Universidad de Valladolid

Escuela de Doctorado Universidad de Valladolid

PROGRAMA DE DOCTORADO EN FÍSICA

TESIS DOCTORAL:

DESIGN AND VALIDATION OF EXPERIMENTAL METHODS FOR PROBING FOAM FORMATION DYNAMICS AND CELLULAR STRUCTURE

Presentada por Paula Cimavilla Román para optar al grado de
Doctora por la Universidad de Valladolid

Dirigida por:
Prof. Dr. Miguel Ángel Rodríguez Pérez

FINANCIACIÓN

Se agradece el apoyo económico aportado por la Consejería de Educación de la Junta de Castilla y León y el Fondo Social Europeo para la realización de esta tesis doctoral a través de las ayudas para la contratación de personal investigador predoctoral Orden EDU/1100/2017. Además, quiero agradecer la financiación recibida por el grupo CellMat, procedente de los siguientes proyectos de investigación:

- Desarrollo materiales micro y nanocelulares: fabricación, caracterización y aplicaciones. Financiado por la Universidad de Valladolid.
- Espumas poliméricas funcionales para el tratamiento de aguas. Financiado por la agencia estatal de investigación, fondos FEDER.
- Polímeros nanocelulares transparentes y aislantes térmicos: fabricación, caracterización y relación proceso-estructura-propiedades. Financiado por la agencia estatal de investigación, fondos FEDER.
- Desarrollo y fabricación en continuo de aislantes térmicos avanzados basados en polímeros. Financiado por los fondos FEDER, Ministerio de economía y competitividad.

FUNDING

Financial support provided by the Consejería de Educación de la Junta de Castilla y León and the European Social Fund for the completion of this doctoral thesis through the grants for the recruitment of pre-doctoral research staff Order EDU/1100/2017 is gratefully acknowledged. In addition, I would like to thank the CellMat group for the funding received from the following research projects:

- Development of micro and nanocellular materials: manufacture, characterisation and applications. Funded by the University of Valladolid.
- Functional polymeric foams for water treatment. Funded by the state research agency, FEDER funds.
- Transparent and thermally insulating nanocellular polymers: fabrication, characterisation and process-structure-properties relationship. Funded by the state research agency, FEDER funds.
- Development and continuous manufacturing of advanced polymer-based thermal insulators. Financed by FEDER funds, Ministry of Economy and Competitiveness.

Nichts ist drinnen, nichts ist draußen;
Denn was innen, das ist außen

J.W. Goethe, 1827

Nada hay dentro, nada hay fuera;
Pues lo que hay dentro, eso hay fuera.

J.W. Goethe, 1827

AGRADECIMIENTOS

Hay etapas en el desarrollo de una tesis que parecen estar señaladas casi desde el día en que te matriculas: el primer artículo publicado, los nervios de la primera charla en un congreso, la estancia de doctorado, el índice de la tesis, y también, en esta lista de momentos anticipados, se encuentran los agradecimientos. Aunque agradecer debería ser casi un ritual diario, una de las ventajas de escribir una tesis es que te proporciona la plataforma para dar las gracias sin ser tachada de ñoña.

Son muchas las personas sin las que yo no hubiese podido ni empezar a vislumbrar esta investigación, no obstante, hay una en especial sin la cual nada de lo vivido y aprendido en estos años hubiese sido posible. Miguel Ángel, gracias por darle a una insegura estudiante de tercer año de carrera la oportunidad de hacer las prácticas de empresa en CellMat Technologies, por descubrirme toda la física y ciencia que hay detrás de los materiales, y, por supuesto, por todas las oportunidades que vinieron después. No puedo imaginar un lugar mejor para formarse e investigar que CellMat. Gracias por hacerme sentir que esta es mi casa.

Me gustaría también agradecer a la profesora Paula Moldenaers la oportunidad de realizar mi estancia de doctorado en SMaRT. Los meses en Leuven no solo me permitieron aprender sobre reología, sino también sobre las muy distintas formas en las que la investigación académica puede realizarse y, no menos importante, me dieron la oportunidad de conocer a personas y lugares maravillosos que permanecerán siempre en mi memoria.

A los compañeros de CellMat Technologies. Cristina y Ester, gracias por todas las colaboraciones de los últimos años y por todo lo que me habéis enseñado. También por demostrarme que aspirar a combinar todos los colores de una diapositiva no es de bicho raro sino un TOC frecuente entre los que trabajamos en CellMat. Alberto, para mi has sido lo más parecido a un mentor durante estos años en el laboratorio, primero como supervisor de las prácticas de empresa y luego como director de trabajo de fin de grado; lo he repetido mil veces, pero no por ello deja de ser menos cierto, para mi trabajar contigo ha sido un placer e incluso un aliciente en muchas ocasiones.

A Leandra, Suset y Javier, gracias por todo vuestro interés y apoyo durante la tesis. Por todas las horas de trabajo compartidas y por pensar en mi cuando se abrían nuevas vías de investigación o posibles proyectos. A los técnicos del laboratorio: Blanca, gracias

por toda tu ayuda con los experimentos de DMA, por aconsejarme siempre que me encontraba en apuros y por seguir impidiendo que el laboratorio sea devorado por el caos. Laura, gracias por tu paciencia y por siempre intentar mejorar el grupo, nuestra forma de trabajar y, en general, la vida en el laboratorio. A Puri, por cada historia y consejo. Pablo, gracias por todas las fotos de SEM, las conversaciones y por hacerme creer que, si la ciencia falla, tengo futuro como repostera de tartas de queso. Javi, gracias por tu buena disposición a ayudar en cualquier experimento, por todas las parladas y ratos en el despacho. Sergio, gracias por toda tu ayuda con Autocell.

A mis compañeros de doctorado, mil gracias por hacer del laboratorio mucho más que un lugar de trabajo. Mikel, gracias por ser capaz de animar cualquier habitación con tus bromas, por tu naturalidad y tu sentido del humor tan envidiable. Dani, gracias por toda tu paciencia y buen humor, por ser capaz de quitarle hierro a cualquier situación y por ayudarme tanto con el equipo de rayos X. Ismael, gracias por tu sonrisa eterna, por acompañarme en mil turnos de tarde durante la época de la pandemia y por darme tantos ánimos e ideas descabelladas para arreglar el sistema de crio-tomo. Patricia, gracias por tu ayuda en los proyectos del grupo de poliuretanos, tu honestidad y tu capacidad de trabajo. Bea, mil gracias por tu buen rollo y tu naturalidad, por nunca dejar de intentar crear buen ambiente entre los que te rodean. A Vicky gracias por descubrirme libros increíbles. Colaborar contigo en campañas, investigación y proyectos ha sido una experiencia maravillosa por tu forma metódica y detallista de trabajar que tan bien combina con mi carácter. Judith, gracias por tu buen corazón, tu paciencia y todos los buenos consejos sobre cómo lidiar con los primeros años de tesis y docencia. A las nuevas incorporaciones en el grupo: Vanesa, gracias por tu dulzura y tu tacto. Ana, Karina, Álvaro, Lidia, Mónica, Ángel, Alba, Félix y Edu gracias por renovar el ambiente, recordarnos a los que llevamos más tiempo que es lo que nos une y ayudarnos a hacer piña de nuevo. Ojalá haber colaborado y pasado más tiempo con vosotros.

A mis últimas compañeras de despacho: Yayan, María y Clara. Sois súper especiales y si algo me duele es no poder coincidir más tiempo con vosotras. En mis meses de más desanimo, durante la escritura de la tesis y vértigo al futuro, conseguíais que me sintiese una más y no como una doctoranda terminal.

No obstante, de todas las personas de CellMat hay cuatro que tienen un lugar especial en mi corazón por todo el tiempo y el apoyo continuado que me han dado. Con

ellos he compartido doctorado, pero también frustraciones, miedos y alegrías. Merce, todas estas palabras son pocas para expresar lo que te debo. Me ayudaste desde el primer minuto de la forma más desinteresada. Además, a partir de ese momento hemos compartido muchísimas horas dentro y fuera del laboratorio. Esta tesis es tan tuya como mía, porque sin tu paciencia, tus explicaciones y tu actitud, muchos de los trabajos no hubiesen visto la luz. Gracias de corazón. Edu, creo que te debo la cordura de estos años de tesis por toda la calma y serenidad que me aportabas en nuestros cafés de sobremesa. En medio de las obsesiones del día a día, poder hablar contigo de viajes, libros e idiomas es como una bocanada de oxígeno. Santi, gracias por tanto. Eres una persona maravillosa y con un gran corazón. Me has ayudado, escuchado y aguantado lo indecible incluso cuando suponía poner en pausa lo que tuvieses entre manos. Hay pocas personas tan brillantes y redondas como tú. Por último, Alberto. Creo que eres la única persona del grupo con la que puedo quedar fuera del laboratorio y ni acordarnos de lo que sucede dentro. Además, sin ti jamás hubiese batido esta especie de récord personal basado en ver estrenos de películas extranjeras que muchas veces acaban siendo un bodrio. Contigo sé que me llevo un amigo para siempre. En este grupo de personas con las que he compartido mucho tiempo y vivencias no me puedo olvidar de Josías y de Saúl. Gracias Saúl por toda tu paciencia y tu guía durante mis primeros años de doctorado. Por trasmitirme todo lo que tú sabías y animarme a ser independiente y proactiva. Josías, eres un maquina en todos los sentidos. No sé qué hubiese sido de mi tesis sin tu ayuda para apañar montajes experimentales.

Como no solo en laboratorio se vive, no puedo dejar de agradecerle a mis amigos y familia el haberme ayudado tanto durante estos años de doctorado. A mis amigas de siempre, gracias Bea, Noelia, Paula y Elisa, por todos nuestros años de amistad, por cada consejo, por escuchar audios interminables y estar siempre junto a mí. Ander, gracias por seguir aguantándome, improvisar planes para cada fin de semana y por nunca dejar de proponérmelos. Sean, gracias por tu amistad y por enseñarme a disfrutar del aprendizaje de un idioma. También le debo a Julia mi cordura de los últimos meses, por motivarme a correr un kilómetro más cuando yo solo quería saltarme la carrera y pasar directamente al café. Gracias por, no se muy bien cómo, acabar haciendo de esas horas de entrenamiento una especie de terapia de grupo

De todos mis amigos hay un grupo de trece personas sin los que mi vida sería indudablemente más gris. Gracias en mayúsculas al Comando por ser el mejor grupo de

amigos que una pueda imaginar, por nuestras escapadas por Europa, por las casas rurales, por el rol, el parchís y el pinturillo, por las noches, las mañanas, los vermús y los brunches. Gracias porque solo con vosotros es posible hacer cualquier cosa y que se convierta en instante memorable. Hace tiempo que sé que lo mejor que me ha dado estudiar física sois vosotros [1].

A Tim, por nuestros días perfectos y por todos los momentos compartidos.

Gracias a Nieves por ser mi mejor consejera, por ser capaz de ponerme frente al espejo, por desmontar mis castillos de naipes y despejar las brumas que se posan sobre mi cabeza con más frecuencia de la que me gustaría. Para mi tu amistad y tu compañía son como un amuleto de la suerte. Esta tesis la hemos hecho a medias.

A mi hermana Marta, gracias por ser siempre mi mejor amiga, mi guía, mi protectora y mi modelo a seguir. Gracias por escucharme siempre, por tu dulzura y tu buen humor. Por tener una visión tan diáfana de lo que merece la pena y lo que no. Por nunca parar de repetirme que el trabajo son los garbanzos, y por quitarle peso a todas mis miedos. Además, a la peque Inés le debo cada una de sus diminutas risas y el recordarme la emoción de los primeros descubrimientos. A Rubén, por estar dispuesto siempre a escuchar y a darme buenos consejos. Y en general, gracias también a toda mi familia, especialmente a mis tíos y a mis primos.

Por último, a las dos personas sin las que yo no sería nada, es difícil resumir en unas pocas palabras todo lo que os debo. Papá, gracias por apoyarme en absolutamente todo lo que hago. Por todo lo que me has enseñado, por todo lo que sigo aprendiendo de ti, por nunca ponerme barreras y por ayudarme a derribar las que van surgiendo en el camino. Gracias por darme alas e impulsarme a encontrar el equilibrio dentro de mí misma. Mamá, has hecho y continúas haciendo lo indecible por Marta y por mí. Te debo mis valores y mis cimientos, gracias por nunca dejar de enseñarnos el valor del trabajo duro y la constancia sin los cuales hubiese mandado a la porra esta tesis en múltiples ocasiones. Pero sobre todo gracias por enseñarme que para ser feliz primero hay que ser fuerte. Esta tesis es tan vuestra como mía.

TABLE OF CONTENTS

Chapter 0	**Resumen en Español**	**19**
	0.1. Marco de la tesis	24
	0.2. Objetivos	26
	0.3. Principales novedades de la tesis	28
	0.4. Estructura de la tesis	29
	0.5. Porfolio doctoral	31
	0.6. Metodología de trabajo	35
	0.7. Principales resultados	37
	0.8. Conclusiones	42
	0.9. Referencias	43
Chapter 1	**Introduction**	**49**
	1.1. Framework of the thesis	53
	1.2. Objectives	55
	1.3. Main novelties of the thesis	57
	1.4. Thesis structure	58
	1.5. Doctoral portfolio	59
	1.6. References	64
Chapter 2	**Background**	**71**
	2.1. Rigid Polyurethane foams	71
	2.2. Polyurethane reactive foaming	72
	2.2.1. Chemical background	72
	2.2.2. Formulation components	73
	2.2.3. Polymer morphology development	74
	2.2.4. Cellular structure development	76
	2.2.5. Final cellular structure	80

2.3. Probing into polyurethane reactive foaming 84

2.3.1. Reaction kinetics 84

2.3.2. Matrix polymerisation 91

2.3.3. Foaming mechanisms 97

2.3.4. Advanced imaging of the final structure 105

2.4. Thermal insulation properties of foams 109

2.4.1. Gas conduction 109

2.4.2. Solid conduction 110

2.4.3. Radiation 110

2.5. Case studies: Relevant foam systems 111

2.5.1. Polyurethane-aerogel composite foams 111

2.5.2. Recycled glass foams 112

2.6. References 113

Chapter 3 Experimental 123

3.1. Materials 123

3.1.1. Rigid Polyurethane foam formulations 125

3.1.2. Rigid Polyurethane foam production 126

3.1.3. Externally supplied foams 127

3.2. Experimental methods 128

3.2.1. Standard characterisation techniques 129

3.2.2. Non-standard and newly developed techniques 130

3.3. References 131

PART 1 DEVELOPMENT OF METHODOLOGIES 133

Chapter 4 Rheological behaviour during Polyurethane foaming 137

4.1. Introduction 137

4.2. *Dynamic mechanical analysis during polyurethane foaming: relationship between modulus build-up and reaction kinetics* 138

4.3. *The influence of viscosity build-up on the foaming dynamics of Rigid Polyurethane foams* 166

Chapter 5 **Early structure generation during Polyurethane foaming** **193**

5.1. Introduction 193

5.2. *Cryogenic X-ray Tomography of Polyurethane foams: Early structural development* 194

Chapter 6 **Solid matrix distribution in Polymeric foams** **215**

6.1. Introduction 215

6.2. *Sub-pixel tomographic methods for characterising the solid architecture of foams* 216

PART 2 **APPLICATION OF THE DEVELOPED METHODOLOGIES** **245**

Chapter 7 **Influence of aerogel on the synthesis of Polyurethane foams** **249**

7.1. Introduction 249

7.2. *Influence of silica aerogel particles on the foaming process and cellular structure of rigid polyurethane foams* 251

7.3. *The effects of Silica Aerogel on the rheological behaviour and polymer matrix structure of Rigid Polyurethane foams* 278

Chapter 8 **Thermal insulation in low density foams** **305**

8.1. Introduction 305

8.2. *The influence of Silica Aerogel on the Thermal Conductivity of Rigid Polyurethane Foams* 307

8.3. *Modelling of the mechanisms of heat transfer in recycled glass foams* 322

Chapter 9 **Conclusions and Future Work** **355**

9.1. Conclusions 355

9.1.1. Development and validation of experimental methods 355

9.1.2. Application of the developed methodologies 358

9.2. Future work 362

9.3. References 364

CAPÍTULO 0

Resumen en Español

0 RESUMEN EN ESPAÑOL

Ya sea en forma de pompas de jabón o como colchones para nuestras camas, los materiales espumados son omnipresentes en nuestro día a día. Técnicamente, las espumas son sistemas bifásicos en los que una fase gaseosa está dispersa en una fase sólida. Se encuentran prácticamente en todas partes (Figura 0-1). En la naturaleza, se considera que la espuma más antigua es la de la madera, que puede entenderse como espuma de celulosa [1]. En nuestro plato, las espumas comestibles son fácilmente reconocibles en forma de pan, palomitas de maíz o mousse de chocolate. Por otro lado las espumas sintéticas se encuentran prácticamente en todos los sectores, desde la automoción y la construcción hasta los envases y los deportes [2].

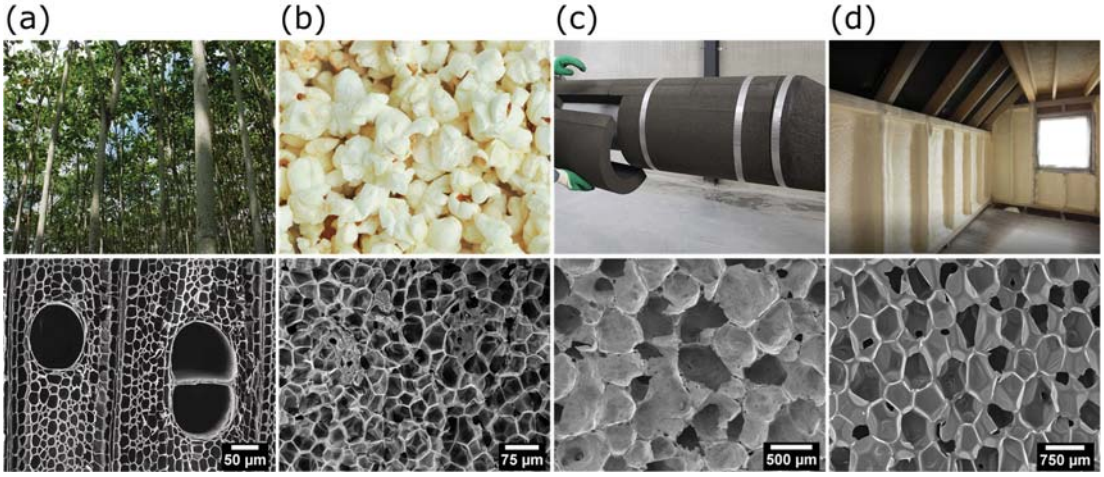

Figura 0-1: Estructura celular característica de (a) la madera de balsa, (b) las palomitas de maíz, (c) las espumas de vidrio y (d) el aislamiento de espuma de poliuretano.

Hoy en día, las espumas sintéticas pueden producirse con casi cualquier tipo de matriz sólida, desde metal, cerámica, vidrio o polímero [3]. Sin embargo, las espumas poliméricas son las más frecuentes en nuestra vida cotidiana. Desde su desarrollo a principios del siglo XX, las tecnologías de producción han avanzado mucho, facilitando la irrupción de las espumas en el mercado de los polímeros. De hecho, el consumo de espumas no ha dejado de aumentar en el último siglo. En 2021 el tamaño del mercado se estimó en 93.900

millones de dólares y se prevé que alcance los 118.900 millones en 2026, con una tasa de crecimiento anual del 4,8% entre 2021 y 2026 [4]. Este vasto consumo de espumas sintéticas sólo puede entenderse a la luz de las ventajas que presentan los materiales espumados frente a sus homólogos sólidos. Los materiales celulares o espumas destacan por ser ligeros y buenos aislantes térmicos. Otras ventajas son su resistencia mecánica relativamente alta por unidad de peso, su resistencia al impacto y su menor constante dieléctrica en comparación con los polímeros sólidos [1].

Sin embargo, la formación de una espuma es un proceso complejo y dinámico en el que intervienen varios mecanismos fisico-químicos [2]. Los factores relacionados con las propiedades del material de partida, como la viscosidad de cizalla y extensional, la temperatura de transición vítrea y el peso molecular, así como con las condiciones de procesado, temperatura, presión y humedad, pueden limitar la expansión y deteriorar la estructura final de las espumas (Figura 0-2) [5–7]. Por ejemplo, viscosidades altas pueden reducir la velocidad de difusión del gas y dificultar el crecimiento de la espuma [6]. Mientras que viscosidades extensionales bajas pueden dar lugar a materiales de baja calidad en los que se dan fenómenos de colapso y degeneración durante el espumado [8].

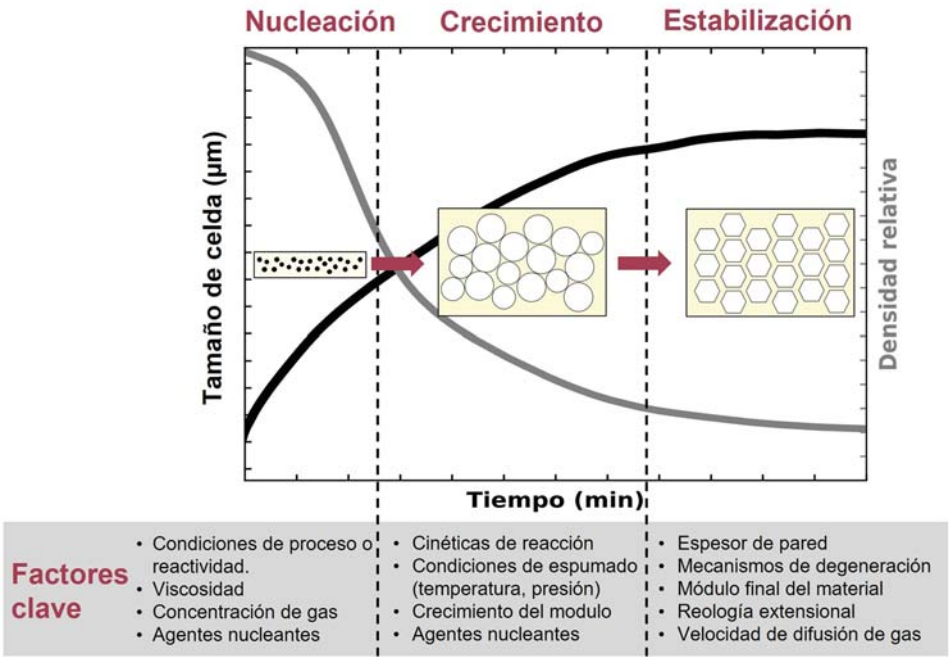

Figura 0-2: Evolución esquemática de la densidad relativa de la espuma (parámetro inverso al grado expansión) y del tamaño de las celdas a lo largo del tiempo, junto con los factores que influyen en la estructura final (adaptado de [9]).

La naturaleza estocástica del proceso de espumado da lugar a materiales en los que la estructura celular final es inhomogénea y varía mucho entre materiales. En las espumas

poliméricas se han identificado varias topologías celulares posibles. La forma de las celdas va desde dodecaedros pentagonales en las espumas de poliuretano (PU) hasta tetracaidecaedros en las espumas de polietileno de baja densidad (PE) [10]. Asimismo, el espesor y la cantidad del material sólido que encierra las celdas puede variar entre las paredes, las aristas y los vértices (Figura 0-3). Por ejemplo, en las espumas de PU la mayor parte de la masa sólida se encuentra en las aristas mientras que en las espumas de PE las paredes, las aristas y los vértices tienen un grosor similar, ya que la masa sólida se distribuye homogéneamente entre ellos [10,11].

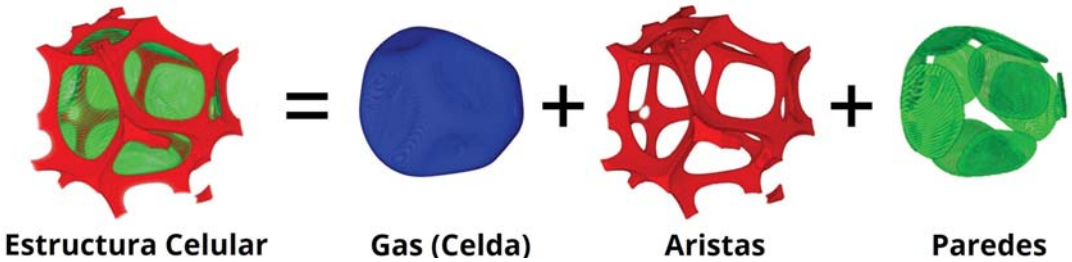

Figura 0-3: Partes de la estructura celular en las espumas (reproducido de [10]).

La complejidad del proceso de espumado y de la organización de la estructura final en las espumas ha motivado el desarrollo de múltiples técnicas experimentales con las que profundizar en la relación procesado-estructura-propiedades [10,12]. Aunque, en general, la porosidad y la naturaleza de la matriz sólida dominan las aplicaciones y propiedades finales de la espuma, estas últimas no pueden entenderse sin considerar también la estructura celular interna [3]. Esta dependencia de las propiedades con la estructura justifica el por qué espumas de diferentes matrices, generadas mediante distintos procesos de fabricación, pueden mostrar propiedades similares. Por ejemplo, las espumas flexibles de PU de celda abierta y de PE de celda abierta tienen ambas excelente capacidad para atenuar el sonido [13,14]. Ambos materiales tienen en común una estructura interconectada y de celdas muy abiertas que favorece la atenuación del sonido, independientemente de la matriz sólida. En el otro extremo se encuentran los materiales basados en PU. Las espumas basadas en PU pueden tener una morfología polimérica y porosidad similares, pero estructuras y propiedades completamente diferentes. La reacción de poliadición del uretano entre el isocianato y los átomos de hidrógeno activos (poliol) es la fuente de una gran variedad de materiales, que van desde los termoplásticos a los termoestables y desde rígidos (RPU) a flexibles (FPU), como se ve en la Figura 0-4.

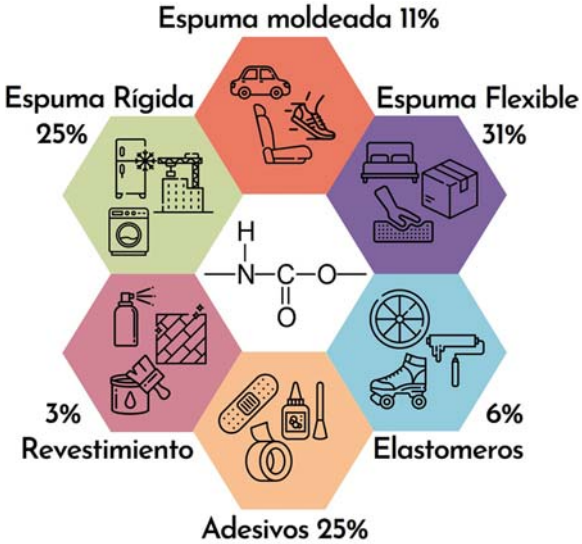

Figura 0-4: Consumo mundial de poliuretanos según el tipo de producto y sus aplicaciones [15].

Las espumas de PU, tanto rígidas como flexibles, se producen siguiendo un proceso de espumado reactivo en el que la polimerización y el espumado tienen lugar simultáneamente. Tras la reacción del isocianato con el poliol, los componentes iniciales de baja viscosidad se transforman en una red supramolecular de alta reticulación [16]. Durante la reacción, también se generan moléculas de gas capaces de crear puntos de nucleación en la mezcla. Poco después, los núcleos crecen hasta formar una estructura celular que llena el espacio, mientras que la matriz sigue cambiando tanto en su morfología como en su comportamiento reológico. A pesar de que la química y el proceso de espumado del poliuretano rígido (RPU) y flexible (FPU) es similar, ambos materiales muestran una estructura celular final completamente diferente. Las espumas de RPU tienen una estructura celular homogénea y cerrada que proporciona a este material buenas propiedades de aislamiento térmico (Figura 0-5 (a)). Por el contrario, las espumas de FPU presentan una estructura celular abierta que las hace adecuadas para aplicaciones destinadas al confort y amortiguación (Figura 0-5 (b)). Estas diferencias tienen su origen en el proceso de espumado. En las espumas FPU, las finas paredes de las celdas se rompen al alcanzar una elevada expansión, mientras que las paredes celulares de las espumas RPU son lo suficientemente elásticas como para soportar las tensiones generadas por el gas al liberarse. Aunque este ejemplo constituye un escenario extremo, entre espumas de la misma familia cambios no deseados en los mecanismos de espumado también pueden ser perjudiciales para la estructura y las propiedades. Además, los cambios en el proceso de espumado del PU pueden desencadenarse con facilidad debido a ligeras modificaciones en la formulación o en los parámetros de procesado, como la

temperatura de reacción, el perfil de viscosidad, la tensión superficial o la presión del gas en la mezcla [17].

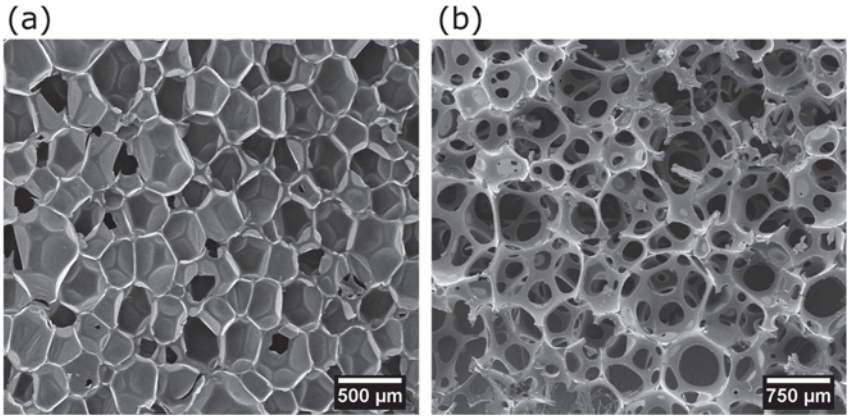

Figura 0-5: (a) Espuma rígida de poliuretano con estructura celular cerrada y (b) wspumas flexibles de poliuretano con estructura celular abierta.

El caso de las espumas de PU es especialmente interesante, ya que es un material que adopta muchas formas y es, con diferencia, una de las espumas poliméricas más utilizadas actualmente [4,18]. Sin embargo, para el desarrollo futuro del PU hay dos retos principales: una mayor sostenibilidad y un mejor rendimiento. Este último se refleja, por ejemplo, en la producción de espumas de celdas cerrada de menor tamaño y en la mejora de las capacidades de aislamiento térmico. Sin embargo, el cumplimiento de las normas medioambientales y de rendimiento para este tipo de materiales requiere el desarrollo de nuevas formulaciones, así como la optimización de las existentes. Para optimizar eficazmente las formulaciones es esencial conocer a fondo los parámetros y variables que modifican la generación de las espumas de PU. Esto puede lograrse mediante modelos digitales o técnicas de monitorización in situ [18]. En los últimos años, se ha trabajado mucho para intentar comprender las relaciones entre la formulación, la estructura y las propiedades mediante la simulación y la modelización, sin depender únicamente de la investigación experimental [19–26]. Sin embargo, los modelos de predicción de estructuras y propiedades necesitan, en última instancia, de datos experimentales para proporcionar parámetros de entrada a los modelos o confirmar su validez. Por estos motivos, también se ha avanzado en el desarrollo de nuevas técnicas experimentales [27–33].

En el marco de esta tesis, todo lo anterior ha motivado el diseño de nuevos métodos experimentales que permitan la caracterización estructural y la monitorización de los mecanismos de formación de espuma de poliuretano utilizando equipos de laboratorio. Se espera que estos métodos faciliten la identificación de cómo las formulaciones y parámetros

de proceso modifican la estructura y propiedades de las espumas. Además, la aplicación de estos enfoques puede ayudar a acelerar y optimizar el trabajo de investigación y desarrollo de nuevos materiales con mejores propiedades.

0.1. MARCO DE LA TESIS

Esta investigación forma parte de las actividades de investigación del Laboratorio CellMat del Departamento de Física de la Materia Condensada de la Universidad de Valladolid (cellmat.es) y ha sido supervisada por el Prof. Dr. Miguel Ángel Rodríguez-Pérez, director del laboratorio.

El Laboratorio CellMat fue fundado en 1999 por el Prof. Dr. José Antonio de Saja y el Prof. Dr. Miguel Ángel Rodríguez-Pérez. Desde su fundación, el laboratorio ha crecido no sólo en miembros sino también en el número de programas de investigación activos y en equipamiento. Si bien, en sus inicios la investigación se centraba en la caracterización de materiales celulares basados en poliolefinas [34–36], a lo largo de los años las actividades de investigación se han diversificado y ahora abarcan más temas de investigación y han dado lugar a más de 275 publicaciones y 34 tesis doctorales.

Actualmente, la investigación realizada en CellMat se centra en cinco áreas temáticas: materiales nanocelulares [9,37], materiales celulares multifuncionales [10,38], nanocompuestos celulares [39,40], materiales celulares bioplásticos [41,42] y espumas de poliuretano [39,43]. En todas estas áreas de investigación, el grupo se esfuerza en dilucidar el vínculo entre producción, estructura, propiedades y aplicaciones. Este objetivo constituye la base de la investigación en CellMat (Figura 0-6) y se consigue mediante la investigación de los mecanismos de espumado y la modelización de las propiedades. Por un lado, la aplicación de métodos avanzados para investigar los mecanismos de espumado ha permitido comprender cómo la formulación y el procesado pueden condicionar la estructura celular final [44–48]. Por otro lado, la caracterización en profundidad de la estructura celular ha permitido modificar y desarrollar nuevos modelos analíticos para predecir las propiedades de los materiales celulares [49–51].

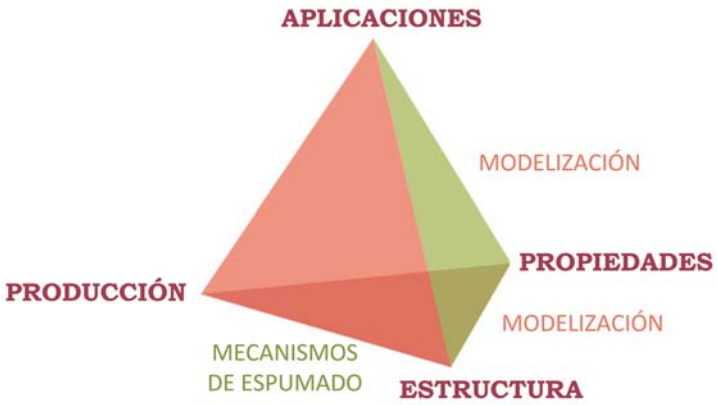

Figura 0-6: Base de la investigación en CellMat: el tetraedro de materiales celulares.

La investigación realizada en esta tesis se basa en el tetraedro de los materiales celulares (Figura 0-6) y profundiza en los mecanismos de espumado y en su modelización. La investigación sobre los mecanismos de espumado en CellMat se inició con la tesis doctoral del Dr. Samuel Pardo Alonso. Esta tesis allanó el camino para el desarrollo y la aplicación de métodos experimentales no convencionales para visualizar las dinámicas de generación de la estructura celular y caracterizar la estructura celular mediante tomografía de rayos X de alta resolución [38]. A esta investigación le siguieron las tesis doctorales de los doctores Mercedes Santiago Calvo y Saúl Pérez Tamarit. La primera investigó el proceso de polimerización y espumación de las espumas de RPU utilizando principalmente espectroscopia FTIR, analizando en detalle la cinética de reacción y cómo se ve afectada por la adición de diferentes cargas [43,52,53]. Además, esta tesis demostró la viabilidad de utilizar los conocimientos obtenidos sobre los mecanismos de espumado para modificar eficazmente las formulaciones y, a su vez, mejorar las propiedades de los materiales [45,46]. Por el contrario, la tesis del Dr. Saúl Pérez Tamarit exploró nuevos métodos para caracterizar con precisión la estructura celular de las espumas con diversas matrices poliméricas [11,50,54]. Esta tesis se basó en el uso de tomografía de rayos X de sincrotrón para estudiar en 3D la microestructura celular y polimérica tanto durante el espumado como en el material final [11,55].

La presente tesis se basa en gran medida en estos precedentes, ya que pretende explorar tanto la formación reactiva de espumas RPU utilizando nuevos enfoques, así como la obtención de un método de caracterización estructural mediante tomografía de rayos X de laboratorio a la par de la de Sincrotrón.

0.2. OBJETIVOS

El propósito de esta tesis ha sido el de desarrollar nuevas técnicas para profundizar en la relación proceso-estructura-propiedades en las espumas (Figura 0-7). Para lograr este objetivo se definieron dos objetivos específicos. En primer lugar, investigar los cambios viscoelásticos y la evolución de la estructura celular durante el espumado del PU utilizando métodos específicos. Para lograr este objetivo, la investigación se centró en investigar formulaciones modelo para la producción de espumas de poliuretano. Además, para comprender cómo el proceso de espumado afecta a la topología de la matriz polimérica (distribución del espesor de la fase sólida) se desarrollaron metodologías de análisis de imagen basadas en la tomografía de rayos X de laboratorio. En segundo lugar, utilizando los métodos de caracterización anteriores, se buscó dilucidar la relación proceso-estructura-propiedades en diferentes materiales. Para ello, los sistemas seleccionados fueron espumas rígidas de PU con partículas de aerogel de sílice y espumas de vidrio.

Figura 0-7: Objetivo general de esta tesis.

Para alcanzar los objetivos generales anteriores, la investigación de esta tesis se desglosó en varios objetivos específicos.

1) Desarrollo de métodos experimentales para esclarecer la relación espumado-estructura en espumas RPU (Figura 0-8).

- Estudiar in situ los cambios viscoelásticos en espumas reactivas de RPU. Para ello, se utilizaron dos técnicas complementarias: una nueva metodología basada en Análisis Mecánico Dinámico (DMA) y la adaptación de un método de medida basado en reología de cizalla para espumas reactivas (capítulo 4).
- Utilizar los resultados de DMA y reología como medida del proceso de polimerización. A continuación, se compararon estos resultados con las cinéticas de

reacción y la evolución de la estructura celular de las espumas RPU medidas con otras técnicas bien establecidas: Espectroscopia FTIR y radioscopia de rayos X, respectivamente (Capítulo 4).

- Diseñar e implementar un método basado en tomografía de rayos X de laboratorio para monitorizar en 3D la generación de la estructura celular en las espumas RPU (Capítulo 5). Esto se logró desarrollando una metodología para realizar experimentos de tomografía de rayos X a muy bajas temperaturas.
- Desarrollar metodologías de análisis de imagen que permitan la caracterización de la matriz sólida mediante tomografía de rayos X de laboratorio. En particular, cuando el tamaño de píxel del sistema es superior al espesor del sólido, es decir, en condiciones subpíxel (Capítulo 6).

Figura 0-8: Esquema que resume los pasos esenciales para lograr el objetivo 1.

2) Aplicar los métodos experimentales para comprender la estructura final y las propiedades de sistemas de espumas complejos (Figura 0-9).

- Aplicar los métodos de caracterización desarrollados a dos casos prácticos: Espumas compuestas de RPU-Aerogel de Sílice y espumas de vidrio reciclado.
- Dilucidar la influencia de la polimerización y la cinética de espumado en la topología de la matriz polimérica y la estructura celular de las espumas compuestas de RPU-Aerogel (Capítulo 7).
- Estudiar la influencia de la estructura celular y la topología de la matriz polimérica en la capacidad de aislamiento térmico de espumas de vidrio reciclado y las espumas compuestas de RPU-aerogel (Capítulo 8).

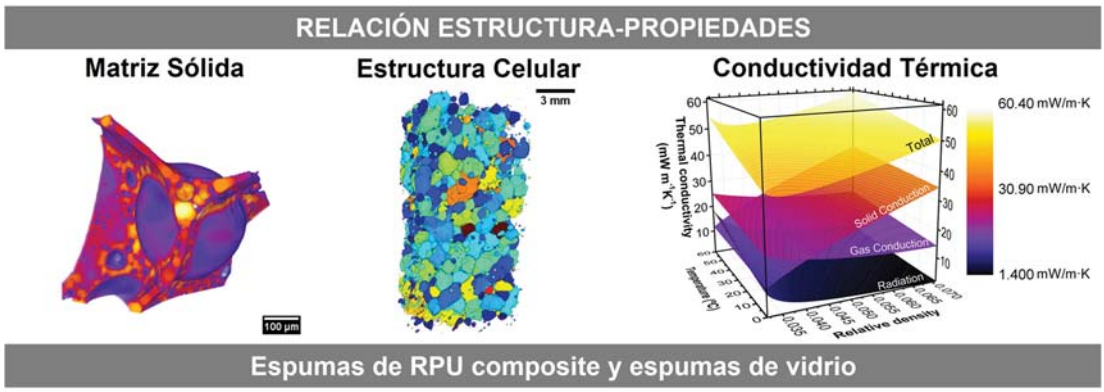

Figura 0-9: Resumen de las medidas adoptadas para alcanzar el objetivo 2.

0.3. PRINCIPALES NOVEDADES DE LA TESIS

El cumplimiento de los objetivos anteriores ha permitido avanzar en el estado del arte. Las principales novedades de la tesis se resumen a continuación.

- Por primera vez se han monitorizado las cinéticas de polimerización y la evolución del módulo en espumas RPU mediante DMA. La eficacia de la técnica se verificó utilizando formulaciones de diferente reactividad y por comparación con los resultados proporcionados por la espectroscopia FTIR. Esta nueva aplicación de DMA representa un avance en el rango de aplicaciones de la técnica y así como en el conjunto de los métodos que permiten monitorizar el espumado reactivo.
- Asimismo, en el transcurso de esta tesis se desarrolló un nuevo método experimental basado en la tomografía criogénica de rayos X. Este método permitió observar en 3D la estructura celular de las espumas RPU a distintos tiempos de reacción.
- El desarrollo de nuevos métodos de análisis de imagen permitió la caracterización de la distribución de la masa sólida (fracción de masa en aristas) en espumas de matriz más delgada que la resolución del equipo de rayos X. Esto ha permitido ampliar la gama de caracterizaciones posibles con sistemas de tomografía de rayos X de resolución limitada. Por lo tanto, la resolución espacial limitada ya no es un obstáculo para el análisis de la matriz sólida en espumas de baja densidad.
- Se ha estudiado el impacto de partículas de aerogel de silice superaislantes en la nucleación, la dinámica de espumado, la reología de los reactivos iniciales, la cinética de reacción y la polimerización de las espumas de RPU mediante técnicas de caracterización no convencionales.
- Se han esclarecido los mecanismos de transferencia de calor en las espumas de vidrio reciclado. Además, se ha determinado la contribución de cada mecanismo a la

conductividad térmica de estas espumas. Se espera que este avance facilite la tarea de identificar rutas para reducir la conductividad térmica en este tipo de materiales.

0.4. ESTRUCTURA DE LA TESIS

Esta tesis se ha redactado como compendio de publicaciones. Los resultados obtenidos están avalados por ocho publicaciones, cinco de las cuales están publicadas en revistas Q1 y las tres restantes están pendientes de aceptación. Esta tesis cumple los requisitos para obtener el grado de Doctor con Mención Internacional. La investigación presentada se articula en torno al mapa conceptual que se muestra en la Figura 0-10. La tesis consta de 9 capítulos y los capítulos de resultados se agrupan, a su vez, en dos secciones.

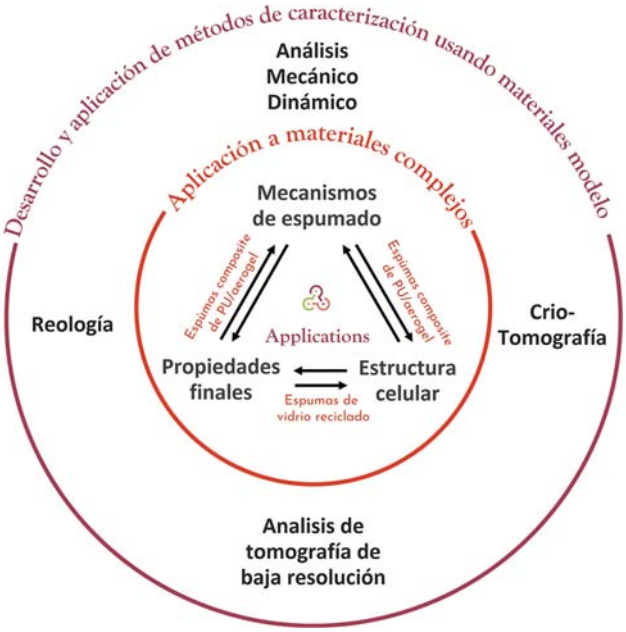

Figura 0-10: Mapa conceptual de la tesis.

El **capítulo 1** (Introducción) ofrece una visión general del tema de la tesis. En él se exponen los objetivos y la estructura de la tesis. Además, se incluyen los logros científicos (publicaciones, conferencias, proyectos) alcanzados durante esta tesis.

El **capítulo 2** (Antecedentes) presenta los principales conceptos y el estado de los conocimientos en los que se basa la investigación realizada. Abarca temas que van desde la cinética de reacción, las dinámicas de espumado y el desarrollo reológico de las espumas de PU hasta la conductividad térmica en las espumas.

El **capítulo 3** (Experimental) describe las materias primas utilizadas en esta investigación y las diferentes técnicas aplicadas para identificar los mecanismos de espumado y caracterizar la estructura celular.

PARTE I. DESARROLLO DE METODOLOGÍAS

El **capítulo 4** (Comportamiento reológico durante el espumado reactivo de poliuretano) comprende dos publicaciones acerca de cuatro formulaciones tipo de RPU con diferentes concentraciones de catalizador y agente espumante. La primera de las publicaciones proporciona una comparativa entre las cinéticas de reacción y el desarrollo del módulo medido mediante una metodología basada en DMA. La segunda de las publicaciones revela el impacto del comportamiento reológico de las espumas reactivas en la generación de la estructura celular.

El **capítulo 5** (Primeros instantes de formación de la estructura celular en espumas de poliuretano) incluye una breve comunicación sobre el desarrollo de una nueva técnica basada en la tomografía criogénica de rayos X. La técnica se aplica para seguir ex-situ y en 3D el desarrollo de la estructura celular de las espumas de RPU en los primeros estadios del proceso de espumado.

El **capítulo 6** (Distribución de la matriz sólida en espumas poliméricas) presenta tres metodologías de análisis de imagen para la caracterización de la matriz polimérica de las espumas escaneadas con tomografía de rayos X de baja resolución. La eficacia de los métodos se demuestra con tres espumas de diferentes matrices: poliestireno, polietileno y poliuretano.

PARTE II. APLICABILIDAD DE LAS METODOLOGÍAS DESARROLLADAS

El **capítulo 7** (Influencia de la incorporación del aerogel de sílice en la síntesis de espumas de RPU) contiene dos artículos que tratan de espumas compuestas de RPU y aerogel de sílice. En estas publicaciones, se estudia el efecto del aerogel de sílice en la formación de la estructura celular (radioscopia de rayos X), la cinética de reacción (espectroscopia FTIR), el desarrollo de las propiedades viscoelásticas (reología de cizalla), la matriz polimérica final y la estructura celular (tomografía de rayos X de laboratorio).

En el **capítulo 8** (Propiedades de aislamiento térmico en espumas de baja densidad) se presentan dos publicaciones que abordan las propiedades de aislamiento térmico de las espumas compuestas de RPU-Aerogel de sílice y de las espumas de vidrio reciclado. La estructura celular de estas espumas se caracterizó mediante tomografía de rayos X de laboratorio y se evalúa la relación estructura-aislamiento térmico.

El **capítulo 9** (Conclusiones) resume los resultados de esta investigación. Además, se discuten los futuros trabajos de investigación.

0.5. PORFOLIO DOCTORAL

En este apartado se recogen las publicaciones científicas (Tabla 0-1 y Tabla 0-2) conferencias (Tabla 0- 3 y Tabla 0-4), cursos (Tabla 0-5), estancias de investigación (Tabla 0-6) y proyectos (Tabla 0-7 y Tabla 0-8) que se han realizado a lo largo de la presente tesis doctoral.

Tabla 0-1: Publicaciones parte de esta tesis.

	Referencia de la Publicación	Capítulo
1	P. Cimavilla-Román, M. Santiago-Calvo, M.A. Rodríguez-Pérez. Dynamic Mechanical Analysis during polyurethane foaming: Relationship between modulus build-up and reaction kinetics, Polym. Test. 103 (2021) 107336	**4**
2	P. Cimavilla-Román, M. Santiago-Calvo, A. Vananroye, P. Moldenaers, M.A. Rodríguez-Pérez. The influence of viscosity build-up on the foaming dynamics of Rigid Polyurethane foams, *Submitted*	**4**
3	P. Cimavilla-Román, M. Santiago-Calvo, M.A. Rodríguez-Pérez. Cryogenic X-ray Tomography of Polyurethane foams: Early structural development, *Submitted*	**5**
4	P. Cimavilla-Román, S. Pérez-Tamarit, S. Barroso-Solares, J. Pinto, M.A. Rodríguez-Pérez. Sub-pixel tomographic methods for characterizing the solid architecture of foams. Microsc. Microanal. (2022)	**6**
5	P. Cimavilla-Román, S. Pérez-Tamarit, M. Santiago-Calvo, MA. Rodríguez-Pérez, Influence of silica aerogel particles on the foaming process and cellular structure of rigid polyurethane foams, Eur. Polym. J. 135 (2020) 109884	**7**
6	P. Cimavilla-Román, S. Pérez-Tamarit, A. Vananroye, P. Moldenaers, M.A. Rodríguez-Pérez. The effects of Silica Aerogel on the rheological behaviour and polymer matrix structure of Rigid Polyurethane foams, Eur. Polym. J. 176 (2022) 111398	**7**
7	P. Cimavilla-Román, J. Villafañe-Calvo, A. López-Gil, J. König, MA. Rodríguez-Perez, Modelling of the mechanisms of heat transfer in recycled glass foams, Constr. Build. Mater. 274 (2021) 122000	**8**
8	P. Cimavilla-Román, S. Pérez-Tamarit, M. Santiago-Calvo, MA. Rodríguez-Pérez, Influence of silica aerogel particles on thermal insulation properties of rigid polyurethane foams, *Submitted*	**8**

Tabla 0-2: Publicaciones en coautoría durante la tesis.

	Referencia de la Publicación
1	A. Ballesteros, E. Laguna-Gutierrez, P. Cimavilla-Roman, M.L. Puertas, A. Esteban-Cubillo, J. Santaren, M.A. Rodriguez-Perez, Influence of the dispersion of Nanoclays on the cellular structure of foams based on polystyrene, J. Appl. Polym. Sci. 138 (2021)
2	J. Martín-de León, P. Cimavilla-Román, V. Bernardo, E. Solórzano, N. Kardjilov, M.A. Rodríguez-Pérez, Cold neutron transmission for the in-situ analysis of the gas diffusion in polymers, J. Supercrit. Fluids. 177 (2021)
3	S. Barroso-Solares, P. Cimavilla-Roman, M.A. Rodriguez-Perez, J. Pinto, Non-invasive approaches for the evaluation of the functionalization of melamine foams with in-situ synthesized silver nanoparticles, Polymers (Basel). 12 (2020)
4	S. Barroso-Solares, B. Merillas, P. Cimavilla-Román, M.A. Rodriguez-Perez, J. Pinto, Enhanced nitrates-polluted water remediation by polyurethane/sepiolite cellular nanocomposites, J. Clean. Prod. 254 (2020)
5	J. König, A. Lopez-Gil, P. Cimavilla-Roman, M.A. Rodriguez-Perez, R.R. Petersen, M.B. Østergaard, N. Iversen, Y. Yue, M. Spreitzer, Synthesis and properties of open- and closed-porous foamed glass with a low density, Constr. Build. Mater. 247 (2020)
6	J. Martín-de León, V. Bernardo, P. Cimavilla-Román, S. Pérez-Tamarit, M.A. Rodríguez-Pérez, Overcoming the Challenge of Producing Large and Flat Nanocellular Polymers: A Study with PMMA, Adv. Eng. Mater. 1900148 (2019)
7	M. Santiago-Calvo, S. Pérez-Tamarit, P. Cimavilla-Román, V. Blasco, C. Ruiz, R. París, F. Villafañe, M. A. Rodríguez-Pérez, X-ray radioscopy validation of a polyol functionalized with graphene oxide for producing rigid polyurethane foams with improved cellular structures, Eur. Polym. J. 118 (2019)
8	D. Batey, S. Cipiccia, X. Shi, S. Williams, K. Wanelik, A. Wilson, S. Pérez-Tamarit, P. Cimavilla, M.A. Ródriguez-Pérez, C. Rau, Coherence Branch at I13, DLS: The Multiscale, Multimodal, Ptycho-tomographic End Station, Microsc. Microanal. 24 (2018)
9	C. Rau, M. Storm, S. Marathe, A.J. Bodey, S. Cipiccia, D. Batey, X. Shi, M.-C. Zdora, I. Zanette, S. Perez-Tamarit, P. Cimavilla, M.A. Rodriguez-Perez, F. Doring, C. David, Multi-Scale Imaging at the Coherence and Imaging Beamline I13 at Diamond, Microsc. Microanal. 24 (2018)

Tabla 0-3: Resumen de las comunicaciones en conferencias relacionadas con el tema de la tesis.

	Congresos
1	P. Cimavilla-Román., M. Santiago-Calvo, M.A. Rodríguez-Pérez. Cryogenic X-ray tomography of Rigid Polyurethane foams. *FOAMS2021*-September 13-16, 2021, Virtual conference. Oral Communication
2	P. Cimavilla-Román; J. Villafañe-Calvo; A. López-Gil; J. König; M. A. Rodríguez Pérez. Modelling of the mechanisms of heat transfer in glass foams at different temperatures. *CELLMAT2020*-October 7-9, 2020, Virtual conference. Poster
3	P. Cimavilla-Román; M. Santiago-Calvo; M. A. Rodríguez Pérez. In-situ Dynamic Mechanical Analysis during polyurethane foaming: relationship between modulus build-up and reaction kinetics. *CELLMAT2020*-October 7-9, 2020, Virtual conference. Oral Communication
4	P. Cimavilla-Román; S. Pérez-Tamarit; M. Santiago-Calvo; M. A. Rodríguez Pérez. Influence of nanoporous aerogel on the foaming process and properties of Rigid Polyurethanes foams from a physicochemical perspective. *FOAMS2019*-October 1-3, 2019. Valladolid, Spain. Poster
5	J König, U. Hribar, P. Cimavilla-Román, A. Lopez-Gil, M.A. Rodriguez-Pérez, R.R. Petersen, Y. Yue. Comparison of open- and closed-porous foamed glass. *25th International Congress on Glass*-June 9-14, 2019. Boston, USA. Oral Communication
6	P. Cimavilla-Román, S. Pérez-Tamarit, M. Santiago-Calvo, M. A. Rodríguez-Pérez. In-situ physicochemical analysis of the foaming process of aerogel-rigid polyurethane composite foams. *EUFOAM2018*-July 9-12, 2018. Liege, Belgium. Oral Communication
7	P. Cimavilla-Román, S. Pérez-Tamarit, E. Sólorzano, A. Hilger, I. Manke, M. A. Rodríguez-Pérez. Novel subresolution tomographic methods for quantifying fraction of mass in Plateau borders of solid polymeric foams. *EUFOAM2018*-July 9-12, 2018. Liege, Belgium. Poster
8	P. Cimavilla-Román, S. Pérez-Tamarit, M. Santiago-Calvo, M. A. Rodríguez-Pérez. In-situ analysis, by X-ray radioscopy, of the foaming process of aerogel-polyurethane cellular composites. *ESMolNa2017* – May 7-11, 2017. Oral Communication

Tabla 0-4: Contribuciones adicionales a conferencias no relacionadas con el tema de la tesis.

	Congresos
1	V. Bernardo, J. Martín-de Leon, F. Van Loock, N. A. Fleck, P. Cimavilla-Román, S. Pérez-Tamarit, M. A. Rodríguez Pérez. Nanocellular polymers based on PMMA/Sepiolite nanocomposites: characterization of the mechanic behaviour. *CELLMAT2018*-October 24-26, 2019. Bad Staffestein, Germany. Poster
2	S. Barroso-Solares, B. Merillas, P. Cimavilla-Román, M. A. Rodríguez Pérez, J. Pinto. Nitrates and other pollutants removal from water resources using multifunctional polyurethane foams. *Water Waste*-July 18-20, 2018, Madrid, Spain. Oral Communication
3	S. Pérez-Tamarit, P. Cimavilla-Román, S. Barroso-Solares, M. A. Rodríguez Pérez. X-Ray Imaging as a useful tool for a training program on polymer foams. *EDULEARN18*–July 2-4, 2018, Palma (Spain). Oral Communication
4	P. Cimavilla-Román, S. Pérez-Tamarit, J. Martín-de León, E. Solórzano, I. Manke, N. Kardjilov, M. A. Rodríguez Pérez. In-situ neutron tomography of the gas diffusion process of high pressure CO_2 on PMMA. *38th Berlin School on Neutron Scattering* - March 1-9, 2018. Berlin (Germany). Poster

Tabla 0-5: Estancias en centros internacionales de investigación.

	Estancias de investigación
1	KU Leuven (Belgium) – Agosto 2021 – Noviembre 2021 Tema: Reología de cizalla durante el proceso de espumación reactiva del poliuretano
2	Synchrotron Beamtime BESSY II (Germany) – Julio 2019 Tema: Estudio de la estructura de fibras poliméricas huecas mediante tomografía de rayos X
3	Synchrotron Beamtime Diamond Light Source (UK) – Febrero 2019 Tema: Ticotomografía de polímeros microcelulares y submicrocelulares
4	Synchrotron Beamtime Diamond Light Source (UK) – Enero 2018 Tema: Ticotomografía de polímeros microcelulares y submicrocelulares

Tabla 0-6: Cursos realizados durante esta tesis.

	Cursos
1	Termografía infrarroja con procesamiento de imágenes Universidad de Valladolid – Valladolid, España, Junio 2018
2	38th Berlin School on Neutron Scattering Helmholtz Zentrum Berlin - Berlin, Alemania, Marzo 2018
3	Jornadas Prof Antonio de Saja: Envases Plásticos: Fundamentos, Normativa y Tendencias Leical, CellMat Technologies - Valladolid, España, Febrero 2018
4	Jornadas Prof Antonio de Saja: Caracterización de materiales poliméricos Leical, CellMat Technologies - Valladolid, España, Diciembre 2016

Tabla 0-7: Proyectos de financiación pública en los que ha colaborado la autora.

	Proyectos de financiación pública
1	Functional polymeric foams for water treatment Agencia estatal de investigación, FEDER. 2019-2022
2	Reduction of energy consumption in buildings through transparent and thermally insulating nanocellular polymers: production, characterisation and process-structure-properties relationship Ente público Regional de la Energía de Castilla y León (EREN). 2019-2021
3	CleanTechBlock - Sustainable Multi-functional Building Block Basics M-ERA.NET. 2017-2019
4	Development and continuous manufacturing of advanced polymer-based thermal insulators Ministerio de Economia y Competitividad, FEDER. 2016-2019
5	Development of micro- and nanocellular materials: fabrication, characterization and application Universidad de Valladolid. 2015-2016

Tabla 0-8: Proyectos de financiación privada en los que ha colaborado el autor.

	Proyectos de financiación privada
1	Study of polyisocyanurate foam formulations DuPont (USA). 2019-2020
2	Research on the applications of advanced carbon nanomaterials to improve the performance of polyurethane (PU) matrices with interest to the automotive sector. Grupo Antolin ingeniería SA. 2017-2019
3	Development of new foaming techniques to lighten rigid plastic parts and generate soft touch surfaces: structural and functional foaming technologies. Grupo Antolin ingeniería SA. 2017-2019

0.6. METODOLOGÍA DE TRABAJO

En esta sección se describe la metodología que se ha seguido en el desarrollo de esta tesis doctoral.

0.6.1. Materiales seleccionados

Se ha trabajado con dos grupos de formulaciones de PU, así como con una serie de muestras comerciales de interés para la validación de los métodos desarrollados en la tesis.

En el primer grupo de formulaciones se han probado distintos contenidos de catalizador (POLYCAT 8, Evonik) y agentes espumantes (agua destilada) para generar espumas de diferente estructura celular y densidad.

En el segundo grupo de formulaciones se ha empleado un único contenido de catalizador y agente espumante, pero se han empleado distintos contenidos de partículas. Las partículas seleccionadas fueron un polvo micrométrico de aerogel de sílice comercial (Enova® Aerogel IC3100) distribuido por Cabot. La fabricación de espumas con distintos contenidos de aerogel (0 wt.%, 0.5 wt.%, 1.0 wt.% y 3.0 wt.%) permite obtener espumas de PU de diferente estructura y propiedades.

El método de fabricación de las espumas de PU se basó en el proceso de espumado reactivo. La mezcla a altas revoluciones de los dos principales componentes de la formulación, isocianato y poliol promueve la reacción de polimerización. Esta reacción es responsable de la generación de un polímero altamente entrecruzado y termoestable. Además, cuando se añade agua a la formulación, el isocianato reacciona con los grupos OH del agua dando lugar a la reacción de espumado, responsable de la generación de CO_2 gas y grupos urea.

Los materiales comerciales se destinaron al estudio de la arquitectura de la matriz polimérica en espumas de baja densidad de PU (suministrada por BASF), en una espuma de polietileno (suministrada por Zotefoams) y una espuma de poliestireno extruida (suministrada por Dow).

Además, se han estudiado espumas de vidrio producidas con material de vidrio reciclado proveniente de pantallas de tubos de rayos catódicos. Estas espumas fueron producidas en el marco del proyecto M-ERA.NET (Tabla 0-7) en el Jožef Stefan Institute, en Liubliana, Eslovenia [56].

0.6.2. Metodologías de caracterización

Los métodos empleados para la caracterización del proceso de espumado, estructura celular y propiedades de los materiales se pueden dividir en dos grupos (Figura 0-11).

En primer lugar, aquellos métodos bien establecidos para el análisis y la caracterización de la estructura y propiedades de polímeros y espumas. La caracterización de las materias primas para producir espumas de PU se centró en el estudio de la viscosidad mediante reología de cizalla. Además, las partículas de aerogel se estudiaron microscópicamente (Microscopia electrónica de barrido, SEM) y mediante espectroscopía infrarroja para

determinar su tamaño y los grupos superficiales, respectivamente. Por otro lado, de las espumas finales se caracterizó su densidad, estructura celular, contenido de celda abierta y conductividad térmica.

En segundo lugar, se han aplicado y desarrollado metodologías no convencionales para el seguimiento de la síntesis de las espumas de PU. Estas metodologías permiten estudiar el desarrollo de la estructura celular, la evolución de las propiedades reológicas y las cinéticas de reacción de las espumas de PU.

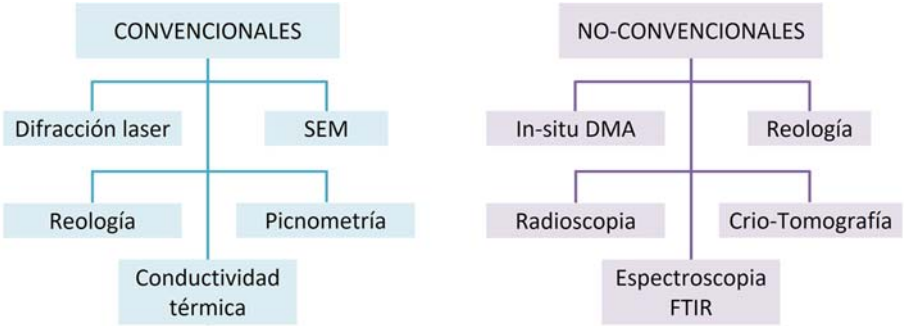

Figura 0-11: Esquema de las técnicas de caracterización.

0.7. PRINCIPALES RESULTADOS

0.7.1. Desarrollo de metodologías de seguimiento del proceso

Para la validación de las nuevas metodologías desarrolladas se han empleado las formulaciones de PU fabricadas con distintos contenidos de catalizador y de agente espumante (sección 0.6.1.). El uso combinado de DMA y Reología ha permitido obtener información sobre los estadios de desarrollo de la morfología polimérica así como validar los resultados entregados por la nueva técnica basada en DMA (Capítulo 4). Ambos métodos muestran cómo, independientemente de la formulación, a tiempos cortos de reacción el módulo de la muestra se mantiene bajo durante la expansión de la espuma (Figura 0-12). A continuación, ambos módulos se cruzan en el punto de gel, momento en el que el material empieza a adquirir propiedades elásticas. En una segunda etapa, el módulo comienza a crecer de forma rápida. En este estadio se produce un máximo en la *tan δ,* o un hombro en el módulo de perdidas, que corresponde al instante de vitrificación. En este punto, la morfología se congela, disminuyendo la movilidad de las cadenas y, por tanto, reduciéndose la velocidad de curado. A partir de este momento, la reacción pasa a estar controlada por fenómenos de difusión y el módulo evoluciona más lentamente hasta alcanzar la región de

curado. Además, a través del estudio de distintas formulaciones se ha verificado que la velocidad del desarrollo del módulo está relacionada con la cinética de reacción.

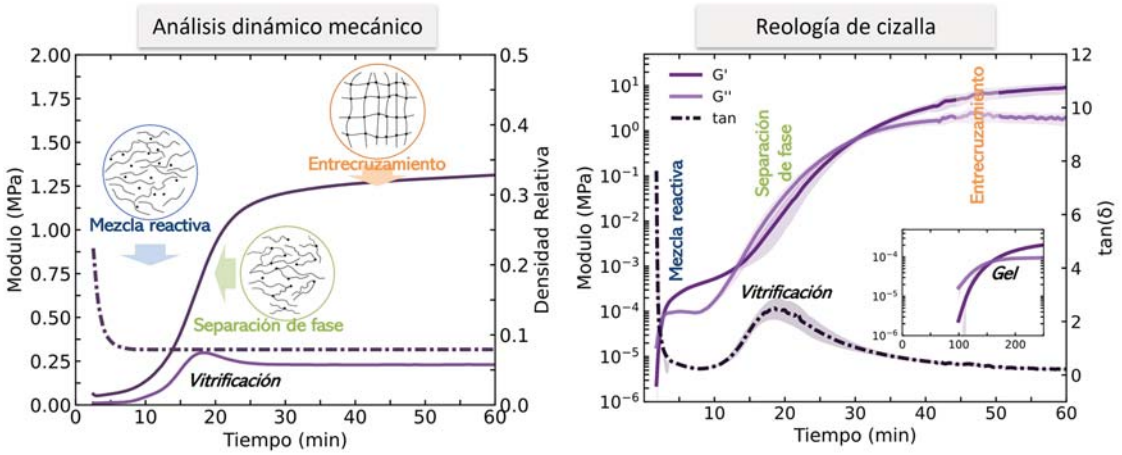

Figura 0-12: Desarrollo del módulo de almacenamiento y de pérdidas durante el espumado de RPU.

Las cinéticas de reacción se han estudiado a través de la adquisición secuencial de espectros de infrarrojo (FTIR). Se ha observado como a mayor velocidad de conversión de isocianato más rápido es el desarrollo del módulo de la espuma. En los resultados (Capítulo 4) también se comprobado que los materiales en los que la densidad de entrecruzamiento (número de grupos uretano) es mayor el módulo final también es más elevado a igual densidad.

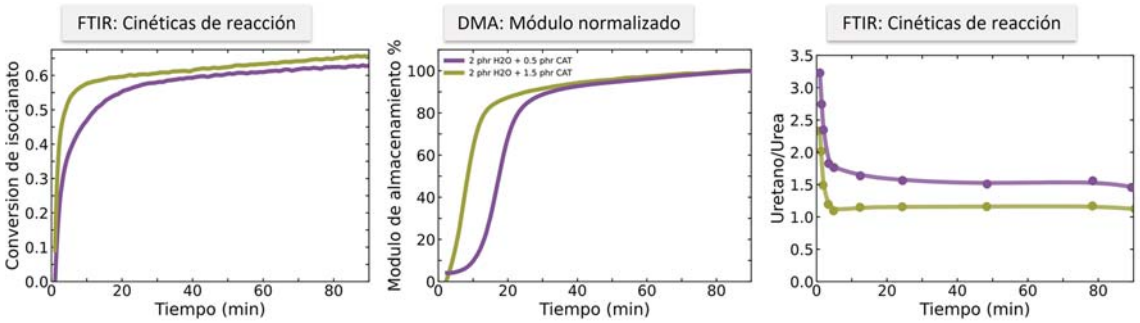

Figura 0-13: Ejemplo de los resultados de evolución de las cinéticas de reacción y el módulo de almacenamiento para una espuma con contenido alto de catalizador (verde) y bajo (morado).

La nueva técnica de tomografía criogénica de Rayos X (Capítulo 5) permite medir de forma directa, y con mayor precisión que a través de radioscopía, el incremento en la densidad de nucleación con la incorporación de más agua y catalizador. Un incremento de 1 parte por peso de catalizador conlleva que la densidad de nucleación aumenta desde 8.7 10^5 celdas cm^{-3} a 1.6 10^6 celdas cm^{-3}, casi un factor 2. De forma similar, al aumentar el contenido de agua en 3 partes resulta en un incremento menor, de 8.7 10^5 celdas cm^{-3} a 1.1 10^6 celdas cm^{-3}. El análisis conjunto del desarrollo del módulo y de la estructura celular ha

permitido determinar que el rápido incremento en viscosidad que sufren las muestras con mayor catalizador tiene un efecto nucleante más potente que la generación de más moles de gas.

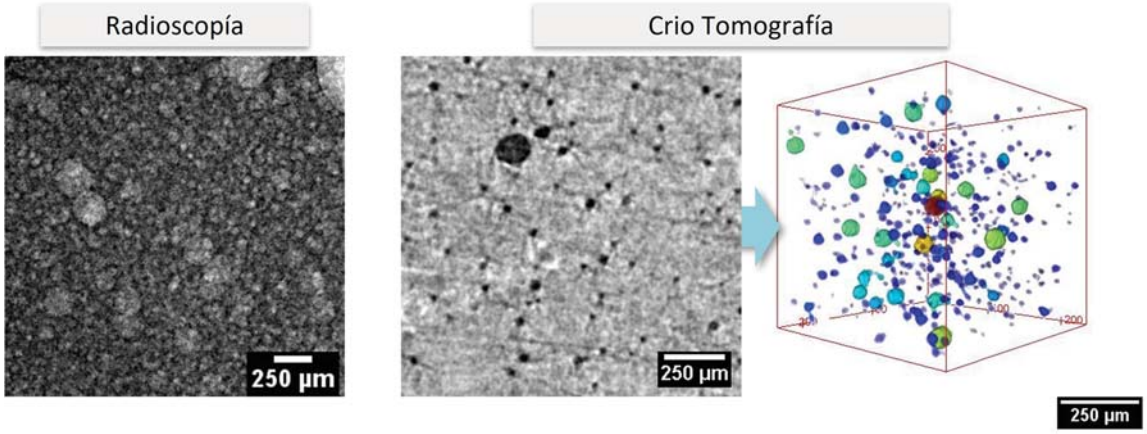

Figura 0-14: Ejemplo de la estructura celular a tiempos cortos de rección obtenida mediante Radioscopía y Crio-Tomografía.

Por último, el desarrollo de nuevos protocolos de análisis de imagen ha permitido caracterizar la fracción de masa en las aristas de espumas de baja densidad mediante tomografía de baja resolución. Comparando los resultados obtenidos con una caracterización previa mediante tomografía de alta resolución [11] se ha comprobado que el análisis es más preciso cuanto mayor es el contenido de masa en las aristas. Mientras que la mayor desviación se produce en materiales cuyo matriz tiene un espesor cercano a la resolución del equipo. Se han desarrollado varios métodos de análisis destacando la buena precisión de algunos de ellos (Función densidad de atenuación en verde en la Figura 0-15).

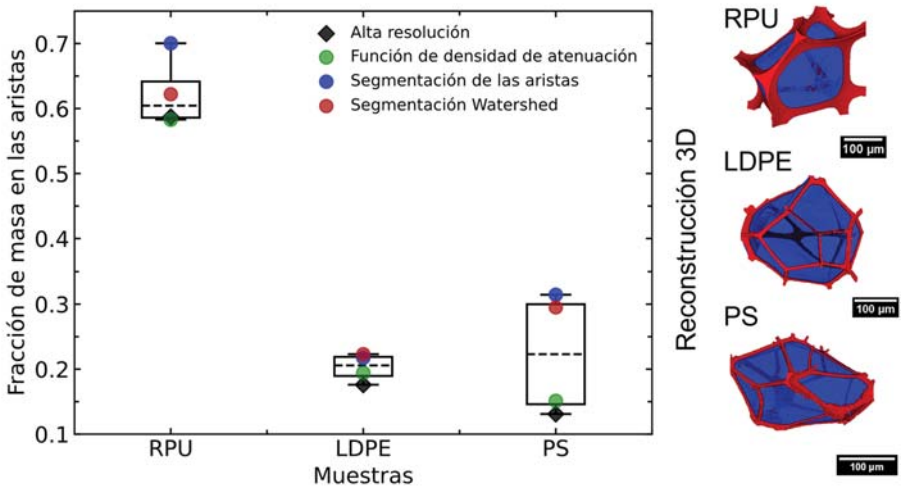

Figura 0-15: Resultados de la fracción de masa en las aristas obtenidos aplicando los métodos desarrollados en el Capítulo 6.

0.7.2. Aplicación a casos prácticos

De la investigación del proceso de síntesis de las espumas compuestas de PU-Silica aerogel se han obtenido los siguientes resultados (Capítulo 7):

La adición de partículas de aerogel conlleva un incremento significativo de la viscosidad del isocianato empleado para producir las espumas (Figura 0-16 (a)). Además, para contenidos cercanos a 2.5 wt% de partículas se alcanza el límite de percolación y la dispersión comienza a revelar un comportamiento propio de un gel en el que la componente elástica predomina sobre la viscosa. La presencia de partículas de aerogel supone un incremento en la nucleación de celdas al inicio del espumado reactivo (Figura 0-16 (b)). Sin embargo, a tiempos largos de espumado se producen intensos fenómenos de degeneración, de modo que tan solo para contenidos bajos de partículas (por debajo de 1 wt%) la estructura final muestra un tamaño de celda inferior a la espuma de referencia sin partículas.

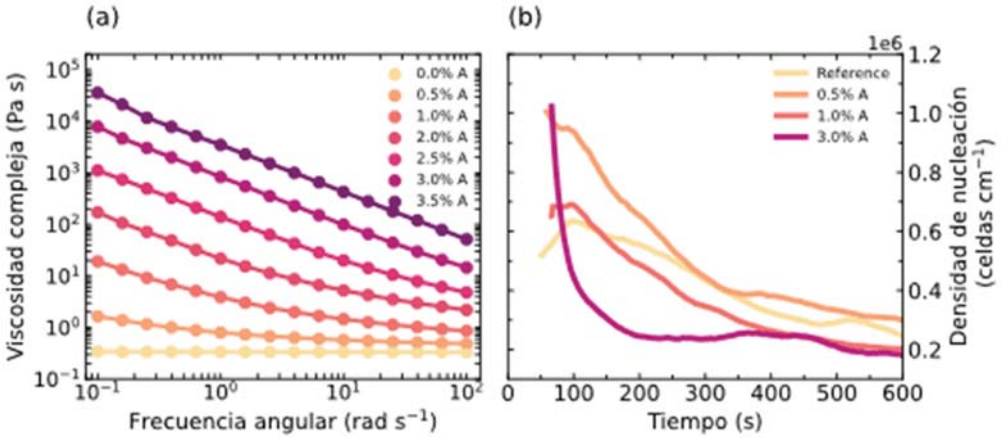

Figura 0-16: (a) Evolución de la viscosidad para las dispersiones de isocianato/aerogel, (b) evolución con el tiempo de la densidad de nucleación.

El estudio de la evolución del módulo con el tiempo de reacción ha demostrado que la velocidad de polimerización disminuye por la presencia de partículas. Este retraso en la polimerización es mínimo a bajos contenidos de partículas, pero muy significativo a altos contenidos, lo cual explica la mayor degeneración detectada para contenidos de partículas del 3 wt.%. Además, la espuma con un 3 wt% de partículas comienza el proceso de espumado en un estado de gel. A través del análisis de la fase sólida se observó como a contenidos de partículas por debajo del 1 wt% la fracción de masa en las aristas aumenta con la adición de partículas debido al drenaje de material reactivo durante el espumado. Sin embargo, a contenidos altos, 3 wt%, la fracción de masa en las aristas se reduce con respecto

a las otras espumas (Figura 0-17). Esto es debido a una reducción en el drenaje a causa de la mayor viscosidad y el comportamiento tipo de gel de la mezcla reactiva.

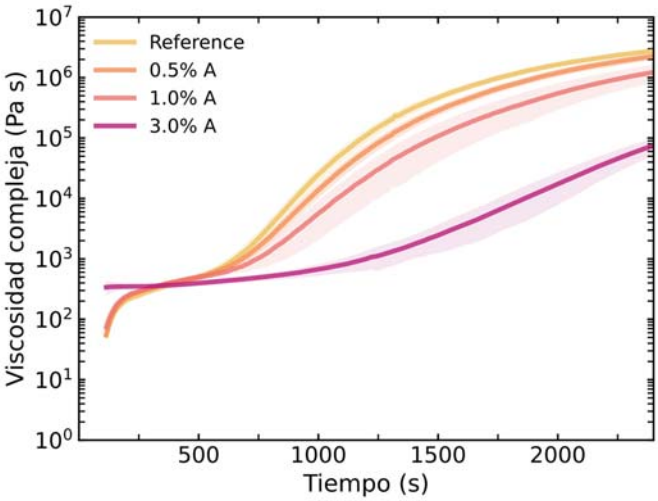

Aerogel (wt%)	Fracción de masa en las aristas
0.0% A	0.739
0.5% A	0.745
1.0% A	0.860
3.0% A	0.790

Figura 0-17: Evolución de la viscosidad de las espumas compuestas de PU-Aerogel con el tiempo de espumado y el efecto de la viscosidad en la fracción de masa en las aristas de la espuma final.

La conductividad térmica de las espumas compuestas de PU-aerogel (hasta un contenido del 1 wt%) disminuyó hasta 1.4 mW m^{-1} K^{-1} comparada con la espuma sin partículas. El estudio de los mecanismos de trasferencia de calor demostró que la reducción en la conductividad térmica tenía dos causas. Por un lado, la reducción del término de conducción a través de la fase sólida, debido a la menor conductividad de las partículas de aerogel. Por otro lado, a la reducción de la trasferencia de calor radiativa, debido al menor tamaño de celda.

Por último, se aplicó la metodología de caracterización de la fracción de masa en las aristas y se analizó la conductividad térmica en espumas de vidrio reciclado. La fracción de masa en las aristas aumenta a medida que bajaba la densidad de las espumas, lo cual implicaba una reducción de la conducción a través de la matriz sólida. En conjunto se observó como la conductividad térmica de las espumas alcanzaba un valor mínimo a una densidad relativa 0.032 para volver a subir a menores densidades debido a un incremento en la trasferencia de calor radiativo.

0.8. CONCLUSIONES

Uno de los principales objetivos de este trabajo era “desarrollo de métodos experimentales para esclarecer la relación espumado-estructura en espumas RPU”. Esto implicaba el diseño y la validación protocolos para el estudio experimental del proceso de

síntesis de las espumas de RPU. De los trabajos completados en torno a este tema, se pueden extraer las siguientes conclusiones:

- El nuevo método basado en DMA entrega resultados equivalentes a la Reología en relación con las velocidades de desarrollo del módulo en espumas de RPU producidas con distintos tipos de formulaciones. Además, el estudio de las cinéticas de reacción mediante FTIR ha permitido comprobar que existe una correlación entre la velocidad de conversión de isocianato y la velocidad de desarrollo del módulo. También se ha comprobado que, a igual densidad, las espumas que alcanzan una mayor polimerización (más grupos uretanos) tienen un mayor módulo.
- La comparativa entre los resultados de desarrollo de la estructura celular (Radioscopía) y del módulo (Reología y DMA) ha permitido verificar que una mayor velocidad de desarrollo del módulo limita la aparición de mecanismos de degeneración y permite una estabilización más temprana de la estructura celular.
- La nueva metodología basada en Crio-tomografía permite detectar de forma precisa la densidad de nucleación a tiempos cortos de reacción. Además de revelar que a tiempos cortos de reacción apenas se producen mecanismos de degeneración debido al gran espesor de la matriz entre celdas.
- Se han desarrollado y validado tres metodologías de análisis de imagen que permiten la caracterización de la matriz sólida mediante tomografía de rayos X de laboratorio. La validación se ha llevado a cabo comparando con una caracterización previa de la fase sólida realizada con tomografía de alta resolución [11]. La comparación desveló que el análisis resultaba más preciso para materiales de alta fracción de masa en las aristas. Además, el método basado en el análisis de los coeficientes de atenuación de la fase sólida era el de mayor precisión de entre los tres.

Respecto al segundo de los objetivos: “Aplicar los métodos experimentales para comprender la estructura final y las propiedades de las espumas complejas”, ha sido posible entender en detalle como la presencia de partículas condiciona la relación proceso-estructura-propiedades en espumas compuestas de PU-Aerogel.

- La presencia de altos contenidos de partículas tiene un efecto disruptivo sobre la generación de la estructura celular. Las partículas tienen tamaños superiores a 1 μm por lo que su aglomeración causa rupturas en las paredes de las celdas y aumenta el contenido de celda abierta en la espuma final.

- También se ha comprobado que a medida que aumenta el contenido de partículas la velocidad de desarrollo del módulo disminuye. Esta reducción en la velocidad de polimerización disminuye la resistencia y elasticidad de las paredes celulares durante el espumado, promoviendo una mayor degeneración celular.
- La fabricación de espumas con dispersiones líquido-partículas en estado de percolación supone una disminución en el drenaje de material reactivo de las paredes celulares a las aristas. Esto da lugar a espumas con una menor fracción de masa en las aristas.
- La estructura celular final en las espumas compuestas de PU-Aerogel es la combinación de un incremento en la nucleación y degeneración de la estructura. A bajos contenidos de partículas el tamaño de celda es menor que la espuma de Referencia sin partículas dando lugar a espumas de menor conductividad térmica.

Los resultados de esta tesis evidencian que la producción de espumas compuestas de PU-Aerogel es una estrategia acertada para reducir la conductividad térmica de espumas convencionales de PU. Para obtener aún mejores propiedades de aislamiento térmico sería necesario modificar la formulación de la espuma de RPU para producir espumas con un 3 wt% de partículas de aerogel. Aumentar el contenido de catalizador permitiría incrementar la velocidad de polimerización y desarrollo del módulo y así reducir la degeneración.

Por último, las espumas de vidrio reciclado constituyen una alternativa interesante a los actuales materiales de aislamiento térmico. Además, la producción de espumas de vidrio de alta porosidad, densidad relativa 0.032, permite obtener materiales de conductividad térmica de casi 40 mW m^{-1} K^{-1}. Estos valores de conductividad térmica están cerca de los obtenidos para espumas de PU producidas con agua como agente espumante. Sin embargo, gracias a la modelización de los mecanismos de trasferencia de calor se ha observado que es necesario implementar estrategias para bloquear la radiación infrarroja si se quiere reducir aún más la conductividad térmica de estos materiales

0.9. REFERENCIAS

[1] J.G. Drobny, Processing Methods Applicable to Thermoplastic Elastomers, Handb. Thermoplast. Elastomers. (2014) 33–173.

[2] N.S. Ramesh, S.T. Lee, Polymeric Foams: Mechanisms and Materials, First Ed, CRC Press, Boca Raton, 2004.

[3] L.J. Gibson, M.F. Ashby, Cellular solids: Structure and Properties, Cambridge: Cambridge Solid State Science Series, Cambridge, 1997.

[4] Foam Market Global Forecast to 2026 | MarketsandMarkets, (n.d.). (accessed February 7, 2022).

[5] V. Bernardo, J. Martin-de Leon, E. Laguna-Gutierrez, T. Catelani, J. Pinto, A. Athanassiou, M.A. Rodriguez-Perez, Understanding the role of MAM molecular weight in the production of PMMA/MAM nanocellular polymers, Polymer (Guildf). 153 (2018) 262–270.

[6] J.M. de León, V. Bernardo, E. Laguna-Gutiérrez, M.Á. Rodríguez-Pérez, Influence of the viscosity of poly(methyl methacrylate) on the cellular structure of nanocellular materials, Polym. Int. 69 (2020) 72–83.

[7] J. Martín-de León, P. Cimavilla-Román, V. Bernardo, E. Solórzano, N. Kardjilov, M.A. Rodríguez-Pérez, Cold neutron transmission for the in-situ analysis of the gas diffusion in polymers, J. Supercrit. Fluids. 177 (2021).

[8] E. Laguna-Gutierrez, Understanding the Foamability of Complex Polymeric Systems By Using Extensional Rheology, Universidad de Valladolid, 2016.

[9] V. Bernardo, Production and Characterization of Nanocellular Polymers Based on Nanostructured PMMA Blends and PMMA Nanocomposites, University of Valladolid, 2019.

[10] S. Pérez Tamarit, Structural characterization of solid cellular polymers by X-ray tomography and light scattering, University of Valladolid, 2019.

[11] S. Pérez-Tamarit, E. Solórzano, A. Hilger, I. Manke, M.A. Rodríguez-Pérez, Multi-scale tomographic analysis of polymeric foams: A detailed study of the cellular structure, Eur. Polym. J. 109 (2018) 169–178.

[12] S. Pardo-Alonso, X-Ray Imaging Applied to the Characterization of Polymer Foams' Cellular Structure and Its Evolution, Universidad de Valladolid, 2014.

[13] S.-T. Lee, C.B. Park, Foam Extrusion: Principles and Practice, 2nd Ed, CRC Press 2014, 2000.

[14] E. López González, Analysis of the composition-structure- properties relationship of open-cell polyolefin-based foams with tailored levels of gas-phase tortuosity, University of Valladolid, 2019.

[15] N. V. Gama, A. Ferreira, A. Barros-Timmons, Polyurethane Foams: Past, Present, and Future, Mater. 2018, Vol. 11, Page 1841. 11 (2018) 1841.

[16] R.D. Priester, J. V. Mcclusky, R.E. O'neill, R.B. Turner, M.A. Harthcock, B.L. Davis, FT-IR-A Probe into the Reaction Kinetics and Morphology Development of Urethane Foams, J. Cell. Plast. 26 (1990) 346–367.

[17] N.C. Hilyard, A. Cunningham, Low density cellular plastics, 1st Ed, Springer Science & Business Media, 2012, London, 1994.

[18] B. Eling, Ž. Tomović, V. Schädler, Current and Future Trends in Polyurethanes: An Industrial Perspective, Macromol. Chem. Phys. 221 (2020).

[19] P. Ferkl, I. Kršková, J. Kosek, Evolution of mass distribution in walls of rigid polyurethane foams, Chem. Eng. Sci. 176 (2018) 50–58.

[20] J. Kosek, P. Ferkl, I. Kršková, PU foams: Mathematical modelling of morphology development, in: Comput. Aided Chem. Eng., Elsevier, 2017: pp. 1009–1014.

[21] T. Chaloupka, A. Zubov, J. Kosek, Real-time Hybrid Monte Carlo Method for Modelling of 4 Monomer Semi-Batch Emulsion Copolymerization, Elsevier Masson SAS, 2017.

[22] P. Ferkl, A. Nistor, M. Podivinska, M. Vonka, J. Kosek, PU foams: Modelling of heat insulation properties and their degradation in time, Comput. Aided Chem. Eng. 40 (2017) 475–480.

[23] P. Ferkl, M. Toulec, E. Laurini, S. Pricl, M. Fermeglia, S. Auffarth, B. Eling, V. Settels, J. Kosek, Multi-scale modelling of heat transfer in polyurethane foams, Chem. Eng. Sci. 172 (2017) 323–334.

[24] P. Ferkl, M. Karimi, D.L. Marchisio, J. Kosek, Multi-scale modelling of expanding

polyurethane foams: Coupling macro- and bubble-scales, Chem. Eng. Sci. 148 (2016) 55–64.

[25] H. Al-Moameri, Y. Zhao, R. Ghoreishi, G.J. Suppes, Simulation of liquid physical blowing agents for forming rigid urethane foams, J. Appl. Polym. Sci. 132 (2015) 1–7.

[26] Y. Zhao, F. Zhong, A. Tekeei, G.J. Suppes, Modeling impact of catalyst loading on polyurethane foam polymerization, Appl. Catal. A Gen. 469 (2014) 229–238.

[27] M.J. Elwell, A.J. Ryan, H.J.M. Grunbauer, H.C. VanLieshout, An FTIR study of reaction kinetics and structure development in model flexible polyurethane foam systems, Polymer (Guildf). 37 (1996) 1353–1361.

[28] L.D. Artavia, C.W.W. Macosko, Foam Kinetics, J. Cell. Plast. 26 (1990) 490–511.

[29] M.J. Elwell, S. Mortimer, A.J. Ryan, A Synchrotron SAXS Study of Structure Development Kinetics during the Reactive Processing of Flexible Polyurethane Foam, Macromolecules. 27 (1994) 5428–5439.

[30] M.J. Elwell, A.J. Ryan, H.J.M. Grunbauer, H.C. Van Lieshout, In-situ studies of structure development during the reactive processing of model flexible polyurethane foam systems using FT-IR spectroscopy, synchrotron SAXS and rheology, Macromolecules. 29 (1996) 769–770.

[31] S. Pardo-Alonso, E. Solórzano, S. Estravís, M.A. Rodríguez-Perez, J.A. de Saja, In situ evidence of the nanoparticle nucleating effect in polyurethane–nanoclay foamed systems, Soft Matter. 8 (2012) 11262.

[32] M. Santiago-Calvo, S. Pérez-Tamarit, J. Tirado-Mediavilla, F. Villafañe, M.A. Rodríguez-Pérez, Infrared expandometry: A novel methodology to monitor the expansion kinetics of cellular materials produced with exothermic foaming mechanisms, Polym. Test. 66 (2018) 383–393.

[33] J. Reignier, P. Alcouffe, F. Méchin, F. Fenouillot, The morphology of rigid polyurethane foam matrix and its evolution with time during foaming – New insight by cryogenic scanning electron microscopy, J. Colloid Interface Sci. 552 (2019) 153–165.

[34] M.A. Rodriguez Pérez, Propiedades térmicas y mecánicas de espumas de poliolefina, Universidad de Valladolid, 1998.

[35] O. Almanza, Caracterización y Modelización de las Propiedades Térmicas y Mecánicas en Espumas con Base Polietileno, University of Valladolid, 2000.

[36] S. Díez-Gutiérrez, M.A. Rodríguez-Pérez, J.A. De Saja, J.I. Velasco, Dynamic mechanical analysis of injection-moulded discs of polypropylene and untreated and silane-treated talc-filled polypropylene composites, Polymer (Guildf). 40 (1999) 5345–5353.

[37] J. Martin-de Leon, Understanding the Production Process of Nanocellular Polymers Based on PMMA Driven By a Homogeneous nucleation, University of Valladolid, 2019.

[38] S. Pardo-Alonso, X-Ray Imaging Applied to the Characterization of Polymer Foams ' Cellular Structure and Its Evolution, Universidad de Valladolid, 2014.

[39] S. Estravis, Cellular Nanocomposites Based on Rigid Polyurethane and Nanoclays : Fabrication , Characterization and Modeling of the Mechanical and Thermal, Universidad de Valladolid, 2014.

[40] J. Escudero Arconada, Polyolefin based cellular materials. Development of new production routes and optimization of barrier and mechanical properties by the addition of nanoclays, Universidad de Valladolid, 2016.

[41] A. López Gil, Development of Environmentally Friendly Cellular Polymers for Packaging and Structural Applications . Study of the Relationship Cellular Structure-Mechanical Properties, Universidad de Valladolid, 2016.

[42] D. Velasco Nieto, Desarrollo de biomateriales celulares en base EVA, PLA y PHB, fabricación y caracterización., Universidad de Valladolid, 2016.

[43] M. Santiago-Calvo, Synthesis , Foaming Kinetics and Physical Properties of Cellular Nanocomposites Based on Rigid Polyurethane, University of Valladolid, 2019.

[44] E. Solórzano, S. Pardo-Alonso, J.A. De Saja, M.A. Rodriguez-Perez, X-ray radioscopy in-situ studies in thermoplastic polymer foams, Colloids Surfaces A Physicochem. Eng. Asp. 438 (2013) 167–173.

[45] M. Santiago-Calvo, V. Blasco, C. Ruiz, R. París, F. Villafañe, M.-Á. Rodríguez-Pérez, Synthesis, characterization and physical properties of rigid polyurethane foams prepared with poly(propylene oxide) polyols containing graphene oxide, Eur. Polym. J. 97 (2017) 230–240.

[46] M. Santiago-Calvo, V. Blasco, C. Ruiz, R. París, F. Villafañe, M.Á. Rodríguez-Pérez, Improvement of thermal and mechanical properties by control of formulations in rigid polyurethane foams from polyols functionalized with graphene oxide, J. Appl. Polym. Sci. 136 (2019) 1–10.

[47] E. Lopez-Gonzalez, L.O. Salmazo, A. Lopez-Gil, E. Laguna-Gutierrez, M.A. Rodriguez-Perez, Analysis of the foaming mechanisms of materials based on high-density polyethylene (HDPE) crosslinked with different irradiation doses, J. Appl. Polym. Sci. 135 (2018) 46276.

[48] L. Oliveira Salmazo, A. Lopéz-Gil, Z.M. Ariff, M.L. Rodriguez-Mendez, A.E. Job, M.A. Rodriguez Perez, Study of the Foaming Kinetics in Epoxidized Natural Rubber Foams Crosslinked by Electron Beam Irradiation, Macromol. Chem. Phys. 219 (2018).

[49] V. Bernardo, J. Martin-de Leon, J. Pinto, R. Verdejo, M.A. Rodriguez-Perez, Modeling the heat transfer by conduction of nanocellular polymers with bimodal cellular structures, Polymer (Guildf). 160 (2019) 126–137.

[50] S. Pérez-Tamarit, E. Solórzano, A. Hilger, I. Manke, M.A. Rodríguez-Pérez, Effect of solid phase corrugation on the thermo-mechanical properties of low density flexible cellular polymers, Mater. Des. 161 (2019) 106–113.

[51] P. Cimavilla-Román, J. Villafañe-Calvo, A. López-Gil, J. König, M.Á. Rodríguez-Perez, Modelling of the mechanisms of heat transfer in recycled glass foams, Constr. Build. Mater. 274 (2021) 122000.

[52] M. Santiago-Calvo, J. Tirado-Mediavilla, J.L. Ruiz-Herrero, M.Á. Rodríguez-Pérez, F. Villafañe, The effects of functional nanofillers on the reaction kinetics, microstructure, thermal and mechanical properties of water blown rigid polyurethane foams, Polymer (Guildf). 150 (2018) 138–149.

[53] M. Santiago-Calvo, S. Pérez-Tamarit, P. Cimavilla-Román, V. Blasco, C. Ruiz, R. París, F. Villafañe, M.Á. Rodríguez-Pérez, X-ray radioscopy validation of a polyol functionalized with graphene oxide for producing rigid polyurethane foams with improved cellular structures, Eur. Polym. J. 118 (2019) 404–411.

[54] S. Pérez-Tamarit, E. Solórzano, M.A. Rodriguez-Perez, Efficient prediction of cell size in solid polymeric foams by numerically solving the diffusion approximation of light scattering equation, Colloids Surfaces A Physicochem. Eng. Asp. 534 (2017) 130–137.

[55] S. Pérez-Tamarit, E. Solórzano, R. Mokso, M.A. Rodríguez-Pérez, In-situ understanding of pore nucleation and growth in polyurethane foams by using real-time synchrotron X-ray tomography, Polymer (Guildf). 166 (2019) 50–54.

[56] J. König, A. Lopez-Gil, P. Cimavilla-Roman, M.A. Rodriguez-Perez, R.R. Petersen, M.B. Østergaard, N. Iversen, Y. Yue, M. Spreitzer, Synthesis and properties of open- and closed-porous foamed glass with a low density, Constr. Build. Mater. 247 (2020) 11857

C APT

Introduction

1 INTRODUCTION

Whether in the form of soap bubbles blown by children or as mattresses for our beds foams surround us in an almost imperceptible way. Technically speaking, foams are two-phase systems in which a gas phase is dispersed in a continuous solid phase. They are found practically everywhere (Figure 1-1). In nature, the oldest occurring foam is considered to be wood, which can be regarded as cellulose foam [1]. On our plate, edible foams can be easily recognised in the form of bread, popped corns or chocolate mousse. Similarly, synthetic foams are found in practically every sector, from automotive, construction to packaging and sports [2].

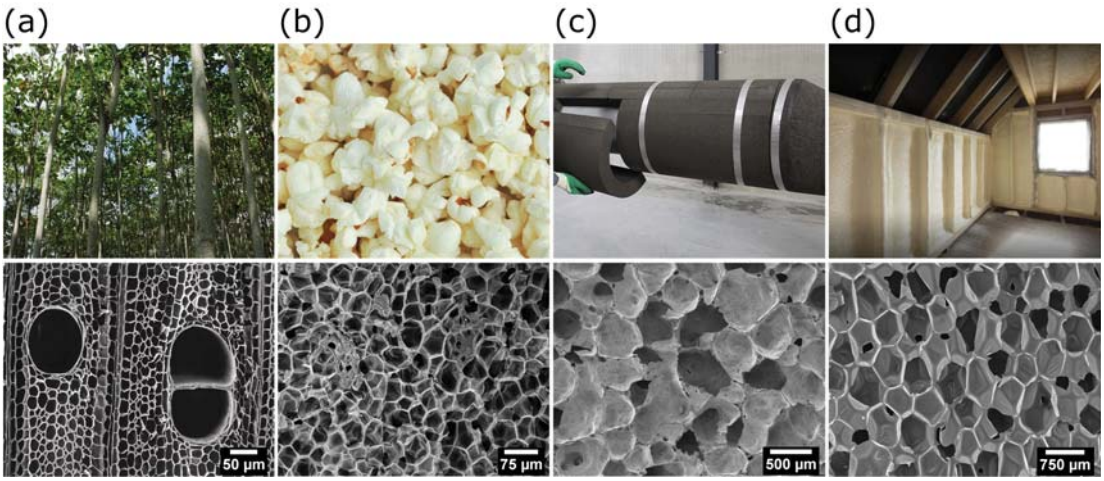

Figure 1-1: Characteristic cellular structure of (a) balsa wood, (b) popcorn, (c) glass foams and (d) polyurethane foam insulation.

Nowadays, synthetic foams can be produced with almost any type of solid matrices, such as metal, ceramics, glass and polymers [3]. Yet, by far polymeric foams are the most often encountered in daily life. Since their development in the early 20th century production technologies have greatly advanced facilitating the irruption of foams into the polymer market. In fact, foam consumption has never ceased to increase in the last century. In 2021 market size was estimated at $93.9 billion and is projected to reach $118.9 billion by 2026, at an annual growth rate of 4.8% between 2021 and 2026 [4]. This vast consumption of

foam products can only be understood in light of the advantages presented by polymer foams against their solid counterparts. These stand out for being lightweight and good thermal insulators. Other advantages are their relatively high strength per unit weight, impact strength and lower dielectric constant when compared to solid polymers [1].

However, foam formation is a complex and dynamic process in which several physico-chemical mechanisms are at play [2]. Factors related to the starting material properties, such as shear and extensional viscosity, glass transition temperature and molecular weight, as well as to the processing conditions, temperature, pressure and humidity, can limit expansion and deteriorate the final structure of the foams (Figure 1-2) [5–7]. For instance, high viscosities can reduce the speed of gas diffusion and hinder the foam expansion [6]. Whereas low extensional viscosities can yield poor quality materials in which collapse, and degeneration events take place during foaming [8].

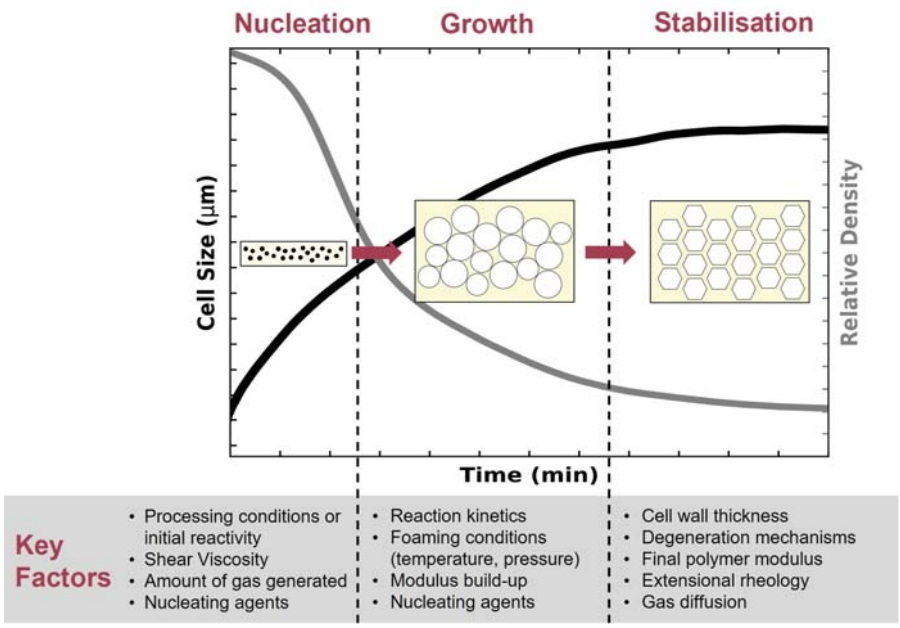

Figure 1-2: Schematic evolution of the foam relative density (inverse of expansion ratio) and cell size over time together with the factors influencing the final structure (adapted from [9]).

The stochastic nature of the foaming process leads to foams in which the final cellular structure is rather inhomogeneous and can vary greatly among materials. In polymeric foams several possible cell topologies have been identified. The cell shape can vary from pentagonal dodecahedrons in polyurethane (PU) foams to tetrakaidecahedrons in low density polyethylene (PE) foams [10]. Likewise, the thickness and amount of solid material enclosing the cells can vary between the walls, edges, and vertices (Figure 1-3). For instance, in PU foams most solid mass is located on edges and vertices (struts), while in PE foams

walls, edges and vertices have similar thickness as the solid mass is homogeneously distributed among them [10,11].

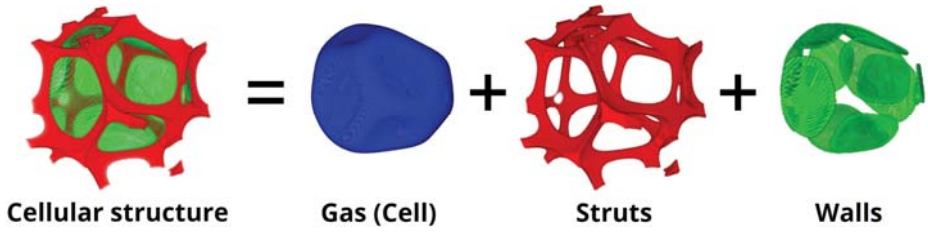

Figure 1-3: Parts of the cellular structure in foams (reproduced from [10]).

The complexity of the foaming process and final structure organisation in foams has motivated the development of multiple experimental techniques with which to delve into the foaming process-structure-properties relationships [10,12,13]. While, in general, porosity and the nature of the solid matrix dominate the final foam applications and properties, the latter cannot be understood without also considering the internal cellular structure [3]. The structure-dependent properties explain how foams of different matrices, generated using different production processes can still reveal similar properties. For instance, flexible open cell PU and open cell PE foams can both be excellent sound absorbers [14,15]. These two materials have in common a highly open cell and interconnected structure which enhances sound attenuation regardless of the matrix. At the other end of the scale, polyurethane materials are found. PU-based foams may have similar polymer morphology and porosity yet completely different structures and properties. The urethane polyaddition reaction between isocyanate and active hydrogen atoms (polyol) is the root of a wide variety of materials, ranging from thermoplastic to thermoset and from rigid (RPU) to flexible (FPU) as seen in Figure 1-4.

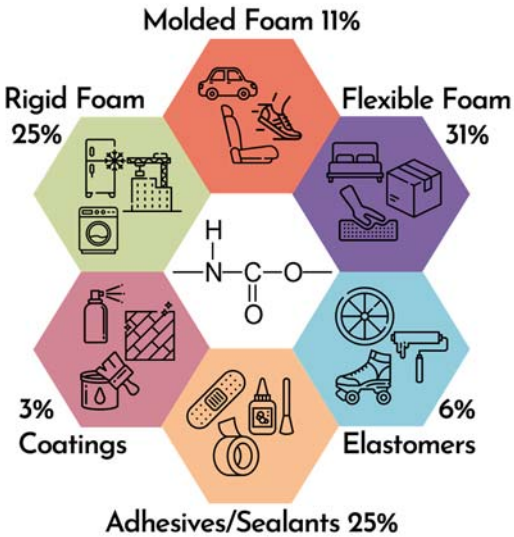

Figure 1-4: Global consumption of polyurethanes by product type and their applications [16].

Both rigid and flexible PU foams are produced following a reactive foaming process in which polymerisation and foaming take place simultaneously. Upon reaction of isocyanate with the polyol, the initial low viscosity components transform into a supramolecular crosslinked polymer network [17]. During the reaction, gas molecules are generated and create nucleation points in the mixture. Soon after, nuclei grow into a space-filling cellular structure while the matrix continues to change both in its morphology and rheological behaviour. Despite the similar chemistry and foaming process of rigid and flexible PU foams, they reveal a completely different final cellular structure. RPU foams have a homogeneous and closed cell cellular structure which provides this material with good thermal insulation properties (Figure 1-5 (a)). On the contrary, FPU foams present an open cell structure making them suitable for comfort and cushioning applications (Figure 1-5 (b)). These differences are rooted in the foaming process. In FPU foams thin cell walls break at maximum expansion, whereas the cell walls of RPU foams are elastic enough to withstand tensions. While this is an extreme scenario, within RPU foams unsought changes in the foaming mechanisms can also be detrimental to the structure and properties. Furthermore, changes in the PU foaming process are easily triggered by slight modifications in formulation variables or processing parameters such as reaction temperature, viscosity profile, surface tension or gas pressure in the mixture [18].

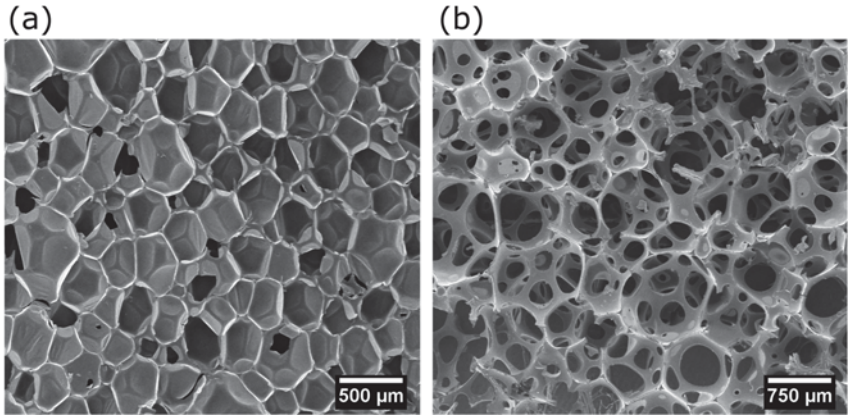

Figure 1-5: (a) Rigid Polyurethane foam with closed cell structure and (b) Flexible Polyurethane foams with open cell structure.

The case of PU foams is particularly interesting as it comes in many forms and it is by far one of the most consumed polymer foams [4,19]. Yet, for the future development of PU, there are two main challenges: increased sustainability and improved performance. The latter is reflected, for instance, in the production of closed cell foams of smaller cell size and improved thermal insulation capacities. However, meeting latest environmental and

performance standards for these materials necessarily passes through developing new and optimising existing PU foam formulations. To efficiently optimise formulations, without relying on trial and error approaches, it is essential to have a thorough understanding of the parameters and variables modifying the generation of PU foams. This can be achieved by either digital models or in-situ monitorisation techniques [19]. In recent years, much work has been done in trying to understand the formulation-structure-property relations through simulation and modelling, thereby without relying on experimental research [20–27]. However, structure and property predictive models ultimately necessitate experimental data either to provide input to the models or confirm their validity. For such reasons, advances have also been made in the development of novel experimental techniques [28–34].

In the framework of this thesis, all the aforementioned has motivated the design of new experimental methods to obtain in detail structural characterisation and track foam formation mechanisms of polyurethane foams using laboratory equipment. These methods are expected to ease the identification of how formulations modify parameters essential to the foam formation, from viscosity build-up and surface tension to temperature and pressure. Moreover, the applicability of these approaches can help accelerate and optimise research and development work on these foams.

1.1. FRAMEWORK OF THE THESIS

This investigation is part of the research activities at CellMat Laboratory in the Condensed Matter Physics Department of the University of Valladolid (cellmat.es) and was supervised by Prof. Dr Miguel Ángel Rodríguez-Pérez, head of the laboratory.

CellMat Laboratory was founded in 1999 by Prof. Dr. José Antonio de Saja and Prof. Dr. Miguel Ángel Rodríguez-Pérez. Since its foundation, the lab has grown not only in members but also in the number of active research programs and equipment. While at the start research was focused on the characterisation of cellular materials based on polyolefins [35–37], throughout the years, research activities have diversified and they now encompass several research topics and have resulted in over 275 publications and 34 PhD thesis.

Currently, the research conducted at CellMat focuses on five main topic areas: nanocellular materials [9,38], multifunctional cellular materials [10,39], cellular nanocomposites [40,41], bioplastic cellular materials [42,43] and polyurethane foams [40,44]. In all these research areas, the group strives to elucidate the link between

production, structure, properties and applications. This goal constitutes the basics of research at CellMat (Figure 1-6) and is achieved through the investigation of the foaming mechanisms and properties modelling. On the one hand, advanced methods for experimental research on the foaming mechanisms have enabled the group to understand how formulation and processing may condition the final cellular structure [45–49]. On the other hand, in-depth characterisations of the cellular structure have permitted to modify and develop new analytical models predicting the properties of cellular materials [50–52].

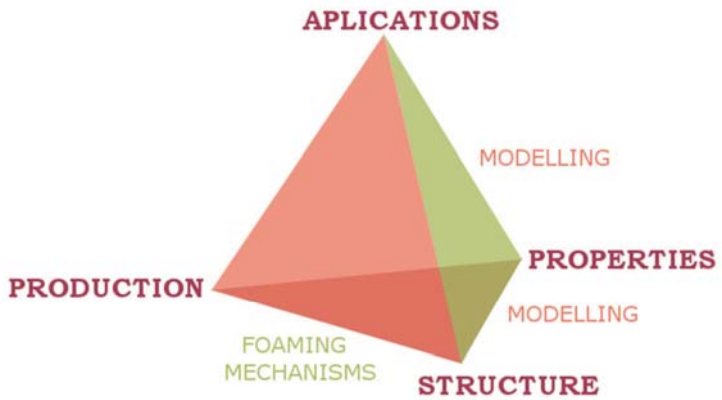

Figure 1-6: Research basis at CellMat: the cellular materials tetrahedron.

The investigation carried out in this thesis lies on the base of the cellular materials tetrahedron (Figure 1-6) and delves into the foaming mechanisms and modelling. Research on the foaming mechanisms in CellMat was initiated with the PhD thesis of Dr Samuel Pardo Alonso. This thesis paved the way for the development and application of non-standard experimental methods to visualise the dynamics of cellular structure generation and perform in-depth characterisations of the cellular structure through high-resolution X-ray tomography [39]. This research was followed by the PhD theses of Dr Mercedes Santiago Calvo and Dr Saúl Pérez Tamarit. The former investigated the polymerisation and foaming process of RPU foams using mainly FTIR spectroscopy, analysing in detail the reaction kinetics and how they are affected by the addition of different fillers [44,53,54]. Moreover, this thesis proved the feasibility of using the knowledge gained to effectively modify formulations and in turn improve the properties of the materials [46,47]. By contrast, the thesis of Dr Saúl Pérez Tamarit explored new methods of precisely characterising the cellular structure of foams with various polymer matrices [11,51,55]. This thesis relied on Synchrotron X-ray tomography to study in 3D the cellular and polymer microstructure both during foaming and in the final material [11,56].

The present thesis draws heavily on these precedents as it aims to explore both the reactive formation of RPU foams using new approaches and the feasibility of obtaining structural characterisation using laboratory X-ray tomography on a par with Synchrotron tomography.

1.2. OBJECTIVES

The purpose of this thesis was to **develop novel techniques to delve into the foaming process–structure-properties relationship in foams** (Figure 1-7). To accomplish this broad goal two specific targets were defined. Firstly, to investigate the viscoelastic changes and cellular structure evolution during PU foaming using newly developed and previously established methods. To achieve this goal, research focused on investigating model formulations to produce PU foams. In addition, to understand how the foaming process affects the polymer matrix topology (solid-phase thickness distribution) image analysis methodologies based on laboratory X-ray tomography were developed. And secondly, using the previous characterisation methods, it was sought to elucidate the structure-properties relationship in different materials. To that end, the selected systems were rigid PU foams containing silica aerogel particles and glass foams.

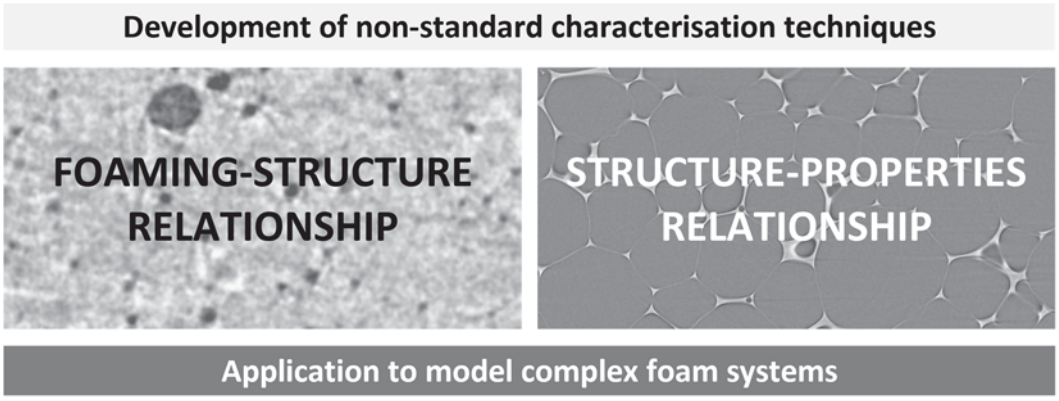

Figure 1-7: General objective of this thesis.

To achieve the previous general objectives the research in this thesis was broken down into several specific targets. These targets are categorised below according to the objective they intend to fulfil.

1) Development of novel experimental methods to unravel the foaming-structure relationship in RPU foams (Figure 1-8).

- Study in-situ the viscoelastic changes during the reactive foaming of RPU foams. To that end, two complementary techniques were used: a novel methodology based on

Dynamic Mechanical Analysis (DMA) and a pre-existing oscillatory shear rheology protocol for expanding foams (Chapter 4).

- Use the measurements of DMA and rheology as a measure of the extent of the polymerisation reaction. Then, compare and understand these results in light of the reaction kinetics and cellular structure evolution of RPU foams measured with well-established techniques: FTIR Spectroscopy and X-ray radioscopy, respectively (Chapter 4).
- Design and implement a laboratory X-ray tomography method to monitor in 3D the cellular structure generation in RPU foams (Chapter 5). This was accomplished by developing the methodology to perform Cryogenic X-ray Tomography experiments.
- Develop image analysis methodologies permitting the characterisation of the solid matrix structure in foams using laboratory X-ray tomography with pixel size above the solid thickness, *i.e.,* sub-pixel conditions (Chapter 6).

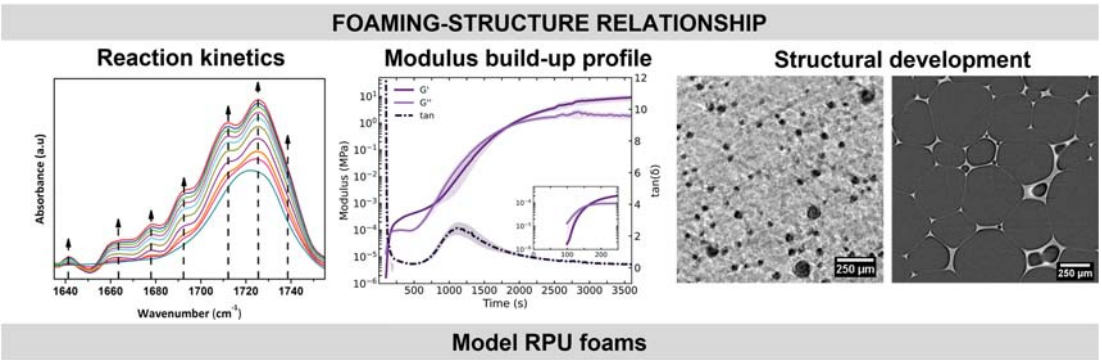

Figure 1-8: Scheme summarising the essential steps to achieve objective 1.

2) Application of the developed experimental methods to understand the final structure and properties of complex foams (Figure 1-9).

- Apply the non-standard characterisation methods to two case studies: RPU-Silica aerogel composite foams and recycled glass foams.
- Elucidate the influence of polymerisation and foaming kinetics on the polymer matrix topology and cellular structure of RPU-Aerogel composite foams (Chapter 7).
- Study the influence of the cellular structure and polymer matrix topology on the thermal insulation capacities of complex foam systems, in particular, recycled glass foams and RPU-Aerogel composite foams (Chapter 8).

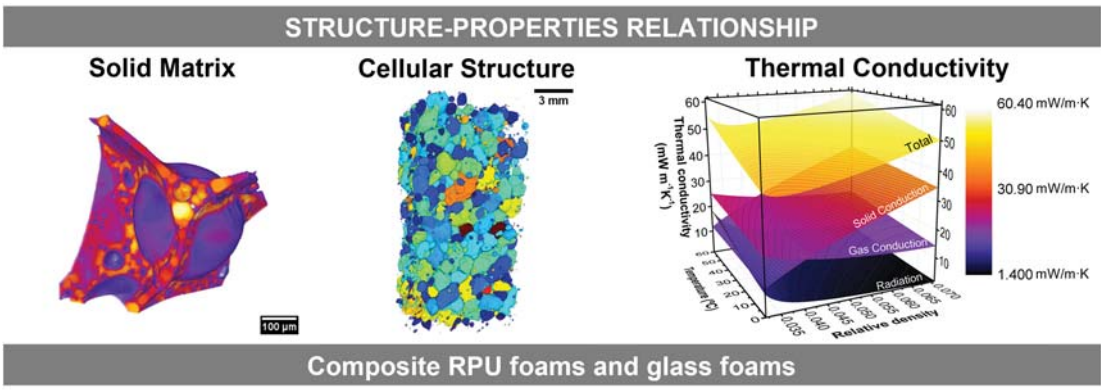

Figure 1-9: Summary of the steps taken to achieve objective 2.

1.3. MAIN NOVELTIES OF THE THESIS

The completion of the previous objectives has permitted us to make progress beyond the state of the art. The main novelties of the thesis are summarised hereafter.

- For the first time, the polymerisation kinetics and modulus build-up in RPU foams have been monitored using in-situ DMA. The efficiency of the technique was verified using simple formulations of different reactivity and by comparison with the results provided by FTIR Spectroscopy. This new experimental method for DMA represents an advancement in the range of applications of the technique and in the methods to in-situ analyse reactive foams.
- Likewise, in the course of this thesis, a new experimental method based on cryogenic X-ray tomography was developed. It enabled observation in 3D of the RPU foams cellular structure at early reaction times.
- The development of new image analysis methods renders possible the characterisation of the solid mass distribution in foams whose matrix is thinner than the X-ray tomography set-up spatial resolution. This has permitted to expand the range of characterisations possible with X-ray tomography systems of low resolution. Therefore, limited spatial resolution is no longer a setback for the analysis of the solid matrix in low density foams.
- The impact of super-insulating aerogel particles on the nucleation, foaming dynamics, rheology of the initial reactants, reaction kinetics and polymerisation of RPU foams has been unravelled using non-standard characterisation techniques.
- The heat transfer mechanisms in recycled glass foams have been elucidated. Moreover, the contribution of each mechanism to the thermal conductivity of these

foams has been determined. This breakthrough is expected to ease the task of identifying routes for reducing thermal conductivity in this system.

1.4. THESIS STRUCTURE

This dissertation was written as a compendium of publications. The obtained results are supported by eight publications, five of which are published in Q1 journals at the time of submission of this dissertation (August 2022) and the remaining three are currently pending acceptance. This thesis fulfils the requirements to obtain the degree of Doctor in Philosophy with International Mention. The presented research is articulated around the conceptual map shown in Figure 1-10. The dissertation consists of 9 chapters and the results chapters are, in turn, grouped into two sections.

Chapter 1 (Introduction) provides an overview of the thesis topic. It states the objectives and structure of the thesis. In addition, the scientific achievements (publications, conferences, projects) accomplished during the competition of this thesis are reported.

Chapter 2 (Background) introduces the main concepts and state of knowledge underpinning the conducted research. It covers topics from reaction kinetics, foaming dynamics and rheological development of PU foams to thermal conductivity in foams.

Chapter 3 (Experimental) describes the raw materials and the different standard and novel techniques implemented to identify the foaming mechanisms and characterise the cellular structure in foams.

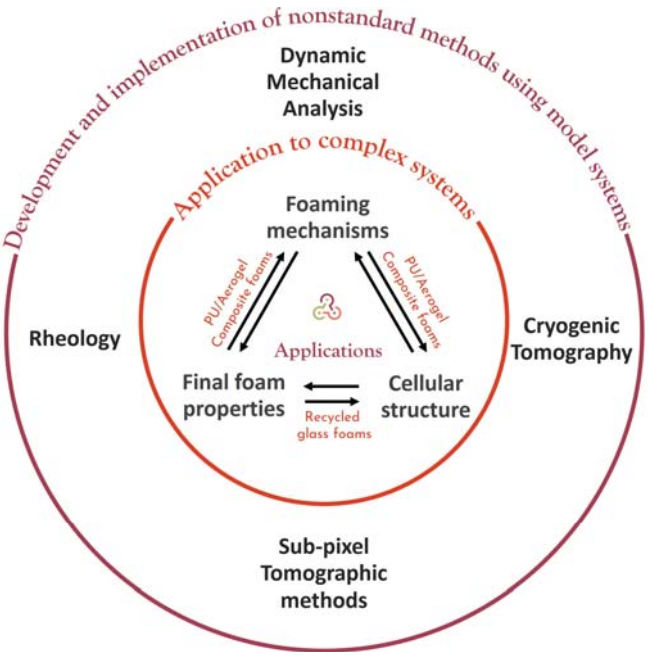

Figure 1-10: Conceptual map of the thesis.

PART I. DEVELOPMENT OF METHODOLOGIES

Chapter 4 (Rheological behaviour during Polyurethane foaming) comprises two publications and deals with four model RPU formulations of different catalyst and blowing agent concentrations. The first of the publications provides a comparison of the reaction kinetics of the model RPU foams with their modulus build-up profile measured using a novel methodology based on in-situ DMA. The second of the publications reveals the impact of the rheological behaviour of reactive foams on the cellular structure generation.

Chapter 5 (Early cellular structure generation in Polyurethane foams) includes one short communication about the development of a new technique based on cryogenic X-ray tomography. The technique is applied to follow ex-situ and in 3D the cellular structure development of RPU foams at early foaming stages.

Chapter 6 (Solid matrix distribution in polymeric foams) reports three image analysis methodologies for the characterisation of the polymer matrix of foams scanned with sub-pixel X-ray tomography. The efficiency of the methods is proved with three foams of different matrices: polystyrene, polyethylene and polyurethane.

PART II. APPLICABILITY OF THE DEVELOPED METHODOLOGIES

Chapter 7 (Influence of aerogel on the synthesis of Polyurethane) contains two articles dealing with RPU-Silica aerogel composites foams. In these publications, the effect of Silica aerogel particles on the cellular structure formation (X-ray radioscopy), reaction kinetics (FTIR Spectroscopy), viscoelastic properties development (Shear Rheology) and final polymer matrix and cellular structure (laboratory X-ray tomography) is addressed.

Chapter 8 (Thermal insulation properties in low density foams) presents two publications addressing the thermal insulation properties of RPU-Silica aerogel composites foams and recycled glass foams. The cellular structure of these foams was characterised using laboratory X-ray tomography and the structure-thermal insulation relationship is evaluated.

Chapter 9 (Conclusions and Future Work) summarises the findings of this research. In addition, future research work is discussed.

1.5. DOCTORAL PORTFOLIO

This section gathers the scientific publications (Table 1-1 and Table 1-2) conferences (Table 1-3 and Table 1-4), courses (Table 1-5), research stays (Table 1-6) and projects (Table 1-7 and Table 1-8) that have been carried out during the course of the present PhD thesis.

Table 1-1: Publications included in this thesis.

	Publication Reference	Chapter
1	P. Cimavilla-Román, M. Santiago-Calvo, M.A. Rodríguez-Pérez. Dynamic Mechanical Analysis during polyurethane foaming: Relationship between modulus build-up and reaction kinetics, Polym. Test. 103 (2021) 107336	**4**
2	P. Cimavilla-Román, M. Santiago-Calvo, A. Vananroye, P. Moldenaers, M.A. Rodríguez-Pérez. The influence of viscosity build-up on the structure generation of rigid polyurethane foams, *Submitted*	**4**
3	P. Cimavilla-Román, M. Santiago-Calvo, M.A. Rodríguez-Pérez. Cryogenic X-ray Tomography of Polyurethane foams: Early structural development, *Submitted*	**5**
4	P. Cimavilla-Román, S. Pérez-Tamarit, S. Barroso-Solares, J. Pinto, M.A. Rodríguez-Pérez. Sub-pixel tomographic methods for characterizing the solid architecture of foams. Microsc. Microanal. (2022)	**6**
5	P. Cimavilla-Román, S. Pérez-Tamarit, M. Santiago-Calvo, MA. Rodríguez-Pérez, Influence of silica aerogel particles on the foaming process and cellular structure of rigid polyurethane foams, Eur. Polym. J. 135 (2020) 109884	**7**
6	P. Cimavilla-Román, S. Pérez-Tamarit, A. Vananroye, P. Moldenaers, M.A. Rodríguez-Pérez. The effects of Silica Aerogel on the rheological behaviour and polymer matrix structure of Rigid Polyurethane foams, Eur. Polym. J. 176 (2022) 111398	**7**
7	P. Cimavilla-Román, J. Villafañe-Calvo, A. López-Gil, J. König, MA. Rodríguez-Perez, Modelling of the mechanisms of heat transfer in recycled glass foams, Constr. Build. Mater. 274 (2021) 122000	**8**
8	P. Cimavilla-Román, S. Pérez-Tamarit, M. Santiago-Calvo, MA. Rodríguez-Pérez, Influence of silica aerogel particles on thermal insulation properties of rigid polyurethane foams, *Submitted*	**8**

Table 1-2: Co-authored publications during the thesis.

	Publication Reference
1	A. Ballesteros, E. Laguna-Gutierrez, P. Cimavilla-Roman, M.L. Puertas, A. Esteban-Cubillo, J. Santaren, M.A. Rodriguez-Perez, Influence of the dispersion of Nanoclays on the cellular structure of foams based on polystyrene, J. Appl. Polym. Sci. 138 (2021)
2	J. Martín-de León, P. Cimavilla-Román, V. Bernardo, E. Solórzano, N. Kardjilov, M.A. Rodríguez-Pérez, Cold neutron transmission for the in-situ analysis of the gas diffusion in polymers, J. Supercrit. Fluids. 177 (2021)
3	S. Barroso-Solares, P. Cimavilla-Roman, M.A. Rodriguez-Perez, J. Pinto, Non-invasive approaches for the evaluation of the functionalization of melamine foams with in-situ synthesized silver nanoparticles, Polymers (Basel). 12 (2020)
4	S. Barroso-Solares, B. Merillas, P. Cimavilla-Román, M.A. Rodriguez-Perez, J. Pinto, Enhanced nitrates-polluted water remediation by polyurethane/sepiolite cellular nanocomposites, J. Clean. Prod. 254 (2020)
5	J. König, A. Lopez-Gil, P. Cimavilla-Roman, M.A. Rodriguez-Perez, R.R. Petersen, M.B. Østergaard, N. Iversen, Y. Yue, M. Spreitzer, Synthesis and properties of open- and closed-porous foamed glass with a low density, Constr. Build. Mater. 247 (2020)
6	J. Martín-de León, V. Bernardo, P. Cimavilla-Román, S. Pérez-Tamarit, M.A. Rodríguez-Pérez, Overcoming the Challenge of Producing Large and Flat Nanocellular Polymers: A Study with PMMA, Adv. Eng. Mater. 1900148 (2019)
7	M. Santiago-Calvo, S. Pérez-Tamarit, P. Cimavilla-Román, V. Blasco, C. Ruiz, R. París, F. Villafañe, M. A. Rodríguez-Pérez, X-ray radioscopy validation of a polyol functionalized with graphene oxide for producing rigid polyurethane foams with improved cellular structures, Eur. Polym. J. 118 (2019)
8	D. Batey, S. Cipiccia, X. Shi, S. Williams, K. Wanelik, A. Wilson, S. Pérez-Tamarit, P. Cimavilla, M.A. Ródriguez-Pérez, C. Rau, Coherence Branch at I13, DLS: The Multiscale, Multimodal, Ptycho-tomographic End Station, Microsc. Microanal. 24 (2018)
9	C. Rau, M. Storm, S. Marathe, A.J. Bodey, S. Cipiccia, D. Batey, X. Shi, M.-C. Zdora, I. Zanette, S. Perez-Tamarit, P. Cimavilla, M.A. Rodriguez-Perez, F. Doring, C. David, Multi-Scale Imaging at the Coherence and Imaging Beamline I13 at Diamond, Microsc. Microanal. 24 (2018)

Table 1-3: Summary of conference communications related to the thesis topic.

	Conferences
1	P. Cimavilla-Román., M. Santiago-Calvo, M.A. Rodríguez-Pérez. Cryogenic X-ray tomography of Rigid Polyurethane foams. *FOAMS2021*-September 13-16, 2021, Virtual conference. Oral Communication
2	P. Cimavilla-Román; J. Villafañe-Calvo; A. López-Gil; J. König; M. A. Rodríguez Pérez. Modelling of the mechanisms of heat transfer in glass foams at different temperatures. *CELLMAT2020*-October 7-9, 2020, Virtual conference. Poster
3	P. Cimavilla-Román; M. Santiago-Calvo; M. A. Rodríguez Pérez. In-situ Dynamic Mechanical Analysis during polyurethane foaming: relationship between modulus build-up and reaction kinetics. *CELLMAT2020*-October 7-9, 2020, Virtual conference. Oral Communication
4	P. Cimavilla-Román; S. Pérez-Tamarit; M. Santiago-Calvo; M. A. Rodríguez Pérez. Influence of nanoporous aerogel on the foaming process and properties of Rigid Polyurethanes foams from a physicochemical perspective. *FOAMS2019*-October 1-3, 2019. Valladolid, Spain. Poster
5	J König, U. Hribar, P. Cimavilla-Román, A. Lopez-Gil, M.A. Rodriguez-Pérez, R.R. Petersen, Y. Yue. Comparison of open- and closed-porous foamed glass. *25th International Congress on Glass*-June 9-14, 2019. Boston (USA). Oral Communication
6	P. Cimavilla-Román, S. Pérez-Tamarit, M. Santiago-Calvo, M. A. Rodríguez-Pérez. In-situ physicochemical analysis of the foaming process of aerogel-rigid polyurethane composite foams. *EUFOAM2018*-July 9-12, 2018. Liege (Belgium). Oral Communication
7	P. Cimavilla-Román, S. Pérez-Tamarit, E. Sólorzano, A. Hilger, I. Manke, M. A. Rodríguez-Pérez. Novel subresolution tomographic methods for quantifying fraction of mass in Plateau borders of solid polymeric foams. *EUFOAM2018*-July 9-12, 2018. Liege (Belgium). Poster
8	P. Cimavilla-Román, S. Pérez-Tamarit, M. Santiago-Calvo, M. A. Rodríguez-Pérez. In-situ analysis, by X-ray radioscopy, of the foaming process of aerogel-polyurethane cellular composites. *ESMolNa2017* – May 7-11, 2017. El Escorial (Spain) Oral Communication

Table 1-4: Additional conference contributions unrelated to the main thesis topic.

	Conferences
1	V. Bernardo, J. Martín-de Leon, F. Van Loock, N. A. Fleck, P. Cimavilla-Román, S. Pérez-Tamarit, M. A. Rodríguez Pérez. Nanocellular polymers based on PMMA/Sepiolite nanocomposites: characterization of the mechanic behaviour. *CELLMAT2018*-October 24-26, 2019. Bad Staffestein (Germany). Poster
2	S. Barroso-Solares, B. Merillas, P. Cimavilla-Román, M. A. Rodríguez Pérez, J. Pinto. Nitrates and other pollutants removal from water resources using multifunctional polyurethane foams. *Water Waste*-July 18-20, 2018, Madrid (Spain.) Oral Communication
3	S. Pérez-Tamarit, P. Cimavilla-Román, S. Barroso-Solares, M. A. Rodríguez Pérez. X-Ray Imaging as a useful tool for a training program on polymer foams. *EDULEARN18*–July 2-4, 2018, Palma (Spain). Oral Communication
4	P. Cimavilla-Román, S. Pérez-Tamarit, J. Martín-de León, E. Solórzano, I. Manke, N. Kardjilov, M. A. Rodríguez Pérez. In-situ neutron tomography of the gas diffusion process of high pressure CO_2 on PMMA. *38th Berlin School on Neutron Scattering* - March 1-9, 2018. Berlin (Germany). Poster

Table 1-5: Stays at International Research Centres.

	Research stays
1	KU Leuven (Belgium) – August 2021 – November 2021 Topic: Oscillatory shear rheology during the reactive foaming process of polyurethane
2	Synchrotron Beamtime BESSY II (Germany) – July 2019 Topic: Study of the internal structure of a hollow polymeric fibres by X-ray tomography
3	Synchrotron Beamtime Diamond Light Source (UK) – February 2019 Topic: Ptychotomography of microcellular and sub-microcellular polymers
4	Synchrotron Beamtime Diamond Light Source (UK) – January 2018 Topic: Ptychotomography of microcellular and sub-microcellular polymers

Table 1-6: Courses completed during this thesis.

	Courses
1	Termografía infrarroja con procesamiento de imágenes Universidad de Valladolid – Valladolid, Spain, June 2018
2	38th Berlin School on Neutron Scattering Helmholtz Zentrum Berlin - Berlin, Germany, March 2018
3	Jornadas Prof Antonio de Saja: Envases Plásticos: Fundamentos, Normativa y Tendencias Leical, CellMat Technologies - Valladolid, Spain, February 2018
4	Jornadas Prof Antonio de Saja: Caracterización de materiales poliméricos Leical, CellMat Technologies - Valladolid, Spain, December 2016

Table 1-7: Projects of public funding in which the author has collaborated.

	Projects of public funding
1	Functional polymeric foams for water treatment Agencia estatal de investigación, FEDER. 2019-2022
2	Reduction of energy consumption in buildings through transparent and thermally insulating nanocellular polymers: production, characterisation and process-structure-properties relationship Ente público Regional de la Energía de Castilla y León (EREN). 2019-2021
3	CleanTechBlock - Sustainable Multi-functional Building Block Basics M-ERA.NET. 2017-2019
4	Development and continuous manufacturing of advanced polymer-based thermal insulators Ministerio de Economia y Competitividad, FEDER. 2016-2019
5	Development of micro- and nanocellular materials: fabrication, characterization and application Universidad de Valladolid. 2015-2016

Table 1-8: Projects of private funding in which the author has collaborated

	Projects of private funding
1	Study of polyisocyanurate foam formulations DuPont (USA). 2019-2020
2	Research on the applications of advanced carbon nanomaterials to improve the performance of polyurethane (PU) matrices with interest to the automotive sector. Grupo Antolin ingeniería SA. 2017-2019
3	Development of new foaming techniques to lighten rigid plastic parts and generate soft touch surfaces: structural and functional foaming technologies. Grupo Antolin ingeniería SA. 2017-2019

1.6. REFERENCES

[1] J.G. Drobny, Processing Methods Applicable to Thermoplastic Elastomers, Handb. Thermoplast. Elastomers. (2014) 33–173.

[2] N.S. Ramesh, S.T. Lee, Polymeric Foams: Mechanisms and Materials, First Ed, CRC Press, Boca Raton, 2004.

[3] L.J. Gibson, M.F. Ashby, Cellular solids: Structure and Properties, Cambridge: Cambridge Solid State Science Series, Cambridge, 1997.

[4] Foam Market Global Forecast to 2026 | MarketsandMarkets, (n.d.). (accessed February 7, 2022).

[5] V. Bernardo, J. Martin-de Leon, E. Laguna-Gutierrez, T. Catelani, J. Pinto, A. Athanassiou, M.A. Rodriguez-Perez, Understanding the role of MAM molecular weight in the production of PMMA/MAM nanocellular polymers, Polymer (Guildf). 153 (2018) 262–270.

[6] J.M. de León, V. Bernardo, E. Laguna-Gutiérrez, M.Á. Rodríguez-Pérez, Influence of the viscosity of poly(methyl methacrylate) on the cellular structure of nanocellular materials, Polym. Int. 69 (2020) 72–83.

[7] J. Martín-de León, P. Cimavilla-Román, V. Bernardo, E. Solórzano, N. Kardjilov, M.A. Rodríguez-Pérez, Cold neutron transmission for the in-situ analysis of the gas diffusion in polymers, J. Supercrit. Fluids. 177 (2021) 105331.

[8] E. Laguna-Gutierrez, Understanding the Foamability of Complex Polymeric Systems By Using Extensional Rheology, Universidad de Valladolid, 2016.

[9] V. Bernardo, Production and Characterization of Nanocellular Polymers Based on Nanostructured PMMA Blends and PMMA Nanocomposites, University of Valladolid, 2019.

[10] S. Pérez Tamarit, Structural characterization of solid cellular polymers by X-ray tomography and light scattering, University of Valladolid, 2019.

[11] S. Pérez-Tamarit, E. Solórzano, A. Hilger, I. Manke, M.A. Rodríguez-Pérez, Multi-scale tomographic analysis of polymeric foams: A detailed study of the cellular structure, Eur. Polym. J. 109 (2018) 169–178.

[12] S. Pardo-Alonso, X-Ray Imaging Applied to the Characterization of Polymer Foams' Cellular Structure and Its Evolution, Universidad de Valladolid, 2014.

[13] C. Brondi, E. Di Maio, L. Bertucelli, V. Parenti, T. Mosciatti, Competing bubble formation mechanisms in rigid polyurethane foaming, Polymer (Guildf). 228 (2021) 123877.

[14] S.-T. Lee, C.B. Park, Foam Extrusion: Principles and Practice, 2nd Ed, CRC Press 2014, 2000.

[15] E. López González, Analysis of the composition-structure- properties relationship of open-cell polyolefin-based foams with tailored levels of gas-phase tortuosity, University of Valladolid, 2019.

[16] N. V. Gama, A. Ferreira, A. Barros-Timmons, Polyurethane Foams: Past, Present, and Future, Mater. 2018, Vol. 11, Page 1841. 11 (2018) 1841.

[17] R.D. Priester, J. V. Mcclusky, R.E. O'neill, R.B. Turner, M.A. Harthcock, B.L. Davis, FT-IR-A Probe into the Reaction Kinetics and Morphology Development of Urethane Foams, J. Cell. Plast. 26 (1990) 346–367.

[18] N.C. Hilyard, A. Cunningham, Low density cellular plastics, 1st Ed, Springer Science & Business Media, 2012, London, 1994.

[19] B. Eling, Ž. Tomović, V. Schädler, Current and Future Trends in Polyurethanes: An Industrial Perspective, Macromol. Chem. Phys. 221 (2020) 2000114.

[20] P. Ferkl, I. Krškova, J. Kosek, Evolution of mass distribution in walls of rigid polyurethane foams, Chem. Eng. Sci. 176 (2018) 50–58.

[21] J. Kosek, P. Ferkl, I. Krškova, PU foams: Mathematical modelling of morphology development, in: Comput. Aided Chem. Eng., Elsevier, 2017: pp. 1009–1014.

[22] T. Chaloupka, A. Zubov, J. Kosek, Real-time Hybrid Monte Carlo Method for Modelling of 4 Monomer Semi-Batch Emulsion Copolymerization, Comput. Aided Chem. Eng. 40 (2017) 259–264.

[23] P. Ferkl, A. Nistor, M. Podivinska, M. Vonka, J. Kosek, PU foams: Modelling of heat insulation properties and their degradation in time, Comput. Aided Chem. Eng. 40 (2017) 475–480.

[24] P. Ferkl, M. Toulec, E. Laurini, S. Pricl, M. Fermeglia, S. Auffarth, B. Eling, V. Settels, J. Kosek, Multi-scale modelling of heat transfer in polyurethane foams, Chem. Eng. Sci. 172 (2017) 323–334.

[25] P. Ferkl, M. Karimi, D.L. Marchisio, J. Kosek, Multi-scale modelling of expanding polyurethane foams: Coupling macro- and

bubble-scales, Chem. Eng. Sci. 148 (2016) 55–64.

[26] H. Al-Moameri, Y. Zhao, R. Ghoreishi, G.J. Suppes, Simulation of liquid physical blowing agents for forming rigid urethane foams, J. Appl. Polym. Sci. 132 (2015) 1–7.

[27] Y. Zhao, F. Zhong, A. Tekeei, G.J. Suppes, Modeling impact of catalyst loading on polyurethane foam polymerization, Appl. Catal. A Gen. 469 (2014) 229–238.

[28] M.J. Elwell, A.J. Ryan, H.J.M. Grunbauer, H.C. VanLieshout, An FTIR study of reaction kinetics and structure development in model flexible polyurethane foam systems, Polymer (Guildf). 37 (1996) 1353–1361.

[29] L.D. Artavia, C.W.W. Macosko, Foam Kinetics, J. Cell. Plast. 26 (1990) 490–511.

[30] M.J. Elwell, S. Mortimer, A.J. Ryan, A Synchrotron SAXS Study of Structure Development Kinetics during the Reactive Processing of Flexible Polyurethane Foam, Macromolecules. 27 (1994) 5428–5439.

[31] M.J. Elwell, A.J. Ryan, H.J.M. Grunbauer, H.C. Van Lieshout, In-situ studies of structure development during the reactive processing of model flexible polyurethane foam systems using FT-IR spectroscopy, synchrotron SAXS and rheology, Macromolecules. 29 (1996) 769–770.

[32] S. Pardo-Alonso, E. Solórzano, S. Estravís, M.A. Rodríguez-Perez, J.A. de Saja, In situ evidence of the nanoparticle nucleating effect in polyurethane–nanoclay foamed systems, Soft Matter. 8 (2012) 11262.

[33] M. Santiago-Calvo, S. Pérez-Tamarit, J. Tirado-Mediavilla, F. Villafañe, M.A. Rodríguez-Pérez, Infrared expandometry: A novel methodology to monitor the expansion kinetics of cellular materials produced with exothermic foaming mechanisms, Polym. Test. 66 (2018) 383–393.

[34] J. Reignier, P. Alcouffe, F. Méchin, F. Fenouillot, The morphology of rigid polyurethane foam matrix and its evolution with time during foaming – New insight by cryogenic scanning electron microscopy, J. Colloid Interface Sci. 552 (2019) 153–165.

[35] M.A. Rodriguez Pérez, Propiedades térmicas y mecánicas de espumas de poliolefina, Universidad de Valladolid, 1998.

[36] O. Almanza, Caracterización y Modelización de las Propiedades Térmicas y Mecánicas en Espumas con Base Polietileno, University of Valladolid, 2000.

[37] S. Díez-Gutiérrez, M.A. Rodríguez-Pérez, J.A. De Saja, J.I. Velasco, Dynamic mechanical analysis of injection-moulded discs of polypropylene and untreated and silane-treated talc-filled polypropylene composites, Polymer (Guildf). 40 (1999) 5345–5353.

[38] J. Martin-de Leon, Understanding the Production Process of Nanocellular Polymers Based on PMMA Driven By a Homogeneous nucleation, University of Valladolid, 2019.

[39] S. Pardo-Alonso, X-Ray Imaging Applied to the Characterization of Polymer Foams ' Cellular Structure and Its Evolution, Universidad de Valladolid, 2014.

[40] S. Estravis, Cellular Nanocomposites Based on Rigid Polyurethane and Nanoclays : Fabrication , Characterization and Modeling of the Mechanical and Thermal, Universidad de Valladolid, 2014.

[41] J. Escudero Arconada, Polyolefin based cellular materials . Development of new production routes and optimization of barrier and mechanical properties by the addition of nanoclays, Universidad de Valladolid, 2016.

[42] A. López Gil, Development of Environmentally Friendly Cellular Polymers for Packaging and Structural Applications . Study of the Relationship Cellular Structure-Mechanical Properties, Universidad de Valladolid, 2016.

[43] D. Velasco Nieto, Desarrollo de biomateriales celulares en base EVA, PLA y PHB, fabricación y caracterización., Universidad de Valladolid, 2016.

[44] M. Santiago-Calvo, Synthesis , Foaming Kinetics and Physical Properties of Cellular Nanocomposites Based on Rigid Polyurethane, University of Valladolid, 2019.

[45] E. Solórzano, S. Pardo-Alonso, J.A. De Saja, M.A. Rodriguez-Perez, X-ray radioscopy in-situ studies in thermoplastic polymer foams, Colloids Surfaces A Physicochem. Eng. Asp. 438 (2013) 167–173.

[46] M. Santiago-Calvo, V. Blasco, C. Ruiz, R. París, F. Villafañe, M.-Á. Rodríguez-Pérez, Synthesis, characterization and physical properties of rigid polyurethane foams prepared with poly(propylene oxide) polyols containing graphene oxide, Eur. Polym. J. 97 (2017) 230–240.

[47] M. Santiago-Calvo, V. Blasco, C. Ruiz, R. París, F. Villafañe, M.Á. Rodríguez-Pérez, Improvement of thermal and mechanical properties by control of formulations in rigid polyurethane foams from polyols functionalized with graphene oxide, J. Appl. Polym. Sci. 136 (2019) 1–10.

[48] E. Lopez-Gonzalez, L.O. Salmazo, A. Lopez-Gil, E. Laguna-Gutierrez, M.A. Rodriguez-Perez, Analysis of the foaming mechanisms of materials based on high-density polyethylene (HDPE) crosslinked with different irradiation doses, J. Appl. Polym. Sci. 135 (2018) 46276.

[49] L. Oliveira Salmazo, A. Lopéz-Gil, Z.M. Ariff, M.L. Rodriguez-Mendez, A.E. Job, M.A. Rodriguez Perez, Study of the Foaming Kinetics in Epoxidized Natural Rubber Foams Crosslinked by Electron Beam Irradiation, Macromol. Chem. Phys. 219 (2018) 1800295.

[50] V. Bernardo, J. Martin-de Leon, J. Pinto, R. Verdejo, M.A. Rodriguez-Perez, Modeling the heat transfer by conduction of nanocellular polymers with bimodal cellular structures, Polymer (Guildf). 160 (2019) 126–137.

[51] S. Pérez-Tamarit, E. Solórzano, A. Hilger, I. Manke, M.A. Rodríguez-Pérez, Effect of solid phase corrugation on the thermo-mechanical properties of low density flexible cellular polymers, Mater. Des. 161 (2019) 106–113.

[52] P. Cimavilla-Román, J. Villafañe-Calvo, A. López-Gil, J. König, M.Á. Rodríguez-Perez, Modelling of the mechanisms of heat transfer in recycled glass foams, Constr. Build. Mater. 274 (2021) 122000.

[53] M. Santiago-Calvo, J. Tirado-Mediavilla, J.L. Ruiz-Herrero, M.Á. Rodríguez-Pérez, F. Villafañe, The effects of functional nanofillers on the reaction kinetics, microstructure, thermal and mechanical properties of water blown rigid polyurethane foams, Polymer (Guildf). 150 (2018) 138–149.

[54] M. Santiago-Calvo, S. Pérez-Tamarit, P. Cimavilla-Román, V. Blasco, C. Ruiz, R. París, F. Villafañe, M.Á. Rodríguez-Pérez, X-ray radioscopy validation of a polyol functionalized with graphene oxide for producing rigid polyurethane foams with improved cellular structures, Eur. Polym. J. 118 (2019) 404–411.

[55] S. Pérez-Tamarit, E. Solórzano, M.A. Rodriguez-Perez, Efficient prediction of cell size in solid polymeric foams by numerically solving the diffusion approximation of light scattering equation, Colloids Surfaces A Physicochem. Eng. Asp. 534 (2017) 130–137.

[56] S. Pérez-Tamarit, E. Solórzano, R. Mokso, M.A. Rodríguez-Pérez, In-situ understanding of pore nucleation and growth in polyurethane foams by using real-time synchrotron X-ray tomography, Polymer (Guildf). 166 (2019) 50–54.

C APT Background

BACKGROUND

2.1. RIGID POLYURETHANE FOAMS

Rigid polyurethane (RPU) foams are a well-established class of thermosetting cellular polymers of closed cell structure. Since its introduction in the early 1950s, low-density RPU foams have been used for thermal insulation purposes due to their low thermal conductivity. Their extensive consumption for thermal insulation purposes is related to its high compressive strength, low thermal conductivities between 18 and 30 mW (m K)$^{-1}$, and good imperviousness to water. Nowadays, they can be found in home appliances, building construction and automotive applications among others (Figure 2-1).

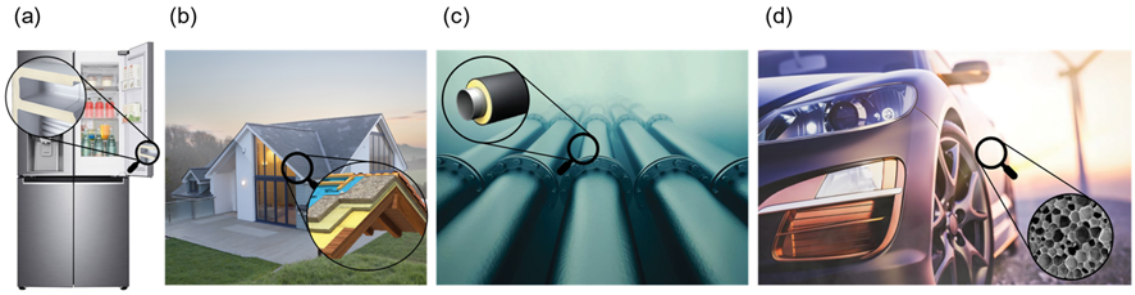

Figure 2-1: Application of RPU foams: (a) insulation for home appliances, (b) panels for building insulation, (c) pipe insulation and (d) structural component in car parts such as roofs and doors.

Thermal conductivity in RPU foams is a combination of a closed-cell cellular structure, high porosity and low thermal conductivity of both the polymer and the gas inside the cells. In fact, RPU foams can reach thermal conductivity values as low as 18 mW (m K)$^{-1}$ [1]. Traditionally, the gases most commonly used to blow RPU foams were chlorofluorocarbons (CFCs) for their very low thermal conductivity and boiling points [2]. However, the Montreal Protocol advised against the use of CFCs due to their contribution to the depletion of the ozone layer of the atmosphere. For such reasons, these blowing agents have progressively been replaced with hydrocarbons (HCs), hydrofluorocarbons (HFCs), hydrofluorolefins (HFOs) and CO_2 (generated via the isocyanate-water reaction) [3,4]. Nowadays, RPU foams in the European market are blown with a combination of chemical

blowing agents, water, and physical blowing agents, mainly hydrocarbons and hydrofluorolefins, reaching densities close to 30 kg m^{-3} and cell sizes in the 100-500 μm range with initial thermal conductivities around 20 mW $(m\ K)^{-1}$ and aged thermal conductivities lower than 30 mW $(m\ K)^{-1}$.

2.2. POLYURETHANE REACTIVE FOAMING

From a physicochemical perspective, RPU foams are prepared by mixing two low viscosity and low molecular weight components. Component A—isocyanate—and component B—a blend of polyol, catalyst, blowing agent and surfactant. The mixing results in several exothermic chemical reactions leading to foam expansion and polymerisation.

2.2.1. Chemical Background

The high reactivity of isocyanate groups is responsible for initiating several simultaneous reactions upon mixing the components. At the centre of PU foam formation are two reactions: polymerisation and blowing. Polymerisation, also known as gelling, occurs via an addition reaction between polyol and isocyanate. When polyfunctional reagents (polyisocyanates and polyols) are used, the polyaddition reaction leads to the generation of urethane crosslinks which yields a high molecular weight polymer network (Figure 2-2). This reaction is exothermic with a heat of reaction of -93.9 kJ mol^{-1} [5,6].

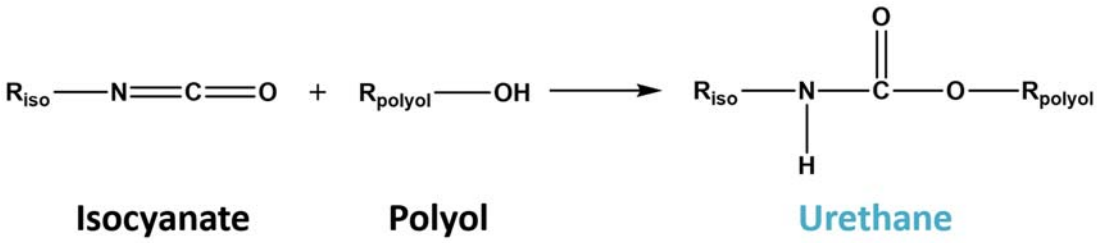

Figure 2-2: Polymerisation or gelling reaction.

In water-blown polyurethane foams, isocyanate reacts with water in a step condensation polymerisation reaction (Figure 2-3). This reaction is responsible for the generation of unstable carbamic acid, which spontaneously decomposes releasing amine and CO_2 gas as a by-product. In this reaction, every two moles of isocyanate react with one mole of water yielding one mole of CO_2 gas [7]. The amine is generated in the first step. Later through addition reaction, it reacts with a second isocyanate group generating urea hard segments [8]. The released gas is the driving force for blowing the foam and generating the cellular

structure. It is often accepted that the water-isocyanate reaction is completed before the polyol-isocyanate reaction [9,10]. This means that the blowing of the foam takes place at faster paces than polymerisation. Both reactions in Figure 2-3 are exothermic with -125.5 kJ mol^{-1} total heat of reaction [5].

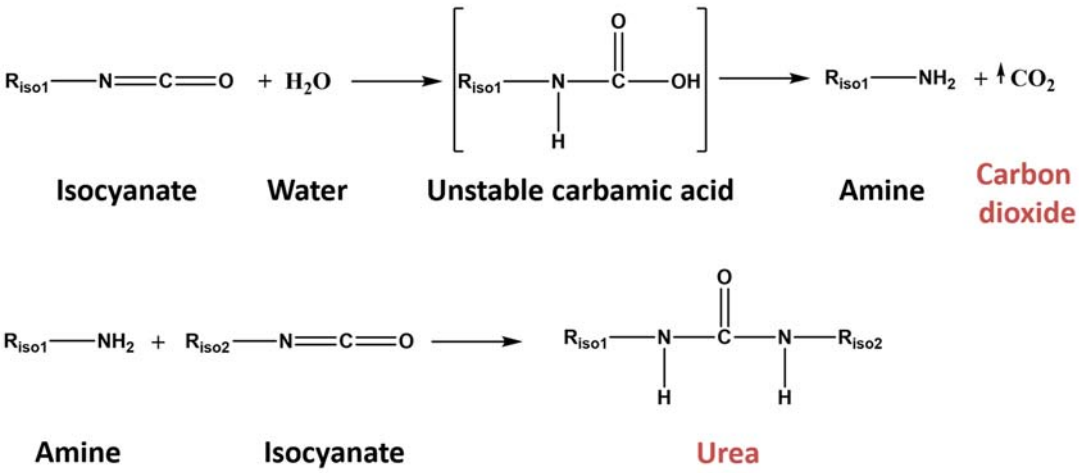

Figure 2-3: Blowing or foaming reaction.

Besides these two main reactions, the remaining isocyanate in the mixture can further react with other isocyanate groups and with urethane and urea products. Notable by-products of these reactions are allophanates, biuret, isocyanurate and carbodiimides [3,11].

2.2.2. Formulation Components

To produce RPU foams several commercial components are available. While polyols and isocyanates are by far the most important ingredients of the formulation other components such as, catalysts, blowing agents and surfactants, are essential to achieve full reaction of the isocyanate, more homogeneous cellular structures and improved properties.

On the one hand, polyols are the main source of hydroxyl groups in the reaction. When producing RPU foams they typically have high functionalities, larger than 3, and high OH numbers in the order of 400 mg KOH g^{-1}. Commonly used polyols can be either polyethers or polyesters, being polyether polyols the most commonly encountered [12]. On the other hand, isocyanates are typically aromatic isocyanates, such as toluene diisocyanate (TDI) or diphenylmethane diisocyanate (MDI). However, to obtain rigid foams, polymeric MDI is most commonly used, as it presents higher functionality than pure MDI or TDI and is much less hazardous. In the formulation of RPU foams, more isocyanate is added than what is theoretically needed to react with the hydrogen active groups in the formulation. This is reflected in the formulation of foams using the isocyanate index (eq. (2-1)) above 100 [13].

$$NCO\ index = \frac{Actual\ amount\ of\ isocyanate\ used}{Theoretical\ amount\ of\ isocyanate\ requiered} x100 \qquad (2\text{-}1)$$

Other additives are also added to the polyol component. First, catalysts are introduced to increase the reaction rate and modify the reaction balance in the formulation, enhancing either the polymerisation or blowing reaction [14]. The most commonly used catalysts are tertiary amines and tin catalysts [11]. Likewise, silicone surfactants are added to produce foams with more homogeneous cellular structures and prevent cell wall thinning [15]. Last but not least, other blowing agents besides water are often added to the formulation to boost gas generation and increase foam porosity without modifying the reaction balance. Two types of blowing agents are most commonly employed, chemical blowing agents which react with the isocyanate to produce gas, such as water, and physical blowing agents which are liquids of a low boiling point that vaporise by the heat released in the polyurethane reaction, common examples of physical blowing agents are hydrocarbons, hydrofluorocarbons and hydrofluorolefins [16].

2.2.3. Polymer Morphology Development

The development of the final polymer morphology in polyurethane foams is a complex process involving several rheological and physicochemical transformations [3]. On the one hand, the polymerisation reaction is responsible for creating a chemical crosslinking network based on urethane structures. Whereas, on the other hand, the blowing reaction generates CO_2 and polyurea-based hard segments which are chemically incompatible with polyol soft segments and tend to microphase separation with polyureas aggregating via hydrogen bonding (Figure 2-4). Once the chemical reactions stop, the final polymer morphology exhibits a close-meshed crosslinked structure reinforced with polyurea hard segments [17].

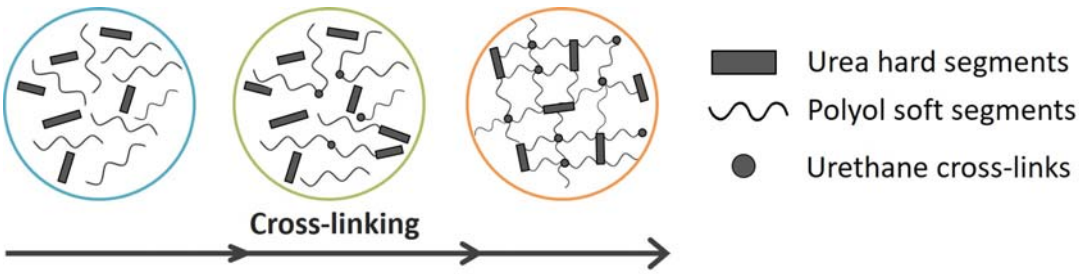

Figure 2-4: Development of the polymer morphology of RPU foams.

Simultaneous to the development of the polymer morphology the material transitions from a liquid state into a solid state as corresponding to a curing thermoset [18]. In RPU foaming, the heat needed to cure the foam is provided by the isocyanate exothermic reactions (Section 2.2.1) [13]. However, complete curing of RPU foams is a slow process and the final build-up of the polymer morphology can take up to several hours or even days to complete [3]. Nonetheless, several transformations can be recognised during the process.

Initially, the starting isocyanate and polyol are low viscosity polyfunctional monomers of low molecular weight, around 500 g mol^{-1}, and low glass transition temperature, -30 °C [19,20]. These monomers are fusible and partly soluble liquids [21]. Upon reaction, they progressively transform into an insoluble gel of evolving glass transition temperature, whilst the mixture starts to attain solid-like behaviour (Figure 2-5) [17,21,22]. At gelation, an incipient crosslinking polymer network forms. This instance is also characterised by a dramatic increase in the viscosity of the mixture and the weight average molecular weight goes to infinity [22]. As the reaction progresses a second transformation of major importance is reached, vitrification. At this stage, the material solidifies transforming into a glassy polymer. From this point on, the reaction rates are significantly reduced, the polymer morphology freezes, and the process of polymerisation becomes diffusion controlled [3]. This change in the polymer structure is accompanied by an increase of several orders of magnitude in the polymer modulus. Vitrification is also characterised by marking the point at which the evolving glass transition temperature of the polymer equals or surpasses the cure temperature [23]. After vitrification, the moduli and glass transition temperature slowly continue to grow until cure stops.

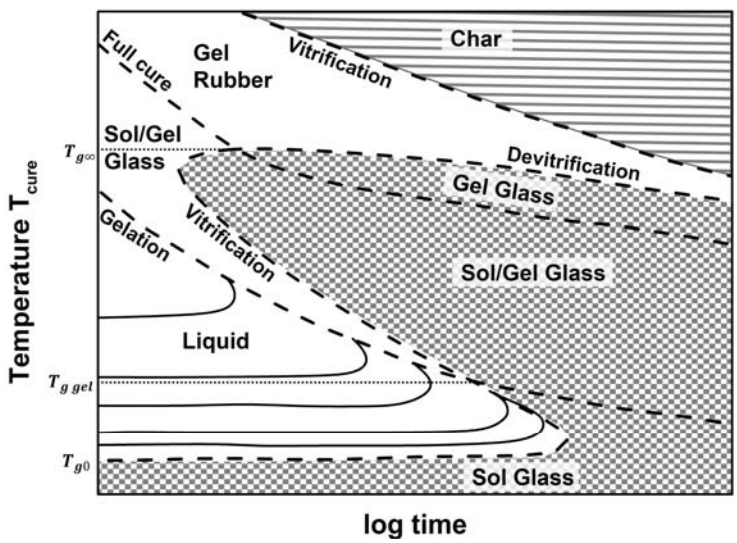

Figure 2-5: Schematic time-temperature-transformation (TTT) isothermal cure diagram for a thermosetting system. Reproduced from [22].

All these transformations take place at different paces depending on the formulation and largely vary with the reaction temperature (Figure 2-5). In Figure 2-5 the curing TTT diagram for a thermoset is displayed, showing three critical temperatures, T_{go}, $T_{g\ gel}$, $T_{g\infty}$ representing the glass transition temperature of the starting reactants, of the gel point and of the fully cured thermoset, respectively. In addition, the different states during cure are displayed: liquid, sol/gel rubber, gel rubber, sol/gel glass, gel glass, sol glass, and char. Although curing of RPU foams does not take place under isothermal conditions, the temperature inside the foam follows a quasi-parabolic profile [20,24], gelation takes place first and is followed by vitrification. Moreover, under normal processing conditions, the states of matter undergone by the polymer are liquid to gel rubber and finally to amorphous glass.

2.2.4. Cellular Structure Development

In thermosetting PU foams, cellular structure development takes place simultaneously with the polymer morphology build-up. Both events are mutually dependent and significantly condition the final cellular structure and properties. For instance, fast polymerisation and high matrix viscosities can restrict foam expansion early in the foaming process leading to foams of high density. In contrast, slow modulus build-up can cause excessive expansion and cellular structure degeneration due to weak cell walls. Therefore, appropriate timing of the competing reactions is a critical issue that can significantly modify foaming dynamics. In this section, the main events and models describing the cellular structure formation are detailed, namely nucleation, cell growth, cell degeneration and stabilisation.

2.2.4.1. Nucleation

Cell nucleation is the process responsible for forming gas nuclei in a liquid/gas medium after a change in the thermodynamic conditions [25]. According to classical nucleation theories, there are two possible mechanisms for the formation of nuclei in polymer foaming: homogeneous and heterogeneous nucleation [12,15,26]. Homogeneous or self-nucleation takes place in a homogeneous medium supersaturated with gas when the free energy of the system exceeds activation energy given by eq.(2-2) where σ is the surface tension of the liquid, and ΔP is the differential pressure between the system and the surroundings [3].

$$\Delta G^*{}_{homo} = \frac{16\pi\sigma^3}{3\Delta P^2} \tag{2-2}$$

Moreover, the homogeneous nucleation theory predicts that for a nucleus to spontaneously grow its radius has to be larger than the critical nuclei radius, r_{cr}, given by eq. (2-3).

$$r_{cr} = \frac{2\sigma}{\Delta P} \tag{2-3}$$

Yet, self-nucleation is not considered the primary mechanism by which most nuclei form in foams, since the activation energy required is too high [26]. In contrast, heterogeneous nucleation is supported by the presence of a second phase in the initial system. The presence of a secondary phase, such as solid nanoparticles or microbubbles, acts as a nucleating agent. Nucleation usually takes place on the surface of the nucleating agent and reduces the activation energy needed for nucleation (eq. (2-2)) [26]. In many processes, without solid nucleating agents, the liquid phase contains microbubbles of air, which serve as seeds for bubble growth [27].

As discussed in section 2.2.1 gas generation in water-blown PU foams is caused by the water-isocyanate reaction. Theoretically, nucleation should be induced when the gas exceeds the solubility limit of the mixture [2]. However, the mechanical agitation needed to trigger foam formation constitutes a well-known source of air entrapment in the mixture [2,4,28]. As aforementioned, the entrapped microbubbles may act as seeds for nucleation hindering self-nucleation by the dissolved CO_2 molecules [4,29]. Hence, in most cases, CO_2 diffusion into the entrapped air bubbles proceeds so quickly that nucleation of new bubbles is prevented. Macroscopically the characteristic timescale of nucleation in PU foams can be detected by a change in colour (from dark brown to white) of the reactive mixture. This constitutes the instance at which CO_2 gas dissolved in the liquid exceeds the solubility limit triggering cell growth. This instant is usually known as cream time as the mixture acquires a creamy viscous appearance [20].

2.2.4.2. Cell Growth

After cell nucleation bubbles grow due to the diffusion of the CO_2 gas molecules from regions of higher pressure, the reactive mixture, to regions of lower pressure, the nuclei. The process involves the expansion of several bubbles with a limited supply of gas [30]. This competitive growth of cells in a liquid medium is governed by coupled mass and momentum

conservation equations where several factors are at play, mainly diffusion, temperature, viscosity, and surface tension [2]. To describe the evolving radius of a spherical cell, Amon and Denson [30,31] introduced the concept of the liquid envelope of radius *S(t),* which represents the specific amount of liquid saturated with gas for each cell. This model accounts for the growth of a given number of bubbles with limited gas supply and assumes that no degenerations mechanisms take place. Every cell is assumed to be spherical and consists of a single glass bubble surrounded by its concentric liquid envelope. Initially, the cell has a radius R_o and internal pressure P_{go}. As the bubble radius, *R(t)*, increases the radius of the envelope, *S(t)* thins while its initial size is conditioned by the number of nucleated cells, N_{cells}, which is assumed to remain constant in the cell model [30].

$$S_o = \left(\frac{3}{4\pi N_{cells}}\right)^{1/3} \tag{2-4}$$

$$S(t) = (S_o^3 + R(t)^3 - R_o^3)^{1/3} \tag{2-5}$$

As the bubble starts to grow a concentration gradient, *c(r,t)*, is established inside the liquid envelope whose evolution is governed by the diffusion equation (eq. (2-6)). The gas in the liquid is assumed to behave as an ideal gas of constant diffusivity, *D*, during expansion.

$$\frac{dc}{dt} + \frac{\dot{R}\,R^2}{r^2}\left(\frac{\partial c}{\partial r}\right) = \frac{D}{r^2}\frac{\partial}{\partial r}\left(r^2\frac{\partial c}{\partial r}\right) \tag{2-6}$$

As diffusion proceeds, the pressure inside the cell will decrease. Through the conservation of mass equation on the bubble surface, it is possible to obtain a relationship (eq. (2-7)) between gas pressure, P_g, inside the cells and the bubble radius, *R* [32]. In eq. (2-7), R_g is the universal gas constant, ρ is the density of the polymer mixture, *T* is the gas temperature, and *M is* the molecular weight of the gas.

$$\frac{dP_g}{dt} = \frac{a}{R}\left(\frac{dc}{dr}\right)_{r=R} - 3P_g\left(\frac{\dot{R}}{R}\right) \; where\ a = \frac{3R_gT\rho D}{M} \tag{2-7}$$

In addition, the conservation of momentum equation permits to calculate the cell radius assuming that the liquid reactive mixture is a Newtonian incompressible fluid of viscosity η_o.

$$\frac{dR}{dt} = R\left(\frac{P_g - P_a - 2\sigma/R}{4\eta_o}\right)\left(\frac{S^3}{S^3 - R^3}\right) \tag{2-8}$$

By solving the coupled system of equations formed by eq. (2-5), (2-6), (2-7) and (2-8) it is possible to obtain the evolution of cell size with time.

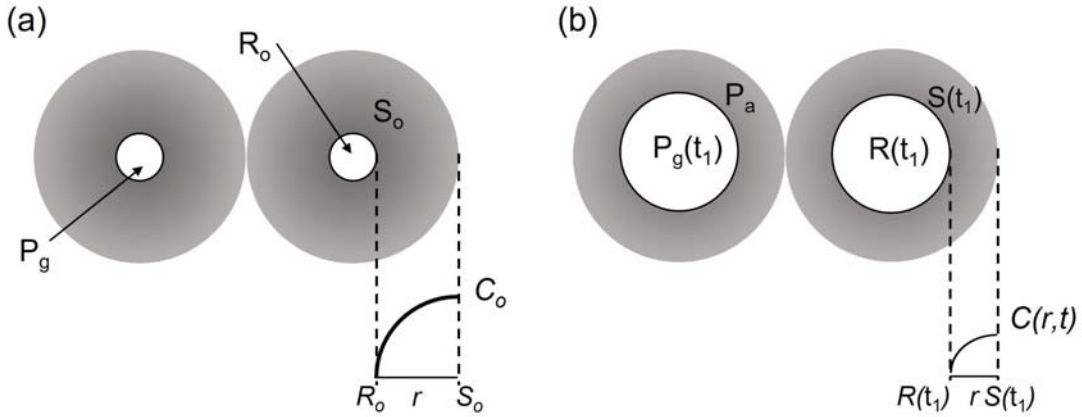

Figure 2-6: Schematic representation of the Amon and Denson cell model: (a) start of cell growth with the hypothetical concentration profile in the liquid envelope, (b) after cell growth the envelope thins while the gas concentration profile flattens.

2.2.4.3. Cell Degeneration and Stabilisation

During foaming continuous gas generation leads to the impingement of the growing cells. This wet-dry transition is responsible for the cells losing their spherical geometry and, as they come into close contact, they begin to attain polyhedral shapes [33]. At this stage, the thickness of the liquid matrix between the cells minimises which constitutes a potential source of cell wall ruptures. Degeneration mechanisms are responsible for decreasing the cell density in the foam and increasing cell size due to the merging of neighbouring cells. In this section three degeneration mechanisms are discussed: drainage, coalescence and coarsening [2].

Drainage is caused by capillary forces action that produces transport of liquid material from the cell walls towards the edges and struts of the cells. This mechanism is most frequently found in the case of low viscosity systems, such as flexible PU foams. It can also take place in rigid PU foams, and it modifies the amount of material in the edges and struts. Progressive thinning below the critical thickness of the cell walls can cause wall ruptures and eventually coalesce [2]. Coalescence is the degeneration mechanism by which a cell wall breaks and two adjacent cells merge increasing the average size of the cells in the foam. Last but not least, coarsening consists of gas motion promoted by diffusion from the smaller cells (with higher internal pressure) to the larger adjacent cells (with lower internal pressure). Therefore, the small cells reduce its size and eventually can disappear increasing the average

size of those remaining. This mechanism can also produce heterogeneous cellular structures with large and small cells (bimodal cell size distribution) [20].

While degeneration is a naturally occurring phenomenon in most low density foams it must be avoided if obtaining fine structures of small cells is the objective. In rigid PU foams, stabilisation is achieved through the addition of surfactants and by crosslinking of the reacting system. In these foams, expansion and degeneration proceed even once gelation has taken place. Degeneration in PU foams takes place in many cases as a consequence of the mismatch between the time scales of viscosity growth (polymerisation reaction) and expansion rate (blowing reaction).

Macroscopically, two main characteristic times can be observed during the cell growth and stabilisation stage. In the first place, string time can be identified as the time when the matrix has developed enough gel strength and strings of polymer can be pulled out by dipping a sharp object into the foam mixture. While rise time is the time at which the foam stops growing [20].

2.2.4.4. Solidification and Final Cure

After bubble growth and degeneration, structural changes are arrested by vitrification. At this stage, full solidification of the cellular structure is reached. Solidification is the result of a large increase in the modulus of the polymer matrix yielding the cell walls with enough strength to withstand the gas pressure inside the cells. The foam starts to cool down by slowly dissipating the heat produced in the chemical reactions. However, curing is still ongoing as the modulus of the foam continues to increase at a slow pace until residual reactivity stops and the covalent crosslinks are completed. This last stage of curing is typically only associated to a change in the polymer morphology, and it rarely involves changes in the cellular structure.

2.2.5. Final Cellular Structure

Once the foaming process concludes the cells form a closed-packed structure in which individual cells have polyhedral shapes and are separated by thin solid regions in closed cell foams. This high degree of close-packing is characteristic of materials of high volume expansion. The expansion degree can be understood in terms of its relative density, ρ_r, which represents the fraction of solid material in the final foam (eq. (2-9)). It is calculated as the ratio of the foam density, ρ_f, by the density of the solid matrix, ρ_s.

$$\rho_r = \frac{\rho_f}{\rho_s} \tag{2-9}$$

The relative density of the foam can be used to estimate the total porosity, V_f, of the material which is defined according to eq. (2-10). Just like relative density represents the volume fraction of solid, likewise porosity accounts for the volume fraction of gas in the foam.

$$V_f = 1 - \rho_r \tag{2-10}$$

The gas and solid phase organisation in foams can be better understood using various structural descriptors. Some of the most widespread descriptors in the literature are detailed in the following sections.

2.2.5.1. Gas Phase Descriptors

Average cell size, Φ, typically corresponds to the average diameter of the cells assuming that they have quasi-spherical geometry. As foams are intrinsically heterogeneous materials with cells of different sizes, it is important to analyse a large number of cells to have statistically reliable data and obtain the cell size distribution. The homogeneity of the cellular structure can be inferred from the analysis of the sizes of a large population of cells. The ratio of the standard deviation, *SD*, of the cell size distribution by the average cell size, SD/Φ, represents the homogeneity of the structure. The larger this descriptor is, the more heterogeneous is the cellular structure.

In certain cases, the cells can be elongated or flattened in one of their dimensions. In such cases, the anisotropy of the cell can be quantified using the *anisotropy ratio*, *AR*, which is defined as the ratio between the cell size in two perpendicular directions (eq. (2-11)). When *AR* exceeds or falls below 1 the structure is characterised by a strong anisotropy in one of the directions. By contrast, *AR* values close to 1 correspond to isotropic structures (Figure 2-7). The concept of anisotropy can be extended to all cells and an average anisotropy ratio for the cellular structure can be used to quantify the degree of cells orientation in the foam.

$$AR = \frac{\Phi_y}{\Phi_x} \tag{2-11}$$

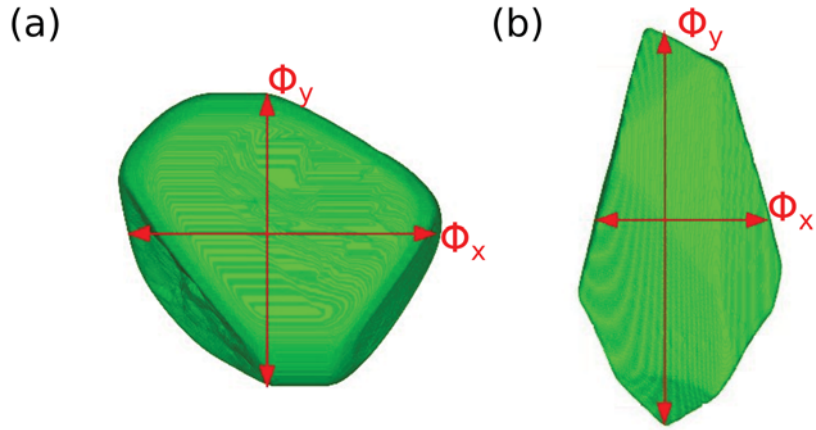

Figure 2-7: Tomographic 3D rendering of an (a) isotropic cell in the directions X and Y and (b) anisotropic cell elongated in the Y direction.

The *cell density*, N_v, in foams is simply defined as the number of cells per unit volume of foam. Theoretically, this magnitude is related to the relative density of the foam and the average cell size as given by eq. (2-12) [34].

$$N_v = \frac{6}{\pi \Phi^3}(1 - \rho_r) \tag{2-12}$$

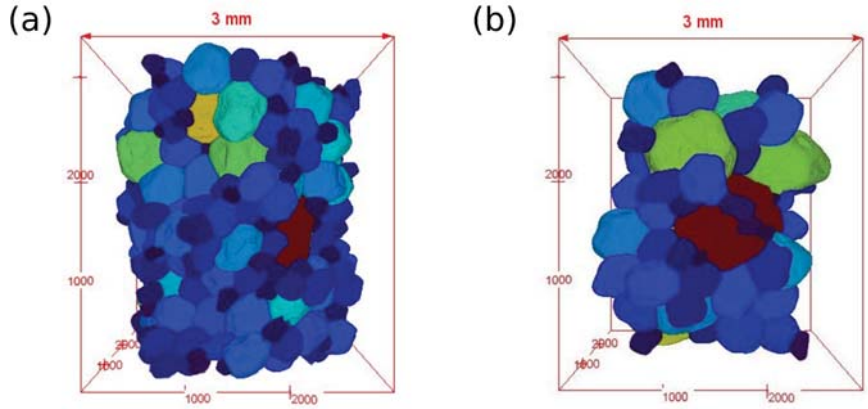

Figure 2-8: Tomographic 3D rendering of two foams of similar density but different cell density

The cellular structure of foams can be very diverse and, for instance, foams with the same relative density can have very different cell densities and as a consequence cell sizes (Figure 2-8). In addition, from the cell density and assuming that there were no degeneration events during the foaming process the *cell nucleation density* can be obtained, N_o, following eq. (2-13). The expression in eq. (2-13) gives an estimation of the number of nucleation sites per volume of solid material. If this parameter were measured over time during the foaming process it can give an estimation of the initial number of nucleation sites or the presence of degeneration mechanisms if N_o decreases during foaming [35,36].

$$N_o = \frac{N_v}{\rho_r} \tag{2-13}$$

2.2.5.2. Solid Phase Descriptors

Within the solid matrix, two main structures can be distinguished: cell walls and struts. Assuming that the cells are polyhedral units the faces are the cell walls, while, the edges and vertices of the polyhedrons constitute the struts, also known as Plateau borders [37]. The solid fraction is divided between these two different regions. The study of the solid phase distribution is of great significance as it has influence on the material physical properties, such as thermal conductivity or mechanical performance [38,39].

These structures can be recognised either by their thickness or by their relative contribution to the total solid volume: *fraction of mass in the struts*. On the one hand, the *thickness of the struts*, ζ, is typically quite large. The struts are the thickest elements in the matrix, as they constitute the merging point of three or more cell walls. Conversely, *cell walls thickness*, δ, is rather low near 1 µm for most low density foams. Walls are the thinnest elements in the matrix as the foaming process minimises the separation between adjacent cells (section 2.2.4.3). On the other hand, the solid mass can be either preferentially located in the struts or the cell walls. For PU foams the solid mass is preferentially located in the struts leading to foams with a high fraction of mass in the struts (Figure 2-9) [40].

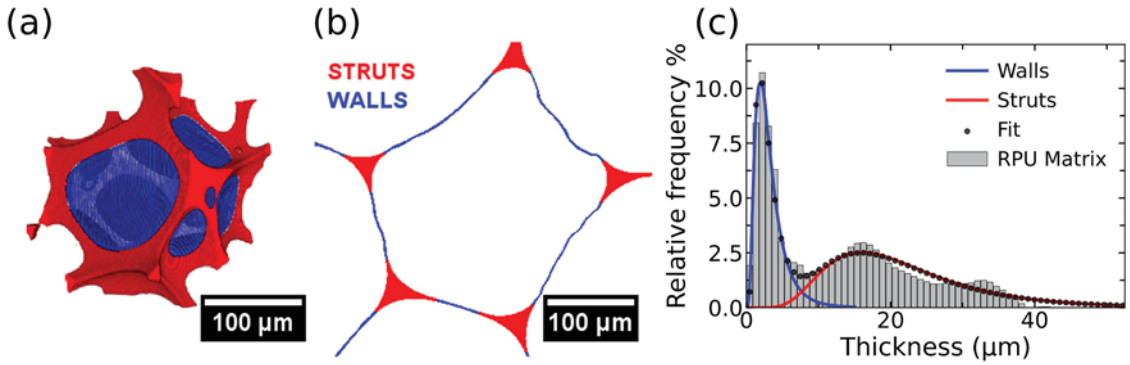

Figure 2-9: (a) Tomographic 3D rendering of a cell showing the struts (red) and the cell walls (blue) of a PU foam (b) cross-sectional view of the solid matrix of a single cell and (c) thickness distribution of the solid matrix of a PU foam in which walls and struts contribution have been separated by a deconvolution process.

Hence, one of the most useful parameters to describe the solid matrix organisation is the *fraction of mass in the struts*, f_s (eq. (2-14)). It represents the volumetric or mass fraction of material located in the struts, m_s, with respect to the entire solid matrix, walls, m_w, and struts, m_s.

$$f_s = \frac{m_s}{m_w + m_s} \tag{2-14}$$

2.3. PROBING INTO POLYURETHANE REACTIVE FOAMING

As highlighted in previous sections, the reactive foaming process is a complex phenomenon in which several mechanisms are at play. For such reason, there is a quest for developing experimental protocols permitting to probe into the morphological, rheological and chemical development of PU foams. In this section, the state of the art of these techniques is discussed.

2.3.1. Reaction Kinetics

In the current literature, there are a few well-established methods to follow the reaction kinetics of PU foams. Among them, three techniques stand out: Adiabatic Temperature Rise, Small Angle X-ray Scattering (SAXS) and Fourier Transform Infrared (FTIR) spectroscopy.

2.3.1.1. Adiabatic Temperature Rise

Firstly, the Adiabatic Temperature Rise method permits monitoring the heat released as a result of the exothermic polyurethane reactions, section 2.2.1 [41,42]. To that end, thermocouples are inserted inside the beaker where the foaming is going to take place. Typically, reactants are mixed in a different container and then poured into the beaker containing the thermocouples. As the cellular structure of the RPU foam is being formed, the centre of foam is isolated from its surroundings, so it can be considered an adiabatic system. The thermocouples provide the temperature profile during foaming which is mainly related to the consumption of isocyanate groups [42]. In general, high reaction temperatures are related to high isocyanate conversion levels. Also, higher water concentrations are associated with higher foaming temperatures, as the blowing reaction is more exothermic than the polymerisation reaction (section 2.2.1) [43]. This method is the most straightforward of all those permitting probing into the PU reaction kinetics. For such reason, in the literature, there are numerous reports concerning the influence of blowing agents, catalysts and fillers on the PU reaction temperature profile [24,43,44].

Zhao et al. [44] studied the impact of different catalysts and catalyst loadings on the reaction kinetics of RPU foams using the Adiabatic Temperature Rise method. The authors observed how the catalyst concentration is directly proportional to the reaction rate. Hence, increasing catalyst loading leads to higher reaction rates and temperatures (Figure 2-10 (a)).

Moreover, the presence of fillers has also been proved to significantly modify the reaction temperatures.

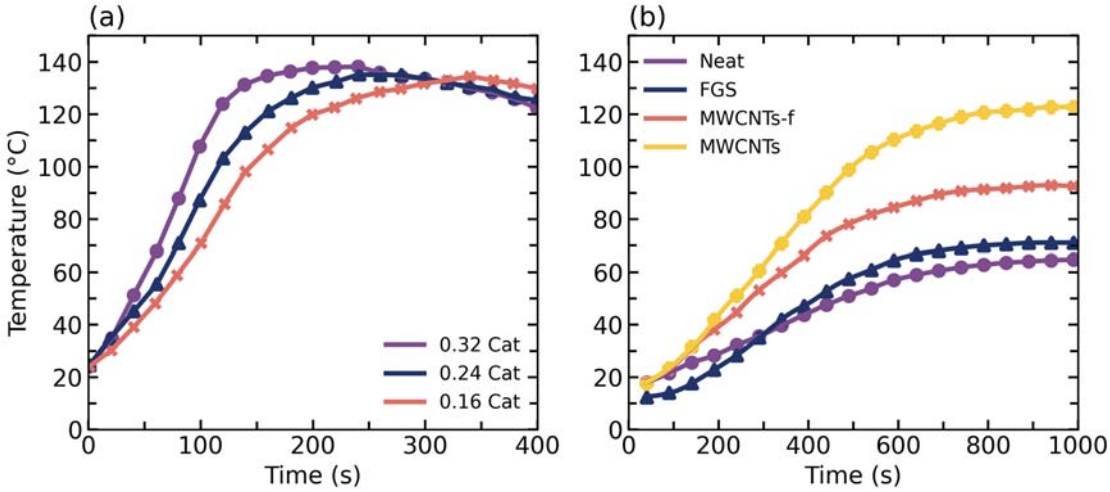

Figure 2-10: Evolution of the internal reaction temperature of (a) RPU foams with different catalyst concentrations [44] and (b) RPU nanocomposite foams in the study of Bernal et al [45].

Bernal et al. [45] recorded the temperature rise profile in nanocomposite foams. A thermocouple was located in the centre of the foam during its expansion. The authors observed how the addition of multi-walled carbon nanotubes (MWCNTs) and graphene sheets (FGS) drastically increased the internal temperature during the formation of RPU foams (Figure 2-10 (b)). The nanofillers increased the thermal conductivity of the reactive mixture accelerating in turn the reaction. An in-depth exploration of the reaction kinetics using FTIR spectroscopy revealed that while the final isocyanate conversion is similar for the reference and the nanocomposite RPU foams, at the start of the reaction the nanocomposite foams have faster conversion rates.

2.3.1.2. Small Angle X-ray Scattering

Another technique for monitoring the reaction kinetics is Small Angle X-ray Scattering (SAXS). This technique is a powerful way of measuring the degree of hard/soft segment segregation. However, it is less widespread as it requires synchrotron X-ray intensity [46–48]. In SAXS experiments the scattered X-ray intensity by the evolving foams is sequentially collected. By representing the scattered intensity versus the scattering vector at different reaction times (Figure 2-11 (a)) it is possible to observe the curve evolution from a flat profile, when the mixture was a homogeneous liquid, into a peak representing the

development of a microphase separated morphology which progressively increases until vitrification of the morphology is reached [46].

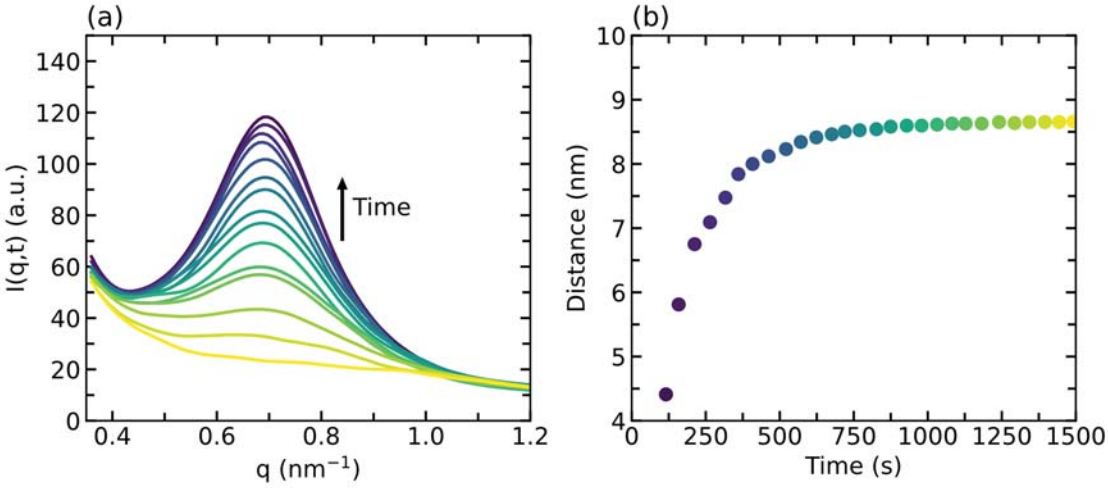

Figure 2-11: (a) Evolution of the scattered intensity, *I(q, t)* vs the scattering vector, *q*, with reaction time and (b) evolution of the interdomain spacing with time for a flexible PU foam. Reproduced from [46].

The maximum in the scattered intensity curves is indicative of the existence of a periodic structure. Periodicity arises from the urea hard segments, thereby the average interdomain spacing can be evaluated using Bragg's Law (eq. (2-15)) and the scattering vector at the maximum of Figure 2-11 (a) [46].

$$distance = \frac{2\pi}{q_{max}} \tag{2-15}$$

Some authors have ascribed the increase in the interdomain spacing (Figure 2-11 (b)) to an increase in the size of the urea hard segments [49]. In the literature, this type of analysis of the polymer morphology build-up is most frequent for flexible polyurethane foams since these materials exhibit stronger microphase separation [46,48,49].

2.3.1.3. In situ FTIR Spectroscopy

Lastly, FTIR spectroscopy constitutes one of the most frequently used techniques to follow the polyurethane reaction kinetics [43,50]. In the acquired PU spectra (Figure 2-12), several specific bands provide information about the extent of the polymerisation and blowing reactions, Figure 2-2 and Figure 2-3. The band at 2270 cm^{-1} corresponds to the asymmetric stretching vibrations of the isocyanate group. The intensity of the isocyanate band decreases over time as the polymer morphology develops at the expense of the isocyanate groups being consumed in the reaction.

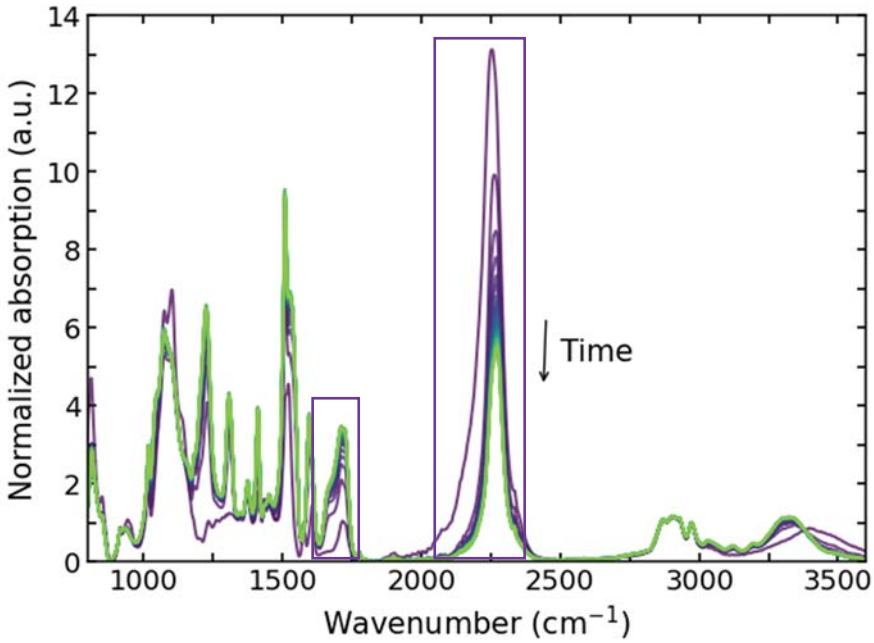

Figure 2-12: Evolution of the FTIR spectra of a RPU foam with the reaction time. The main regions of interest (isocyanate and carbonyl band) are highlighted.

In addition, the region of the spectra between 1800-1600 cm^{-1} corresponds to the carbonyl or amide I band which represent the stretching vibrations of the carbonyl groups present in reaction products. However, this region of the spectra conceals many hidden peaks resulting from the groups generated in the polymerisation (Figure 2-13) and blowing reactions (Figure 2-14). To obtain the individual contributions of each group or at least the urethane/urea relative contribution a deconvolution procedure of the amide, I region has been used [51].

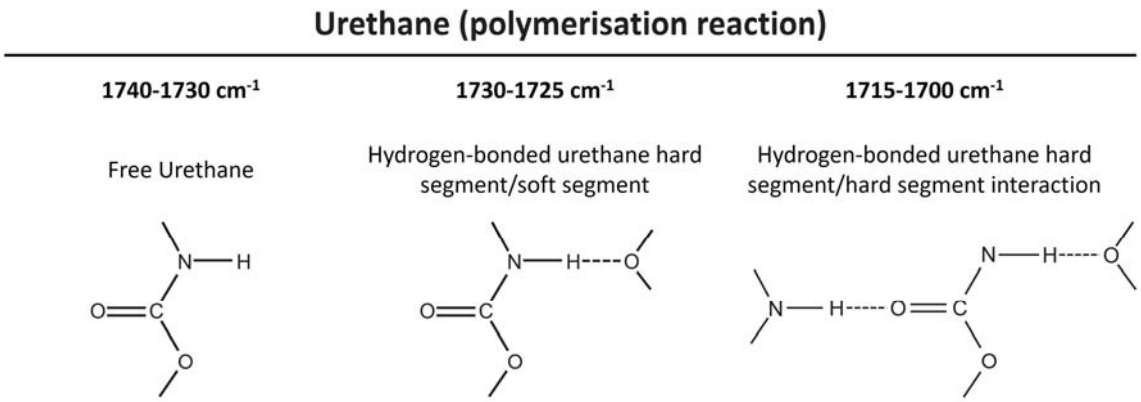

Figure 2-13: Characteristic frequencies of the urethane groups present in the carbonyl region including free urethane and hydrogen-bonded urethane [49,50,52–56].

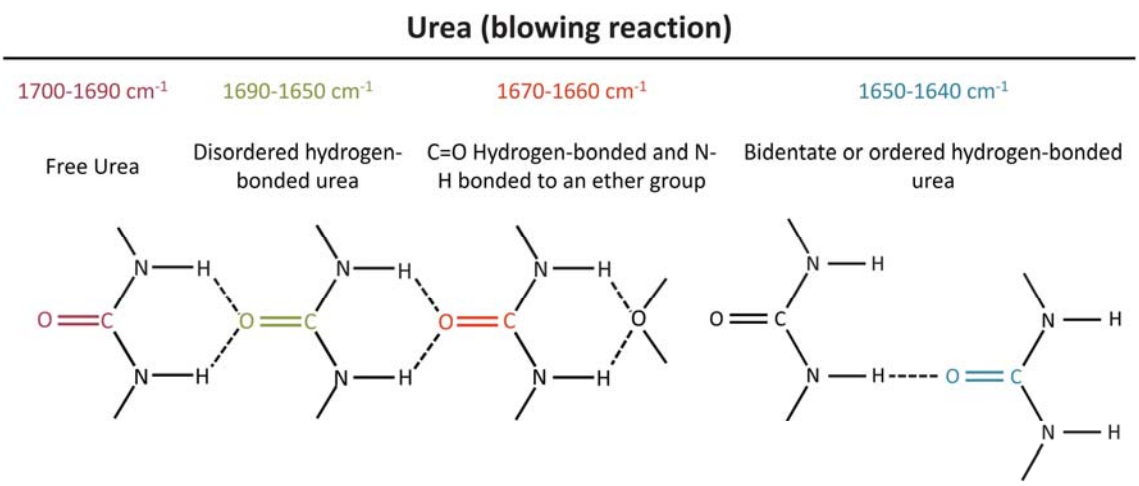

Figure 2-14: Characteristic frequencies of the urea groups generated during the blowing reaction including free urea and hydrogen-bonded urea [49,50,56–60].

Examples of the use of dynamic FTIR spectroscopy to follow the reaction kinetics of PU foams are frequently found in the literature [24,43,50,51,61,62]. Historically, FTIR was used to probe the reaction kinetics of flexible polyurethane foams [50,57]. Yet, in recent years, partly due to the increasing popularity of nanocomposite foams, it has been mostly applied to investigate the impact of additives and fillers on the isocyanate conversion and reaction balance [24,51,61,62]. The literature on this technique is ever-growing, hence only a few selected works are discussed here as characteristic examples.

Akkoyun et al. [62] studied the effects of shape, surface area, surface functional groups and concentration of different nanofillers, such as titanium dioxide, zinc oxide, and magnetite (1 or 10 wt. % in polyol), on the RPU foam formation reaction. They calculated the isocyanate consumption at different reaction times using eq. (2-16) which relates the area under the normalised isocyanate band at time 0 of reaction, A_o, with the normalised area, A_t, under the isocyanate band at time t.

$$P_{NCO}(t) = 1 - \frac{A_t}{A_o} \qquad (2\text{-}16)$$

The results revealed a non-linear response of the isocyanate consumption with the concentration of nanofillers. For low concentrations of nanofillers, isocyanate consumption changed slightly with respect to the unfilled foam. Consumption was dominated by the viscosity of the reactants rather than by the shape or type of nanofiller. For high concentrations, the consumption rate increased indicating that above a critical concentration, the nanofillers may act as catalysts for the reaction. This behaviour was related to the critical surface area of the nanofillers, above a critical surface area (30 $m^2\ g^{-1}$

in this study), regardless of the nanofiller type, the reaction rate increased with increasing surface area. Moreover, the nanofillers reduced the final cell size of the foam when added below the critical surface area, whereas above this critical value the cell size distribution became wider. Thus, the increase of the reaction rate, induced by the high concentration of nanofillers, lead to coalescence which resulted in a more heterogeneous cellular structure.

Santiago-Calvo et al. [51] investigated the impact of functional nanofillers on the reaction kinetics of RPU foams using ATR-FTIR spectroscopy. The carbonyl region in the spectra (1800-1600 cm^{-1}) was deconvoluted to evaluate how the balance of the reactions was disrupted by the nanofiller presence. The amide I region (Figure 2-15 (a)) was deconvoluted in 7 peaks each associated with the vibrations of the urea and urethane groups produced in the reaction (Figure 2-13 and Figure 2-14). Detection of the hidden peaks in the spectra was achieved by examining the second derivative of the spectra (Figure 2-15 (b)). The deconvolution procedure enabled the authors to obtain the relative contribution of urea and urethane products as well as the urethane/urea ratio in every foam as a function of time [51]. The quantification was achieved by applying eq. (2-17), (2-18) and (2-19).

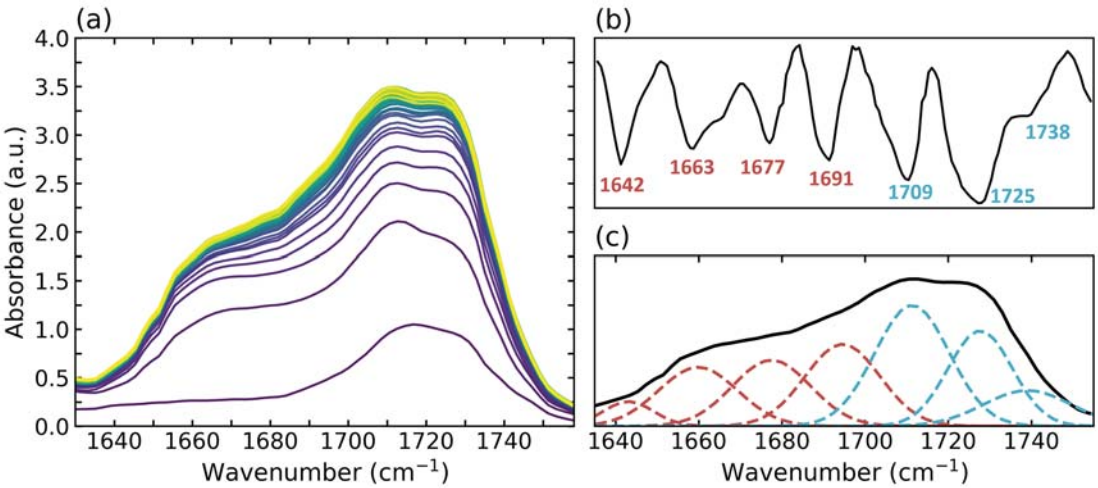

Figure 2-15: Example of the deconvolution of amide I region for a RPU foam (a) evolution of the amide I region. (b) Second derivate of the amide I region. (c) Curve-fitting for the amide I region

$$Relative\ Area\ Urea\ \% = \frac{\sum A_{C=O\ Urea}}{\sum A_{amide\ I}} \quad (2\text{-}17)$$

$$Relative\ Area\ Urethane\ \% = \frac{\sum A_{C=O\ Urethane}}{\sum A_{amide\ I}} \quad (2\text{-}18)$$

$$Urethane/Urea\ Ratio = \frac{\sum A_{C=O\ Urethane}}{\sum A_{C=O\ Urea}} \quad (2\text{-}19)$$

The authors observed how at short times the urethane/urea ratio decreased for all foams as a result of the fast consumption of water to blow the foam. In addition, fillers with hydrophilic surface treatments enhanced the blowing reaction as a consequence of the water absorbed in their surface. This enhancement led to higher urea ratios in the final foam morphology.

In another work by Santiago-Calvo et al. [24] foams were synthesised using polyols functionalised with different concentrations of graphene oxide (GO) nanoparticles. The authors analysed the isocyanate consumption and product generation during the nanocomposites foaming. They observed how the introduction of GO reduces the overall isocyanate consumption (Figure 2-16 (a)) and reaction temperature (measured by the Adiabatic Temperature Rise method). The decrease in isocyanate consumption for the nanocomposite foam was ascribed to the higher viscosity of the polyol functionalised with GO nanoparticles. The particle addition also caused an increase in the polymerisation reaction at the early stages of the foaming process (Figure 2-16 (b)). This enhancement resulted in an increased foam expansion and finer cellular structures. The authors elucidated that the faster polymerisation reaction promoted more efficient retention of the CO_2 gas by the mixture.

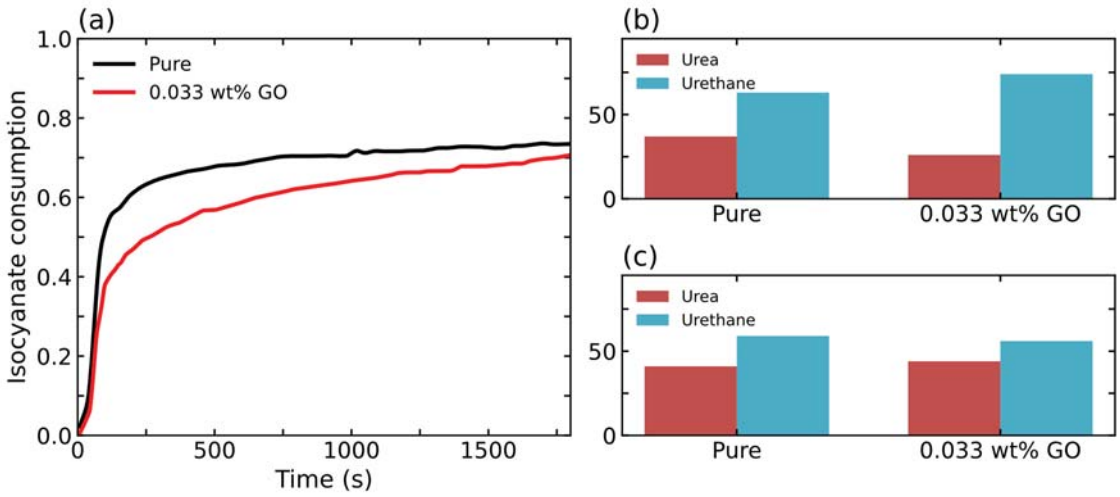

Figure 2-16: (a) Isocyanate conversion versus time for pure foam and for the foam with 0.033 wt.% GO. Relative area percentage of the absorbances of urea or urethane (b) at the initial time, (c) one month after the production of the foam [24].

In addition, the previous information was used to modify formulations seeking to improve the insulation and mechanical performance of the final foams. To that end in a later study, the isocyanate index, as well as the surfactant and catalyst concentrations, were fine-

tuned to obtain more homogenous and smaller cells in the cellular structure of these materials [63].

2.3.2. Matrix Polymerisation

The discussion in the previous section was articulated around the techniques enabling monitoring of the extent of the chemical reactions in PU foams. However, the curing of PU foams involves complex transformations from mobile liquids to rubbery, or even rigid, foams which cannot be fully understood in terms of reaction kinetics. To date, the main methods used to follow the curing process in thermosetting foams rely either on electrical resistivity and sound absorption measurements or on rheological characterisations of the evolving foam [18,23,61,64–70].

2.3.2.1. Electrical Resistivity and Sound Attenuation

The use of electrical resistivity measurements to identify the start/end of the main stages of PU foam formation (cream, rise, packing, gelation and solidification) and polymerisation rate was first suggested by Torres-Sánchez et al. [64,65]. The proposed method registered electrical resistivity in the material during foaming. The sample was immersed in a water bath of controlled temperature and subjected to ultrasound irradiation (sonicated). Electrical measurements revealed that resistivity varies greatly when the foam evolves from a liquid mixture into a crosslinked network (Figure 2-17 (a)).

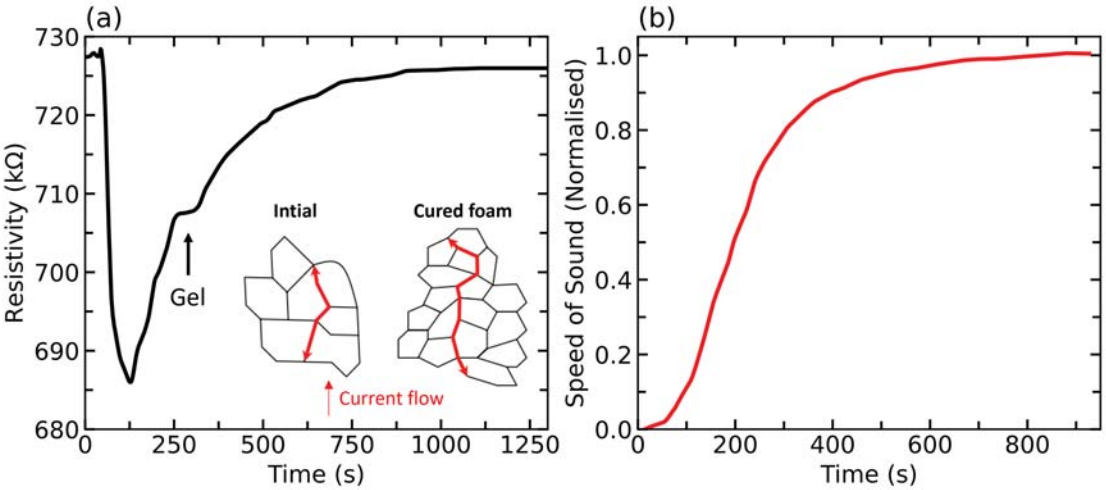

Figure 2-17: (a) Electrical resistivity profile evolution with reaction time and (b) normalised speed of sound (equivalent to the curing degree) evolution during foaming as reported by Torres-Sanchez [64] and Holt [65], respectively.

The resistivity profile (Figure 2-17 (a)) shows an asymptotic behaviour. Initially, resistivity decreases down to a minimum which corresponds with the start of the reaction. Later, it increases until stabilisation indicating the end of the reaction. The asymptote represents the time at which maximum expansion is reached and the material undergoes a transition from a wet to a dry regime. In addition, a distinctive 'shoulder' step appeared in the electrical resistivity measurements indicating the instance of gelation.

In a follow-up study, Holt et al. [65] measured the speed of sound during foaming for sound waves travelling perpendicular to the foam expansion direction (Figure 2-17 (b)). The sound waves were generated by a signal generator connected to an oscilloscope and an amplifier. The propagated waves were registered by a transducer located opposite the emitter transducer. The receiver transducer was connected to an oscilloscope that records the signal. From the recorded speed of sound and eq.(2-20), the degree of cure (assuming 100% cure at the end of the process) was calculated.

$$\alpha = \frac{c_i - c_o}{c_\infty - c_o} \tag{2-20}$$

In eq. (2-20) c_i is the instantaneous speed of sound, c_∞ is the final speed of sound and c_0 is the speed of sound at time 0.

While both works are interesting contributions to the topic, these techniques present several shortcomings as the real viscoelastic properties of the foam cannot be measured and the identification of the main stages of foam polymerisation can result ambiguous. Hence, other approaches permitting direct measurement of the rheological properties have been developed.

2.3.2.2. Rheology

Rheological methods are by far the most widespread when studying the curing kinetics of thermosets. To that end, either vane rheometers or flooded parallel plate rheometers are used [57,66,67,69,71,72]. Mora et al. [67] were the first to suggest the use of oscillatory shear rheology with a flooded parallel plate geometry to measure the viscoelastic properties development in expanding flexible PU foams (Figure 2-19). The technique is known for permitting analysis of the linear viscoelastic properties of polymers. During the test, the sample was deformed in an oscillatory shear flow in a plate-cup configuration at a gap of 2.5 mm (Figure 2-19 (a)). The upper plate oscillated with a certain angular frequency, ω, while the bottom cup remained stationary. A constant 5% strain deformation at 6.28 rad s^{-1} was

used for the measurements. In these experiments, the viscoelastic response of the polymer can be identified by the phase shift, δ, (Figure 2-18) between the applied shear strain, ε, (eq. (2-21)) and shear stress, σ, (eq. (2-22)) curves.

$$\varepsilon = \varepsilon_0 \, sin(\omega t) \tag{2-21}$$

$$\sigma = \sigma_0 \, sin(\omega t + \delta) \tag{2-22}$$

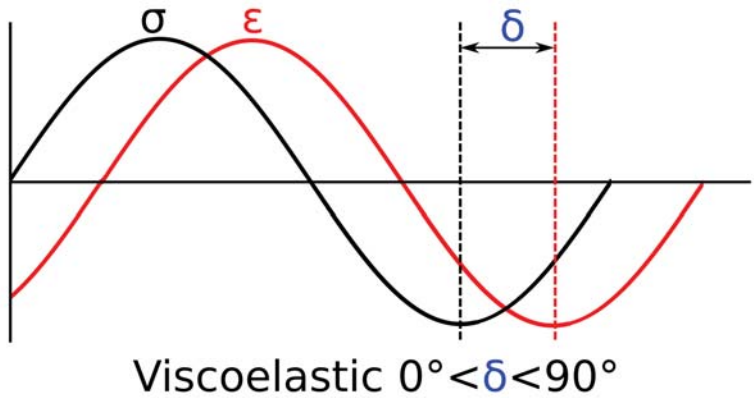

Figure 2-18: Sinusoidal behaviour of the stress, σ, and strain, ε, for a viscoelastic material. The phase angle between both curves varies between 0° and 90°.

The phase shift is also known as the loss angle. It indicates whether the material behaves as an ideal elastic solid, $\delta=0°$, or as an ideal viscous liquid if $\delta=90°$. However, in most polymeric materials the loss angle is between 0° and 90°. In addition, the storage or elastic modulus, G' (eq. (2-23)), and the loss or viscous modulus, G'' (eq. (2-24)), were registered and they are a measure of the deformation energy stored and the deformation energy dissipated by the sample during the shear process, respectively.

$$G' = \frac{\sigma_0}{\varepsilon_0} cos(\delta) \tag{2-23}$$

$$G'' = \frac{\sigma_0}{\varepsilon_0} sin(\delta) \tag{2-24}$$

If the material is purely elastic, it means that it stores the whole deformation energy applied and shows reversible deformation behaviour. In contrast, viscous materials show irreversible deformation behaviour as they consume energy [73].

In the work performed by Mora et al., the storage and loss modulus evolution with reaction time was registered (Figure 2-19 (b)). They identified four main phenomenological stages related to the main events of PU foam formation. In the first stage, the loss modulus is higher than the storage modulus as corresponding to the viscous reactants. Afterwards, both moduli of the reactive foam rise in more than two decades. At the end of this stage, the

storage modulus has a higher value than the loss modulus indicating a solid-like behaviour of the mixture [67]. Microscopically, this region corresponds to the bubble nucleation stage. In the second stage, the moduli remain relatively unchanged with the material exhibiting a solid-like behaviour characteristic of liquid foams [74]. At this point, the matrix is a low modulus gel of low molecular weight and low viscosity. Thirdly, at the onset of phase separation, both moduli undergo a rapid rise due to the stiffening of the polymer matrix. For flexible PU foams, this stage has also been recognised to occur simultaneously with the opening of the cell walls at maximum foam expansion [67]. Afterwards, the reactions continue but become diffusion controlled, the foam reaches its maximum temperature and final modulus.

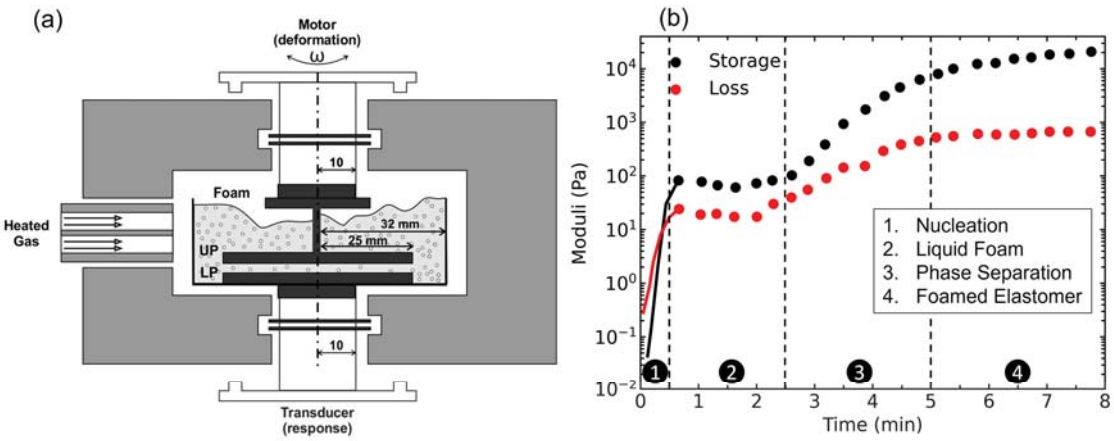

Figure 2-19: (a) Schematic of the flooded parallel plate set-up and (b) rheological evolution and main stages of foam formation reproduced from the work by Mora et al. [67].

This work besides being the first to recognise the main regions of rheological development during PU foaming also studied the changes in modulus build-up when the water and catalyst level in the foams changed. The authors detected that as the concentration of catalyst increased, the speed of modulus build-up increased accelerating the cell opening and gelation of the polymer. Similarly, as the concentration of water increased, the modulus build-up speed was also observed to accelerate [67].

However, using a parallel plate configuration to study expanding systems has several drawbacks as it is only possible to investigate a few layers of cells in the foam, precise temperature control of the material between the plates is difficult to achieve and, as the expanding foam grows over the plate, the modulus values can only be considered an apparent measurement [68]. Hence, other geometries and techniques have been researched to register the modulus rise in the bulk of reactive PU foams [66,75]. Among them, the use of a vane geometry (Figure 2-20) attached to a shear rheometer has been proposed [66,75].

The vane fixture consists of four blades which are immersed in the foam as it grows. Moreover, foams of volume up to 2 L can be studied. Due to the large dimensions of the samples the experiments could be conducted without using a temperature program [66]. Despite the advances in new accessories and geometries, conventional rheometers present certain limitations related to the strict geometric requirements for the accurate determination of the modulus and complexity of the analysis of the results. Hence, these difficulties have fostered the development of other techniques to study the viscoelastic properties build-up in reactive foams.

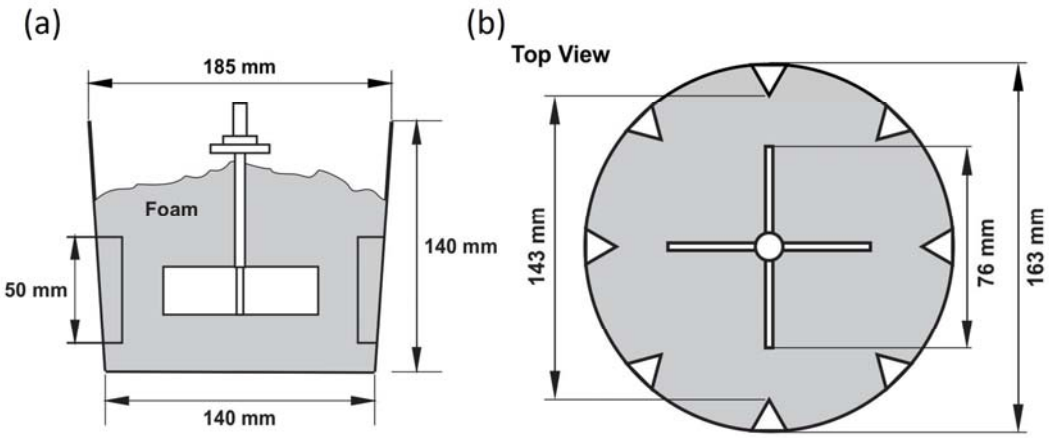

Figure 2-20: (a) Side view and (b) top view of the vane rheometer during PU foaming [66].

2.3.2.3. Scanning Vibrating Needle Curemeter

In the literature, there are reports of commercial devices designed for the characterisation of the cure profiles of thermosetting materials, such as the Scanning Vibrating Needle Curemeter (SVNC) by Rapra Technology Ltd. [76,77]. This instrument consists of a carbon needle (50 cm long) set to vibrate at an adjustable frequency in an electrically driven vibrator. The back electromotive force of the vibrator gives a measure of the vibration amplitude, and the vibration frequency is computer-controlled to maintain the maximum amplitude. Hence, the equipment is capable of providing the elastic and viscous response of the foaming material by measuring both the resonant frequency and amplitude. As the viscosity of the curing liquid increases, it damps the vibration of the probe which is seen as a decrease in the amplitude. Once the material passes through the gel point, it starts to develop elastic properties which result in a shift of the resonance to higher frequencies. The output data is presented as the vibrating frequency, which is related to the storage or elastic modulus, *G'*, and the vibrating amplitude, which is related to the viscosity (before gelation) and the loss or viscous modulus, *G''* (after gelation). Bernal et al. [61] used

this method to follow in situ the foaming of flexible PU foam nanocomposites reinforced with dispersed and functionalized carbon nanotubes. The authors were able to identify the main stages of PU foam rheological development. Frequency, *G'*, increased over the entire monitored time (Figure 2-21 (a)), while the amplitude of the vibration, *G"*, started at a maximum and decreased sharply in a few minutes of reaction (Figure 2-21 (b)). This amplitude response is related to the onset of phase separation of the urea hard segments domains. After this stage, the amplitude levelled off, but the frequency continued to increase as the polymerisation proceeded. At last, the amplitude stabilised at a constant value while the frequency continues to increase until the cure stops. Among samples, it was detected how nanocomposites with 0.5 phpp of carbon nanotubes had superior storage modulus implying that the incorporation of 0.5 phpp of nanotubes lead to a reinforcement of the matrix, while lower contents (0.1 phpp) did not.

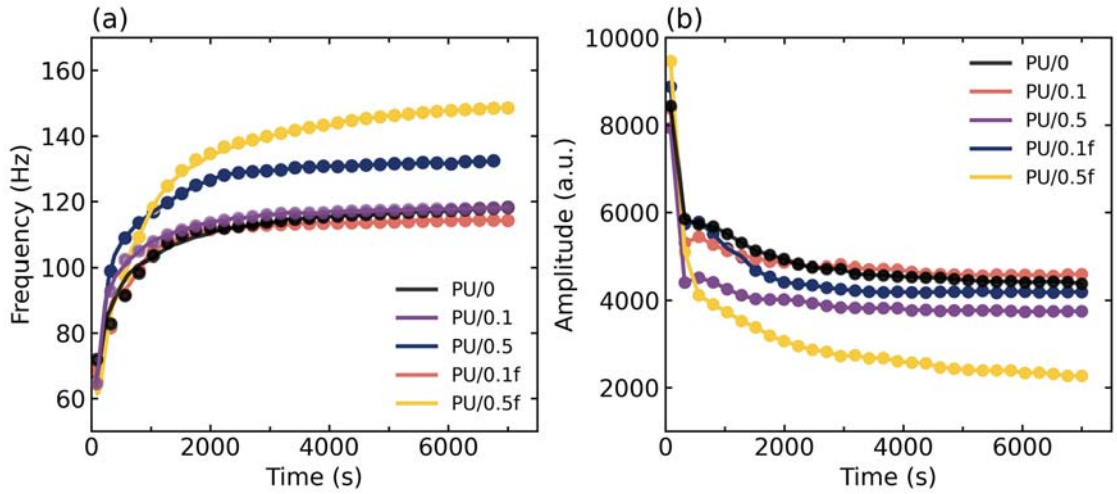

Figure 2-21: Data obtained using the Needle Curemeter in the work by Bernal et al. [61]. (a) Frequency of vibration, or elastic behaviour, and (b) amplitude of vibration, or damping behaviour, for FPU foams with different contents of dispersed (PU/0.1 and PU/0.5) and functionalized (PU/0.1f and PU/0.5f) nanotubes.

As demonstrated throughout Section 2.3.2, the application of these methods can give insights into the viscoelastic properties in reactive PU foams. However, most of these methods fail to measure the real foam modulus. The Needle Curemeter as well as the Electrical and Sound measurements only provide indirect information of the cure process. In contrast the vane and flooded parallel plate rheometers give accurate information on the reaction times and main transformation but the modulus measured can only be considered an estimation. Nonetheless, to study the viscoelastic properties of polymers not only rheometers but also Dynamic Mechanical Analysers (DMA) can be employed. Despite, the

widespread use of DMA for thermoplastics and cured thermosets, prior to this thesis the technique had never been used to probe the polymerisation and cure of reactive foams. Therefore, in this thesis we have aimed at developing a new characterisation route to probe the PU foam polymerisation using DMA (Chapter 4). In addition, we investigated how the dynamics of polymerisation relate to the reaction kinetics measured with FTIR Spectroscopy. The comparison of the reaction kinetics and rheological response was proved to be an efficient way of demonstrating the accuracy of the DMA results.

2.3.3. Foaming Mechanisms

The analysis of the reaction kinetics of the solid matrix is not enough to understand the formation process of PU foams. It is also necessary to monitor the cellular structure development by techniques such as sequential acquisition of microscopy images, X-ray radioscopy, cryogenic scanning electron microscopy and real-time Synchrotron X-ray tomography [15,36,78]. In the following sections we describe these techniques and some of the key results obtained when they are applied to PU systems.

2.3.3.1. Optical Imaging

For PU foams, the first report on the in situ investigation of the foaming dynamics is attributed to E. Minogue [15]. The author used in situ light microscopy to follow the cellular structure generation in small and thin PU samples (0.15 mm thick and 2.5 mm diameter) [15]. In this work, sequential optical micrographs were acquired of the evolving cellular structure. The author used a temporal resolution of 3 s and observed the structure formation from the end of the mixing of the reactants until the stabilisation of the structure. The analysis of the microscopy images was performed manually and focused mainly on quantifying the cell size and number of evolving nuclei with time (Figure 2-22).

This type of analysis allowed the identification of the main stages of cellular structure development. The first region (I) in Figure 2-22 (b) corresponds to the induction period, *i.e.,* the time required for bubble nucleation. Afterwards, in region II the number of bubbles continues to grow linearly with time. In a later stage (region III), the number of bubbles begins to stabilise. This instance corresponds to the point of gelling. Lastly (region IV), the number of present bubbles can either remain stable with time, in the absence of cell degeneration, or otherwise decrease over time. In addition, Minogue [15] observed good correspondence between the stages of structure generation and those of rheological

development (Section 2.3.2) observed by Mora et al. [67]. Additionally, a curve depicting the cell growth is displayed in Figure 2-22 (a) which is accompanied by representative optical micrographs of each stage. In this plot, a quick cell size increase with time can be detected in the first minutes of foaming. This region corresponds to the period in which spherical bubbles grow radially undisturbed from bubbles of a few microns to more than 80 µm. Once the bubbles become in contact, they lose their spherical shape and the rate of cell growth levels off. In this particular example, the final cell size established at around 100 µm and in less than 200 s since the beginning of the reaction.

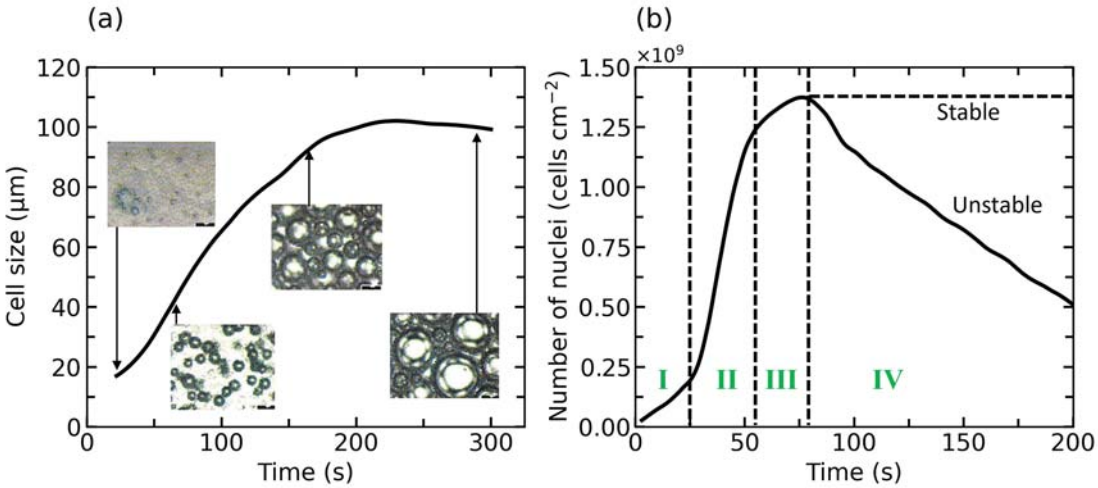

Figure 2-22: (a) Cell growth and (b) density of nuclei evolution with time for an RPU foam obtained with in situ optical microscopy by Minogue [15].

More recently, Brondi et al. [78–80] also used an optical imaging set-up to investigate the foaming dynamics of PU foams. The experimental set-up is displayed in Figure 2-23 (a)-(d). It consisted of a high-speed optical camera focused on the bottom of a plastic beaker in which the polyurethane foam reaction was triggered. The optical camera had a spatial resolution of 2.4 µm. This set-up enabled to analyse the cellular structure formation in samples of larger size than those studied by Minogue [15]. Yet, it only permitted the observation of the bottom of the foam. This could be a disadvantage as the bottom layer of the foam may undergo different structural development than the foam core. The micrographs analysis focused on measuring the average cell size and cell density in the images. Cells selection was performed manually and cell density was estimated as the number of cells divided by the image area following Kumar's approximation [81]. An example of the micrographs obtained during the cellular structure development of pentane blown RPU foam can be seen in Figure 2-23 (e)-(i).

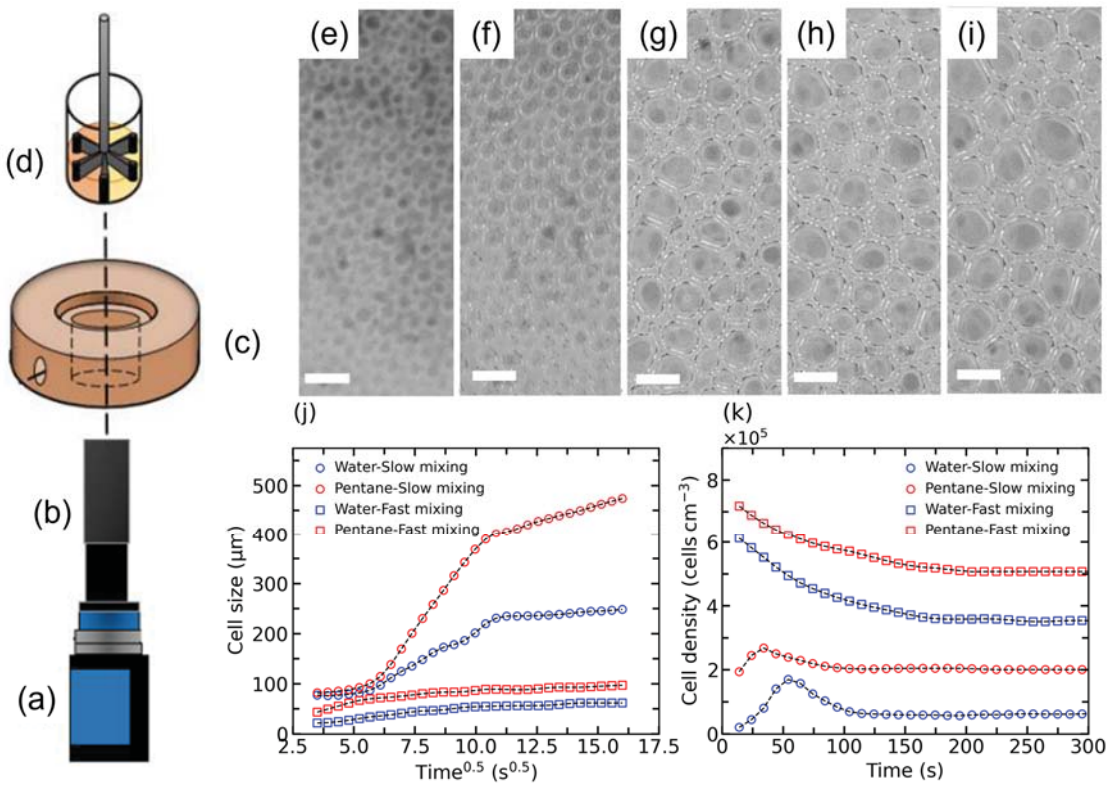

Figure 2-23: Experimental set-up: (a) high-speed camera, (b) bi-telecentric lens, (c) copper plate used to keep the (d) sample holder. Example micrographs (scale bars 200 μm) of pentane blown foam at times: (a) 10 s, (b) 30 s, (c) 40 s, (d) 120 s and (e) 300 s. (j) Cell size and (k) cell density evolution of RPU foams blown with water and water-pentane and mixed at fast and slow speeds reproduced from [78].

The target of the in-situ studies by Brondi et al. [78] was to increase the understanding on how foaming dynamics change with the introduction of air bubbles in the reactive mixture. The authors prepared PU and PIR (polyisocyanurate foams) using different blowing agents (water and water-pentane) and mixing conditions (slow and fast mixing at 50 rpm for 20 s and 1000 rpm for 8 s, respectively) [78]. Both fast and slow mixing conditions were tested, and it was proved that under fast mixing conditions the introduction of air bubbles in the mixture was severe. From the cell size evolution curves, it was possible to detect two stages of growth. The first one corresponds to the growth of round bubbles isolated in the liquid. While the second stage corresponds to the growth of the cells after impingement when the speed of cell growth decreases.

Brondi et al. also quantified the cell nucleation density evolution with time (Figure 2-23 (k)). At a glance, it is possible to observe that nucleation was more intense under fast mixing conditions and when a mixture of water-pentane as blowing agent was employed. When fast mixing conditions were used the foams show maximum cell density as soon as monitoring began. Hence, the authors hypothesize that there was no nucleation of new cells and that

the detected cell nucleation came solely from the air bubbles introduced during mixing. Yet, under slow mixing conditions, a growth in the number of nucleated cells is detected during the monitored time. This is owed to the generation of new nuclei due to the saturation of gas in the mixture. For all systems, after nearly 40 s of reaction degeneration mechanisms start to dominate the foaming process and the density of cells in the foam drops (Figure 2-23 (k)). Under slow mixing conditions, the cellular structure stabilised relatively quickly approximately after 100 s of reaction.

Moreover, this set-up also permitted the authors to experimentally probe that in many situations pre-existing gas bubbles are solely responsible for the final cell density. When air bubbles are introduced into the mixture the gas generated by the blowing agents is not used in the generation of new nucleation points. In fact, gas coming from the blowing agents diffuses into the dispersed air bubbles. Observation of the cellular structure evolution over time permitted to identify the main degeneration mechanisms at play in PU foaming: coalescence and Ostwald ripening (coarsening).

2.3.3.2. X-ray Radioscopy

Other works report the use of X-ray imaging to investigate the cellular structure and porosity generation in foams [36,82–87]. X-ray imaging is an extremely powerful technique in the field of materials science. Thanks to the strong penetrating power of X-rays, it is possible to investigate non-destructively the internal structure of low atomic number materials, such as polymers. In addition, the sequential acquisition of X-ray radiographs, *i.e.,* X-ray radioscopy, permits observation of dynamic phenomena, such as the foaming process of different materials [82,84,88]. Hence, this technique can be applied to polymeric foams, both thermoplastic and thermosetting [36,83,86,87,89,90]. In particular, Pardo-Alonso et al. [36] were the first to perform X-ray radioscopy experiments on PU foams to investigate the cellular structure and porosity generation. The authors used an in-house X-ray imaging system consisting of a laboratory X-ray source and a high sensitivity flat panel detector (Figure 2-24) [90]. In these experiments, a drop of the reactive mixture was allowed to expand freely in two directions in a low-thickness (0.6 mm) foaming mould. The thickness of the sample was constrained during expansion. The spatial resolution of the set-up was fixed at 14 μm [36].

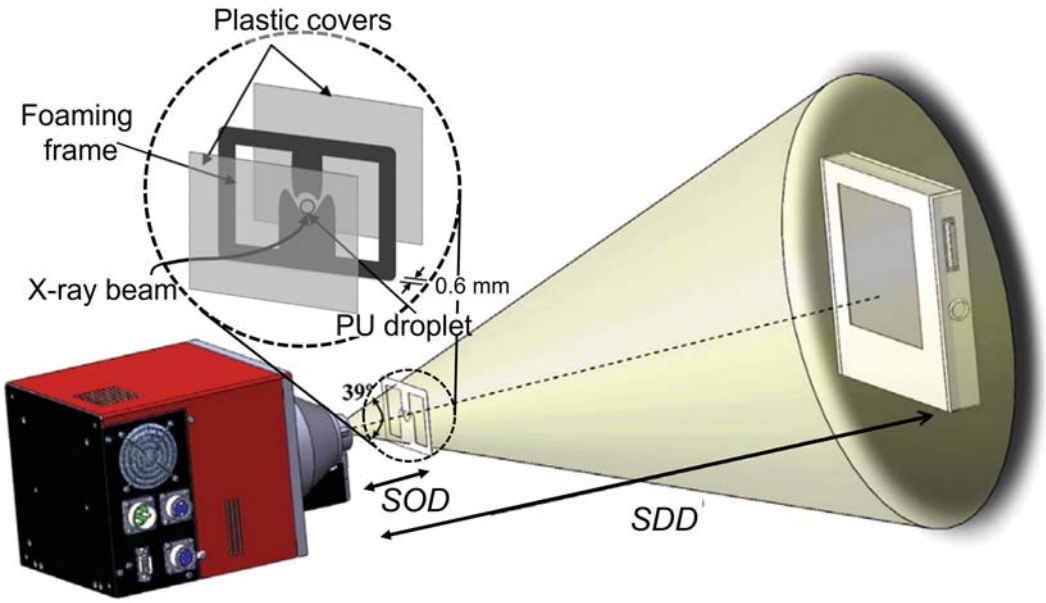

Figure 2-24: Schematic view of the X-ray radioscopy system used by Pardo-Alonso et al. [36]. It includes the foaming frame placed between the source and the detector.

When compared with optical methods, X-ray imaging presents the advantage of enabling simultaneous research of the relative density evolution in the sample and the cellular structure development. In X-ray absorption imaging, attenuation of an X-ray beam is related to the linear attenuation coefficient, μ, sample density, ρ, and thickness of the sample, t, through Beer-Lambert's law (eq. (2-25)). Hence, density analysis is possible thanks to the relationship between the original intensity coming from the source, I_0, and the transmitted intensity, $I(x,y)$ as seen in eq. (2-25).

$$I(x,y) = I_0\, exp(-\mu\, \rho_{foam}\, d) \qquad (2\text{-}25)$$

The density evolution in the sample was obtained by applying appropriate calibration with materials of known density (air and final droplet-foam density) [85].

Cell size, Φ, growth and cell density, N_v, evolution could also be investigated using X-ray radioscopy. The cell size analysis was performed automatically by binarizing the image sequences. Binarization was achieved by applying a different threshold to each image which varied logarithmically with the reaction time. After binarization, a watershed-based algorithm was applied to separate individual cells. The average size of the cells corresponds to the average diameter assuming that the cells had spherical shapes. Last but not least, Pardo-Alonso et al. [36] obtained the evolution of cell density using the theoretical approximation in eq. (2-26).

$$N_v = \frac{6}{\pi \Phi^3}\left(\frac{\rho_{solid}}{\rho_{foam}} - 1\right) \tag{2-26}$$

Pardo-Alonso et al. [36] applied this methodology to study the nucleation power of nanoparticles in PU-nanoclays foams. To that end, nanocomposite foams with different clays concentrations were investigated using X-ray radioscopy. It was detected that the nanoclays presence did not significantly modify the relative density evolution of the neat PU foam. However, the nanocomposite foams presented lower cell sizes than the neat PU foam during the entire foaming process. The foam with 5% nanoclays underwent a 50% reduction in the final cell size compared to the neat PU foam (Figure 2-25). The authors ascribed the cell size reduction to an increase in the number of nucleation points as a result of the nanoclays presence. In addition, there was no sign of degeneration in the studied systems.

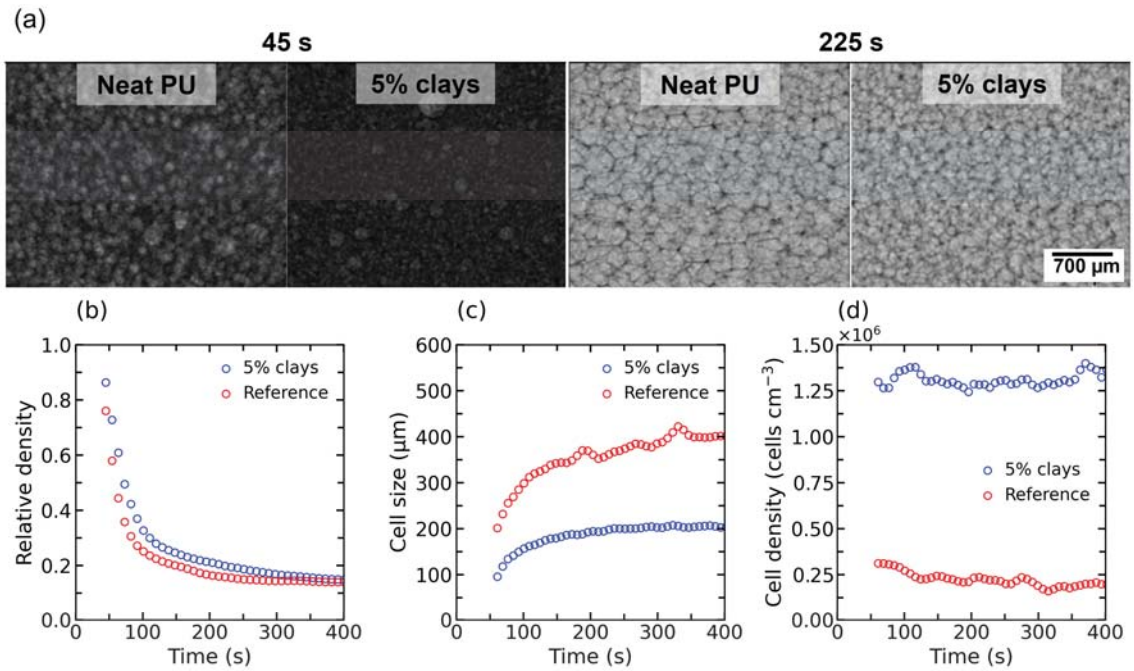

Figure 2-25: (a) Comparative sequence of acquired radiographies of neat PU and 5% nanoclays/PU at 45 and 225 seconds reaction time (b) relative density, (c) cell size and (d) cell density evolution during the PU foaming process [36].

The effectiveness of this approach is confirmed by the number of research works that have successfully investigated the nucleation and degeneration effect of different nanofillers types in PU foams [36,85,87,89]. However, the analysis of the cellular structure generation alone does not permit to elucidate which are the responsible chemo-rheological mechanisms. Hence, a combined analysis of the structure with the rheological and chemical methods can be beneficial. In this thesis, we have continued to apply X-ray radioscopy

together with FTIR Spectroscopy and rheological methods to obtain a holistic view of the reactive foaming process of a novel type of composite foam, RPU-aerogel composite foams (Chapter 7) [91,92].

2.3.3.3. Cryogenic Scanning Electron Microscopy

While all the previous methods gave insights into the density of nucleation at the early stages of the foaming process, the limited spatial resolution of the set-ups did not provide direct identification about the nuclei. Recently, Reignier et al. [4] reported the first observation of the evolving morphology of PU foams using cryogenic scanning electron microscopy (SEM). The high resolution of SEM enabled the authors to visualize the morphology on the sub-micron scale. Reignier et al. [4] investigated the premixes and reactive mixtures of different PU formulations. Formulations were prepared with water and isopentane as blowing agents. Also, formulations without blowing agents were prepared to observe the morphology of air bubbles dispersed in the mixture before reactive mixing. Small quantities of the mixtures at times close to the cream time of the formulation were placed directly in SEM specimen holders and quickly frozen by plunging them into liquid nitrogen. The high resolution of SEM allowed the authors to visualize both micro-and nanometre nuclei in the reactive mixture. Exploration of the stirred premixes revealed that dispersed air bubbles have sizes of about 5 μm diameter (Figure 2-26 (a)) and their number per unit volume is near 10^6 bubbles cm^{-3}. In contrast, isopentane droplets (Figure 2-26 (b)) dispersed in the reactive mixture matrix have sizes in the nanometre scale, *ca.* 100 nm, and appear in a much higher density, ~10^{12} droplets cm^{-3}. In addition, the reactive mixture also presented a morphology consisting of a dispersed phase/matrix with dispersed nodules of around 2.5 μm. The isopentane droplets generally appear dispersed in the matrix but also at the interphase of the dispersed phase/matrix (polyol/isocyanate). Near the cream time, some of the isopentane droplets previously seen near the polyol/isocyanate interphase have disappeared. However, the disappearance of the isopentane droplets is not generalised and some can still be detected as seen in Figure 2-26 (c). However, at times longer than the cream time (Figure 2-26 (d)) the cavities made by isopentane droplets have completely disappeared and so have the dispersed phase nodules. These results meant that isopentane molecules dissolved in the matrix do not generate new nuclei on their own as there is no cell growth stemming from the dispersed isopentane droplets. In addition, this work also

contributed to proving that air entrapments during mixing are the key factor promoting the generation of a cellular structure in PU foams [4].

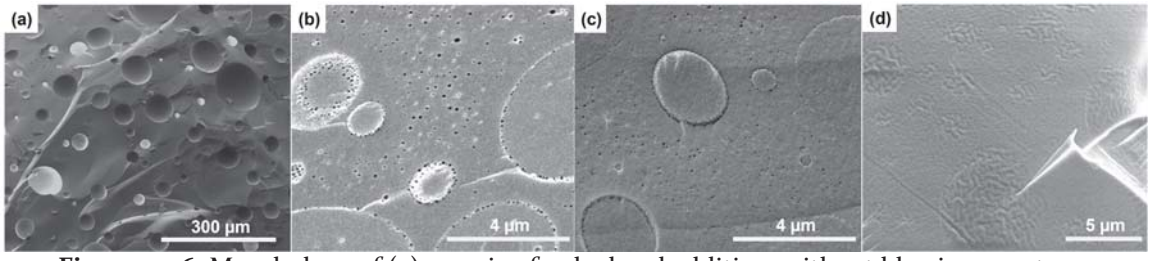

Figure 2-26: Morphology of (a) premix of polyol and additives without blowing agent nor isocyanate showing air bubbles and reactive mixture (b) at 13 s (before cream time), (c) 24 s (near cream time) and (d) 37 s (after cream time) of reaction (micrographs reproduced from [4]).

2.3.3.4. Real-time Synchrotron X-ray Tomography

Lastly, it is also worth mentioning the contribution of Pérez-Tamarit et al. [93] to the state-of-the-art techniques probing into the foaming dynamics. In his 2019 work, real-time synchrotron X-ray tomography was used to investigate the microstructure generation in nanocomposite PU foams. X-ray tomography is an increasingly popular technique to visualise and analyse the internal structure of materials. In addition, recent advances in synchrotron facilities enable the acquisition of X-ray tomography scans at extremely fast speeds. In the aforementioned study, one tomography was acquired in 156 ms at a resolution of 3.2 µm and with a span time of 1.4 s between scans.

The authors investigated the relative density (Figure 2-27 (b)), cell size (Figure 2-27 (c)) and cell density (Figure 2-27 (d)) evolution for 100 s since the start of the reaction. They found three regimes of microstructure generation: nucleation, growth and wet-dry transition. Firstly, in the nucleation stage ($t < 15$ s) the relative density slowly decreased, the cell nucleation density increased at a constant rate while the cell size remained practically constant. In a subsequent stage, growth took place until the cells start touching each other (50–65 s). At this stage relative density had dropped to nearly the final value, cell nucleation density remained constant and cell size increased almost linearly with $t^{0.5}$. The authors found that the inclusion of nanosilica slowed cell growth and lead to a relative density decrease. After the wet-dry transition (50 s and 65 s for nanocomposite and neat PU respectively), both density and cell growth speed decreased whereas cell nucleation density remained constant indicating the absence of degeneration mechanisms in these foams. In addition, the impact of nanosilicas on the cell nucleation density was also evidenced by the increase in more than one order of magnitude in the final cell density (Figure 2-27 (d)).

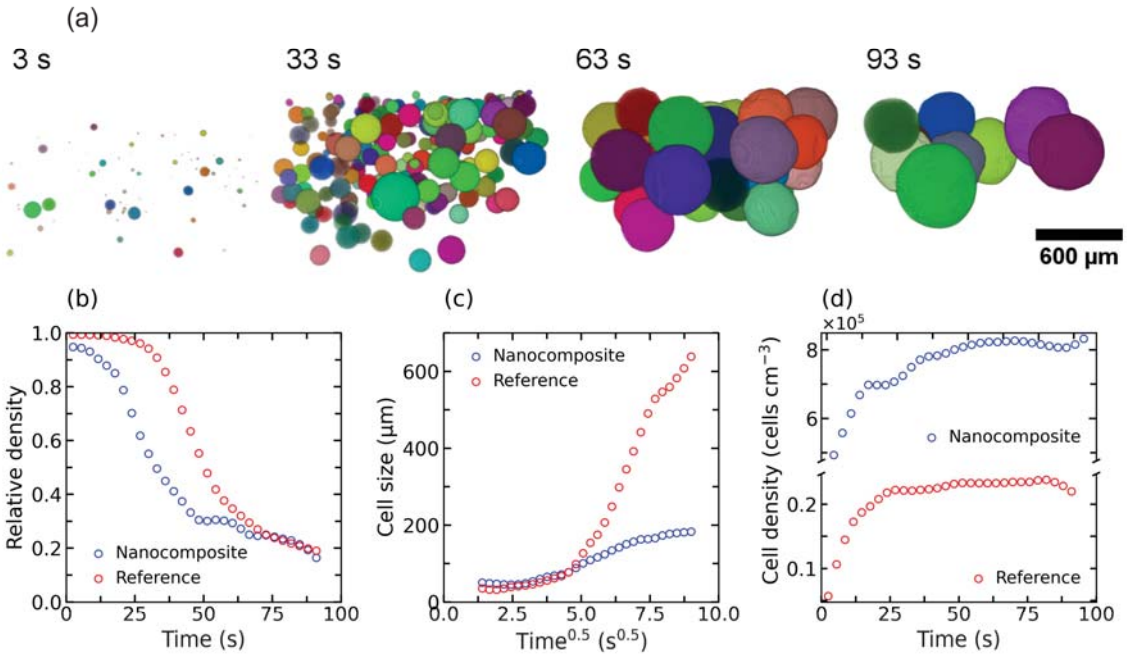

Figure 2-27: (a) 3D rendering of the structure of Reference foam at different times, (b) relative density, (c) average cell size and (d) cell density for Reference and Nanocomposite (3 wt.% nanosilica) foam (reproduced from [93]).

In this thesis, we have explored the feasibility of conducting a 3D characterisation of the PU evolving structure using lab-scale X-ray tomography. This research is in line with the ultimate goal of the thesis of developing novel characterisation methods. However, since laboratory X-ray tomography takes on average more than 1 h per scan [40] performing tomography on evolving PU foams is not possible, as full structure formation takes less than 10 minutes [85,87]. Hence, in this thesis, the exploration in 3D of the structure of non-cured PU samples was achieved by performing X-ray tomography scans on frozen PU samples at different reaction times (Chapter 5) [4]. Therefore, this new method was brought about by the Reignier and Pérez-Tamarit et al. studies [4,93]. In the past, this methodology, known as cryogenic X-ray tomography, has found application in biological systems [94–96] and with this thesis we pave the way for its application in the field of reactive foams.

2.3.4. Advanced Imaging of the Final Cellular Structure

The analysis of the final cellular structure of foams typically focuses on studying gas-phase descriptors (Section 2.2.5.1). In the literature, these descriptors are usually measured using standard microscopy techniques, such as SEM and optical microscopy [34]. The analysis of the micrographs is performed by manual or semi-automated procedures which facilitate the task of obtaining reliable structural characterisations of all types of foams [34].

However, the solid phase distribution in foams is often overlooked. In recent years detailed characterisation of topology of the solid phase (Section 2.2.5.2) has acquired some relevance as it is an essential factor in the understanding of certain properties, such as thermal conductivity and mechanical response [38,39]. Yet, while the gas phase of the foams can be easily characterised using standard micrographs, the solid phase organisation can hardly be studied using 2D techniques. X-ray tomography is the preferred method when investigating the solid matrix of foams. Standard X-ray tomography relies on absorption contrast to retrieve the 3D internal structure of foams. In X-ray tomography experiments hundreds of radiographs are acquired at different orientations of the sample, which rotates 360° during the scan. Using an appropriate algorithm, the radiography data is used to obtain cross-sectional (reconstructed) images of the internal foam structure (Figure 2-28). A lengthier explanation of the fundamentals of X-ray tomography can be found in the PhD dissertation by S. Pérez-Tamarit [97].

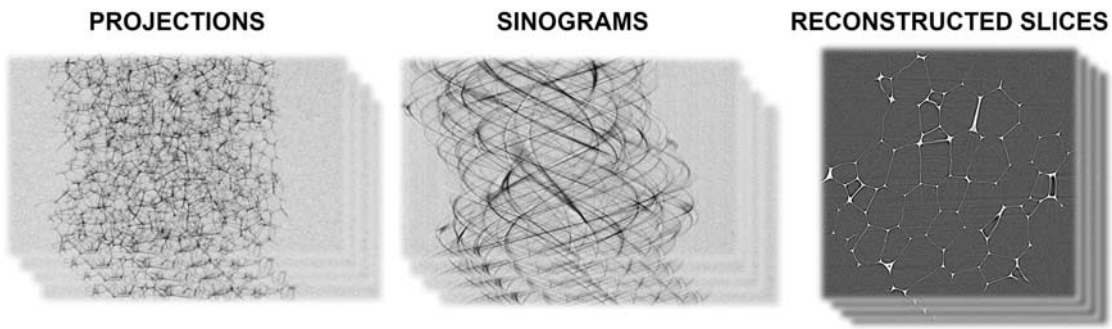

Figure 2-28: Main steps of the tomography process. Projections acquisition, sinograms generation and reconstruction (modified from [97]).

Nonetheless, the analysis of the X-ray tomography volumes is not straightforward [40,98–100]. Particularly, the process of de-structuring the solid matrix into struts and cell walls can result rather ambiguous. For such reason, several image analysis protocols for X-ray tomography scans have been developed in recent years [40,101–103]. They enable quantification of the solid phase descriptors presented in Section 2.2.5, namely *cell wall thickness*, *struts thickness* and the *fraction of mass in the struts*.

In 2015, Pardo-Alonso et al. [101] proposed a series of analysis strategies to analyse the solid phase of closed cell polymeric foams in X-ray tomography scans. The authors used a de-structuration approach based on calculating the moments of inertia of each voxel in the solid phase. Those voxels with a moment of inertia ratio b/c higher than a given threshold (b>> c) were associated with wall voxels. Once the walls and struts voxels had been identified it was possible to calculate the fraction of mass in the struts, f_s, as the ratio of the

struts voxels divided by the number of solid phase voxels. In addition, a local thickness analysis was performed to obtain the average thickness of the walls and struts. While the authors studied mainly thermoplastic foams of low density polyethylene (LDPE) and ethylene-vinyl acetate copolymer (EVA) matrix, their approaches could easily be extrapolated to RPU foams.

In a later study, Pérez-Tamarit et al. [40] performed synchrotron X-ray tomography experiments on RPU foams of different densities. The scans were performed with high spatial resolution. The authors proposed the application of the local thickness algorithm to the binarised solid matrix of the foams. The local thickness distribution was calculated from the images. The distribution is the result of two overlapping contributions, struts and walls. To obtain the weight of each contribution the authors implemented a fitting procedure using a two-peak deconvolution process (Figure 2-29). With this methodology, the area under the peaks (A_w and A_s respectively) represented the fraction of each constituent. Then, the fraction of mass in the struts was calculated using eq. (2-27).

$$f_s = \frac{A_s}{A_s + A_w} \tag{2-27}$$

In addition, using the fitted data for each of the distributions the authors obtained the mean thickness values for cell walls and struts. Finally, the mean thickness of the structure was obtained by calculating the weighted average of the original thickness distribution. Hence, in this method de-structuration of the walls and struts was not performed directly over the images but during the analysis.

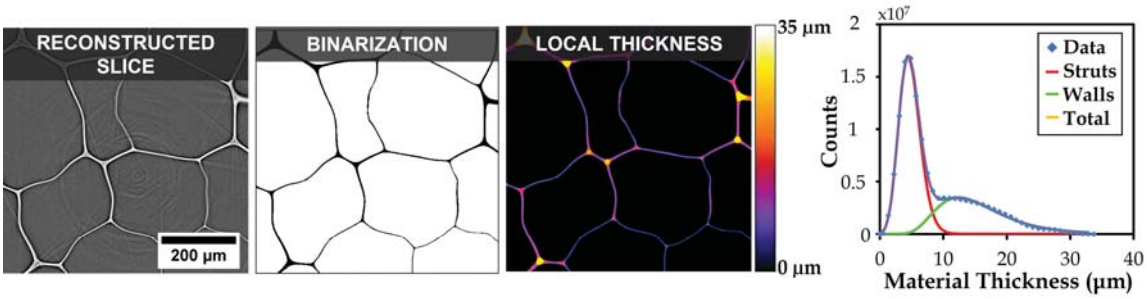

Figure 2-29: Main steps of the imaging analysis protocol of the solid matrix used by Pérez-Tamarit et al. [40].

The most recent contribution to this topic is the work by Chen et al. from 2021 [103]. In this work, X-ray tomography scans of commercial styrene-acrylonitrile (SAN) and polyvinyl chloride (PVC) foams were analysed at a resolution of 1.5 µm/pixel. The process starts with the binarisation of the solid matrix (Figure 2-30 (a)). On the binarised matrix, a

distance transform algorithm was applied (Figure 2-30 (b)). The algorithm computes the distance of one solid pixel to its nearer neighbour. This approach revealed that the medial axes of the walls can be assigned to watershed lines. Hence, a watershed algorithm was applied to the distance image (Figure 2-30 (c)). The resulting watershed image was used to identify junctions of the medial axes. If a pixel is on the border of more than two regions, then it is considered a junction or strut. From the watershed image, the junctions were subtracted leading to an image with the disconnected medial axes of the walls (Figure 2-30 (d)). Following this classification approach, the thickness of each wall can be obtained by finding out the intensities of solid pixels.

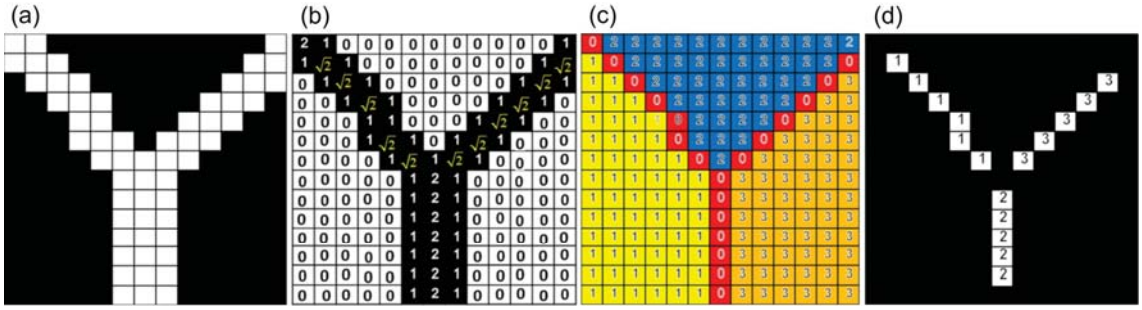

Figure 2-30: Illustration of the process of wall thickness measurement used by Chen et al. [103]: (a) binary image containing three cell walls, (b) distance image, (c) watershed image, (d) disconnected and labelled medial axes of the cell walls.

Despite the previous advances, one prevailing difficulty to study the solid phase distribution in low density foams is that they require high spatial resolution [101,103,104]. The need of high resolution arises from the thin solid cell walls present in most low density foams. Laboratory X-ray imaging set-ups commonly have spatial resolutions above the micron, in the range of 2-3 μm per pixel. Hence, with most common laboratory X-ray imaging systems is not possible to perform a full solid matrix characterisation. In this research work we have aimed at mitigating this difficulty by designing image analysis methods to retrieve sub-pixel information (Chapter 6). In such way, it will be possible to infer the cell wall thickness and estimate the solid mass distribution between walls and struts provided that the struts can be properly characterised. This is for instance the case in RPU foams whose struts thickness is considerably larger than the cell walls thickness.

2.4. THERMAL INSULATION PROPERTIES OF FOAMS

Good thermal insulation is one of the most attractive features of low density foams. Thermal transport in porous materials is the result of three major modes of heat transfer:

convection, conduction and radiation [105]. Convection is the mechanism of heat transfer resulting from the movement of fluid, gas and liquid [105]. Heat transfer by conduction is a diffusion process, whereby thermal energy is transferred from a hot end of a medium to its colder end via an intermolecular energy exchange [106]. While, conduction can occur in solids, liquids and gases, it is the predominant mode of heat transfer in solids. In contrast, heat transfer by radiation is a process by which electromagnetic waves (in the infrared region) are emitted, absorbed, or transmitted by bodies at a certain temperature. Unlike the previous mechanisms, heat can be transported by radiation in the absence of an intervening medium. Hence, the thermal conductivity in a foam is the sum of these contributions of heat transfer (eq. (2-28)).

$$\lambda = \lambda_s + \lambda_g + \lambda_r + \lambda_c \tag{2-28}$$

In eq. (2-28) λ_s accounts for conduction by the solid matrix, λ_g is the conduction by the gas phase inside the cells, λ_r is the radiation term, and λ_c represents the convection of the gas inside the cells. However, several authors have noted that convection only contributes to the thermal conductivity when the cells exceed sizes of 4 mm [6,107]. Therefore, for most polymeric foams this term can be neglected as they have cell sizes below 1 mm.

During this research, our efforts have also focused on understanding how the foaming process and the cellular structure impact the thermal conductivity through modelling of the heat transfer mechanisms. Due to this, the state of the art related to the analytical modelling of the thermal conductivity of low density foams is explained in the next paragraphs.

2.4.1. Gas Conduction

In low density foams, gas is the predominant component and can represent up to 98% of the total foam volume. For such reason, the main contribution to the total foam thermal conductivity is owed to the gas filling the cells. In foams with only one gas filling the cells this term can be easily calculated following eq. (2-29) where V_g is the volume fraction of gas and λ_{gas} is the thermal conductivity of the gas filling the cells.

$$\lambda_g = V_g \, \lambda_{gas} \tag{2-29}$$

2.4.2. Solid Conduction

In the literature, different equations have been proposed to analytically predict the thermal conductivity by conduction of the solid phase in a cellular material [108]. In this

work, we have used an expression that has been proven to give accurate results in the case of low density polymeric foams [39]. It is known as Glicksman equation (eq. (2-30)) [109]. It breaks the conduction of the solid in two terms, one accounting for the conduction due to struts and the other one due to cell walls. In this equation ρ_r is the relative density, λ_{solid} is the thermal conductivity of the solid phase, AR is the anisotropy ratio and f_s is the fraction of mass in the struts.

$$\lambda_s = \lambda_{struts} + \lambda_{walls} = \frac{\rho_r}{3} \cdot f_s \lambda_{solid} \sqrt{AR} + \frac{2}{3} \rho_r (1 - f_s) \lambda_{solid} AR^{1/4} \qquad (2\text{-}30)$$

2.4.3. Radiation

The contribution of radiation to the thermal conductivity can be estimated using Rosseland's approximation [109]. The foam is modelled as a combination of randomly oriented cell walls that absorb radiation and blackbody struts, which scatter all the radiation incident upon them. Hence, the average distance (mean free path) that radiation can travel without being scattered or absorbed is relatively short specially in comparison to the dimensions of the material. Thus, it is possible to model radiative heat transport as a diffusion process inside the foam, result known as Rosseland diffusion equation (eq. (2-31)). This equation considers the extinction coefficient of the foam, $K_{e,R}$, Stefan–Boltzmann constant, σ, and the temperature of the sample, T.

$$q_r = \frac{4}{3K_{e,R}} \frac{\partial e_b}{\partial x} = \frac{-16\sigma T^3}{3K_{e,R}} \frac{\partial T}{\partial x} = -\lambda_r \frac{\partial T}{\partial x} \qquad (2\text{-}31)$$

$$\lambda_r = \frac{16\sigma T^3}{3K_{e,R}} \qquad (2\text{-}32)$$

The extinction coefficient, $K_{e,R}$, of foams can be modelled using an equation proposed by Glicksmann et al.[109]. The struts have a contribution to the foam's extinction coefficient that depends on the cellular structure and density. Cell walls have an extinction coefficient, K_{ws}, that is a function of the amount of material in the walls and the extinction coefficient of the material contained in the walls K_w (eq. (2-33)).

$$K_{e,R} = K_s + K_{ws} = 4.10 \frac{\sqrt{f_s \cdot \rho_r}}{\Phi} + (1 - f_s) \rho_r K_w \qquad (2\text{-}33)$$

2.5. CASE STUDIES: RELEVANT FOAM SYSTEMS

In recent years, the increasing need of more performant and sustainable insulating materials has motivated intensive research and innovation in new foam systems to be used as thermal insulators. In this PhD thesis work, we have concentrated our efforts on two innovative materials with the potential to replace conventional RPU foam insulators: RPU-Aerogel composite foams and recycled glass foams. In the next paragraphs a brief description of the state of the art of these materials is included.

2.5.1. Polyurethane-Aerogel Composite Foams

Aerogels are lightweight (0.003-0.35 g cm^{-3}) and porous materials with a nanoporous structures (pore size ~ 5 nm). In these nanoporous materials, the gas phase is confined in nanometric pores with sizes close to or below the main free path length of the gas molecules (~70 nm) [110]. This phenomena is the so-called Knudsen effect which significantly reduces heat transfer by gas-phase conduction [111]. In addition, in these materials there is very intense scattering of phonons in the boundaries of the nanometric particles forming the aerogel that reduce the heat flow by conduction through the solid phase. For these reasons, some aerogels present extremely low thermal conductivities (~12 mW $(m\ K)^{-1}$ in room conditions) reason why they are often labelled as super-insulators. They are produced via a sol-gel route by which both inorganic and organic aerogel can be obtained [112–115]. Among inorganic aerogels, silica aerogels are the most widespread and they can be synthesised in several forms, from powders to monoliths [116]. Lately, organic aerogels are also being developed. Polyurethane aerogels were first developed in the 1990s but recently there have been commercialization efforts by companies such as BASF and Aerogel technologies [113,117].

However, monolithic Polyurethane aerogels present several drawbacks related to their poor mechanical performance, and they are still far from a final-application format [112]. Some studies have highlighted the possibility of benefiting from the excellent properties of aerogels by using them as reinforcement for composite polyurethane foams [91,92,118,119]. The addition of aerogels in the form of micro- or nanoparticles can enhance the thermal insulation performance of PU foams by two mechanisms: reducing the heat transfer by conduction of the polyurethane matrix and decreasing heat transfer by radiation. On the one hand, during the synthesis of composite foams, the particles are

dispersed within the cell walls and struts of the PU matrix. Hence, as the aerogel particles have lower conductivity than the matrix, they can contribute to decrease the overall heat conductivity of the matrix, λ_{solid}. On the other hand, the addition of fillers is a well-known way of reducing the average cell size of the foam [39]. Lower cell sizes are responsible for higher extinction coefficients of the foams. Hence, finer cellular structures can reduce radiative heat transfer in the material.

In the current literature, there are some examples of the efficiency of aerogel particles in the decrease of the thermal conductivity of PU foams [91]. For instance, Zhao et al. [18] reported a decrease in the thermal conductivity of PIR foams of approximately 35% when adding 8 wt.% of silica aerogel particles. In addition, the flame retardant properties of PIR foams also improved when adding silica aerogel. Nazeran and Moghaddas [119] also reported an improvement in the thermal insulation properties when adding aerogel particles to RPU foams. The thermal conductivity decreased by about 10% the thermal conductivity of the unfilled RPU foam when adding 3 wt.% of aerogel particles.

Throughout this thesis work we studied in depth the influence of silica aerogels and its potential to improve the properties of RPU foams. Moreover, we have demonstrated its effect on the initial reactants and foaming process from different standpoints (reaction kinetics, rheological- and structural-wise) and connected it with the final thermal conductivity of the composite foams (Chapter 7 and Chapter 8).

2.5.2. Recycled Glass Foams

Glass foams are lightweight materials with a closed-cell structure, which can be produced from waste glass and glass-forming minerals [120]. Its full inorganic composition and closed-cell structure result in several advantages compared with conventional thermal insulation materials, e.g., water and steam resistance, freeze-thaw cycle tolerance, excellent chemical and thermal stability, incombustibility, long lifespan equal to the lifespan of bricks and concrete, and superior mechanical properties [121–124]. The combination of good thermal stability and mechanical properties enables the use of foam glass as a functional, and load-bearing component. In addition, glass foams are also 100% recyclable and environmentally friendly [125]. Due to all these reasons, there is a growing interest both in academia and industry (currently commercialised by FOAMGLAS and GLAPOR) to further develop this sustainable insulating material.

Nowadays, the most performant glass foams are produced from powdered glass, which is prepared from minerals and recycled glass, after being melted at temperatures above 1000 °C [124]. The powder mixture with carbon as a blowing agent is foamed at around 850 °C [126,127]. Currently, glass foams can be prepared with up to 95% of recycled glass. The best glass foams produced up to now have thermal conductivities near 38 mW $(m{\cdot}K)^{-1}$ at densities of about 100 kg m^{-3} [124]. However, the disadvantage of this product is its high price and the higher thermal conductivity compared to conventional foam insulators such as PU foams.

During this research work we have applied the developed solid phase characterisation methodology and used these results to estimate the thermal conductivity and fully comprehend the structure and thermal conductivity connection in these materials. Our analysis show that radiation plays an important role in the thermal conductivity of low density glass foams (Chapter 8).

2.6. REFERENCES

[1] K.H. Choe, D.L. Soo, W.J. Seo, W.N. Kim, Properties of Rigid Polyurethane Foams with Blowing Agents and Catalysts, Polym. J. 2004 365. 36 (2004) 368–373.

[2] S.T. et al. Lee, Polymeric Foams: Science and Technology, Taylor & Francis, Boca Raton, 2007.

[3] N.S. Ramesh, S.T. Lee, Polymeric Foams: Mechanisms and Materials, First Ed, CRC Press, Boca Raton, 2004.

[4] J. Reignier, P. Alcouffe, F. Méchin, F. Fenouillot, The morphology of rigid polyurethane foam matrix and its evolution with time during foaming – New insight by cryogenic scanning electron microscopy, J. Colloid Interface Sci. 552 (2019) 153–165.

[5] S. Tan, T. Abraham, D. Ference, C.W. Macosko, Rigid polyurethane foams from a soybean oil-based Polyol, Polymer (Guildf). 52 (2011) 2840–2846.

[6] N.C. Hilyard, A. Cunningham, Low density cellular plastics, 1st Ed, Springer Science & Business Media, 2012, London, 1994.

[7] M.L. Pinto, Formulation, Preparation, and Characterization of Polyurethane Foams, J. Chem. Educ. 87 (2010) 212–215.

[8] B.E. Obi, Polymer Chemistry and Synthesis, in: Polym. Foam. Struct., 2018: pp. 17–40.

[9] H.J.M. Grünbauer, J.A. Thoen, J.C.W. Folmer, H.C. Van Lieshout, Polymer Morphology of Water-Blown Rigid Polyurethane Foams: Development of New Polyols, J. Cell. Plast. 28 (1992) 36–47.

[10] N. Mahmood, J. Kressler, K. Busse, Structure analysis in polyurethane foams at interfaces, J. Appl. Polym. Sci. 98 (2005) 1280–1289.

[11] K. Ashida, Polyurethane and Related Foams: Chemistry and Technology, 1st Ed, Taylor & Francis Group, Boca Raton, 2007.

[12] D. Klempner, K.C. Frisch, Cellular Structure and Properties of Foamed Polymers, in: Handb. Polym. Foam. Foam Technol., 2nd Ed, Hanser, Munich, 2004.

[13] M. Szycher, Szycher's handbook of Polyurethanes, 2nd Ed, Taylor & Francis Group, London, 2013.

[14] P. Cognard, Handbook of Adhesives and Sealants: Volume 1, 2005.

[15] E. Minogue, An in-situ study of the nucleation process of polyurethane rigid foam formation, Dublin City University, 2000.

[16] B.E. Obi, Foaming Processes, in: Polym. Foam. Struct., 2018: pp. 131–188.

[17] B.E. Obi, Fundamentals of Structure–Property Relationships of Polyurethane Foams, in: Polym. Foam. Struct., 2018: pp. 209–254.

[18] R.R. Rao, L.A. Mondy, K.N. Long, M.C. Celina, N. Wyatt, C.C. Roberts, M.M. Soehnel, V.E. Brunini, The kinetics of polyurethane structural foam formation: Foaming and polymerization, AIChE J. 63 (2017) 2945–2957.

[19] D. Radojčić, M. Ionescu, Z.S. Petrović, Novel potentially biodegradable polyurethanes from bio-based polyols, Contemp. Mater. 4 (2013) 9–21.

[20] M. Santiago-Calvo, Synthesis , Foaming Kinetics and Physical Properties of Cellular Nanocomposites Based on Rigid Polyurethane, University of Valladolid, 2019.

[21] M.T. Aronhime, J.K. Gillham, Time-Temperature-Transformation (TTT) Cure Diagram of Thermosetting Polymeric Systems., Adv. Polym. Sci. 78 (1986) 83–113.

[22] C. Block, B. Van Mele, P. Van Puyvelde, G. Van Assche, Time-temperature-transformation (TTT) and temperature-conversion-transformation (TxT) cure diagrams by RheoDSC: Combined rheometry and calorimetry on an epoxy-amine thermoset, React. Funct. Polym. 73 (2013) 332–339.

[23] L.M. Chiacchiarelli, J.M. Kenny, L. Torre, Kinetic and chemorheological modeling of the vitrification effect of highly reactive poly(urethane-isocyanurate) thermosets, Thermochim. Acta. 574 (2013) 88–97.

[24] M. Santiago-Calvo, V. Blasco, C. Ruiz, R. París, F. Villafañe, M.-Á. Rodríguez-Pérez, Synthesis, characterization and physical properties of rigid polyurethane foams prepared with poly(propylene oxide) polyols containing graphene oxide, Eur. Polym. J. 97 (2017) 230–240.

[25] D. Niyogi, R. Kumar, K.S. Gandhi, Modeling of bubble-size distribution in free rise polyurethane foams, J. Appl. Polym. Sci. 131 (2014) 9098–9110.

[26] L. Wang, H. Zhou, X. Wang, J. Mi, Evaluation of Nanoparticle Effect on Bubble Nucleation in Polymer Foaming, J. Phys. Chem. C. 120 (2016) 26841–26851.

[27] V. Bergeron, P. Walstra, Foams, in: Fundam. Interface Colloid Sci., 2005: pp. 1–38.

[28] M. del M. Bernal Ortega, Estudio de nanocompuestos de espumas de poliuretano reforzadas con nanocargas en base carbono, Universidad de Valencia, 2012.

[29] B. Kanner, T.G. Decker, Urethane Foam Formation— Role of the Silicone Surfactant, J. Cell. Plast. 5 (1969) 32–39.

[30] M. Amon, C.D. Denson, A study of the dynamics of foam growth: Analysis of the growth of closely spaced spherical bubbles, Polym. Eng. Sci. 24 (1984) 1026–1034.

[31] R. Elshereef, J. Vlachopoulos, A. Elkamel, Comparison and analysis of bubble growth and foam formation models, Eng. Comput. 27 (2010) 387–408.

[32] S. Costeux, I. Khan, S.P. Bunker, H.K. Jeon, Experimental study and modeling of nanofoams formation from single phase acrylic copolymers, J. Cell. Plast. 51 (2014) 197–221.

[33] Y. Furuta, N. Oikawa, R. Kurita, Close relationship between a dry-wet transition and a bubble rearrangement in two-dimensional foam, Sci. Rep. 6 (2016) 1–8.

[34] J. Pinto, E. Solorzano, M.A. Rodriguez-Perez, J.A. de Saja, Characterization of the cellular structure based on user-interactive image analysis procedures, J. Cell. Plast. 49 (2013) 555–575.

[35] L. Oliveira Salmazo, A. Lopéz-Gil, Z.M. Ariff, M.L. Rodriguez-Mendez, A.E. Job, M.A.

Rodriguez Perez, Study of the Foaming Kinetics in Epoxidized Natural Rubber Foams Crosslinked by Electron Beam Irradiation, Macromol. Chem. Phys. 219 (2018).

[36] S. Pardo-Alonso, E. Solórzano, S. Estravís, M.A. Rodríguez-Perez, J.A. de Saja, In situ evidence of the nanoparticle nucleating effect in polyurethane–nanoclay foamed systems, Soft Matter. 8 (2012) 11262.

[37] I. Cantat, S. Cohen-Addad, F. Elias, F. Graner, R. Höehler, O. Pitois, F. Rouyer, A. Saint-Jalmes, Foams: structure and dynamics, First Ed, Oxford University Press, Oxford, 2013.

[38] S. Pérez-Tamarit, E. Solórzano, A. Hilger, I. Manke, M.A. Rodríguez-Pérez, Effect of solid phase corrugation on the thermo-mechanical properties of low density flexible cellular polymers, Mater. Des. 161 (2019) 106–113.

[39] S. Estravís, J. Tirado-Mediavilla, M. Santiago-Calvo, J.L. Ruiz-Herrero, F. Villafañe, M.A. Rodríguez-Pérez, Rigid polyurethane foams with infused nanoclays: Relationship between cellular structure and thermal conductivity, Eur. Polym. J. 80 (2016) 1–15.

[40] S. Pérez-Tamarit, E. Solórzano, A. Hilger, I. Manke, M.A. Rodríguez-Pérez, Multi-scale tomographic analysis of polymeric foams: A detailed study of the cellular structure, Eur. Polym. J. 109 (2018) 169–178.

[41] J.H. Marciano, A.J. Rojas, R.J.J. Williams, Curing kinetics of a rigid polyurethane foam formulation, Polymer (Guildf). 23 (1982) 1489–1492.

[42] L.D. Artavia, C.W.W. Macosko, Foam Kinetics, J. Cell. Plast. 26 (1990) 490–511.

[43] R.D. Priester, J. V. Mcclusky, R.E. O'neill, R.B. Turner, M.A. Harthcock, B.L. Davis, FT-IR-A Probe into the Reaction Kinetics and Morphology Development of Urethane Foams, J. Cell. Plast. 26 (1990) 346–367.

[44] Y. Zhao, F. Zhong, A. Tekeei, G.J. Suppes, Modeling impact of catalyst loading on polyurethane foam polymerization, Appl. Catal. A Gen. 469 (2014) 229–238.

[45] M.M. Bernal, M. Martin-Gallego, I. Molenberg, I. Huynen, M.A. López Manchado, R. Verdejo, Influence of carbon nanoparticles on the polymerization and EMI shielding properties of PU nanocomposite foams, RSC Adv. 4 (2014) 7911–7918.

[46] M.M. Bernal, M. Martin-Gallego, L.J. Romasanta, A.-C.C. Mortamet, M.A. L?pez-Manchado, A.J. Ryan, R. Verdejo, M.A. López-Manchado, A.J. Ryan, R. Verdejo, Effect of hard segment content and carbon-based nanostructures on the kinetics of flexible polyurethane nanocomposite foams, Polymer (Guildf). 53 (2012) 4025–4032.

[47] G. Trovati, E.A. Sanches, S.M. De Souza, A.L. Dos Santos, S.C. Neto, Y.P. Mascarenhas, G.O. Chierice, Rigid and semi rigid polyurethane resins: A structural investigation using DMA, SAXS and le Bail method, J. Mol. Struct. 1075 (2014) 589–593.

[48] M.J. Elwell, S. Mortimer, A.J. Ryan, A Synchrotron SAXS Study of Structure Development Kinetics during the Reactive Processing of Flexible Polyurethane Foam, Macromolecules. 27 (1994) 5428–5439.

[49] W. Li, A.J. Ryan, I.K. Meier, Effect of chain extenders on the morphology development in flexible polyurethane foam, Macromolecules. 35 (2002) 6306–6312.

[50] M.J. Elwell, A.J. Ryan, H.J.M. Grunbauer, H.C. VanLieshout, An FTIR study of reaction kinetics and structure development in model flexible polyurethane foam systems, Polymer (Guildf). 37 (1996) 1353–1361.

[51] M. Santiago-Calvo, J. Tirado-Mediavilla, J.L. Ruiz-Herrero, M.Â. Rodríguez-Pérez, F. Villafañe, The effects of functional nanofillers on the reaction kinetics, microstructure, thermal and mechanical properties of water blown rigid polyurethane foams, Polymer (Guildf). 150 (2018) 138–149.

[52] A.G. Strikovsky, V. V Zharkov, Infra-red spectroscopy study of equilibrium association of urethane groups in poly(ether urethane)s, Polymer (Guildf). 34 (1993) 3397–3401.

[53] V. V Zharkov, A.G. Strikovsky, T.E. Verteletskaya, Amide I absorption band: description of the urethane group association scheme in polyether urethane elastomers, Polymer (Guildf). 34 (1993).

[54] N. Luo, D.N. Wang, S.K. Ying, Hydrogen-bonding properties of segmented polyether poly(urethane urea) copolymer, Macromolecules. 30 (1997) 4405–4409.

[55] M.M. Coleman, M. Sobkowiak, G.J. Pehlert, P.C. Painter, T. Iqbal, Infrared temperature studies of a simple polyurea, Macromol. Chem. Phys. 198 (1997) 117–136.

[56] A.L. Daniel-da-Silva, J.C.M. Bordado, J.M. Martín-Martínez, Moisture curing kinetics of isocyanate ended urethane quasi-prepolymers monitored by IR spectroscopy and DSC, J. Appl. Polym. Sci. 107 (2008) 700–709.

[57] M.J. Elwell, A.J. Ryan, H.J.M. Grunbauer, H.C. Van Lieshout, In-situ studies of structure development during the reactive processing of model flexible polyurethane foam systems using FT-IR spectroscopy, synchrotron SAXS and rheology, Macromolecules. 29 (1996) 769–770.

[58] M.M. Bernal, M.A. Lopez-Manchado, R. Verdejo, In situ foaming evolution of flexible polyurethane foam nanocomposites, Macromol. Chem. Phys. 212 (2011) 971–979.

[59] A. Marcos-Fernández, A.E. Lozano, L. González, A. Rodríguez, Hydrogen bonding in copoly(ether-urea)s and its relationship with the physical properties, Macromolecules. 30 (1997) 3584–3592.

[60] R.M. Versteegen, R.P. Sijbesma, E.W. Meijer, Synthesis and characterization of segmented copoly(ether urea)s with uniform hard segments, Macromolecules. 38 (2005) 3176–3184.

[61] M.M. Bernal, M.A. Lopez-Manchado, R. Verdejo, In situ foaming evolution of flexible polyurethane foam nanocomposites, Macromol. Chem. Phys. 212 (2011) 971–979.

[62] M. Akkoyun, E. Suvaci, Effects of TiO2, ZnO, and Fe3O4 nanofillers on rheological behavior, microstructure, and reaction kinetics of rigid polyurethane foams, J. Appl. Polym. Sci. 133 (2016) 1–14.

[63] M. Santiago-Calvo, V. Blasco, C. Ruiz, R. París, F. Villafañe, M.Á. Rodríguez-Pérez, Improvement of thermal and mechanical properties by control of formulations in rigid polyurethane foams from polyols functionalized with graphene oxide, J. Appl. Polym. Sci. 136 (2019) 1–10.

[64] C. Torres-Sánchez, J. Corney, Identification of formation stages in a polymeric foam customised by sonication via electrical resistivity measurements, J. Polym. Res. 16 (2009) 461–470.

[65] J.A. Holt, C. Torres-Sanchez, P.P. Conway, Monitoring the continuous manufacture of a polymeric foam via a thermokinetic-informed acoustic technique, Proc. Inst. Mech. Eng. Part E J. Process Mech. Eng. 235 (2021) 1998–2007.

[66] X.D. Zhang, D.W. Giles, V.H. Barocas, K. Yasunaga, C.W. Macosko, Measurement of foam modulus via a vane rheometer, J. Rheol. (N. Y. N. Y). 42 (1998) 871–889.

[67] E. Mora, L.D. Artavia, C.W. Macosko, Modulus development during reactive urethane foaming, J. Rheol. 35 (1991) 921–940.

[68] L.D. Artavia, C.W. Macosko, Polyurethane flexible foam formation, Low Density Cell. Plast. (1994) 22–55.

[69] R. Bouayad, J. Bikard, J.F. Agassant, Compressible flow in a plate/plate rheometer: Application to the experimental determination of reactive expansion's models parameters for polyurethane foam, Int. J. Mater. Form. 2 (2009) 243–260.

[70] F. Dimier, N. Sbirrazzuoli, B. Vergnes, M. Vincent, Curing kinetics and chemorheological analysis of Polyurethane formation, Polym. Eng. Sci. 44 (2004) 518–527.

[71] R.A. Neff, C.W. Macosko, Simultaneous measurement of viscoelastic changes and cell opening during processing of flexible polyurethane foam, Rheol. Acta. 35 (1996) 656–666.

[72] W. Li, A.J. Ryan, I.K. Meier, Morphology development via reaction-induced phase separation in flexible polyurethane foam, Macromolecules. 35 (2002) 5034–5042.

[73] T. Mezger, The Rheology Handbook: For users of rotational and oscillatory rheometers, 4 th, 2014.

[74] H.M. Princen, A.D. Kiss, Rheology of foams and highly concentrated emulsions: IV. An experimental study of the shear viscosity and yield stress of concentrated emulsions, J. Colloid Interface Sci. 128 (1989) 176–187.

[75] H.A. Barnes, Q.D. Nguyen, Rotating vane rheometry-a review, J. Nonnewton. Fluid Mech. 98 (2001) 1–14.

[76] S.A. Jones, K.W. Scott, B.G. Willoughby, E.A. Sheard, Monitoring of polyurethane foam cure, J. Cell. Plast. 38 (2002) 285–299.

[77] B.G. Willoughby, K.W. Scott, Understanding Cure With the Scanning Vibrating Needle Curemeter (Scanning Vnc), Rapra Technol. Ltd. 44 (1996).

[78] C. Brondi, E. Di Maio, L. Bertucelli, V. Parenti, T. Mosciatti, Competing bubble formation mechanisms in rigid polyurethane foaming, Polymer (Guildf). 228 (2021) 123877.

[79] C. Brondi, E. Di Maio, N. Federico, T. Mosciatti, V. Parenti, L. Bertucelli, The effect of air bubbles inclusion on polyurethane foaming - Insight into bubble nucleation and growth mechanisms, in: SPE Foam. 2019 Conf., Valladolid, Spain, 2019.

[80] C. Brondi, Polyurethane foams : novel processing and novel additives for improved thermal insulation properties, University of Naples Federico II, 2020.

[81] V. Kumar, N.P. Suh, A process for making microcellular thermoplastic parts, Polym. Eng. Sci. 30 (1990) 1323–1329.

[82] F. Garcia-Moreno, E. Solórzano, J. Banhart, Kinetics of coalescence in liquid aluminium foams, Soft Matter. 7 (2011) 9216.

[83] E. Solórzano, S. Pardo-Alonso, J.A. de Saja, M.A. Rodríguez-Pérez, Study of aqueous foams evolution by means of X-ray radioscopy, Colloids Surfaces A Physicochem. Eng. Asp. 438 (2013) 159–166.

[84] F.G. Moreno, M. Fromme, J. Banhart, Real-time X-ray radioscopy on metallic foams using a compact micro-focus source, Adv. Eng. Mater. 6 (2004) 416–420.

[85] M. Santiago-Calvo, S. Pérez-Tamarit, P. Cimavilla-Román, V. Blasco, C. Ruiz, R. París, F. Villafañe, M.Á. Rodríguez-Pérez, X-ray radioscopy validation of a polyol functionalized with graphene oxide for producing rigid polyurethane foams with improved cellular structures, Eur. Polym. J. 118 (2019) 404–411.

[86] E. Solórzano, S. Pardo-Alonso, J.A. De Saja, M.A. Rodriguez-Perez, X-ray radioscopy in-situ studies in thermoplastic polymer foams, Colloids Surfaces A Physicochem. Eng. Asp. 438 (2013) 167–173.

[87] M. Mar Bernal, S. Pardo-Alonso, E. Solórzano, M.Á. Lopez-Manchado, R. Verdejo, M.Á. Rodriguez-Perez, Effect of carbon nanofillers on flexible polyurethane foaming from a chemical and physical perspective, RSC Adv. 4 (2014) 20761.

[88] F. Garcia-Moreno, M. Mukherjee, C. Jiménez, A. Rack, J. Banhart, Metal Foaming Investigated by X-ray Radioscopy, Metals (Basel). 2 (2011) 10–21.

[89] S. Pardo-Alonso, E. Solórzano, M.A. Rodriguez-Perez, Time-resolved X-ray imaging of nanofiller-polyurethane reactive foam systems, Colloids Surfaces A Physicochem. Eng. Asp. 438 (2013) 119–125.

[90] E. Solórzano, J. Pinto, S. Pardo, F. Garcia-Moreno, M.A. Rodriguez-Perez, Application of a microfocus X-ray imaging apparatus to the

study of cellular polymers, Polym. Test. 32 (2013) 321–329.

[91] C. Zhao, Y. Yan, Z. Hu, L. Li, X. Fan, Preparation and characterization of granular silica aerogel/polyisocyanurate rigid foam composites, Constr. Build. Mater. 93 (2015) 309–316.

[92] K.J. Chang, Y.Z. Wang, K.C. Peng, H.S. Tsai, J.R. Chen, C.T. Huang, K.S. Ho, W.F. Lien, Preparation of silica aerogel/polyurethane composites for the application of thermal insulation, J. Polym. Res. 21 (2014).

[93] S. Pérez-Tamarit, E. Solórzano, R. Mokso, M.A. Rodríguez-Pérez, In-situ understanding of pore nucleation and growth in polyurethane foams by using real-time synchrotron X-ray tomography, Polymer (Guildf). 166 (2019) 50–54.

[94] M. Kampschulte, G. Erdmann, J. Sender, G. Martels, W. Böcker, T. Elkhassawna, C. Heiß, A.C. Langheinrich, E. Roeb, M. Roderfeld, G.A. Krombach, The development and validation of micro-CT of large deep frozen specimens, Scanning. 37 (2015) 63–72.

[95] S.M. Jorgensen, B. Blank, E.L. Ritman, Cryostatic micro-CT imaging of transient processes, Dev. X-Ray Tomogr. III. 4503 (2002) 140.

[96] A. Corral, M. Balcerzyk, Á. Parrado-Gallego, I. Fernández-Gómez, D.R. Lamprea, A. Olmo, R. Risco, Assessment of the cryoprotectant concentration inside a bulky organ for cryopreservation using X-ray computed tomography, Cryobiology. 71 (2015) 419–431.

[97] S. Pérez Tamarit, Structural characterization of solid cellular polymers by X-ray tomography and light scattering, University of Valladolid, 2019.

[98] K. Mader, R. Mokso, C. Raufaste, B. Dollet, S. Santucci, J. Lambert, M. Stampanoni, Quantitative 3D characterization of cellular materials: Segmentation and morphology of foam, Colloids Surfaces A Physicochem. Eng. Asp. 415 (2012) 230–238.

[99] A. Nistor, M. Toulec, A. Zubov, J. Kosek, Tomographic Reconstruction and Morphological Analysis of Rigid Polyurethane Foams, Macromol. Symp. 360 (2016) 87–95.

[100] S. Pardo-Alonso, E. Sorlórzano, L. Brabant, P. Vanderniepen, M. Dierick, L. Van Hoorebeke, M.A. Rodríguez-Peréz, E. Solórzano, L. Brabant, P. Vanderniepen, M. Dierick, L. Van Hoorebeke, M.A. Rodríguez-Pérez, 3D Analysis of the progressive modification of the cellular architecture in polyurethane nanocomposite foams vía X-ray microtomography, Eur. Polym. J. 149 (2013) 999–1006.

[101] S. Pardo-Alonso, E. Solórzano, J. Vicente, L. Brabant, M.L. Dierick, I. Manke, A. Hilger, E. Laguna, M.A. Rodriguez-Perez, μCT-Based Analysis of the Solid Phase in Foams: Cell Wall Corrugation and other Microscopic Features, Microsc. Microanal. 21 (2015) 1361–1371.

[102] S. Pardo-Alonso, E. Sorlórzano, L. Brabant, P. Vanderniepen, M. Dierick, L. Van Hoorebeke, M.A. Rodríguez-Peréz, 3D Analysis of the progressive modification of the cellular architecture in polyurethane nanocomposite foams vía X-ray microtomography, Eur. Polym. J. 149 (2013) 999–1006.

[103] Y. Chen, R. Das, H. Wang, M. Battley, Characterization of microstructures of SAN foam core using micro-computed tomography:, Cell. Polym. 40 (2021) 143–164.

[104] C. Rau, M. Storm, S. Marathe, A.J. Bodey, S. Cipiccia, D. Batey, X. Shi, M.-C. Zdora, I. Zanette, S. Perez-Tamarit, P. Cimavilla, M.A. Rodriguez-Perez, F. Doring, C. David, Multi-Scale Imaging at the Coherence and Imaging Beamline I13 at Diamond, Microsc. Microanal. 24 (2018) 256–257.

[105] F. Hu, S. Wu, Y. Sun, Hollow-Structured Materials for Thermal Insulation, Adv. Mater. 31 (2019) 1801001.

[106] F. Kreith, R.M. Manglik, M.S. Bohn, Principles of Heat Transfer, Seventh Ed, Global Engineering, Stanford, 2010.

[107] R. Hasanzadeh, M.M. Darvishi, T. Azdast, Synergetic effect of MWCNT/nanoclays on microcellular polystyrene hybrid nanocomposite foams, Carbon Lett. (2019).

[108] A.G. Leach, The thermal conductivity of foams. I: Models for heat conduction, J. Phys. D. Appl. Phys. 26 (1993) 733–739.

[109] L.R. Glicksmann, Heat transfer in foams, in: N.C. Hilyard, A. Cunningham (Eds.), Low Density Cell. Plast., First Ed, 1994: pp. 104–152.

[110] B. Eling, Ž. Tomović, V. Schädler, Current and Future Trends in Polyurethanes: An Industrial Perspective, Macromol. Chem. Phys. 221 (2020) 1–11.

[111] P. Ferkl, R. Pokorný, M. Bobák, J. Kosek, Heat transfer in one-dimensional micro- and nano-cellular foams, Chem. Eng. Sci. 97 (2013) 50–58.

[112] B. Eling, Ž. Tomović, V. Schädler, Current and Future Trends in Polyurethanes: An Industrial Perspective, Macromol. Chem. Phys. 221 (2020).

[113] B. Merillas, J. Martín-De León, F. Villafañe, M.A. Rodríguez-Pérez, Transparent Polyisocyanurate-Polyurethane-Based Aerogels: Key Aspects on the Synthesis and Their Porous Structures, ACS Appl. Polym. Mater. 2021 (2021) 4607–4615.

[114] A.A. Pisal, A. Venkateswara Rao, Development of hydrophobic and optically transparent monolithic silica aerogels for window panel applications, J. Porous Mater. 24 (2017) 685–695.

[115] G.M. Pajonk, Transparent silica aerogels, J. Non. Cryst. Solids. 225 (1998).

[116] A. Soleimani Dorcheh, M.H. Abbasi, Silica aerogel; synthesis, properties and characterization, J. Mater. Process. Technol. 199 (2008) 10–26.

[117] Z. Zhu, G.M.B.F. Snellings, M.M. Koebel, W.J. Malfait, Superinsulating Polyisocyanate Based Aerogels: A Targeted Search for the Optimum Solvent System, ACS Appl. Mater. Interfaces. 9 (2017) 18222–18230.

[118] S. Alasti Bonab, J. Moghaddas, M. Rezaei, In-situ synthesis of silica aerogel/polyurethane inorganic-organic hybrid nanocomposite foams: Characterization, cell microstructure and mechanical properties, Polymer (Guildf). 172 (2019) 27–40.

[119] N. Nazeran, J. Moghaddas, Synthesis and characterization of silica aerogel reinforced rigid polyurethane foam for thermal insulation application, J. Non. Cryst. Solids. 461 (2017) 1–11.

[120] M.B. Østergaard, Preparation and characteristics of glass foam, Aalborg University, 2019.

[121] R. Lebullenger, S. Chenu, J. Rocherullé, O. Merdrignac-Conanec, F. Cheviré, F. Tessier, A. Bouzaza, S. Brosillon, Glass foams for environmental applications, J. Non. Cryst. Solids. 356 (2010) 2562–2568.

[122] J. König, R.R. Petersen, Y. Yue, Influence of the glass particle size on the foaming process and physical characteristics of foam glasses, J. Non. Cryst. Solids. 447 (2016) 190–197.

[123] G. Scarinci, G. Brusatin, E. Bernardo, Glass foams: Cellular Ceramics: Structure, Manufacturing, Properties and Applications, 2006.

[124] J. König, A. Lopez-Gil, P. Cimavilla-Roman, M.A. Rodriguez-Perez, R.R. Petersen, M.B. Østergaard, N. Iversen, Y. Yue, M. Spreitzer, Synthesis and properties of open- and closed-porous foamed glass with a low density, Constr. Build. Mater. 247 (2020) 118574.

[125] V. Göswein, C. Rodrigues, J.D. Silvestre, F. Freire, G. Habert, J. König, Using anticipatory life cycle assessment to enable future sustainable construction, J. Ind. Ecol. 24 (2020) 178–192.

[126] R.R. Petersen, J. König, Y. Yue, The mechanism of foaming and thermal conductivity of glasses foamed with MnO2, J. Non. Cryst. Solids. 425 (2015) 74–82.

[127] M.B. Østergaard, R.R. Petersen, J. König, Y. Yue, Effect of alkali phosphate content on foaming of CRT panel glass using Mn3O4 and carbon as foaming agents, J. Non. Cryst. Solids. 482 (2018) 217–222.

C APT Experimental

EXPERIMENTAL

3

3.1. MATERIALS

3.1.1. Rigid Polyurethane Foam Formulations

In this thesis, five polyurethane formulations were designed and studied. The raw materials for the formulations were commercially supplied by different companies. Their specifications and properties, as listed in the technical data sheet, are reported in Table 3-1, Table 3-2, Table 3-3 and Table 3-4. All the reported densities and viscosities were measured at 25 °C. The blowing agent used for all the foams in this thesis was distilled water.

Table 3-1: Polyether polyol properties.

Function	Commercial name	Supplier	OH value (mg KOH g^{-1})	Functionality	η (mPa s)	ρ (g cm^{-3})
Polyol	Alcupol R4520	Repsol	455	4.5	5250	1.08
Polyol	Alcupol R3810	Repsol	380	3	350	1.05

Table 3-2: Surfactant properties.

Function	Commercial name	Supplier	pH value	η (mPa s)	ρ (g cm^{-3})
Surfactant	Tegostab B5822	Evonik	7.0	600-1000	1.05

Table 3-3: Catalyst properties.

Function	Commercial name	Supplier	Purity	η (mPa s)	ρ (g cm^{-3})
Catalyst	Polycat 8/DMCHA	Evonik	≥99.0%	2.0	0.87

Table 3-4: Properties of the polymeric diphenylmethane diisocyanate (pMDI).

Function	Commercial name	Supplier	NCO%	η (mPa s)	ρ (g cm^{-3})
Isocyanate	IsoPMDI 92140	BASF	31.5	170-250	1.23

Throughout this text four of the formulations are labelled as *model formulations* (Table 3-5). These have been prepared with the minimum necessary components i.e., polyol, isocyanate, catalyst, blowing agent and surfactant. In these formulations, the effect of the

catalyst and blowing agent (water) concentration was assessed by independently varying their content. The catalyst was varied between 0.5 and 1.5 parts per weight (ppw) and water was modified between 2 and 5 ppw. Results regarding these formulations can be found in Chapter 4 and Chapter 5.

Table 3-5: Model RPU formulations.

Sample	Isocyanate Index	Polyol: R4520 (ppw)	Surfactant: B5822 (ppw)	Catalyst: DMCHA (ppw)	Water (ppw)
REF	110	100	1	0.5	2
BAF	110	100	1	0.5	5
GCF	110	100	1	1.5	2
GBF	110	100	1	1.5	5

By contrast, the fifth formulation was used for the production of RPU-Silica Aerogel composite foams (Table 3-6). This formulation differs from those in Table 3-5 in the incorporation of a second polyol (R3810) and in the concentration of catalyst and water which were fixed at 0.4 and 4 ppw, respectively.

Table 3-6: Composite RPU-Silica Aerogel formulations.

Sample	Isocyanate Index	Polyol: R4520 (ppw)	Polyol: R3810 (ppw)	Surfactant: B5822 (ppw)	Catalyst: DMCHA (ppw)	Water (ppw)	Aerogel (wt.%)
Reference	110	90	10	1	0.4	4	0.0
0.5% A	110	90	10	1	0.4	4	0.5
1.0% A	110	90	10	1	0.4	4	1.0
3.0% A	110	90	10	1	0.4	4	3.0

The selected filler for the production of these composites is a super-insulating and low density silica aerogel powder provided by Cabot. The concentration of fillers introduced in the formulation (Table 3-6) was calculated as the corresponding weight percentage (wt %) over the total mass of reactants used to prepare the foam. The thermal conductivity, λ, of the powder and other relevant properties provided by the supplier are listed in Table 3-7.

Table 3-7: Properties of commercial Silica Aerogel Powder.

Filler	Commercial name	Supplier	Particle size (μm)	Pore diameter (nm)	ρ (g cm^{-3})	λ (mW/m K)
Silica Aerogel	Enova Aerogel IC3100	Cabot	2-40	20.0	0.15	12

This powder is made of Silica particles with a hydrophobic [(trimethylsilyl)oxy] superficial treatment. This treatment replaces the hydrophilic unreacted OH groups on the surface of the aerogel skeleton (Figure 3-1 (a)) by [(trimethylsilyl)oxy] groups that inhibit the absorption of water, resulting in hydrophobic aerogels (Figure 3-1 (b)).

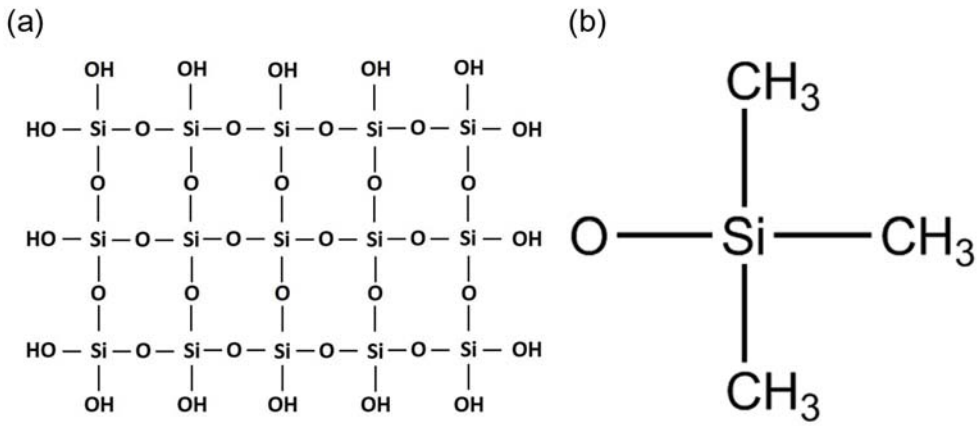

Figure 3-1: (a) Chemical structure of the Silica Aerogel particles, (b) Surface modification, OH is replaced by CH_3 groups.

This filler was selected for the low thermal conductivity of aerogel (12 mW (mK)$^{-1}$) which has the potential of decreasing the thermal conductivity of the RPU foams provided that the foaming process is not severely disrupted by the presence of particles. The results dealing with the production and characterization of these composites can be found in Chapter 7 and Chapter 8.

3.1.2. Rigid Polyurethane Foam Production

The RPU foams in this thesis were prepared by the reactive foaming process (Figure 3-2) of isocyanate with a blend of polyol, catalyst, water, and surfactant, following the formulations in Table 3-5 and Table 3-6.

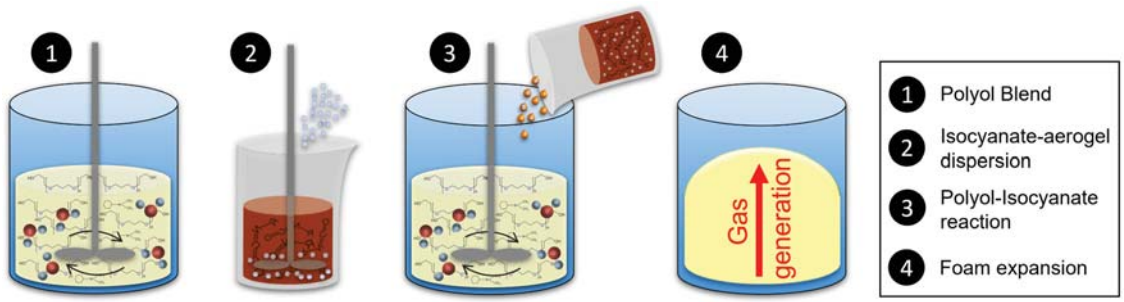

Figure 3-2: Preparation procedure for RPU composite foams. Non-composite foams were prepared following the same procedure but excluding step 2.

Firstly, the blend of the polyol with the other components (catalyst, water, and surfactant) was prepared using an overhead stirrer (EUROSTAR 60 control from IKA), equipped with a 50 mm diameter Vollrath™ Lenart-disc stirrer. The components were mixed at 250 rpm for 2 min. When preparing the composite RPU foams, the isocyanate component was mixed with the corresponding weight of aerogel particles (Table 3-6) using the same overhead stirrer at 250 rpm for 5 min. Immediately after performing the dispersion, the reactive foaming was triggered. Hence the composite foams (Table 3-6) were prepared by mixing a total mass of 50 g of liquid reactants together with 0.25 g (0.5 wt.%), 0.5 g (1.0 wt.%) and 1.5 g (3.0 wt.%) of aerogel particles. The polyol blend and isocyanate-particle dispersion were mixed at 1200 rpm for 10 s. Whereas, the *model formulations* (Table 3-5) were prepared by simply mixing a total mass of 40 g of the polyol blend and isocyanate using the same speed (1200 rpm) for the same time (10 seconds).

The mixture of the components and later growth of the foam took place inside a disposable plastic cup 10 cm in diameter and 15 cm tall. The curing of the foams took place in the same disposable cup for at least 48 hours at room temperature.

3.1.3. Externally supplied foams

Non-polyurethane foams have also been researched to prove the applicability of the developed image analysis characterisation methods (Chapter 6) to other materials. The foams selected for this purpose were: recycled glass foams, low density polyethylene (LDPE) foam and extruded polystyrene (XPS) foam. Glass foams were produced at Jožef Stefan Institute Ljubljana, Slovenia in the context of a collaborative project with CellMat Laboratory (Chapter 1, Table 1-7). LDPE and XPS foams were commercial materials supplied by the companies Zotefoams and Dow Chemical, respectively. Some insights into the production and properties of these foams are given in this section to provide context to the reader.

3.1.3.1. Glass foams

Glass foams were produced at Jožef Stefan Institute using recycled cullets of cathode-ray-tube (CRT) panel glass [1]. The foams were prepared from CRT panel glass mixed with 0.44 wt.% carbon black and 5.97 wt.% Mn_3O_4. The starting materials were homogenized using a Planetary Ball Mill PM200 (Retsch, Haan, Germany). Then, the ground powder was inserted into a stainless-steel form and gently pressed using a flat surface. The steel form was covered with alumina fibres and a metal plate. Samples were heat-treated in a flow of CO_2 (10 mL min^{-1}). Depending on the final density of the samples, these were prepared by heating at 5 °C min^{-1} to a temperature ranging from 740 to 820 °C for 40 min. In general, the higher the temperature the lower the final density of the foam [1]. Afterwards, foams were cooled at 7 °C min^{-1} to 550 °C and then naturally cooled down to room temperature in the furnace.

In this thesis, 8 samples of different porosity (97-93%) were considered. All foams have a closed cell structure with large cell sizes ranging from 2000 to 800 μm depending on the density. In addition, these foams present a multi-scale structure with pores of a few millimetres and micrometric pores embedded in the solid matrix (Figure 3-3). This complex structure makes these foams very suitable for studying their solid matrix structure using the new image analysis methods (Chapter 6) developed in this thesis for laboratory X-ray tomography. Moreover, the structure-thermal insulation properties relationship was also investigated (Chapter 8).

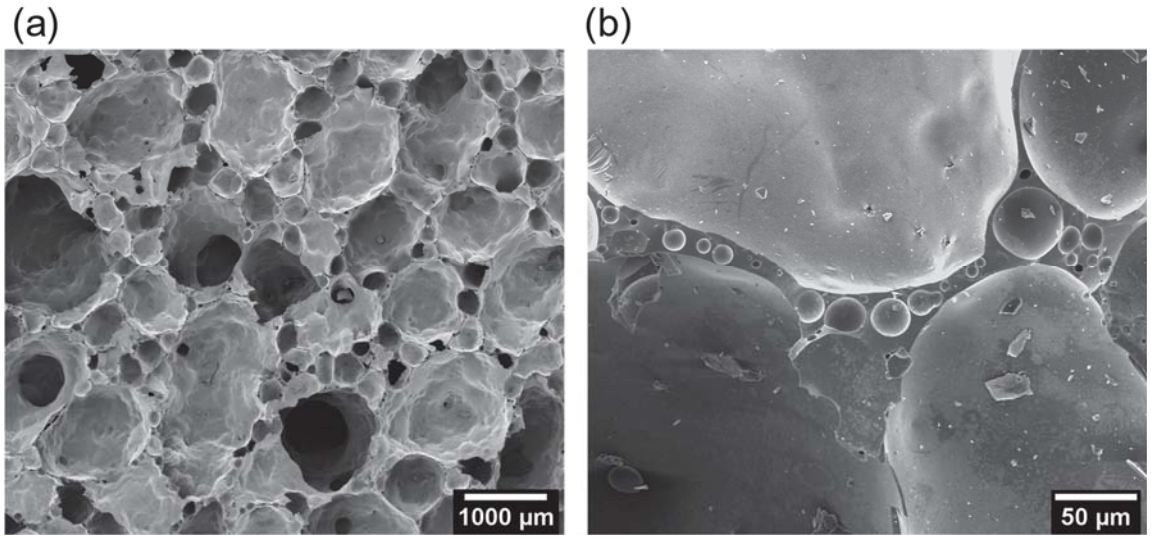

Figure 3-3: SEM micrographs displaying the cellular structure of one of the glass foams with a porosity of 94.4% (a) general view of the structure (b) close-ups of the cells in the solid phase.

3.1.3.2. Thermoplastics foams: XPS and LDPE

The XPS foam was produced following extrusion foaming by Dow Chemical. This process yields foams of low density (35 kg m^{-3}) with a homogeneous cellular structure and thin cell walls and struts (Figure 3-4 (a)). The average struts and cell walls thickness is around 1-2 μm and the fraction of mass in the struts is extremely low, close to 0.1.

Likewise, the LDPE foam was a commercial product produced by Zotefoams (UK) and manufactured following the gas dissolution foaming process [2]. The density of the sample was 33.1 kg m^{-3}. The cells had polyhedral geometry with the solid material homogeneously distributed in the matrix (Figure 3-4 (b)). The fraction of mass in the struts for LDPE foams is rather low, meaning that most of the polymeric mass is located homogeneously between cell walls and struts. These foams were selected to verify whether the image analysis methods developed to characterise the polymer matrix are precise for materials beyond RPU foams (Chapter 6). As can be observed in Figure 3-4 the solid phase topology is very different for RPU foams.

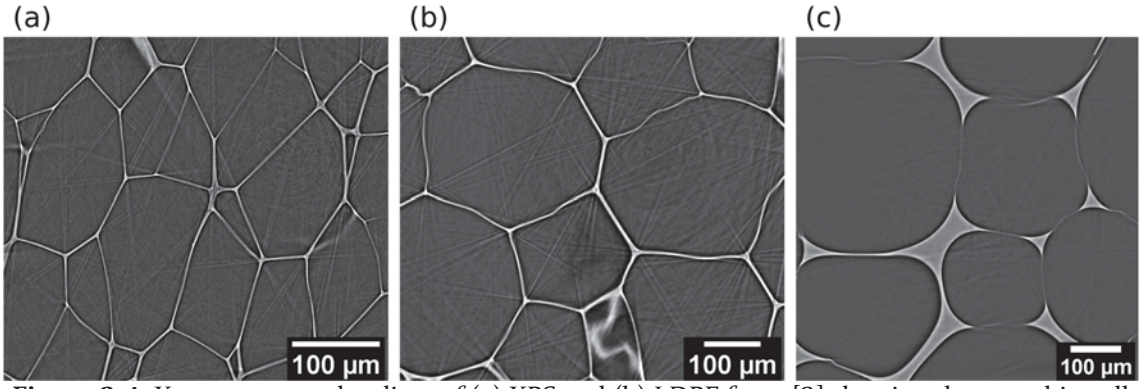

Figure 3-4: X-ray tomography slices of (a) XPS and (b) LDPE foam [2] showing the very thin cell walls and struts for these particular materials compared to (c) RPU foams.

3.2. EXPERIMENTAL METHODS

Several experimental techniques were employed to study the raw materials, foaming mechanisms and final foams covered in this dissertation. Two groups of characterisation techniques are defined. In the first group, it is possible to find standard characterisation methods for polymers and foams. By contrast, in the second group, non-conventional techniques and methods developed within the scope of this work can be found. The fundamentals and measurement protocols of all the experimental techniques are described thoroughly in the corresponding chapters. Hence, in the following sections, the methods used are collected and classified according to their purpose.

3.2.1. Standard characterisation techniques

3.2.1.1. Raw materials

Characterisation efforts at this level focused on the Silica aerogel particles, the initial formulations in Table 3-5 and the isocyanate-particle dispersions used to prepare the RPU composite foams (Section 3.1.2). A summary of the techniques can be seen in Table 3-8. For an exhaustive explanation of how each technique was used, the reader is referred to the corresponding results chapters.

Table 3-8: Characterisation techniques of the raw materials.

Chapter	Technique	Purpose
7	Laser Diffraction	Measure the size distribution of the silica aerogel particles
7, 8	Oscillatory Shear Rheology	Measure the viscosity of the initial formulations (Table 3-5)
		Asses the dispersion state of the aerogel particles in the isocyanate [3]
7	FTIR-ATR	Study the chemical structure and surface modification of the aerogel particles
7	SEM	Visualise the morphology and porous structure of the Silica Aerogel particles

The rheological characterisations mentioned in Table 3-8 were performed at the SMaRT (Soft Matter Rheology and Technology) group part of the Department of Chemical Engineering at KU Leuven (Belgium).

3.2.1.2. Final foams

An overview of the characterisation techniques applied to investigate the foams (Section 3.1.1 and 3.1.3) covered in this thesis can be found in Table 3-9. Characterisation of the final foams mainly focused on their structure and thermal insulation properties (thermal conductivity).

Table 3-9: Experimental methods to characterise the final foams.

Chapter	Technique	Purpose
4, 7, 8	SEM	Visualise and characterise the cellular structure of foams using a dedicated image analysis software based on FIJI/ImageJ [4]
4, 5, 6, 7, 8	ASTM D1622–08	Measure the apparent density of rigid foams [5]
7, 8	Gas pycnometer	Obtain the open cell content of foams [6]
6, 7, 8	X-ray Tomography	Characterise in 3D the cellular structure through image analysis [7,8]
8	Heat-flow Meter	Measure the thermal conductivity by the stationary method UNE12667 [9]

3.2.2. Non-standard and newly developed techniques

Within the scope of this thesis, three novel characterisation methods were developed (Table 3-10). Two of them aim to shed light on the mechanisms involved in the synthesis of RPU foams. Whereas the third method is, in fact, a collection of three image analysis strategies to characterise the solid matrix topology in low density foams. The novelty of this method is that it permits the analysis of the fraction of mass in the struts even when the cell walls have a thickness below the spatial resolution of the X-ray tomography scanner.

Table 3-10: Experimental methods developed in the context of this thesis.

Chapter	Technique	Purpose
4	Time-resolved DMA	Measure the modulus build-up, porosity generation and polymerisation kinetics in reactive foams [10]
5	Cryogenic X-ray Tomography	Study in 3D and ex-situ the cellular structure generation of RPU foams
6	Sub-pixel X-ray Tomography	Develop analysis methods to characterise the solid matrix in foams using low-resolution laboratory X-ray tomography

In Table 3-11 four techniques for tracking the cellular structure generation and reaction kinetics of RPU foams are listed. These techniques were initially developed by other authors but due to their complexity, they are still non-standard characterisation methods. Time-resolved FTIR spectroscopy, reaction temperature recording and X-ray Radioscopy belong to this group and have been recently established at CellMat [11,12]. Conversely, Shear Rheology experiments of expanding RPU foams were carried out at the SMaRT group in Leuven (Belgium).

Table 3-11: Non-standard characterisation techniques to follow the foaming process of PU.

Chapter	Technique	Purpose
4, 7	Time-resolved FTIR	Monitor over time the isocyanate consumption and the urethane and urea groups generation in RPU foams [12,13]
7	Adiabatic Temperature Rise	Measure the internal reaction temperature of RPU foams assuming adiabatic conditions inside the foam [12]
4, 7	Oscillatory Shear Rheology	Study the polymerisation and viscoelastic properties development during the reactive foaming of RPU foams [14]
4, 7	X-ray Radioscopy	Visualise and analyse the cellular structure and porosity generation in a drop of reacting RPU [11,15]

The results obtained with the methods in Table 3-11 were contrasted with the information obtained using the newly developed methods (Table 3-10). Hence, the comparison permitted validation of the new experimental methods and provided additional information on the foaming mechanisms of RPU foams (Table 3-5 and Table 3-6).

3.3. REFERENCES

[1] J. König, A. Lopez-Gil, P. Cimavilla-Roman, M.A. Rodriguez-Perez, R.R. Petersen, M.B. Østergaard, N. Iversen, Y. Yue, M. Spreitzer, Synthesis and properties of open- and closed-porous foamed glass with a low density, Constr. Build. Mater. 247 (2020) 118574.

[2] S. Pérez Tamarit, Structural characterization of solid cellular polymers by X-ray tomography and light scattering, University of Valladolid, 2019.

[3] F.J. Galindo-Rosales, P. Moldenaers, J. Vermant, Assessment of the dispersion quality in polymer nanocomposites by rheological methods, Macromol. Mater. Eng. 296 (2011) 331–340.

[4] J. Pinto, E. Solorzano, M.A. Rodriguez-Perez, J.A. de Saja, Characterization of the cellular structure based on user-interactive image analysis procedures, J. Cell. Plast. 49 (2013) 555–575.

[5] ASTM D1622-08: Standard Test Method for Apparent Density of Rigid Cellular Plastics, (n.d.).

[6] ASTM D6226-10. Standard Test Method for Open Cell Content of Rigid Cellular Plastics, (n.d.).

[7] S. Pardo-Alonso, E. Sorlórzano, L. Brabant, P. Vanderniepen, M. Dierick, L. Van Hoorebeke, M.A. Rodríguez-Peréz, E. Solórzano, L. Brabant, P. Vanderniepen, M. Dierick, L. Van Hoorebeke, M.A. Rodríguez-Pérez, 3D Analysis of the progressive modification of the cellular architecture in polyurethane nanocomposite foams vía X-ray microtomography, Eur. Polym. J. 149 (2013) 999–1006.

[8] S. Pérez-Tamarit, E. Solórzano, A. Hilger, I. Manke, M.A. Rodríguez-Pérez, Multi-scale tomographic analysis of polymeric foams: A detailed study of the cellular structure, Eur. Polym. J. 109 (2018) 169–178.

[9] UNE-EN 12667:2002. Thermal performance of building materials and products. Determination of thermal resistance by means of guarded hot plate and heat flow meter methods. Products of high and medium thermal resistance, 2020.

[10] P. Cimavilla-Román, M. Santiago-Calvo, M.Á. Rodríguez-Pérez, Dynamic Mechanical Analysis during polyurethane foaming: Relationship between modulus build-up and reaction kinetics, Polym. Test. 103 (2021) 107336.

[11] S. Pardo-Alonso, X-Ray Imaging Applied to the Characterization of Polymer Foams ' Cellular Structure and Its Evolution, Universidad de Valladolid, 2014.

[12] M. Santiago-Calvo, Synthesis , Foaming Kinetics and Physical Properties of Cellular Nanocomposites Based on Rigid Polyurethane, University of Valladolid, 2019.

[13] M. Santiago-Calvo, J. Tirado-Mediavilla, J.L. Ruiz-Herrero, M.Á. Rodríguez-Pérez, F. Villafañe, The effects of functional nanofillers on the reaction kinetics, microstructure, thermal and mechanical properties of water blown rigid polyurethane foams, Polymer (Guildf). 150 (2018) 138–149.

[14] E. Mora, L.D. Artavia, C.W. Macosko, Modulus development during reactive urethane foaming, J. Rheol. 35 (1991) 921–940.

[15] S. Pardo-Alonso, E. Solórzano, S. Estravís, M.A. Rodríguez-Perez, J.A. de Saja, In situ evidence of the nanoparticle nucleating effect in polyurethane–nanoclay foamed systems, Soft Matter. 8 (2012) 11262.

Part 1

DEVELOPMENT OF METHODOLOGIES

C APT

Rheological behaviour during Polyurethane foaming

RHEOLOGICAL BEHAVIOUR DURING POLYURETHANE FOAMING

4

4.1. INTRODUCTION

This chapter includes two publications dealing with the development and validation of experimental methods to understand the rheological behaviour of RPU foams during their synthesis. In these publications, four model formulations have been studied. These formulations present independent modifications in their catalyst and water content. In the first publication (P. Cimavilla-Román et al. Polym. Test. 103, 107336 (2021). doi: 10.1016/j.polymertesting.2021.107336) the robustness of a new measuring protocol based on dynamic mechanical analysis (DMA) for expanding and curing foams is determined. In addition, the impact of the reaction kinetics on the viscoelastic properties development over time has been explored. The second publication (The influence of viscosity build-up on the foaming dynamics of Rigid Polyurethane foams, submitted) accomplishes two objectives. On the one hand, it presents the evolution of the viscoelastic properties for the same model formulations during foaming using Shear Rheology. This approach permits validating the accuracy of the DMA-based methodology presented in the previous publication. On the other hand, it sheds light on the influence of the modulus build-up kinetics on cellular structure generation. Moreover, cell growth was simulated under different gas concentrations and viscosities. The experimental and modelled results are compared to understand the influence of the modulus build-up speeds on the degeneration of the cellular structure.

Section 4.2.

Dynamic mechanical analysis during polyurethane foaming: relationship between modulus build-up and reaction kinetics

Paula Cimavilla-Román[a], Mercedes Santiago-Calvo[a], Miguel Ángel Rodriguez-Pérez[a,b]

[a] Cellular Materials Laboratory (CellMat), Condensed Matter Physics Department, University of Valladolid, Paseo Belen 7, Valladolid, 47011, Spain

[b] BioEcoUva. Research Institute on Bioeconomy, University of Valladolid, Spain

Published in: Polymer Testing, 103, 107336 (2021)

DOI: 10.1016/j.polymertesting.2021.107336

Graphical Abstract

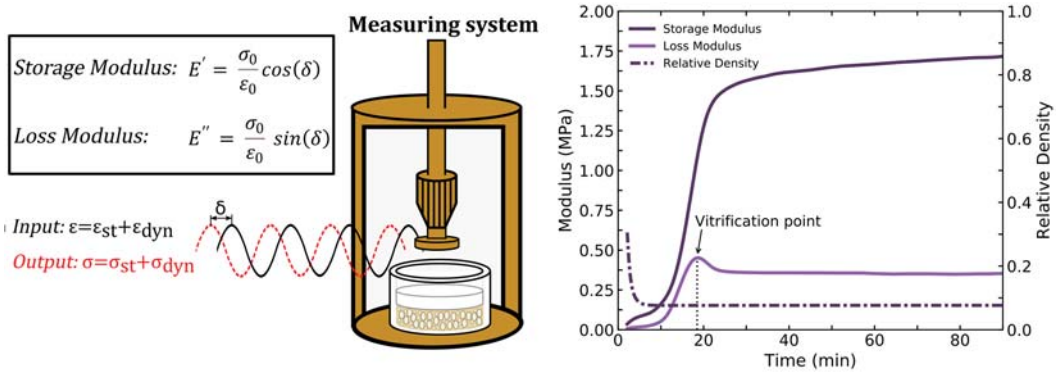

Polym. Test. 103, 107336 (2021)

ABSTRACT

The modulus build-up and relative density evolution during the reactive foaming of four standard polyurethane formulations was monitored in-situ by Dynamic Mechanical Analysis (DMA) with a customised set-up in parallel plate geometry. The modulus increased from 0.01 MPa in the first minutes to over 1.2 MPa within 20 minutes. The set-up also enabled the recording of vitrification followed by curing times. These typically occur within 3 minutes of each other. The results of DMA are corroborated by measurements of the reaction kinetics with Infrared Spectroscopy. This goes to show that the modulus remains nearly unchanged during the stage of swiftest isocyanate conversion, while the point of gel conversion is accompanied by their increase.

KEYWORDS

Dynamic Mechanical Analysis; Rheokinetics; FTIR Spectroscopy; Rigid Polyurethane foams; Chemical reactions.

1. INTRODUCTION

By the end of 2019, polyurethane (PU) products represented more than 9% of the European plastic consumption [1]. Unlike other polymers, PU encompasses a wide variety of materials ranging from thermosets adhesives to thermoplastic elastomers and foam products. The versatility of this polymer is the main reason accounting for its extensive consumption. Among these PU-based materials, foams represent around 67% of their global consumption [2]. There are two main types of PU foams. On the one hand, flexible foams are mainly used in comfort applications and transportation due to their load-bearing capacity and resilience [3]. On the other hand, due to its low thermal conductivity and excellent mechanical properties, rigid polyurethane foams (RPU) are used in a myriad of applications, such as insulating materials for construction, insulators for refrigeration systems as well as structural elements in the automotive industry [4–6]. Modern society's demands and increasing pressure from governmental institutions require constant research on these materials to enhance properties, ensure their sustainability and expand their applicability limits [2,7–9].

Enhancing the properties of RPU foams' unavoidably involves modifying current formulations and production routes [10–15]. As a consequence of the complexity of the foaming process of these materials, fine-tuning formulations or changing the initial raw materials by a trial-and-error approach is an arduous task. Boosting these material's performance requires a deep understanding of the modifications undergone by the initial raw materials by the reaction. RPU foams are the result of two exothermic reactions, one between isocyanate with hydrogen active groups stemming from the polyol and another one between isocyanate and water. The reaction between isocyanate and polyol, *gelling reaction,* is responsible for generating urethane cross-links. While the reaction between isocyanate and water, known as *blowing reaction,* releases CO_2 gas and generates urea hard segments. The release of CO_2 at early stages of the reaction, when the polymer is still a low modulus and low molecular weight gel, leads to foam expansion. Prior to the foam expansion, the CO_2 gas generated saturates the reactive mixture. Once the amount of gas in the mixture exceeds the solubility limit, this thermodynamic instability leads to the nucleation of cells, which later grow due to the ongoing blowing reaction [16]. Cell growth progresses until the polymer matrix has reached a limiting stiffness from which the foam expansion can no longer continue.

Polym. Test. 103, 107336 (2021)

Therefore, producing foams with optimum properties requires attaining a delicate balance between cell nucleation, cell growing, cellular structure stabilisation, fast polymerisation of the initial reactive mixture and a swift viscosity increase of the polymer matrix. Any additional components, such as catalysts, surfactants or fillers, drastically modify this balance [13,17,18]. Hence, it is vital to characterise the equilibrium between the different phenomena and physical magnitudes that ultimately condition the final cellular structure, polymer morphology and foams' properties[17]. This is why there has been a rise in the number of *in-situ* techniques enabling researchers to gain insight into the RPU foam formation in the last years [14,19–21].

These *in-situ* techniques can be divided into two groups depending on whether they follow the chemical or physical events leading to the foam formation. On the chemical side, infrared expandometry, foaming temperature measurements, FTIR spectroscopy, and small-angle X-ray scattering (SAXS) are well-established techniques that give information about the system's reactivity [13,19,22,23]. FTIR spectroscopy and SAXS provide information about the kinetics of both gelling and blowing reactions, and about the development of a microphase separated polymer morphology [13,19,22]. In addition, PU foaming is exothermic and the foaming temperature evolution can be monitored by inserting thermocouples into the material. [23]. Similarly, infrared expandometry allows probing the sample's surface temperature as well as the foam expansion [24]. On the physical side, imaging techniques and rheology have been used to understand the mechanisms of foam formation. On the one hand, X-ray Radioscopy and *in-situ* optical imaging have been used to observe cell growth and degeneration of the cellular structure [16,25]. On the other hand, previous studies have also shown that by employing shear rheology, it is possible to measure the evolution of the foam's modulus with time [20,26,27]. Using a rheometer with a flooded parallel plate geometry, Mora et al. [26] studied the evolution of flexible PU foams' shear modulus with time. During the reactive foaming process, the authors were able to identify four phenomenological stages, corresponding to bubble nucleation, liquid foam, phase separation and a final stage corresponding to the already foamed material.

Despite the success of rheology in measuring the foam's modulus development and identifying the different foam formation stages, this technique is not as widespread as the previously mentioned *in-situ* techniques. The reason lies in the relative complexity of the method, a reputation for mathematical complexity, and the technical difficulty of keeping the growing foam between the equipment plates [28]. The latter necessitates a small gap

between the parallel plates, which limits the sample's mass to a low value. Thus, only foams of a few layers of cells in thickness can be investigated [29]. In order to avoid this, there are reports of flooded parallel-plate geometries with which larger samples can be accommodated [26]. The trade-off is the variation of the foam's mass between the plates during the experiment, which limits the accuracy of the experimental results.

Another common technique for the determination of the viscoelastic properties of polymers is Dynamic Mechanical Analysis (DMA). DMA provides information on major and minor transitions of solid polymers and it has been used extensively to measure the mechanical properties of viscoelastic materials as a function of temperature or frequency [28]. In addition, DMA has been also employed to measure the curing process of thermosets [28]. However, the technique has never been applied to investigate the simultaneous polymerisation and growth of polyurethane foams. This absence of reports on the application of DMA during the foaming process of thermosets could be explained by the disparate transformations undergone by solids and foams during polymerisation. In fact, non-foaming polymers during cure experience a minimum volume change which pales in comparison to that suffered by a foaming thermoset; for instance some PU foams experience a volume increase superior to thirty times [24,30]. Therefore, the existing methods to measure the modulus of curing thermosets cannot be directly translated to materials undergoing a simultaneous foaming process. Nonetheless, employing a customised fixture, like the one reported in this work, it is possible to keep the growing foam in contact with the measuring plate while maintaining the mass constant underneath it. This allows measuring the expansion ratio simultaneously to the modulus increase, which cannot be achieved with rheometers [28]. In this study, we propose a simple methodology based on DMA to measure the modulus development of RPU foams for the first time. To establish the method and determine its accuracy, we investigated four conventional RPU formulations with varying blowing agent (water) and catalyst content. The approach proposed here can deepen the understanding of the foaming process of PU systems, and the results obtained, modulus and viscosity increase vs time, could be implemented in existing models for the growing stage of RPU foams.

Polym. Test. 103, 107336 (2021)

2. EXPERIMENTAL

2.1. Materials

2.1.1. Reactants of RPU foams

The polyol component was a high functionality polyether polyol, Alcupol R4520 (4.5 functionality, OH value of 455 mg·KOH g^{-1}, viscosity 5250 mPa·s) from Repsol S.A. The isocyanate was a polymeric diphenylmethane diisocyanate (pMDI), IsoPMDI 92140 (2.7 functionality, 31.5% NCO, density 1.23 g cm^{-3}, viscosity 170-250 mPas) supplied by BASF. TEGOAMIN® DMCHA (N,N-dimethylcyclohexylamine) from Evonik was employed as a catalyst, a tertiary amine used primarily to promote urethane (polyol-isocyanate) reaction. TEGOSTAB® B8522 (a non-hydrolysable polyether-polydimethyl-siloxane–stabiliser) from Evonik was used as a surfactant to obtain superior cell structures. Distilled water was chosen as a blowing agent.

2.1.2. Preparation of RPU foams

Four different RPU foams were prepared, maintaining a constant isocyanate index. The formulations are presented in Table 4-1-1. While the polyol and surfactant contents were kept constant, the amount of catalyst (0.5 and 1.5 parts per weight (ppw)) and blowing agent (2 and 5 ppw) was changed independently.

The different components were mixed with an overhead stirrer (EUROSTAR 60 control from IKA), equipped with a 50 mm diameter VollrathTM Lenart-disc. A homogeneous polyol blend with the additives (catalyst, surfactant and blowing agent) was produced at 250 rpm for 2 minutes. To trigger the foaming reaction, a total mass of 40 g of isocyanate and polyol blend was mixed during 10 s at 1200 rpm in a plastic cup. The start of the stirring process between polyol blend and isocyanate is set to time 0 of the reaction.

Table 4-1-1. Components and concentrations for each RPU formulation.

Sample	Isocyanate Index	Polyol (ppw)	Surfactant (ppw)	Gelling catalyst (ppw)	Water (ppw)
REF	110	100	1	0.5	2
BAF	110	100	1	0.5	5
GCF	110	100	1	1.5	2
GBF	110	100	1	1.5	5

Following the formulations in Table 4-1-1, RPU foams with 40 g of material (large samples) were produced. Foams with low blowing agent content REF (Reference Formulation) and GCF (Gelling Catalyst Formulation) reached foam volumes of *ca*. 750 cm^3. In contrast, foams with high blowing agent content, BAF (Blowing Agent Formulation) and GBF (Gelling Blowing Formulation) attained foam volumes of nearly 1200 cm^3. These foams were left to cure at room temperature for one week. After this period the foams were cut, and the final density was characterised. DMA experiments were carried out to obtain stress-strain curves and the complex modulus of the cured foams.

In addition, around 100 mg from the reactive mixture were extracted from the plastic cup just after the stirring process to study the viscoelastic properties by time-resolved DMA experiments, the reaction kinetics by time-resolved FTIR spectroscopy and the reactivity of the foams by measuring the characteristic times of foam formation (see next sections for a detailed explanation of these measurements).

2.2. Methods

2.2.1. Reactivity of the foams

The system's reactivity can be roughly estimated by measuring characteristic times of the RPU foam formation, *i.e*. cream time, string or gel time, rise time, and tack-free time [21]. These times were determined using samples of similar mass to those tested in DMA experiments (100 mg). The samples were kept inside a furnace at 50 °C during the testing.

2.2.2. Density characterisation of the foams

Foam density was measured as described by ASTM D1622/D1622M-14 [31]. Density was measured on three different samples for each material, with a diameter of 30 mm and a height of 20 mm. Relative density was obtained as the ratio between the foam density and the solid material density (1160 kg/m^3).

Polym. Test. 103, 107336 (2021)

2.2.3. Dynamic Mechanical Analysis

Viscoelastic properties during the growing and curing of foams in Table 4-1-1 have been measured using a Perkin-Elmer DMA 7. The equipment was operated in compression mode, employing a 10 mm-diameter parallel plate configuration where the upper plate is mobile, and the lower plate is fixed. DMA's operating principle is based on supplying an oscillatory force to a sample and studying its response. This force causes a sinusoidal stress to the sample under study, $\sigma = \sigma_0 \sin(wt)$, which generates a strain wave, $\varepsilon = \varepsilon_0 \sin(wt + \delta)$ as a response. Depending on the material's viscous or elastic character, the strain wave will be shifted by a certain phase angle, δ. Provided that the material is purely elastic, the wave response will be in-phase with the applied oscillation (δ=0). On the contrary, a purely viscous material will respond with an out-of-phase strain wave ($\delta=\pi/2$). Therefore, by measuring the amplitude and the phase of the response strain wave, it is possible to calculate the storage modulus (eq. (4-1-1)), E', the loss modulus (eq. (4-1-2)), E'', the complex modulus (eq. (4-1-3)), E^*, and loss tangent (eq. (4-1-4)), or damping, $tan\ \delta$, as well as the equivalent viscosity values.

$$E' = \frac{\sigma_0}{\varepsilon_0} cos(\delta) \tag{4-1-1}$$

$$E'' = \frac{\sigma_0}{\varepsilon_0} sin(\delta) \tag{4-1-2}$$

$$E^* = E' + iE'' = \sqrt{(E')^2 + (E'')^2} \tag{4-1-3}$$

$$tan(\delta) = \frac{E''}{E'} \tag{4-1-4}$$

Although DMA is well established as a technique with which to investigate the properties of solids and their transitions [28], it is rarely applied to the study of fluids or low viscosity samples. For this, rotational rheometers are more often employed. Whereas fluids in a rotational rheometer can shear and glide because the applied force is parallel to the strain, in a DMA, the force is normal to the material. Usually, fluids subjected to normal stress will merely flow away from the compression plate, thereby providing meaningless information. Hence, to study the foam's rheological properties during the expansion process, it was necessary to develop a customised accessory (Figure 4-1-1). The designed fixture enables to accommodate unreacted and growing foams, which experience a quick transition from a fluid of low viscosity to a high modulus solid material. The accessory

comprises a 15 mm-internal diameter Teflon cup with a piston of the same diameter and material. The customised piston can glide with low friction inside the container by the force of either the expanding foam or the compression plate (Figure 4-1-1 component 6). This piston also ensures that no leakage of the growing foam occurs. Due to the limited dimensions of the measuring system, the maximum foam volume that the cup can hold is *ca*. 2.5 cm^3. In addition, the height of the foam can be recorded, and from it, the sample volume can be calculated. Using the value of the initial mass and this calculated volume, it is possible to measure the density and relative density as a function of time.

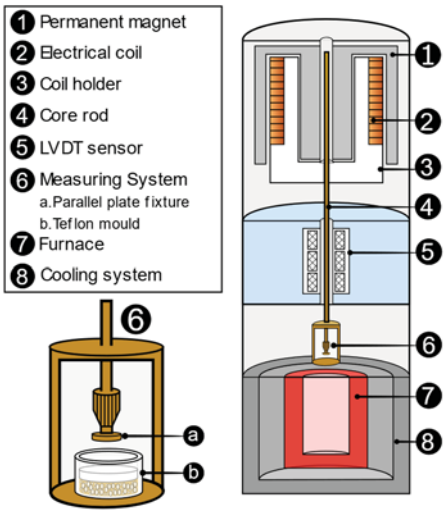

Figure 4-1-1: Scheme of the main components in the DMA 7 analyser and the measuring set-up.

Experimental procedure of time-resolved DMA

The samples for the DMA tests were produced following the method detailed in Section 2.1.2. A few microliters were extracted from the cup containing the reactive mixture with a syringe and injected into the Teflon container (Figure 4-1-1 component 6 b.). Simultaneously, the mass of the reactive mixture injected into the container was weighed using a precision balance. In order to ensure the reproducibility of the obtained results, the sample's mass was kept around 100 mg in all the experiments.

Once the sample was prepared, the piston was inserted into the cup, and the mould was placed in the measuring system (Figure 4-1-1 component 6). The plate was lowered to record the initial height, after which the experiment began. The first experimental data point was recorded 2 minutes after the initiation of the reaction, meaning that the foam growth had already begun once the acquisition started. The experiment ended after 90 minutes since the start of the RPU foam reaction.

Polym. Test. 103, 107336 (2021)

During these experiments, we chose to work under constant temperature (50 °C), constant frequency of oscillation (1 Hz) and controlled stress conditions. Data points were acquired every 6 s; thus, a total of 880 measurements were performed during the experiment. The sample was subjected to static stress of 509.3 Pa (static force: 90 mN) meant to hold the sample in place and to oscillatory or dynamic stress of 424.4 Pa (dynamic force: 75 mN) throughout the experiment. Under these conditions, the dynamic strain sinks from *ca*. 3%, when the mixture is soft, to *ca*. 0.05% at the end of the experiment. The low stresses applied were selected to obtain reliable values of the mechanical properties while still allowing the expansion of the foam.

An example of the technique's typical output when applied to investigate the foaming and curing process of an RPU foam can be seen in Section 3.3. Additionally, to ensure the method's reproducibility, at least three measurements were performed for every formulation.

DMA experiments of the cured foams

The mechanical properties of the foams produced ex-situ with 40 g of material (section 2.1.2) were also measured with DMA. The foams were cut into three sections; the central section had 20 mm of height and was extracted from mid-height of the foam. From the central section, at least two cylindrical samples of 13 mm of diameter were extracted, and all were investigated one week after their production. The experiment temperature and frequency were fixed at 50 °C and 1 Hz, respectively. The foams were subjected to a stress-strain test during which the dynamic stress increased linearly from 7.71 Pa to 7676.57 Pa. The static stress changed accordingly, and a ratio of 1.2 between the static and dynamic stress was kept constant for the entire run. In addition, to ensure comparability with the in-situ experiments, the complex modulus of the cured foams was calculated for the same values of force employed during the in-situ tests. [32].

2.2.4. Dynamic Mechanical Analysis

Time-resolved FTIR spectroscopy is a common technique for monitoring the reaction kinetics of PU foams [13,27,33]. In order to validate the modulus build-up kinetics, FTIR spectra of the samples during foaming were collected using a Bruker ALPHA spectrometer in attenuated total reflectance (ATR) mode. From the 40 g reacting mixture (section 2.1.2), 1 mL was extracted and poured onto the ATR cell's surface. The FTIR experiments lasted 90

minutes. A spectrum was acquired every 30 s - 180 spectra in total. The experiment's temperature was set to 50 °C, as it was for the DMA measurements. The isocyanate (NCO) consumption is extracted from the decrease in the area of the isocyanate band asymmetric stretching vibration at 2270 cm^{-1} [17]. To monitor the number of reaction products of the blowing and polymerisation reactions, the Amide I region (carbonyl region) located in the wavenumber range between 1610 and 1760 cm^{-1} was deconvoluted into 7 different bands encompassing all the urethane and urea compounds as indicated in the literature [13,34,35].

3. RESULTS

3.1. Reactivity of the foams

In order to evaluate the reactivity of the foams, the characteristic times of RPU foaming reaction were measured: cream time, string time, rise time and tack-free time. Firstly, cream time corresponds to the start of bubble nucleation, physically characterised by a change in the mixture's colour from a translucent dark brownish liquid to one cream-like. Secondly, the string time is the time at which the foam starts to polymerise or gel. It can be recognised by the thin strands or strings that can be pulled out of the foam when touching its surface with a sharp object. Thirdly, the rise time is the time at which the foam reaches its maximum expansion. Lastly, tack-free time is the time when the foam's surface loses its tackiness. It can be taken as the surface cure time of RPU foams. The characteristic times for the four RPU foams can be found in Table 4-1-2. On the one hand, REF and BAF foams were obtained using the same amount of gelling catalyst in the PU formulation (0.5 ppw), lower than that used in foams GCF and GBF (1.5 ppw). And since the gelling catalyst promotes the PU reactions, it can be observed that the characteristic times of the two latter materials are shortened. On the other hand, when RPU foams with the same amount of gelling catalyst and different water amount are compared (REF versus BAF, and GCF versus GBF), those materials with higher amounts of water in the PU formulation (BAF and GBF) reveal slightly lower characteristic times. On the whole, the addition of water and catalyst promotes the system's reactivity, shortening the reaction times in line with expectations.

Polym. Test. 103, 107336 (2021)

Table 4-1-2: Characteristic times of the RPU foams.

Samples	Catalyst (ppw)	Water (ppw)	Cream time (min)	String time (min)	Rise time (min)	Tack-free time (min)
REF	0.5	2	1.2 ± 0.1	4.2 ± 0.6	5.7 ± 0.9	14.9 ± 2.0
BAF	0.5	5	0.9 ± 0.1	3.7 ± 0.9	4.3 ± 0.2	15.6 ± 1.2
GCF	1.5	2	0.7 ± 0.02	2.0 ± 0.3	2.7 ± 0.3	6.7 ± 1.4
GBF	1.5	5	0.4 ± 0.7	1.4 ± 0.2	1.7 ± 0.1	5.7 ± 0.5

3.2. Foam Density Characterisation

In order to verify the evolution of the foam density detected during the DMA tests, the final geometric density of the foams produced with 40 g of material was measured (Section 2.1.2). Table 4-1-3 shows that the Reference foam (REF) with the lowest catalyst and water content (0.5 ppw and 2 ppw, respectively) has the highest density, followed by the foam produced with 1.5 ppw of gelling catalyst and 2 ppw of water (GCF). In contrast, the foams with 5 ppw of water (BAF and GBF) show the highest foam density decrease with respect to REF and GCF. Moreover, the lowest density was achieved for the foam with the highest water and catalyst content (GBF), which also presents the swiftest reaction kinetics according to Table 4-1-2. Therefore, the density is mainly determined by the amount of blowing agent and catalyst. A greater amount of water and gelling catalyst in the PU formulation gives rise to foams with lower densities.

Table 4-1-3: Density and relative density of the foams produced following Section 2.1.2

Samples	Catalyst (ppw)	Water (ppw)	Density (kg/m3)	Relative Density
REF	0.5	2	60.4 ± 1.1	0.052
BAF	0.5	5	37.7 ± 1.1	0.033
GCF	1.5	2	59.5 ± 3.7	0.051
GBF	1.5	5	33.1 ± 1.6	0.029

3.3. Foaming and curing kinetics: Time-resolved DMA

Figure 4-1-2 illustrates the main results obtained from a single DMA experiment for the formulation with a low concentration of blowing agent and catalyst (REF). From these data, the different chemical and physical events that lead to changes in the sample's viscoelastic properties can be identified [20,26,27,36]. Firstly, it can be appreciated how the sample's modulus remained rather low and unchanged during the foam expansion (at times lower

than 10 min). However, due to the relatively long loading time, the sample's porosity was already high when the run started. In fact, relative density was below 0.63 at the beginning of the experiment, and this value decreased to a final relative density of 0.1 in less than five minutes. Because of the low modulus values, it can be concluded that the mixture was still a low-molecular-weight gel that expanded due to the force of the CO_2 gas being generated during this stage. The second stage, at times longer than the string time (Table 4-1-2), was accompanied by the rapid build-up of both moduli. This increase was due to the stiffening of the polymer matrix by the generation of a stable cross-linking network [37]. In this stage, the loss modulus progressed to a maximum that several authors have previously ascribed to the Berghams or vitrification point [25,38,39]. From a thermokinetic point of view, vitrification is reached when the reactive mixture's glass transition temperature becomes equal to the curing temperature [40]. At vitrification, the morphology freezes, decreasing the chain mobility and hence reducing the curing rate. From this point on, the reaction becomes diffusion-controlled [41]. Finally, once the reactivity of the system had quenched, the polymerisation speed decreased, and the storage modulus reached a plateau region. After this, the moduli continued to grow. Although the speed of increase is reduced considerably, and the remaining changes in moduli result from the long reactivity of RPU foams, which continue to cure long after the reaction starts. In addition, for this specific formulation, the storage modulus attained nearly 75% of its final value after 20 minutes from the reaction start.

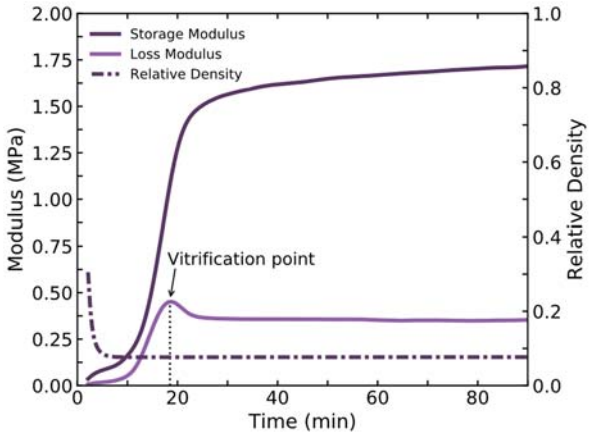

Figure 4-1-2: Example of the results obtained during a typical DMA experiment for sample REF (0.5 ppw catalyst and 2 ppw water)

All the formulations in Table 4-1-1 were studied according to the same experimental procedure detailed in Section 2.2.3. Figure 4-1-3 represents the average values and the standard deviation of the storage and loss modulus after repeating the measurements three

times for different samples produced with the same formulation. As can be seen, the standard deviation is considerable, yet the differences between the foams are clear, and it is possible to distinguish not only the final foam's modulus but most notably the reaction speeds.

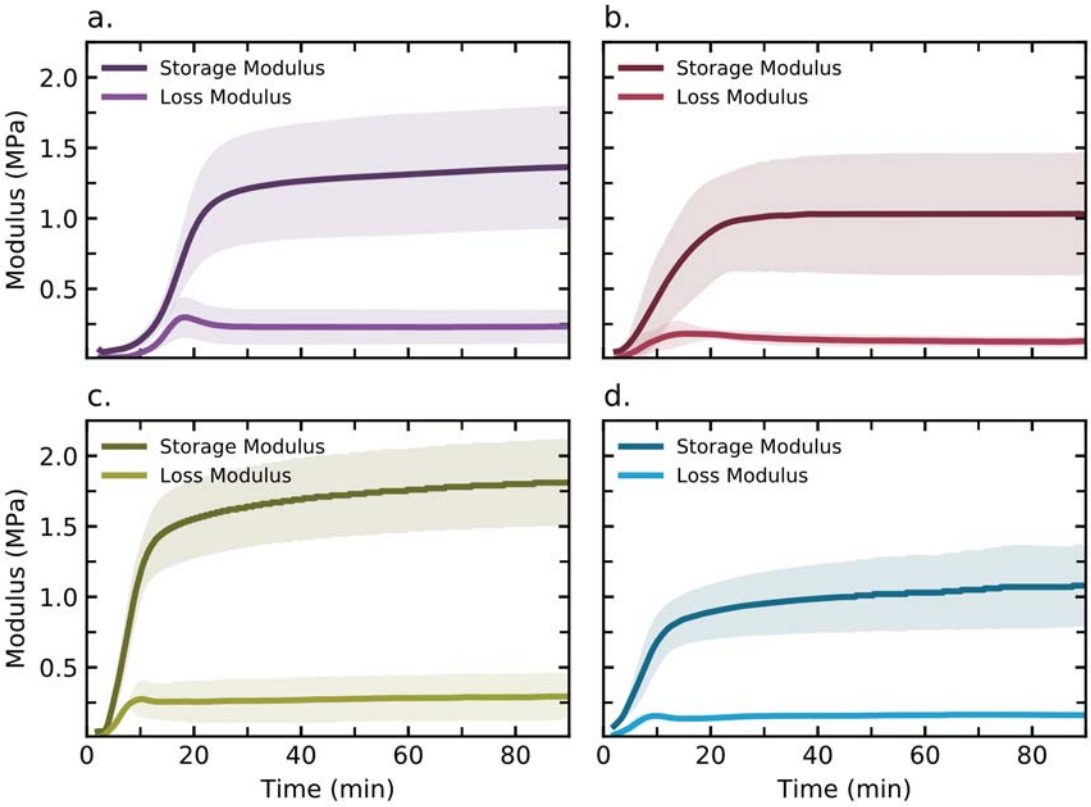

Figure 4-1-3. Moduli development as a function of time for each of the foams in Table 4-1-1 (a) REF (0.5 ppw catalyst and 2 ppw water), (b) BAF (0.5 ppw catalyst and 5 ppw water), (c) GCF (1.5 ppw catalyst and 2 ppw water), and (d) GBF (1.5 ppw catalyst and 5 ppw water).

It can be observed how the onset of the storage modulus build-up and the time at which the foams' modulus stabilised was longer for the formulations with the least catalyst content (Figure 4-1-3 (a) and (b)). In fact, foams REF (Figure 4-1-3 (a)) and BAF (Figure 4-1-3 (b)) took more than 30 minutes to reach the storage modulus plateau. In contrast, formulations with the highest catalyst dosage (Figure 4-1-3. (c) and (d)) show the opposite trend. An almost immediate modulus development is appreciable as soon as the experiment starts. This is followed by a quick modulus build-up. Apart from this, the relative density decrease was also faster for the foams with more catalyst (Figure 4-1-4), an observation that is in good agreement with the rise times reported in Table 4-1-2. Lastly, information can also be extracted from the slope of the storage modulus increase: foams with higher blowing agent content (Figure 4-1-3 (b) and (d)) revealed a slower transition from a low modulus gel to a

cross-linked solid. Particularly, BAF (Figure 4-1-3 (b)) and GBF (Figure 4-1-3 (d)) presented slopes of 0.063 and 0.083 MPa/min, respectively, whereas foams REF (Figure 4-1-3 (a)) and GCF (Figure 4-1-3 (c)) reached much higher speeds of modulus increase in the region of 0.099 and 0.190 MPa min^{-1}, respectively. Therefore, on average, formulations with less water exhibited twice the speed of elastic modulus increment.

As alluded to previously, the loss modulus also provides some information regarding each foam's curing and polymerisation kinetics. Most importantly, the vitrification time is observed to decline with decreasing catalyst content (Table 4-1-4). This implies that the samples with weaker catalysis take longer to achieve the glassy state characteristic of amorphous thermosetting PU and thus to reach the glass transition temperature of the final material [42]. It can be surmised that vitrification stands for a form of curing time at which the polymer reaches the high stiffness characteristic of RPU foams. This rationale is in agreement with the curing kinetics that can be inferred from the storage modulus evolution. In fact, it is observed that shortly after the vitrification time, the foams attained nearly 75% of their final modulus in the time-resolved DMA experiments (Table 4-1-4). However, due to the long loading times and the lower precision of DMA when the foam is in a fluid state, it was not possible to identify the gelation time, which in principle should be at the crossover between the storage and loss modulus [26,42,43].

Table 4-1-4. Vitrification times (extracted from the average loss modulus in Figure 4-1-3) and time at which the storage modulus had progressed to 75% of the final value.

Samples	Catalyst (ppw)	Water (ppw)	Vitrification time (min)	75% of cure time (min)
REF	0.5	2	18.6 ± 1.1	21.5 ± 1.9
BAF	0.5	5	15.3 ± 1.9	15.9 ± 2.6
GCF	1.5	2	9.4 ± 1.3	10.6 ± 1.6
GBF	1.5	5	9.3 ± 1.1	13.1 ± 3.7

Furthermore, the DMA measurements also mapped the relative density evolution of the samples during growth (Figure 4-1-4). The relative density evolution shows that the foams with more catalyst presented a faster decrease in relative density. This observation is in good agreement with the rise times reported in Table 4-1-2. Although the samples produced during the DMA tests achieved higher relative densities, the final values are related to those measured on the ex-situ produced samples (Table 4-1-3). Foams with higher water dosage

(BAF and GBF) always reveal lower densities throughout the whole experiment. However, the effect of the catalyst level is less evident in the DMA samples. A minor decrease in the final density was detected in the large samples when the catalyst level was increased. No appreciable effect was observed for the small samples since slight densification was found with respect to the lower catalyst counterparts. This could be due to the lower curing temperatures or the degasification induced by the constant stress applied to the samples during expansion [20].

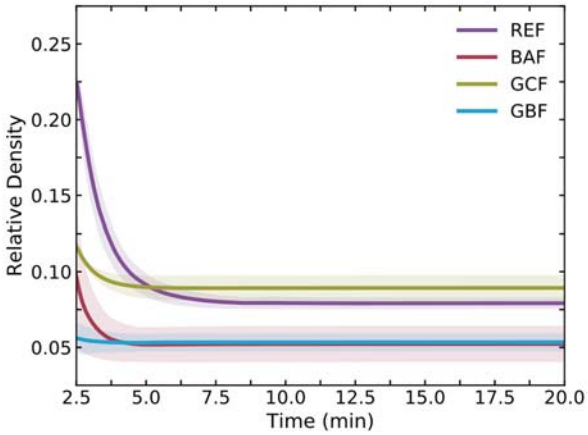

Figure 4-1-4. Relative density evolution with time during 20 minutes from the reaction start for each of the foams in Table 4-1-1: REF (0.5 ppw catalyst and 2 ppw water), BAF (0.5 ppw catalyst and 5 ppw water), GCF (1.5 ppw catalyst and 2 ppw water) and GBF (1.5 ppw catalyst and 5 ppw water).

Regarding the standard deviation among repeated runs for the same formulation, the coefficient of variation is significantly lower in the temporal scale than in the absolute values of the modulus. On the one hand, the temporal events that can be detected by means of this technique were well defined in all the experiments. For instance, among repeated experiments for each foam, the coefficient of variation of the vitrification time was found to be below 12% in all cases (Table 4-1-4). Additionally, when the curves in Figure 4-1-3 were normalised so that their final modulus is equal to 1, the time at which the foams reach 75% of the last recorded modulus remains fairly constant among repetitions (Table 4-1-4). On average, the coefficient of variation for this value is around 20% for these materials. On the other hand, when considering the modulus final values for each of the formulation's subsequent runs, the coefficient of variation was found to be slightly larger.

Regardless of this, conclusions can be drawn from the hierarchy of each sample's final modulus (Figure 4-1-3). Foams with more water content (BAF and GBF) showed lower final modulus values, whereas lower water dosages yielded foams with a higher modulus (REF

and GCF). Several factors can account for this phenomenon, such as differences in the cross-linking densities, changes in the polymer matrix's stiffness, or the higher density of the foams with less water. To ensure the accuracy of the final modulus values measured by time-resolved DMA experiments (Figure 4-1-3), the mechanical properties of the cured foams produced in the cup were also measured with DMA. The complex modulus was calculated under the same stress conditions as the time-resolved DMA tests. The obtained values can be compared to the complex moduli measured in-situ (see Table 4-1-5). Similar conclusions to those drawn from the *in-situ* results (Figure 4-1-3) can be made from the data summarised in Table 4-1-5. The higher the catalyst content, the higher the moduli in comparison to the foams with the same water content. The higher the water content, the lower the modulus with respect to the foams with the same catalyst content. Therefore, a greater amount of water and catalyst in the foam formulation gives rise to materials with lower densities and lower modulus and vice versa. Regarding the absolute values, the cured foams' complex modulus is undoubtedly lower than that of the samples foamed during the time-resolved DMA experiments. This difference can be due to several factors, such as the lower density of the foams produced in a cup, the skin developed by the samples produced in the mould during in-situ DMA (section 2.2.3) or the different degree of polymerisation attained by the in-situ and ex-situ samples.

Table 4-1-5. Complex and Young's modulus obtained from the linear region of the stress-strain curves.

Samples	Catalyst (ppw)	Water (ppw)	Complex modulus after 90 min (MPa)	Complex modulus of the cured foams (MPa)
REF	0.5	2	1.38 ± 0.44	0.54 ± 0.09
BAF	0.5	5	1.05 ± 0.34	0.31 ± 0.03
GCF	1.5	2	1.84 ± 0.33	0.55 ± 0.09
GBF	1.5	5	1.19 ± 0.13	0.30 ± 0.02

Nevertheless, to fully comprehend the changes observed in the samples' viscoelastic properties, it is fundamental to have some information about the reaction kinetics of these systems.

Polym. Test. 103, 107336 (2021)

3.4. Reaction kinetics: FTIR Spectroscopy

In order to investigate the temporal evolution of the moduli and its connection to the reactivity of each system, FTIR spectra of the reacting foams were acquired. In this study, two main aspects of the RPU reaction kinetics were monitored: the consumption of isocyanate and the generation of the main products of the gelling and blowing reactions [13,44].

3.4.1. Isocyanate consumption

Figure 4-1-5 depicts the average isocyanate conversion from three experiments with each of the foams in Table 4-1-1. None of the foams had fully reacted by the end of the experiment since they reached an isocyanate conversion of around 0.65. Furthermore, the curves of isocyanate conversion for all samples reached around 0.6 in the first 30 minutes of the foam formation, which is equivalent to more than 90% of their final isocyanate conversion. This reveals that the reaction rates are considerably reduced early in the curing process, even if there are still a high number of isocyanate functional groups available to react. Moreover, the speed of isocyanate consumption was calculated for every foam. The time at which the rate of conversion decreases to nearly zero (below 0.025 min^{-1}) varies significantly with the catalyst content. Foams with 1.5 ppw of gelling catalyst (GCF and GBF) reach such speeds after 12 minutes, whereas foams with 0.5 ppw of gelling catalyst (REF and BAF) take more than 25 minutes to experience such a decrease in their reaction rate. No significant effect was observed when the water content was changed. The speeds of conversion seem to be in good agreement with the vitrification times reported in Table 4-1-4, suggesting that after vitrification, the reactions were nearly halted, and the conversion fell to nearly zero [39,44]. Surprisingly, there are no notable differences in the final degree of conversion among foams. Regardless of the concentration of catalyst or water, they all attained conversions close to 0.65. Yet, the different catalysis levels influenced the degree of NCO consumption greatly at short reaction times. Most notably, foams REF and BAF (with 0.5 ppw of catalyst) present lower reaction rates than GCF and GBF with a high catalyst content of 1.5 ppw. Moreover, if samples with the same catalyst content are compared, that with more water has a higher reaction rate.

Concerning the variation between repeated measurements of foams with the same formulation, those with 0.5 ppw of catalyst concentration present higher deviation among

experiments (on average, 18% for foam REF and 9% for foam BAF). On the contrary, foams with 1.5 ppw of catalyst reveal lower deviation among repetitions, less than 8% for foam GBF and barely 2% for foam GCF. Therefore, the low catalyst concentration in RPU foams seems to be accountable for a higher degree of dispersion between experiments. This behaviour is in agreement with that observed during the DMA experiments.

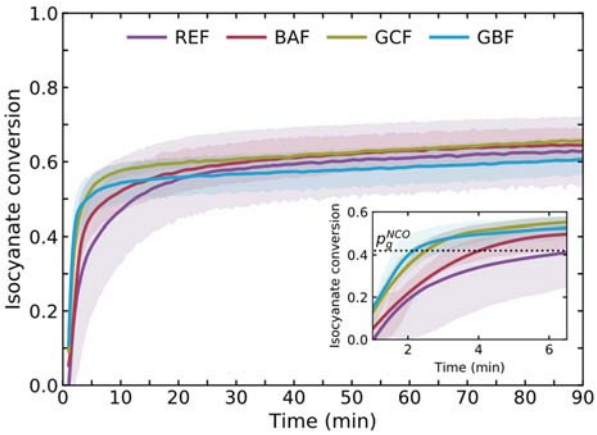

Figure 4-1-5: Average isocyanate conversion versus time for the foams under study: REF (0.5 ppw catalyst and 2 ppw water), BAF (0.5 ppw catalyst and 5 ppw water), GCF (1.5 ppw catalyst and 2 ppw water) and GBF (1.5 ppw catalyst and 5 ppw water).

In addition, the theoretical isocyanate conversion at gel point (p_g^{NCO}) was calculated by means of eq. (4-1-5) as proposed by Macosko and Miller [45]:

$$p_g^{NCO} = \sqrt{\frac{1}{(f-1)\,(g-1)\,r}} \qquad (4\text{-}1\text{-}5)$$

In this equation, f and g represent the functionalities of the polyol and the isocyanate (reported in Section 2.1.1), respectively. The variable r stands for the formulation's stoichiometry ratio (OH/NCO molar ratio), an alternative definition of the isocyanate index (Table 4-1-1). This ratio is most commonly used when dealing with PU adhesives or elastomers [46]. Applying this equation, the conversion at the theoretical gel point was found to be 0.427. Thus, it is possible to compare the times at which the foams reach this conversion value (dotted line in the inset of Figure 4-1-5) with the string times measured on the growing foams (Table 4-1-2). For foams with high catalyst amount (GCF and GBF), the times at the gelation conversion point are rather short, 2.5 and 2 minutes, respectively. For the foams with low catalyst dosage, the gel conversion time is notably larger, 4 and 6.5 minutes for BAF and REF, respectively. These gel times are in good agreement with the string time reported in Table 4-1-2, and only for foam REF, the gel time was slightly longer (6.5 minutes versus 4 minutes).

3.4.2 Products generation

Another key aspect for the characterisation of PU foam formation is the number and rate at which the different reaction products are generated. To gain insight into this, the increasing area of the carbonyl band observed in the ATR-FTIR spectra was analysed by a deconvolution procedure detailed in previous works [6,13,34]. The area under each of the bands corresponding to the blowing and gelling reactions has been added to give the total number of urea and urethane products, respectively.

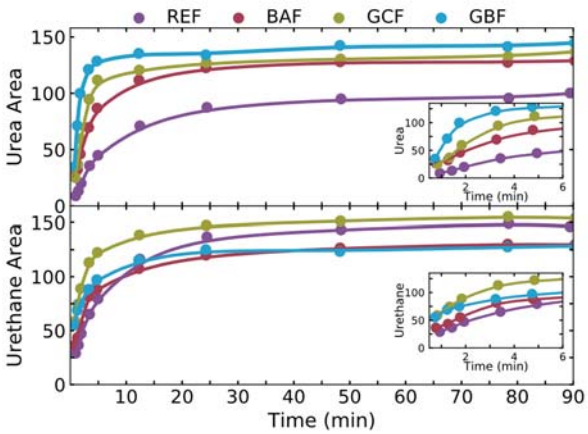

Figure 4-1-6: Total area of urea and urethane products generated with time for the foams under study: REF (0.5 ppw catalyst and 2 ppw water), BAF (0.5 ppw catalyst and 5 ppw water), GCF (1.5 ppw catalyst and 2 ppw water) and GBF (1.5 ppw catalyst and 5 ppw water).

The evolution of the number of urea and urethane products with time and the evolution of the ratio of urethane versus urea products can be seen in Figure 4-1-6 and Figure 4-1-7, respectively. In the first five minutes of reaction, the cross-linking was faster for foams with higher catalyst concentration (GCF and GBF), as proven by the rapid generation of urethane bonds. In addition, these foams suffered a swift increase in their number of urea products, which can be witnessed in the close-ups of Figure 4-1-6. For times longer than 5 minutes after the beginning of the reaction, the urea band's area continued to grow more slowly, suggesting an ongoing gas generation caused by the high reactivity of the water and isocyanate reaction. Yet, from Figure 4-1-4, it is clear that the expansion of foams GBF and GCF halted less than 4 minutes after the reaction started. This time interval coincides with the largest generation of products from both gelling and blowing reactions and the highest isocyanate conversion. Therefore, the faster cross-linking and vitrification of the matrix hampered larger expansions of these samples. Conversely, foams with low catalyst dosage (BAF and most notably REF) underwent a steadier increase in the number of urethane

groups. This is in accordance with the isocyanate consumption rates (Figure 4-1-5) and the modulus build-up trends (Figure 4-1-3).

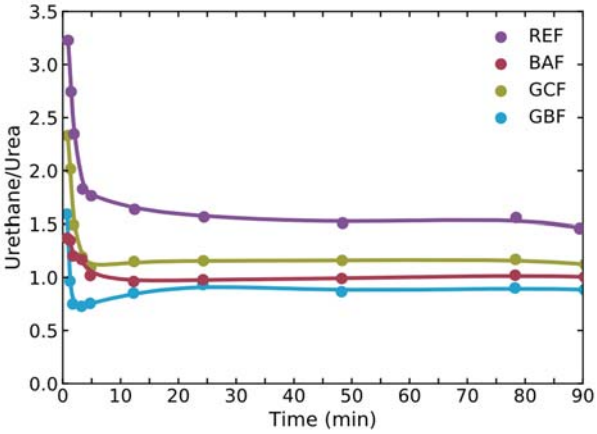

Figure 4-1-7: Ratio of urethane/urea products evolution with time for the foams under study: REF (0.5 ppw catalyst and 2 ppw water), BAF (0.5 ppw catalyst and 5 ppw water), GCF (1.5 ppw catalyst and 2 ppw water) and GBF (1.5 ppw catalyst and 5 ppw water).

However, due to the competitive nature of the blowing and gelling reactions, as polymerisation progressed, the foams with less water content (REF and GCF) were biased towards the generation of urethane bonds surpassing the number of urethane bonds of foams with higher water content. A more linear trend with time can be observed for the urea products. The reference foam (REF) generated fewer urea hard segments. Adding more water to this formulation (BAF) leads to an expected increase in the amount of urea to the detriment of the gelling reaction. Surprisingly, the addition of 1.5 ppw of catalyst in GCF and GBF samples also results in a remarkable increase in the number of ureas with respect to the materials with 0.5 ppw of catalyst (REF and BAF samples) (see Figure 4-1-6). As complementary information to the above, the decrease in the ratio of urethane versus urea (Figure 4-1-7) suggests that the selected catalyst has a dominant role in the blowing reaction.

3.5. Discussion

Moduli evolution of reactive foams can be understood on the basis of the different transformations undergone by the initial raw materials upon reaction, *i.e.* density decrease due to gas generation, development of a stable cellular structure, formation of a highly cross-linked network etc. For the interpretation, we have considered that the results obtained with DMA can be decoupled in two different aspects. On the one hand, the evolution of the

Polym. Test. 103, 107336 (2021)

moduli as a consequence of the matrix polymerisation and, on the other hand, the final modulus values attained.

First of all, to discard any effect of the density on the modulus values, these have been divided by the squared relative density $\left(E_{foam}/E_{polymer} = (\rho_{foam}/\rho_{solid})^2\right)$. In such a way, it is possible to observe the impact on the stiffness of the polymer matrix of the different polymer morphologies and reaction products [47,48]. In addition, to obtain a clearer understanding of the relationship between the system's reactivity and the modulus rise, the evolution of the normalised storage modulus, $E_{polymer}$, was plotted against the isocyanate conversion (Figure 4-1-8). Different phenomenological stages can be observed. All materials present an induction stage during which the isocyanate conversion is swift due to the initial components' high reactivity. During this time, the molecular weight is increasing, and the system is being transformed from a rubbery liquid (sol) into a solid network (gel) [38]. Yet, during this first stage, the modulus remains low and practically unchanged since the urethane matrix's cross-linking is still minimal. However, after the gelation conversion point (p_g^{NCO}= 0.427) the modulus of all materials begins to rise. This effect has been reported in previous works for PU thermosets which showed a sudden and steep increase in the complex viscosity after gelation [39]. Notably, during the stage in which the modulus increase is the fastest, the reactivity of the system slows down considerably. Additionally, foams with higher urea content (BAF and GBF, as seen in Figure 4-1-6) show a steeper increase in the polymer's modulus. Last but not least, when the consumption has nearly halted and the reactivity of the system is residual, a slight increase in the modulus is still detected. This increase corresponds to the plateau region of modulus development observed in Figure 4-1-3.

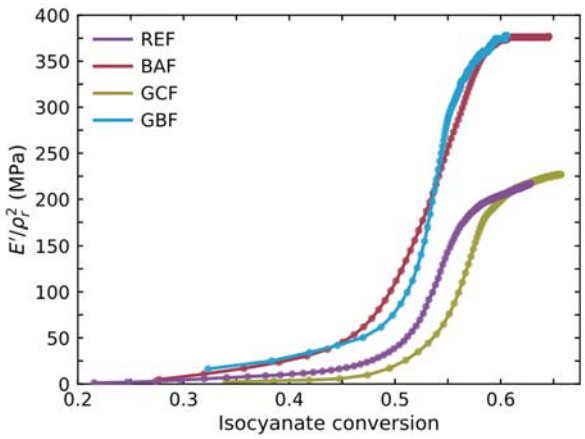

Figure 4-1-8: Evolution of the storage modulus normalised to the relative density as a function of the isocyanate conversion.

Concerning the final modulus values, in Figure 4-1-9, the final foam's complex modulus (Table 4-1-5) was normalised to the relative density and is presented against the last value of the normalised complex modulus measured during the *in-situ* experiments. There is a good correspondence between the properties of the samples produced under compression during the DMA experiments and those of the large-sized foams which underwent a free foaming process (R^2 of the linear fit 0.927). There undoubtedly two groups of foams. The materials with low water content present lower polymer moduli (REF and GCF), whereas those produced with higher water content exhibit higher polymer moduli (BAF and GBF). These results reveal that the modulus trend is similar to that of the ratio of urethane versus urea (Figure 4-1-7), so that the higher the enhancement of the blowing reaction (more urea products), the greater the modulus [49–51]. Furthermore, the addition of water and catalyst (GBF) provides the highest increment in the modulus of the polymer matrix. This increment may be due to the higher number of urea hard segments (Figure 4-1-6), which combined with a good cross-linking, resulted in an increase in the mechanical properties of the polymer matrix. Moreover, these results prove the strong influence of the density on the results reported in Table 4-1-5 and Figure 4-1-3.

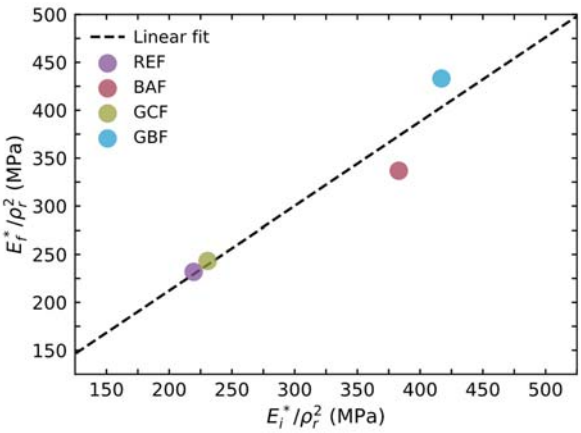

Figure 4-1-9: Normalised Young's modulus of the cured samples (after one week) versus the normalised complex modulus (after 90 minutes) measured in-situ.

Throughout this work, the results obtained by means of *in-situ* DMA have been presented in terms of the modulus. Yet, when modelling the evolution of viscoelastic properties and their influence on the generation of a stable-cellular structure, the rheological properties are expressed in terms of the polymer viscosity. The DMA modulus values can be converted to viscosity via division by a constant factor (eq. (4-1-6)) [28].

$$\eta^* = \frac{G^*}{\omega} = \frac{E^*}{2\,\omega\,(1-\upsilon)} \qquad (4\text{-}1\text{-}6)$$

Polym. Test. 103, 107336 (2021)

In eq. (4-1-6), the complex viscosity is connected to the complex modulus through the sample's Poisson's Ratio, υ, and the experiment's radial frequency, ω, which is equal to $2\pi f$ where f is the applied frequency measured in Hertz. In our experiments, the frequency was fixed to 1 Hz, and in general, the Poisson's Ratio is low and close to 0.1 for polymeric foams [47]. Therefore, at a constant frequency of 1 Hz, the calculated complex viscosity has the shape of the complex modulus (Figure 4-1-10). Since viscosity increases with the resistance to flow, it is logical that the complex viscosity increases during polymerisation, from low viscosities of around 2000 Pa at the beginning of the polymerisation to practically 50 times the initial value after 90 min of reaction.

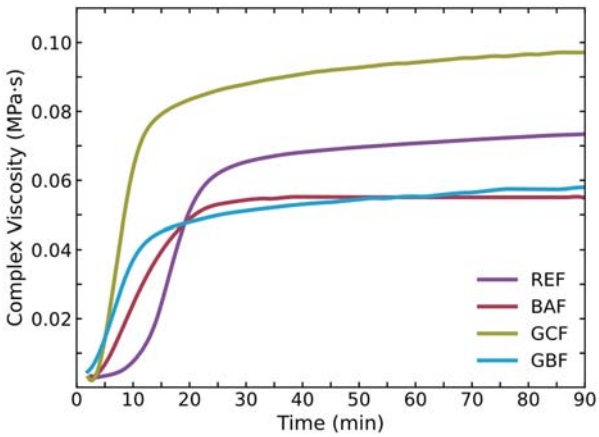

Figure 4-1-10: Complex viscosity as a function of time for each of the foams in Table 4-1-1

Likewise, it is possible to divide the complex modulus into two contributions, an in-phase and an out-of-phase component (eq. (4-1-7)). The in-phase component, η', is a measure of the energy losses representing the fluid properties of the system and the out-of-phase component, η'', is a measure of the energy stored.

$$\eta^* = \eta' - i\eta'' \qquad (4\text{-}1\text{-}7)$$

Therefore, the proposed approach can also be used to determine the complex viscosity and its components, which are key parameters for modelling foam growth and degeneration mechanisms in foaming processes.

4. CONCLUSIONS

In this study, the modulus evolution of reactive foams was measured by a newly developed time-resolved DMA method. By means of a customised set-up, it was possible to follow simultaneously the modulus evolution and relative density of reactive foams. The specificity and the reproducibility of the technique were verified by performing repeated

experiments on RPU formulations of very different reactivity and final density. From a kinetic point of view, time-resolved DMA's results were verified with ATR-FTIR spectroscopy. Therefore, it was possible to confirm that the foam's polymerisation kinetics had a considerable influence on the dynamics of the modulus development.

Together with these findings and previous rheological models, it was possible to obtain the materials' viscosity development of the materials with time. Classical theories for modelling cell nucleation, cell growth and foam stabilisation phenomena use viscosity-related magnitudes to investigate these mechanisms. Thus, the development of this methodology paves the way for the study of the foaming process of these complex systems.

In short, it has been demonstrated the possibility of obtaining relevant information for the understanding of the foaming process of RPU foams by using a straightforward approach based on time-resolved Dynamic Mechanical Analysis.

5. ACKNOWLEDGEMENTS

Financial assistance from the Junta of Castile and Leon (VA202P20) and Spanish Ministry of Science, Innovation and Universities (RTI2018-098749-B-I00) is gratefully acknowledged. Financial support from Junta de Castilla y Leon predoctoral grant of P. Cimavilla-Román, co-financed by the European Social Fund, is also acknowledged.

6. REFERENCES

[1] Market data: PlasticsEurope, (n.d.). (accessed January 15, 2021).

[2] N. V. Gama, A. Ferreira, A. Barros-Timmons, Polyurethane foams: Past, present, and future, Materials (Basel). 11 (2018).

[3] M. del M. Bernal Ortega, Estudio de nanocompuestos de espumas de poliuretano reforzadas con nanocargas en base carbono, Universidad de Valencia, 2012.

[4] D. Klempner, Handbook of Polymeric Foams and Foam Technology, Hanser Gardner Publications, 2004.

[5] K. Ashida, Polyurethane and Related Foams: Chemistry and Technology, 1st Ed, Taylor & Francis Group, Boca Raton, 2007.

[6] M. Santiago-Calvo, Synthesis , Foaming Kinetics and Physical Properties of Cellular Nanocomposites Based on Rigid Polyurethane, University of Valladolid, 2019.

[7] J.O. Akindoyo, M.D.H. Beg, S. Ghazali, M.R. Islam, N. Jeyaratnam, A.R. Yuvaraj, Polyurethane types, synthesis and applications-a review, RSC Adv. 6 (2016) 114453–114482.

[8] A. Kausar, Polyurethane Composite Foams in High-Performance Applications: A Review, Polym. - Plast. Technol. Eng. 57 (2018) 346–369.

[9] B. Eling, Ž. Tomović, V. Schädler, Current and Future Trends in Polyurethanes: An Industrial Perspective, Macromol. Chem. Phys. 221 (2020) 1–11.

[10] B. Grignard, J.M. Thomassin, S. Gennen, L. Poussard, L. Bonnaud, J.M. Raquez, P. Dubois, M.P. Tran, C.B. Park, C. Jerome, C. Detrembleur, CO2-blown microcellular non-isocyanate polyurethane (NIPU) foams: From bio- and CO2-sourced monomers to potentially thermal insulating materials, Green Chem. 18 (2016) 2206–2215.

[11] A. Lee, Y. Deng, Green polyurethane from lignin and soybean oil through non-isocyanate reactions, Eur. Polym. J. 63 (2015) 67–73.

[12] N. V. Gama, B. Soares, C.S.R. Freire, R. Silva, C.P. Neto, A. Barros-Timmons, A. Ferreira, Bio-based polyurethane foams toward applications beyond thermal insulation, Mater. Des. 76 (2015) 77–85.

[13] M. Santiago-Calvo, J. Tirado-Mediavilla, J.L. Ruiz-Herrero, M.Á. Rodríguez-Pérez, F. Villafañe, The effects of functional nanofillers on the reaction kinetics, microstructure, thermal and mechanical properties of water blown rigid polyurethane foams, Polymer (Guildf). 150 (2018) 138–149.

[14] M. Santiago-Calvo, J. Tirado-Mediavilla, J.L. Ruiz-Herrero, F. Villafañe, M.Á. Rodríguez-Pérez, Long-term thermal conductivity of cyclopentane–water blown rigid polyurethane foams reinforced with different types of fillers, Polym. Int. 68 (2019) 1826–1835.

[15] D. V. Pikhurov, A.S. Sakhatskii, V. V. Zuev, Rigid polyurethane foams with infused hydrophilic/hydrophobic nanoparticles: Relationship between cellular structure and physical properties, Eur. Polym. J. 99 (2018) 403–414.

[16] E. Minogue, An in-situ study of the nucleation process of polyurethane rigid foam formation, Dublin City University, 2000.

[17] P. Cimavilla-Román, S. Pérez-Tamarit, M. Santiago-Calvo, M.Á. Rodríguez-Pérez, Influence of silica aerogel particles on the foaming process and cellular structure of rigid polyurethane foams, Eur. Polym. J. 135 (2020) 109884.

[18] M.M. Bernal, M.A. Lopez-Manchado, R. Verdejo, In situ foaming evolution of flexible polyurethane foam nanocomposites, Macromol. Chem. Phys. 212 (2011) 971–979.

[19] M.J. Elwell, S. Mortimer, A.J. Ryan, A Synchrotron SAXS Study of Structure Development Kinetics during the Reactive Processing of Flexible Polyurethane Foam, Macromolecules. 27 (1994) 5428–5439.

[20] R. Bouayad, J. Bikard, J.F. Agassant, Compressible flow in a plate/plate rheometer: Application to the experimental determination of reactive expansion's models parameters for polyurethane foam, Int. J. Mater. Form. 2 (2009) 243–260.

[21] J. Reignier, P. Alcouffe, F. Méchin, F. Fenouillot, The morphology of rigid polyurethane foam matrix and its evolution with time during foaming – New insight by cryogenic scanning electron microscopy, J. Colloid Interface Sci. 552 (2019) 153–165.

[22] R.D. Priester, J. V. Mcclusky, R.E. O'neill, R.B. Turner, M.A. Harthcock, B.L. Davis, FT-IR-A Probe into the Reaction Kinetics and Morphology Development of Urethane Foams, J. Cell. Plast. 26 (1990) 346–367.

[23] M. Kurańska, A. Prociak, S. Michałowski, K. Zawadzińska, The influence of blowing agents type on foaming process and properties of rigid polyurethane foams, Polimery/Polymers. 63 (2018) 672–678.

[24] M. Santiago-Calvo, S. Pérez-Tamarit, J. Tirado-Mediavilla, F. Villafañe, M.A. Rodríguez-Pérez, Infrared expandometry: A novel methodology to monitor the expansion kinetics of cellular materials produced with exothermic foaming mechanisms, Polym. Test. 66 (2018) 383–393.

[25] M. Mar Bernal, S. Pardo-Alonso, E. Solórzano, M.Á. Lopez-Manchado, R. Verdejo, M.Á. Rodriguez-Perez, Effect of carbon nanofillers on flexible polyurethane foaming from a chemical and physical perspective, RSC Adv. 4 (2014) 20761.

[26] E. Mora, L.D. Artavia, C.W. Macosko, Modulus development during reactive urethane foaming, J. Rheol. (N. Y. N. Y). 35 (1991) 921–940.

[27] M.J. Elwell, A.J. Ryan, H.J.M. Grunbauer, H.C. Van Lieshout, In-situ studies of structure development during the reactive processing of model flexible polyurethane foam systems using FT-IR spectroscopy, synchrotron SAXS and rheology, Macromolecules. 29 (1996) 769–770.

[28] K.P. Menard, Dynamic Mechanical Analysis: A Practical Introduction, First Edit, CRC Press, Boca Raton, 2008.

[29] S. Takeda, M. Ohashi, O. Kuwano, M. Kameda, M. Ichihara, Rheological tests of polyurethane foam undergoing vesiculation-deformation-solidification as a magma analogue, J. Volcanol. Geotherm. Res. 393 (2020) 106771.

[30] Y. Nawab, S. Shahid, N. Boyard, F. Jacquemin, Chemical shrinkage characterization techniques for thermoset resins and associated composites, J. Mater. Sci. 48 (2013) 5387–5409.

[31] ASTM D1622-08: Standard Test Method for Apparent Density of Rigid Cellular Plastics, (n.d.).

[32] S. Ebnesajjad, P.R. Khaladkar, Fluoropolymer Applications in the Chemical Processing Industries, Second Edi, Plastics Design Library, 2017.

[33] M.J. Elwell, A.J. Ryan, H.J.M. Grunbauer, H.C. VanLieshout, An FTIR study of reaction kinetics and structure development in model flexible polyurethane foam systems, Polymer (Guildf). 37 (1996) 1353–1361.

[34] D.P. Queiroz, M.N. De Pinho, C. Dias, ATR-FTIR studies of poly(propylene oxide)/polybutadiene bi-soft segment urethane/urea membranes, Macromolecules. 36 (2003) 4195–4200.

[35] A. Marcos-Fernández, A.E. Lozano, L. González, A. Rodríguez, Hydrogen bonding in copoly(ether-urea)s and its relationship with the physical properties, Macromolecules. 30 (1997) 3584–3592.

[36] C. Torres-Sánchez, J. Corney, Identification of formation stages in a polymeric foam customised by sonication via electrical resistivity measurements, J. Polym. Res. 16 (2009) 461–470.

[37] S. Farzaneh, S. Riviere, A. Tcharkhtchi, Rheokinetic of Polyurethane Crosslinking Time-Temperature-Transformation Diagram for Rotational Molding, J. Appl. Polym. Sci. 152 (2012) 2658–2667.

[38] Z. Yang, H. Peng, W. Wang, T. Liu, Rheological Investigation of Cure Kinetics and Adhesive Strength of Polyurethane Acrylate Adhesive, J. Appl. Polym. Sci. 116 (2010) 2658–2667.

[39] L.M. Chiacchiarelli, J.M. Kenny, L. Torre, Kinetic and chemorheological modeling of the vitrification effect of highly reactive poly(urethane-isocyanurate) thermosets, Thermochim. Acta. 574 (2013) 88–97.

[40] M. Rochery, T.M. Lam, Chemorheology of polyurethane. I. Vitrification and gelation studies, J. Polym. Sci. Part B Polym. Phys. 38 (2000) 544–551.

[41] M. Stanko, M. Stommel, Kinetic prediction of fast curing polyurethane resins by model-free isoconversional methods, Polymers (Basel). 10 (2018).

[42] M.T. Aronhime, J.K. Gillham, Time-Temperature-Transformation (TTT) Cure Diagram of Thermosetting Polymeric Systems., Adv. Polym. Sci. 78 (1986) 83–113.

[43] R. Muller, E. Gérard, P. Dugand, P. Rempp, Y. Gnanou, Rheological Characterization of the Gel Point: A New Interpretation, Macromolecules. 24 (1991) 1321–1326.

[44] J.K. Fink, Epoxy Resins, in: React. Polym. Fundam. Appl., Plastics Design Library, 2018: pp. 139–223.

[45] C.W. Macosko, D.R. Miller, A New Derivation of Average Molecular Weights of Nonlinear Polymers, Macromolecules. 9 (1976) 199–206.

[46] S. Oprea, Synthesis and properties of polyurethane elastomers with castor oil as crosslinker, JAOCS, J. Am. Oil Chem. Soc. 87 (2010) 313–320.

[47] L.J. Gibson, M.F. Ashby, Cellular solids: Structure and Properties, Cambridge: Cambridge Solid State Science Series, Cambridge, 1997.

[48] R.A. Neff, C.W. Macosko, Simultaneous measurement of viscoelastic changes and cell opening during processing of flexible polyurethane foam, Rheol. Acta. 35 (1996) 656–666.

[49] A.K. Yusuf, P.A.P. Mamza, A.S. Ahmed, U. Agunwa, Physico-Mechanical Properties of Rigid Polyurethane Foams Synthesized From Modified Castor Oil Polyols, Int. J. Sci. Res. Publ. 6 (2016) 548–556.

[50] Z. Yang, H. Peng, W. Wang, T. Liu, Crystallization behavior of poly(ε-caprolactone)/layered double hydroxide nanocomposites, J. Appl. Polym. Sci. 116 (2010) 2658–2667.

[51] W.J. Seo, H.C. Jung, J.C. Hyun, W.N. Kim, Y.B. Lee, K.H. Choe, S.B. Kim, Mechanical, morphological, and thermal properties of rigid polyurethane foams blown by distilled water, J. Appl. Polym. Sci. 90 (2003) 12–21.

Section 4.3.

The influence of viscosity build-up on the foaming dynamics of Rigid Polyurethane foams

Paula Cimavilla-Román [a*], Pablo Álvarez-Zapatero [b], Anja Vananroye [c], Paula Moldenaers [c], Miguel Ángel Rodriguez-Pérez [a,d]

[a] Cellular Materials Laboratory (CellMat), Condensed Matter Physics Department, University of Valladolid, Paseo Belen 7, Valladolid, 47011, Spain

[b] Departamento de Física Teórica, Atómica y Óptica, University of Valladolid, Valladolid 47071, Spain

[c] Department of Chemical Engineering, KU Leuven, 3001 Leuven, Belgium

[d] BioEcoUva. Research Institute on Bioeconomy, University of Valladolid, Spain

Manuscript submitted

Graphical Abstract

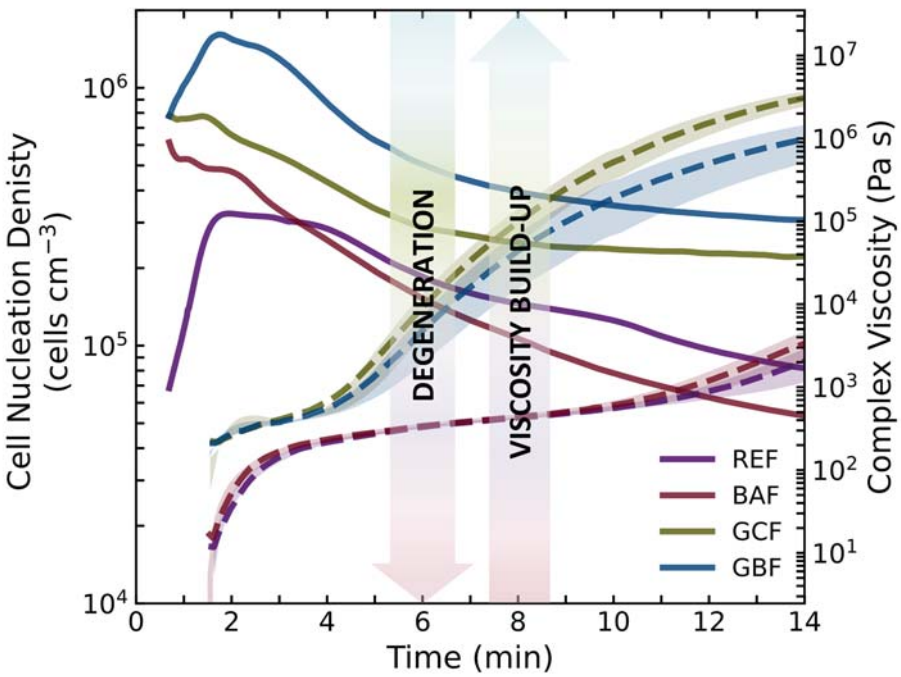

ABSTRACT

The viscoelastic properties development during the reactive foaming of four standard polyurethane formulations was monitored using a flooded parallel plate rheometer. The measurements permitted to show how foams of low catalyst content took longer than 10 minutes to increase their viscosity from 1 to 10^3 Pa s, while foams with higher catalysts saw this increase in less than 4 minutes. The speed of polymerisation had a deep impact on the cellular structure degeneration during foaming. Foams with high catalyst stabilised in their final cell size in 4-5 minutes concurring with the stage of largest viscosity build-up. In contrast, the foams of low catalyst content underwent strong degeneration as a result of the slow gelification and stiffening of the matrix. Simulation results also revealed that stabilisation of the cellular structure was much faster in the absence of degeneration and for foams of higher blowing agents content.

KEYWORDS

Flooded Parallel-Plate Rheology; Rheokinetics; Foaming Dynamics; Rigid Polyurethane foams; Cell growth; Degeneration

1. INTRODUCTION

Polyurethane (PU) foams are one of the most consumed polymer foams [1,2]. As with other cellular materials, the final properties of PU foams are heavily dependent on their internal cellular structure. Hence, to obtain materials of superior properties and performance it is fundamental to have a good understanding of the foaming process. The synthesis of PU foams is the result of the reaction of isocyanate with hydrogen active compounds [3]. The reaction between isocyanate and polyol, gelling or polymerisation reaction, is responsible for generating urethane crosslinks. While the reaction between isocyanate and water, known as blowing or foaming reaction, releases CO_2 gas and generates urea hard segments. The release of CO_2 at the initial stages of the reaction, when the polymer is still a low modulus and low molecular weight gel, leads to foam expansion. Before the foam expansion, the CO_2 gas generated saturates the reactive mixture. Once the amount of gas in the mixture exceeds the solubility limit, this thermodynamic instability leads to the nucleation of cells, which later grow due to the ongoing blowing reaction [4]. The growth of the cells progresses until the polymer matrix has reached a limiting stiffness from which the structure freezes.

The understanding of how cells grow during PU foaming is often achieved through simulation and modelling [5–8]. Typically, the competitive growth of cells in a liquid medium is modelled through a system of coupled mass and momentum conservation equations in which several factors intervene, mainly diffusion, temperature, viscosity, and surface tension [6,8]. Traditional models consider the growth of cells with a limited gas supply in a Newtonian medium of constant viscosity, result known as the bubble shell model [6]. More recently, specific models for reactive PU foams have been developed [5,9]. These models permit coupling the reaction kinetics and viscosity build-up with the foam expansion, cell growth and cell wall evolution [10,11]. Ferkl et al. [10] modelled the evolution of the cell wall thickness and cell size in PU foams. The authors observed that the initial concentration of the blowing agent and cell nucleation density directly impacted cell growth. In contrast, the growth of the cells and the viscosity of the reactive mixture are critical factors for the evolution of the cell wall thickness. The simulation results also confirmed that wall stretching by cell growth and polymer drainage are the mechanisms responsible for the final matrix thickness of the foam.

Experimentally, sequential X-ray imaging (X-ray radioscopy) has been widely used to investigate bubble nucleation and growth in PU foams produced using different formulations and nanoparticles as nucleating agents [12–15]. However, the analysis of the mechanisms of cell growth and degeneration in PU foams is often conducted without taking into account the extent of the chemical reactions or the viscosity of the reactive material [12–16]. While the reaction kinetics have been widely investigated using FTIR Spectroscopy [17–19], the rheological behaviour of the reactive mixture is far less considered. Recently, we developed a new experimental methodology based on Dynamic Mechanical Analysis (DMA) to follow the modulus build-up and polymerisation of PU foams [20]. In that study, we demonstrated that the reaction kinetics of PU foaming significantly modify the speeds of modulus build-up [20]. However, such system did not allow to measure the viscosity at the early stages of the foaming process. To that end, shear rheology is a more adequate method as it permits direct contact of the geometry with the mixture. Moreover, rheometers are more suited to measure low viscous materials and liquids [21,22]. In this work, we use a controlled strain rheometer and a flooded parallel plate fixture to monitor the rheological transformations and the viscosity build-up during PU foaming. By coupling this information with the foaming dynamics studied with X-ray radioscopy the mechanisms responsible for cell nucleation and degeneration are inferred. In addition, the cell growth is modelled theoretically under different conditions of blowing agent concentration and viscosity. By comparing the experimental and simulation results of cell growth it is possible to understand the effect of cell degeneration, reaction kinetics and viscosity build-up on the structure generation.

2. MATERIALS AND METHODS

2.1. Raw materials of RPU foams

The polyol component used to prepare the RPU foams was a high functionality polyether polyol from Repsol S.A, Alcupol R4520 (functionality of 4.5, OH value of 455 mg·KOH g^{-1}, viscosity of 5.25 Pa s at 25 °C). The isocyanate was a polymeric diphenylmethane diisocyanate (pMDI), IsoPMDI 92140 (31.5% NCO, density 1.23 g cm^{-3}, viscosity of 0.17-0.25 Pa s at 25 °C) supplied by BASF. POYCAT 8 from Evonik was employed as a catalyst, which is a tertiary amine used primarily to promote the urethane (polyol-isocyanate) reaction. TEGOSTAB® B8522 (a non-hydrolysable polyether-polydimethylsiloxane–

stabilizer) from Evonik was used as a surfactant to obtain superior cell structures. Distilled water was employed as a blowing agent.

2.2. Preparation of RPU foams

Four different RPU foams were prepared while maintaining a constant isocyanate index. The formulations are presented in Table 4-2-1. While the polyol and surfactant contents were kept constant, the amount of catalyst (0.5 and 1.5 parts per weight (ppw)) and blowing agent (2 and 5 ppw) was changed independently.

The different components were mixed with an overhead stirrer (EUROSTAR 60 control from IKA), equipped with a 50 mm diameter VollrathTM Lenart-disc. A homogeneous polyol blend with the additives (catalyst, surfactant and blowing agent) was produced at 250 rpm for 2 minutes. To promote the RPU reaction, a mass of 40 g, including the isocyanate and polyol blend, was mixed for 10 s at 1200 rpm in a 1 L plastic cup. The start of the stirring process between polyol blend and isocyanate is considered as time 0 of the reaction.

Table 4-2-1. Components and concentrations for each RPU formulation.

Sample	Isocyanate Index	Polyol (ppw)	Surfactant (ppw)	Gelling catalyst (ppw)	Water (ppw)
REF	110	100	1	0.5	2
BAF	110	100	1	0.5	5
GCF	110	100	1	1.5	2
GBF	110	100	1	1.5	5

Following the formulations in Table 4-2-1, RPU foams with 40 g of material were produced. Foams with low water content REF (Reference Formulation) and GCF (Gelling Catalyst Formulation) reached foam volumes of *ca*. 750 cm^3. In contrast, foams with high blowing agent content, BAF (Blowing Agent Formulation) and GBF (Gelling Blowing Formulation) attained foam volumes of nearly 1200 cm^3. These foams were left to cure at room temperature for one week. After this period the foams were cut, and the final density and cellular structure were measured.

Additionally, a few millilitres of the reactive mixture were extracted from the plastic cup just after the stirring process to perform characterisations *in-situ* during the foaming process (see next sections for a detailed explanation of these *in-situ* measurements).

2.3. Density and cellular structure characterisation

Foam density, ρ, was measured as described by ASTM D1622/D1622M-14 [23]. Relative density, ρ_r, was obtained as the ratio between the foam density and the solid material density (1160 kg m^{-3}). In addition, the internal cellular structure was imaged in the free rise direction using Scanning Electron Microscopy, SEM (JEOL JSM-820 microscope.). Cell size, ϕ_{3D}, anisotropy ratio of the cells in the foam rise direction, *AR*, and cell density, N_v, were measured using a dedicated ImageJ script [24]. Cell nucleation density, N_o, was estimated by dividing cell density by the relative density. However, for this estimation to be accurate no degeneration should have taken place during cell growth [24]. On average more than 100 cells were measured to obtain the mean descriptors of the cellular structure.

2.4. Viscosity measurements

The viscosity of the isocyanate and the polyol premixes was measured using a cone and plate rheometer (model ARES G2 from TA Instruments). Cone angle and diameter of the fixture were 0.04 rad and 25 mm, respectively. The truncation GAP was 58 µm. Frequency sweeps from 0.1 to 100 rad s^{-1} were performed at 25 °C. The shear viscosity was obtained from the average of the viscosity values over the entire frequency range.

2.5. Rheology

The development of the viscoelastic properties during foaming was followed using an AR-G2 rheometer from TA Instruments. Due to the large expansion suffered by polyurethane upon reaction, a flooded parallel plate geometry was employed as suggested by Mora et al. [21]. The fixture consisted of a 25 mm stainless steel plate, upper geometry, and a 55 mm diameter stainless steel cup, lower geometry. The cup was inserted in a Peltier Concentric Cylinder which allowed control of the sample temperature. During these experiments, the temperature was maintained at 25 °C.

A reactive mixture volume of 5 mL was loaded into the rheometer cup immediately after preparation. Then, the rheometer head was lowered to a GAP of 2 mm between the plate and the bottom of the cup. The time required to transfer the sample and start the experiment was approximately 1.5 min.

To characterise the rheological behaviour of PU, oscillatory time sweeps were performed under controlled strain conditions. Frequency was kept constant at 1 rad s^{-1}, whereas strain

was reduced during the experiment to accommodate the large modulus build-up experienced by these foams during cure. A summary of the experimental conditions can be seen in Table 4-2-2. Four repetitions were performed for each material to ensure reproducibility.

Table 4-2-2: Applied strain and run times for the rheology experiments

Sample	Time (s)	Step 1		Step 2		Step 3	
		γ_1 %	t_1 (s)	γ_2 %	t_2 (s)	γ_3 %	t_3 (s)
REF	2700	0.5	1200	0.05	1200	0.005	300
BAF	2700	0.5	1200	0.05	1200	0.005	300
GCF	2700	0.25	500	0.125	500	0.025	1700
GBF	2700	0.25	500	0.125	500	0.025	1700

2.6. X-ray Radioscopy

Time-resolved X-ray imaging (X-ray Radioscopy) was used to investigate the dynamics of cell structure generation of RPU foams (see the sketch in Figure 4-2-1). The imaging set-up consisted of a laboratory X-ray source from Hamamatsu with a maximum output power of 20 W (spot size: 5 μm, voltage: 20-100 kV, current: 0-200 μA). The X-rays go out of the source window forming a cone-beam which allows magnifying the sample up to 20 times. A flat panel detector (C7940DK-02, Hamamatsu. 2240×2344 pixels, 50 μm pixel size) collected the transmitted X-rays and formed the images.

For this study, X-ray voltage was fixed to 40 kV and current to 120 μA. Source-detector distance (SDD) was fixed at 581 mm, while source object distance (SOD) was 46.4 mm. This configuration yielded an optical magnification of 12.5. In addition, due to the fast dynamics of cell growth, the selected image acquisition time was low, 800 ms (speed 1.25 fps). However, to increase contrast in the radiographs the detector applied a 2x2 binning to the acquired images, which, in turn, reduced the effective pixel size by a factor of 2. Hence, the spatial resolution of the acquired images increased from 4 to 8 μm.

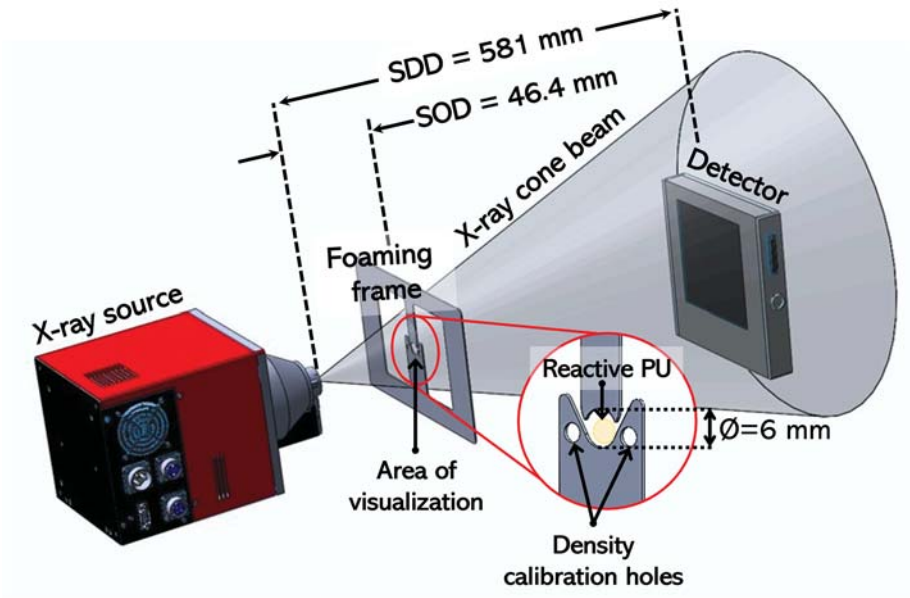

Figure 4-2-1: 3D Sketch of the X-ray imaging set-up used to monitor the cellular structure development of RPU foams.

To monitor the foam generation dynamics a drop of the reactive mixture was extracted from the beaker where the large foams were prepared (Section 2.2). During the experiment, the drop was kept inside a low thickness frame (0.6 mm) where the material could grow freely in two dimensions (Figure 4-2-1). The thickness of the PU drop was constant during foaming thanks to two polypropylene covers which forced the flow of the sample towards the two evacuation channels in the foaming frame. The sequential acquisition of radiographs enables to visualise the cellular structure development in the drop. Moreover, from the image sequence, it was possible to measure relative density evolution, cell size and cell nucleation density [12,15]. Relative density, ρ_r, evolution can be obtained thanks to Beer-Lambert's Law (eq. (4-2-1)), which relates the transmitted intensity, I, through the sample with the material absorption coefficient, μ, density, ρ, and thickness, d.

$$I = I_{air} e^{-\mu\rho(x,z)d} \tag{4-2-1}$$

Applying eq. (4-2-1) to the two reference materials in the calibration holes (air, $\rho_r = 0$), and solid polyurethane (TPU, $\rho_r = 1$) an expression for the relative density of the expanding foam is obtained (eq. (4-2-2)) [12,13].

$$\rho_r = \frac{log\left(\frac{I}{I_{air}}\right)}{log\left(\frac{I_{TPU}}{I_{air}}\right)} \tag{4-2-2}$$

Cell size, ϕ_{3D}, was measured on each radiography image by means of a dedicated ImageJ script which automatically binarizes and segments the cells in the image. The ImageJ tool

measures the cell diameter of every cell in 2D and the results are transformed to 3D by multiplying the scale factor 1.273 [25]. The procedure permitted obtaining the temporal evolution of the average size of the cells in the drop. Moreover, cell nucleation density, N_o, can be estimated using Kumar's theoretical approximation and assuming spherical cells (eq. (4-2-3))

$$N_o = \frac{6}{\pi \Phi^3}\left(\frac{1}{\rho_r} - 1\right) \tag{4-2-3}$$

2.7. Model of cell growth and simulation

Cell growth was simulated following the bubble-shell model originally developed by Amon and Denson [6]. To describe the evolving radius of a spherical cell the model introduces the concept of the liquid envelope of radius *S(t)* which represents the specific amount of liquid saturated with gas for each cell. This model accounts for the growth of a given number of bubbles with a limited gas supply and assumes that there is no degeneration during growth. Every cell is assumed to be spherical and consists of a single glass bubble surrounded by its concentric liquid envelope or shell. Initially, the cell has a radius R_o and internal pressure P_{go}. As the bubble radius, *R(t)*, increases the radius of the shell, *S(t)* thins while its initial size is conditioned by the number of nucleated cells, N_{cells}, which is assumed to remain constant in the cell model [6].

$$S_o = \left(\frac{3}{4\pi N_{cells}}\right)^{1/3} \tag{4-2-4}$$

$$S(t) = (S_o^3 + R(t)^3 - R_o^3)^{1/3} \tag{4-2-5}$$

As the bubble starts to grow a concentration gradient, *c(r,t)*, is established inside the liquid envelope whose evolution is governed by the diffusion equation (eq. (4-2-6)). The gas in the liquid is assumed to behave as an ideal gas with constant diffusivity, *D*, during expansion.

$$\frac{dc}{dt} + \frac{\dot{R}\,R^2}{r^2}\left(\frac{\partial c}{\partial r}\right) = \frac{D}{r^2}\frac{\partial}{\partial r}\left(r^2\frac{\partial c}{\partial r}\right) \tag{4-2-6}$$

As diffusion proceeds, the pressure inside the cell will decrease. Through the conservation of mass equation on the bubble surface, it is possible to obtain a relationship (eq. (4-2-7)) between gas pressure, P_g, inside the cells and the bubble radius, *R* [26]. In eq. (4-2-7), R_g is the universal gas constant, ρ_s is the density of the polymer mixture, *T* is the gas temperature, and *M is* the molecular weight of the gas.

$$\frac{dP_g}{dt} = \frac{a}{R}\left(\frac{dc}{dr}\right)_{r=R} - 3P_g\left(\frac{\dot{R}}{R}\right) \; where \; a = \frac{3R_g T \rho_s D}{M} \tag{4-2-7}$$

In addition, the conservation of momentum equation permits the calculation of the cell radius assuming that the liquid reactive mixture is a Newtonian incompressible fluid of viscosity η_o.

$$\frac{dR}{dt} = R\left(\frac{P_g - P_a - 2\sigma/R}{4\eta_o}\right)\left(\frac{S^3}{S^3 - R^3}\right) \tag{4-2-8}$$

The system of coupled system of equations formed by (4-2-5), (4-2-6), (4-2-7) and (4-2-8) was solved using the explicit Runge-Kutta-Fehlberg 4(5) method as implemented in SciPy. Despite the stiffness of the problem, we checked that same results were obtained when a very small time step was forced. At each time step, the diffusion equation is discretized using a logarithmic mesh of 50 points, in order to more accurately sample at the gas-liquid interface. The fineness of the mesh was also determined by means of a convergence criterion, so considering more points does not substantially improve the results. Furthermore, the central finite difference derivative scheme was used for the spatial derivatives.

3. RESULTS

3.1. Foam density and cellular structure characterisation

Table 4-2-3 displays the density and relative density of the large foams prepared in a beaker following the procedure in Section 2.2. As reported in previous work [20], density only decreases slightly when boosting the catalysis of the foams. Conversely, density dropped approximately 1.6 times when the content of water rose from 2 to 5 ppw. For the selected isocyanate index this change resulted in a twofold increase in the moles of water in the formulation. Since one mole of CO_2 is produced from each mole of water, the number of moles of CO_2 released also doubles (BAF and GBF) and ideally, the density should have also been reduced by a factor of two [27,28]. The lesser expansion of foams BAF and GBF might be due to CO_2 lost to the surroundings during blowing or supersaturated in the polymer phase.

Table 4-2-3: Density, relative density and main descriptors of the cellular structure obtained from SEM micrographs.

Sample	ρ (kg m^{-3})	ρ_r	Φ_{3D} (μm)	AR	N_v (cells cm^{-3})	N_o (cells cm^{-3})
REF	59.7 ± 1.6	0.051	416.0 ± 91.8	1.2	2.5 10^4	4.5 10^5
BAF	34.4 ± 0.2	0.030	488.3 ± 151.9	1.4	1.6 10^4	4.8 10^5
GCF	52.3 ± 1.1	0.045	322.5 ± 73.7	1.3	5.4 10^4	1.1 10^6
GBF	34.5 ± 0.1	0.030	356.0 ± 87.2	1.5	4.1 10^4	1.4 10^6

The increase in the gelling catalyst concentration significantly improved the cellular structure of the foams (Figure 4-2-2). Cell size was reduced by 23% for GCF with respect to REF and by almost 30% for GBF compared to BAF, Table 4-2-3. Cell density decreased with the addition of water suggesting an increased number of degeneration of events during foaming. On the contrary, cell density rose with catalyst concentration. Similarly, cell nucleation density increased by more than a factor 2 with the addition of more catalyst and only slightly with the addition of water. Nonetheless, the real cell nucleation density is expected to have been larger than the values in Table 4-2-3 as degeneration events are likely to have taken place in these foams during synthesis. Regarding anisotropy, all foams showed a structure with cells elongated in the foam growth direction. Yet, anisotropy was higher for samples of lower density (BAF and GBF).

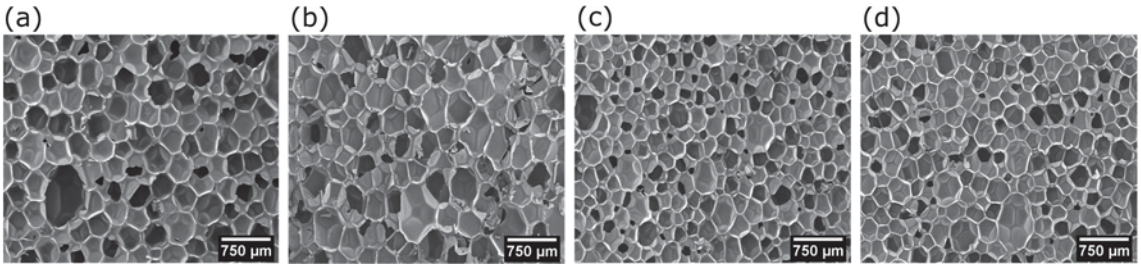

Figure 4-2-2: SEM micrographs of the cellular structure of foams (a) REF (2 ppw water, 0.5 ppw catalyst), (b) BAF (5 ppw water, 0.5 ppw catalyst), (c) GCF (2 ppw water, 1.5 ppw catalyst) and (d) GBF (5 ppw water, 1.5 ppw catalyst)

3.2. Viscosity of the raw materials

Table 4-2-4 shows the shear viscosities of the raw materials used to prepare the RPU foams in Table 4-2-1. The measured isocyanate viscosity is close to the value declared by the manufacturer (section 2.1). For all premixes, a decrease in the viscosity with respect to the pure polyol was found (section 2.1). The premixes with 5 ppw of water present the lowest viscosity. Taking into account the similar viscosity of the raw materials it is possible

to confirm that all the foams had a similar viscosity at the start of the reactive foaming process.

Table 4-2-4: Shear viscosities of the polyol premixes and isocyanate.

Material	REF	BAF	GCF	GBF	Isocyanate
Viscosity (Pa s)	3.4 ± 0.2	2.5 ± 0.1	3.5 ± 0.2	2.5 ± 0.2	0.3 ± 0.003

3.3. Rheological development

As seen in Figure 4-2-3 polymerisation of thermosetting RPU foams goes through four main viscoelastic stages regardless of the formulation. Initially, the viscous character of the mixture dominates over the elastic one, as evidenced by the large value of the damping factor, *tan (δ)* (loss modulus larger than storage as seen in the insets of Figure 4-2-3 (a) and (b)). Yet, in less than three minutes of reaction, the two moduli cross at the gel point [29,30]. This crossover represents a liquid to gel transition, and it is followed by a period of minimum increase in the moduli. The loss modulus remains practically constant with time while the storage modulus steadily grows over the loss component. This behaviour has been linked to that of a liquid foam [21]. The foam has already expanded, but the material forming the matrix is still a low molecular weight gel [20]. As polymerisation progresses a second transformation is found, vitrification. Vitrification can be recognized from the maximum in the damping factor. At this point, the material transforms from gel to glass which causes an increase of several orders of magnitudes in the moduli. At vitrification, the polymer morphology freezes, decreasing the chain mobility and reducing the curing rate. From this point on, the reaction becomes diffusion-controlled [31]. The last stage constitutes the final curing of the sample, the moduli continue to increase at a slow pace until they stabilise.

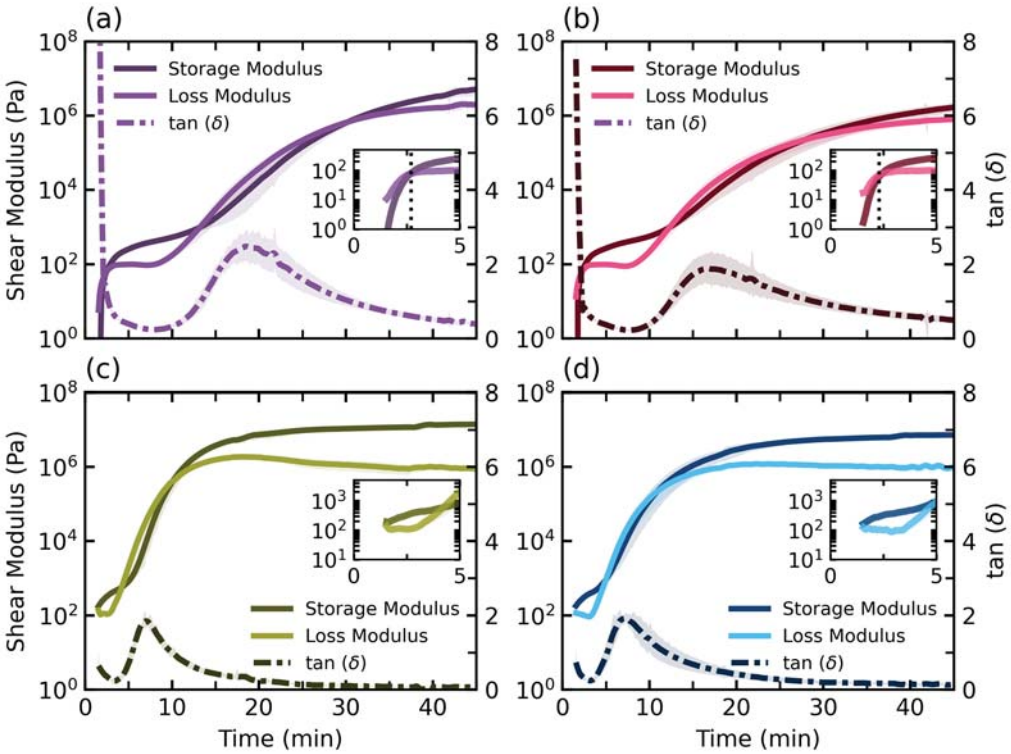

Figure 4-2-3: Shear modulus build-up profiles for (a) REF (2 ppw water and 0.5 ppw catalyst) (b) BAF (5 ppw water and 0.5 ppw catalyst), (c) GCF (2 ppw water and 1.5 ppw catalyst), (d) GBF (5 ppw water and 1.5 ppw catalyst).

While all formulations in Table 4-2-1 undergo similar transformations from liquid to glass, the concentration of blowing agent and catalyst substantially modifies the reaction rate and absolute modulus value. On the one hand, the increase in the blowing agent (from 2 to 5 ppw) leads to more than a twofold decrease in the final modulus (Table 4-2-5) [20]. This drop in the moduli is related to the lower density of the foams with 5 ppw of water (BAF and GBF). On the other hand, the impact of the catalyst on the final modulus is less marked. Yet, the reaction rate is significantly influenced by its concentration. (Table 4-2-5: reaction times). It has been demonstrated that PU foams catalysed with amine-based catalysts have reaction rate constants directly proportional to the amount of catalyst loading [32,33]. Zhao et al. [33] showed that increasing catalyst concentration makes the reaction kinetics faster which gives higher temperatures. For the formulations in Table 4-2-1, an increase of 1 part per weight in the catalyst (from REF to GCF, and from BAF to GBF) translates to 2.7 times faster vitrification. In fact, using this value as a scaling factor of the time axis permits overlapping of the modulus build-up profiles. Hence, moduli profiles in Figure 4-2-3 (a) and (b) can be collapsed into Figure 4-2-3 (c) and (d), enabling us to infer the missing gelling times of systems GCF and GBF: 56.1 s and 53.0 s respectively.

Table 4-2-5: Characteristic reaction times and storage modulus after 45 minutes of reaction measured with shear rheology.

Sample	Gelation (min)	Vitrification (min)	Final G'(MPa)
REF	2.6 ± 0.1	19.2 ± 2.3	5.2 ± 1.1
BAF	2.3 ± 0.1	18.9 ± 2.6	1.6 ± 0.4
GCF	< 1.5	6.9 ± 0.2	13.8 ± 1.5
GBF	< 1.5	7.3 ± 0.7	7.1 ± 0.8

3.4. Foaming dynamics

Immediately after finishing the stirring of the polyol and isocyanate components a drop of the reactive mixture was placed on the foaming frame (Figure 4-2-1). The radiographies acquisition started approximately 36 s after the onset of the reaction. For all the materials the full development of the cellular structure was captured, and an overview is displayed in Figure 4-2-4 (see Supporting Information for the videos corresponding to the complete X-ray radioscopy sequences). Initially, the formulations with low catalyst concentration (REF and BAF) revealed a high liquid fraction and a structure populated by cells of less than 50 μm in diameter. The ongoing CO_2 generation together with a slow viscosity build-up (Figure 4-2-3) led to a significant decrease in the relative density in the next minutes (1.5-5.5 min). During this time cell growth raised in more than one order of magnitude as a combination of CO_2 diffusion to the cells and, potentially, cell degeneration mechanisms. On the contrary, formulations with high catalyst dosage (GCF and GBF) underwent a fast foaming process. In less than 1 minute the materials had reached low liquid fractions due to their increased reactivity [20]. In addition, the cellular structure development with time halted early in the foaming process (Figure 4-2-4: 96 s) and only slight changes in the cell size are noticeable after 2 minutes of reaction.

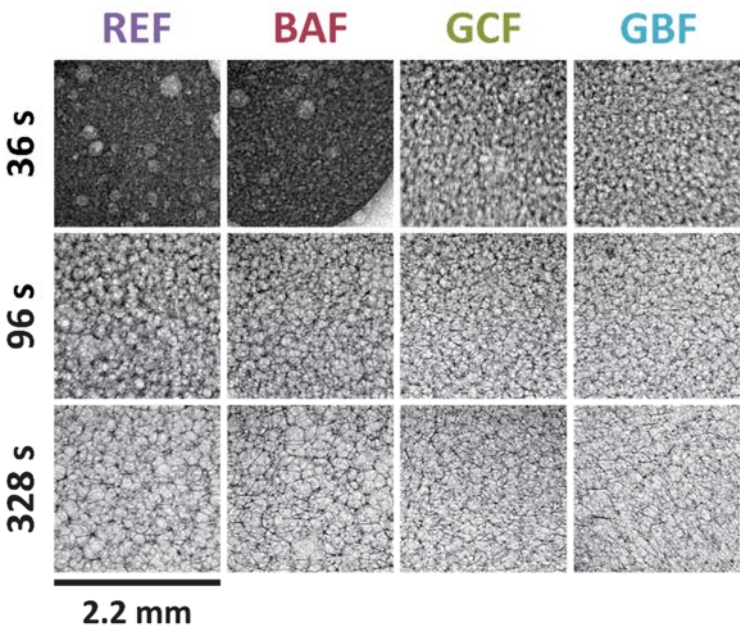

Figure 4-2-4: X-ray radiographies of the materials at three distinctive instants of the foaming process

The analysis of the image sequences was conducted following the procedure in Section 2.6 and yields the results in Figure 4-2-5 and Figure 4-2-6. Firstly, Figure 4-2-5 (a) displays the evolution of the relative density for the samples over time, where noticeable differences can be found in the relative density at short foaming times. For foams with 0.5 ppw of catalyst (REF and BAF), a marked decrease in the relative density is visible during the first 2.5 minutes of reaction. This decrease took place while the polymer still presented a fluid behaviour as evidenced by the high values of the damping factor (Figure 4-2-3). After gelation (Table 4-2-5) expansion slowed down, and the relative density approached its stabilisation value. In contrast, samples with 1.5 ppw of catalyst (GCF and GBF) attained low relative densities shortly after the start of the monitoring as a consequence of their fast modulus build-up which hardened the polymer matrix, thus hampering foam expansion (Figure 4-2-3). However, after the gelling point, GCF and GBF revealed some shrinkage leading to slight densification of the PU drop (this effect is likely to be caused by the small size of the sample). At the end of the foaming process (*ca.* 6 minutes), foams attained relative densities somewhat higher than that of the large foams (Table 4-2-3). In the foaming frame, foams REF and GCF reached final relative densities of around 0.2, while BAF and GBF dropped to values close to 0.13. Hence, the relative density hierarchy was preserved between samples of different volume.

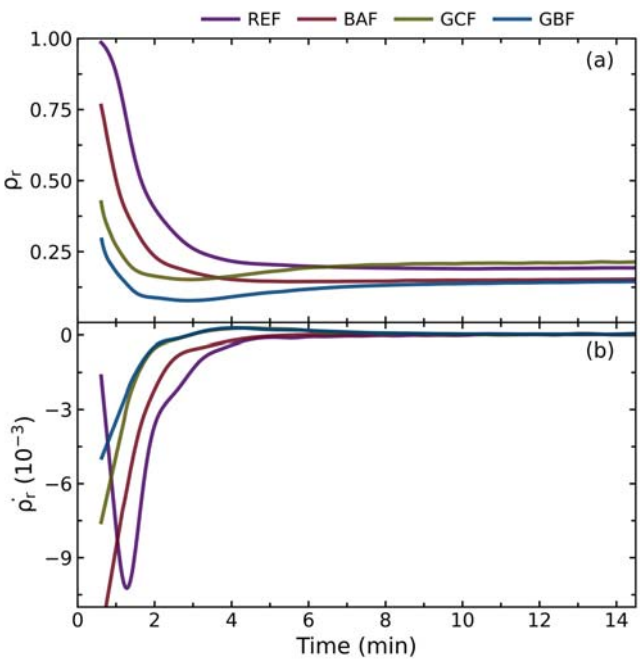

Figure 4-2-5: (a) Measured relative density evolution and (b) speed of relative density change with time obtained from the first derivate of (a).

Cell growth during polymerization of the RPU foams was measured and is shown in Figure 4-2-6 (a). The curves reveal the drastic differences in the cell growth behaviour experienced by the samples with different catalyst and water dosages. Foams with 0.5 ppw of catalyst (REF and BAF) started the foaming process with a cellular structure consisting of small cells (*ca*. 50 μm). Yet, they experienced a quick increase in less than 1 minute of foaming due to the low viscosity of the matrix at this time (Figure 4-2-3 (a) and (b)). This is translated into speeds of cell growth of nearly 5 μm s^{-1} (Figure 4-2-6 (b)). However, at long foaming times (larger than 6 minutes), when expansion had nearly halted, the average cell size of REF and BAF continued to grow. By contrast, catalyst loadings of 1.5 ppw led to a cell evolution profile practically flat over time. On the one hand, the fast blowing (Figure 4-2-3) of these foams led to a large cell growth at reaction times earlier than the start of the image acquisition. On the other hand, the fast viscosity increase (Figure 4-2-3) together with the quick matrix gelification (*ca*. 0.8 min) hindered the growth of cells after less than 4 minutes of reaction (Figure 4-2-6). In the Supporting Information, the time-sequences for the radioscopy images of GCF and GBF also manifest how after vitrification of the matrix (vitrification time in Table 4-2-5) the cell structure freezes, and no shrinkage or movement of any type is detected in the structure.

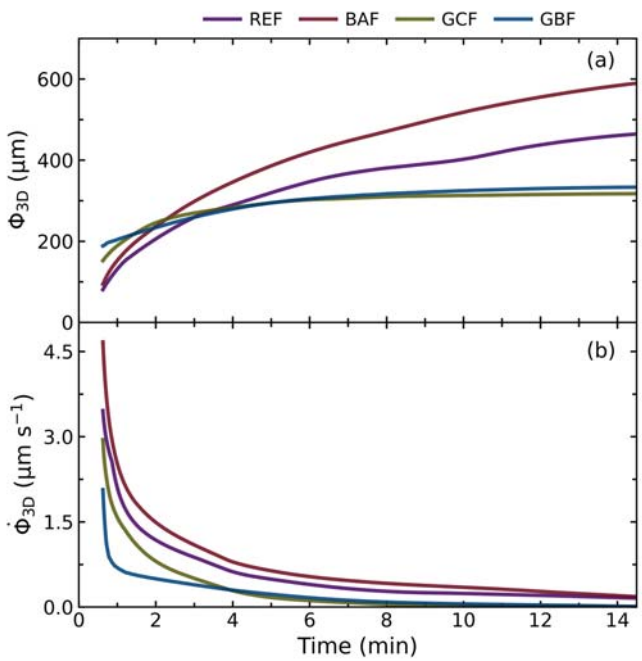

Figure 4-2-6: (a) Mean cell diameter and (b) rate of cell growth evolution with time calculated as the first derivate of the curves in (a)

Cell nucleation density was estimated using eq. (4-2-3) and the measured values of relative density and average cell size (Figure 4-2-7). This equation provides an estimation of the number of cells per cubic centimetre of solid material, which permits the comparison of nucleation in foams of different relative densities.

At short foaming times, an inspection of the cell nucleation density curves revealed a higher number of cells nucleated for higher contents of water and catalyst. On the one hand, the increase of 3 parts per weight in the number of moles of water in the formulation (Table 4-2-1) resulted in a jump in the maximum of the nucleation density curves. From 3.2 10^5 cells cm^{-3} (REF) to 7.3 10^5 cells cm^{-3} (BAF) and from 7.8 10^5 cells cm^{-3} (GCF) to 1.6 10^6 cells cm^{-3} (GBF). In the case of foams BAF and GBF, this enhancement in cell nucleation density was due to the increase in the number of CO_2 molecules available for nucleation compared to foams with less water in the formulation (REF and GCF). On the other hand, catalyst loading impacted nucleation by boosting the viscosity build-up of the reactive mixture at short reaction times (Figure 4-2-3) [34,35]. High viscosity is expected to favour greater cell nucleation densities by hindering degeneration at short reaction times and preventing losses of CO_2 to the surroundings. Both water and catalyst increments tested had a similar impact in boosting nucleation and led to an increase in the maximum cell nucleation density of approximately a factor of 2.3.

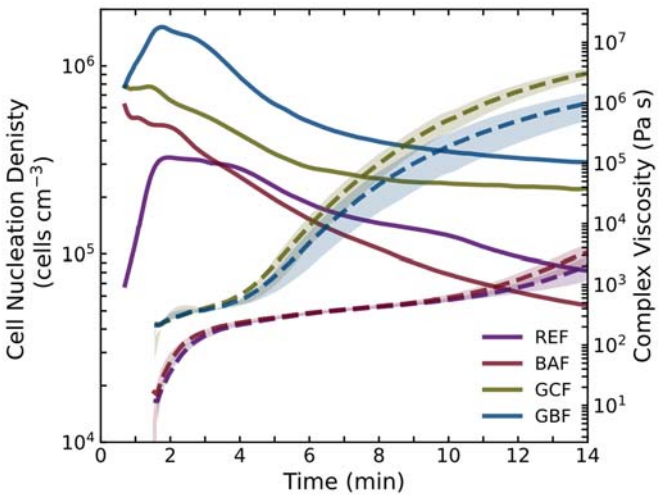

Figure 4-2-7: Calculated cell nucleation density (solid lines) data over time and complex viscosity build-up (dashed lines).

After 8 minutes of foaming the foams with higher catalyst dosage (GCF and GBF) stabilised at a constant cell nucleation density indicating the absence of degeneration mechanisms. However, foams of low catalyst dosage (REF and BAF) experienced a continuous decrease in their cell nucleation density even long after the blowing reaction had stopped (stabilisation of the relative density in Figure 4-2-5 (a)). This reduction in cell nucleation density together with the fast cell growth at long foaming times points out the existence of cell degeneration mechanisms in these foams. Moreover, the foam with low catalyst and high water content (BAF) presents the sharpest reduction in cell nucleation density of more than one order of magnitude over the scanned time. The strong decrease in the cell nucleation density of this foam is due to the higher amount of CO_2 gas generated which causes larger stretching of the cell walls contributing to degeneration due to the low modulus of the walls.

3.5. Cell growth simulation

To understand how cell growth, for the foams of Table 4-2-1, would proceed under ideal conditions and in the absence of degeneration mechanisms the evolution of cell size was calculated following the method detailed in Section 2.7. The constants needed to model cell growth were obtained from the literature and are summarised in Table 4-2-6 and Table 4-2-7 [9,10,34,36]. The constants whose value is considered to be independent of the formulation can be found in Table 4-2-6.

Table 4-2-6: Summary of operating conditions.

Property	Value
ρ_s (kg m^{-3})	1160
P_a (Pa)	101325
M_{CO_2} (kg mol^{-1})	0.044
D_{CO_2} (m^{2}s^{-1})	2.0 10^{-11}
H_{CO_2} (mol m^{-3}Pa^{-1})	1.1 10^{-4}
σ (N m^{-1})	0.025
T (K)	383

In contrast, modifying the amount of water and catalyst in the formulation is known to have an impact on the initial concentration of CO_2 in the mixture and on the reactive mixture viscosity, respectively. Attending to the mass of reactants, increasing the amount of water in the formulation from 2 ppw to 5 ppw increases the amount of CO_2 generated from 175 mmol to 363 mmol. In principle, according to Henry's Law (eq. (4-2-9)) this change in the amount of gas generated translates to an increase in the gas concentration, c_{CO_2}, and, consequently, in the saturation pressure of CO_2 in the reactive mixture, $P_{g,o}$.

$$c_{CO_2} = H_{CO_2} P_{g,o} \tag{4-2-9}$$

If all the gas was generated simultaneously at the start of the cell growth, we could in principle use Henry's Law to calculate the initial pressure of the gas. However, during PU foaming gas is not generated instantaneously but over time because of the continuous blowing reaction of water with isocyanate [20]. Hence, due to the difficulty of modelling a changing initial gas pressure, $P_{g,o}$, we decided to use approximate values of the initial gas pressure similar to those in the literature [9]. For the simulation, we translated the increase in water (BAF and GBF) as a slight increase in the initial gas pressure (Table 4-2-7) [9]. For viscosity, we took the average of the experimental complex viscosity during the first 5 minutes of reaction as registered with Shear Rheology. Last but not least, it has also been detected how varying the initial content of catalyst and water also modified the cell nucleation density (Figure 4-2-7). As the model does not account for degeneration events, this magnitude is going to have a pivotal impact on the maximum cell size that each foam can reach. Hence, the maximum size that the cells can reach is the diameter of the bubble shell, 2 x S_o.

Table 4-2-7: Summary of the cell growth variables changing with the formulation.

Sample	η (Pa s)	$P_{g,o}$ (Pa)	$2\ x\ S_o$ (μm)
REF	300	261325	328.0
BAF	300	561325	150.0
GCF	2000	261325	126.8
GBF	2000	561325	138.0

Assuming the previous constants as representative of the cell growth process in the foams in Table 4-2-1 the results in Figure 4-2-8 are obtained. Some interesting facts can be perceived. First of all, the final cell sizes achieved by the foams are ordered from lowest to highest cell nucleation density. REF and BAF achieve the highest cell sizes. REF grows to larger cell sizes since the material has the lowest viscosity and cell nucleation density. By comparison with the experimental results in Figure 4-2-6 (a), it is evident that BAF shows strong cell degeneration, which is in accordance with the results in Figure 4-2-7. According to the simulation results, stabilisation is achieved much faster for all foams than in the X-ray radioscopy experiments. Only REF takes slightly longer than 4 minutes to reach the final cell size. Yet, the samples with higher water and catalyst stabilise after only 1 minute of foaming. Moreover, the slope of cell growth of foams with the same initial saturation pressure is the same. In fact, the lower the differential pressure between the gas and the mixture the slower the cell growth. This phenomenon is also appreciated in the experimental results. In the X-ray radioscopy sequences, BAF experiences quicker cell growth (Figure 4-2-6 (b)). Similarly, GBF also experienced a quicker cell growth since the first experimental measurement showed the highest cell size of all four foams.

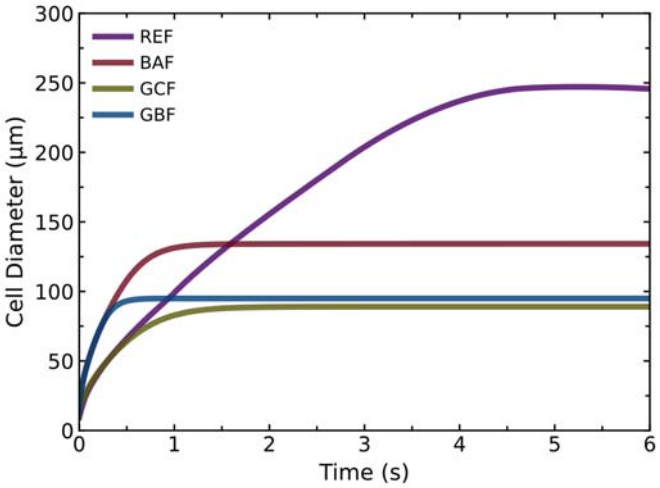

Figure 4-2-8: Cell growth for foams of different catalysts and water content.

When these results (Figure 4-2-8) are compared with those in Figure 4-2-6, it is clear that the mechanism responsible for the stabilisation of the cellular structure is radically different. While in the Amon and Denson model cells stop growing because they become into contact with each other, in PU foaming degeneration events are frequent causing a decrease in the number of cells. Hence, viscosity build-up is the limiting mechanism of cell degeneration and for stopping cell growth.

4. CONCLUSIONS

In this work, it has been demonstrated, both through experimental and simulation results, the impact of the viscosity of the reactive mixture on the foaming dynamics of PU. X-ray radioscopy revealed that foams of slow modulus build-up (REF and BAF) underwent a prolonged cell growth for nearly 15 minutes of reaction. Initially, cell growth was motivated by the ongoing generation of CO_2 gas. However, at long reaction times when the gas generation had practically stopped the cell size continued to increase. Analysing the cell nucleation density evolution over time confirmed the intensity of the degeneration mechanisms in foams of low catalyst content. For foam BAF (low water and catalyst) nucleation density dropped from 6 10^5 to 6 10^4 cells cm^{-3}, practically one order of magnitude. Degeneration was caused by the low stiffness of the cell walls which barely increased during the first 15 minutes of reaction. In contrast, the high viscosity and fast modulus build-up of foams with higher catalyst content restricted cell growth at the early stages of reaction without restraining the foam expansion. The investigation of the final cellular structure confirmed that the foam with the higher catalyst and water dosage revealed a higher cell density and smaller cell sizes. Hence, proving that a fast modulus build-up is beneficial to obtaining optimum cellular structures.

Simulation results also revealed that the viscosity of the mixture and gelification has a strong impact on the initial cell nucleation density. In turn, under the assumption of no degeneration, higher cell nucleation densities lead to smaller cell sizes and a faster stabilisation of the cellular structure. The initial blowing agent concentration also proved to have a pivotal influence on the initial speeds of cell growth. Hence, simulation of cell growth using the bubble shell model permits understanding the different speeds of stabilisation and cell growth of different formulations. However, to properly comprehend the dynamics of cellular structure generation it would be necessary to improve the shell model. Two possible improvements of the model would be to integrate the effect of the ongoing CO_2 generation

on the initial gas pressure and also an evolving viscosity of the mixture accounting for the foams reaction kinetics.

5. ACKNOWLEDGEMENTS

Financial assistance from the Junta of Castile and Leon (VA202P20) and Spanish Ministry of Science, Innovation and Universities (RTI2018-098749-B-I00 and RTI2018 - 097367-A-I00) is gratefully acknowledged. Financial support from Junta de Castilla y Leon predoctoral grant of P. Cimavilla-Román, co-financed by the European Social Fund, is also acknowledged.

6. REFERENCES

[1] N.S. Ramesh, S.T. Lee, Polymeric Foams: Mechanisms and Materials, First Ed, CRC Press, Boca Raton, 2004.

[2] J. Reignier, P. Alcouffe, F. Méchin, F. Fenouillot, The morphology of rigid polyurethane foam matrix and its evolution with time during foaming – New insight by cryogenic scanning electron microscopy, J. Colloid Interface Sci. 552 (2019) 153–165.

[3] M. Szycher, Szycher's handbook of Polyurethanes, 2nd Ed, Taylor & Francis Group, London, 2013.

[4] E. Minogue, An in-situ study of the nucleation process of polyurethane rigid foam formation, Dublin City University, 2000.

[5] P. Ferkl, I. Kršková, J. Kosek, Evolution of mass distribution in walls of rigid polyurethane foams, Chem. Eng. Sci. 176 (2018) 50–58.

[6] M. Amon, C.D. Denson, A study of the dynamics of foam growth: Analysis of the growth of closely spaced spherical bubbles, Polym. Eng. Sci. 24 (1984) 1026–1034.

[7] S. Costeux, L. Zhu, Thermoplastic nanocellular foams with low relative density using CO2 as the blowing agent, SPE Foam. 2011 Conf. (2011) 1–5.

[8] R. Elshereef, J. Vlachopoulos, A. Elkamel, Comparison and analysis of bubble growth and foam formation models, Eng. Comput. 27 (2010) 387–408.

[9] D. Niyogi, R. Kumar, K.S. Gandhi, Modeling of bubble-size distribution in free rise polyurethane foams, J. Appl. Polym. Sci. 131 (2014) 9098–9110.

[10] P. Ferkl, I. Kršková, J. Kosek, Evolution of mass distribution in walls of rigid polyurethane foams, Chem. Eng. Sci. 176 (2018) 50–58.

[11] P. Ferkl, M. Karimi, D.L. Marchisio, J. Kosek, Multi-scale modelling of expanding polyurethane foams: Coupling macro- and bubble-scales, Chem. Eng. Sci. 148 (2016) 55–64.

[12] P. Cimavilla-Román, S. Pérez-Tamarit, M. Santiago-Calvo, M.Á. Rodríguez-Pérez, Influence of silica aerogel particles on the foaming process and cellular structure of rigid polyurethane foams, Eur. Polym. J. 135 (2020) 109884.

[13] M. Santiago-Calvo, S. Pérez-Tamarit, P. Cimavilla-Román, V. Blasco, C. Ruiz, R. París, F. Villafañe, M.Á. Rodríguez-Pérez, X-ray radioscopy validation of a polyol functionalized with graphene oxide for producing rigid polyurethane foams with improved cellular structures, Eur. Polym. J. 118 (2019) 404–411.

[14] S. Pardo-Alonso, E. Solórzano, M.A. Rodriguez-Perez, Time-resolved X-ray imaging of nanofiller-polyurethane reactive foam systems, Colloids Surfaces A Physicochem. Eng. Asp. 438 (2013) 119–125.

[15] S. Pardo-Alonso, E. Solórzano, S. Estravís, M.A. Rodríguez-Perez, J.A. de Saja, In situ evidence of the nanoparticle nucleating effect in polyurethane–nanoclay foamed systems, Soft Matter. 8 (2012) 11262.

[16] M. Mar Bernal, S. Pardo-Alonso, E. Solórzano, M.Á. Lopez-Manchado, R. Verdejo, M.Á. Rodriguez-Perez, Effect of carbon nanofillers on flexible polyurethane foaming from a chemical and physical perspective, RSC Adv. 4 (2014) 20761.

[17] J. V. McClusky, R.D. Priester, W.R. Willkomm, M.D. Heaney, M.A. Capel, The use of FT-IR and dynamic saxs to provide an improved understanding of the matrix formation and viscosity build of flexible polyurethane foams, J. Cell. Plast. 29 (1993) 465.

[18] M.J. Elwell, S. Mortimer, A.J. Ryan, A Synchrotron SAXS Study of Structure Development Kinetics during the Reactive Processing of Flexible Polyurethane Foam, Macromolecules. 27 (1994) 5428–5439.

[19] M. Santiago-Calvo, Synthesis , Foaming Kinetics and Physical Properties of Cellular Nanocomposites Based on Rigid Polyurethane, University of Valladolid, 2019.

[20] P. Cimavilla-Román, M. Santiago-Calvo, M.Á. Rodríguez-Pérez, Dynamic Mechanical Analysis during polyurethane foaming: Relationship between modulus build-up and reaction kinetics, Polym. Test. 103 (2021) 107336.

[21] E. Mora, L.D. Artavia, C.W. Macosko, Modulus development during reactive urethane foaming, J. Rheol. 35 (1991) 921–940.

[22] L.D. Artavia, C.W. Macosk, R.D. Priester, A.K. Schrock, R.B. Turner, Volume rise during flexible urethane foaming, Polym. React. Eng. 1 (1993) 203–227.

[23] ASTM D1622-08: Standard Test Method for Apparent Density of Rigid Cellular Plastics, (n.d.).

[24] J. Pinto, E. Solorzano, M.A. Rodriguez-Perez, J.A. de Saja, Characterization of the cellular structure based on user-interactive image analysis procedures, J. Cell. Plast. 49 (2013) 555–575.

[25] ASTM D3572, Annu. B. ASTM Stand. 8.02 (1994).

[26] S. Costeux, I. Khan, S.P. Bunker, H.K. Jeon, Experimental study and modeling of nanofoams formation from single phase acrylic copolymers, J. Cell. Plast. 51 (2014) 197–221.

[27] R.R. Rao, L.A. Mondy, K.N. Long, M.C. Celina, N. Wyatt, C.C. Roberts, M.M. Soehnel, V.E. Brunini, The kinetics of polyurethane structural foam formation: Foaming and polymerization, AIChE J. 63 (2017) 2945–2957.

[28] M.L. Pinto, Formulation, Preparation, and Characterization of Polyurethane Foams, J. Chem. Educ. 87 (2010) 212–215.

[29] H. Winter, H, Can the gel point of a cross-linking polymer be detected by the G' - G" crossover?, Polym. Eng. Sci. 27 (1987).

[30] R. Bouayad, J. Bikard, J.F. Agassant, Compressible flow in a plate/plate rheometer: Application to the experimental determination of reactive expansion's models parameters for polyurethane foam, Int. J. Mater. Form. 2 (2009) 243–260.

[31] M. Stanko, M. Stommel, Kinetic prediction of fast curing polyurethane resins by model-free isoconversional methods, Polymers (Basel). 10 (2018).

[32] Y. Zhao, Modeling and Experimental Study of Polyurethane Foaming Reactions, University of Missouri-Columbia, 2015.

[33] Y. Zhao, F. Zhong, A. Tekeei, G.J. Suppes, Modeling impact of catalyst loading on polyurethane foam polymerization, Appl. Catal. A Gen. 469 (2014) 229–238.

[34] C. Brondi, E. Di Maio, L. Bertucelli, V. Parenti, T. Mosciatti, Competing bubble formation mechanisms in rigid polyurethane foaming, Polymer (Guildf). 228 (2021) 123877.

[35] B. Merillas, F. Villafañe, M.Á. Rodríguez-Pérez, Nanoparticles Addition in PU Foams: The Dramatic Effect of Trapped-Air on Nucleation, Polym. 2021, Vol. 13, Page 2952. 13 (2021) 2952.

[36] S. Pérez-Tamarit, E. Solórzano, R. Mokso, M.A. Rodríguez-Pérez, In-situ understanding of pore nucleation and growth in polyurethane foams by using real-time synchrotron X-ray tomography, Polymer (Guildf). 166 (2019) 50–54.

C APT

Early structure generation during Polyurethane foaming

EARLY STRUCTURE GENERATION DURING POLYURETHANE FOAMING

5

5.1. INTRODUCTION

In this chapter, we present a publication (Cryogenic X-ray Tomography of Polyurethane foams: Early structural development, manuscript submitted to Polymer) reporting an innovative approach to investigate in 3D the cellular structure generation during the synthesis of PU foams. From the previous chapter (Section 4.2) it becomes evident that while X-ray radioscopy is a powerful method to obtain an overview of foaming dynamics of PU, the limited resolution hinders direct observation of the nucleated cells. In fact, cell nucleation density can only be measured indirectly due to the partial overlap of cells and constant flow of reactive material outside of the mould. Hence, in this chapter, we describe a new approach based on laboratory X-ray tomography to characterise in 3D the structure of foams before cure. However, as seen in Chapter 4, the foaming of PU is a fast process which is often completed in less than 15 minutes. On the contrary, conventional laboratory X-ray tomography takes on average longer than 1 hour per scan. Hence, to investigate the internal cellular structure of PU foams by X-ray tomography, the synthesis was stopped at different reaction times by drastically reducing the temperature of the sample. In the publication collected in this chapter, we present the freezing methodology for stopping the synthesis of PU foams. In addition, since the sample must be preserved at low temperatures during the scan, we report the design of a cooling system for laboratory X-ray tomography systems. With the aforementioned design, we could visualise and analyse the internal cellular structure in 3D of RPU foams. In this publication the initial stages of the cellular structure generation of the model formulations used in chapter 4 were observed and analysed right after nucleation took place. The reason behind the reaction times choice is the difficulty of observing nucleation and the early cellular structure using other state-of-the-art methods such as, X-ray radioscopy (Chapter 4, Section 4.3).

Section 5.2.

Cryogenic x-ray tomography of polyurethane foams: early structural development

Paula Cimavilla-Román[a], Mercedes Santiago-Calvo[a], Miguel Ángel Rodriguez-Pérez[a,b]

[a] Cellular Materials Laboratory (CellMat), Condensed Matter Physics Department, University of Valladolid, Paseo Belen 7, Valladolid, 47011, Spain

[b] BioEcoUva. Research Institute on Bioeconomy, University of Valladolid, Spain

Submitted Manuscript

Graphical Abstract

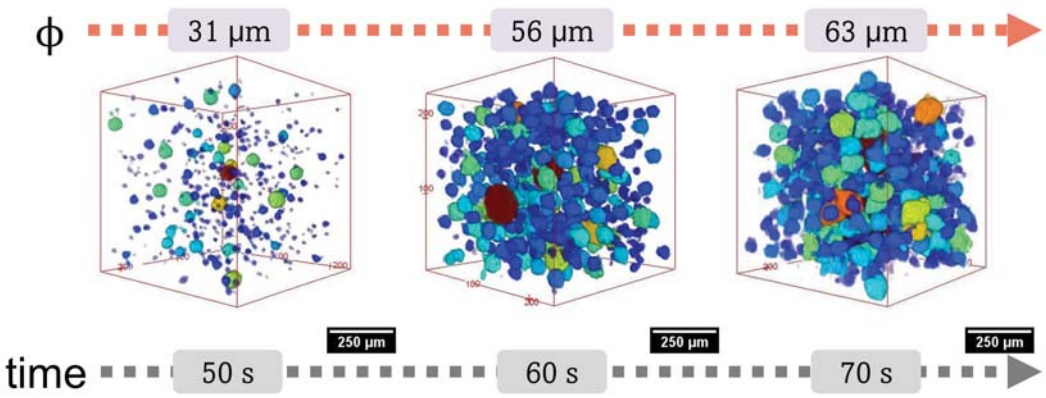

ABSTRACT

Cryogenic X-ray tomography is used for the first time to study the cellular structure development of polyurethane foams. The method permits studying ex-situ and in 3D the internal morphology of frozen polyurethane samples at different reaction times. Nucleation and growth during the first seconds of reaction were studied in foams with different contents of blowing agent and catalyst. It was detected how increasing catalyst in 1 part per weight, led to a rise in cell nucleation density, from 8.9 10^5 to 1.9 10^6 cells cm^{-3}, as well as to a faster structural development. In contrast, an increase in the content of water to 5 parts per weight only increases nucleation slightly but leads to fast speeds of cell growth of 2.6 μm s^{-1} at early reaction times. Overall, the analysis of the tomographies provides a precise characterization of the foam morphology and an overview of how porosity, cell size, cell density and solid phase thickness evolve during the initial stages of foaming.

KEYWORDS

Polyurethane foam; X-ray tomography; Cellular Structure; Foaming

1. INTRODUCTION

The foaming of thermosetting Polyurethane (PU) foams is a complex process in which the generation of a cellular structure is simultaneous to the polymer morphology build-up [1]. At the centre of the formation of Rigid Polyurethane (RPU) foams is the reaction of isocyanates with compounds containing active hydrogen, in particular polyols and water. The reaction of isocyanate with polyol (polymerisation or gelling reaction) leads to the generation of urethane crosslinks which builds the polymer morphology [2]. Whereas, the reaction of isocyanate with water (blowing or foaming reaction) is responsible for the generation of unstable carbamic acid, which spontaneously decomposes releasing amine and CO_2 gas as a by-product [3]. According to classical nucleation theories the released CO_2 gas should be responsible for saturating the liquid reactive mixture with gas. This phenomena results in the nucleation of cells in the mixture and later blowing of the cells [4–6]. Yet, there are still open questions about the process of nucleation in PU foams. Some authors argue that supersaturation with CO_2 gas is not achieved in the reactive mixture and thus the dissolved gas does not spontaneously create nuclei [4,7–9]. In contrast, the mechanical agitation needed to trigger foam formation constitutes a well-known source of air entrapments in the mixture [8,10,11]. The entrapped microbubbles can act as seeds for nucleation hindering self-nucleation by the dissolved CO_2 molecules [8,9]. Hence, in most cases, CO_2 diffusion into the entrapped air bubbles proceeds so quickly that the nucleation of new bubbles is prevented.

Due to the complexity of this foaming process, in recent years, much work has been done to develop techniques capable of probing the cellular structure formation in PU foams. Among them, sequential X-ray imaging (X-ray radioscopy) has been widely used to investigate bubble nucleation and growth in PU foams produced using different types nanoparticles as nucleating agents [12–15]. However, this technique has several drawbacks as it only provides 2D information, the sample must have reduced thickness and the results present a long time span from the beginning of the reaction until the start of the radiographs acquisition (~60 s). For this reason, the technique does not permit characterising the cellular structure development near the instance of nucleation. In fact, detection of nucleation sites or following the growth of individual cells is difficult when using X-ray radioscopy. In a later study, Pérez-Tamarit et al. [16] used synchrotron X-ray tomography to investigate the microstructure generation in nanocomposite PU foams. Thanks to the

advances in synchrotron facilities, the authors could acquire X-ray tomography scans at extremely fast speeds. In standard tomography set-ups the acquisition can take up to 1 h whereas using fast-tomography one scan could be acquired in only 156 ms at a resolution of 3.2 μm [16]. The high spatial and temporal resolution provided 3D information on the cellular structure generated in PU foams filled with and without nanoparticles. From a scientific point of view, this is an ideal approach to study the foaming behaviour of PU systems, but it is impossible to reproduce with laboratory set-ups. In follow up to the previous works, Reignier et al. [8] proved the potential of cryogenic scanning electron microscopy (cryo-SEM) to ex-situ image the cellular structure development of PU foams. The high resolution of SEM enabled visualization of the structure on the sub-micron scale. The authors focused on studying the structure at short reaction times. Using cryo-SEM they visualised the cavities generated by vaporised isopentane droplets as well as the morphology of the entrapped air bubbles introduced while mixing the reactants. Both structures revealed a drastically different morphology. Isopentane cavities had nanometric sizes and their number density was close to 10^{12} droplets cm^{-3}. However, air bubbles had micrometric sizes (5-100 μm) and their number density was much lower, *ca*. 10^6 cells cm^{-3}, which is in the same order of magnitude as the final cell density in the cured foam. These observations together with the disappearance of the isopentane cavities with the reaction time led the authors to infer that cell nucleation was exclusively due to the air bubbles entrapped during mixing [8]. While this approach provides high resolution, it does not allow to analyse the cell volumes or to characterise the solid matrix thickness over time.

Taking into account the state of the art, in the present study, we make a new contribution to the techniques allowing the investigation of the structure generation during PU foaming. We suggest a new approach based on cryogenic X-ray tomography to ex-situ explore in 3D the cellular structure evolution. To this end, an X-ray cryo-tomography set-up has been developed in which the samples are maintained at -120 °C during the scan. To the best of our knowledge, this is the first time that the evolution of PU foams has been studied in 3D by means of cryogenic tomography. This approach allows a detailed analysis of cellular structure descriptors of the gas and of the solid phase in 3D.

2. MATERIALS AND METHODS

2.1. Raw materials of the composite RPU foams

The polyol used was a high functionality polyether polyol from Repsol S.A, Alcupol R4520 (functionality of 4.5, OH value of 455 mg·KOH g^{-1}, viscosity: 5250 mPa s at 25 °C). The isocyanate was a polymeric diphenylmethane diisocyanate (pMDI), IsoPMDI 92140 (31.5% NCO, density 1.23 g cm^{-3}, viscosity 170-250 mPa s at 25 °C) supplied by BASF. Polycat 8 (N,N-dimethyl cyclohexylamine) is a tertiary amine. It was supplied by Evonik, and it is used primarily to promote the urethane reaction. TEGOSTAB® B8522 (a non-hydrolysable polyether-polydimethylsiloxane–stabilizer) also from Evonik was used as a surfactant to obtain superior cell structures. The blowing agent was distilled water.

2.2. Preparation of RPU foams

In this study three RPU foam formulations were prepared (Table 5-1) [17]. Polyol, isocyanate index and surfactant contents were maintained constant. Yet, the concentration of catalyst and blowing agent was changed to observe its impact on the early structural development. The selected concentrations were 0.5 and 1.5 parts per weight (ppw) of catalyst and 2 and 5 ppw of water.

The components were blended together using an overhead stirrer (EUROSTAR 60 control from IKA), connected to a 50 mm diameter VollrathTM Lenart-disc. First, a blend of polyol with additives (catalyst, surfactant and blowing agent) was prepared by mixing at 250 rpm for 2 minutes. Afterwards, the RPU foam reaction was triggered when mixing a total mass of 40 g, including the isocyanate and polyol blend, for 10 s at 1200 rpm in a 1 L plastic cup. The start of the stirring process between polyol blend and isocyanate is considered as time 0 of the reaction.

Table 5-1. Components and concentrations for each RPU formulation.

Sample	Isocyanate Index	Polyol (ppw)	Surfactant (ppw)	Gelling catalyst (ppw)	Water (ppw)
REF	110	100	1	0.5	2
BAF	110	100	1	0.5	5
GCF	110	100	1	1.5	2

2.3. Density and cellular structure characterisation of the cured foam

Foam density, ρ, was measured following ASTM D1622/D1622M-14 [17]. The relative density, ρ_r, is the ratio between the density of the foam and that of the solid PU (1160 kg m^{-3}). Additionally, the cellular structure was observed in growth direction of the foam using Scanning Electron Microscopy, SEM (JEOL JSM-820 microscope). Descriptors of the cellular structure such as cell size, ϕ_{3D}, anisotropy ratio of the cells in the foam rise direction, *AR*, and cell density, N_v, were measured using a dedicated ImageJ script [18]. Cell nucleation density, N_o, was estimated by dividing cell density by the relative density. However, it is important to note that cell nucleation density might be lower than in reality, since the approximation assumes that there are no degeneration mechanisms during foaming [18]. To ensure the accuracy of the analysis more than 100 cells per sample were measured.

2.4. Sample preparation and freezing

To prepare the samples for the cryogenic X-ray tomography experiments a few millilitres of the mixture were extracted from the cup (Section 2.2) and injected into the X-ray tomography sample holder (Figure 5-1 component 6 (b)). The sample holder is a hollow cylindrical Kapton container of 4 mm in diameter and 2 cm in height. It can accommodate a maximum volume of 0.25 mL. In order to ensure the reproducibility between experiments, the injected sample volume was fixed to 0.1 mL, and then the liquid was allowed to expand in the container until the corresponding freezing time. The foam expansion was first stopped with the vapours of liquid nitrogen (LN_2) and after a few seconds immersed in liquid nitrogen to achieve full freezing. The time elapsed since the start of the mixing and the instant at which the samples were cooled with liquid nitrogen was taken as the overall foaming time of the material.

2.5. Cryogenic X-ray tomography

The tomography experiments were performed using a laboratory X-ray microtomography system. The set-up consisted of an X-ray microfocus source (Hamamatsu) and a flat panel detector connected to a frame grabber (Dalsa-Coreco), which records the projection images [19]. This high-resolution detector is composed of a matrix of 2240x2344 pixels, each with a size of 50 μm. In these experiments, the tube voltage was set to 55 kV, the tube current to 170 μA, the detector exposure time was 1 s, and each projection was the result of averaging three consecutive images to reduce noise. On the whole, 1200 projections were acquired, resulting in long scan times of *ca*. 90 min. The spatial resolution was fixed to 3.5 μm.

The described microtomography set-up per se lacked the cooling system required to keep the samples at cryogenic temperatures during the scan. Hence, a cooling stage was implemented to ensure the dimensional stability of the foams during the inspection [20]. Figure 5-1 shows a scheme of the X-ray cryo-tomography set-up.

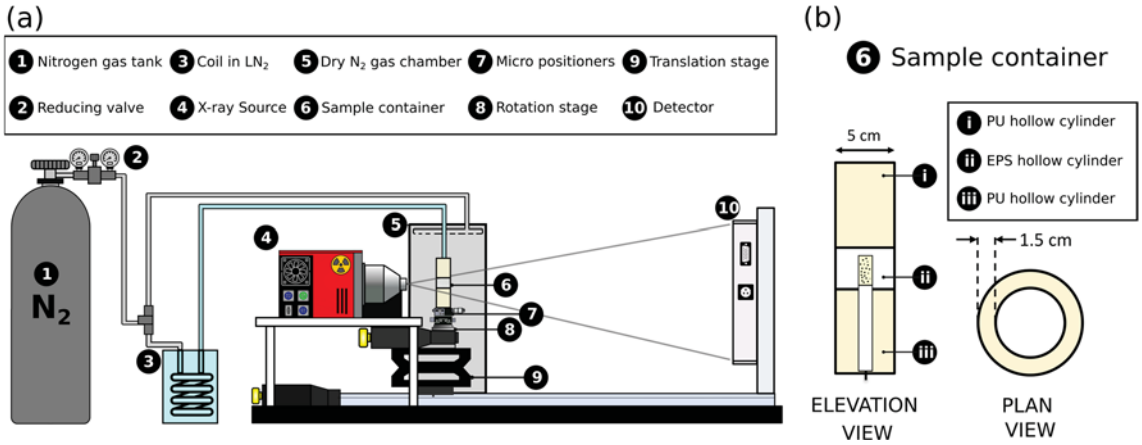

Figure 5-1: (a) Scheme of the cooling and X-ray tomography system. Nitrogen (N_2) gas (1), at room temperature, passes through a reducing valve (2) to a coil (3) immersed in liquid nitrogen. The cooled gas enters the insulating container (6) through a tube. Both the sample and the sample container sit on top of the rotation stage (8) which is inside a dry gas chamber (5). (b) Elevation and plan view of the insulating container with sample superimposed on the elevation view.

The reactive sample (prepared as specified in Section 2.2) is located inside a thermal insulating container. The container was a hollow cylinder of 5 cm in diameter and walls of 1.5 cm in thickness (Figure 5-1 (b)). The material making up the walls of the container was low density foam for its high insulation capacity. The main material making up the container was PU foam except for the region in the X-ray beam path which was made of expanded polystyrene (EPS) foam. EPS is the optimum material in terms of X-ray transparency as it has extremely low density and low attenuation to the X-rays. In the X-ray tomography set-

up both the container and the sample stand on top of a rotation stage (Figure 5-1 (a), (8)) so that the sample and container rotate synchronously with the stage.

Low temperatures in the sample are achieved by making dry nitrogen gas (N_2), coming from a pressurized gas bottle, pass through a copper coil immersed in liquid nitrogen. After the gas is cooled, it is directed towards the X-ray set-up and into the sample container. In addition, as seen in Figure 5-1, the entire sample set-up (sample container and rotational stage) was enclosed inside a chamber filled with N_2 gas at room temperature. As the chamber is not airtight, N_2 gas coming from the tank is flowing continuously in and out of the chamber (Figure 5-1). The continuous flow of N_2 gas is essential to prevent the formation of frost on the surface of the sample container. Avoiding the formation of frost is a critical factor when performing cryogenic X-ray tomography since the dynamic generation of frost would hinder the reconstruction of the acquired tomographies [20]. For this work, the operating pressure for both the cold N_2 and the room temperature N_2 was maintained at 1.5 bar. This pressure ensured that the temperature of the gas when reaching the sample was sufficiently low to keep the material frozen. The temperature inside the sample container (Figure 5-1 component 6) was measured with a type K thermocouple during the scan. The temperature was logged with a Data Logger from Picolog and during the experiment time the temperature was approximately -117.1 ± 7.4 °C.

2.6. Image analysis

The reconstruction of the cryogenic X-ray tomographies was carried out using Octopus reconstruction package [21]. The process produces slices or cross-section images of the scanned volumes. From the total reconstructed volume, the analysis of the foam microstructure was investigated on a minimum of four sub-volumes of 5.5 mm^3. These volumes were analysed using ImageJ/FIJI software tool [22]. The analysis focused on characterising the cellular structure (gas phase) and the thickness of the reactive mixture matrix (solid phase). The gas phase was studied using the MorphoLibJ plugin implemented on ImageJ/FIJI [23]. Firstly, an edge-preserving filter was applied to reduce noise in the images and enhance the contrast between the solid and gas phases. Afterwards, the gas phase was binarized to separate both phases. From the binarized volumes cell size, ϕ, cell density, N_v and relative density, ρ_r were measured in 3D. Relative density was estimated simply as the number of solid voxels divided by the total number of voxels in the analysed volume. Cell size was obtained assuming that the cells had spherical shapes. Hence, the

average cell size is the average diameter of the cells. Cell density was calculated by dividing the total number of cells by the volume of the analysed region. Employing Kumar's method [24] cell nucleation density (eq. (5-1)) was calculated, N_o. For the analysis, more than 10^4 cells were studied.

$$N_o = \frac{6}{\pi \Phi^3}\left(\frac{1}{\rho_r} - 1\right) \tag{5-1}$$

After binarization, the solid phase thickness was measured using a Local Thickness algorithm implemented on FIJI [25]. The plugin returns a thickness map of the binarized phase. From the thickness map, the histogram representing the matrix thickness distribution was calculated and from it, the average histogram thickness can be calculated providing the intercell distance, δ.

3. RESULTS AND DISCUSSION

3.1. Cured foams: Density and cellular structure

Table 5-2 displays the density and relative density of the cured foams prepared with 40 g of material as indicated in Section 2.2. As reported in previous work [26], density only decreases slightly when boosting the catalysis of the foams. Conversely, density dropped approximately 1.6 times when the content of water rose from 2 to 5 ppw. For the selected isocyanate index this change resulted in a twofold increase in the moles of water in the formulation. Since one mole of CO_2 is produced from each mole of water, the number of moles of CO_2 released also doubles (BAF) and ideally, the density should have also been reduced by a factor of two [27,28]. The lesser expansion of foam BAF might be due to CO_2 lost to the surroundings during blowing or supersaturated in the polymer phase.

Table 5-2: Density, relative density and main descriptors of the cellular structure obtained from SEM micrographs.

Sample	ρ (kg m^{-3})	ρ_r	Φ_{3D} (μm)	AR	N_v (cells cm^{-3})	N_o (cells cm^{-3})
REF	59.7 ± 1.6	0.051	416.0 ± 91.8	1.2	2.5 10^4	4.5 10^5
BAF	34.4 ± 0.2	0.030	488.3 ± 151.9	1.4	1.6 10^4	4.8 10^5
GCF	52.3 ± 1.1	0.045	322.5 ± 73.7	1.3	5.4 10^4	1.1 10^6

The increase in the gelling catalyst concentration significantly improved the cellular structure of the final foams (Figure 5-2). Cell size was reduced by 23% for GCF with respect

to REF, Table 5-2. Cell density decreased with the addition of water suggesting an increased number of degeneration of events during foaming. On the contrary, cell density rose with catalyst concentration. Similarly, cell nucleation density increased by more than a factor 2 with the addition of more catalyst and only slightly with the addition of water. Nonetheless, the real cell nucleation density is expected to have been larger than the values in Table 5-2 as degeneration events are likely to have taken place in these foams during synthesis. Regarding anisotropy, all foams showed a structure with cells elongated in the foam growth direction. Yet, anisotropy was higher for samples of lower density (BAF).

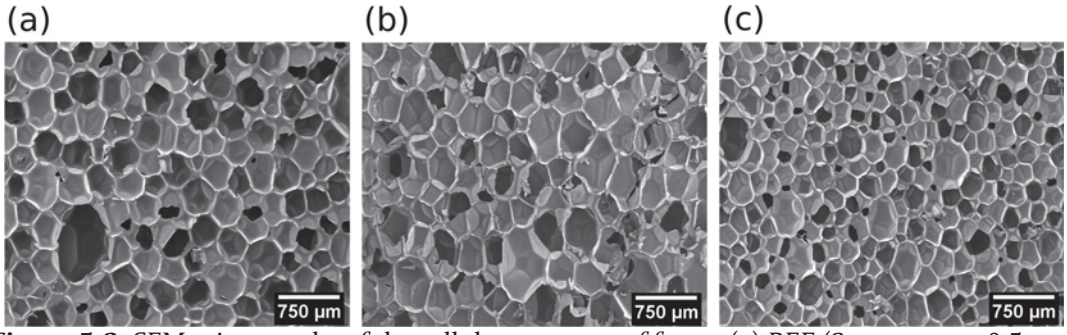

Figure 5-2: SEM micrographs of the cellular structure of foams (a) REF (2 ppw water, 0.5 ppw catalyst), (b) BAF (5 ppw water, 0.5 ppw catalyst) and (c) GCF (2 ppw water, 1.5 ppw catalyst).

3.2. Early cellular structure evolution

The reactivity of these foams was studied in previous work [26]. It was detected that the time required for the cells to nucleate (cream time) decreased from 72 s (REF) to 42 s (GCF) with the increase of 1 ppw of catalyst. However, the increase in blowing agent reduced slightly the cream time from 72 s (REF) to 54 s (BAF). To understand the early cellular structure development of RPU foams the analysed times were always near the cream time. For systems REF and BAF, the selected freezing times were: 50, 60 and 70 s. Whereas, due to its high reactivity, for the system GCF the freezing times for the analysis were: 25, 32 and 40 s. In Figure 5-3 the structure of the frozen PU samples obtained by Cryogenic X-ray tomography following the method detailed in section 2.5 can be appreciated.

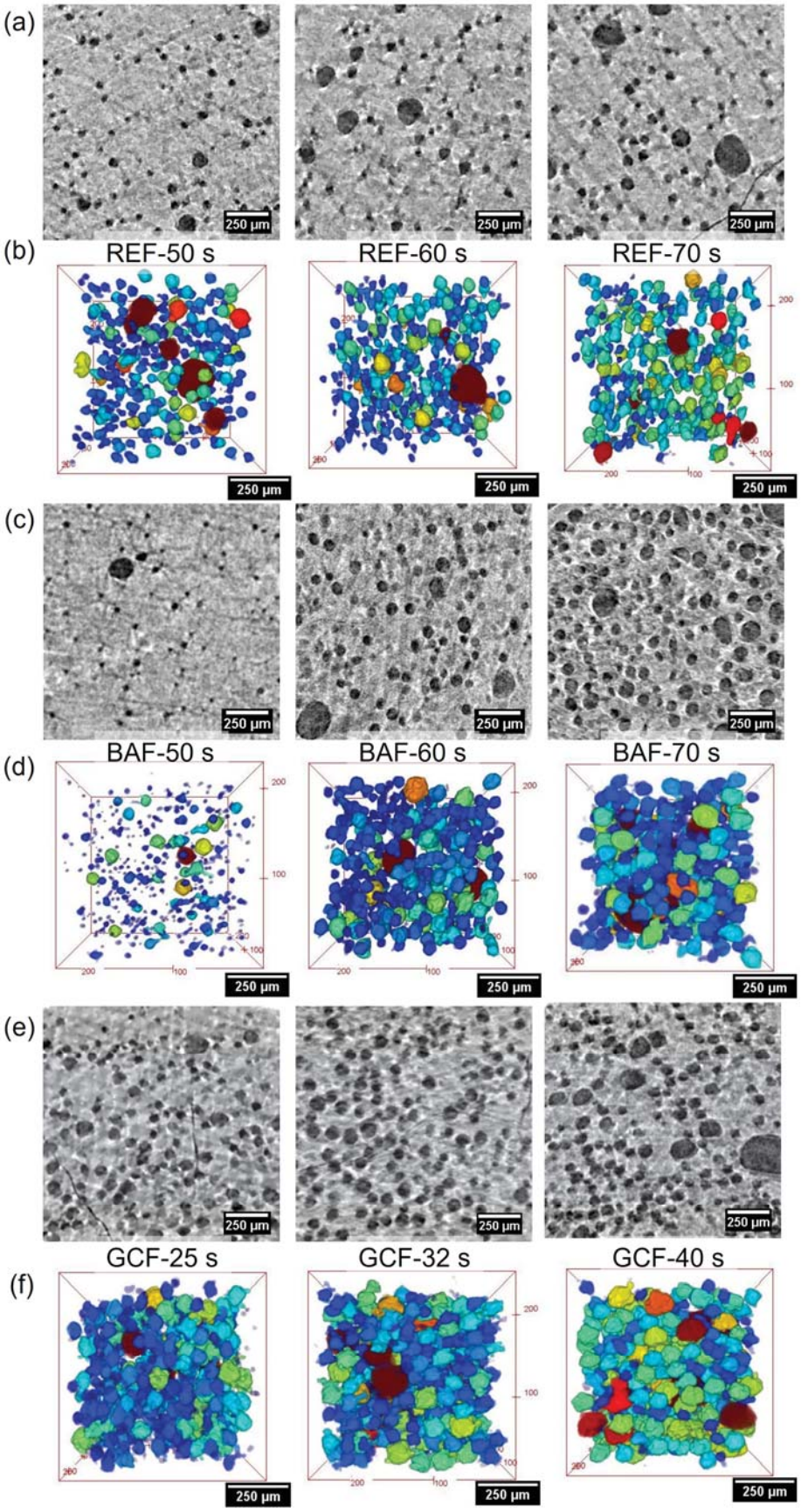

Figure 5- 3: (a), (c) and (e) Reconstructed cross-sections and (b), (d) and (f) 3D renderings of the analysed cells for the systems REF, BAF and GCF at different times.

From Figure 5-3, it is possible to appreciate the main qualitative differences between samples. REF (Figure 5-3 (a) and (b)) structure remains practically unchanged at short foaming times. Whereas BAF (Figure 5-3 (c) and (d)) quickly transitions from a liquid, scattered with nascent cells of only a few microns, into a foamed material in which cells have spherical shapes but are still isolated from each other. Lastly, despite being examined at shorter reaction times, foam GCF (Figure 5-3 (d) and (e)) revealed higher porosity and larger cells than the previous systems with catalyst concentration of 0.5 ppw. From the tomography volumes, the main descriptors of the cellular structure were measured (Table 5-3).

The relative density results gathered in Table 5-3 evidence that all systems with low catalyst content (0.5 ppw) undergo little gas generation before their cream time. Before the onset of foam growth, the porosity of foams REF and BAF was below 10%. This fact is particularly noticeable in system REF whose cream time is close to 72 s. This system reveals relatively low expansion in the characterised reaction times. Likewise, the cell growth experienced by foam REF, before its cream time, is almost negligible (0.5 μm s^{-1}) compared to typical cell growth rates (~3 μm s^{-1}) observed, after the cream time when using X-ray radioscopy [12].

After the onset of foam expansion (54 s), BAF samples suffer a quick growth as anticipated by the images in Figure 5-3. In only 20 s, relative density decreased to about 79% of the pre-cream value. Additionally, there is a drastic increase in the cell size in less than 10 s (from 50 s to 60 s of reaction time). This translates into a speed of cell growth of approximately 2.6 μm s^{-1}. The fast speed of cell growth is a consequence of the high content of water in the formulation. In PU foams, the blowing (urea) reaction proceeds at a faster pace than the polymerisation [29,30]. Hence, the CO_2 gas generated as a by-product of the urea reaction quickly diffuses into the nuclei blowing the cells. In contrast, the formulation with a higher catalyst content (GCF) undergoes quite different structural development. Firstly, even at times lower than cream, the system has low relative densities and large cell sizes compared to foams REF and BAF. Yet, the higher reactivity and viscosity build-up of this foam will stop cell growth at earlier foaming times leading to lower cell sizes in the cured foam as seen in Figure 5-2 [26]. In the 20 s of monitored reaction time, the speed of cell growth was close to 1.2 μm s^{-1}, below that of foam BAF.

Table 5-3: Evolution of the main structural descriptors near the cream time for foams in Table 5-1.

Sample	Reaction time (s)	ρ_r	ϕ (μm)	SD/ϕ	N_v (cells cm^{-3})	N_o (cells cm^{-3})	δ (μm)
REF	50	0.92	39.5 ± 18.1	0.46	8.0 10^5	8.7 10^5	148.4 ± 40.9
	60	0.90	43.6 ± 20.3	0.47	8.5 10^5	9.5 10^5	139.9 ± 41.0
	70	0.90	49.3 ± 20.7	0.42	8.0 10^5	8.9 10^5	143.6 ± 42.6
BAF	50	0.95	31.2 ± 13.5	0.43	1.1 10^6	1.1 10^6	138.8 ± 38.9
	60	0.88	56.4 ± 20.3	0.36	9.1 10^5	1.0 10^6	106.9 ± 39.1
	70	0.75	62.9 ± 24.5	0.39	1.1 10^6	1.5 10^6	70.5 ± 29.0
GCF	25	0.84	51.9 ± 18.1	0.35	1.3 10^6	1.6 10^6	93.9 ± 47.5
	32	0.76	60.3 ± 20.7	0.34	1.3 10^6	1.8 10^6	69.9 ± 30.6
	40	0.69	70.5 ± 18.5	0.26	1.2 10^6	1.9 10^6	63.6 ± 31.3

In addition, after analysing a large number of cells, more than 10^4, the cell size distributions were calculated (Figure 5-4). In the foam REF, cell distributions remain unchanged before the cream time in accordance with the average cell size values. In 20 s, only a slight displacement of the distribution to higher cell sizes is observed (Figure 5-4 (a)). In contrast, system BAF shows a remarkably different distribution at different reaction times. From the cell size distribution (Figure 5-4 (b)), cells with sizes as small as 8 μm were detected at this foaming stage. Nonetheless, shortly after the beginning of the foam expansion, the sample showed a fast cell growth, and the minimum cell size increased to more than 20 μm. Moreover, the generation of gas due to the blowing reaction resulted in a change of the cellular structure heterogeneity (parameter SD/ϕ: normalised standard deviation). The lower SD/ϕ the more homogenous is the structure. Hence, the structure of foam BAF becomes more homogenous with time. Last but not least, the increase in catalyst content caused the cell distribution to move to higher cell sizes at early reaction times compared to the other foams. However, at 32 s of reaction a population of small-sized cells (<20 μm) prevailed. In contrast near the cream time (40 s), the cell distribution of GCF had completely shifted to higher sizes, while it had also narrowed indicating a more homogeneous structure (SD/ϕ=0.25).

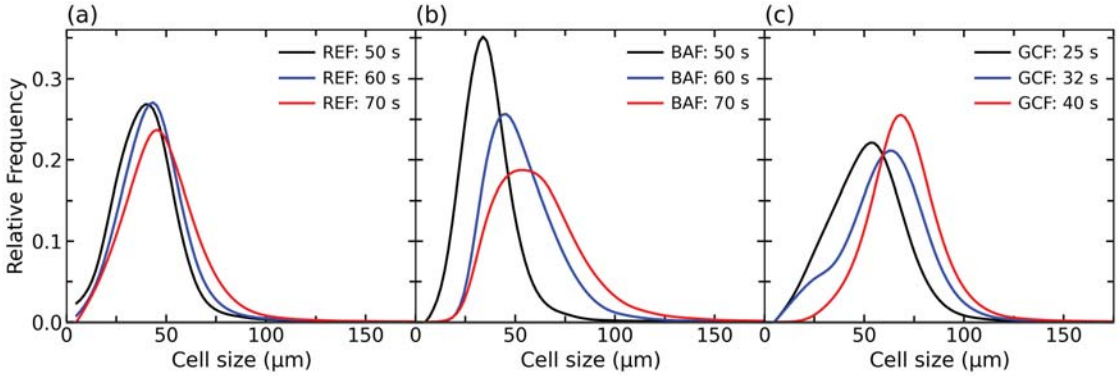

Figure 5- 4: Cell size distributions for systems at three different reaction times for systems: (a) REF, (b) BAF, and (c) GCF.

Cell density (Table 5-3) provides an estimation of the number of cells per unit volume of foam. Hence, if the number of nuclei remains constant over time, as porosity increases cell density should, in principle, decrease over time as the volume of foam increases. In contrast, cell nucleation density values give insights into the number of nucleation sites initially present in the mixture. As seen in Table 5-3, cell density remains rather constant and only varies over time in approximately 10^5 cells cm^{-3}. While cell nucleation density remains constant for REF and increases over the monitored time for foams BAF and GCF. In principle, this points out to an ongoing nucleation near the cream time for the latter foams. However, in previous studies [8,31] it has been argued that nucleation in PU foams is typically the result of air bubbles being entrapped during the mixing of reactants. Hence, another possible explanation for the apparent increase in cell nucleation density is the limited resolution (3.5 μm) of the X-ray system. The limited spatial resolution may hinder the visualisation of cells below or near the spatial resolution at early reaction times. The ongoing generation of gas blows the cells which, as they grow above 7 μm (twice the spatial resolution), become more easily detectable by the analysis. Regardless of this fact, the results show that the foam with the highest cell nucleation density was the one with higher catalyst content (GCF). This agrees with the final cellular structure of the cured foam (Figure 5-2). It has been argued that a fast viscosity build-up can promote more air entrapments and act as a driver for cell nucleation [31,32]. Moreover, previous studies have hinted at the role of the reactive mixture viscosity in entrapping and retaining the CO_2 gas generated more efficiently [31,33]. In addition, the stability of the cell nucleation density values over time indicates that there is no degeneration of the structure at short foaming times.

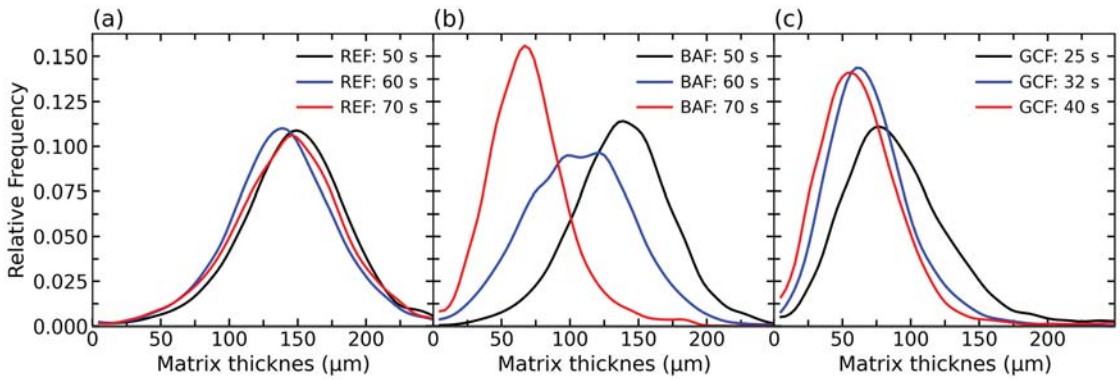

Figure 5- 5: Thickness of the solid matrix at three different reaction times for systems: (a) REF, (b) BAF, and (c) GCF.

From Figure 5-3 and Figure 5-5, it can be observed how the matrix thickness is clearly in the micrometric range. At high relative densities ($\rho_r > 0.9$) the thickness of the reactive mixture is above 100 μm. Whereas the increase in cell density and cell size with the foaming time reduces the intercell distance to approximately 65 μm. The high intercell distance also supports the apparent absence of degeneration mechanisms. In PU foams coalescence is one of the most common degeneration mechanisms, and it is triggered by the reduction of the wall thickness below the micron [34,35]. However, during the times studied in this work, cells have spherical shapes and are separated from each other by more than 5 μm as reported in Figure 5-5 making it unlikely the appearance of coalescence events. Overall, the high cell density and cell size caused system GCF to present a lower intercell distance compared to foams BAF and REF. Yet, BAF foam revealed a fast reduction in the matrix thickness, whereas REF intercell distance remained practically unchanged.

4. CONCLUSIONS

In this work, the development of a new technique probing the fast-changing cellular structure of PU foams is reported. The proposed approach permits the ex-situ investigation of the foaming process of PU and relies on cryogenic temperatures to vitrify the cellular structure of the foam at different reaction times. By employing an in-house cooling system, the dimensional stability of frozen PU samples was ensured, and their microstructure could be explored in 3D with laboratory X-ray tomography.

Thanks to this technique, the cellular structure of PU foams of different reactivity was studied near their cream time. For foams of low catalyst content, the cell size and intercell distance remained practically unchanged before the cream time. Whereas, after the cream time the cell size nearly doubled and the average distance between cells dropped. Initially,

cells were isolated from each other by large solid regions as thick as 250 μm. Nonetheless, the intercell distance rapidly decreased with time and halved in only 20 s. For foams with high catalyst content (1.5 ppw) the cell growth and reduction of intercell distance started slightly before the cream time. In addition, the cell growth rate was slower than in foams with higher water content due to the fast viscosity build-up caused by the high reactivity of the foam. The cell nucleation density was the highest for the foam with higher catalyst content as well, most probably as a consequence of a more efficient gas entrapment by the higher viscosity mixture.

5. ACKNOWLEDGEMENTS

Financial assistance from the Junta of Castile and Leon (VA202P20), Spanish Ministry of Science, Innovation and Universities (RTI2018-098749-B-I00 and RTI2018 - 097367-A-I00) and "Ente Público Regional de la Energía de Castilla y León" (EREN) is gratefully acknowledged. Financial support from Junta de Castilla y Leon predoctoral grant of P. Cimavilla-Román, co-financed by the European Social Fund, is also acknowledged.

6. REFERENCES

[1] M.M. Bernal, M.A. Lopez-Manchado, R. Verdejo, In situ foaming evolution of flexible polyurethane foam nanocomposites, Macromol. Chem. Phys. 212 (2011) 971–979.

[2] M. Szycher, Szycher's handbook of Polyurethanes, 2nd Ed, Taylor & Francis Group, London, 2013.

[3] R.A. Neff, C.W. Macosko, Simultaneous measurement of viscoelastic changes and cell opening during processing of flexible polyurethane foam, Rheol. Acta. 35 (1996) 656–666.

[4] L. Wang, H. Zhou, X. Wang, J. Mi, Evaluation of Nanoparticle Effect on Bubble Nucleation in Polymer Foaming, J. Phys. Chem. C. 120 (2016) 26841–26851.

[5] D. Niyogi, R. Kumar, K.S. Gandhi, Modeling of bubble-size distribution in free rise polyurethane foams, J. Appl. Polym. Sci. 131 (2014) 9098–9110.

[6] N.S. Ramesh, S.T. Lee, Polymeric Foams: Mechanisms and Materials, First Ed, CRC Press, Boca Raton, 2004.

[7] C. Brondi, E. Di Maio, L. Bertucelli, V. Parenti, T. Mosciatti, Competing bubble formation mechanisms in rigid polyurethane foaming, Polymer (Guildf). 228 (2021) 123877.

[8] J. Reignier, P. Alcouffe, F. Méchin, F. Fenouillot, The morphology of rigid polyurethane foam matrix and its evolution with time during foaming – New insight by cryogenic scanning electron microscopy, J. Colloid Interface Sci. 552 (2019) 153–165.

[9] B. Kanner, T.G. Decker, Urethane Foam Formation— Role of the Silicone Surfactant, J. Cell. Plast. 5 (1969) 32–39.

[10] M. del M. Bernal Ortega, Estudio de nanocompuestos de espumas de poliuretano reforzadas con nanocargas en base carbono, Universidad de Valencia, 2012.

[11] S.T. Lee, Polymeric Foams: Science and Technology, Taylor & Francis, Boca Raton, 2007.

[12] P. Cimavilla-Román, S. Pérez-Tamarit, M. Santiago-Calvo, M.Á. Rodríguez-Pérez, Influence of silica aerogel particles on the foaming process and cellular structure of rigid polyurethane foams, Eur. Polym. J. 135 (2020) 109884.

[13] M. Santiago-Calvo, S. Pérez-Tamarit, P. Cimavilla-Román, V. Blasco, C. Ruiz, R. París, F. Villafañe, M.Á. Rodríguez-Pérez, X-ray radioscopy validation of a polyol functionalized with graphene oxide for producing rigid polyurethane foams with improved cellular structures, Eur. Polym. J. 118 (2019) 404–411.

[14] S. Pardo-Alonso, E. Solórzano, M.A. Rodriguez-Perez, Time-resolved X-ray imaging of nanofiller-polyurethane reactive foam systems, Colloids Surfaces A Physicochem. Eng. Asp. 438 (2013) 119–125.

[15] S. Pardo-Alonso, E. Solórzano, S. Estravís, M.A. Rodríguez-Perez, J.A. de Saja, In situ evidence of the nanoparticle nucleating effect in polyurethane–nanoclay foamed systems, Soft Matter. 8 (2012) 11262.

[16] S. Pérez-Tamarit, E. Solórzano, R. Mokso, M.A. Rodríguez-Pérez, In-situ understanding of pore nucleation and growth in polyurethane foams by using real-time synchrotron X-ray tomography, Polymer (Guildf). 166 (2019) 50–54.

[17] ASTM D1622-08: Standard Test Method for Apparent Density of Rigid Cellular Plastics, (n.d.).

[18] J. Pinto, E. Solorzano, M.A. Rodriguez-Perez, J.A. de Saja, Characterization of the cellular structure based on user-interactive image analysis procedures, J. Cell. Plast. 49 (2013) 555–575.

[19] E. Solórzano, J. Pinto, S. Pardo, F. Garcia-Moreno, M.A. Rodriguez-Perez, Application of a microfocus X-ray imaging apparatus to the study of cellular polymers, Polym. Test. 32 (2013) 321–329.

[20] A. Corral, M. Balcerzyk, Á. Parrado-Gallego, I. Fernández-Gómez, D.R. Lamprea, A. Olmo, R. Risco, Assessment of the cryoprotectant concentration inside a bulky organ for cryopreservation using X-ray computed tomography, Cryobiology. 71 (2015) 419–431.

[21] J. Vlassenbroeck, B. Masschaele, V. Cnudde, M. Dierick, K. Pieters, L. Van Hoorebeke, P. Jacobs, Octopus 8: A High Performance Tomographic Reconstruction Package for X-ray Tube and Synchrotron micro-CT, Adv. X-Ray Tomogr. Geomaterials. (2010) 167–173.

[22] J. Schindelin, I. Arganda-Carreras, E. Frise, V. Kaynig, M. Longair, T. Pietzsch, S. Preibisch, C. Rueden, S. Saalfeld, B. Schmid, J.Y. Tinevez, D.J. White, V. Hartenstein, K. Eliceiri, P. Tomancak, A. Cardona, Fiji: an open-source platform for biological-image analysis, Nat. Methods 2012 97. 9 (2012) 676–682.

[23] D. Legland, I. Arganda-Carreras, P. Andrey, MorphoLibJ: Integrated library and plugins for mathematical morphology with ImageJ, Bioinformatics. 32 (2016) 3532–3534.

[24] V. Kumar, N.P. Suh, A process for making microcellular thermoplastic parts, Polym. Eng. Sci. 30 (1990) 1323–1329.

[25] R. Dougherty, K.-H. Kunzelmann, Computing Local Thickness of 3D Structures with ImageJ, Microsc. Microanal. 13 (2007) 1678–1679.

[26] P. Cimavilla-Román, M. Santiago-Calvo, M.Á. Rodríguez-Pérez, Dynamic Mechanical Analysis during polyurethane foaming: Relationship between modulus build-up and reaction kinetics, Polym. Test. 103 (2021) 107336.

[27] R.R. Rao, L.A. Mondy, K.N. Long, M.C. Celina, N. Wyatt, C.C. Roberts, M.M. Soehnel, V.E. Brunini, The kinetics of polyurethane structural foam formation: Foaming and polymerization, AIChE J. 63 (2017) 2945–2957.

[28] M.L. Pinto, Formulation, Preparation, and Characterization of Polyurethane Foams, J. Chem. Educ. 87 (2010) 212–215.

[29] H.J.M. Grünbauer, J.A. Thoen, J.C.W. Folmer, H.C. Van Lieshout, Polymer Morphology of Water-Blown Rigid Polyurethane Foams: Development of New Polyols, J. Cell. Plast. 28 (1992) 36–47.

[30] N. Mahmood, J. Kressler, K. Busse, Structure analysis in polyurethane foams at interfaces, J. Appl. Polym. Sci. 98 (2005) 1280–1289.

[31] B. Merillas, F. Villafañe, M.Á. Rodríguez-Pérez, Nanoparticles Addition in PU Foams: The Dramatic Effect of Trapped-Air on Nucleation, Polymers (Basel). 13 (2021) 2952.

[32] P. Cimavilla-Román, S. Perez-Tamarit, A. Vananroye, P. Moldenaers, M. Ángel Rodriguez-Pérez, The effects of silica aerogel on the rheological behaviour and polymer matrix structure of Rigid Polyurethane foams, Eur. Polym. J. 176 (2022) 111398.

[33] M. Santiago-Calvo, V. Blasco, C. Ruiz, R. París, F. Villafañe, M.-Á. Rodríguez-Pérez, Synthesis, characterization and physical properties of rigid polyurethane foams prepared with poly(propylene oxide) polyols containing graphene oxide, Eur. Polym. J. 97 (2017) 230–240.

[34] R. Verdejo, F.J. Tapiador, L. Helfen, M.M. Bernal, N. Bitinis, M.A. Lopez-Manchado, Fluid dynamics of evolving foams, Phys. Chem. Chem. Phys. 11 (2009) 10860–10866.

[35] F. Garcia-Moreno, E. Solórzano, J. Banhart, Kinetics of coalescence in liquid aluminium foams, Soft Matter. 7 (2011) 9216.

C APT

Solid matrix distribution in Polymeric foams

SOLID MATRIX DISTRIBUTION IN POLYMERIC FOAMS

6

6.1. INTRODUCTION

This chapter presents a publication entitled "Sub-pixel tomographic methods for characterising the solid architecture of foams" published in 2022 on Microscopy and Microanalysis (P. Cimavilla-Román et al. Microsc. Microanal. 1 (2022), doi: 10.1017/S1431927622000447). This publication deals with a prevalent problem when characterising low density foams using laboratory X-ray tomography: the insufficient resolution to investigate the solid matrix organisation. To tackle this problem, in the present publication we report three image analysis methodologies which permit measuring the fraction of mass in the struts even when the cell walls thickness is lower than the pixel size of the set-up. The developed methods provide different approaches to characterise the solid matrix. Two of the approaches rely on binarisation methodologies and on macroscopic measurements (geometric density of the foam) to obtain accurate predictions of the fraction of mass in the struts of the foams. Whereas the third of the methodologies relies on the different attenuation coefficients of the under-resolved regions of the solid matrix compared to the real attenuation coefficient of the solid matrix. In all cases, the accuracy of the methods was achieved following a twofold strategy. On the one hand, foams of different fraction of mass in the struts and matrix thickness were characterised using the three developed methods. On the other hand, the obtained results were compared with the fraction of mass in the struts obtained using high resolution X-ray tomography. While the high resolution measurements were taken as ground truth in terms of analysis accuracy, in the present publication the standard deviation of the fraction of mass in the struts was explored by analysing different regions of the foam.

Section 6.2.

Sub-pixel tomographic methods for characterising the solid architecture of foams

Paula Cimavilla-Román [a*], Saúl Pérez-Tamarit [a], Suset Barroso-Solares [a,b], Javier Pinto [a,b], Miguel Ángel Rodríguez-Pérez [a,b]

[a] Cellular Materials Laboratory (CellMat), Condensed Matter Physics Department, University of Valladolid, Paseo Belen 7, Valladolid, 47011, Spain

[b] BioEcoUva. Research Institute on Bioeconomy, University of Valladolid, Spain

Published in: Microscopy and Microanalysis (2022)

DOI: 10.1017/s1431927622000447

Graphical Abstract

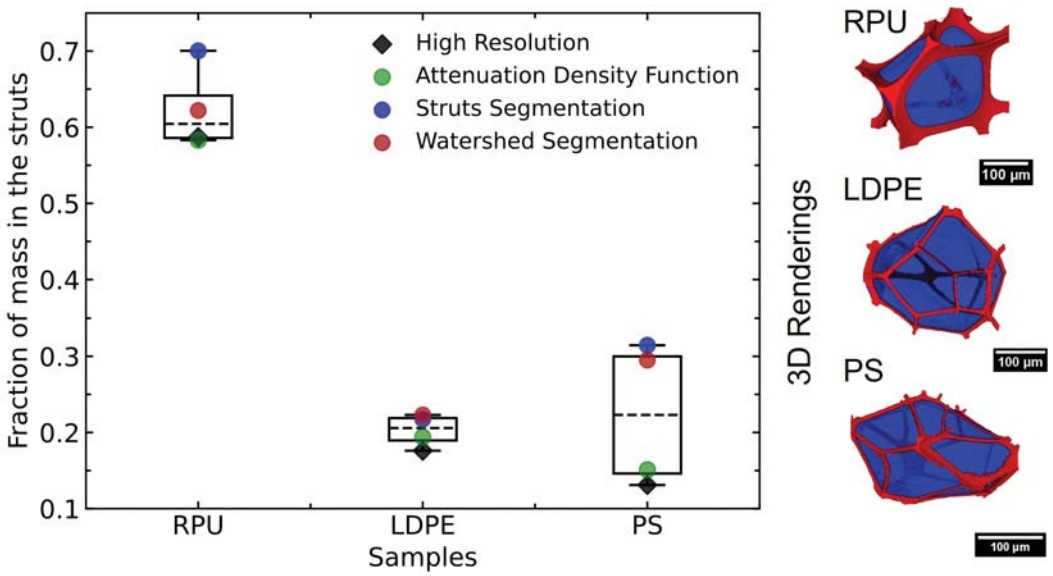

Microsc. Microanal. 28, 689 (2022)

ABSTRACT

Three independent analysis methods were developed to investigate the distribution of solid mass in foams analyzed by X-ray tomography with effective pixel sizes larger than the thickness of the solid network (sub-pixel conditions). Validation of the methods was achieved by a comparison with the results obtained employing high-resolution tomography for the same set of foams. The foams showed different solid mass distribution, which varied from being preferentially located on the edges, with a fraction of mass in the struts nearing 0.6, to materials in which the fraction of mass in the struts was low, under 0.15. In all cases, the accuracy of the proposed approaches was greater for materials with a higher fraction of mass in the struts. The method based on deconvolution of the attenuation probability density function yielded the closest results to the high-resolution characterizations. In contrast, analysis of the solid matrix thickness distribution after watershed segmentation, and binarization of high thickness regions (struts segmentation) required normalization through macroscopic measurements and revealed higher deviations with respect to the high-resolution results. However, segmentation-based methods allowed investigation of the heterogeneity of the fraction of mass in the struts along the sample.

KEYWORDS

Microtomography; Foams characterisation; Fraction of mass in the struts; 3D analysis; Sub-pixel; Cellular structure.

1. INTRODUCTION

Nowadays, foams are produced from a wide range of solids and can be found in a myriad of applications. Cellular solids manufactured from organic materials such as polyolefins are often used for body protection or vibration dampening [1,2]. Others, such as porous glass, are employed for thermal insulation [3,4]. Polymer foams are the most frequently encountered in daily appliances [5]. They can be generated following various production routes and from various types of polymers. While properties and applications of these foams are conditioned by the starting polymer, the quality of the material and final performance are also strongly conditioned by subtle differences in their internal cellular structure [6–9].

From a structural viewpoint, polymer foams are composed of a continuous polymer network in which a gas phase is dispersed [4]. In cellular polymers, gas is distributed in an organised manner around the solid forming cells. For highly porous foams, these cells are polyhedral units described by faces, edges, and vertices. The faces of the polyhedrons make up the walls of the cells. Typically, at least three walls intersect forming the edges (Plateau borders) and four of them join at the vertices [10]. Nonetheless, when characterising the architecture of solid foams, no distinction is made between edges and vertices, and both elements are labelled as struts. Despite the lack of a universal definition for the boundary between struts and cell walls, struts are often identified as the higher thickness elements in the matrix or, geometrically, as the elements whose cross-section forms an equilateral triangle with concave sides (Figure 6-1).

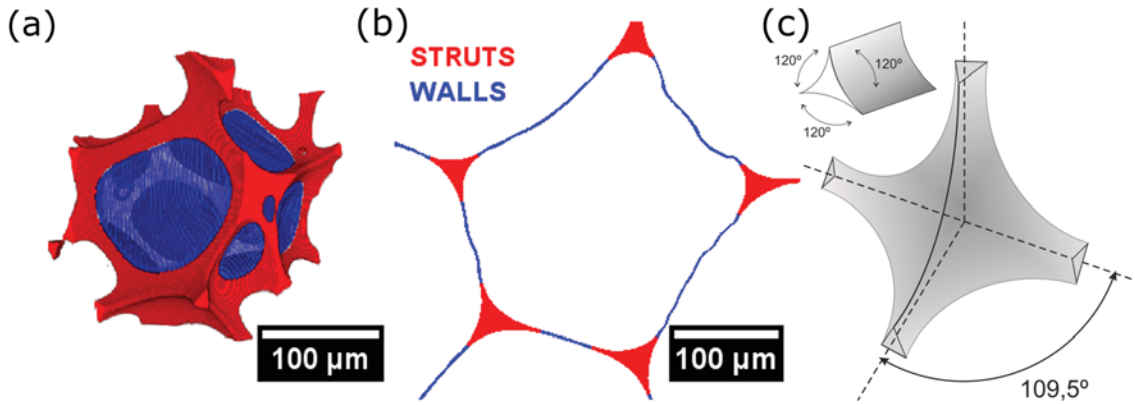

Figure 6-1: (a) Struts (red) and cell walls (blue) in a 3D render of a Polyurethane foam (modified with permission from [11] (b) cross-sectional view of the solid matrix of a pore in a Polyurethane foam and (c) idealised representation of the struts meeting in a fourfold junction (vertex)

Microsc. Microanal. 28, 689 (2022)

When it comes to characterising the cellular structure, descriptors are divided into two large groups: those depicting the arrangement of cells in space—*gas phase descriptors*—and those concerning the solid mass distribution in the matrix—*solid phase descriptors*. The former includes cell size (diameter of a sphere with equivalent volume to that of the cell), cellular structure homogeneity, and cell anisotropy. In contrast, the latter comprises magnitudes such as the fraction of mass in the struts, cell walls and struts thickness. The fraction of mass in the struts, f_s, defined as the solid mass in the struts, m_{st}, divided by the total mass in the struts and walls, m_w eq. (6-1), is often studied since it can significantly modify the mechanical or thermal performance [12–14].

$$f_s = \frac{m_{st}}{m_{st} + m_w} \tag{6-1}$$

While the gas phase descriptors of the cellular structure can be analysed using a wide range of microscopy techniques, a precise characterisation of the solid phase distribution can hardly be accomplished using 2D techniques. To that end, non-destructive X-ray tomography is the preferred choice. It permits measuring in 3D the thickness of the solid phase and estimating the repartition of solid mass [11].

However, when it comes to characterising low-density polymeric foams, spatial resolution is a critical factor. Although the gas phase is distributed in cells of diameter ranging from 100 to 500 μm, the polymer phase is confined in regions of a few microns thick, often as low as 0.5 μm. This fact restricts the successful investigation of polymeric foams to set-ups with high spatial resolution. Yet, the acquisition of high-resolution tomographies of these materials poses several inconveniences. Firstly, as resolution increases, the field of view decreases and hence, the number of cells inside the scanned volume drops (*ca.* 6 cells in thickness [11]). Secondly, the likelihood of damaging the internal morphology of the foams during sample preparation rises when the sample size is reduced to a few cells in thickness. Last but not least, the number of commercial set-ups with resolution below the micron is scarce, and the availability of high-resolution synchrotron beamlines is limited.

To tackle the aforementioned problems, some authors suggest using a region-of-interest (ROI) scan in which only part of the sample is irradiated and reconstructed, this permits achieving higher resolution without the need to physically reduce the size of the sample [15,16]. This strategy also reduces the number of projections and duration of the scan. However, the reconstruction process requires advanced correction methods as there is

laterally truncated projection data in the scan [16]. In other cases, when a full characterisation of the cellular structure is needed, several imaging platforms or magnifications are used (for instance, combining X-ray tomography with SEM). This is a well-known problem when imaging live microorganisms which has fostered the development of many varieties of correlative imaging [17,18]. Nevertheless, correlative imaging is still a time-consuming approach in which different set-ups have to be employed to obtain complementary information from the same sample. Thus, there is also great interest in developing methods to maximise the attainable information from standard imaging experiments. In the field of X-ray tomography, previous studies proposed analysis methodologies to estimate the main descriptors of the gas phase morphology [11,19]. However, there are fewer reports on workflows enabling the retrieval of information for material confined in regions smaller than the pixel size, *i.e.,* sub-pixel information. Hitherto, the prevalent literature presents techniques to attain increasing resolution using, coherent imaging, X-ray dark-field tomography or advanced reconstruction/post-processing algorithms. Lauridsen et al. (2015) confirmed that X-ray dark-field tomography could be used to detect sub-pixel cracks in solid materials. Wang et al. (2018), proposed algorithms to reconstruct 3D high-resolution porous structures by combining a set of increasing resolution tomography images. Minaee et al. (2021) proved the superior performance of deep learning algorithms in tasks of image segmentation. In particular, Furat et al. (2019) successfully applied machine learning algorithms to achieve precise segmentation of different phases in low contrast and under-resolved tomography volumes of an AlCu sample.

In this work, we explore the feasibility of characterising the solid phase distribution of a series of low-density polymeric foams using laboratory X-ray tomographies acquired with pixel size larger than the solid thickness, *i.e.,* under sub-pixel conditions. To that end, a set of simple and computationally low demanding methods are conceptualised and tested. This work stems from the results of a previous high-resolution synchrotron characterisation of the same samples [11]. These results are taken as reference in the present paper and permit the validation of the proposed methods, *i.e.,* sub-pixel methods, to characterise the solid phase imaged with pixel size above its thickness.

Microsc. Microanal. 28, 689 (2022)

2. MATERIALS AND METHODS

2.1. Materials

To begin with, the PU-based material was produced employing a commercial formulation provided by BASF Poliuretanos Iberia S.A (Barcelona, Spain). The material was produced as a result of a reactive foaming process between two main reactants, a resin or polyol blend (part A) with polymeric diisoycanate (part B). The reaction was triggered by mixing both components at high speeds (1200 rpm) for a short period (25 s). The mixture of the different components was performed with an overhead stirrer (EUROSTAR 60 control from IKA), equipped with a 50 mm diameter Vollrath^{TM} Lenart-disc stirrer.

For the second sample, cross-linked low-density polyethylene foams were provided by Zotefoams Plc (Croydon, United Kingdom). The production route for these materials consists of a three-stage foaming process. In the first stage, low-density polyethylene (LDPE) was extruded into a solid sheet which is heated while passing through an oven, activating the cross-linking. Afterwards, the polymer was subjected to high pressures inside an autoclave until the sheet was completely saturated with nitrogen gas. In the third and last stage, the nitrogen-saturated sheets were transferred into a lower-pressure autoclave and heated above the melting point. Due to the lower pressure, the nitrogen expanded, and the sheet was transformed into a low density foam.

The last sample selected for this work was provided by Dow Chemical Europe (Horgen, Switzerland). It is an extruded polystyrene foam (XPS), most commonly known as Styrofoam. This material was produced as a result of an extrusion foaming process. Raw polystyrene pellets (PS) were heated above their melt temperature during the process. A small amount of talc (lower than 1%) was used as a nucleating agent in the foaming process. The molten polymer was mixed with a combination of two blowing agents (CO_2 and ethanol). Once the mixture between the gas and polymer was homogeneous, the material moved to the cooling zone of the extrusion equipment to reduce the temperature to a level in which the polymer had enough extensional viscosity to be foamed. The material was foamed and shaped to its final form when it reached the die of the extrusion equipment.

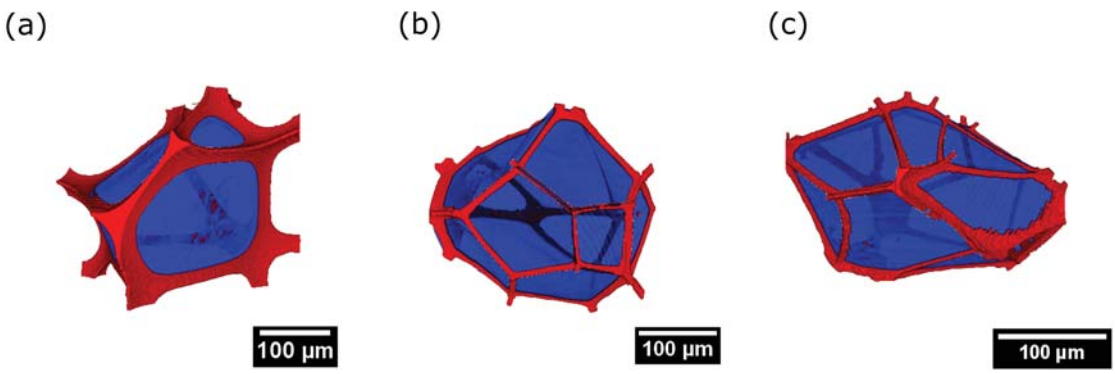

Figure 6-2: High resolution 3D renders of foams: (a) RPU, (b) LDPE and (c) XPS.

As seen in Table 6-1, foams of very similar relative density were selected to minimise the impact of the solid fraction on the subsequent analysis. Nonetheless, due to the different production processes and polymeric matrices, these foams show differences in terms of their properties and applications. For the same reasons, they also reveal disparate cellular structures (a 3D rendering of one cell for each foam can be seen in Figure 6-2). Several works have previously underlined the dissimilar distribution of cells in terms of size, shape, and the number of neighbours [12,24,25], but thorough investigations of the solid phase of the foams are scarce.

Table 6-1: Density and relative density of the samples.

Samples	Density (kg m^{-3})	Relative density
RPU	32.5	0.028
LDPE	33.1	0.036
XPS	31.2	0.030

2.2. Density characterisation of the foams

Foam density was measured as described in ASTM D1622/D1622M-14. Density, ρ, was measured on five different samples for each material using the geometric volume which was obtained from cubes of 3 x 3 x 3 cm3. Relative density, ρ_r^{Geo} which also stands for the volume fraction of solid, V_{solid}, in the foam, was obtained as the ratio between the foam geometric density and the solid material density, ρ_s (PU solid density, 1160 kg/m^3, LDPE solid density 910 kg/m^3, and PS solid density: 1050 kg/m^3).

2.3. Experimental set-up

The X-ray tomographies studied in this work were acquired using two different set-ups.

Microsc. Microanal. 28, 689 (2022)

Samples in Table 6-1 were scanned in the high-resolution μ-CT beamline located in Berlin, BESSY II synchrotron (BAMline). The selected magnification yielded an effective pixel size of 0.438 μm, which enabled the precise characterisation of the solid phase distribution of the samples [11]. At this resolution, the field of view was limited and the samples had reduced dimensions (prisms of less than 1 mm^2 of base and 4 mm in height). The detector was a PCO 4000 camera (4008×2672 $pixels^2$, 9 μm of pixel size). The energy of the X-rays in the line was fixed at a value of 9.8 keV, while the selected exposure time of the detector was 3000 ms and the rotation step was 0.08°.

Samples extracted from the same foams were also scanned using a laboratory X-ray tomography set-up (Solórzano et al., 2013). The set-up consists of an X-ray microfocus source (Hamamatsu) with a maximum output power of 20 W (spot size: 5 μm, voltage: 20-100 kV, current: 0-200 μA). Emitted X-rays form a cone beam of 39°, allowing up to 20 times magnification. The transmitted X-ray intensity is collected with a high sensitivity flat panel connected to a frame grabber (Dalsa-Coreco), which records the projection images. The detector is composed of a matrix of 2240x2344 $pixels^2$, each with a size of 50 μm. Samples were cylinders of around 7 mm^2 of base and 4 mm in height. The tube voltage, current and exposure time were set to 50 kV, 170 μA and 1 s. Each projection was the average of three consecutive radiographies for noise reduction. The highest possible magnification of the set-up was selected according to the cut-off frequency, calculated as described by [26]. At this magnification, blurring effects were negligible and the effective pixel size was 2.5 μm. The pixel size is considerably larger than the features of the solid matrix of polymeric foams leading to under-resolved areas in the tomography. Hence, these tomographies were acquired under sub-pixel conditions and conventional methods cannot be applied to characterise the solid phase morphology of foams [27,28].

2.4. Synchrotron X-ray Tomography: data analysis

To estimate the accuracy of the sub-pixel methods, the selected samples were compared to previously performed synchrotron tomography characterisations [11]. From these tomographies, the fraction of mass in the struts was calculated following the methodology proposed by [11]. The method consisted of binarising the solid phase followed by the application of a Local Thickness algorithm to the solid phase (foreground) which renders a thickness map of the binarised phase [29]. For every pixel, the plugin computes the maximum sphere that contains the pixel and fits into the solid phase without intersecting

with the gas phase. After applying the plugin, the histogram representing the solid thickness distribution was calculated. Due to the thickness overlap between struts and walls in the histograms, the contribution of walls and struts is not clear. To obtain the weight of each element a mixture of two asymmetric Log-Normal distributions was fitted. Thereby, it was possible to obtain the relative weight of walls and struts to the matrix and from it, the fraction of mass in the struts which in their method is the ratio between the area under the struts distribution and the area under the total matrix distribution.

2.5. Laboratory X-ray Tomography: data analysis

The reconstruction of laboratory tomographies was carried out using Octopus reconstruction package [30]. The process allows obtaining cross-sections images (bit depth: 32 bits) of the scanned volumes. In Figure 6-3, a representative slice for each of the foams can be seen. In these reconstructed grey-scale images, the pixel grey values can be approximated to an apparent attenuation coefficient of the material (μ) located in that pixel, as obtained when taking logarithms to the Beer-Lambert Law eq. (6-2).

$$\mu = \frac{1}{t} ln \frac{I_0}{I} \tag{6-2}$$

With t the path length, and I the transmitted X-ray intensity. However, laboratory sources emit multispectral X-rays, and the Beer-Lambert Law is only true for monochromatic beams. As attenuation coefficients of all materials depend on the photon energy, the X-ray spectrum will vary when traversing the material. Low energy photons are attenuated more easily than photons with high energy (beam hardening effect). Hence, the effective attenuation coefficient ($\bar{\mu}_{eff}$) depends on both the energy and the thickness of the material. In samples for which the thickness of attenuating species is low (low-density foams) beam hardening effect is not prevalent. Therefore, the expression predicting X-ray attenuation is equivalent to eq. (6-2) after replacing the attenuation coefficient with the effective multispectral one [26,31].

Microsc. Microanal. 28, 689 (2022)

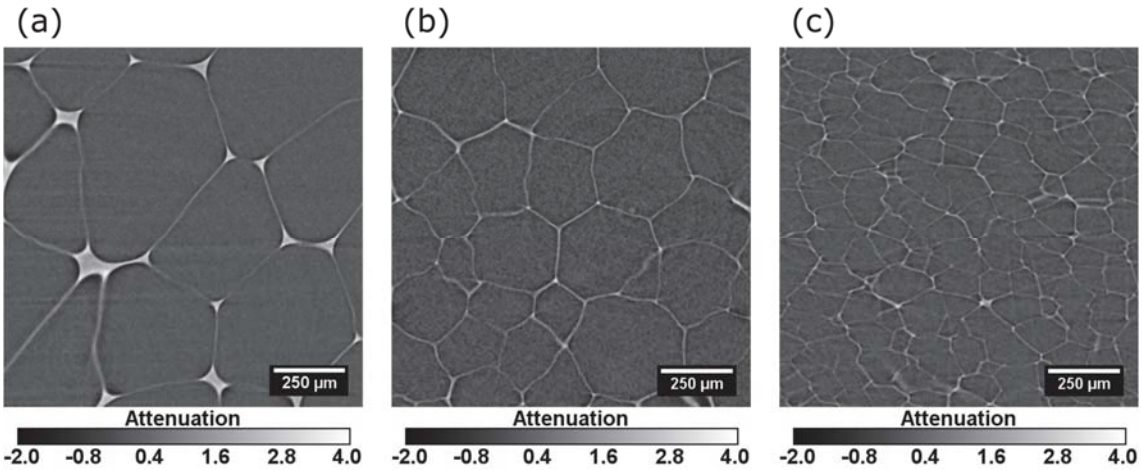

Figure 6-3: Representative laboratory X-ray tomography slices of (a) RPU, (b) LDPE, and (c) XPS foams.

2.5.1. Deconvolution of the Attenuation Density Function

In the low-resolution laboratory tomographies different polymer regions (walls and struts) present different attenuation coefficients ($\bar{\mu}_{eff}$). High thickness elements have attenuation values corresponding only to the solid polymer, whereas. thin regions, with respect to the pixel size, revealed grey level values that are a combination of the polymer and gas attenuation coefficients (partial volume effect).–These regions have attenuation coefficients which are accepted to be the weighted average of the attenuation coefficients of each of the phases partially located on the pixel eq. (6-3) [32]. In eq. (6-3), f is the volume fraction of solid in the pixel *(x,y,z)*, $\bar{\mu}_s$ is the attenuation coefficient of the solid, and $\bar{\mu}_g$ the attenuation coefficient of the gas.

$$\bar{\mu}_{eff}(x,y,z) = f\,\bar{\mu}_s + (1-f)\,\bar{\mu}_g \qquad (6\text{-}3)$$

In Figure 6-4 (a), the probability density function depicting the attenuation coefficients of the RPU foam is presented. It was obtained from a dense histogram depicting the relative frequency of each attenuation coefficient. Then, the attenuation density function (ADF) was obtained by performing a spline interpolation to every data point. From Figure 6-4 it can be appreciated how the high porosity (higher than 96 %) of the foam has a considerable influence on the appearance of the curve. The presence of a solid phase is only manifest at low relative frequencies and large attenuation values (see Figure 6-4 (a) inset). In addition, negative values of the attenuation coefficient are also present. These have a non-physical meaning and arise from gas pixels in the boundary with the polymer phase (appreciable by the edges of the RPU foam struts, Figure 6-3). They are due to shading artifacts appearing by the edges of the polymer phase which lower the real attenuation of the gas phase [33].

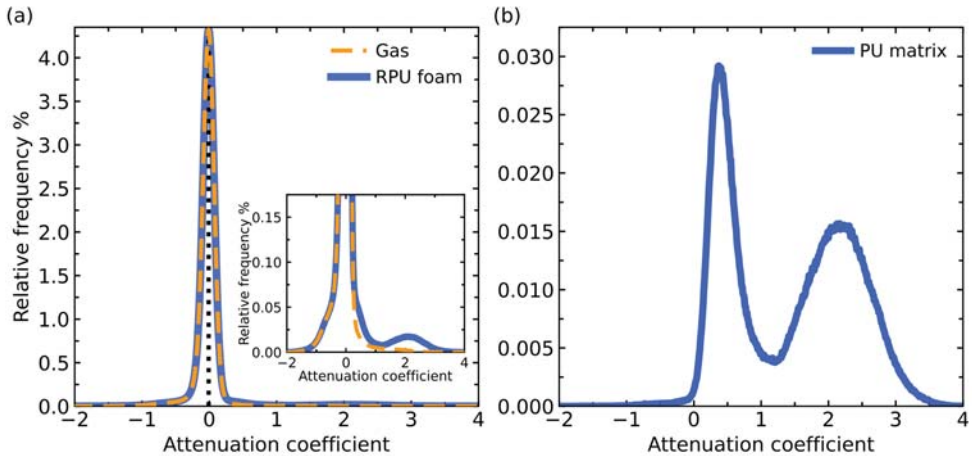

Figure 6-4: Attenuation probability density functions for the (a) Gas and Foam volumes in the laboratory tomographies and (b) RPU matrix.

Since the regions of interest in this study are only those of the confined polymer matrix, the gas probability density curve was subtracted from that of the RPU foam to investigate the distribution of attenuation coefficients in the solid phase. To retrieve the solid phase (Figure 6-4 (b)) the gas enclosed by the solid was selected for subtraction. Other approaches were explored such as employing the attenuation values of gas outside the foam, but it did not provide accurate results since it could not correct the effect of shading artifacts, *i.e.*, negative attenuation values in Figure 6-4 (a). A detailed workflow for the correction of the attenuation probability curve can be found in the Supplementary Material.

In Figure 6-4 (b), two distinct regions can be detected: a wide peak at high attenuation coefficients and a thin distribution with higher relative frequencies at low attenuation coefficients. Inspection of the scanned volumes confirmed that pixels showing attenuation coefficients higher than 1 corresponded to thick polymer regions. On the contrary, attenuation coefficients ranging from 0 to 1 represent the polymer matrix confined in sub-pixel regions, which are the cell walls.

Additionally, due to the overlap between struts and cell walls, a deconvolution procedure was applied to quantify the fraction of mass in the struts. Thereby two asymmetric Log-Normal functions representing the walls and struts distributions were fitted using a peak fitting application (such as Peakfit or Origin Peak Analyzer [34,35]). The position of the peaks was found using the first derivate method which permits finding hidden peaks in the distribution. This was followed by the subtraction of the fitted distribution from the original data. If there are more hidden peaks they arise as positive peaks in the residual plot. The precision of the fitting (R^2) was in all cases above 0.99. This type of fitting, based on the second or first derivative, is a common way of finding hidden

Microsc. Microanal. 28, 689 (2022)

peaks in FTIR spectra [36–38]. After the deconvolution, it was visually confirmed whether the x-limits of the peaks were within the observable attenuation values for the struts and walls in the reconstructed tomographies. From the numeric fit, the areas under the walls (A_w) and struts (A_{st}) distributions were used to calculate the fraction of mass in the struts eq. (6-4).

$$f_s = \frac{A_{st}}{A_{st} + A_w} \tag{6-4}$$

2.5.2. Struts Thresholding

Segmentation by thresholding is often the core of many image analysis workflows [39,40]. However, several difficulties arise when trying to threshold the solid phase of foams scanned under sub-pixel conditions. Since a high percentage of the solid matrix has sub-pixel thicknesses, segmentation of these regions leads to overestimations of the polymer phase or noise arising from gas phase pixels with similar attenuation to those of the under-resolved polymer regions. For these reasons, a partial segmentation procedure was applied in which only elements with sizes clearly above the pixel size were thresholded. For the majority of foams, these elements are almost always struts (Figure 6-5).

In the first stage, prior to binarisation, an anisotropic diffusion filter (details on the parameters used can be found in Supplementary Material) was applied to decrease noise without inducing edge blurring [41]. Afterwards, a threshold pixel value for the struts binarisation was selected using information about the cell walls and struts attenuation values distribution in the tomographies. This can be obtained from the Deconvolution of the Attenuation Density Function (Figure 6-2 (b)). The selected optimum threshold level was refined based on the observation of the volume cross-sections—that is, the threshold value must only include regions where at least three or more cell walls merge. Due to the overlap of attenuation values an ideal binarization, in which only struts are included, is difficult to achieve and in such cases, minimisation of the fraction of walls binarised was sought. A visual example of the optimum threshold level (RPU: 1.55, LDPE: 1.40 and XPS: 1.20) for the lab-scale tomographies can be seen in Figure 6-5.

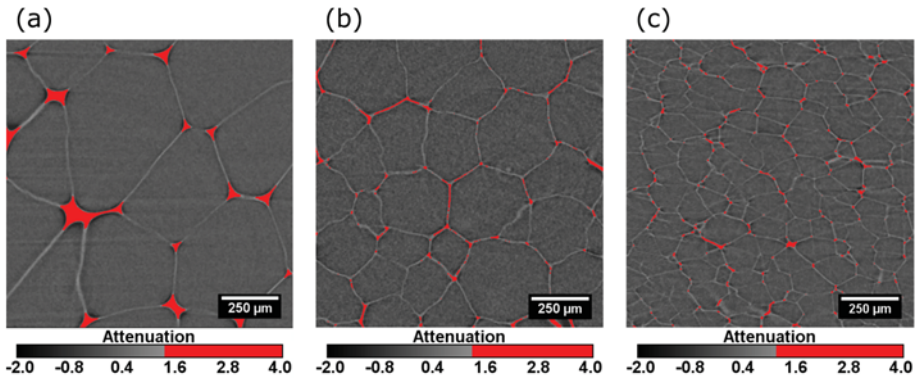

Figure 6-5: Representative laboratory X-ray tomography slices of (a) RPU, (b) LDPE, and (c) XPS foams, in red, the binarised struts are presented after thresholding.

Provided that only struts were segmented, their real volume (V_{st}) can be measured from the binarised images. From these volumes, it is possible to obtain the relative density of a foam supposing that it was only composed of struts (ρ_r^{st}). To this end, the volume occupied by struts pixels was divided by that of the analysed foam volume. By comparing this value with the geometrical density (ρ_r^{Geo}: Section 2.2) an estimate of the fraction of mass in the struts can be calculated eq. (6-5).

$$f_s = \frac{V_{st}}{V_{st} + V_w} = \frac{V_{st}/V_{foam}}{(V_{st} + V_w)/V_{foam}} = \frac{\rho_r^{st}}{\rho_r^{Geo}} \qquad (6\text{-}5)$$

Eq. (6-1) was converted into eq. (6-5) simply through a simple density transformation since the polymer density in the struts and cell walls is the same.

Furthermore, this methodology was selected to investigate the presence of f_s gradients throughout the height of the sample due to its computational speed. The scanned tomography volumes were divided into subsets of around 2 mm³ (V_{foam}) in which their height was fixed to at least once the average cell size (0.5 mm). On these sets, the struts volume was measured by the same segmentation procedure detailed above. Afterwards, the projections acquired during the tomography acquisition were also divided into sets of equal size and the same relative z-position with regard to the slices used for the struts characterisation. This guarantees that the same regions were analysed in the X-ray projections and the reconstructed slices.

The projection sets were employed to investigate the relative density of the foam. Knowing the transmitted X-ray intensity through the bulk sample (I_{foam}) of polymer concentration c_{foam}, and the concentration of gas (c_{gas}) in a region of transmitted intensity I_{gas} it was possible to calculate the polymer fraction (c_{solid}), which is the same as the relative

Microsc. Microanal. 28, 689 (2022)

density, at any point *(x, y)* of the projections by transforming Beer-Lambert's law eq. (6-2) into eq. (6-6) [26].

$$c_{solid}(x,y) = c_{foam} + \frac{ln\left(I_{foam}/I(x,y)\right)}{ln\left(I_{foam}/I_{gas}\right)}(c_{gas} - c_{foam}) \quad (6\text{-}6)$$

Therefore, it was possible to obtain the average relative density of the selected sets and connect it with the evolution of f_s inside the sample. The method enabled establishing whether changes in f_s are related to phenomena such as densification or drainage, which can occur during the manufacturing of these foams.

2.5.3. Watershed segmentation

As with the previous method, the starting point was the binarisation of the solid matrix (Figure 6-6 (a)). In the binarised cross-sections, cells were interconnected due to the absence of cell walls (Figure 6-6 (b)). Previous studies have shown that touching objects such as cells or particles can be separated using watershed algorithms [11]. In our particular case, we employed the Distance Transform Watershed (3D) algorithm implemented in the MorphoLibJ library in Fiji/ImageJ [42,43]. The basic idea behind the algorithm is to create borders as far as possible from the centre of the touching cells. To that end, the plugin calculates the inverse of the distance transform from the binary image and then applies the watershed to it. Moreover, the library also provides several Distance Map and Watershed options that permit controlling the location, number and shape of the border in the final result. The watershed option *Dynamic* permits controlling the number of cells that merge and split. The higher the number, the more cells merge. Similarly, selecting a low value of *Connectivity* (6) permits obtaining more rounded cells. For the particular case of low-density polymer foams, we found that the Quasi-Euclidian Distance Map, Connectivity-6 and a value of 2 for Dynamic intensity for the search of regional minima yields the best results. With these conditions, we retrieved rounded cells and avoided over-segmentation. Following this procedure, walls of 1-pixel thickness were created, isolating neighbour cells (Figure 6-6 (c)). Afterwards, the Local Thickness plugin implemented in the default version of Fiji/ImageJ was applied to obtain the thickness distribution of the solid phase in the previous step (Figure 6-6 (d)) [29]. The plugin returns a thickness map of the reconstructed volume in which pixel grey levels are local thickness values.

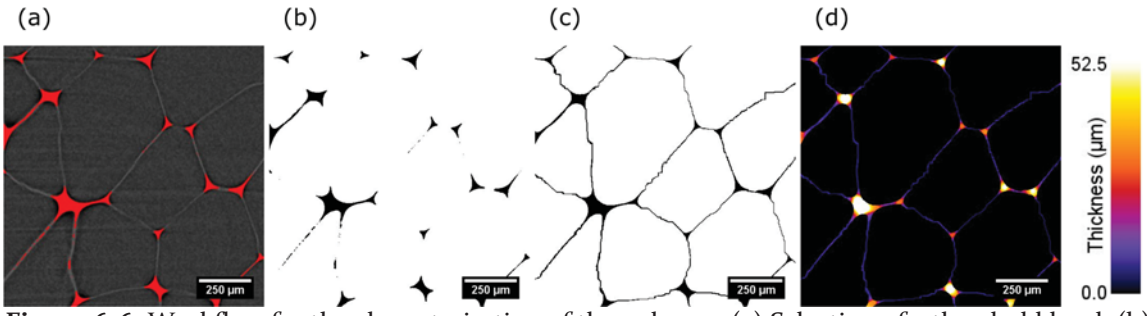

Figure 6-6: Workflow for the characterisation of the polymer: (a) Selection of a threshold level, (b) binarisation, (c) generation of cell walls via distance transform watershed and (d) local thickness map of the solid skeleton.

As shown by [11], quantitative information can be extracted about the solid phase distribution from the local thickness volumes. The histogram depicting the relative frequency of each thickness value in the polymeric matrix was computed (Figure 6-7). After this step, the thickness histogram was fitted using a combination of two asymmetric Log-Normal functions, depicting the cell walls and the struts. To this end, a peak fitting procedure equivalent to that described in Section 2.5.1 was applied. By measuring the area under the struts and walls distributions, it is possible to quantify the weight of walls and struts to the total solid skeleton and, employing eq. (6-4), determine the tomographic f_s value, f_s^{Tomo}.

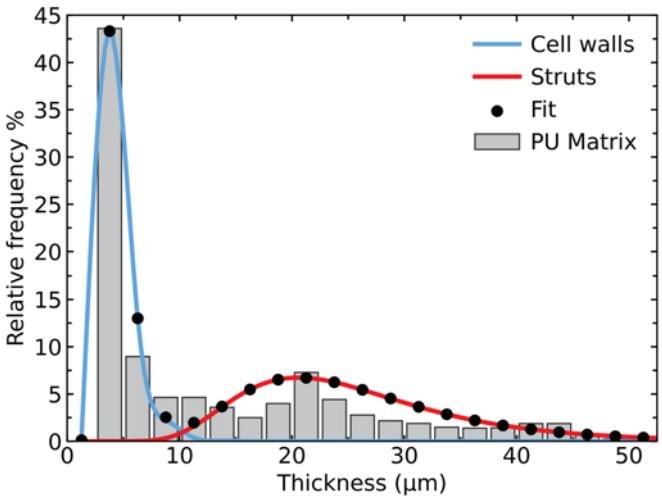

Figure 6-7: Local thickness distribution of the RPU foam solid matrix calculated from the low resolution laboratory tomographies.

However, the tomography f_s^{Tomo} value estimates the struts volume supposing foams in which cell walls are those generated during the watershed step (Figure 6-6 (c)). However, the cell walls generated during the watershed step are constant in width and have a thickness of 2.5 µm. Yet, real foams neither present constant wall thickness nor have a lower width limit of 2.5 µm. Therefore, to obtain an accurate value of f_s, it is also necessary to

Microsc. Microanal. 28, 689 (2022)

normalise the value obtained when applying eq. (6-4). For the correction, the relative density differences between the tomography ($\rho_r{}^{Tomo}$) and the geometrically measured relative density of the foam ($\rho_r{}^{Geo}$: Section 2.2) were used eq. (6-7).

$$f_s{}^{Real} = f_s{}^{Tomo} \frac{\rho_r{}^{Tomo}}{\rho_r{}^{Geo}} \tag{6-7}$$

The correction is based on the assumption that the area under the struts distribution employed in eq. (6-4) is accurate, and hence the volume of struts in the tomography corresponds to that of the real foam. A derivation of eq. (6-7) can be found in the Supplementary Material.

3. RESULTS

3.1. High-resolution: Reference analysis

The solid architecture observed in synchrotron tomographies was analysed, according to the procedure described in Section 2.4, to calculate the fraction of mass in the struts and the average polymer thickness of the foams shown in Table 6-1.

Table 6-2: Fraction of mass in the struts obtained from high-resolution (HR) X-ray Tomography.

Samples	HR-f_s
RPU	0.587
LDPE	0.176
XPS	0.131

The thickness distributions for the foams in Table 6-1 are depicted in Figure 6-8. Despite the similar density of all the samples, the thickness of the solid elements varies remarkably among materials. The solid phase of the polyurethane foam presents a remarkably wide skeleton of a few tens of microns in average thickness (Figure 6-8). As described in previous works [11,19], the foaming process undergone by RPU foams leads to a large number of degeneration events, for example, drainage and coalescence, which contribute to the thickening of struts at the expense of the cell walls. On the contrary, LDPE and XPS revealed an overall thin solid phase skeleton, in which the overlap between cell walls and struts is considerable (25 % of the LDPE cell walls with the struts, while for XPS more than 40 % of the cell walls thickness distribution is inside the struts range). In addition, this overlapping influences notably the distribution of mass among walls and struts. The less the overlap, the lower the fraction of polymer in the struts (Table 6-2).

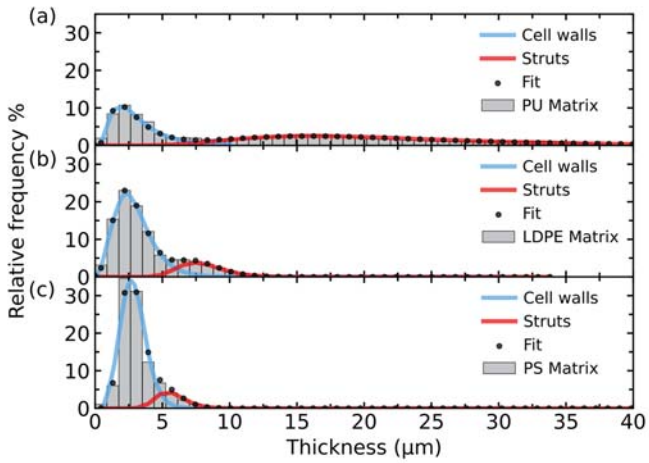

Figure 6-8: High resolution polymer thickness distributions (bin size 2 times the spatial resolution) for (a) RPU, (b) LDPE and (c) XPS.

3.2. Low-resolution: Proof of the methods

3.2.1. Deconvolution of the Attenuation Density Function

The RPU matrix is composed of two well-defined independent anisotropic Log-Normal distributions. The narrow peak appearing at low attenuation values corresponds to the thin and partially unresolved cell walls detected in the tomography volumes, Figure 6-3. Whereas, at higher attenuation values, a wide peak emerges due to higher thickness elements, where cell walls join and form struts. Furthermore, these two independent distributions barely intersect. The overlapping area was calculated to be below 1.9% of the total area of the probability density function, *i.e.*, less than 3% of the area under the struts function overlaps with the walls. The delocalisation of these functions is caused by the drastic differences in polymer concentration presented by these elements in the solid skeleton.

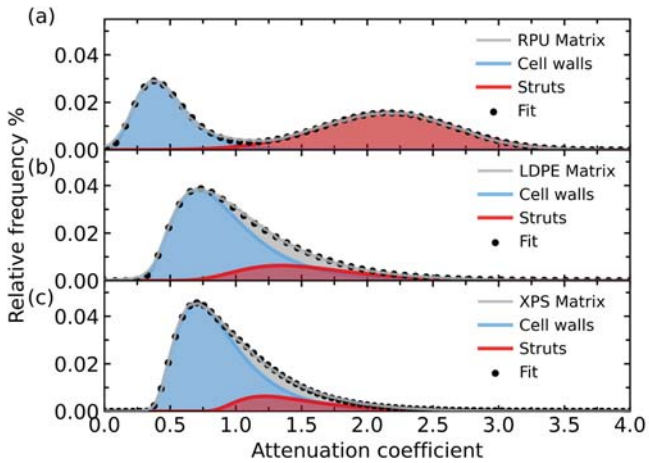

Figure 6-9: Attenuation probability density functions for (a) PU, (b) LDPE and (c) PS matrix in the laboratory tomographies.

Microsc. Microanal. 28, 689 (2022)

The distribution of attenuation values for the two other samples is substantially different. Figure 6-9 (b) and (c) reveal the strong overlap between attenuation density functions of the strut and walls, 16.5% and 14.1% for LDPE and XPS, respectively. For LDPE, nearly 85% of the struts distribution intersects with the area below the cell walls function. In the case of XPS, this number rises to more than 92% of the overlapping area. Conversely to what was detected for the RPU foam.

A clear correlation can be established between the reference thickness distributions, Figure 6-8 and the fitted attenuation density functions in Figure 6-9. The distribution of attenuation values is notably wider for the material composed of a thicker matrix, RPU foam. In contrast, the overall thinner solid phase of LDPE and XPS foams gives rise to narrower attenuation values distribution. The cell walls and struts are strongly convolved, resulting in only one signal in the attenuation density function of the polymeric matrix. Likewise, the high overlap between apparent attenuation values of cell walls and struts is a direct consequence of the similar thickness shown by the elements in the polymeric matrix. This analysis method also points out the bigger volume of the struts with respect to the cell walls in the RPU foam (see Table 6-3). Meanwhile, thermoplastic foams showed a very low value of f_s as expected from the low prominence of the struts grey levels distribution compared to the cell faces. The relationship between attenuation and solid thickness below the pixel size is further discussed in the Supplementary Material.

Table 6-3: Fraction of mass in the struts obtained from the laboratory tomographies using the deconvolution of the Attenuation Density Function method (ADF).

Samples	ADF-f_s
RPU	0.583
LDPE	0.194
XPS	0.151

3.2.2. Struts Thresholding

The variation of the fraction of mass in the struts eq. (6-5) with decreasing threshold values was investigated (Figure 6-10). The curves in Figure 6-10 can be understood as the cumulative frequency of the solid phase attenuation density function shown in Figure 6-9. The change of convexity detected in the RPU f_s curve results from the nearly negligible overlap between the walls and struts distributions. Moreover, the second derivative of the f_s curve revealed an inflexion point for the RPU foam in the vicinity of 1.55. On the contrary,

the lack of any significant feature in the XPS and LDPE f_s curves and their second derivatives, stresses the continuity of the attenuation density function of the matrix of these foams (Figure 6-9). For XPS and LDPE foams, when the threshold value decreases below 0.75, f_s rises above 1. In other words, the relative density measured in the tomographies exceeded the real relative density of the foams. This overestimation of the matrix volume fraction is due to the reduced thickness of the walls and struts which leads to the thresholding of a high number of pixels representing mixed gas and polymer phases as soon as the threshold includes low attenuation values. For the selected optimum threshold value (Figure 6-5) the obtained fraction of mass in the struts can be found in Table 6-4.

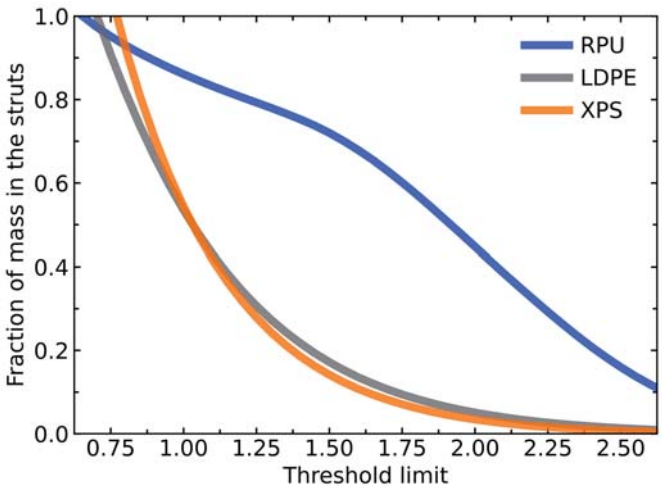

Figure 6-10: Evolution of the fraction of mass in the struts in the laboratory tomographies with varying limits of the threshold for the solid phase.

A refinement of the above calculation consists of employing the relative density profile of the sample extracted from the radiography images, as a replacement for the geometric density in eq. (6-5). The density variations along the height of the sample are depicted in Figure 6-11 (a). It can be seen how the relative density along the height of the foams does not follow any clear trend since the values are scattered around the geometrically measured points (discontinuous lines). Likewise, f_s remained practically constant within the scanned volume of XPS and LDPE foams (Figure 6-11 (b)). On the contrary, for RPU an increase in the fraction of mass in the struts with decreasing relative density was detected towards the bottom of the sample.

Microsc. Microanal. 28, 689 (2022)

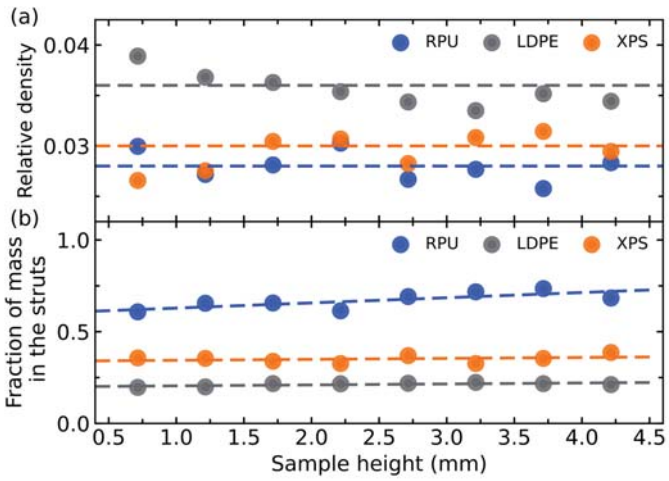

Figure 6-11: (a) Relative density profile measured on the sample height (dots) and the geometrically measured relative density for the entire sample (dashed lines). (b) Fraction of mass in the struts (obtained from the laboratory tomographies) evolution with the height of the foam (dots) and linear fit to the experimental points (dashed lines). Sample height represents the top of the set measured with respect to the first pixel row of the volume acquired during the experiment.

The nature of the production process of polyurethane foams (reactive free foaming in the vertical direction) fosters an abundance of degeneration mechanisms that often vary in intensity along the foam rise direction [44,45]. The main mechanism influencing the value of f_s is drainage, which causes the flow of polymer from the cell windows into the struts [46]. Here, given the sample size, it is premature to assert that this effect accounts for a systematic increase in the fraction mass in the struts due to drainage. Yet, it is a clear indicator that inhomogeneities in the value of f_s are to be expected in this type of foam.

Table 6-4: Fraction of mass in the struts obtained from the laboratory tomographies using the deconvolution of the struts thresholding method (ST).

Samples	SS- f_s
RPU	0.700
LDPE	0.218
XPS	0.315

3.2.3. Watershed segmentation

Lab-scale tomographies were thresholded seeking to maximise the available information on the solid skeleton of the foam. After cell walls reconstruction by watershed transformation, the solid fraction increased to nearly three times the real relative density (Table 6-5). The overestimation of the solid fraction of the foams is linear with the overall matrix thickness (Figure 6-8), the lower the matrix thickness, the higher the overestimation induced by the watershed. The thickness distribution of the tomographic solid fraction can

be seen depicted in Figure 6-12, which bears a strong resemblance to those presented in Figure 6-8 and Figure 6-9. Yet, as a consequence of the watershed transformation, the cell walls distribution shows a minimum thickness of 2.5 μm well above the real minimum width of cell walls. Therefore, the fitting of the histograms in Figure 6-12 leads to a disproportionated contribution of the cell walls to the matrix.

Table 6-5: Fraction of mass in the struts obtained from the laboratory tomographies using the watershed segmentation method (WS).

Sample	Threshold value	V_s after thresholding	V_s after walls reconstruction	f_s^{Tomo}	WS-f_s^{Real}
RPU	1.00	0.0234	0.0363	0.484	0.622
LDPE	0.60	0.0381	0.0601	0.124	0.223
XPS	0.55	0.0386	0.0967	0.092	0.295

However, since the weight of the struts can be considered to be correctly estimated by the Log-Normal curve fitted to high thicknesses, it is possible to normalise the tomographic f_s value (f_s^{Tomo}) using eq. (6-7). Following normalisation f_s^{Real} can be seen to near the values obtained from high-resolution tomographies (Table 6-2).

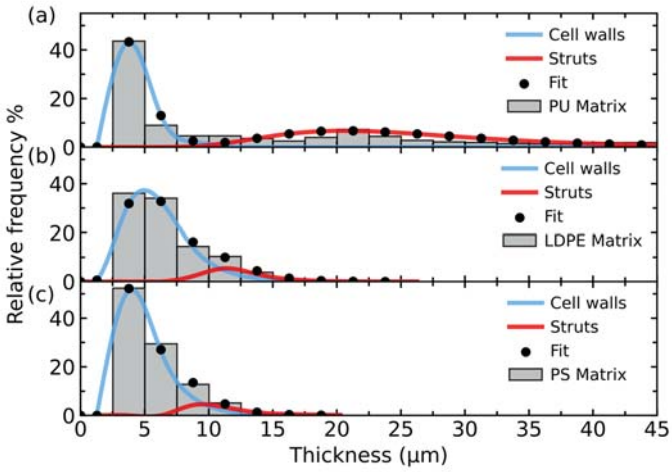

Figure 6-12: (a) RPU, (b) LDPE and (c) XPS solid thickness distributions after watershed segmentation of the laboratory tomographies, bin size of 2.5 μm.

4. DISCUSSION

The fraction of mass in the struts of polymeric foams with different cellular structures and undergoing different foaming processes was studied employing three different methodologies. The results of the analysis are summarised in the box and whisker plot of Figure 6-13. For every sample, high-resolution reference values are found in the lower whisker of the plot. These are closely followed and at times even concurring (RPU) with the

Microsc. Microanal. 28, 689 (2022)

values of f_s calculated on the low-resolution laboratory tomographies using the deconvolution of the Attenuation Density Function method. The good agreement between the calibrated f_s values (Table 6-2) and those yielded by deconvolution of the Attenuation Density Function (Table 6-3) stress the high accuracy of this sub-pixel approach. In contrast, applying the Struts Thresholding and Watershed Segmentation methods on the low-resolution laboratory tomographies led to f_s values above the mean of all the proposed approaches and farther from the high-resolution reference values. Remarkably, the values of f_s returned by the Struts Thresholding method are always located on the higher whisker and outside the interquartile range. For our samples, the Watershed Segmentation method proved to be the most accurate of those based on image segmentation.

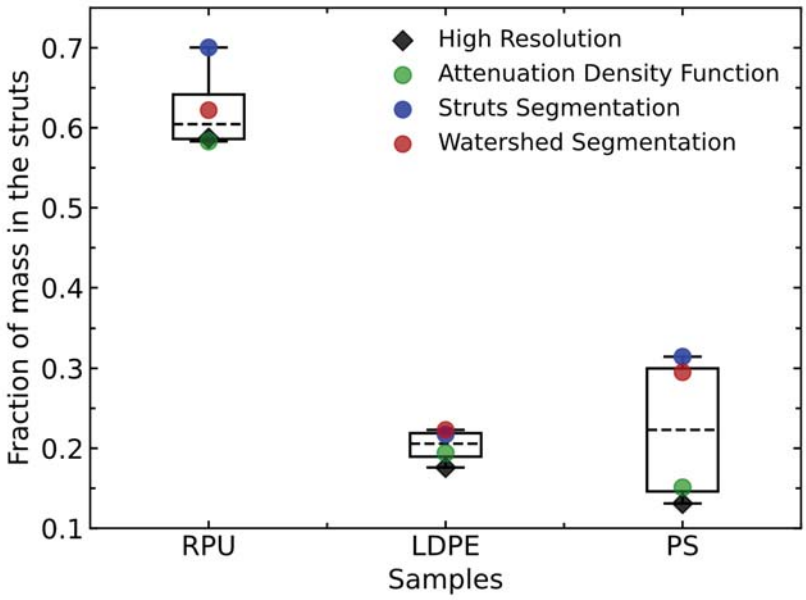

Figure 6-13: Box and whiskers plot depicting the variation of the fraction of mass in the struts with the analysis methodology and the foam type.

The performance of each method varies largely with the material. For instance, all methods show satisfactory effectiveness in yielding an accurate fraction of mass in the struts for the LDPE foam. For this material, the interquartile range is narrow, and all measurements fall in this range (Figure 6-13). Using the deviation between high-resolution and segmentation of the laboratory tomographies it was estimated that less than 5% of the walls are lost during the characterisation of the laboratory tomographies. Similar success was observed when the methods were applied to the RPU sample, except for the Struts Thresholding approach (Section 2.5.2). In this case, the mismatch with other results is most likely due to the higher width of some cell walls in the matrix, which cannot be easily excluded from the binarised regions. However, in light of the results in Figure 6-11 (b), it is

plausible that the higher dispersion was due to the intrinsic variability of the polymer mass distribution along the growth direction during foaming.

The results for XPS present undoubtedly the largest discrepancies between high-resolution and sub-pixel methods. In this case, thresholding methodologies appear to be the least accurate. This is due to the reduced thickness of the polystyrene skeleton, which hinders thresholding without leading to over dilation of polymer pixels or even gas pixels binarisation. Despite the normalisations implemented for the segmentation methods (Struts Thresholding and Watershed segmentation), it is estimated that nearly 25 % of thin cell walls are lost for XPS due to the insufficient resolution of the scan.

Nevertheless, care should also be taken when interpreting the results returned by the high-resolution analysis. Samples scanned with synchrotron radiation had, on average, a three times smaller volume than those scanned with laboratory X-ray tomography. For instance, the RPU sample scanned with synchrotron radiation revealed less than two cells in thickness. Therefore, high-resolution analysis is far more local than that performed here under sub-pixel conditions. Considering the intrinsic heterogeneity of these materials, especially materials resulting from a chemical foaming process (RPU), the so-called reference f_s values should be treated with caution. Therefore, a certain standard deviation in the value of f_s is to be expected as it is with any other microscopic descriptor of the foams cellular structure.

5. CONCLUSIONS

In this work, the feasibility of studying the polymer mass distribution of foams using laboratory X-ray tomography (with pixel size above the solid phase thickness) was proved. Three methodologies were implemented and validated. These permitted the retrieval of sub-pixel information about the polymer phase. The validation was possible by comparison with high-resolution X-ray tomographies performed on the same materials and characterised employing previously published workflows [11].

The three proposed approaches enabled quantifying the main descriptor accounting for the polymer mass distribution in foams: the fraction of mass in the struts. It was proved that investigating the solid phase through the attenuation probability density function of the matrix yielded the most accurate results. However, segmentation methodologies provided information about the fraction of mass struts evolution throughout the foam.

These findings confirm that the reported methods allow obtaining accurate 3D information about the polymer phase in foams by using a straightforward approach both mechanically and computationally. Moreover, the proposed methodologies are suitable for all types of foamed products acquired with pixel size larger than the thickness of the cell walls.

6. ACKNOWLEDGEMENTS

Financial assistance from the Junta of Castile and Leon (VA202P20) and the Spanish Ministry of Science, Innovation and Universities (RTI2018-098749-B-I00 and RTI2018 - 097367-A-I00) is gratefully acknowledged. Financial support from Junta de Castilla y Leon predoctoral grant of P. Cimavilla-Román, co-financed by the European Social Fund, is also acknowledged. We acknowledge the support from BESSY II (HZB, Berlin, Germany) to complete this work (proposal 14100497-ST).

7. REFERENCES

[1] Nigel J. Mills, Polymer Foams Handbook: Engineering and Biomechanics Applications and Design, 2007.

[2] R. Verdejo, Gas Loss and Durability of EVA foams used in Running Shoes, The University of Birmingham, 2003.

[3] J. König, A. Lopez-Gil, P. Cimavilla-Roman, M.A. Rodriguez-Perez, R.R. Petersen, M.B. Østergaard, N. Iversen, Y. Yue, M. Spreitzer, Synthesis and properties of open- and closed-porous foamed glass with a low density, Constr. Build. Mater. 247 (2020) 118574.

[4] L.J. Gibson, M.F. Ashby, Cellular solids: Structure and Properties, Cambridge: Cambridge Solid State Science Series, Cambridge, 1997.

[5] F. García-Moreno, Commercial Applications of Metal Foams: Their Properties and Production, Materials (Basel). 9 (2016) 85.

[6] M.K. Williams, E.S. Weiser, J.E. Fesmire, B.W. Grimsley, T.M. Smith, J.R. Brenner, G.L. Nelson, Effects of cell structure and density on the properties of high performance polyimide foams, Polym. Adv. Technol. 16 (2005) 167–174.

[7] A.G. Dement'ev, O.G. Tarakanov, Effect of cellular structure on the mechanical properties of plastic foams, Polym. Mech. 6 (1970) 519–525.

[8] V. Bernardo, E. Laguna-Gutierrez, A. Lopez-Gil, M.A. Rodriguez-Perez, Highly anisotropic crosslinked HDPE foams with a controlled anisotropy ratio: Production and characterization of the cellular structure and mechanical properties, Mater. Des. 114 (2017) 83–91.

[9] B. Zhao, R. Wang, Y. Li, Y. Ren, X. Li, X. Guo, R. Zhang, C.B. Park, Dependence of electromagnetic interference shielding ability of conductive polymer composite foams with hydrophobic properties on cellular, J. Mater. Chem. C. 8 (2020) 7401–7410.

[10] I. Cantat, S. Cohen-Addad, F. Elias, F. Graner, R. Höehler, O. Pitois, F. Rouyer, A. Saint-Jalmes, Foams: structure and dynamics, First Ed, Oxford University Press, Oxford, 2013.

[11] S. Pérez-Tamarit, E. Solórzano, A. Hilger, I. Manke, M.A. Rodríguez-Pérez, Multi-scale tomographic analysis of polymeric foams: A detailed study of the cellular structure, Eur. Polym. J. 109 (2018) 169–178.

[12] D. Klempner, K.C. Frisch, Cellular Structure and Properties of Foamed Polymers, in: Handb. Polym. Foam. Foam Technol., 2nd Ed, Hanser, Munich, 2004.

[13] S. Estravís, J. Tirado-Mediavilla, M. Santiago-Calvo, J.L. Ruiz-Herrero, F. Villafañe, M.A. Rodríguez-Pérez, Rigid polyurethane foams with infused nanoclays: Relationship between cellular structure and thermal conductivity, Eur. Polym. J. 80 (2016) 1–15.

[14] N.C. Hilyard, A. Cunningham, Low density cellular plastics, 1st Ed, Springer Science & Business Media, London, 1994.

[15] Y. Ma, J. Hua, D. Liu, Y. He, T. Zhang, J. Chen, F. Yang, X. Ning, Z. Yang, J. Zhang, C.H. Pai, Y. Gu, W. Lu, Region-of-interest micro-focus computed tomography based on an all-optical inverse Compton scattering source, Matter Radiat. Extrem. 5 (2020) 064401.

[16] C. Maaß, M. Knaup, M. Kachelrie, New approaches to region of interest computed tomography, Med. Phys. 38 (2011) 2868–2878.

[17] J. Caplan, M. Niethammer, R.M. Taylor, K.J. Czymmek, The power of correlative microscopy: Multi-modal, multi-scale, multi-dimensional, Curr. Opin. Struct. Biol. 21 (2011) 686–693.

[18] Y. Liu, A.M. Kiss, D.H. Larsson, F. Yang, P. Pianetta, To get the most out of high resolution X-ray tomography: A review of the post-reconstruction analysis, Spectrochim. Acta - Part B At. Spectrosc. 117 (2016) 29–41.

[19] S. Pardo-Alonso, E. Sorlórzano, L. Brabant, P. Vanderniepen, M. Dierick, L. Van Hoorebeke, M.A. Rodríguez-Peréz, E. Solórzano, L. Brabant, P. Vanderniepen, M. Dierick, L. Van Hoorebeke, M.A. Rodríguez-Pérez, 3D Analysis of the progressive modification of the cellular architecture in polyurethane nanocomposite foams vía X-ray microtomography, Eur. Polym. J. 149 (2013) 999–1006.

[20] T. Lauridsen, M. Willner, M. Bech, F. Pfeiffer, R. Feidenhans'l, Detection of sub-pixel fractures in X-ray dark-field tomography, Appl. Phys. A Mater. Sci. Process. 121 (2015) 1243–1250.

[21] Y. Wang, J.Y. Arns, S.S. Rahman, C.H. Arns, Three-dimensional porous structure reconstruction based on structural local similarity via sparse representation on micro-computed-tomography images, Phys. Rev. E. 98 (2018) 1–16.

[22] S. Minaee, Y.Y. Boykov, F. Porikli, A.J. Plaza, N. Kehtarnavaz, D. Terzopoulos, Image Segmentation Using Deep Learning: A Survey, IEEE Trans. Pattern Anal. Mach. Intell. 44 (2021) 3523–3542.

[23] O. Furat, M. Wang, M. Neumann, L. Petrich, M. Weber, C.E. Krill, V. Schmidt, Machine learning techniques for the segmentation of tomographic image data of functional materials, Front. Mater. 6 (2019) 145.

[24] N.S. Ramesh, S.T. Lee, Polymeric Foams: Mechanisms and Materials, First Ed, CRC Press, Boca Raton, 2004.

[25] D. Eaves, Handbook of Polymer Foams, Rapra Technology Limited, Shrewsbury, 2004.

[26] E. Solórzano, J. Pinto, S. Pardo, F. Garcia-Moreno, M.A. Rodriguez-Perez, Application of a microfocus X-ray imaging apparatus to the study of cellular polymers, Polym. Test. 32 (2013) 321–329.

[27] É. Maire, J. Adrien, C. Petit, Structural characterization of solid foams, Comptes Rendus Phys. 15 (2014) 674–682.

[28] C. Petit, S. Meille, É. Maire, E. Maire, Cellular solids studied by x-ray tomography and finite element modeling-a review Cellular solids studied by X-ray tomography and finite element modelling-a review, J. Mater. Res. 28 (2013) 2191–2201.

[29] R. Dougherty, K.-H. Kunzelmann, Computing Local Thickness of 3D Structures with ImageJ, Microsc. Microanal. 13 (2007) 1678–1679.

[30] M. Dierick, B. Masschaele, L. Van Hoorebeke, Octopus, a fast and user-friendly tomographic reconstruction package developed in LabView®, Meas. Sci. Technol. 15 (2004) 1366–1370.

[31] M. Baur, N. Uhlmann, T. Pöschel, M. Schröter, Correction of beam hardening in X-ray radiograms, Rev. Sci. Instrum. 90 (2019) 025108.

[32] S.R. Stock, Micro computed tomography, methodology and applications, CRC Press, Boca Raton, 2009.

[33] J. Hsieh, Computed Tomography: Principles, Design, Artifacts, and Recent Advances, 3rd ed., Wiley, Bellingham, Washington, 2003.

[34] R.A. May, K.J. Stevenson, Software Review of Origin 8, J. Am. Chem. Soc. 131 (2009) 872.

[35] C. Ruan, Y. Zhu, X. Zhou, N. Abidi, Y. Hu, J.M. Catchmark, Effect of cellulose crystallinity on bacterial cellulose assembly, Cellulose. 23 (2016) 3417–3427.

[36] P. Laurson, P. Raudsepp, H. Kaldmäe, A. Kikas, U. Mäeorg, The deconvolution of FTIR-ATR spectra to five Gaussians for detection of small changes in plant–water clusters, AIP Adv. 10 (2020) 085214.

[37] M. Santiago-Calvo, J. Tirado-Mediavilla, J.L. Ruiz-Herrero, M.Á. Rodríguez-Pérez, F. Villafañe, The effects of functional nanofillers on the reaction kinetics, microstructure, thermal and mechanical properties of water blown rigid polyurethane foams, Polymer (Guildf). 150 (2018) 138–149.

[38] L.F. Leopold, N. Leopold, H.A. Diehl, C. Socaciu, Quantification of carbohydrates in fruit juices using FTIR spectroscopy and multivariate analysis, Spectroscopy. 26 (2011) 93–104.

[39] V. Bernardo, F. Van Loock, J. Martin-de Leon, N.A. Fleck, M.A. Rodriguez-Perez, Mechanical Properties of PMMA-Sepiolite Nanocellular Materials with a Bimodal Cellular Structure, Macromol. Mater. Eng. 304 (2019) 1–12.

[40] J.C. Russ, The Image Processing Handbook, 3rd Ed., CRC Press, Boca Raton, 2006.

[41] J. Roels, F. Vernaillen, A. Kremer, A. Gonçalves, J. Aelterman, H.Q. Luong, B. Goossens, W. Philips, S. Lippens, Y. Saeys, An interactive ImageJ plugin for semi-automated image denoising in electron microscopy, Nat. Commun. 11 (2020) 1–13.

[42] D. Legland, I. Arganda-Carreras, P. Andrey, MorphoLibJ: Integrated library and plugins for mathematical morphology with ImageJ, Bioinformatics. 32 (2016) 3532–3534.

[43] D. Legland, I. Arganda-Carreras, MorphoLibJ-User manual, 2016.

[44] G. Huang, P. Wang, Effects of preparation conditions on properties of rigid polyurethane foam composites based on liquefied bagasse and jute fibre, Polym. Test. 60 (2017) 266–273.

[45] D.R. Harbron, C.J. Page, R.K. Scarrow, Methods of minimising density gradients in rigid polyurethane foams, J. Cell. Plast. 37 (2001) 43–57.

[46] X.D. Zhang, C.W. Macosko, H.T. Davis, A.D. Nikolov, D.T. Wasan, Role of silicone surfactant in flexible polyurethane foam, J. Colloid Interface Sci. 215 (1999) 270–279.

Supplementary information

Sub-pixel tomographic methods for characterising the solid architecture of foams

Paula Cimavilla-Román [a*], Saúl Pérez-Tamarit [a], Suset Barroso-Solares [a,b], Javier Pinto [a,b], Miguel Ángel Rodríguez-Pérez [a,b]

[a] Cellular Materials Laboratory (CellMat), Condensed Matter Physics Department, University of Valladolid, Paseo Belen 7, Valladolid, 47011, Spain

[b] BioEcoUva. Research Institute on Bioeconomy, University of Valladolid, Spain

Published in: Microscopy and Microanalysis (2022)

DOI: 10.1017/s1431927622000447

S1. ATTENUATION DENSITY FUNCTION OF THE POLYMER MATRIX

Figure 6-2 (b) in the manuscript was obtained after applying the workflow detailed in Figure 6-S1. To obtain the gas phase histogram (Figure 6-S1 (f)) the original tomography volumes had to be binarised. A satisfactory binarisation of the gas phase was achieved after applying the 2D Anisotropic Diffusion filter implemented in Fiji (parameters: 20 iterations, smooth 1, diffusion limiter along minimal variation 0.5, diffusion limiter along maximal variation 0.9, time step 20, and edge threshold 10). The diffusion filter permitted to homogenise the attenuation values of gas inside the cells. To ensure correct subtraction of the attenuation density functions the volume fraction of gas binarised had to be equivalent to the macroscopic porosity of the sample. Finally, to obtain Figure 6-2 (b) in the manuscript the subtraction of the probability density plots in Figure 6-S1 (b) and (f) was performed numerically.

Microsc. Microanal. 28, 689 (2022)

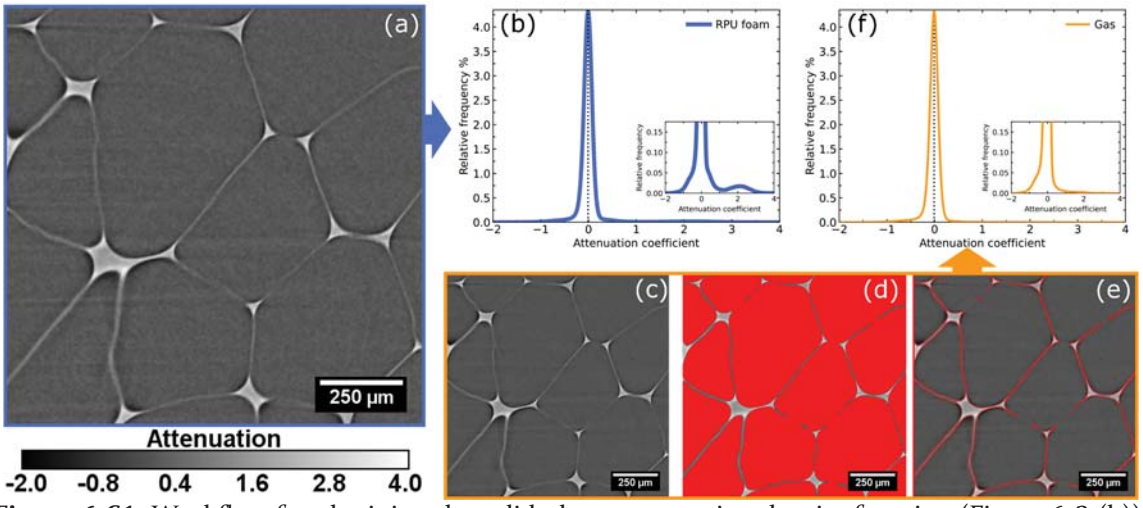

Figure 6-S1: Workflow for obtaining the solid phase attenuation density function (Figure 6-2 (b)). From the lab-scale tomography volumes (a), the attenuation density function for the foam (gas + polymer) is then calculated performing a spline interpolation to the attenuation values histogram (bin size: 0.01) (b). Next, an anisotropic diffusion filter was applied to the lab-scale tomography volumes (c), and the filtered volume was binarised to obtain the gas phase inside the cells (d). ROIs were created from the binarised volume (e) and after applying them on the original lab-scale reconstructed volumes (a) the attenuation density function of the gas could be computed (f).

S2. NORMALISATION FACTOR: WATERSHED SEGMENTATION METHOD

Eq. (6-7) in the manuscript is obtained following the derivation detailed in Figure 6-S2.

Condition: $V_{st}^{Tomo} = V_{st}^{Real} = V_{st}$

$$(1)\ f_s^{Tomo} = \frac{V_{st}}{V_{st} + V_w^{Tomo}}$$

$$(2)\ f_s^{Real} = \frac{V_{st}}{V_{st} + V_w^{Real}}$$

$$(5)\ \frac{f_s^{Real}}{f_s^{Tomo}} = \frac{V_{st} + V_w^{Tomo}}{V_{st} + V_w^{Real}}$$

$$(3)\ \rho_r^{Tomo} = \frac{V_{st} + V_w^{Tomo}}{V_{sample}}$$

$$(4)\ \rho_r^{Real} = \frac{V_{st} + V_w^{Real}}{V_{sample}}$$

$$(6)\ \frac{\rho_r^{Tomo}}{\rho_r^{Real}} = \frac{V_{st} + V_w^{Tomo}}{V_{st} + V_w^{Real}}$$

$$(7)\ \frac{\rho_r^{Tomo}}{\rho_r^{Real}} = \frac{f_s^{Real}}{f_s^{Tomo}} \rightarrow f_s^{Real} = f_s^{Tomo}\frac{\rho_r^{Tomo}}{\rho_r^{Real}}$$

Figure 6-S2: Steps to obtain the normalisation factor for the fraction of mass in the struts obtained from laboratory tomographies using the Watershed segmentation method.

S3. VOLUME FRACTION OF POLYMER IN SUB-PIXEL CELL WALLS

Using eq. (6-3) in the manuscript and the right attenuation coefficients of the gas and polymer phase it is possible to obtain the fraction of polymer in the under-resolved cell walls. However, the choice of an attenuation coefficient for each phase is not obvious since gas or high thickness polymer regions (struts) show a spectrum of attenuation values (Figure 6-S1 (f) and Figure 6-9). To obtain reasonable results $\bar{\mu}_s$ must be the minimum attenuation

value of solid with thickness above the pixel size (for RPU foams that is the minimum value of the struts attenuation density function Figure 6-9 (a)). Using larger attenuation values for $\bar{\mu}_s$ would imply that solid elements thicker than the pixel size are, according to eq. (6-3), a mix of gas and solid phase. Therefore, any value below $\bar{\mu}_s$ will correspond to regions with sizes below the pixel size. For the gas phase the representative attenuation coefficient ($\bar{\mu}_g$) can be obtained from the probability density function in Figure 6-S1 (f). The average value of the density function is approximately 0 (exact value -0.007) excluding shading areas. In Figure 6-S3 (a) the change in attenuation with the volume fraction of polymer can be seen. In addition, the cell walls attenuation probability density function in Figure 6-9 (a) was transformed into volume fraction of solid using eq. (6-3). Then, assuming that the solid thickness in partial pixels is equal to the volume fraction times the pixel size the probability density function of the cell walls can be expressed in terms of its thickness (Figure 6-S3 (b)).

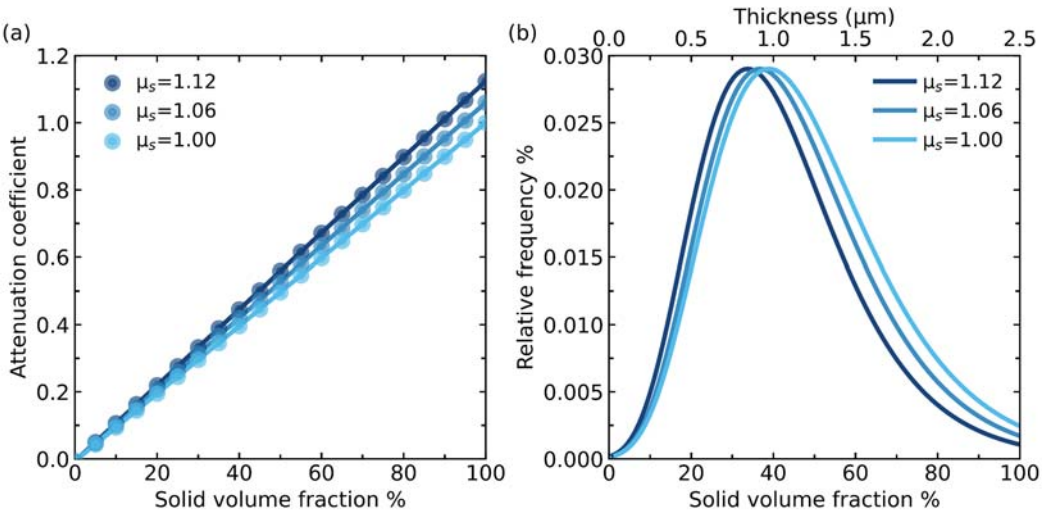

Figure 6-S3: (a) The increase in attenuation coefficient of partial pixels (solid+gas) with the fraction of solid is calculated for three different values of $\bar{\boldsymbol{\mu}}_{\boldsymbol{s}}$ (pure solid attenuation). (b) The cell walls probability density function is presented in terms of the fraction of solid and solid thickness for three different values of $\bar{\boldsymbol{\mu}}_{\boldsymbol{s}}$.

Part 2

APPLICATION OF THE DEVELOPED METHODOLOGIES

C APT

Influence of aerogel on the synthesis of Polyurethane foams

INFLUENCE OF AEROGEL ON THE SYNTHESIS OF POLYURETHANE

7

7.1. INTRODUCTION

In this chapter are collected two publications dealing with the effect of super-insulating Silica Aerogel particles on the foaming process of RPU foams. In this context, the non-standard methods to probe the synthesis (Chapter 4 and Chapter 5) and final structure of PU foams (Chapter 6) find application. The first of the publications is entitled "Influence of silica aerogel particles on the foaming process and cellular structure of rigid polyurethane foams" and was published in 2020 in European Polymer Journal (P. Cimavilla-Román et al., Eur. Polym. J. 135, 109884 (2020), doi: 10.1016/j.eurpolymj.2020.109884). This publication deals with the application of X-ray radioscopy and FTIR spectroscopy to understand the effect of aerogel on the physicochemical mechanisms of PU foam formation. The application of X-ray radioscopy at reaction times longer than 50 s permits inferring the nucleation effect of aerogel particles. However, the composite foams revealed strong degeneration, the higher the content of aerogel particles the more disruptive their effect on the cellular structure. Hence, only composite foams produced with low aerogel contents revealed smaller cell sizes at the end of the foaming process. Moreover, for these foams, it was detected an enhancement of the polymerisation reaction, and higher crosslinking density, which helps in stabilising the structure of the composite foams at low aerogel contents.

The second of the publications, entitled "The effects of Silica Aerogel on the rheological behaviour and polymer matrix structure of Rigid Polyurethane foams" published in 2022 in European Polymer Journal (P. Cimavilla-Román et al., Eur. Polym. J. 176, 111398 (2022), doi: 10.1016/ j.eurpolymj.2022.111398), follows up with the previous research (Section 7.2). In this work, it was detected how the aerogel particles strongly modify the rheological behaviour of the initial raw materials. The complex viscosity of the isocyanate undergoes a stepwise increase with the addition of particles. However, at particle contents above 2.5 wt%, the isocyanate experiences a liquid to gel transition which impacts the kinetics of

viscoelastic properties development and the cellular structure stabilisation mechanisms. The speed of modulus build-up of the composite foams is significantly delayed at high particle contents. Being this delay one of the reasons behind the strong degeneration observed at high particle contents. Last but not least, the application of the sub-pixel methods for the X-ray tomography characterisation (Chapter 6) has permitted the investigation of the polymeric matrix in the composite foams. The analysis revealed that the fraction of mass in the struts decreased at high aerogel contents due to the lower drainage caused by the gel-like behaviour of the mixture combined with its slow modulus build-up.

Eur. Polym. J. 135, 109884 (2020)

Section 7.2.

Influence of silica aerogel particles on the foaming process and cellular structure of rigid polyurethane foams

Paula Cimavilla-Román [a]*, Saúl Pérez-Tamarit [a], Mercedes Santiago-Calvo [a], Miguel Ángel Rodríguez-Pérez [a,b]

[a] Cellular Materials Laboratory (CellMat), Condensed Matter Physics Department, University of Valladolid, Paseo Belen 7, Valladolid, 47011, Spain

[b] BioEcoUva. Research Institute on Bioeconomy, University of Valladolid, Spain

Published in: European Polymer Journal, 135, 109884, (2020)

DOI: 10.1016/j.eurpolymj.2020.109884

Graphical Abstract

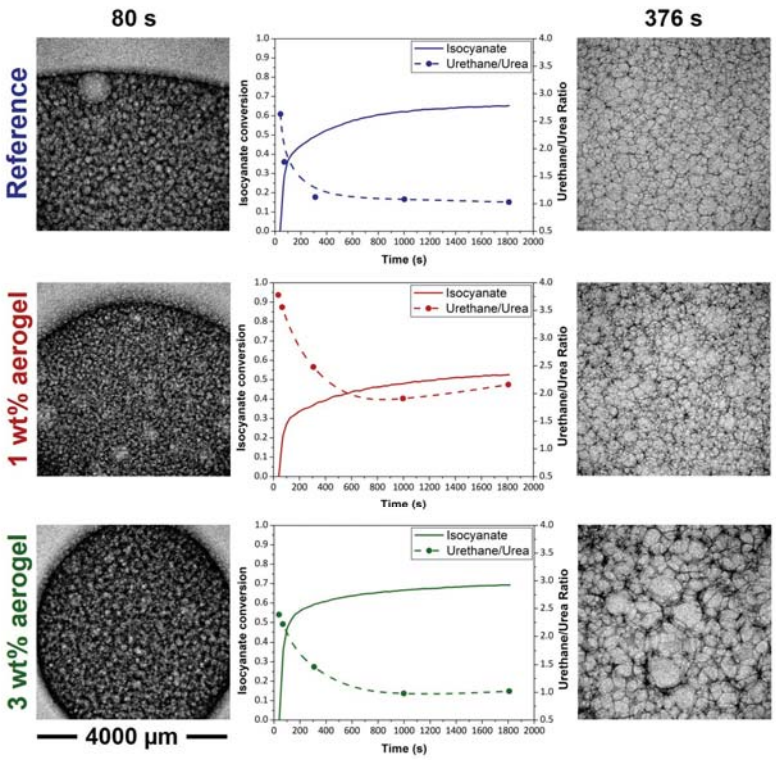

ABSTRACT

Water blown rigid polyurethane (RPU) composite foams were produced using different concentrations of nanoporous silica aerogel micrometric powder (0.5, 1 and 3 wt%). The effect of these particles on the foaming kinetics was analysed from a physical and chemical viewpoint. On the physical side, the foaming process was studied by in-situ X-ray radioscopy. The inclusion of aerogel particles in the system delays the foam expansion and enhances the nucleation of cells. However, high amounts of these particles (3 wt%) lead to intense cell coalesce during foam evolution. On the chemical side, the reaction kinetics was investigated by in-situ FTIR spectroscopy and reaction temperature measurements. The addition of low contents of aerogel (below 3 wt%) reduces the conversion of isocyanate while favouring the generation of urethane groups, which explains the higher density of the foams with low aerogel contents. However, the foam with high contents of aerogel (3 wt%) does not change the reaction balance in comparison to the reference. Therefore, this foam presents similar expansion and density to those of Reference. Furthermore, higher reaction temperatures were reached by the reference foam during the foaming process, and higher dissipation speeds of these temperatures were detected for the foams containing aerogel with respect to those of the reference foam.

KEYWORDS

Polyurethane foam; Composite foams; Nanoporous silica aerogel; X-ray radioscopy; Reaction kinetics; FTIR spectroscopy; In-situ studies

Eur. Polym. J. 135, 109884 (2020)

1. INTRODUCTION

Polymer composite foams are very promising materials due to the enhanced properties that result from the synergy of the polymer and filler particle attributes. Micro and nanosized fillers reinforce the polymer matrix and modify the final cellular structure. These synergistic effects can result in materials with increasing strength [1,2], fire resistance [3] and thermal insulation capabilities [4–6]. In addition, the inclusion of fillers permits tailoring the cellular structure. For all these reasons, these materials have significant potential in the automotive, construction and electronic industries [7].

One of the most interesting thermoset polymeric foams is rigid polyurethane (RPU) foam, widely employed in the construction industry. RPU foams are one of the most popular thermal insulation materials for their low thermal conductivity (16–35 mW m^{-1} K^{-1}) and low density (25–50 kg m^{-3}) [8]. These materials are produced as a result of two main exothermic reactions: polymerization reaction between isocyanate and polyol; and blowing reaction between isocyanate and water. The polymerization reaction is responsible for the generation of urethane linkages and the consequent polymerization process [8]. Meanwhile, the blowing reaction forms urea hard segments and promotes the production of CO_2 gas resulting in the foam rise. The presence of fillers has been reported to introduce significant modifications not only on the final foam properties but also on the physical mechanisms that are responsible for the foam formation [9,10] and the chemical balance between RPU reactions [5,10,11]. Among other effects, the use of fillers has been proven to permit the production of foams with more homogeneous cellular structures, smaller cells and lower densities, becoming materials particularly suitable for thermal insulation purposes [4,12,13]. Due to these cellular structure improvements, many types of fillers have been tested to improve the applicability and performance of RPU foams, such as nanoclays [4,14], nanosilicas [15], graphite [16] and different carbon fillers [11,13,17]. In addition, over the last few years, the use of advanced and multi-functional materials, like super-insulating silica aerogel, as fillers for composite materials, has started to attract increasing attention [5,18–21]. Nanoporous silica aerogels presents exceptional properties that make them very suitable thermal insulators and a very attractive additive to reduce the thermal conductivity of RPU foams. Some of the key properties of these materials are a low thermal conductivity between (10–30 mW m^{-1} K^{-1}), a low density (0.003-0.35 g cm^{-3}), a high porosity (~85%-99.87%) and a high specific surface area (~600-1000 m^2 g^{-1}) [22,23]. However, some

characteristics of these aerogels like its highly open structure, low connections between secondary particles, low density and high porosity make this material brittle which dramatically limits their exploitation as insulation materials by themselves [24].

Despite the interesting properties of this material, the use of silica aerogel as an additive of polymeric materials has just started to be exploited. Most research works that can be found in the literature are focused on studying the effect of aerogel on the thermal conductivity of RPU foams [18–20]. Zhao et al. [18] prepared Polyisocyanurate rigid (PIR) foams containing 1 wt%, 2 wt%, 3 wt%, 4 wt%, 5 wt%, 6 wt% and 8 wt% of granular silica aerogel. The foam with 8 wt% of aerogel showed a reduction of the thermal conductivity by 34.6%. The oxygen index of the same foam was also measured, revealing an improvement in flame retardant properties. Although the cellular structure was not characterised in depth, SEM images showed how the incorporation of aerogel alters the homogeneity of the PIR foams cellular structure. Nazeran and Moghaddas [20] produced cyclopentane blown RPU foams reinforced with different contents of non-commercial nanometric silica aerogel (1 wt%, 3 wt%, and 5 wt%). The composite foams were produced following two different routes, one adding silica aerogel to MDI raw material and second to the polyol phase. In both cases, the authors observed more homogeneous cellular structures and a reduction in the cell size when adding aerogel particles up to a 3 wt%. However, increasing the aerogel content up to the 5 wt% increased the mean cell size due to the viscosity increase of the polyol and the isocyanate. Comparison of the cellular structures produced by the two production routes revealed that the addition of aerogel to the MDI matrix results in materials with smaller cells and narrower cell size distribution, probably due to the low viscosity of MDI relative to the polyol. Concerning the thermal insulation capabilities, by increasing the silica aerogel content from 0 wt% to 5 wt%, the thermal conductivity was reduced by 14.6%. Dourbash et al. [19] prepared silica aerogel rigid polyurethane composite foams. Contents of 3 wt% and 4 wt% of both granular (with particle size from 0.7 to 4 mm) and powdered (particle size from 0.05 to 1 mm) silica aerogel particles were used to prepare the foams. The resulting composite foams did not show a reduction in the thermal conductivity, which was explained considering the deterioration of the cellular structure, and the increase in the average cell size. As mentioned previously, these research works are mainly focused on the properties of the RPU foams containing aerogel particles, but they did not analyse the foaming process and in particular the influence on the aerogel particles on the physical and chemical mechanisms taking place during the production of the RPU

Eur. Polym. J. 135, 109884 (2020)

foams. Therefore, there is still a lack of knowledge about how aerogel particles affect the reactive foaming process and the final cellular structure.

Hence, this work aims at evaluating the influence of powdered silica aerogel on the physicochemical mechanisms leading to the formation of water blown RPU foams. To this end, different *in-situ* techniques have been used due to the impossibility of stopping the chemical reactions responsible for the generation of RPU foams. On the one hand, the foaming process has been studied from a physical perspective using X-ray radioscopy. This technique enables to monitor the evolution of the main features of RPU foams while foaming, such as relative density, cell size and cell nucleation density [9,25] and allows to analyse nucleation, growing and degeneration mechanisms. On the chemical side, the kinetics of the two main reactions of the RPU foam formation have also been followed. The generation of urethane and urea products has been monitored by means of *in-situ* FTIR spectroscopy. Furthermore, thanks to the exothermic nature of these reactions it has been possible to obtain the internal temperature evolution while foaming by suitably positioning thermocouples inside the foaming mould [5] providing information about the global reaction kinetics of the materials under analysis.

The knowledge gained by this research will be useful to optimise RPU formulations containing silica aerogels in order to take full advantage of the excellent properties of this nanoporous material to reduce the thermal conductivity of RPU foams.

2. MATERIALS AND METHODS

2.1. Materials

2.1.1. Reactants of RPU foams

The polyol component used was a blend of two high functionality polyether polyols, Alcupol R4520 (functionality of 4.5, OH value of 455 mg·KOH g^{-1}) and Alcupol R3810 cross-linker (functionality of 3, OH value of 380 mg·KOH g^{-1}), both from Repsol S.A. The isocyanate was a polymeric diphenylmethane diisocyanate (pMDI), IsoPMDI 92140 (31.5% NCO, density 1.23 g cm^{-3}, viscosity 170-250 mPas) supplied by BASF. TEGOAMIN® DMCHA (N,N-dimethylcyclohexylamine) from Evonik was employed as a catalyst, that is a tertiary amine used primarily to promote the urethane (polyol-isocyanate) reaction. TEGOSTAB® B8522 (a non-hydrolysable polyether-polydimethyl-siloxane–stabilizer) from

Evonik was used as a surfactant to obtain superior cell structures. Distilled water was employed as a blowing agent.

2.1.2. Silica Aerogel fillers

Enova® Aerogel IC3100 powder, provided by Cabot, was the filler selected for the manufacturing of RPU composite foams. According to the supplier, Enova aerogels are nanoporous lightweight materials with a particle size from 2 to 40 μm, an average pore diameter of 20 nm, a particle density near 150 kg m^{-3} and a very low thermal conductivity of 12 mW m^{-1} K^{-1}. This powder is made from silica particles with a hydrophobic [(trimethylsilyl)oxy] superficial treatment [26]. This treatment replaces the hydrophilic unreacted OH groups on the surface of the aerogel skeleton (Figure 7-1-1 (a)) by [(trimethylsilyl)oxy] groups that inhibit the absorption of water, resulting in hydrophobic aerogels (Figure 7-1-1 (b)).

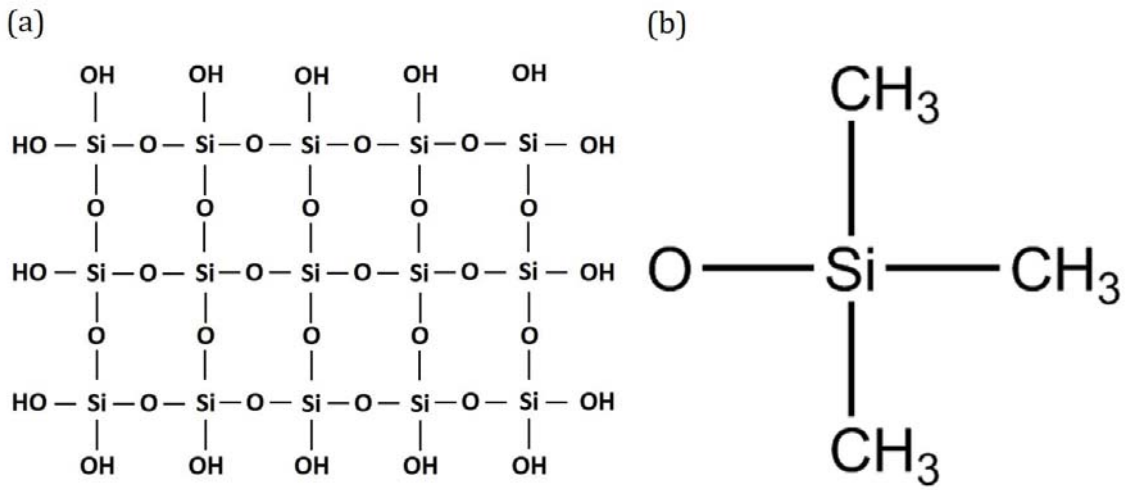

Figure 7-1-1: (a) Schematic representation of the silica aerogel particles, and (b) representation of the surface modifiers groups replacing the OH groups in the left scheme.

2.2. Methods

2.2.1. Preparation of RPU composite foams

RPU foams were prepared from 90 phpp (parts per hundred parts of polyol) of Alcupol R4520, 10 phpp of Alcupol R3810, 1 phpp of TEGOSTAB B8522, 0.4 phpp of TEGOAMIN DMCHA, 4 phpp of distilled water and 197 phpp of IsoPMDI 92140. For comparison purposes, four foams with different filler content (0 wt%, 0.5 wt%, 1 wt%, 3 wt%) dispersed in the isocyanate were produced.

Eur. Polym. J. 135, 109884 (2020)

The blend of the polyols with the different components was performed with an overhead stirrer (EUROSTAR 60 control from IKA), equipped with a 50 mm diameter Vollrath™ Lenart-disc stirrer. First, the mixture of the polyol with the additives (catalyst, surfactant and blowing agent) was performed at 250 rpm for 2 minutes. The dispersion of the aerogel powder in the isocyanate component was carried out at low shear stress values of 250 rpm for 5 minutes. Finally, to promote the foam formation, a mixture of 50 g of isocyanate and polyol components was produced using 1200 rpm during 10 s.

A lower amount of TEGOAMIN DMCHA catalyst (0.4 ppw) is used in this study because a long cream time (around 50 s in our formulation) is necessary to properly observe the foaming behaviour with the X-ray setup [9,11,25]. The placement of the evolving sample inside the X-ray cabinet takes around 50 s, time in which monitoring with the setup used in this research is not possible.

2.2.2. Fillers characterisation

Two methods were used for the characterisation of the commercial Enova aerogel particles. Surface groups and chemical structure have been investigated employing an FTIR spectrometer model Tensor 27 (Bruker), working in the attenuated total reflectance (ATR) mode. The morphology and porous structure of the particles have been observed using high-resolution micrographs obtained by a scanning electron microscope (SEM) model QUANTA 200 FEG. Prior to the observation, the particles were dissolved in ethanol and sonicated for 30 minutes to avoid agglomerates. Then, a drop of the solution was deposited on an SEM specimen stub for the observation.

2.2.3. Density, cell size and open cell content characterisation

The produced foams were characterised using the following techniques. Foam density was measured as described by ASTM D1622/D1622M-14 [27]. Density was determined in three different samples for each material, with a diameter of 30 mm and a height of 30 mm. After measuring the densities in the samples, open cell content, *OC%*, was measured by using a gas pycnometer Accupyc II 1340 from Micromeritics, according to ASTM D6226-10 [28]. Relative density was obtained as the ratio between the foam density and the solid material density (1180 kg m^{-3}). A micro-computed tomography scan (resolution of 2.5 μm) was performed on cylindrical samples of 2.5 mm in diameter to measure the average cell size [29].

2.2.4. Time-resolved radiography (X-ray radioscopy)

The setup used for radiography acquisition (Figure 7-1-2 (a)) consists of an X-ray microfocus source from Hamamatsu with a maximum output power of 20 W (spot size: 5 µm, voltage: 20-100 kV, current: 0-200 µA). X-rays come out of the source window, forming a cone-beam of 39°, which allows to obtain up to 20 times magnification [15]. The X-ray transmitted radiation is detected by a high sensitivity flat panel connected to a frame grabber (Dalsa-Coreco) that records the radiographic images. This high-resolution detector is composed of a matrix of 2240x2344 pixels with a pixel size of 50 µm. The digital output is a 12 bits grey depth resolution, and the maximum acquisition rate goes up to 9 fps (at 4x4 pixel binning) [11].

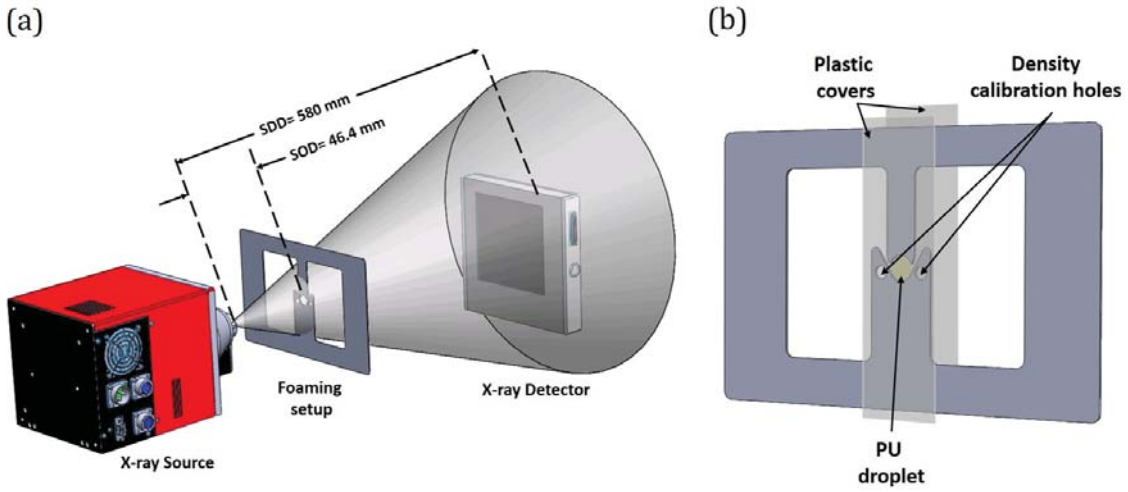

Figure 7-1-2: X-ray setup employed for the radioscopy experiments. (a) X-ray system and position of the foaming frame with respect to the X-ray source and detector and (b) Stainless steel mould for PU foaming (foaming frame).

This setup is optimised for low absorbing materials such as polymers and typically works at low energies and high currents (40 kV, 120 µA) to optimise the contrast in the radiographs. To this end, the exposure time should always be set between 1-2 s. However, as the foaming process of RPU foams is swift, high acquisition rates are required to obtain images containing sharp features. For this reason, the detector was set to work under 2x2 binning mode [30] with an acquisition time of 800 ms (1.25 fps) (thus effective exposure time of 3.2 s). Consequently, the effective pixel size (after applying 2x2 binning) is increased from 3.85 µm to 7.70 µm.

In these experiments, a 0.6 mm-thick stainless-steel frame was employed (Figure 7-1-2 (b)) to produce the foams. This frame has a circular cavity (Ø =6 mm) where a PU reacting droplet of approximately 0.02 mL is placed. The droplet is taken from the cup where the 50

Eur. Polym. J. 135, 109884 (2020)

g polyol-isocyanate mixture is performed (section 2.2.1). Two evacuating conducts facilitate the foam evacuation out of the central circular cavity improving the X-ray imaging in the central region of the cavity; therefore, cell growth can be visualised and further analysed. In order to avoid the PU drop from flowing and growing in the thickness direction, two polypropylene covers (thickness~50 μm) were employed. This ensured having a quasi-bidimensional foam system with a constant thickness in which only a few cells are present in the thickness direction. Besides, two circular holes (Figure 7-1-2 (b)) located in the frame hold two reference materials, air (density 1 kg m^{-3}, porosity 1) and a thermoplastic polyurethane (TPU) pellet of thickness 0.6 mm (density 1106.9 kg m^{-3}, porosity 0), which are used for relative density calibration purposes.

Once the radiography sequence has been acquired, it is necessary to treat the images to obtain numerical results. The evolution of three different foam descriptors were measured: density, cell size, and cell nucleation density.

The density can be calculated from each radiograph, thanks to Beer-Lambert law [31] eq. (7-1-1). This expression predicts the attenuation of an incident monochromatic X-ray beam, I_{air}, by an exponential function of the linear absorption coefficient, μ, the density of the material, ρ, and the thickness, d.

$$I = I_{air} e^{-\mu\rho(x,z)d} \tag{7-1-1}$$

Relative density, ρ_r, (density of the foamed sample divided by the density of the solid polymer) of the evolving sample can be calculated after applying a logarithmic conversion to eq. (7-1-1). Given that the thickness of the foam is constant and equal to that of the TPU solid pellet used for calibration, it is possible to propose two equations like eq. (7-1-1). One of the equations refers to the attenuation suffered by the incident X-ray beam, I_{air}, by solid polyurethane, I_{TPU}, and another to the evolving foam, I_f. After equalizing both equations, it is possible to obtain the relative density of the foam using eq. (7-1-2).

$$\rho_r = \frac{log\left(\frac{I_f}{I_{air}}\right)}{log\left(\frac{I_{TPU}}{I_{air}}\right)} \tag{7-1-2}$$

For the determination of the cell size evolution, Φ, during the foaming process, every image that conforms the radioscopy has been analysed following a sequential process. First of all, the images are scaled to convert pixels into distances. Afterwards, a minimum filter is

applied to enhance the darker solid phase pixels (solid phase is more X-ray absorbing). Then, automatic binarization of the radioscopy images was performed. As transmitted intensity through the sample increases during the foaming (meanwhile the relative density decreases), the threshold limits for the binarization of the image increase automatically with the monitored time. Afterwards, a watershed segmentation algorithm is applied to create the cell walls that separate pores. The resulting masks (binarized images) are analysed by a size and roundness selective procedure which enables to remove noise and other artefacts from the images.

Finally, the evolution of cell nucleation density [31] can be calculated according to eq. (7-1-3) employing the measured values of relative density and cell size evolution.

$$N_o = \frac{6}{\pi \Phi^3}\left(\frac{1}{\rho_r} - 1\right) \qquad (7\text{-}1\text{-}3)$$

2.2.5. Kinetic studies

Reaction kinetics for the reference material (Reference) and the materials containing 1 wt% aerogel (1% A) and 3 wt% aerogel (3% A) were studied. To this end, two different techniques were employed: *in-situ* FTIR [5,32] and reaction temperature evolution measurements [5].

In-situ FTIR spectra of the samples were collected using a Bruker ALPHA spectrometer by attenuated total reflectance (ATR) method [5,32]. From the 50 g reacting mixture (section 2.2.1), 1 mL was extracted and poured on the surface of the ATR cell. The FTIR experiments lasted 30 minutes, during this time 60 spectra were acquired, one every 30 s. The temperature of the experiment was set at 70 °C. In addition, to monitor the amount of reaction products of the blowing and polymerization reaction a deconvolution of the amide I region (carbonyl region) was carried out as indicated in the literature [32–34].

The reaction temperature evolution during the foaming process was also measured. Three thermocouples (type K) were introduced in a plastic cup of 11.5 cm of diameter and 14 cm of height to measure the temperature during 60 minutes at three different positions. Three thermocouples were placed vertically in the centre of the plastic cup at the following heights from the base of the cylinder: 0.5 cm (thermocouple 1, T1), 2.0 cm (thermocouple 2, T2) and 6.5 cm (thermocouple 3, T3). The data collected by the thermocouples were registered with a computer. Three experiments were performed for each material.

Eur. Polym. J. 135, 109884 (2020)

3. RESULTS AND DISCUSSION

3.1. Aerogel powder characterisation

FTIR spectra of the silica aerogel particles can be observed in Figure 7-1-3. The strong absorption bands appearing at 1047.74 cm^{-1} and 841.77 cm^{-1} are the characteristic peaks of the asymmetric and symmetric stretching vibration of Si-O-Si, respectively [32,35–37]. On the other hand, the absorption peak located at 1254.49 cm^{-1} is due to the CH_3 deformation in the bond Si-CH_3 [38]. Moreover, the peak intensity detected at 2962.67 cm^{-1} and 756.46 cm^{-1} can be attributed to the C-H stretching and bending vibration, respectively. These weaker peaks confirm the existence of methyl groups belonging to the superficial treatment of the aerogel powder (Figure 7-1-1 (b)). Thus, the FTIR spectra confirm the presence of hydrophobic groups on the surface of the particles. The hydrophobic nature of aerogel can also be verified by the absence of the characteristic peak for the Si-OH bond in silica aerogel (~1630 cm^{-1})[36].

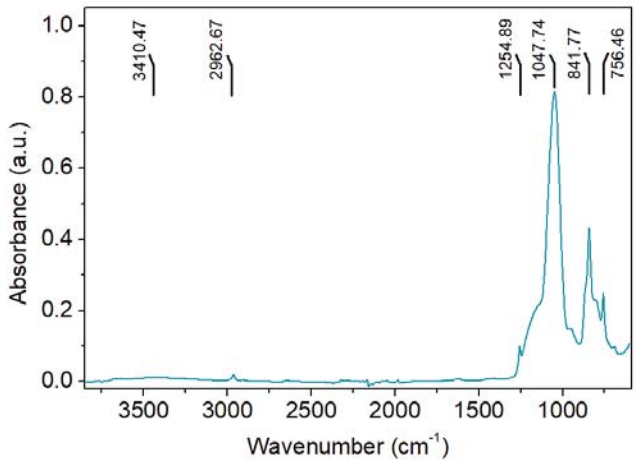

Figure 7-1-3: FTIR spectra of the Enova® Aerogel powder.

The particle morphology has been examined using high-resolution SEM imaging, as seen in Figure 7-1-4. The micrographs (Figure 7-1-4 (a)) reveal the micrometric size of the particles. As it can be observed in this figure, the majority of the particles have sizes close to 15 μm supporting the data provided by the supplier. Concerning the nanoporous structure of the particles, it is possible to appreciate in Figure 7-1-4 (b) a textured surface of the particles. Moreover, darker areas on the surface resemble pores or holes on this surface, with sizes in the range of 15 nm.

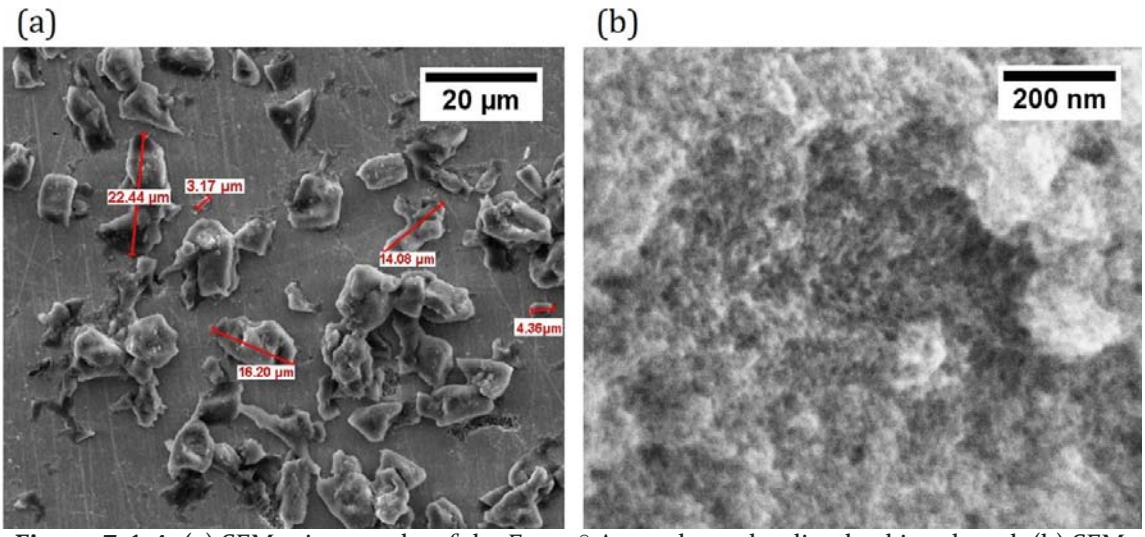

Figure 7-1-4: (a) SEM micrographs of the Enova® Aerogel powder dissolved in ethanol, (b) SEM micrograph of the Enova® Aerogel particles surface.

3.2. Foam density, cell size and open cell content characterisation

To verify the evolution of foam density and cell size with increasing aerogel content the final geometric density and cell size of all foams were investigated and are gathered in Table 7-1-1. Average cell size values were obtained from the equivalent sphere diameter of the cell volumes measured by means of X-ray Tomography (Figure 7-1-5) [29]. Moreover, SEM micrographs were acquired of the foams' growth plane and are shown in Figure 7-1-5.

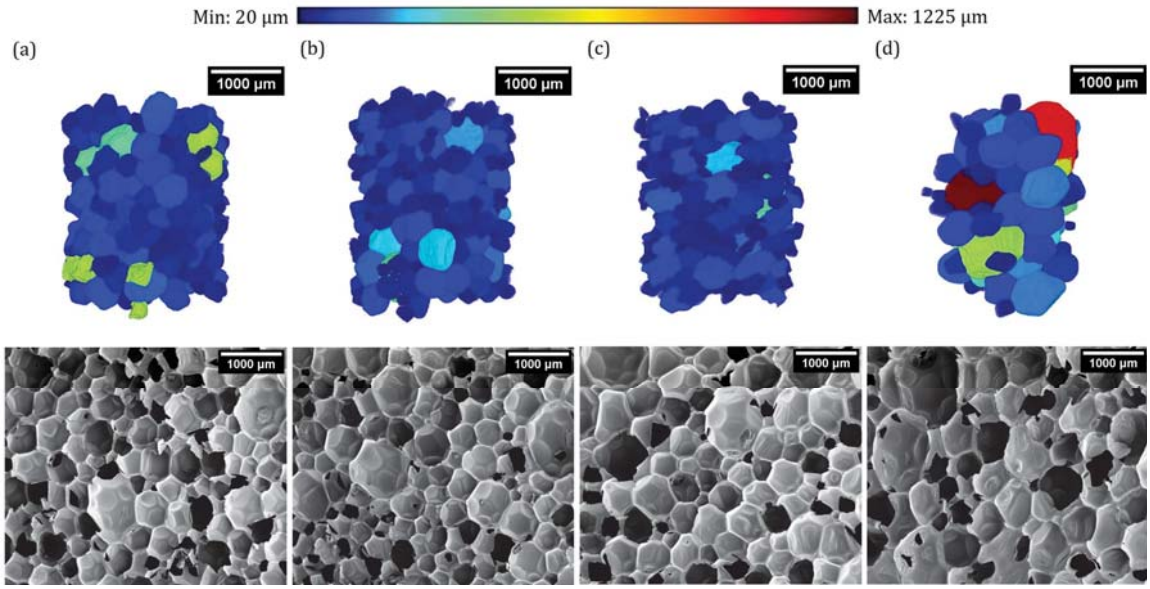

Figure 7-1-5: 3D renderings of the X-ray tomography scanned volumes, coloured according to the displayed colour-size scale, and SEM micrographs of (a) Reference, (b) 0.5% A, (c) 1% A and (d) 3%A.

Table 7-1-1 shows that the foam containing 3 wt% silica aerogel (3% A) has a similar density to that of the reference foam (Reference). In contrast, the foams with 0.5 wt% and

Eur. Polym. J. 135, 109884 (2020)

1 wt% silica aerogel (0.5% A and 1% A) present a slight increase in density with respect to Reference foam (only around 5% increase). Therefore, the introduction of silica aerogel fillers does not significantly alter the density of the RPU cured foam.

Table 7-1-1: Density, relative density and open cell content for every foam manufactured.

Material	Density (kg m^{-3})	Relative density	Open cell content (%)	Cell size (μm)
Reference	38.1 ± 0.5	0.033	6.1 ± 0.1	412.5 ± 122.7
0.5% A	40.3 ± 0.1	0.035	7.5 ± 0.4	309.6 ± 180.0
1% A	39.8 ± 0.8	0.034	8.4 ± 1.6	290.7 ± 168.3
3% A	38.2 ± 0.4	0.033	19.8 ± 3.5	454.7 ± 234.1

On the other hand, the evolution of the open cell content with aerogel concentration has also been studied, as shown in Table 7-1-1. The influence of aerogel silica powder in this magnitude is evident. Open cell content of the RPU foams shows an increase with the addition of aerogel; this effect is the most visible for sample 3% A.

In contrast, the average cell size progressively decreases when low contents of particles (below 1 wt%) are added to the polyurethane matrix, reaching a reduction near the 30% for the foam containing 1% of silica aerogel. Whereas it slightly increases when 3 wt% of aerogel is used. The cell size for this material is similar to that of the reference material.

3.3. Foaming behaviour

3.3.1. Relative density evolution

Figure 7-1-6 shows curves for the relative density evolution during foaming. These results are plotted to take as the initial time the beginning of the isocyanate and polyol stirring process. Therefore, all curves present a time span of 66.4 s that results from the time required to perform the mixture of the polyol with isocyanate, position the RPU drop inside the foaming frame (Figure 7-1-2 (b)) and introduce the sample inside the X-ray cabinet. Therefore, the beginning of the experiments occurs once the foam rise has already started. The first radiography is acquired approximately 10 s after the cream time, which is 50 s.

Figure 7-1-6 reveals how, during the firsts instants of the foaming process, a rapid density decrease takes place, as a consequence of the CO_2 gas generated during the blowing reaction [11]. After that, the expansion rate is reduced due to a combination of polymerization evolution (increasing the material viscosity) and the reduced amount of gas

generated at long times. Attending to the differences observed among curves, Figure 7-1-6 shows how the inclusion of a small amount of these nanoporous particles (0.5 and 1 wt%) slightly increases the density of the aerogel filled foams with respect to the reference at any time during the process. Furthermore, when a higher content in aerogel particles (3 wt%) is introduced into the foam, its density evolution trend is altered, ending with a density similar to the reference despite showing a higher density at short reaction times.

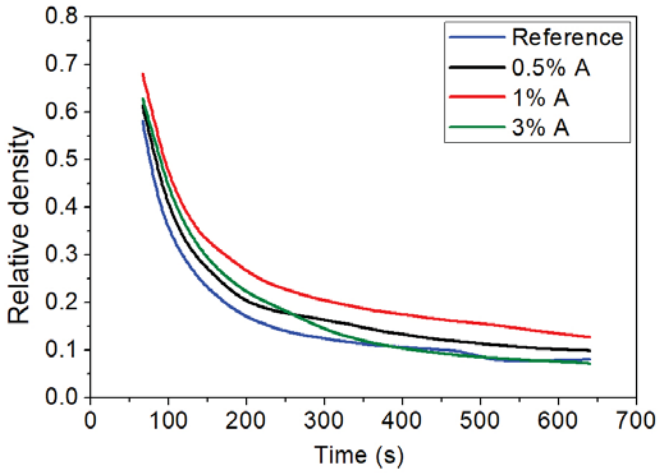

Figure 7-1-6: Representative curves of the relative density evolution versus time of the reference and aerogel composite foams.

In addition, when observing the slopes of the relative density evolution process (Figure 7-1-7), it is detected how at short times Reference material shows a remarkably rapid density decrease, whereas composite foams present a slower evolution. Nevertheless, this trend shifts at times higher than 95 s (Figure 7-1-7 (b)). At longer times, the foams reinforced with aerogel particles decrease their density more readily. Despite this, at the end of the radioscopy experiments, the foams with 0.5 wt% and 1 wt% of aerogels end with higher relative density values than the reference.

Furthermore, the accuracy of the relative density values obtained by radioscopy has been confirmed by measuring the density (Table 7-1-1) of the cured foams. Table 7-1-1 and Figure 7-1-6 at long times show similar results. Both results reveal how the addition of low contents of aerogel (0.5 wt% and 1 wt%) increases the density of the foams, however, when high contents (3 wt%) are employed the density of the foam remains similar to the density of the unfilled foam.

Eur. Polym. J. 135, 109884 (2020)

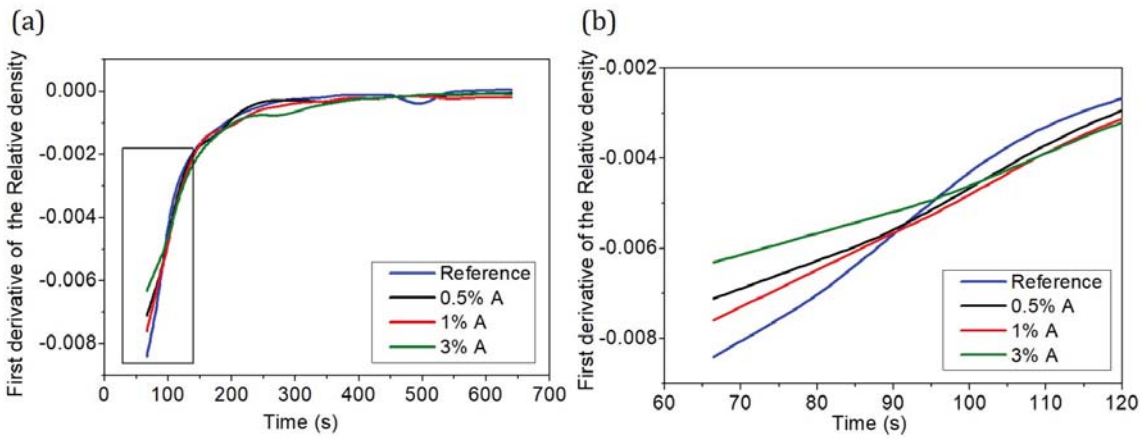

Figure 7-1-7: (a) Relative density decreasing speed versus time for reference foam and aerogel composite foams (0.5% A, 1% A and 3% A). (b) Zoom of the previous figure at short reaction times.

3.3.2. Cell size evolution

A visual comparison between the cellular structure of the four composite foams can be appreciated in Figure 7-1-8. The main changes in cellular structure are observed at two stages of the foam evolution, after the onset of foam rise, 84 s, and once the cellular structure is almost solidified, 580 s. Between these two foaming stages the growth of the cells can be appreciated. In addition, the increase in grey level intensities observed between foams at 84 s and 580 s is related to the reduction in density reported previously (Figure 7-1-6). At early stages, it is challenging to appreciate clear differences from a simple visual inspection. However, at the final stages of the foaming, 580 s, the composite sample with 3 wt% aerogel shows a cellular structure with remarkably larger pores (*ca*. 1 mm) than reference foam and those foams with 0.5 wt% and 1 wt% silica aerogel.

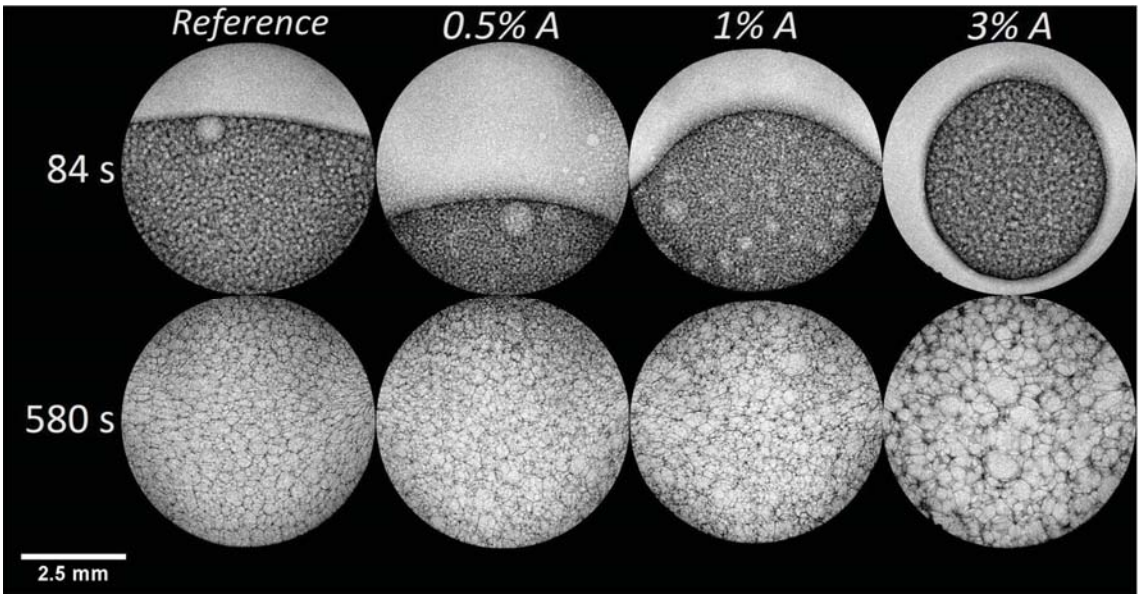

Figure 7-1-8: X-ray radiographs of expanding reference and aerogel composite foams at the beginning and ending of the foaming process.

The qualitative observations that can be extracted from Figure 7-1-8 are confirmed when analysing the radioscopy sequences (Figure 7-1-9 (a)). A dissimilar pore-growing slope for the different materials is observed. During the foam rise, cell growth rate (Figure 7-1-9 (b)) is exceptionally high in the case of the foam with 3 wt% of aerogel (60-120 s), reaching cell size growing speeds of 3 μm s^{-1}. Such expansion rate is not achieved by any other sample. Reference foam reaches cell size expansion speed close to 2 μm s^{-1} whereas composites with low content in aerogel, 0.5 wt%, and 1 wt%, show a rather slow cell growth rate (below 1.5 μm s^{-1}). Furthermore, they present a remarkable cell size reduction compared to the reference at the end of the foaming process. On the other hand, sample 3% A, which starts the foaming process with the smallest cell size, shows the largest pore size at the end of the monitored time due to this quick increase of cell size with time.

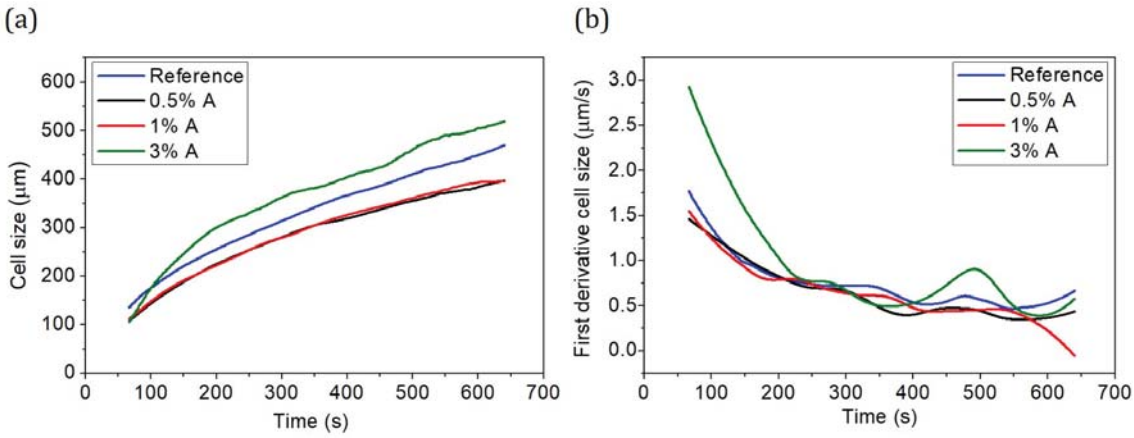

Figure 7-1-9: (a) Cell size evolution with time and (b) Cell size growing speed for all the RPU foams under study.

The quick transition from small to larger pores in the case of sample 3% A can be interpreted as a sign of cellular structure instability, *i.e.* presence of cellular degeneration mechanisms such as coalescence [39]. This mechanism is characterised by the cell wall rupture between adjacent cells, leading to the junction of small-sized cells into bigger ones, especially at low densities when cell walls are thinner [40]. The cellular instability detected here matches the increase in open cell content observed as the content in aerogel increases, Table 7-1-1. This effect was extremely remarkable for the sample containing 3 wt% of aerogel particles, reaching almost 20% of open cell content. On the other hand, it is also interesting to observe that the cell size of samples containing 0,5% or 1% aerogel is reduced at the end of the experiment (same result to that found in Table 7-1-1). Mainly as a consequence of the lower cell size at early stages and a slower increase of cell size with time.

Eur. Polym. J. 135, 109884 (2020)

3.3.3. Cell nucleation density evolution

The obtained results exhibit a fluctuating behaviour depending on the filler amount in the materials (Figure 7-1-10).

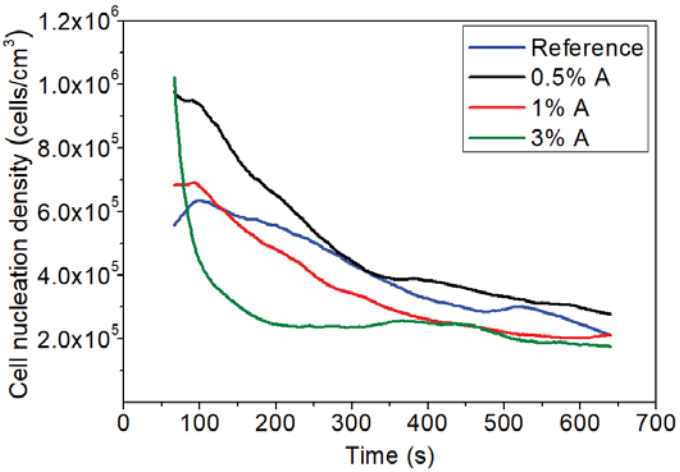

Figure 7-1-10: Cell nucleation density evolution with time for all the foams manufactured.

Initially, the presence of aerogel particles increases the number of nucleation sites with respect to the reference, as described by classical nucleation theories [41]. Even though the nucleation process occurred before the monitoring began, it is possible to confirm this effect due to the higher cell nucleation density of the aerogel-filled foams immediately after the foam rise starts. Moreover, the cell density does not stay constant with time in any of the composite foams though in some cases Reference, 0.5% A and 1% A the variations are small. As it was reported for material 3% A, the swift increase in cell size together with the reduction in cell nucleation density is a clear symptom of cell degeneration mechanisms. These cell degeneration processes prevail at long times over the enhanced nucleation experienced by the composite foams. A possible explanation for these degeneration phenomena could be the broad particle size range of Enova® Aerogel powder (Figure 7-1-4 a) and the high content of particles in this particular system. Fillers are usually hosted in the struts and cell walls of the foam. However, particles with sizes close to 40 μm, could undoubtedly cause cell walls (with thickness around 1-2 μm) to weaken and break, leading to the joining of adjacent cells and increasing of the open cell content (Table 7-1-1).

3.4. Kinetic study

As it was previously commented, the RPU foam formation is a consequence of a reactive foaming process between isocyanate with water (blowing reaction) and polyol

(polymerization reaction). The addition of particles to the RPU formulation can alter the rates of conversion of isocyanate and modify the balance between the generation of urethane and urea products. This type of information is vital to understand the observed changes in the foaming behaviour of RPU when different contents in aerogel particles are introduced. As observed in Figure 7-1-7 and Figure 7-1-10, the relative density and cell size evolution of foams 0.5% A and 1% A are essentially analogous. What is more, their final cellular structure and density also agree (see section 3.2). For these reasons, foam 0.5% A was excluded from this analysis on the assumption that foams with low aerogel contents present the same foaming behaviour. Therefore, the kinetic study discussed below was then performed for the foams Reference, 1% A and 3% A.

3.4.1. FTIR Measurements

The isocyanate consumption can be evaluated with the decrease of the isocyanate asymmetric stretching vibration at 2270 cm^{-1}. In contrast, the generation of urethane and urea products are followed, considering the increase of the carbonyl stretching vibrations of the Amide I Region in the range 1610–1760 cm^{-1}[5].

Firstly, during foaming, the isocyanate group conversion (pNCO) is quantified by the decay eq. (7-2-4) of the isocyanate absorption band; located between 2500 and 2000 cm^{-1}[42]:

$$pNCO = \frac{A_0 - A_{max}}{A_0} \tag{7-1-4}$$

In eq. (7-1-4) A_0 represents the absorbance of the isocyanate band for the first acquired spectra, and A_{max} is the integrated absorbance of the isocyanate band at time ~ 0 [5]. Figure 7-1-11 shows curves for the isocyanate conversion of foams Reference, 1% A and 3% A. It is clear how the foam with the highest content in aerogel particles presents the highest isocyanate consumption, followed by the reference. However, as observed in the relative density evolution curves (Figure 7-1-6), there is not a linear trend in the monitored magnitudes with the addition of aerogel particles. In fact, 3% A and Reference show a similar isocyanate consumption and relative density evolution (at the last minutes of the foaming process). Whereas 1% A presents low values of isocyanate consumption during the complete foaming process. Previous works have noted that depending on the filler content the isocyanate reaction is conditioned either by the viscosity of the initial mixture or the particle

Eur. Polym. J. 135, 109884 (2020)

characteristics [10,32,43]. For low amounts of fillers, the reaction rate is dominated by the viscosity increase. Thus, the addition of 1 wt% of aerogel could increase the viscosity of the isocyanate part triggering a reduction in the mobility of the reacting chains and a smaller isocyanate conversion. Whereas, when high amounts are employed is the fillers' surface treatment which strongly conditions the reaction rates. Since aerogel particles have a hydrophobic surface treatment that does not interact with the OH groups coming from the polyol or water, the isocyanate consumption is enhanced [32]. However, for all foams, it is clear how the isocyanate consumption increases rapidly (in less than 200 s) to almost its maximum value observed in the 30 minutes monitored by *in-situ* FTIR spectra.

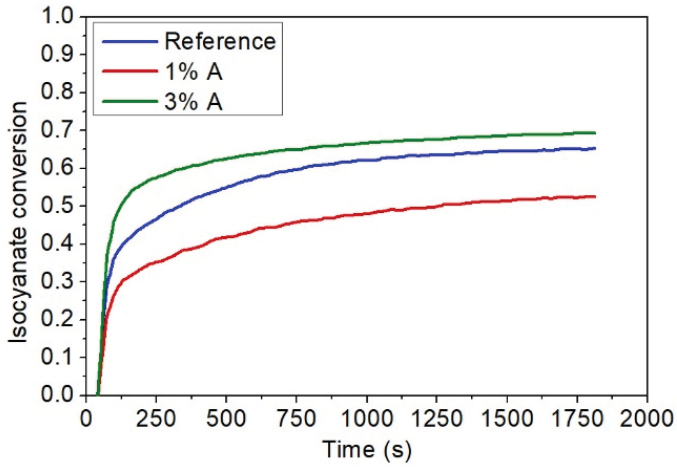

Figure 7-1-11: Average isocyanate conversion versus time for foams Reference, 1% A and 3% A.

The rate of generation of products can be obtained from the deconvolution of the Amide I region of the acquired spectra. This procedure permits separating the different carbonyl groups present in the reaction mixture and obtaining the relative area percentages of ureas and urethanes [34,35]. Relative area percentages of products generated at different times are obtained by dividing the corresponding peak area by the total Amide I area (summing up the areas of all peaks present in this carbonyl region). From this, the urethane/urea ratio at different times is calculated from the relative area percentages of urethanes groups divided by the relative area percentages of ureas groups (Figure 7-1-12). From Figure 7-1-12, it is clear how the reaction kinetics of 1% A are strongly affected by the presence of aerogel, increasing the generation of urethane products with respect to ureas during the whole foaming time. Nevertheless, this trend is not preserved when higher amounts of aerogel are used. 3% A shows a similar behaviour than that of the reference sample.

These results indicate how the addition of low aerogel contents seems to favour the polymerization during the first minutes of foaming. All in all, the trend followed by foams

ratio of urethane/urea is very similar to that observed for the relative density evolution. When the polymerization reaction is favoured, as it is the case of foam containing 1 wt% aerogel, the increase in density is significant because the urethane formation is quicker. Thus, the viscosity is higher during early stages of foaming, giving as a consequence a lower expansion ratio. Meanwhile, a higher amount of ureas, as it is the case of foam 3% A, involves higher CO_2 generation and therefore, a more substantial density decrease.

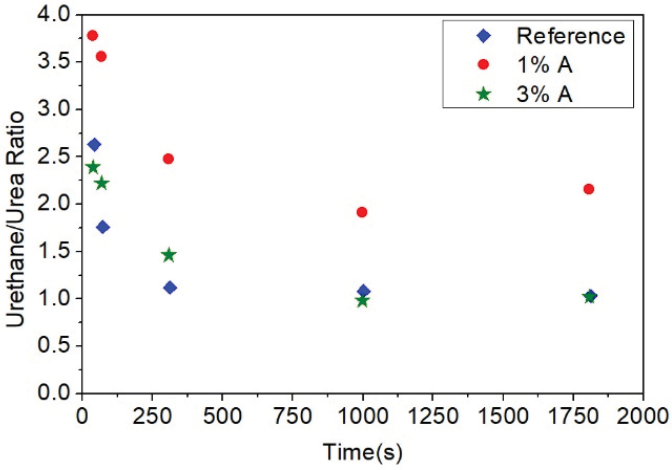

Figure 7-1-12: Relative area percentage of the absorbances of urea or urethane detected in the Amide I region at different stages of the foaming process.

3.4.2. Reaction temperature measurements

The reactions responsible for the generation of RPU foams, polymerization and blowing, are both exothermic. The heat liberated in the polymerization reaction is approximately 24 kJ mol^{-1} of urethane formed, while the blowing reaction releases 47 kJ mol^{-1} of urea generated [44]. During the formation of RPU, the centre of the foam is isolated from its surroundings, making it comparable to an adiabatic system.

Figure 7-1-13 represents the temperature reached by the foams Reference, 1% A and 3% A, versus time at different heights during its growing process. As it can be observed from the data reported in Table 7-1-2, Reference shows higher peak temperatures in all the measured regions of the foams. The higher temperature of the reference is the most remarkable for the upper areas of the foam, near the top, where the temperature recorded by the medium thermocouple inside the reference foam is on average 3.5 ºC higher than for the composite foams. There are also some significant differences when it comes to the time of reaction needed to reach the peak temperature. It is appreciated how the foam 3% A reaches its maximum internal temperature sooner than the reference and 1% A foams (on average around 1 minute before).

Eur. Polym. J. 135, 109884 (2020)

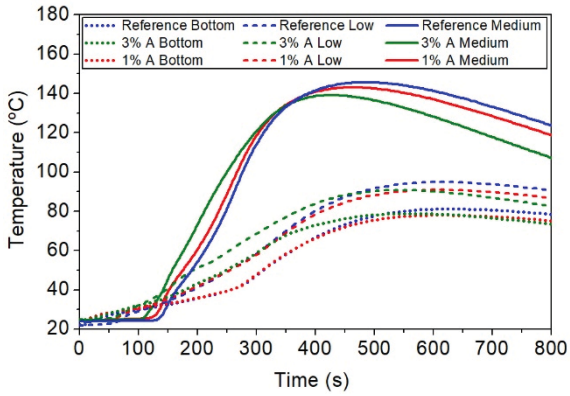

Figure 7-1-13: Temperature evolution during the foaming process detected by thermocouples for all the analysed samples.

Furthermore, since the reaction temperatures have been measured for sixty minutes, it is possible to monitor the temperatures during the cooling down process of the foam, as it progressively equilibrates its temperature to that of its surroundings. Thus, it is also possible to determine the heat dissipation speed of each foam as it cools down (Table 7-1-3). This cooling down rate has been calculated as the slope of the temperature decrease during twelve minutes from the maximum temperature registered.

Table 7-1-2: Maximum temperatures and time to reach them for the foams Reference, 1% A and 3% A.

Material	Bottom: Peak (°C)	Bottom: Peak time (s)	Low: Peak (°C)	Low: Peak time (s)	Medium: Peak (°C)	Medium: Peak time (s)
Reference	81.2 ± 2.3	625.3 ± 15.3	94.9 ± 2.1	611.7 ± 11.4	145.7 ± 1.8	483.3 ± 11.8
0.5% A	78.1 ± 1.0	612.5 ± 12.0	91.0 ± 1.1	609.0 ± 5.7	143.1 ± 1.1	458.5 ± 6.4
3% A	80.5 ± 2.2	534.5 ± 137.9	92.7 ± 2.9	539.5 ± 143.5	141.4 ± 2.8	420.5 ± 84.1

Table 7-1-3 reveals that 3% A has higher heat dissipation speeds in all areas in which the temperature has been monitored. The swifter dissipation speed of this foam is related to its elevated cell opening in contrast with the low open cell content of foams filled with fewer aerogel particles (Table 7-1-1). This cell opening also explains why 3% A seems to reach a lower internal temperature despite presenting the highest isocyanate conversion.

Table 7-1-3: Heat dissipation speed for the RPU foams containing 0 wt%, 1 wt% and 3 wt% of aerogel.

Material	Bottom: Temperature Cooling Speed (°C s^{-1})	Low: Temperature Cooling Speed (°C s^{-1})	Medium: Temperature Cooling Speed (°C s^{-1})
Reference	-0.027 ± 0.0006	-0.036 ± 0.0005	-0.078 ± 0.0013
1% A	-0.024 ± 0.0004	-0.035 ± 0.0016	-0.078 ± 0.0004
3% A	-0.031 ± 0.0049	-0.038 ± 0.0011	-0.093 ± 0.0011

3.5. Discussion

Cell nucleation power of aerogel particles has been demonstrated thanks to X-ray radioscopy. During the early stages of foaming higher cell nucleation density has been observed for all the aerogel concentrations tested (Figure 7-1-10). We have detected how the introduction of micro-sized aerogel particles also induces degeneration of the cellular structure. In the radioscopy sequences, it is appreciated that degeneration shows up as coalescence, which causes a significant reduction in the number of cells and increases the rate of cell growth as it can be seen in Figure 7-1-10. After a few minutes, when the foam expansion is almost completed, low aerogel content composite foams present a reduction of cell size with regard to the reference (around 16%). Meanwhile, the foam with a 3 wt% of aerogel particles suffers the strongest degeneration, showing at the end of the experiment cell sizes 10% larger than the reference. These modifications in the cellular structure with the addition of aerogel are confirmed in the large foams produced with 50 g of material (Section 2.2.1). In the cured samples 0.5% A and 1% A a reduction of approximately 26% has been measured, whereas 3% A reveals a 10% increase in its average cell size (Table 7-1-1). Consequently, in foams with low contents of aerogel, the final cell size is reduced with respect to Reference because nucleation prevails over coalescence in these systems. Whereas, in foams with high contents of aerogel the size and number of these particles boost degeneration which prevails over nucleation leading to a material with larger cells than the reference.

The onset of degeneration mechanisms can be explained when considering the reaction products. The results of Figure 7-1-12 indicate that foams Reference and 3% A follow similar product balance during the monitored time. Both begin with a superior number of urethane products, but after a few minutes, the amount of urethane and urea products equates. We hypothesise that when cells impinge the matrix is still highly viscous, and the presence of large particles induces significant cell wall instability: promoting drainage of material from

Eur. Polym. J. 135, 109884 (2020)

the cell walls to the struts and ruptures of the walls. Besides, it is to be noted that employing a 3 wt% of aerogel (particle density 150 kg m^{-3}) entails introducing into the foam a considerable number of particles, around $7 \cdot 10^9$ particles in total –assuming that they have an average diameter of 15 μm. Considering that for a foam of 40 kg m^{-3}, average cell density is close to $5 \cdot 10^3$ cells cm^{-3} and that cells are shaped like pentagonal dodecahedrons there will be no more than $3 \cdot 10^4$ struts cm^{-3}, it is clear that the majority of particles will be agglomerated in the struts since they are unlikely to be hosted in the cell walls.

On the other hand, the kinetic balance changes significantly when 1 wt% of aerogel is added. In this case, for the whole experiment time, an enhancement of the polymerization reaction (generation of more urethane products) is detected. In turn, an effective cell size reduction is reached, both in the in-situ experiment and in the large-sized foam. A possible rationale to explain this fact may be that a stronger polymerization promotes a swifter cellular structure stabilization. Then the polymer matrix vitrifies more readily, and hence the material that forms the walls attains higher viscosity in less time, making drainage and coalescence events less likely.

Relative density results at initial stages (60 s-150 s) show how aerogel delays the foam expansion. This fact is probably a consequence of the isocyanate's viscosity increase due to the presence of aerogel particles and the enhancement of the polymerization reaction (rise in the number of urethane groups) as observed by *in-situ* FTIR spectroscopy. In the final stages (t>5 min) and final foam Reference and 3% A present comparable expansion (physical interaction) which might be motivated by the similar isocyanate conversion (Figure 7-1-11) and number of products (chemical interaction) measured in both materials (Figure 7-1-12). Yet, foams filled with small amounts of aerogel achieve lower expansion ratio because they undergo a swifter and more intense polymerization (as in-situ measured for foam 1% A). This explains why materials such as 0.5% A and 1% A end the foaming process with a slightly higher density than foams filled with higher aerogel contents.

The relationship between isocyanate conversion and reaction temperature has been studied in previous works [5,44]. It has been proposed that higher internal temperature during foaming may be linked to an increase in the isocyanate consumption and thus, a higher number of products generated. From Figure 7-1-13, it can be appreciated how the foams internal temperature drops with increasing content of particles. Even when the highest consumption of isocyanate was found for foam 3% A followed by Reference and 1% A. Yet, the higher content of open porosity (around 20%) of material 3% A might be acting

as an aid for rapid heat dissipation speed to the surroundings (Table 7-1-3) and consequently overshadowing the real internal temperature reached by this foam. This hypothesis is also supported by the time taken by each material to attain its peak temperature. In essence, 3% A takes on average 1 minute less than the foams with less open cell content. Thus, the faster temperature increase is in good agreement with the higher reaction speed as measured by FTIR spectroscopy.

4. CONCLUSIONS

The foaming evolution of aerogel RPU composite foams was investigated by X-ray radioscopy, FTIR spectroscopy and internal temperature evolution. The influence of aerogel particles on the cellular structure and polyurethane chemical reactions has been studied for the first time using *in-situ* experiments. Relative density evolution is slowed down by the presence of aerogel. The results at early stages also point out to the cell nucleation power of aerogel particles. Cell size evolution is strongly conditioned by the interaction of the particles with the natural reaction kinetics of Reference. Concentrations of aerogel above 1 wt% speed up and enhance the reactivity of the system. Large amounts of aerogel promote substantial coalescence. Particles, bigger than the polymeric matrix features (walls ~2 μm and struts > 15 μm [29]), act as spots for cell wall ruptures; increasing the generation of holes in the cell walls. These holes may act as sinks for heat dissipation and drive to low cell densities in the final foam. However, there is an optimum content of 1 wt% of aerogel that reduces the final foam cell size by boosting the polymerization, which in turn diminishes the number of cell walls ruptures and open cells.

All these results give valuable insight into the modifications suffered by an RPU formulation (Reference) when an external solid additive (aerogel micrometric particles) is dispersed into the raw materials before the foaming. The results obtained in this work can provide strategies to improve the formulations so that larger amounts of particles can be dispersed into the material producing at the same time good quality foams. On the one hand, the formulation could be modified to increase the polymerization reaction speed for all particle contents employing dedicated catalysts and surfactants, and hence preserving the increases in cell nucleation density. On the other hand, the presence of particles bigger than a few microns most certainly fosters cell wall ruptures since most of these particles only fit into the struts.

Regarding the discussion on the number of struts and powder size (section 3.5), it is clear that the particles will inevitably form aggregates. Good dispersion of particles in the matrix is essential when looking to reinforce the material's properties. Therefore, to maximize the benefits of incorporating aerogel, the particle size should be trimmed so that they can also be hosted in the walls and not only agglomerated in the struts.

5. ACKNOWLEDGEMENTS

Financial assistance from the Junta of Castile and Leon (VA275P18) and Spanish Ministry of Science, Innovation and Universities (RTI2018-098749-B-I00) is gratefully acknowledged. Authors thank Cabot Corporation for supplying us with Enova® Aerogel IC3100 powder. Financial support from Junta de Castilla y Leon predoctoral grant of P. Cimavilla-Román, co-financed by the European Social Fund is acknowledged.

6. REFERENCES

[1] L. Chen, L.S. Schadler, R. Ozisik, An experimental and theoretical investigation of the compressive properties of multi-walled carbon nanotube/poly(methyl methacrylate) nanocomposite foams, Polymer (Guildf). 52 (2011) 2899–2909.

[2] X. Han, C. Zeng, L.J. Lee, K.W. Koelling, D.L. Tomasko, Extrusion of polystyrene nanocomposite foams with supercritical CO2, Polym. Eng. Sci. 43 (2003) 1261–1275.

[3] J.Q. Wang, W.K. Chow, A brief review on fire retardants for polymeric foams, J. Appl. Polym. Sci. 97 (2005) 366–376.

[4] S. Estravís, J. Tirado-Mediavilla, M. Santiago-Calvo, J.L. Ruiz-Herrero, F. Villafañe, M.A. Rodríguez-Pérez, Rigid polyurethane foams with infused nanoclays: Relationship between cellular structure and thermal conductivity, Eur. Polym. J. 80 (2016) 1–15.

[5] M. Santiago-Calvo, V. Blasco, C. Ruiz, R. París, F. Villafañe, M.-Á. Rodríguez-Pérez, Synthesis, characterization and physical properties of rigid polyurethane foams prepared with poly(propylene oxide) polyols containing graphene oxide, Eur. Polym. J. 97 (2017) 230–240.

[6] O.A. Almanza, M.A. Rodriguez-Perez, J.A. De Saja, Prediction of the radiation term in the thermal conductivity of crosslinked closed cell polyolefin foams, J. Polym. Sci. Part B Polym. Phys. 38 (2000) 993–1004.

[7] L.J. Lee, C. Zeng, X. Cao, X. Han, J. Shen, G. Xu, Polymer nanocomposite foams, Compos. Sci. Technol. 65 (2005) 2344–2363.

[8] M. Szycher, Szycher's handbook of Polyurethanes, 2nd Ed, Taylor & Francis Group, London, 2013.

[9] S. Pardo-Alonso, E. Solórzano, S. Estravís, M.A. Rodríguez-Perez, J.A. de Saja, In situ evidence of the nanoparticle nucleating effect in polyurethane–nanoclay foamed systems, Soft Matter. 8 (2012) 11262.

[10] M.M. Bernal, M.A. Lopez-Manchado, R. Verdejo, In situ foaming evolution of flexible polyurethane foam nanocomposites, Macromol. Chem. Phys. 212 (2011) 971–979.

[11] M. Mar Bernal, S. Pardo-Alonso, E. Solórzano, M.Á. Lopez-Manchado, R. Verdejo, M.Á. Rodriguez-Perez, Effect of carbon nanofillers

on flexible polyurethane foaming from a chemical and physical perspective, RSC Adv. 4 (2014) 20761.

[12] A. Kausar, Polyurethane Composite Foams in High-Performance Applications: A Review, Polym. - Plast. Technol. Eng. 57 (2018) 346–369.

[13] M.C. Saha, M.E. Kabir, S. Jeelani, Enhancement in thermal and mechanical properties of polyurethane foam infused with nanoparticles, Mater. Sci. Eng. A. 479 (2008) 213–222.

[14] S.H. Kim, M.C. Lee, H.D. Kim, H.C. Park, H.M. Jeong, K.S. Yoon, B.K. Kim, Nanoclay reinforced rigid polyurethane foams, J. Appl. Polym. Sci. 117 (2010) 1992–1997.

[15] S. Pardo-Alonso, E. Solórzano, M.A. Rodriguez-Perez, Time-resolved X-ray imaging of nanofiller-polyurethane reactive foam systems, Colloids Surfaces A Physicochem. Eng. Asp. 438 (2013) 119–125.

[16] J. Li, X. Mo, Y. Li, H. Zou, M. Liang, Y. Chen, Influence of expandable graphite particle size on the synergy flame retardant property between expandable graphite and ammonium polyphosphate in semi-rigid polyurethane foam, Polym. Bull. (2018) 1–18.

[17] W. Wang, H. Pan, B. Yu, Y. Pan, L. Song, K.M. Liew, Y. Hu, Fabrication of carbon black coated flexible polyurethane foam for significantly improved fire safety, RSC Adv. 5 (2015) 55870–55878.

[18] C. Zhao, Y. Yan, Z. Hu, L. Li, X. Fan, Preparation and characterization of granular silica aerogel/polyisocyanurate rigid foam composites, Constr. Build. Mater. 93 (2015) 309–316.

[19] A. Dourbash, C. Buratti, E. Belloni, S. Motahari, Preparation and characterization of polyurethane/silica aerogel nanocomposite materials, J. Appl. Polym. Sci. 134 (2017) 1–13.

[20] N. Nazeran, J. Moghaddas, Synthesis and characterization of silica aerogel reinforced rigid polyurethane foam for thermal insulation application, J. Non. Cryst. Solids. 461 (2017) 1–11.

[21] M. Martin-Gallego, M.M. Bernal, M. Hernandez, R. Verdejo, M.A. Lopez-Manchado, Comparison of filler percolation and mechanical properties in graphene and carbon nanotubes filled epoxy nanocomposites, Eur. Polym. J. 49 (2013) 1347–1353.

[22] A. Soleimani Dorcheh, M.H. Abbasi, Silica aerogel; synthesis, properties and characterization, J. Mater. Process. Technol. 199 (2008) 10–26.

[23] H. Zhang, Y. Qiao, X. Zhang, S. Fang, Structural and thermal study of highly porous nanocomposite SiO2-based aerogels, J. Non. Cryst. Solids. 356 (2010) 879–883.

[24] G. Wei, Y. Liu, X. Zhang, X. Du, Radiative heat transfer study on silica aerogel and its composite insulation materials, J. Non. Cryst. Solids. 362 (2013) 231–236.

[25] E. Solórzano, S. Pardo-Alonso, J.A. De Saja, M.A. Rodriguez-Perez, X-ray radioscopy in-situ studies in thermoplastic polymer foams, Colloids Surfaces A Physicochem. Eng. Asp. 438 (2013) 167–173.

[26] Cabot Corporation, Enova Aerogel Fine Particles, Saf. Data Sheet. (2012) 1–8.

[27] ASTM D1622-08: Standard Test Method for Apparent Density of Rigid Cellular Plastics, (n.d.).

[28] ASTM D6226-10. Standard Test Method for Open Cell Content of Rigid Cellular Plastics, (n.d.).

[29] S. Pérez-Tamarit, E. Solórzano, A. Hilger, I. Manke, M.A. Rodríguez-Pérez, Multi-scale tomographic analysis of polymeric foams: A detailed study of the cellular structure, Eur. Polym. J. 109 (2018) 169–178.

[30] S. Pardo-Alonso, X-Ray Imaging Applied to the Characterization of Polymer Foams ' Cellular Structure and Its Evolution, Universidad de Valladolid, 2014.

[31] E. Solórzano, J. Pinto, S. Pardo, F. Garcia-Moreno, M.A. Rodriguez-Perez, Application of a microfocus X-ray imaging apparatus to the study of cellular polymers, Polym. Test. 32 (2013) 321–329.

[32] M. Santiago-Calvo, J. Tirado-Mediavilla, J.L. Ruiz-Herrero, M.Á. Rodríguez-Pérez, F. Villafañe, The effects of functional nanofillers on the reaction kinetics, microstructure, thermal and mechanical properties of water blown rigid polyurethane foams, Polymer (Guildf). 150 (2018) 138–149.

[33] D.P. Queiroz, M.N. De Pinho, C. Dias, ATR-FTIR studies of poly(propylene oxide)/polybutadiene bi-soft segment urethane/urea membranes, Macromolecules. 36 (2003) 4195–4200.

[34] A. Marcos-Fernández, A.E. Lozano, L. González, A. Rodríguez, Hydrogen bonding in copoly(ether-urea)s and its relationship with the physical properties, Macromolecules. 30 (1997) 3584–3592.

[35] H. Sanaeishoar, M. Sabbaghan, F. Mohave, Synthesis and characterization of micro-mesoporous MCM-41 using various ionic liquids as co-templates, Microporous Mesoporous Mater. 217 (2015) 219–224.

[36] P. Wagh, R. Kumar, R. P. Patel, I. K. Singh, S. Ingale, S. Gupta, D. Mahadik, A. Venkateswara Rao, Hydrophobicity Measurement Studies of Silica Aerogels using FTIR Spectroscopy, Weight Difference Method, Contact Angle Method and K-F Titration Method, J. Chem. Biol. Phys. Sci. Volume 5 (2015) page no. 2350-59.

[37] P.B. Wagh, S. V. Ingale, Comparison of some physico-chemical properties of hydrophilic and hydrophobic silica aerogels, Ceram. Int. 28 (2002) 43–50.

[38] L.M. Johnson, L. Gao, C.W. Shields, M. Smith, K. Efimenko, K. Cushing, J. Genzer, G.P. López, Elastomeric microparticles for acoustic mediated bioseparations, J. Nanobiotechnology. 11 (2013).

[39] I. Cantat, S. Cohen-Addad, F. Elias, F. Graner, R. Höehler, O. Pitois, F. Rouyer, A. Saint-Jalmes, Foams: structure and dynamics, First Ed, Oxford University Press, Oxford, 2013.

[40] F. Garcia-Moreno, M. Mukherjee, C. Jiménez, A. Rack, J. Banhart, Metal Foaming Investigated by X-ray Radioscopy, Metals (Basel). 2 (2011) 10–21.

[41] J.S. Colton, N.P. Suh, Nucleation of microcellular foam: Theory and practice, Polym. Eng. Sci. 27 (1987) 500–503.

[42] M.J. Elwell, A.J. Ryan, H.J.M. Grunbauer, H.C. VanLieshout, An FTIR study of reaction kinetics and structure development in model flexible polyurethane foam systems, Polymer (Guildf). 37 (1996) 1353–1361.

[43] M. Akkoyun, E. Suvaci, Effects of TiO2, ZnO, and Fe3O4 nanofillers on rheological behavior, microstructure, and reaction kinetics of rigid polyurethane foams, J. Appl. Polym. Sci. 133 (2016) 1–14.

[44] N.S. Ramesh, S.T. Lee, Polymeric Foams: Mechanisms and Materials, First Ed, CRC Press, Boca Raton, 2004.

Section 7.3.

The effects of Silica Aerogel on the rheological behaviour and polymer matrix structure of Rigid Polyurethane foams

Paula Cimavilla-Román [a*], Saul Perez-Tamarit [a], Anja Vananroye [b], Paula Moldenaers [b], Miguel Ángel Rodriguez-Pérez [a,c]

[a] Cellular Materials Laboratory (CellMat), Condensed Matter Physics Department, University of Valladolid, Paseo Belen 7, Valladolid, 47011, Spain

[b] Department of Chemical Engineering, KU Leuven, 3001 Leuven, Belgium

[c] BioEcoUva. Research Institute on Bioeconomy, University of Valladolid, Spain

Published in: European Polymer Journal, 176, 111398, (2022)

DOI: 10.1016/j.eurpolymj.2022.111398

Graphical Abstract

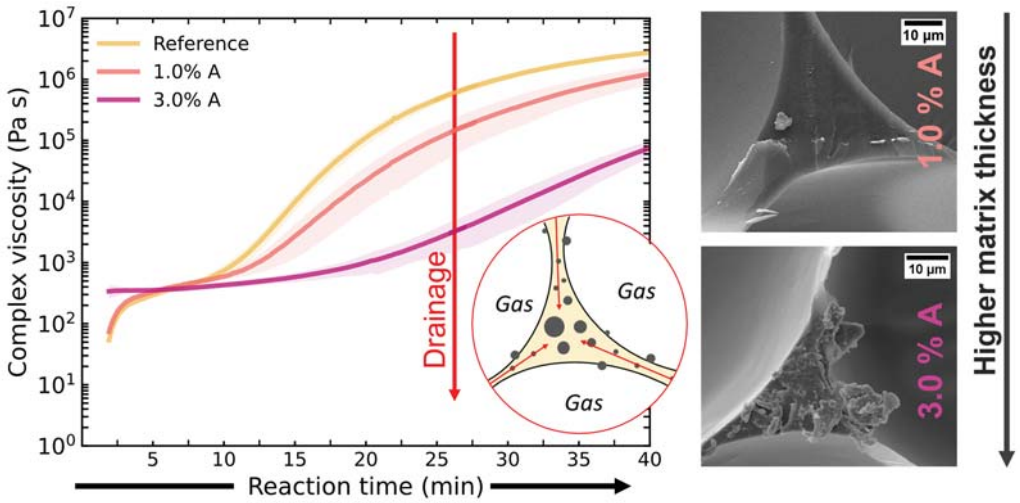

Eur. Polym. J. 176, 111398 (2022)

ABSTRACT

The incorporation of silica aerogel particles into the isocyanate used to prepare Rigid Polyurethane composite foams drastically modifies its rheological behaviour. The isocyanate changes from being a Newtonian fluid of constant viscosity (0.3 Pa s at 25 °C) to a non-linear power-law material with complex viscosity decreasing from 10^4 to 10^1 Pa s with a slope -1 versus frequency. The change in response is caused by the formation of a percolated network of particles at contents above 2.5 wt.% of aerogel. Moreover, the addition of aerogel significantly slows down the modulus-build up kinetics and vitrification of the matrix by approximately 4.5 min with every 1 wt.% of aerogel added. For the foam with 3.0 wt.% of aerogel, the combination of high viscosity at early reaction times coupled with the slow modulus build-up impedes the drainage which leads to a decrease in the fraction of material in the struts of the matrix.

KEYWORDS

Polyurethane foam; Silica aerogel; Rheology; Reaction kinetics; X-ray tomography

1. INTRODUCTION

The production of polymer composite foams is a well-known strategy to enhance the properties of the starting material by introducing a small amount of a secondary phase [1]. Since their establishment, composite foams have been produced using a wide array of fillers as reinforcement (fibres, flakes, micro- and nanoparticles) and all types of polymer matrices (thermoplastic, thermosets, or elastomers). The use of fillers with different morphologies and properties is a way of tailoring the final composite foam performance and range of applications [2,3]. However, obtaining superior foams is also conditioned by the final foam structure, which is affected by the filler dispersion and the matrix-filler interactions during foaming.

Among composite foams, Rigid Polyurethane (RPU) composites are receiving increasing attention for their enhanced mechanical performance and improved thermal insulation. The former is achieved by introducing inorganic reinforcements, *i.e.,* glass fibres, while the latter relies on novel fillers with low thermal conductivity, *i.e.*, aerogels [3–6]. In the case of thermal insulation, PU-aerogel composite foams are promising materials due to the favourable aerogel properties of low density, low thermal conductivity and flame retardancy [7–11]. Recently, several studies have been published dealing with the structure-properties relationship in PU-aerogel composite foams. Zhao et al. prepared Polyisocyanurate rigid (PIR) foams with varying content of granular silica aerogel [8]. The foam with a high content of aerogel (8 wt.%) showed a reduction of the thermal conductivity of 34.6%. However, the addition of aerogel particles does not always translate to a significant improvement of the original PU foam properties. In contrast, Kim et al. reported minimal thermal conductivity reductions when producing PU-silica aerogel foams [11]. This was attributed to the deterioration of the structure with increasing aerogel content. In terms of acoustic insulation notable enhancement was observed when producing Phenolic aerogel-flexible PU foams [10]. Improved sound absorption was attributed to a higher open porosity and reduced cell size caused by the phenolic aerogel incorporation. These discrepancies in the efficiency of aerogel particles are often attributed to either the presence of particle agglomerates or to a modification in the PU foaming reactions caused by the incorporation of the particles [12,13].

In a previous work, we evaluated the influence of different contents of powdered silica aerogel on the cellular structure generation and reaction kinetics of water-blown RPU

Eur. Polym. J. 176, 111398 (2022)

foams [6]. The composite RPU-aerogel foams were produced using isocyanate-aerogel dispersions. It was observed that the final cellular structure of the composite foams was the result of a combination of increased nucleation as well as degeneration caused by the aerogel particles. Moreover, a dissimilar foaming process was observed with increasing aerogel content. It was observed that foams with low contents of aerogel particles (≤1 wt.%) had a higher number of urethane cross-links and final cell sizes below that of the reference foam without particles. High contents of aerogel particles (3 wt.%) led to foams with a coarser cellular structure and larger cell sizes due to an increased number of degeneration events. However, the influence of the starting isocyanate-aerogel component on the cellular structure was not assessed.

Rheology has proven to be a useful method to gain insight into the dispersion quality in composites [14–17]. For instance, the formation of a network of interconnected particles can be detected from the volume fraction dependency of the low frequency storage modulus. By using a power-law relationship it is possible to obtain the percolation threshold of the composite and assess the dispersion state [16]. Both the initial viscosity of the components and the dispersion state influence the dynamic generation of the cellular structure [18,19]. It is well known that a faster polymerisation and modulus build-up can be an effective way of producing foams with smaller cell sizes while preventing degeneration [20,21]. Yet, there are few reports analysing the impact of the initial rheological behaviour and the viscoelastic transformations on the final polymer matrix organisation of RPU foams.

In the present work, the effect of silica aerogel particles on the rheological behaviour of the isocyanate component used to produce the RPU composite foams is evaluated. In addition, the effect of the aerogel particles on the rheological changes experienced during the reaction and curing of the foams is studied *in situ* using oscillatory shear rheology. Moreover, the present paper offers insight into how the rheological properties of the raw materials and reactive mixture modify the final polymer matrix distribution.

2. MATERIALS AND METHODS

2.1. Raw materials of the composite RPU foams

The polyol component was a blend of two high functionality polyether polyols, Alcupol R4520 (functionality of 4.5, OH value of 455 mg·KOH g^{-1}, viscosity: 5250 mPa s at 25 °C)

and Alcupol R3810 cross-linker (functionality of 3, OH value of 380 mg·KOH g^{-}, viscosity 350 mPa s at 25 °C), both from Repsol S.A. The isocyanate was a polymeric diphenylmethane diisocyanate (pMDI), IsoPMDI 92140 (31.5% NCO, density 1.23 g cm^{-3}, viscosity 170-250 mPa s at 25 °C) supplied by BASF. Polycat 8 (N,N-dimethyl cyclohexylamine) from Evonik was employed as a catalyst; it is a tertiary amine used primarily to promote the urethane (polyol-isocyanate) reaction. TEGOSTAB® B8522 (a non-hydrolysable polyether-polydimethylsiloxane–stabilizer) from Evonik was used as a surfactant to decrease the surface tension of the polyol and obtain superior cellular structures. Distilled water was employed as blowing agent.

Silica aerogel particles were provided in powder form by Cabot (Enova® Aerogel IC3100). According to the technical data, the particles have a density close to 0.15 g cm^{-3}, sizes ranging from 2 to 40 μm and an average pore diameter of 20 nm. In addition, the surface of the silica particles had been modified to give the powder a strong hydrophobic character [6]. The surface groups of the Silica Aerogel powder were previously studied by FTIR Spectroscopy which revealed the absence of Si-OH groups on the surface. It also permitted identifying the hydrophonic surface treatment which were Si-CH_3 bonds [6]. In other works the hydrophobicity of the powder was verified by investigating the contact angle of the Enova® Aerogel IC3100 powder with water using the sessile drop method [22]. The method indicated that the contact angle was high and close to 145°.

2.2. Preparation of the aerogel dispersions

The aerogel powder was dispersed in the isocyanate component with an overhead stirrer (EUROSTAR 60 control from IKA), equipped with a 50 mm diameter Vollrath™ Lenart-disc stirrer. Particle dispersions were performed at low shear stress values at 250 rpm for 5 minutes. Six weight concentrations were considered in this study: 0.5, 1.0, 2.0, 2.5, 3.0 and 3.5 wt. % aerogel particles. To prepare the dispersion, the particles were added to 13 g of isocyanate.

2.3. Preparation of RPU foams

Four different RPU foams were prepared while maintaining a constant isocyanate index. The formulations are presented in Table 7-2-1. While the polyol, surfactant, catalyst, and blowing agent contents were kept constant, the concentration of fillers was increased

Eur. Polym. J. 176, 111398 (2022)

resulting in four foams with different aerogel filler content (0 wt.%, 0.5 wt.%, 1 wt.%, 3 wt.%) dispersed in the isocyanate.

The blend of the polyols with the different components was prepared with an overhead stirrer (EUROSTAR 60 control from IKA), equipped with a 50 mm diameter Vollrath™ Lenart-disc stirrer. First, the polyol was mixed with the additives (catalyst, surfactant and blowing agent) at 250 rpm for 2 minutes. Secondly, the dispersion of the aerogel powder in the isocyanate component was carried out as described above (Section 2.2). Finally, to promote foam formation, a mixture of 50 g of isocyanate and polyol components was produced at 1200 rpm for 10 s. These foams were left to cure at room temperature for one week. After this period, the foams were cut, and the final density was measured.

Table 7-2-1. Formulations and aerogel concentration for the RPU composite foams.

Sample	Isocyanate Index	R4520 (ppw)	R3810 (ppw)	Surfactant (ppw)	Catalyst (ppw)	Water (ppw)	Aerogel (wt.%)
Reference	110	90	10	1	0.4	4	0.0
0.5% A	110	90	10	1	0.4	4	0.5
1.0% A	110	90	10	1	0.4	4	1.0
3.0% A	110	90	10	1	0.4	4	3.0

2.4. Particle size characterisation

Particles were characterized using two complementary techniques. The morphology of the particles was explored using high-resolution micrographs obtained with Scanning Electron Microscopy (SEM) model: QUANTA 200 FEG, whereas the average size and size distribution of the commercial aerogel powder was determined using laser diffraction, Malvern Mastersizer 3000 E (Malvern Instruments Ltd.).

2.5. Density determination

Foam densities were measured as described by ASTM D1622/D1622M-14 [23]. The density (ρ) was measured on three different samples for each foam using the geometric volume which was obtained from cylinders of 3 cm height and 3 cm of diameter. The relative density (ρ_r), which equals the volume fraction of solid in the foam, was obtained as the ratio between the foam geometric density and the solid material density (1160 kg m^{-3}).

2.6. Rheology of isocyanate-aerogel dispersions

The rheological behaviour of the aerogel dispersions used to produce the composite foams was studied with a strain-controlled ARES-G2 rotational rheometer (TA Instruments). Two different geometries were used depending on the particle loading of the dispersion. For low particle contents (below 2 wt.%) a double-wall concentric cylinder setup was used. For particle contents above or equal to 2 wt.% a parallel plate geometry (40 mm diameter) was employed with a gap of 1 mm. The use of these two different geometries allows to measure materials with viscosities of several orders of magnitude difference. The temperature was controlled with an Advanced Peltier System (APS) and maintained at 25 °C.

For every measurement, a freshly prepared aerogel dispersion (Section 2.2) was produced. In addition, to ensure reproducible initial conditions, a preshear protocol was applied which consisted of shearing the sample at 5 s^{-1} during 300 s to break the initial particle network. Subsequently, the sample was left at rest for 500 s. The conditioning protocol was followed by a dynamic strain sweep measurement, which permits to assess the linear viscoelastic region of the sample. Data were collected stepwise from 0.01 up to 100 % strain with 5 points per decade at an oscillation frequency of 10 rad s^{-1}. After obtaining the linearity limits, a new sample was loaded and the preshear protocol was applied. Then, dynamic frequency sweep experiments were performed in the linear viscoelastic region using frequencies from 100 to 0.1 rad s^{-1} with 5 points per decade.

2.7. Rheology during foaming

The evolution of the rheological properties during foaming of the raw materials was followed using a stress-controlled AR-G2 rotational rheometer (TA Instruments). Due to the large volume expansion of the mixture during the reaction, a flooded parallel plate geometry was employed as suggested by Mora et al. [24]. The setup consisted of a 25 mm stainless steel plate as upper geometry, and a 55 mm diameter stainless steel cup as bottom geometry. The cup was inserted in a Peltier Concentric Cylinder which allowed accurate control of the sample temperature, fixed to 25 °C.

A sample volume of 6.25 mL was loaded into the rheometer cup immediately after mixing the isocyanate with the polyol component. Then, the rheometer head was quickly lowered to a gap of 2.5 mm between the plate and the bottom of the cup, after which the

Eur. Polym. J. 176, 111398 (2022)

experiment was started. Since the sample starts reacting soon after mixing, the time period between finalizing the mixing and starting the experiment was kept as short as possible, of the order of 1.5 min.

Oscillatory time sweeps at a frequency of 1 rad s^{-1} were performed under controlled strain conditions for 1 h to characterise the rheological changes of the composite foam. To accommodate the large modulus build-up during curing, the strain was stepwise reduced during the experiments to remain below the linear strain limit and within the torque range of the device. A summary of the experimental conditions is given in Table 7-2-2. Each material was analysed in triplicate to check reproducibility. Due to foam expansion, both shear and elongational flow was present during the oscillatory experiment in the plate/plate rheometer. Hence, the obtained material properties are only apparent ones [24,25]. Yet, the comparison is still possible since all foams achieve similar expansion ratios.

Table 7-2-2: Applied strain and run times for the rheology experiments

Time (s)	Step 1		Step 2		Step 3	
	γ_1 %	t_1 (s)	γ_2 %	t_2 (s)	γ_3 %	t_3 (s)
3600	0.5	1200	0.05	1200	0.01	1200

2.8. X-ray Tomography

The X-ray Tomography set-up used in this work is shown in Figure 7-2-1. It consists of a microfocus X-ray source (Hamamatsu) with a maximum output power of 20 W (spot size: 5 µm, voltage: 20-100 kV, current: 0-200 µA). Emitted X-rays form a cone beam of 39°, allowing up to 20 times magnification. The transmitted X-ray intensity is collected with a high sensitivity flat panel detector connected to a frame grabber (Dalsa-Coreco), which records the projection images. The detector is composed of a matrix of 2240 x 2344 pixels^2, each with a size of 50 µm. Samples were mounted on top of a rotation stage (DT-65 N from PI Micos) located between the source and detector (SDD: 581 mm). The rotation stage is positioned on top of a linear stage which permits movement between the source and detector (SOD) while modifying the magnification factor. SOD was set to 29.05 mm, yielding an effective pixel size of 2.5 µm. The scanned samples were cylinders of approximately 7 mm^2 of base and 4 mm in height. Tube voltage, current, rotation step and exposure time were set to 50 kV, 170 µA, 0.3° and 1 s respectively. Each projection was the average of three consecutive radiographies for noise reduction.

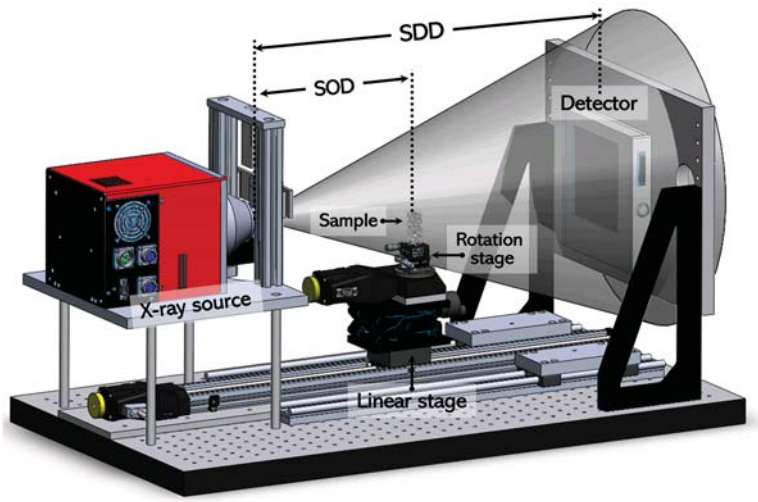

Figure 7-2-1: 3D rendering of the laboratory X-ray tomography set-up.

The tomography reconstructions were carried out using the Octopus package, which allowed obtaining cross-section images of the scanned volumes [26]. In the reconstructed images the fraction of mass in the struts, f_s, and struts thickness was measured using a previously reported image analysis methodology [27]. In this method, solid elements with thickness above the pixel size were binarised. Since the effective pixel size was larger than the thickness of cell walls, these were later retrieved using the Distance Transform Watershed (3D) algorithm implemented in the MorphoLibJ library (Fiji/ImageJ) [28]. Yet, with this procedure, the real walls were not retrieved as the Watershed generated walls had 1-pixel (*i.e.*, 2.5 μm) thickness. Nonetheless, walls were created in the right number and position, permitting to isolate neighbour cells. Afterwards, Local Thickness algorithm (Fiji/ImageJ) was applied to obtain the thickness distribution of the composite RPU-aerogel matrix [27,29].. After this step, the thickness histogram was calculated. The histogram was deconvoluted into two independent distributions depicting cell walls and struts. The deconvolution was achieved using asymmetric Log-Normal functions and from the area under each function, it was possible to obtain the tomographic value of $f_s^{\mu CT}$ using eq. (7-2-1) [27].

$$f_s^{\mu CT} = \frac{A_{st}}{A_{st} + A_w} \tag{7-2-1}$$

In eq. (7-2-1) A_{st} stands for the area under the struts, while A_w represents the area under the watershed walls distribution. To obtain the real f_s, a correction factor was applied (eq. (7-2-2)). The correction was grounded on the different relative densities obtained from the tomographic volumes, $\rho_r^{\mu CT}$, and in the foam samples, ρ_r^{Real} (see Table 7-2-3).

Eur. Polym. J. 176, 111398 (2022)

$$f_s = f_s^{\mu CT} \frac{\rho_r^{\mu CT}}{\rho_r^{Real}} \tag{7-2-2}$$

Struts thickness was calculated as the weighted average of the struts thickness function. In contrast, wall thickness (eq. (7-2-3)) δ was estimated using a theoretical approximation relating the thickness with the relative density of the foam, ρ_r, average cell size, Φ, the fraction of mass in the struts, f_s, and cell shape factor, C_n [29,30].

$$\Phi\,(1 - f_s)\,\rho_r = C_n\,\delta \tag{7-2-3}$$

In eq. (7-2-3) C_n depends on the cell shape and number of faces, n. As cells in RPU foams often take the shape of pentagonal dodecahedrons the value of C_n is 3.46 [30].

3. RESULTS AND DISCUSSION

3.1. Aerogel powder characterisation

The particle size distribution was examined using Laser diffraction (Figure 7-2-2 (a)). The technique revealed that the commercial aerogel particles had sizes ranging from 5 to 25 µm. The largest size detected was close to 25 µm, a considerably smaller value than the maximum size reported by the supplier (Section 2.1). From the volume fraction distribution of particle sizes, the volume mean diameter (eq. (7-2-4)) was calculated using the volume frequency, f_i, of particles in each size range, D_i.

$$D[4,3] = \frac{\sum D_i^4 f_i}{\sum D_i^3 f_i} \tag{7-2-4}$$

The resulting volume mean diameter was 10.9 µm, which agrees with the mean of the distribution in Figure 7-2-2 (a). In addition, SEM micrographs (Figure 7-2-2 (b)) also revealed irregular particles of quasi-spherical shape with a size close to 10 µm.

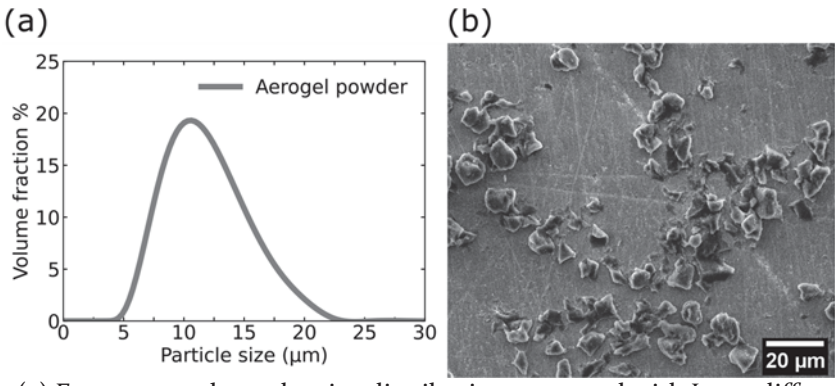

Figure 7-2-2: (a) Enova aerogel powder size distribution measured with Laser diffraction, (b) SEM micrographs of the aerogel powder dispersed in ethanol.

3.2. Composite foams density

Table 7-2-3 summarises the densities and relative densities of the large foams prepared in a 1 L disposable cup following the procedure in Section 2.3. As reported in previous work [32], density scarcely changed with the inclusion of aerogel particles. The sample with 3.0 wt.% of aerogel particles had the same density as the reference foam (without aerogel particles). On the contrary, foams with low aerogel content (0.5% A and 1.0% A) displayed a 5% increase in density with respect to the reference material.

Table 7-2-3: Density, relative density, and cell size of the PU-aerogel composite foams

Sample	Density (kg m-3)	Relative Density	Cell size (μm)
Reference	38.1 ± 0.5	0.033	412.5 ± 122.7
0.5% A	40.3 ± 0.1	0.035	309.6 ± 180.0
1.0% A	39.8 ± 0.8	0.034	290.7 ± 168.3
3.0% A	38.2 ± 0.4	0.033	454.7 ± 234.1

In addition, representative tomographic cross-sections of the cellular structure of the composite foams are shown in Figure 7-2-3. A progressive cell size decrease is seen with increasing aerogel concentration for composites with less than 1 wt.% of aerogel particles while a larger cell size is observed for the sample with 3.0 wt.% of aerogel particles. In Table 7-2-3 the average cell size, calculated as the diameter of a sphere with equivalent volume, is included [6].

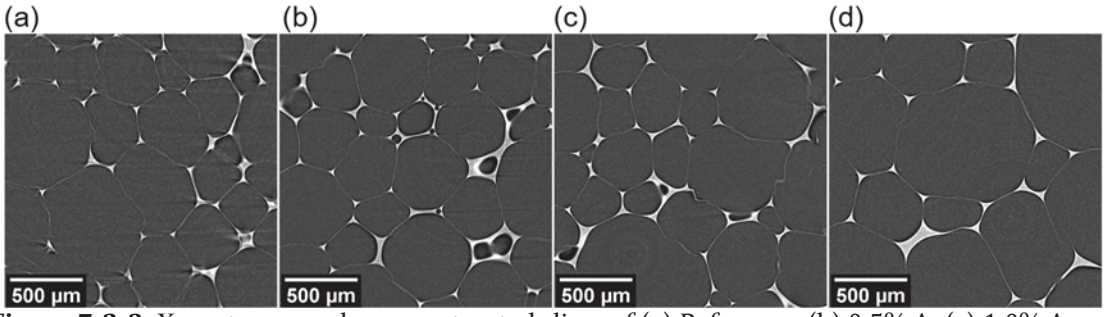

Figure 7-2-3: X-ray tomography reconstructed slices of (a) Reference, (b) 0.5% A, (c) 1.0% A and (d) 3.0% A

3.3. Rheology of the isocyanate-aerogel dispersions

Figure 7-2-4 displays the dependence of the complex viscosity of the isocyanate-aerogel dispersions on the applied angular frequency (ω). The pure isocyanate exhibits a characteristic Newtonian fluid behaviour with its complex viscosity (η^* = 0.32 Pa s) independent of the applied frequency. With the addition of aerogel particles, the complex

Eur. Polym. J. 176, 111398 (2022)

viscosity starts to increase. At high frequencies and low concentrations (≤ 1 wt.%), the dispersions reveal only a slight increase in η^* and a high frequency plateau is still visible. When the particle concentration rises beyond 1 wt.%, η^* increases substantially across the entire frequency range and becomes strongly non-Newtonian and highly dependent on the oscillation frequency. At the highest concentrations, η^* even becomes reversely proportional to ω (slope close to -1). Moreover, at low frequencies, the complex viscosity of the dispersion with only 3 wt.% of aerogel is nearly 5 orders of magnitude higher than the original isocyanate.

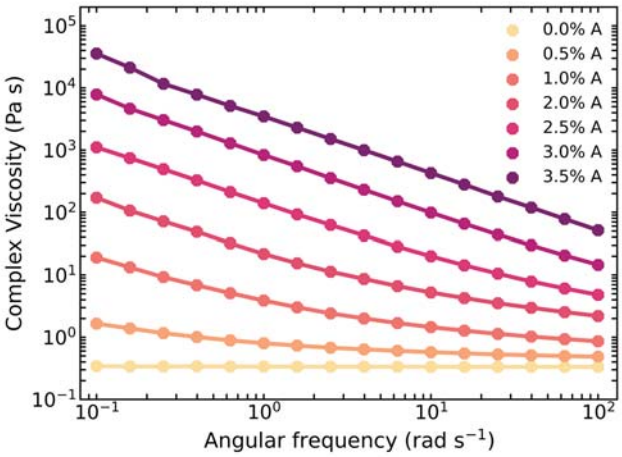

Figure 7-2-4: Complex viscosity as a function of the angular frequency of the isocyanate-aerogel dispersions with different particle loadings.

The viscoelastic nature of the dispersions is further explored by considering the storage (*G'*) and loss (*G''*) modulus variation with angular frequency (Figure 7-2-5). The pure isocyanate exhibits the expected slope of 1 for *G''* versus ω and approaches a slope of 2 for *G'*, corresponding to Newtonian fluids. With the incorporation of aerogel, both *G'* and *G''* increase across the entire frequency spectrum.

In the high-frequency range, the loss modulus of the dispersions (Figure 7-2-5 (b)) still shows viscous behaviour, characteristic of the isocyanate matrix, since curves of *G''* remain parallel to the pure isocyanate. However, with increasing aerogel content (>2.5 wt.%.) *G''* becomes more frequency independent with a small minimum at intermediate frequencies [33].

The impact of the aerogel addition is more severe on the storage modulus. *G'* undergoes a steep increase with increasing particle concentration while the slope of the curve decreases drastically even at low concentrations of aerogel (75% reduction in the slope with the addition of only 0.5 wt. %). As particle concentration increases, *G'* completely exceeds

G" indicating a liquid-to-solid transition at approximately 2.5 wt.%. At this concentration, *G'* starts to display a constant value over the entire frequency range as the slope approaches 0. The typical behaviour of *G'* and *G"* and the corresponding decrease in η^* as a function of frequency at high aerogel concentrations is characteristic of strong gel materials [33,34]., suggesting that the particle-particle interactions dominate over the polymer-particle interactions and a percolating network of touching particles is created providing the dispersions with increased elasticity [15,35].

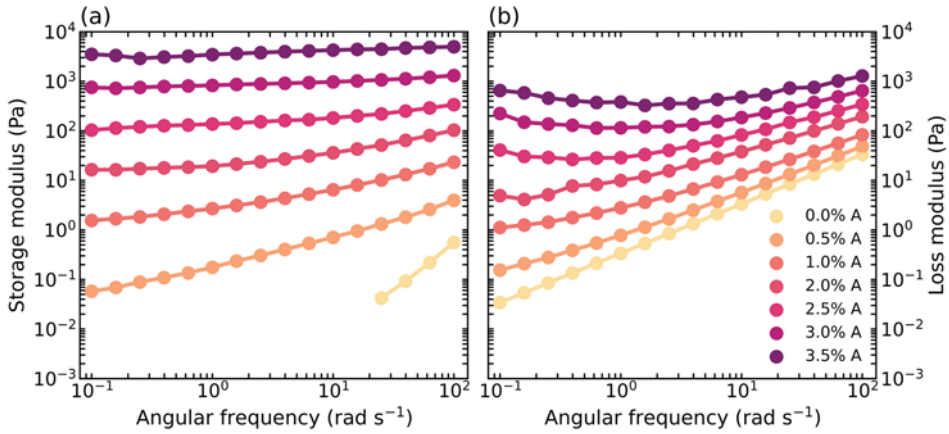

Figure 7-2-5: Frequency sweeps of the isocyanate-aerogel dispersions with different aerogel concentrations. Storage (a) and loss modulus (b) versus angular frequency.

Percolation models indicate that above a certain particle content, the low frequency storage modulus is highly dependent on the volume fraction [15,16]. This dependence of the elastic properties on the volume fraction can be expressed in the form of a power-law relationship.

$$G' \propto (\Phi - \Phi_P)^{\upsilon} \qquad (7\text{-}2\text{-}5)$$

In eq. (7-2-5), *G'* is the storage modulus at low frequencies, Φ stands for the volume fraction of particles, Φ_p is the percolation threshold and υ is the power-law exponent. Hence, by fitting the experimental storage modulus values at the lowest accessible frequency in Figure 7-2-5 (a), the percolation threshold can be calculated. The volume fraction of particles is calculated assuming an aerogel density of 0.15 g cm^{-3} (Section 2.1). Yet, as a reliable fit to eq. (7-2-5) cannot always be obtained, it is assumed that, for volume fractions above the percolation threshold, the storage modulus follows a linear fit and the intersection with the x-axis yields the value of Φ_p (Figure 7-2-6) [13,16]. Using the last three data points in Figure 7-2-6, a percolation threshold of 20.2 vol % is obtained, which corresponds to 2.6 wt. % of aerogel, in agreement with the volume fraction at which the dispersion attains solid-like behaviour (Figure 7-2-5).

Eur. Polym. J. 176, 111398 (2022)

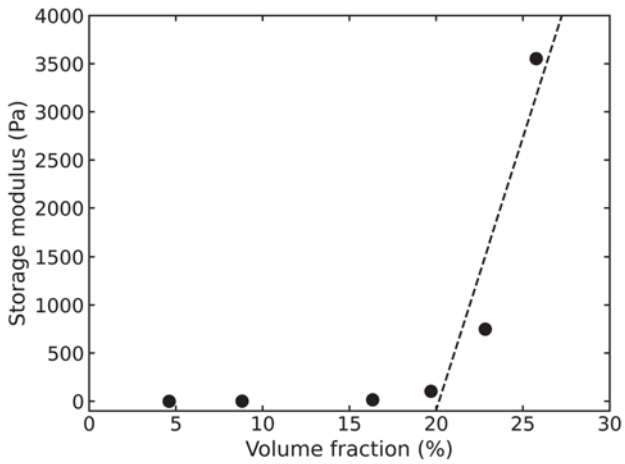

Figure 7-2-6: Variation of the storage modulus at 0.1 rad s^{-1} with the volume fraction of aerogel particles in the dispersion

3.4. Rheology during the composite foam development

The characterised dispersions were used to prepare the composite foams (Table 7-2-4) and their curing process was studied according to the experimental procedure detailed in Section 2.7. The evolution of the dynamic moduli and damping factor, *tan δ*, were monitored for 1 hour (Figure 7-2-7).

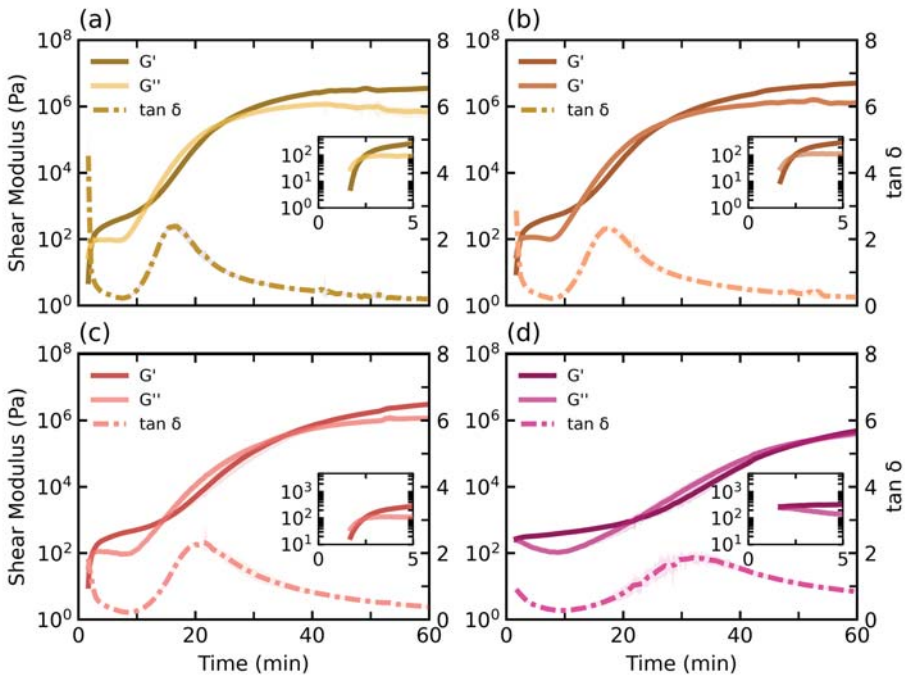

Figure 7-2-7: Shear moduli build-up profiles at 1 rad s^{-1} for (a) Reference (0 wt.% aerogel), (b) 0.5% A (0.5 wt.% aerogel), (c) 1.0% A (1 wt.% aerogel), (d) 3.0% A (3 wt.% aerogel)

The build-up of the viscoelastic moduli is severely impacted by the addition of aerogel particles. Foams prepared with low contents of aerogel (≤ 1 wt.%) begin the foaming

process in a viscous fluid state ($G'' > G'$ and $tan\ \delta > 1$), with the liquid like behaviour of the individual components dominating the behaviour of the mixture. For these samples, gelling (G' and G'' crossover shown in the insets of Figure 7-2-7) takes place approximately 2.3 min after mixing (Table 7-2-4). The composite with 3 wt. % of aerogel particles (Figure 7-2-4 (d)) already displays gel-like properties ($G' > G''$) at the start of the measurement since the dispersion used to produce this material is in a percolated state where particle interactions dominate (Section 3.3). Hence, despite the incorporation of a viscous polyol phase to prepare the composite, the initial rheological response of the mixture is dominated by the gel-like particle dispersion.

Upon gelation, all foams exhibit a solid-like response ($G' > G''$) accompanied by a slow increase of the moduli. During this period, the loss modulus remains nearly constant, while the storage component slowly increases [36]. The duration of this stage depends on the content of particles in the composite. Overall, the higher the aerogel content the longer this intermediate plateau. Previous studies have linked this plateau at early curing times to the behaviour of liquid foams, whose moduli remain nearly constant at high porosities [24,37].

Table 7-2-4: Characteristic times of the polymerisation process of RPU-aerogel foams

Samples	Gel Time (min)	Vitrification time (min)
Reference	2.32 ± 0.04	16.4 ± 0.5
0.5% A	2.35 ± 0.02	17.7 ± 0.7
1.0% A	2.34 ± 0.07	20.9 ± 0.6
3.0% A	/	31.9 ± 1.7

The second transition of major importance can be identified by the peak in the damping factor which represents *vitrification*. While the matrix vitrifies, both moduli undergo an increase of practically three orders of magnitude. At vitrification, molecular mobility is restricted since chemical reactions halt and become diffusion controlled [38]. While gelling times are not significantly affected by the presence of low concentrations of aerogel, vitrification is delayed by approximately 4.5 min with every extra addition of 1 wt.% of aerogel to the composite (Table 7-2-4). This delay is a consequence of the drastic increase in the isocyanate viscosity associated with the aerogel incorporation (Figure 7-2-4). High volume fractions of particles dispersed in isocyanate lower the mobility of the [NCO]

Eur. Polym. J. 176, 111398 (2022)

reacting groups which slows down the urethane reaction between polyol and isocyanate [39].

As curing progresses to the last stages, the increase of the moduli as a function of time levels off. Both moduli reach a plateau, and the material achieves its final properties. The time required to reach the final plateau also depends on the content of particles. Reference and 0.5% A samples reach the final moduli practically at the same time, *ca*. after 40 min. On the contrary, 1.0 % A and 3.0 % A are retarded by 10 and more than 20 min, respectively. Moreover, foam 3.0 % A did not even reach the cure moduli during the 1 hour measurement time.

In Figure 7-2-8, the complex viscosity evolution as a function of the reaction time of the four composites is shown. At early foaming times, a difference of more than one order of magnitude is detected between the low (≤ 1 wt.%) and high aerogel content (3 wt.%) composites. After the first five minutes of reaction, the complex viscosities of all foams with aerogel contents below 1 wt.% start to increase gradually until reaching the onset of vitrification. At this stage the increase slows down until stabilisation is achieved. On the other hand, sample 3 % A displays a constant viscosity during the initial 20 minutes of reaction. After this point the viscosity gradually increases. At equal reaction times, the complex viscosity value reached by each foam decreases with increasing aerogel content.

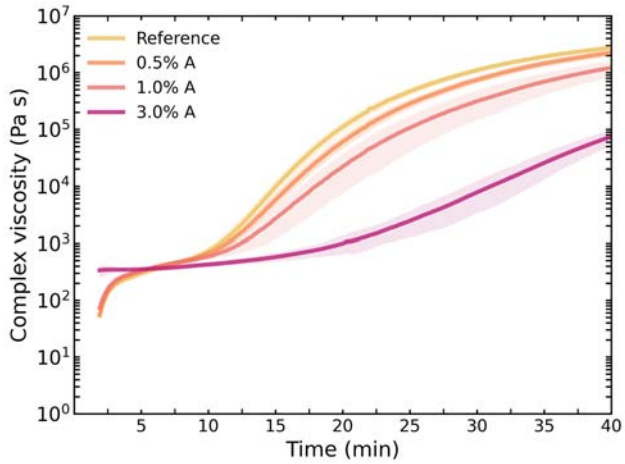

Figure 7-2-8: Complex viscosity evolution at 1 rad s^{-1} during cure obtained from oscillatory time sweeps.

3.5. Solid matrix characterisation

The foams prepared with 50 g of material (Section 2.3) were investigated using X-ray tomography (Section 2.8). Figure 7-2-9 shows the thickness distribution of the polymer matrix. The wall distribution, obtained after performing Watershed segmentation, is

centred at 5 μm. These walls are clearly thicker than real cell walls in RPU foams which normally have thicknesses close to 1 μm [12,40]. In contrast, the struts distribution is an accurate representation of the real struts in the foam. From Figure 7-2-9, it is seen that the thickness of the struts increases with the incorporation of aerogel particles. Reference and 0.5 % A (Figure 7-2-9 (a) and (b)) show very similar struts distribution of analogous maximum thickness, 57.7 μm and 54.3 μm respectively, whereas samples 1.0 % A and, in particular, 3.0 % A have a thicker matrix with a maximum thickness of 61.3 μm and 82.3 μm, respectively. The thickening of the struts with the addition of aerogel particles is also confirmed by the average strut thickness (Table 7-2-5).

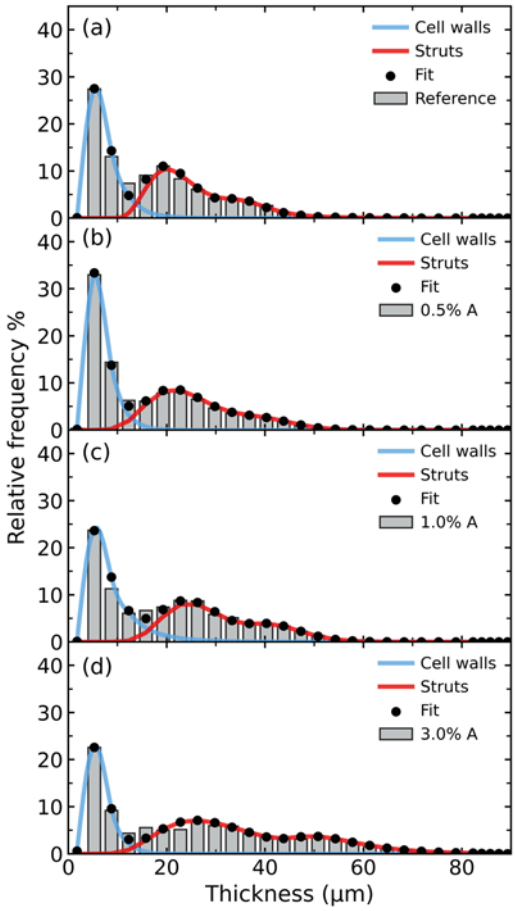

Figure 7-2-9: (a) Reference, (b) 0.5% A, (c) 1.0% A and (d) 3.0% A matrix thickness distributions. In blue, cell walls distributions and red, struts distributions were obtained from a combination of two Log-Normal functions.

The fraction of mass in the struts also changes remarkably with the aerogel content in the composite foams (Table 7-2-5). At low contents of aerogel, the struts' relative volume fraction grows with increasing thickness of these elements, thus the higher the particle content, the higher f_s. However, for the material produced with a percolated dispersion (3

Eur. Polym. J. 176, 111398 (2022)

wt.% of aerogel) the fraction of mass in the struts decreases despite showing thicker struts than the other foams.

In addition, average wall thickness was determined through a theoretical calculation based on eq. (7-2-3). The equation predicts a steady decrease in the cell wall thickness at low contents of aerogel particles. These foams show remarkably thin cell walls, below 1 μm, because of their small cell size and high porosity. In contrast, the cell walls thicken for a particle content of 3 wt.%. This thickening is related to the detected decrease in the fraction of material in the struts.

Table 7-2-5: Fraction of mass in the struts and thickness of the struts and walls (eq. **(7-2-3)**)

Samples	Struts thickness (μm)	Walls thickness (μm)	f_s
Reference	37.46	1.02	0.74
0.5% A	40.56	0.79	0.75
1.0% A	43.69	0.40	0.86
3.0% A	56.42	0.91	0.79

4. DISCUSSION

Polyurethane foams typically reveal polymer phase distributions with thin cell walls and the majority of the material is located in large struts ($f_s \approx 0.7$) [29,39]. The high fraction of mass in the struts is due to a foaming process prone to drainage from the cell walls to the struts when the mixture is in a fluid state. Factors such as the viscosity of the reactive mixture, the amount of gas being generated, and the speed of polymerisation drastically modify the intensity of degeneration mechanisms and the flow of material from the walls to the struts [41-43].

For the composite foams in this study, the thickness of the struts was observed to increase linearly with the addition of aerogel whereas the fraction of polymer in the struts changed non-linearly with the content of particles (Section 3.5). In previous work, the destabilizing effect of aerogel particles on the structure during foaming was revealed [6]. The micrometric particles trigger a large number of degeneration mechanisms, especially coalescence and broken cell walls, which cause cell size to increase long after foam expansion has stopped. Upon coalescence, two growing cells merge as a result of cell wall rupture. It was found that aerogel particles cause degeneration by two mechanisms: local thinning due to drainage and rupture of the walls by particles larger than the thickness of the cell walls [6,44]. The drainage rate is known to be inversely proportional to the viscosity.

Hence, at high viscosities, the flow of the material to the struts is retarded and the walls can remain longer at thickness above the critical rupture value [44].

Figure 7-2-6 shows that mixtures with low aerogel contents (≤1 wt.%) present a fluidlike viscous response at early foaming stages, similar to that of the starting isocyanate-aerogel dispersions (Figure 7-2-5). According to the literature, it is expected that the low viscosity mixture undergoes severe drainage to the struts upon impingement of the cells [43,44]. This intense flow drags most of the aerogel particles to the struts (Figure 7-2-10), explaining the detected thickening of the struts in the final foams (Table 7-2-5). Moreover, drainage involves local thinning of the walls which explains the high number of cell wall ruptures detected at short foaming times (< 5 min) as reported in previous work [6]. Based on SEM images, aerogel particles are also found to detach from the solid matrix and locate inside the cells (Figure 7-2-10). Potentially, a fraction of the large particles or aggregates are forced out of the walls. Drainage and coalescence proceed while the elastic component of the modulus is low ($G' \lesssim 10^3$ Pa). Consequently, upon solidification of the matrix (caused by the onset of vitrification, t ≈ 10 min) foams reveal a structure with a higher fraction of polymer in the struts and lower cell wall thickness than the unfilled reference foam (Table 7-2-5).

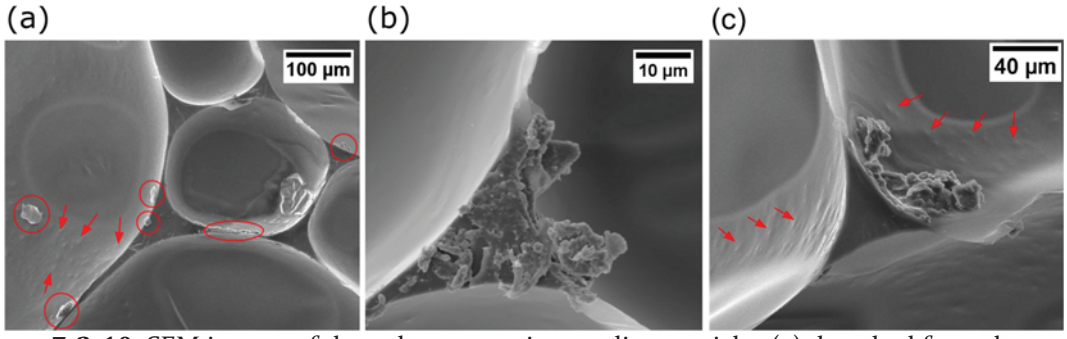

Figure 7-2-10: SEM images of the polymer matrix revealing particles (a) detached from the matrix (foam 1% A), (b) and (c) embedded in the struts (foams 3% A). Arrows indicate particles non exposed by the cross-sectional cut but embedded in the struts and also those showing up as ruggosities.

However, the composite with high content of aerogel particles (3 wt.%) presented a completely different rheological development and final structure. At high aerogel concentrations, a percolating network of particles was created, and the isocyanate dispersion showed the viscoelastic fingerprint of a strong gel (Figure 7-2-5). After stirring the components, the reactive mixture inherited the gel-like behaviour of the isocyanate-aerogel dispersion (Figure 7-2-7). Hence, foaming began with the mixture in a highly viscous gel-like state (Section 3.4) responsible for the slow foam expansion observed in

Eur. Polym. J. 176, 111398 (2022)

previous work [6]. Moreover, the high viscosity of the mixture also slowed down the drainage of reactive material and aerogel to the struts. Despite the reduction in drainage, coalescence in foam 3 % A was not inhibited and in fact, it was detected throughout the whole foaming process (11 min) [6]. On the one hand, the main mechanism responsible for coalescence is the disrupting effect of a high volume fraction (more than 20 vol%) of micrometric particles in the foam matrix. When the particles are located in the stiffening walls, the critical wall thickness is reduced triggering wall ruptures and a partially open cell structure in the final foams, which was not observed in the other composites [6]. Upon coalescence, the polymer mass located in the missing cell wall is redistributed between the struts and walls of the new cell, thickening the overall matrix. On the other hand, the enduring coalescence corresponds to the slower modulus build-up and delayed matrix vitrification, meaning that full hardening of the matrix takes longer to be achieved for the foam 3% A (Table 7-2-4). Therefore, the aforementioned phenomena are responsible for decreasing the fraction of polymer in the struts (Table 7-2-5). To summarise the previous ideas, drainage to the struts is slowed down by the high viscosity of the initial mixture, whereas coalescence, caused by aggregates, leads to larger cells with a thicker surrounding matrix which undergoes slow drainage and results in thicker cell walls than the composites with low aerogel content. Yet, while foam 3% A was prepared with a percolated dispersion of touching particles it was not possible to confirm by X-ray tomography whether the particles were also interconnected within the solid matrix of the foam. However, SEM micrographs of the structure of the composite foams (Figure 7-2-10) revealed the existence of a high density of particles in the struts of the cells. The particles can be detected both in the areas of the struts exposed by the cross-sectional cut and also embedded in the non-exposed struts. These particles show up as rugosities in the otherwise smooth struts. In addition, examination of the SEM micrographs confirmed the absence of aerogel particles in the cell walls. This is most likely due to the reduced thickness of the walls (Table 7-2-5) in which the aerogel particles do not fit due to their large size (~10 μm).

5. CONCLUSIONS

The present study reveals that foams with low contents of aerogel particles (≤ 1 wt.%) undergo an increase in the fraction of mass in the struts with increasing concentration of particles. This increase is accompanied by a thickening of the struts as the result of the drainage of both polymer and aerogel particles from the walls to the struts. This intense

drainage is a consequence of the low viscosity of the isocyanate-aerogel dispersions used to produce the RPU composite foams. At low concentrations of aerogel, the dispersions exhibit a fluid-like response and upon reaction with the polyol, the reactive mixtures have low viscosities until gelation is reached. Conversely, both the rheological behaviour and polymer matrix distribution change drastically at a particle content of 3 wt.%. The analysis of the low frequency values of the storage modulus of the starting isocyanate-aerogel component reveals that the percolation threshold weight fraction is at 2.6 wt%. Hence, in the dispersion with 3 wt.% of aerogel, the particles form an interconnected structure that restrains the motion of the polymer chains. In addition, the isocyanate-aerogel dispersion has a high viscosity which causes the 3.0% A composite foam to start its foaming process already in a gel-like state. For that reason, the material undergoes less drainage during foaming and the final composite foam reveals a polymer matrix distribution with a lower fraction of material in the struts and thicker cell walls.

6. ACKNOWLEDGEMENTS

Financial assistance from the Junta of Castile and Leon (VA202P20) and Spanish Ministry of Science, Innovation and Universities (RTI2018-098749-B-I00 and RTI2018 - 097367-A-I00) is gratefully acknowledged. Financial support from Junta de Castilla y Leon predoctoral grant of P. Cimavilla-Román, co-financed by the European Social Fund, is also acknowledged.

7. REFERENCES

[1] T. Sabu, K. Joseph, S.K. Malhotra, K. Goda, M.S. Sreekala, Polymer Composites, Macro- and Microcomposites, 1st ed., Wiley-VCH Verlag, 2012.

[2] L. Verdolotti, M.R. Di Caprio, M. Lavorgna, G.G. Buonocore, Polyurethane Nanocomposite Foams: Correlation Between Nanofillers, Porous Morphology, and Structural and Functional Properties, in: Polyurethane Polym. Compos. Nanocomposites, Elsevier Inc., 2017: pp. 277–310.

[3] V. Mittal, Polymer Nanocomposite Foams, First Edit, CRC Press, Abu Dhabi, 2013.

[4] H. Sanaeishoar, M. Sabbaghan, F. Mohave, Synthesis and characterization of micro-mesoporous MCM-41 using various ionic liquids as co-templates, Microporous Mesoporous Mater. 217 (2015) 219–224.

[5] K.J. Chang, Y.Z. Wang, K.C. Peng, H.S. Tsai, J.R. Chen, C.T. Huang, K.S. Ho, W.F. Lien, Preparation of silica aerogel/polyurethane composites for the application of thermal insulation, J. Polym. Res. 21 (2014).

[6] P. Cimavilla-Román, S. Pérez-Tamarit, M. Santiago-Calvo, M.Á. Rodríguez-Pérez, Influence of silica aerogel particles on the foaming process and cellular structure of rigid

polyurethane foams, Eur. Polym. J. 135 (2020) 109884.

[7] Y.X. Thong, X. Li, X.J. Yin, Determining the best flame retardant for rigid polyurethane foam—Tris(2-chloroisopropyl) phosphate, expandable graphite, or silica aerogel, J. Appl. Polym. Sci. 139 (2022) 51888.

[8] C. Zhao, Y. Yan, Z. Hu, L. Li, X. Fan, Preparation and characterization of granular silica aerogel/polyisocyanurate rigid foam composites, Constr. Build. Mater. 93 (2015) 309–316.

[9] A. Dourbash, C. Buratti, E. Belloni, S. Motahari, Preparation and characterization of polyurethane/silica aerogel nanocomposite materials, J. Appl. Polym. Sci. 134 (2017) 1–13.

[10] E. Hamamizadeh, H.A. Mahabadi, A. Khavanin, Investigating the Mechanical, Morphological, and Acoustic Properties of the Phenolic Aerogel/Flexible Polyurethane Foam Composite, J. Polym. Environ. (2022) 1–10.

[11] J.-H. Kim, J.-H. Ahn, J.-D. Kim, D.-H. Lee, S.-K. Kim, J.-M. Lee, Influence of Silica-Aerogel on Mechanical Characteristics of Polyurethane-Based Composites: Thermal Conductivity and Strength, Materials (Basel). 14 (2021) 1790.

[12] M. Santiago-Calvo, J. Tirado-Mediavilla, J.L. Ruiz-Herrero, M.Á. Rodríguez-Pérez, F. Villafañe, The effects of functional nanofillers on the reaction kinetics, microstructure, thermal and mechanical properties of water blown rigid polyurethane foams, Polymer (Guildf). 150 (2018) 138–149.

[13] M. Akkoyun, E. Suvaci, Effects of TiO2, ZnO, and Fe3O4 nanofillers on rheological behavior, microstructure, and reaction kinetics of rigid polyurethane foams, J. Appl. Polym. Sci. 133 (2016) 1–14.

[14] F.J. Galindo-Rosales, P. Moldenaers, J. Vermant, Assessment of the dispersion quality in polymer nanocomposites by rheological methods, Macromol. Mater. Eng. 296 (2011) 331–340.

[15] R. Van Hooghten, S. Gyssels, S. Estravis, M.A. Rodriguez-Perez, P. Moldenaers, Understanding the effect of particle surface free energy on the structural and mechanical properties of clay-laden rigid polyurethane foams, Eur. Polym. J. 60 (2014) 135–144.

[16] J. Vermant, S. Ceccia, M.K. Dolgovskij, P.L. Maffettone, C.W. Macosko, Quantifying dispersion of layered nanocomposites via melt rheology, J. Rheol. (N. Y. N. Y). 51 (2007) 429–450.

[17] A. Ballesteros, E. Laguna-Gutierrez, P. Cimavilla-Roman, M.L. Puertas, A. Esteban-Cubillo, J. Santaren, M.A. Rodriguez-Perez, Influence of the dispersion of Nanoclays on the cellular structure of foams based on polystyrene, J. Appl. Polym. Sci. 138 (2021) 1–19.

[18] B. Merillas, F. Villafañe, M.Á. Rodríguez-Pérez, Nanoparticles Addition in PU Foams: The Dramatic Effect of Trapped-Air on Nucleation, Polym. 2021, Vol. 13, Page 2952. 13 (2021) 2952.

[19] M. Mar Bernal, S. Pardo-Alonso, E. Solórzano, M.Á. Lopez-Manchado, R. Verdejo, M.Á. Rodriguez-Perez, Effect of carbon nanofillers on flexible polyurethane foaming from a chemical and physical perspective, RSC Adv. 4 (2014) 20761.

[20] M. Santiago-Calvo, V. Blasco, C. Ruiz, R. París, F. Villafañe, M.-Á. Rodríguez-Pérez, Synthesis, characterization and physical properties of rigid polyurethane foams prepared with poly(propylene oxide) polyols containing graphene oxide, Eur. Polym. J. 97 (2017) 230–240.

[21] M. Santiago-Calvo, S. Pérez-Tamarit, P. Cimavilla-Román, V. Blasco, C. Ruiz, R. París, F. Villafañe, M.Á. Rodríguez-Pérez, X-ray radioscopy validation of a polyol functionalized with graphene oxide for producing rigid polyurethane foams with improved cellular structures, Eur. Polym. J. 118 (2019) 404–411.

[22] F. Raoufi, Z. Ranjbar, S. Rategar, E. Nowak, B. Nazari, Wettability study of super-hydrophobic silica aerogel powders, Prog. Color. Color. Coatings. 13 (2020) 75–83.

[23] ASTM D1622-08: Standard Test Method for Apparent Density of Rigid Cellular Plastics, (n.d.).

[24] E. Mora, L.D. Artavia, C.W. Macosko, Modulus development during reactive urethane foaming, J. Rheol. 35 (1991) 921–940.

[25] R. Bouayad, J. Bikard, J.F. Agassant, Compressible flow in a plate/plate rheometer: Application to the experimental determination of reactive expansion's models parameters for polyurethane foam, Int. J. Mater. Form. 2 (2009) 243–260.

[26] M. Dierick, B. Masschaele, L. Van Hoorebeke, Octopus, a fast and user-friendly tomographic reconstruction package developed in LabView®, Meas. Sci. Technol. 15 (2004) 1366–1370.

[27] P. Cimavilla-Román, S. Pérez-Tamarit, S. Barroso-Solares, J. Pinto, M.Á. Rodríguez-Pérez, Sub-pixel Tomographic Methods for Characterizing the Solid Architecture of Foams, Microsc. Microanal. (2022) 1–12.

[28] D. Legland, I. Arganda-Carreras, P. Andrey, MorphoLibJ: Integrated library and plugins for mathematical morphology with ImageJ, Bioinformatics. 32 (2016) 3532–3534.

[29] R. Dougherty, K.-H. Kunzelmann, Computing Local Thickness of 3D Structures with ImageJ, Microsc. Microanal. 13 (2007) 1678–1679.

[30] S. Pardo-Alonso, E. Sorlórzano, L. Brabant, P. Vanderniepen, M. Dierick, L. Van Hoorebeke, M.A. Rodríguez-Peréz, 3D Analysis of the progressive modification of the cellular architecture in polyurethane nanocomposite foams vía X-ray microtomography, Eur. Polym. J. 149 (2013) 999–1006.

[31] N.C. Hilyard, A. Cunningham, Low density cellular plastics, 1st Ed, Springer Science & Business Media, 2012, London, 1994.

[32] P. Cimavilla-Román, M. Santiago-Calvo, M.Á. Rodríguez-Pérez, Dynamic Mechanical Analysis during polyurethane foaming: Relationship between modulus build-up and reaction kinetics, Polym. Test. 103 (2021) 107336.

[33] C. Vallés, R.J. Young, D.J. Lomax, I.A. Kinloch, The rheological behaviour of concentrated dispersions of graphene oxide, J. Mater. Sci. 49 (2014) 6311–6320.

[34] T. Varzakas, C. Tzia, Food engineering handbook: Food engineering fundamentals, Food Eng. Handb. Food Eng. Fundam. (2014) 1–569.

[35] S. Thankappan Nair, P.P. Vijayan, P. Xavier, S. Bose, S.C. George, S. Thomas, Selective localisation of multi walled carbon nanotubes in polypropylene/natural rubber blends to reduce the percolation threshold, Compos. Sci. Technol. 116 (2015) 9–17.

[36] M.C.D. Jawhar, D. Blanc, P. Chaumont, P. Cassagnau, Study of the Coalescence Mechanisms During Silicone Foaming, Macromol. Mater. Eng. 299 (2014) 336–343.

[37] H.M. Princen, A.D. Kiss, Rheology of Foams and Highly Concentrated Emulsions III. Static Shear Modulus, J. Japanese Soc. Hortic. Sci. 65 (1996) 121–127.

[38] C. Block, B. Van Mele, P. Van Puyvelde, G. Van Assche, Time-temperature-transformation (TTT) and temperature-conversion-transformation (TxT) cure diagrams by RheoDSC: Combined rheometry and calorimetry on an epoxy-amine thermoset, React. Funct. Polym. 73 (2013) 332–339.

[39] M. Abdalla, D. Dean, P. Robinson, E. Nyairo, Cure behavior of epoxy/MWCNT nanocomposites: The effect of nanotube surface modification, Polymer (Guildf). 49 (2008) 3310–3317.

[40] S. Pérez-Tamarit, E. Solórzano, A. Hilger, I. Manke, M.A. Rodríguez-Pérez, Multi-scale tomographic analysis of polymeric foams: A

detailed study of the cellular structure, Eur. Polym. J. 109 (2018) 169–178.

[41] L.W. Schwartz, R. V. Roy, A mathematical model for an expanding foam, J. Colloid Interface Sci. 264 (2003) 237–249.

[42] P. Ferkl, I. Krškova, J. Kosek, Evolution of mass distribution in walls of rigid polyurethane foams, Chem. Eng. Sci. 176 (2018) 50–58.

[43] S.T. Lee, Polymeric Foams: Science and Technology, Taylor & Francis, Boca Raton, 2007.

[44] N.S. Ramesh, S.T. Lee, Polymeric Foams: Mechanisms and Materials, First Ed, CRC Press, Boca Raton, 2004.

C APT

Thermal insulation in low density foams

THERMAL INSULATION IN LOW DENSITY FOAMS

8

8.1. INTRODUCTION

This chapter presents two publications dealing with the influence of the structure on the thermal insulation properties of two types of foams with the potential to replace traditional insulators.

In the first of the publications (The influence of Silica Aerogel on the Thermal Conductivity of Rigid Polyurethane Foams, submitted) we evaluate the influence of the aerogel particle concentration on the thermal properties of RPU foams. In this work, the thermal conductivity of foams with different aerogel concentrations (from 0 wt% to 1 wt%) is measured to understand the effect of the cellular structure and the presence of particles on thermal insulation performance. The thermal conductivity of the composite RPU-Aerogel foams was observed to decrease by about 1.4 mW (m K)$^{-1}$ with respect to the unfilled foam. Modelling of the heat transfer mechanisms revealed that the decrease was due to a combination of reduced cell size, thus, lower radiation heat transfer, and reduced matrix conduction, due to the presence of particles embedded in the matrix.

The second publication is entitled "Modelling of the mechanisms of heat transfer in recycled glass foams" and was published in 2021 in Construction and Building Materials (P. Cimavilla-Román et al., Constr. Build. Mater. 274, 122000 (2021), doi: 10.1016/j.conbuildmat.2020.122000). In this work, the mechanisms of heat transfer in recycled glass foams of various relative densities (from 0.032 to 0.070) were analytically modelled. Through a detailed characterisation of the solid matrix (using the methods discussed in Chapter 6), cellular structure and gas content in the cells, a specific model for these foams was built to predict the thermal conductivity. The predicted and experimental values of the thermal conductivity were compared, being the deviation below 2% for all foams. The thermal conductivity was observed to decrease from values close to 50 mW (m K)$^{-1}$ at 10 °C for a relative density of 0.07 to less than 40 mW (m K)$^{-1}$ for the foams with a

relative density of 0.035. In addition, at low relative densities, a threshold density value was found, below which the thermal conductivity does not further decrease.

Section 8.2.

The influence of Silica Aerogel on the Thermal Conductivity of Rigid Polyurethane Foams

Paula Cimavilla-Román [a]*, Mercedes Santiago-Calvo [a],
Miguel Ángel Rodríguez-Pérez [a,b]

[a] Cellular Materials Laboratory (CellMat), Condensed Matter Physics Department, University of Valladolid, Paseo Belen 7, Valladolid, 47011, Spain

[b] BioEcoUva. Research Institute on Bioeconomy, University of Valladolid, Spain

Submitted Manuscript

Graphical Abstract

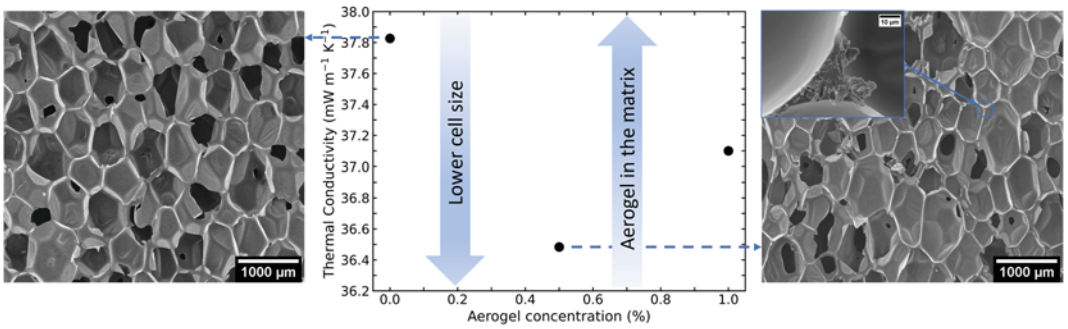

ABSTRACT

The preparation of Rigid Polyurethane-Silica Aerogel composite foams leads to reductions in the cell size of nearly 25% at a 0.5 wt.% aerogel content. The thermal conductivity of foams with 0.5 wt.% and 1.0 wt.% of aerogel was experimentally measured. A decrease of 1.35 mW m^{-1} K^{-1} in the thermal conductivity was obtained for foam 0.5% A compared to the unfilled RPU foam. The analysis of the mechanisms of heat transfer disclosed that the reduction was due to a decrease in the radiative heat transfer. In contrast, the foam with 1.0 wt.% of aerogel resulted in a smaller decrease in the thermal conductivity of 0.75 mW m^{-1} K^{-1}. In this case, the decrease was owed to a reduction in the polymer matrix conduction by the presence of super insulating aerogel particles of 12 mW m^{-1} K^{-1} conductivity.

KEYWORDS

Polyurethane foam; Silica aerogel; Thermal insulation; Thermal Conductivity; Heat Transfer

1. INTRODUCTION

Rigid Polyurethane foams (RPU) are a well-established class of thermal insulation materials widely used in construction and daily appliances [1–3]. Since their introduction in the early 1950s, low-density RPU foams have been used for thermal insulation purposes due to their low thermal conductivity. Nonetheless, the increasing need of more energy efficient materials has motivated intensive research in order to improve their performance. One approach which can help achieve this target is the use of fillers for the production of composite foams [4,5].

In the production of composite RPU foams typically inorganic particles, such as nanoclays and nanosilicas are used [6–9]. The addition of nanoparticles enhances nucleation during foaming and can potentially lead to a decrease in the final cell size of the foams [10]. Decreasing the average cell size in foams is an effective way of improving the thermal insulation properties of the material [11]. Hence, much research has been performed in this direction [12]. However, inorganic nanofillers often have higher thermal conductivities than the polymer matrix. For that reason, their addition is frequently associated to an increase in the heat transfer by solid conduction. Therefore, novel fillers of very low thermal conductivity, i.e., aerogels, have also been employed to prepare RPU composite foams [5,13–15]. PU-aerogel composite foams are promising materials due to the excellent aerogel properties of low density, low thermal conductivity and flame retardancy [16–20]. Recently, several studies have been published dealing with the structure-properties relationship in PU-aerogel composite foams. Zhao et al. prepared Polyisocyanurate rigid (PIR) foams with varying content of granular silica aerogel [17]. The foam with a high content of aerogel (8 wt.%) showed a reduction of the thermal conductivity of 34.6%. However, the addition of aerogel particles does not always translate to a significant improvement of the original PU foam properties. In contrast, Kim et al. reported minimal thermal conductivity reductions when producing PU-silica aerogel foams [20]. This was attributed to the deterioration of the structure with increasing aerogel content. In terms of acoustic insulation notable enhancement was observed when producing Phenolic aerogel-flexible PU foams [19]. Improved sound absorption was attributed to a higher open porosity and reduced cell size caused by the phenolic aerogel incorporation. Cho et al. [21] prepared PU foams with various contents of aerogels particles. The experimental measurement of the thermal

conductivity of aerogel–polyurethane composites revealed a 72% reduction upon 30 wt.% aerogel loading.

In the present work, we build on the previous findings by producing RPU-silica aerogel composite foams at different aerogel concentrations. The structure and thermal conductivity of the composite foams were characterised. Moreover, the mechanisms of heat transfer in the composite foams were modelled using theoretical and analytical models available in the current state of the art. Thanks to the modelling work, we were able to identify the mechanisms responsible for decreasing the thermal conductivity in the composite foam.

2. MATERIALS AND METHODS

2.1. Raw materials of the composite RPU foams

The polyol component was a blend of two high functionality polyether polyols, Alcupol R4520 (functionality of 4.5, OH value of 455 mg·KOH g^{-1}, viscosity: 5250 mPa s at 25 °C) and Alcupol R3810 cross-linker (functionality of 3, OH value of 380 mg·KOH g^{-1}, viscosity 350 mPa s at 25 °C), both from Repsol S.A. The isocyanate was a polymeric diphenylmethane diisocyanate (pMDI), IsoPMDI 92140 (31.5% NCO, density 1.23 g cm^{-3}, viscosity 170-250 mPa s at 25 °C) supplied by BASF. Polycat 8 (N,N-dimethyl cyclohexylamine) from Evonik was employed as a catalyst; it is a tertiary amine used primarily to promote the urethane (polyol-isocyanate) reaction. TEGOSTAB® B8522 (a non-hydrolysable polyether-polydimethylsiloxane–stabilizer) from Evonik was used as a surfactant to decrease the surface tension of the polyol and obtain superior cellular structures. Distilled water was employed as blowing agent.

Silica aerogel particles were provided in powder form by Cabot (Enova® Aerogel IC3100). According to the technical data, the particles have a density close to 0.15 g cm^{-3}, sizes ranging from 2 to 40 μm and an average pore diameter of 20 nm. In addition, the surface of the silica particles had been modified to give the powder a strong hydrophobic character [15].

2.2. Preparation of RPU foams

Four different RPU foams were prepared while maintaining a constant isocyanate index. The formulations are presented in Table 8-1-1. While the polyol, surfactant, catalyst, and

blowing agent contents were kept constant, the concentration of fillers was increased resulting in three foams with different aerogel filler content (0 wt.%, 0.5 wt.%, 1 wt.%) dispersed in the isocyanate.

The blend of the polyols with the different components was prepared in a disposable beaker with an overhead stirrer (EUROSTAR 60 control from IKA), equipped with a 50 mm diameter Vollrath™ Lenart-disc stirrer. First, the polyol was mixed with the additives (catalyst, surfactant and blowing agent) at 250 rpm for 2 minutes. Secondly, the dispersion of the aerogel powder in the isocyanate component was carried out with the same overhead stirrer. Particle dispersions were performed at low shear stress values at 250 rpm for 5 minutes. Finally, to promote foam formation, a mixture of 252.5 g of isocyanate and 135.1 g of polyol blend was produced at 1200 rpm for 10 s. The reactive mixture was immediately poured in an open cardboard mould of dimensions 25 x 20 x 20 cm^3 where the mixture was allowed to grow freely. These foams were left to cure at room temperature for one week. After this period, the foams were cut, and the final density was measured.

Table 8-1-1. Formulations and aerogel concentration for the RPU composite foams.

Sample	Isocyanate Index	R4520 (ppw)	R3810 (ppw)	Surfactant (ppw)	Catalyst (ppw)	Water (ppw)	Aerogel (wt.%)
Reference	110	90	10	1	0.4	4	0.0
0.5% A	110	90	10	1	0.4	4	0.5
1.0% A	110	90	10	1	0.4	4	1.0

2.3. Density determination

Foam densities were measured as described by ASTM D1622/D1622M-14 [22]. The density, ρ, was measured on a large sheet extracted from the middle of the foam. The sheet had dimensions of 15 x 15 x 2.8 cm^3. The relative density, ρ_r, which is equivalent to the volume fraction of solid in the foam, was obtained as the ratio between the foam geometric density and the solid material density (1160 kg m^{-3}).

2.4. Open cell content

The open cell content of the foams was determined in three different samples for each material. The samples had cylindrical dimensions of 30 mm diameter and 30 mm height. After measuring the densities of the cylindrical samples, the open cell content (OC%) was

measured (eq. (8-1-1)) by using a gas pycnometer Accupyc II 1340 from Micromeritics, according to ASTM D6226-10 [23].

$$OC = \frac{V - V_P}{V(1 - \rho_r)} \quad (8\text{-}1\text{-}1)$$

Where V is the geometric volume of the sample corrected to the volume of cells exposed on the surface of the sample, V_p is the volume measured with the pycnometer and $(1 - \rho_r)$ accounts for the porosity of the foam. The Nitrogen pressure used to determine the pycnometer volume was fixed at a constant value of 19.5 psig for all samples. The open cell content reported in this work represents the percentage of the material's porosity that is interconnected inside the sample and to the exterior so the gas can flow inside it.

2.5. Cellular structure

The foams' cellular structure was examined using a Scanning Electron Microscope (model Flex SEM 1000 Hitachi). The main descriptors of the cellular structure were characterised using specific software based on ImageJ/FIJI [24]. First, the average cell size, ϕ_{3D}, has been measured. This cell size in 3D is obtained from the cell size in 2D as $\Phi_{3D} = 1.273\ \Phi_{2D}$ (we have used the correction proposed by ASTM D3576-98 to calculate the cell size in 3D from the data in 2D obtained from SEM images). The standard deviation of the cell size distribution, *SD*, and the normalised standard deviation of the average cell size, *NSD*, have also been calculated. These last two parameters provide information about the cellular structure homogeneity. Besides, the anisotropy ratio, *AR*, was calculated as the ratio between the length of the cells in the foam growth direction divided by the corresponding length in the perpendicular direction. Thus, it represents the elongation of the cells along the foam expansion direction. To ensure the representativeness of the obtained values no less than 150 cells were analysed for each foam.

2.6. Thermal conductivity of the foams

The thermal conductivity measurements were made under steady heat flow conditions through the test samples (model FOX 314), following the ASTM C518-17 method. The measurements were conducted with the samples at a room temperature (20 °C). Thermal conductivity, λ, was calculated by measuring the heat flow through the test sample per time unit, q, as a result of the temperature gradient, ΔT, following Fourier's equation (eq. (8-1-

2)). The thermal conductivity was measured 12 times, but the average value was obtained from the last 5 measurement blocks.

$$q = \lambda A \frac{\Delta T}{d} \tag{8-1-2}$$

In eq. (8-1-2), d stands for the sample thickness, and A is the cross-sectional area of the sample calculated from a standard sample.

3. RESULTS AND DISCUSSION

3.1. Density and cellular structure characterisation

Table 8-1-2 summarises the densities and relative densities of the large prepared in a box following the procedure detailed in Section 2.2. Similarly to what it was observed for small samples [15], the density of the composites scarcely changes with the addition of aerogel. In fact, only a slight increase is observed for the sample with the highest aerogel content 1.0% A.

Table 8-1-2: Density, relative density, open cell and main cellular structure descriptors of the PU-aerogel composite foams.

Sample	ρ (kg m^{-3})	ρ_r	OC (%)	Φ_{3D} (μm)	NSD	AR	f_s
Reference	34.3	0.030	11.96	793.1 ± 160.8	0.20	1.39	0.74
0.5% A	34.3	0.030	18.27	602.1 ± 212.2	0.35	1.52	0.75
1.0% A	36.3	0.031	41.02	665.8 ± 281.4	0.42	1.35	0.86

In addition, representative SEM images of the cellular structure of the composite foams are shown in Figure 8-1-1. A progressive cell size decrease and an increase in the structure heterogeneity, *NSD*, is clearly seen with increasing aerogel concentration. In Table 8-1-2 the average cell size, calculated as described in Section 2.5 is included. Moreover, the anisotropy of the structure along the foam expansion direction is detected to increase substantially at a concentration of 0.5 wt.% of aerogel particles. As it was discussed in previous work [15] the addition of large contents of particles triggers a large number of degeneration mechanisms and cell walls ruptures. The latter is reflected in foam 1.0% A as an increase of the open cell content and small holes on the cell walls (Figure 8-1-1 (c)). When comparing with the structures obtained for smaller samples [15], it is detected that degeneration of the cellular structure happens at lower particle contents in large-sized samples. This scale effect

is not completely unexpected as it is well known that the reaction kinetics and foaming temperatures in PU largely vary depending on the sample mass [1].

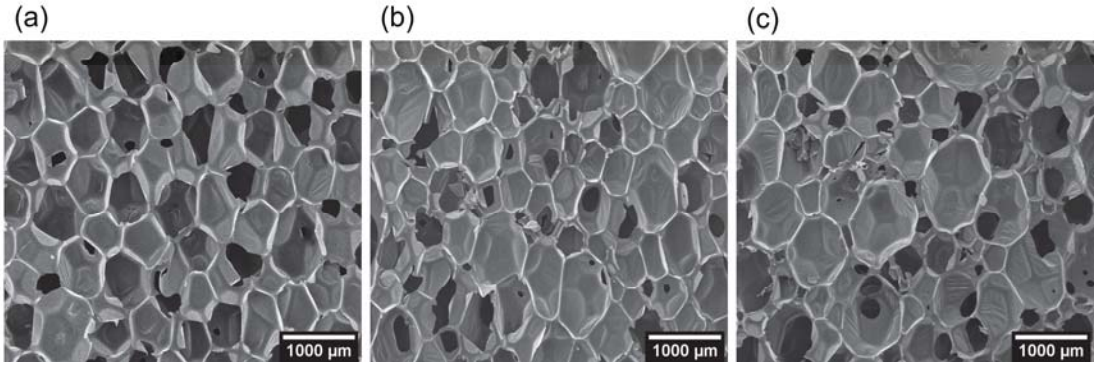

Figure 8-1-1: SEM micrographs of (a) Reference, (b) 0.5% A and (c) 1.0% A.

In previous work the influence of silica aerogel on the solid matrix organisation was studied [25]. The particles were found to be preferentially located in the struts and cell walls leading to an overall thickening of the matrix. In addition, the fraction of mass in the struts was observed to increase for low particle concentration (≤1 wt. %). While, this characterisation was performed on samples produced with low mass (50 g in total), it will be used as an estimation of the fraction of mass (Table 8-1-2) in the struts of the foams produced with 387 g of reactants.

3.2. Experimental: thermal conductivity

The evolution of the thermal conductivity of the foams was studied during the first weeks after production. From Figure 8-1-2 it can be seen how 21 days after production the thermal conductivity of all the foams had nearly stabilised. Previous works have demonstrated that after approximately one month since production, water-blown rigid polyurethane samples had reached a stationary state [6]. After a few weeks since production, most of the CO_2 generated during foaming is expected to have diffused out of the foam and replaced with air.

From Figure 8-1-2 (b) it is possible to detect a decrease in the thermal conductivity of the foams reinforced with aerogel. The foam 0.5% A underwent a decrease of 1.35 mW m^{-1} K^{-1}, whereas foam 1.0% A only underwent a 0.73 mW m^{-1} K^{-1} decrease. In this case, it is remarkable how despite the cell size increase and the appearance of open cells, the foam 1.0% A still reveals superior thermal insulation performance compared to Reference. To understand the reasons behind this thermal conductivity, decrease the analysis of the mechanisms of heat transfer has been previously proved to be helpful [6,7,26].

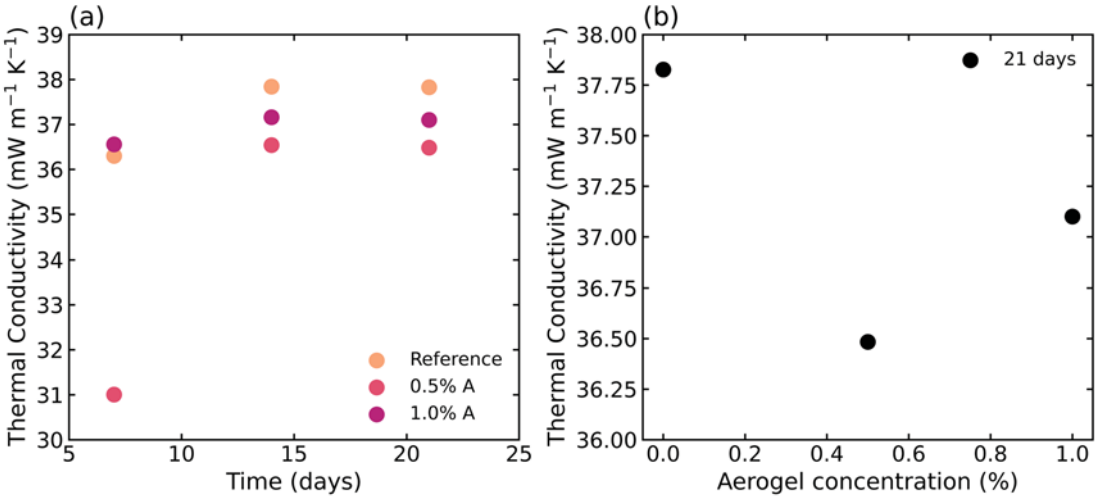

Figure 8-1-2: (a) Thermal conductivity evolution with time and (b) thermal conductivity after stabilisation of the gas diffusion process.

3.3. Prediction of the thermal conductivity

In foams, heat transfer is a combination of four main mechanisms: i) conduction through the gas phase, λ_g; ii) conduction through the solid phase, λ_s; iii) radiation heat transfer, λ_r; and iv) gas convection inside the cells, λ_c. The sum of these four terms represents the effective thermal conductivity of the foam λ_t, eq. (8-1-3).

$$\lambda_t = \lambda_g + \lambda_s + \lambda_r + \lambda_c \tag{8-1-3}$$

Several authors have noted that convection only contributes to the thermal conductivity of the foam when the cells are larger than 4 mm [27,28]. Therefore, for all the foams in Table 8-1-2, this term can be neglected.

In foams, gas is the predominant component. Hence, the main contribution to the total thermal conductivity is due to the gas filling the cells [6,29]. Gas conduction can be easily predicted in the case of foams composed of only one type of gas. This term is simply obtained as the product of the material's porosity and the gas conductivity, eq. (8-1-4). As discussed in Section 2.6, after 21 days since production all the CO_2 in the cells has been exchanged with air. Hence, for the modelling the gas conductivity, λ_{gas}, of air at 20 °C is considered, 25.7 mW m^{-1} K^{-1} [7].

$$\lambda_g = V_g \cdot \lambda_{gas} \tag{8-1-4}$$

The high porosity of RPU foams typically leads to relatively low contributions of the solid phase to the total thermal conductivity, often below 15%. However, it still represents an

non-negligible contribution since the thermal conductivity of the solid phase is typically high and in most cases the addition of nanoparticles contributes to increasing it even more [30]. In the literature, different equations have been proposed to analytically predict the thermal conductivity by conduction of the solid phase in a cellular material [31]. In this work, we use Glicksman equation (eq. (8-1-5)) [32]. It breaks the conduction of the solid in two terms, one accounting for the conduction due to struts and the other one due to cell walls.

$$\lambda_s = \lambda_{struts} + \lambda_{walls} = \frac{\rho_r}{3} \cdot f_s \lambda_{solid} \sqrt{AR} + \frac{2}{3} \rho_r (1 - f_s) \lambda_{solid} AR^{1/4} \qquad (8\text{-}1\text{-}5)$$

At 20 °C, the thermal conductivity of solid polyurethane, λ_{solid}, is close to 260 mW m^{-1} K^{-1} [6]. However, the presence of aerogel particles in the solid phase of the composite foams can impact the thermal conductivity of the matrix [25]. Hence, for the composite foams the value of the matrix conductivity will be reduced by the presence of aerogel. As an estimate of the solid matrix conductivity the rule of mixtures and the corresponding volume fraction of polymer, V_f^{PU}, and aerogel particles, $V_f^{aerogel}$, will be used (eq. (8-1-6)).

$$\lambda_{solid} = V_f^{PU}\, \lambda_{PU} + V_f^{aerogel}\, \lambda_{aerogel} \qquad (8\text{-}1\text{-}6)$$

The thermal conductivity of aerogel, $\lambda_{aerogel}$, reported by the manufacturer is close to 12 mW m^{-1} K^{-1}. This is much lower than the conductivity of the polymer the matrix and thus, the matrix conductivity is reduced by nearly 8% for a concentration of 1 wt.% (Table 8-1-3).

Table 8-1-3: Solid matrix conductivity and extinction coefficient of the foams.

Sample	λ_{matrix} (mW m^{-1} K^{-1})	$K_{e,R}$ (m^{-1})
Reference	260.0	1118.73
0.5% A	248.6	1357.1
1.0% A	238.1	1211.7

Last but not least, the third mechanism contributing to the thermal conductivity of foams is due to the electromagnetic radiation. The transmitted thermal radiation through a material, depends on its thickness and most importantly on its extinction coefficient, $K_{e,R}$, which accounts for all the absorption and scattering events that take place inside the material [32]. The extinction coefficient of foams can be modelled using an equation proposed by Glicksman et al. [32]. The authors considered the foam as a combination of

randomly oriented cell walls that absorb radiation and blackbody struts, which scatter all the radiation incident upon them. The struts contribution to the extinction coefficient depends on the cellular structure and density. Cell walls have an extinction coefficient, K_{ws}, which is a function of the amount of solid in the walls and the extinction coefficient of the matrix K_w (eq. (8-1-7)). In this study, it is assumed that the extinction coefficient of the matrix is that of solid PU, K_w = 460 cm^{-1}, and does not change with the addition of aerogel particles.

$$K_{e,R} = K_s + K_{ws} = 4.10\frac{\sqrt{f_s \cdot \rho_r}}{\Phi} + (1 - f_s)\rho_r K_w \qquad (8\text{-}1\text{-}7)$$

In Table 8-1-3, the extinction coefficient of the composite foams can be seen to increase with respect to the Reference foam. The decrease in cell size caused by the addition of aerogel particles is responsible for increasing the scattering by the struts. Whereas the increase in the fraction of mass in the struts (Table 8-1-1) decreases the scattering by the cell walls.

In low density foams, thermal radiation only travels short distances before suffering from absorption or scattering and it is possible to model radiative heat transport as a diffusion process inside the foam. This result is known as Rosseland diffusion equation (eq (8-1-8)) [32]. For the calculation, this equation considers the extinction coefficient of the foam, $K_{e,R}$, Stefan–Boltzmann constant, σ, and the temperature of the sample, T.

$$\lambda_r = \frac{16\sigma T^3}{3K_{e,R}} \qquad (8\text{-}1\text{-}8)$$

The sum of all contributions leads to the total thermal conductivity of the foam. In Figure 8-1-3 (a) the predicted thermal conductivity values are presented. It is possible to see a similar trend to the one detected experimentally (Figure 8-1-2). The model predicts a reduction of approximately 1.3 mW m^{-1} K^{-1} in the case of foam 0.5% A. Whereas, for foam 1.0% A the decrease is close to 1 mW m^{-1} K^{-1}. The estimated thermal conductivity decrease for foam 0.5% A agrees rather well with the experimental data. However, the predicted thermal conductivity of foam 1.0% A is lower than the experimental value. Most probably, this discrepancy is due to the increase in the open cell content in foam 1.0% A. It is known that the appearance of open cells and broken cell walls causes the thermal conductivity by radiation to increase [8]. However, this factor has not been considered in the thermal conductivity model, hence, constituting a potential source of error.

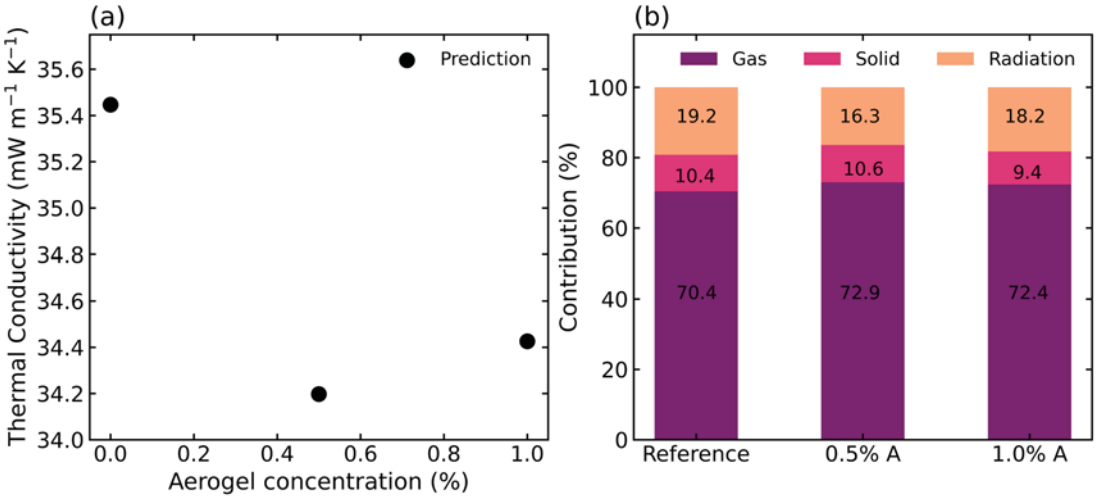

Figure 8-1-3: (a) Predicted thermal conductivity and (b) contribution of each heat transfer mechanisms to the total thermal conductivity.

In absolute terms, for all foams, the predicted values of the thermal conductivity are on average 2 mW m^{-1} K^{-1} smaller than the experimental measurements. This discrepancy between theoretical and experimental values has been often ascribed to the radiation term. The extinction coefficient of the foams might be lower than the real one. Yet, overall, the prediction can be considered rather accurate as the same trends are perceived in the experimental (Figure 8-1-2 (b)) and modelled values (Figure 8-1-3 (b)).

Concerning the relative contributions (Figure 8-1-3 (b)), the gas conduction accounts for more than 70% of the foams conductivity. This contribution is followed by the radiation term. In the case of Reference, radiation accounts nearly for 20% of its thermal conductivity. However, heat transfer by radiation is reduced for all the composite foams due to their higher extinction coefficient. In contrast, heat conduction through the solid matrix represents nearly 10.5% of the total conductivity for foams Reference and 0.5% A. The terms of solid and gas conduction in these materials have relatively similar values due to their similar density and matrix conductivity. However, the detected decrease in thermal conductivity in foam 1.0% A is mainly due to the lower heat conduction through the matrix. In this composite foam, the volume fraction of aerogel particles embedded in the matrix is significant and, thus, it helps reducing the overall thermal conductivity. In addition, also the lower cell size and higher extinction coefficient, also motivates a slight decrease in the radiative heat transfer of foam 1.0% A compared to Reference.

4. CONCLUSIONS

The present study reveals that RPU foams produced with 0.5 wt.% and 1.0 wt.% of aerogel particles presented reductions in the average cell size of approximately 25% and 16% with respect to the unfilled material, respectively. Yet, the cellular structures revealed increasing heterogeneity with the addition of particles due to the presence of degeneration events during foaming [15]. However, at a content of 1.0 wt.% of aerogel the structure revealed significant cell wall ruptures and, hence, open cells. The modifications undergone by the foams upon incorporation of aerogel particles lead to a decrease in the thermal conductivity compared to the unfilled foam, Reference. The decrease in thermal conductivity was owed to two factors. On the one hand, the reduction of radiation heat transfer due to an increase in the extinction coefficient of the foams. Whereas, on the other hand, the matrix conductivity was reduced by the presence of aerogel particles of lower conductivity.

In conclusion, it has been possible to decrease the thermal conductivity of RPU foams by nearly a 4% by using only 0.5 wt.% of aerogel micrometric particles. It is expected that larger contents of aerogel particles, *i.e.*, 3.0 wt.%, could reduce the solid conduction term in practically 1 mW m^{-1} K^{-1}. Hence, provided that the formulations in this study were modified to limit degeneration at large aerogel contents further reductions of the thermal conductivity could be achieved.

5. ACKNOWLEDGEMENTS

Financial assistance from the Junta of Castile and Leon (VA202P20) and Spanish Ministry of Science, Innovation and Universities (RTI2018-098749-B-I00 and RTI2018 - 097367-A-I00) is gratefully acknowledged. Financial support from Junta de Castilla y Leon predoctoral grant of P. Cimavilla-Román, co-financed by the European Social Fund, is also acknowledged.

6. REFERENCES

[1] M. Santiago-Calvo, Synthesis , Foaming Kinetics and Physical Properties of Cellular Nanocomposites Based on Rigid Polyurethane, University of Valladolid, 2019.

[2] N. V. Gama, A. Ferreira, A. Barros-Timmons, Polyurethane foams: Past, present, and future, Materials (Basel). 11 (2018) 1841.

[3] A. Kausar, Polyurethane Composite Foams in High-Performance Applications: A Review,

Polym. - Plast. Technol. Eng. 57 (2018) 346–369.

[4] L. Verdolotti, M.R. Di Caprio, M. Lavorgna, G.G. Buonocore, Polyurethane Nanocomposite Foams: Correlation Between Nanofillers, Porous Morphology, and Structural and Functional Properties, in: Polyurethane Polym. Compos. Nanocomposites, Elsevier Inc., 2017: pp. 277–310.

[5] V. Mittal, Polymer Nanocomposite Foams, First Edit, CRC Press, Abu Dhabi, 2013.

[6] M. Santiago-Calvo, J. Tirado-Mediavilla, J.L. Ruiz-Herrero, F. Villafañe, M.Á. Rodríguez-Pérez, Long-term thermal conductivity of cyclopentane–water blown rigid polyurethane foams reinforced with different types of fillers, Polym. Int. 68 (2019) 1826–1835.

[7] S. Estravís, J. Tirado-Mediavilla, M. Santiago-Calvo, J.L. Ruiz-Herrero, F. Villafañe, M.A. Rodríguez-Pérez, Rigid polyurethane foams with infused nanoclays: Relationship between cellular structure and thermal conductivity, Eur. Polym. J. 80 (2016) 1–15.

[8] M. Santiago-Calvo, J. Tirado-Mediavilla, J.L. Ruiz-Herrero, M.Á. Rodríguez-Pérez, F. Villafañe, The effects of functional nanofillers on the reaction kinetics, microstructure, thermal and mechanical properties of water blown rigid polyurethane foams, Polymer (Guildf). 150 (2018) 138–149.

[9] M. Mar Bernal, S. Pardo-Alonso, E. Solórzano, M.Á. Lopez-Manchado, R. Verdejo, M.Á. Rodriguez-Perez, Effect of carbon nanofillers on flexible polyurethane foaming from a chemical and physical perspective, RSC Adv. 4 (2014) 20761.

[10] S. Pardo-Alonso, E. Solórzano, S. Estravís, M.A. Rodríguez-Perez, J.A. de Saja, In situ evidence of the nanoparticle nucleating effect in polyurethane–nanoclay foamed systems, Soft Matter. 8 (2012) 11262.

[11] V. Bernardo, Production and Characterization of Nanocellular Polymers Based on Nanostructured PMMA Blends and PMMA Nanocomposites, University of Valladolid, 2019.

[12] V. Bernardo, J. Martin-de Leon, J. Pinto, R. Verdejo, M.A. Rodriguez-Perez, Modeling the heat transfer by conduction of nanocellular polymers with bimodal cellular structures, Polymer (Guildf). 160 (2019) 126–137.

[13] H. Sanaeishoar, M. Sabbaghan, F. Mohave, Synthesis and characterization of micro-mesoporous MCM-41 using various ionic liquids as co-templates, Microporous Mesoporous Mater. 217 (2015) 219–224.

[14] K.J. Chang, Y.Z. Wang, K.C. Peng, H.S. Tsai, J.R. Chen, C.T. Huang, K.S. Ho, W.F. Lien, Preparation of silica aerogel/polyurethane composites for the application of thermal insulation, J. Polym. Res. 21 (2014).

[15] P. Cimavilla-Román, S. Pérez-Tamarit, M. Santiago-Calvo, M.Á. Rodríguez-Pérez, Influence of silica aerogel particles on the foaming process and cellular structure of rigid polyurethane foams, Eur. Polym. J. 135 (2020) 109884.

[16] A. Dourbash, C. Buratti, E. Belloni, S. Motahari, Preparation and characterization of polyurethane/silica aerogel nanocomposite materials, J. Appl. Polym. Sci. 134 (2017) 1–13.

[17] Y.X. Thong, X. Li, X.J. Yin, Determining the best flame retardant for rigid polyurethane foam—Tris(2-chloroisopropyl) phosphate, expandable graphite, or silica aerogel, J. Appl. Polym. Sci. 139 (2022) 51888.

[18] C. Zhao, Y. Yan, Z. Hu, L. Li, X. Fan, Preparation and characterization of granular silica aerogel/polyisocyanurate rigid foam composites, Constr. Build. Mater. 93 (2015) 309–316.

[19] E. Hamamizadeh, H.A. Mahabadi, A. Khavanin, Investigating the Mechanical, Morphological, and Acoustic Properties of the Phenolic Aerogel/Flexible Polyurethane Foam Composite, J. Polym. Environ. (2022) 1–10.

[20] J.-H. Kim, J.-H. Ahn, J.-D. Kim, D.-H. Lee, S.-K. Kim, J.-M. Lee, Influence of Silica-Aerogel on Mechanical Characteristics of Polyurethane-Based Composites: Thermal Conductivity and Strength, Materials (Basel). 14 (2021) 1790.

[21] J. Cho, H.G. Jang, S.Y. Kim, B. Yang, Flexible and coatable insulating silica aerogel/polyurethane composites via soft segment control, Compos. Sci. Technol. 171 (2019) 244–251.

[22] ASTM D1622-08: Standard Test Method for Apparent Density of Rigid Cellular Plastics, (n.d.).

[23] ASTM D6226-10. Standard Test Method for Open Cell Content of Rigid Cellular Plastics, (n.d.).

[24] J. Pinto, E. Solorzano, M.A. Rodriguez-Perez, J.A. de Saja, Characterization of the cellular structure based on user-interactive image analysis procedures, J. Cell. Plast. 49 (2013) 555–575.

[25] P. Cimavilla-Román, S. Perez-Tamarit, A. Vananroye, P. Moldenaers, M. Ángel Rodriguez-Pérez, The effects of silica aerogel on the rheological behaviour and polymer matrix structure of Rigid Polyurethane foams, Eur. Polym. J. 176 (2022) 111398.

[26] P. Cimavilla-Román, J. Villafañe-Calvo, A. López-Gil, J. König, M.Á. Rodríguez-Perez, Modelling of the mechanisms of heat transfer in recycled glass foams, Constr. Build. Mater. 274 (2021) 122000.

[27] N.C. Hilyard, A. Cunningham, Low density cellular plastics, 1st Ed, Springer Science & Business Media, London, 1994.

[28] R. Hasanzadeh, M.M. Darvishi, T. Azdast, Synergetic effect of MWCNT/nanoclays on microcellular polystyrene hybrid nanocomposite foams, Carbon Lett. (2019).

[29] M. Santiago-Calvo, V. Blasco, C. Ruiz, R. París, F. Villafañe, M.-Á. Rodríguez-Pérez, Synthesis, characterization and physical properties of rigid polyurethane foams prepared with poly(propylene oxide) polyols containing graphene oxide, Eur. Polym. J. 97 (2017) 230–240.

[30] M.M. Bernal, M. Martin-Gallego, I. Molenberg, I. Huynen, M.A. López Manchado, R. Verdejo, Influence of carbon nanoparticles on the polymerization and EMI shielding properties of PU nanocomposite foams, RSC Adv. 4 (2014) 7911–7918.

[31] A.G. Leach, The thermal conductivity of foams. I: Models for heat conduction, J. Phys. D. Appl. Phys. 26 (1993) 733–739.

[32] L.R. Glicksmann, Heat transfer in foams, in: N.C. Hilyard, A. Cunningham (Eds.), Low Density Cell. Plast., First Ed, 1994: pp. 104–152.

[33] J.R. Howell, Thermal Radiation Heat Transfer, 2010.

Section 8.3.

Modelling of the mechanisms of heat transfer in recycled glass foams

Paula Cimavilla-Román[a]*, Juan Villafañe-Calvo[a], Alberto López-Gil[b], Jakob König[c], Miguel Ángel Rodríguez-Perez[a]

[a] Cellular Materials Laboratory (CellMat), Condensed Matter Physics Department, University of Valladolid, Paseo Belen 7, Valladolid, 47011, Spain

[b] CellMat Technologies S.L., Paseo de Belén 9 A, 47011, Valladolid, Spain

c Advanced Materials Department, Jožef Stefan Institute, Ljubljana, SI-1000, Slovenia

Published in: Construction and Building Materials, 274, 122000, (2021)

DOI: 10.1016/j.conbuildmat.2020.122000

Graphical Abstract

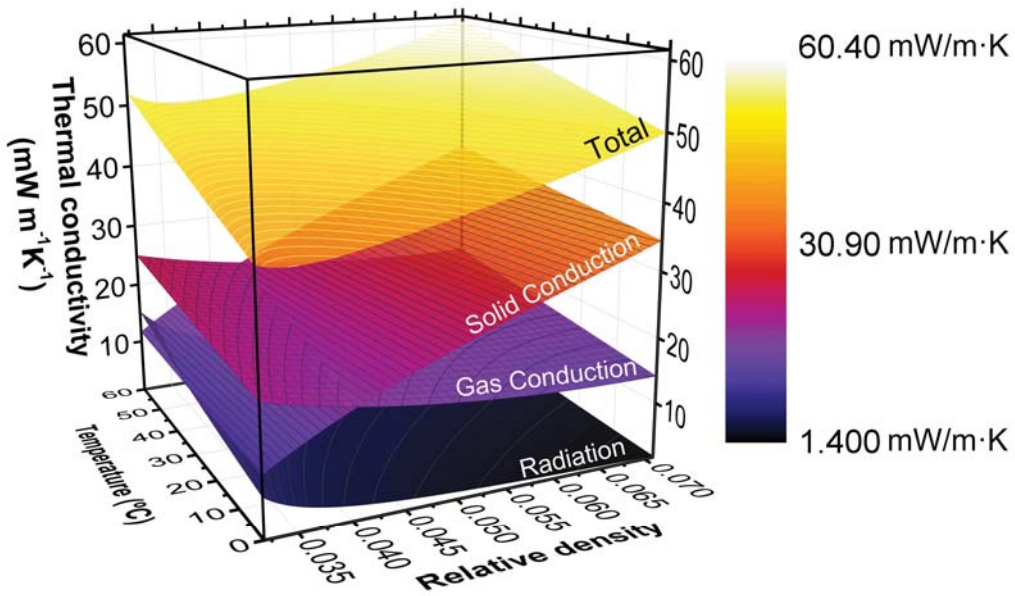

Constr. Build. Mater. 274, 122000 (2021)

ABSTRACT

Glass foams are highly sustainable materials with enormous potential to replace traditional thermal insulators. Current research on glass foams is focused on improving thermal insulation by reducing density, but this is somehow a limited approach. Selecting the best approach to reduce thermal conductivity relies on establishing a detailed knowledge on the heat transfer mechanisms playing the most significant role. We have studied the mechanisms of heat transfer in a set of cathode-ray-tube (CRT) panel glass foams. The influence of relative density, cellular structure, gas composition, glass distribution between cell walls and struts, and radiation on heat transfer is addressed. From a detailed characterisation and state-of-the-art models, we have created a new analytical model adapted to the peculiarities of the foams under analysis. Additionally, the thermal conductivity for varying temperature conditions has been predicted. The obtained results point out to a significant contribution of the heat transfer by radiation for foams with porosities higher than 0.96. The predicted values of thermal conductivity indicate the existence of a plateau region at high porosities. Temperature is proven to shift the contributions of heat transfer, increasing the weight of radiation and gas conduction. The predictions of the new analytical model have been contrasted with experimental measurements of the thermal conductivity at different densities and temperatures obtaining differences below 2%.

KEYWORDS

Glass foams; Cathode-ray-tube panel glass; Thermal conductivity; Mechanisms of heat transfer; Recycled materials

1. INTRODUCTION

For the last decades, European Union directives have aimed to lower energy consumption and increase energy efficiency within its borders. The building sector is crucial in achieving this goal. It contributes to about 40% of the total energy consumption in Europe. Therefore, to minimise the energy employed in space heating and cooling, it is fundamental to increase the thermal insulation efficiency of materials used in the building construction. To this end, all potential solutions pass through ameliorating the insulating materials used in roofs, floors, walls, etc.

Nowadays, polymeric cellular materials are one of the preferred choices when it comes to building insulation [1,2]. Some of the most common plastic insulators, such as extruded polystyrene (XPS) and expanded polystyrene (EPS) present low thermal conductivities in the range of 30-35 mW m·K (at room temperature) and reduced densities [3]. Other insulators, such as polyisocyanurate foams (PIR) can present even lower thermal conductivities depending on the gas used to blow the foam. For instance, PIR foams filled with cyclopentane have thermal conductivities of around 21 mW $m^{-1}K^{-1}$. However, these values are not constant with time. It has been reported that due to the cell walls' permeability to the gases, the thermal conductivity of these foams increases by 30% a few months after production [4]. Thus, the use of these materials implies that frequent renovation of the building envelope would be needed to preserve the energy consumption targets. Furthermore, polymeric insulators are currently under scrutiny for their low sustainability. In addition, they are produced from crude oil, they may contain toxic compounds, are highly flammable and release toxic gases during combustion; besides, being fairly difficult to recycle.

One alternative to traditional insulators are glass foams. These materials are highly porous (porosities larger than 0.9), completely inorganic, and can be produced with closed-cell cellular structures. The intrinsic characteristics of foam glass offer several advantages in comparison to polymeric insulators: water and steam resistance, excellent chemical and thermal stability, incombustibility, long lifespan, and superior mechanical properties. Nowadays, commercial glass foams are produced with excellent control of the glass composition. They present a broad range of thermal conductivities, but the lowest thermal conductivity of industrial products is around 36 mW $m^{-1}K^{-1}$ for a 100 kg m^{-3} density foam. As an added benefit, unlike other building insulation materials, which lose their thermal

performance over time, glass foams long-term thermal conductivity is practically constant [5–7].

One of the main disadvantages of commercial foam glass is its elevated unit price. In recent years, there has been intensive research trying to lower this price and, at the same time, increase the insulation capacity. There is a clear consensus that to reduce costs, the incorporation of glass coming from obsolete cathode ray tubes (CRT) provides the highest benefits [8]. CRT glass abounds in landfills due to its limited recyclability. It contains various types of heavy metal-containing glasses, including lead and barium, which hinder its recyclability following standard procedures [9]. The production of foams from CRT panel-glass is a clever way to reuse this material while lowering the production price in comparison to foams produced from custom-made glass [10,11]. It has also been demonstrated that when using panel glass to produce foams, it is possible to incorporate more than 90% of recycled material and lower the energetic demands of the manufacturing route [10,12]. Several research works have been performed seeking to fine-tune the production process when using CRT panel glass. Recent works have focused on investigating the foaming conditions, foaming agents and optimum glass particle size to ensure that inhomogeneities in the CRT glass composition do not have a detrimental impact on the material properties [8,10]. In the current state of the art, CRT-panel glass foams with densities as low as 107 kg m^{-3} have been prepared, presenting thermal conductivities of 37.5 mW $m^{-1}K^{-1}$ and more than 90% closed porosity [13]. Furthermore, König and co-workers [10] synthesised CRT-glass foams with thermal conductivities lower than that of commercial products of the same density, 42 mW $m^{-1}K^{-1}$ at 140 kg m^{-3}.

Despite the efforts made to improve the insulation capacities of CRT glass foams, few studies have been performed trying to identify the different heat transfer mechanisms and their weight on the total thermal conductivity. In the current state of the art, most authors merely declare linear relationships of thermal conductivity with the foam density, neglecting the influence of pore size and degree of closed/open porosity [14]. Other works have measured indirectly the gas/solid contributions by ignoring radiative heat transfer and measuring the thermal conductivity from atmospheric pressure down to 2 Pa. This method permitted to estimate the solid contribution, which was found to be around 50% for a glass foam of 117 kg m^{-3} in density [15]. But the majority of works concerning glass foams focus on reporting the thermal conductivity of samples produced under various conditions without considering the influence of the different heat transfer mechanisms [10,11].

Therefore, there is still some degree of uncertainty around the contributions of different heat transfer mechanisms in glass foams, and under which conditions it is possible to neglect some of them (*i.e.* radiation). Moreover, the impact of structural and optical factors, such as the fraction of mass in the struts and extinction coefficient of the glass used to produce the foams, has not been addressed for glass foams yet. There are some precedents in the field of polymeric cellular materials which point out to the importance of accounting for changes in the morphology when modelling the thermal conductivity. Solórzano et al. [16] illustrated the impact of radiation on polyethene-based foams. On the one hand, the authors revealed an inflexion point from which the thermal conductivity increased as the density fell below a certain threshold (relative density 0.05 for cell sizes around 900 μm and a fraction of mass in the struts 0.2). The existence of this unexpected trend is due to a progressive thinning of the cell walls as density decreases, which makes the material more transparent to radiation. On the other hand, the struts fraction alone can be accounted for an increment of nearly 13% in the thermal conductivity when the strut fraction increases by a factor of 5 [16,17].

Last but not least, temperature, a factor often overlooked in polymeric cellular materials, is also analysed here. Glass foams, unlike polymeric insulators, are suitable materials to work under demanding conditions of temperature and pressure. They are often employed as insulating materials for reactors and tanks due to their high thermal stability and incombustibility [18]. In these applications, reliable performance, in terms of insulation, is required at conditions most often above ambient temperature. For this reason, the thermal conductivity of glass foams at elevated temperatures cannot be disregarded. Besides, it is expected that the contribution of heat transfer mechanisms will vary significantly when temperature is increased.

In this work, we propose a new model to describe the thermal conductivity, due to conduction and radiation, of glass foams produced from recycled panel glass. This model considers the influence of some less-researched features of the foams such as fraction of mass in the struts, open cell content, extinction coefficient and temperature. Experimental measurements at different temperatures of glass foams presenting different relative density, cellular structure and solid phase architecture confirm the validity of the proposed model. To the authors' knowledge, this is the first time that the impact of structural parameters and radiation on the thermal conductivity of glass foams has been systematically analysed.

2. MATERIALS AND METHODS

2.1. Materials

Cullet of CRT-panel glass with a particle size below 100 µm was supplied by (Averhoff A/S, Aarhus, Denmark). The chemical composition of the cullet was analysed using X-ray fluorescence (PW2400, PANanlytical, The Netherlands) and quantified using oxide standards (Wroxi, PANalytical). The composition of the cullet is shown in Table 8-2-1. The foamed samples were prepared from CRT-panel glass mixed with 0.44 wt% carbon (carbon black, acetylene, Alfa Aesar, Karlsruhe, Germany), and 5.97 wt% Mn_3O_4 (prepared from MnO_2, 98%, Alfa Aesar, by firing at 1250°C for 4 h).

The powder mixtures were homogenised by milling in a yttria-stabilised-zirconia ball mill with 10-mm balls for 25 min using a Planetary Ball Mill PM 200 (Retsch, Haan, Germany). The D50 and D90 particle size of the as-obtained powder were in the ranges 5–6 µm and 15–18 µm, respectively. The ground powder mixture (≈ 35 g) was inserted into a stainless-steel form (10 cm × 8 cm × 4 cm), evenly distributed over the surface and gently pressed with a flat surface. The steel form was covered with alumina fibres and a metal plate. The steel surface was painted with a kaolin suspension to prevent the glass from sticking to the metal. The sample was placed in a laboratory electrical tube furnace in a flow of CO_2 and heated at 5 °C·min^{-1} to 740–830 °C for 40 min. The variation in the foaming temperature led to glass foams with different densities. The samples were then cooled at 7 °C·min^{-1} to 530 °C and then slowly cooled at 1–2 °C·min^{-1} to room temperature. The temperature in the foaming zone was calibrated using an external thermocouple. Further details on the preparation conditions are available in ref. [12].

Table 8-2-1: Composition of the silicate glass measured by XRF.

Oxide	[wt%]
SiO_2	58.4
Al_2O_3	2.4
Na_2O	8.5
K_2O	8.0
PbO	0.12
SrO	7.8
BaO	9.2
MgO	0.5
CaO	0.8
Fe_2O_3	0.3
ZrO_2	2.0

2.2. Methods

2.2.1 Density

The density of the solid materials, ρ_s, was measured in its powder form using a gas pycnometer (Mod AccuPyc II 1340, Micromeritics). Nitrogen is used as the displacement medium, and the gas pressure was fixed at 19.5 psig. The apparent density, ρ, of the glass foams was calculated from the mass of each sample divided by its corresponding volume. Prior to the characterization, the samples were cut into rectangular prims of approximate dimensions of 9 cm x 7 cm x 2 cm. Due to the large size of the samples the experimental uncertainty of this measure was very low, below 0.3 % of the measured values. Relative density, ρ_r, was calculated as the ratio between foam density and the density of the solid with the same chemical composition as the foam's solid matrix.

2.2.2 Open Cell content

The open cell content, *OC*, was determined according to the ASTM Standard D6226-10 using the same gas pycnometer employed to characterise the solid density. The Open Cell Content was measured on cubic samples (dimensions: 4 x 4 x 2 cm) and it is defined as indicated in eq. (8-2-1).

$$OC = \frac{V - V_P}{V(1 - \rho_r)} \qquad (8\text{-}2\text{-}1)$$

Where V is the geometric volume of the sample corrected to the volume of cells exposed on the surface of the sample, V_p is the volume measured with the pycnometer and $(1 - \rho_r)$ accounts for the porosity of the foam. The Nitrogen pressure used to determine the pycnometer volume was fixed at a constant value of 19.5 psig for all samples. The open cell content reported in this work represents the percentage of the material's porosity that is interconnected inside the sample and to the exterior so the gas can flow inside it.

2.2.3 Gas analysis

The gas composition in the closed pores was assessed by crushing a sample (~8 cm^3) in an evacuated, He-filled cylinder connected to a pressure gauge, and subsequent gas analysis using a gas chromatograph (7890A GC System, Agilent Technologies with a split column). The remaining background atmosphere was subtracted, and the reported gas composition is an average of triplicate gas samples. The details on the gas chromatography are reported in ref. [19].

2.2.3 Cellular structure

The foams' cellular structure was examined using a Scanning Electron Microscope (model Flex SEM 1000 Hitachi). The main descriptors of the cellular structure were characterised using specific software based on ImageJ/FIJI [20]. First, the average cell size, ϕ_{3D}, has been measured. This cell size in 3D is obtained from the cell size in 2D by: $\Phi_{3D} = 1.273 \cdot \Phi_{2D}$. (*i.e.* we have used the correction proposed by ASTM D3576-98 to calculate the cell size in 3D from the data in 2D obtained from SEM images). The standard deviation of the cell size distribution, SD, and the normalised standard deviation of the average cell size, NSD, have also been calculated. These last two parameters provide information about the cellular structure homogeneity. Besides, the anisotropy ratio, AR, was calculated as the ratio between the length of the cells in the foam growth direction divided by the corresponding length in the perpendicular direction. Thus, it represents the elongation of the cells along the foam expansion direction. To ensure the representativeness of the obtained values no less than 150 cells were analysed for each foam.

2.2.4 X-Ray Tomography

Solid phase descriptors of the cellular structure were analysed by non-destructive X-ray computed micro-tomography (model V|Tome|X s 240 of GE Sensing & Inspections

Technologies). The experiments consisted of a set of 1800 projections with an exposure time of 1000 ms. The tube current was fixed at 80 kV and 325 μA. The selected magnification yielded an effective pixel size of 1.1 μm. This resolution enabled to resolve the fine elements where the glass phase is confined inside the foam. The field of view at such resolution was limited to only 2.25 x 2.25 mm^2. Therefore, small samples of around 1 mm in diameter were scanned in these experiments

The reconstruction of the tomographies has been carried out using a commercial reconstruction package. The reconstruction procedure allows obtaining the cross-sections of the sample under study. Quantitative data analysis of the reconstructed images was performed following the method of analysis detailed by S. Pérez-Tamarit et al. [21]. To this end, a 3D median filter (2 pixels of radius) was applied to remove noise from the reconstructed images. Afterwards, the solid phase was carefully binarised to preserve the foam's features entirely. Euclidean Distance Transform algorithm was applied to obtain the thickness distribution of the solid elements in the foam. This algorithm enables the user to obtain volumetric information about the average thicknesses of the solid matrix features, such as cell wall thickness, δ, and struts thickness, ς. The solid phase thickness distribution was analysed by means of a two peak deconvolution methodology, which enables to split the histogram into two separates peaks, representative of the walls and struts. The best fitting for this type of materials was achieved using Log-Normal functions.

A key parameter for the modelling of the thermal conductivity can also be obtained thanks to the deconvolution process: the fraction of mass in struts, f_s. This parameter determines the distribution of solid material in the solid phase. If it is close to one, the majority of material is located in the struts and if close to zero the mass is distributed homogeneously between struts and cell walls. Using the deconvolution of the solid phase thickness distribution this parameter can be calculated as the ratio between the area under the struts thickness distribution, A_s, divided by the sum of the areas under the struts and walls distributions, A_w (eq. (8-2-2)).

$$f_s = \frac{A_s}{A_w + A_s} \tag{8-2-2}$$

2.2.5 Thermal conductivity of the foams

The thermal conductivity measurements were made under steady heat flow conditions through the test samples (model FOX 314), following the ASTM C518-17 method. The

measurements were performed with the samples at a temperature of 10 °C, 23 °C, 35 °C, 45 °C and 55 °C. The setpoints temperatures were achieved by creating a 20 °C temperature gradient through the foam. Thermal conductivity, λ, was calculated by measuring the heat flow through the test sample per time unit, q, as a result of the temperature gradient, ΔT, following Fourier's equation (eq. (8-2-3)). The thermal conductivity was measured 12 times, but the average value was obtained from the last 5 measurement blocks.

$$q = \lambda A \frac{\Delta T}{d} \tag{8-2-3}$$

In eq. (8-2-3) d stands for the sample thickness, and A is the cross-sectional area of the sample calculated from a standard sample. Due to the reduced size of the samples (of around 90 mm x 70 mm), they were framed inside a polyurethane mask of known conductivity, λ_{PU}, to cover the entire sensor (100 mm × 100 mm) of the heat flow meter. The thermal conductivity of the glass foam, λ_{gf}, was given by eq. (8-2-4). [22]

$$\lambda_{gf} = \frac{\lambda_m - V_f^{PU}\lambda_{PU}}{V_f^{gf}} \tag{8-2-4}$$

Where λ_m is the measured thermal conductivity, V_f^{PU} is the fraction of the sensor occupied by the polyurethane mask, and V_f^{gf} fraction of the sensor's surface covered by the glass foam. Despite this approximation the obtained thermal conductivity values are highly reliable, in fact the standard deviation between measurements was less than 0.5% of the conductivity value provided by the equipment.

3. RESULTS AND DISCUSSION

3.1. Structural characterisation

Table 8-2-2 collects the main structural characteristics of the foams under. The density, ρ, of the solid glass used to produce the foams was measured to be 2818 kg m^{-3}. The produced foams reach relative density values (density of the foam divided by the density of the solid, ρ_r) as low as 0.033; this fact points out to the significant volume increase suffered by the solid glass (around 30 times its original volume). In expansion terms, it is similar to the one that convectional insulators, such as polymeric foams, undergo during its foaming process [4]. This very low values of relative density correspond to very high values of the porosity, V_g.

Table 8-2-2: Characterised cellular structure descriptors and porosity values for all the foams produced.

Sample	ρ_r	V_g	OC	ϕ_m (μm)	NSD	AR	ϕ_μ (μm)	V_μ	f_s	δ (μm)	ς (μm)
#1	0.033	0.967	0.23	2056.1	0.59	1.05	62.9	0.020	0.81	19.1	34.8
#2	0.035	0.965	0.18	1873.2	0.57	1.13	53.5	0.018	-	-	-
#3	0.038	0.962	0.14	1814.6	0.59	0.89	44.3	0.016	0.59	13.4	23.7
#4	0.040	0.960	0.08	1557.9	0.58	1.09	42.4	0.015	0.50	13.1	23.6
#5	0.045	0.955	0.02	1388.9	0.59	1.06	29.4	0.013	-	-	-
#6	0.052	0.948	0.01	1249.8	0.54	1.10	33.6	0.011	-	-	-
#7	0.056	0.944	0.00	1220.5	0.54	1.07	23.5	0.010	0.36	11.7	18.8
#8	0.069	0.931	0.00	859.6	0.57	1.08	21.9	0.010	-	-	-

Microscopy images of the growth plane of the foams can be observed in Figure 8-2-1. On the one hand, at very low relative densities the foams' cellular structure is characterised for having irregularly shaped cells with sizes, Φ_m, ranging from 150 μm to 3500 μm, with more than 65% of the foam's volume occupied with cells of size above 2000 μm. On the other hand, as the density increases the cell size distribution narrows, with maximum cell size values of 1500 μm for the higher density foams. Therefore, the foam volume occupied by cells of sizes below 1000 μm rises to nearly 80%. Due to the inhomogeneity of the cellular structure, it has been necessary to compute the surface mean diameter (Table 8-2-2, Φ_m), eq. (8-2-5), in order to obtain a representative average cell size [23]. A cut-off cell size of 100 μm was selected to calculate the surface mean diameter of these pores.

$$\Phi_m = \frac{\sum_i^n \Phi_i{}^3 n_i}{\sum_i^n \Phi_i{}^2 n_i} \tag{8-2-5}$$

In eq. (8-2-5), n_i and Φ_i are, respectively, the number and diameter of the cells in a certain cell size fraction. This type of average diameter is often calculated when the cellular structure is composed of a large number of small cells (in this work in the region of 250 μm) and a smaller number of big cells (of a few millimetres) which occupy a significant volume of the foam [24].

The rather inhomogeneous cellular structure is also confirmed by the high values of *NSD* measured (Table 8-2-2). From the images, it is possible to observe that there is no preferential direction of cell growth. The foams can be considered isotropic as suggested by

the anisotropy ratio, *AR*, values measured (Table 8-2-2). Nonetheless, when micrographs are taken at higher magnification (second row of Figure 8-2-1), an unusual solid phase morphology is revealed. Internal porosity inside the struts and cell walls is present, with micrometric cells of sizes of around 50 μm in the case of the lower density foams and cells below 20 μm in the case of higher density materials. A detailed analysis of the solid phase has been carried out, being possible to confirm that the cells hosted by the walls and struts always have sizes below 120 μm irrespective of the foam's relative density. Taking into consideration this threshold size an average cell size representative of the pores inside the solid phase has been measured, ϕ_μ (Table 8-2-2). Furthermore, as with the millimetric pores cell size decreases as relative density rises.

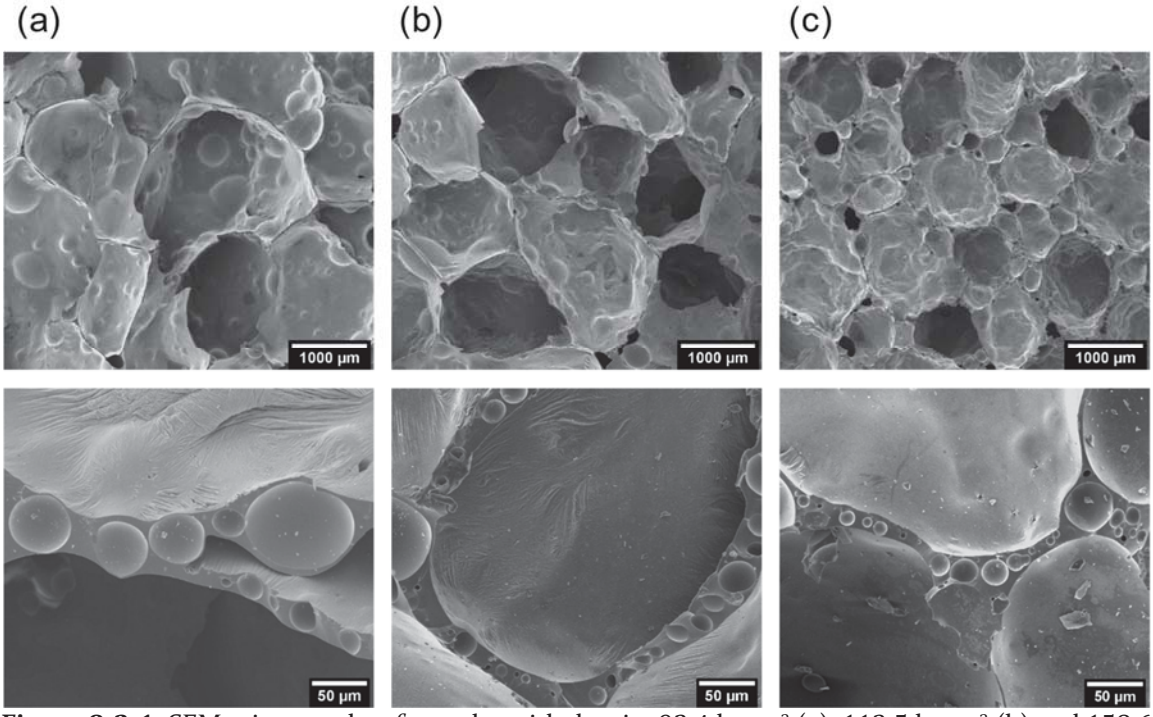

Figure 8-2-1: SEM micrographs of samples with density 92.4 kg m^{-3} (a), 113.5 kg m^{-3} (b) and 158.6 kg m^{-3} (c) foams at low (first row) and high (second row) magnifications.

It is also observed how at high relative densities the open cell content, *OC*, (Table 8-2-2) is low, as it could be expected for closed-cell foams for insulation purposes. However, as density decreases a significant increment in the open cell content is detected. For foams with porosities above 0.96, the open cell content rises to values close to 25%. The fact that open porosity is so high for the lower density foams could be accounting for intense cell degeneration mechanisms resulting in partial cell wall breakage, which are also responsible for the drastic rise in size experienced by the cells as the density falls [25]. These results

point out to the fact that when very low densities are reached, the stability of the cellular structure is compromised.

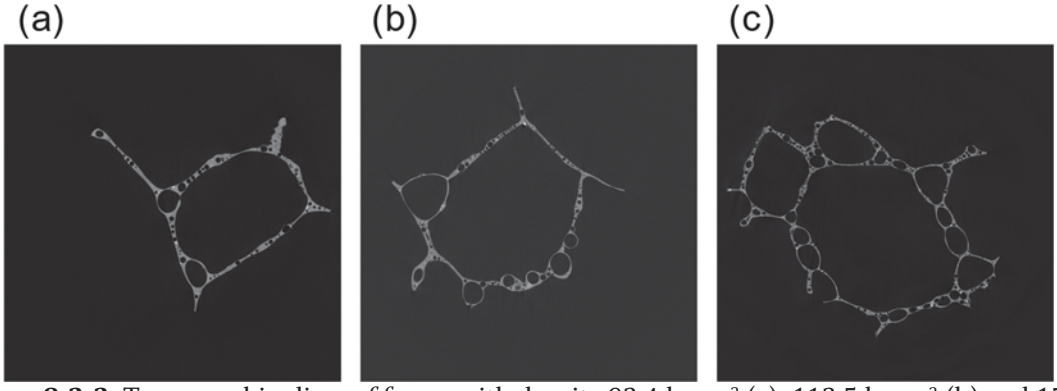

Figure 8-2-2: Tomographic slices of foams with density 92.4 kg m^{-3} (a), 113.5 kg m^{-3} (b) and 158.6 kg m^{-3} (c).

Additionally, using X-ray tomography, four samples were scanned covering the entire density range studied in this work (from 90 to 200 kg m^{-3}). Figure 8-2-2 shows an example of the cellular structure observed with this technique, where it is possible to appreciate the micrometric cells embedded into the solid matrix. However, due to the small dimensions of the scanned sample in each tomography, it was only possible to observe the distribution of solid phase around one or two pores. From the scanned volumes, it has been possible to make a rough estimation of the contribution of sub-100 μm cells to the foams' total porosity, V_μ. All in all, these cells (below 50 μm) account for less than 2% of the foams' porosity (Table 8-2-2). Though, as reported in Table 8-2-2, it has been detected that the porosity due to these cells, V_μ, rises as relative density decreases. Consequently, as detected by SEM (second row of Figure 8-2-1), the *apparent* thickness of the solid matrix increases with porosity.

In contrast, the fraction of mass in the struts, f_s, (Table 8-2-2) increases drastically with decreasing relative density. In line with the increase in open cells, degeneration mechanisms, such as drainage, motivate the flow of glass material from the walls to the struts and seem to be accountable for an increase in the thickness of the struts, ς. Concerning cell walls, an *apparent* increase in their thickness, δ, is also observed according to the results of Table 8-2-2. However, this increase is only partial. On the one hand, the solid phase thins in the border between the sub-50 μm cells and large cells. On the other hand, the increase of porosity reduces the amount of material in the cell walls.

Figure 8-2-3 (a) depicts the progressive modification of f_s as the density increases. At high densities, the glass is distributed more homogeneously between walls and struts prompting low f_s, in a similar manner to how polymeric mass is distributed in low-density

polyethylene foams [21]. Conversely, when density decreases below 110 kg m^{-3}, there is a substantial effect on f_s which abruptly rises from 0.5 to 0.8 whereas the density changes by only 20 kg m^{-3}. This change in f_s makes the concentration of glass more frequent around the struts. Meanwhile, the entire skeleton grows thicker due to the increase in the cell size of the micrometric pores embedded inside the matrix.

To obtain trends for the variation of the most important descriptors of the cellular structure with the density of the foam, the measured values of f_s, cell size and open cell content were adjusted to an exponential decay, a quadratic and an exponential function, respectively (Figure 8-2-3).

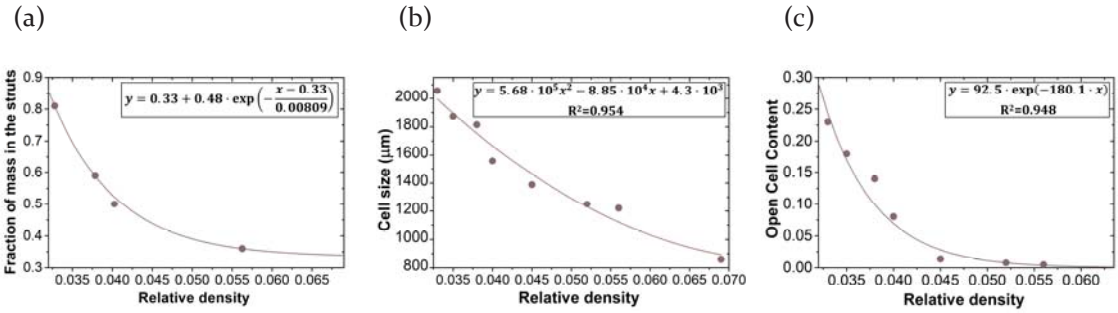

Figure 8-2-3: Fraction of mass in the struts (a), cell size (b) and open cell content (c) as a function of relative density.

3.2. Thermal conductivity modelling

Heat transfer in foams is a combination of four main mechanisms: i) conduction through the gas phase, λ_g; ii) conduction through the glass phase, λ_s, ergo through the struts and cell walls; iii) radiation accounting for the thermal radiation emitted by all bodies at a higher temperature than absolute zero, λ_r; and iv) gas convection inside the cells, λ_c. The sum of these four terms represents the effective thermal conductivity of the foam λ_t, eq. (8-2-6).

$$\lambda_t = \lambda_g + \lambda_s + \lambda_r + \lambda_c \tag{8-2-6}$$

Several authors have noted that convection only contributes to the foam's thermal conductivity when the cells exceed sizes of 4 mm [17,26]. Therefore, for all the glass foams in Table 8-2-2, this term can be neglected.

3.2.1. Gas phase conduction

Gas is the predominant component inside the foams. Typically, the main contribution to the total thermal conductivity, in conventional insulators, is due to the gas filling the

cells. The gas conduction can be easily predicted in the case of foams composed of only one type of gas. This term is simply obtained as the product of the material's porosity and the gas conductivity, eq. (8-2-7).

$$\lambda_g = V_g \cdot \lambda_{gas} \tag{8-2-7}$$

However, when the cells are filled with more than one type of gas the gas conductivity needs to be calculated considering the composition and thermal conductivity of all gases inside the cells eq. (8-2-8). Gas conductivity is a function of the mean free path of the gas molecules. Thus, this value will be altered when a second type of molecules is present. To account for this fact, Wassiljewa derived an empirical model (eq. (8-2-8)) that predicts the conductivity of a gas mixture [17,27]:

$$\lambda_{gas}^{mix} = \sum_{i=1}^{N} \frac{x_i \lambda_i}{\sum_{j=1}^{N} A_{ij} \lambda_j} \tag{8-2-8}$$

In Wassiljewa's equation (eq. (8-2-8)) the conductivity of a gas mixture is obtained from the conductivity of each gas alone, λ_i, the volume fraction of each gas in the mixture, x_i, and a series of adjustable parameters proposed by Lindsay and Bromley, A_{ij} [27]. These coefficients can be interpreted as the ratio of efficiencies with which molecules from gas j impede the transport of heat by molecules of gas i. The expression of A_{ij} is given in eq. (8-2-9). Here μ_i represents the viscosity of the pure gas i, M_i is the molecular weight of gas i, T is the temperature of the gas, and S_i is known as the Sutherland's constant which depends on the boiling temperature, T_b, of the gas at 1 atm, $S_i=1.5 \cdot T_b$. S_{ij} accounts for the collisions of the gases in the mixture and its value depends on the polarity of the molecules: for a polar and a non-polar gas $S_{ij}=0.73 \cdot \sqrt{S_i S_j}$; whilst for gases with the same polarity S_{ij} is only $\sqrt{S_i S_j}$.

$$A_{ij} = \frac{1}{4}\left\{1 + \left[\frac{\mu_i}{\mu_j}\left(\frac{M_j}{M_i}\right)^{0.75} \frac{\left(1+\frac{S_{ij}}{T}\right)}{\left(1+\frac{S_j}{T}\right)}\right]^{1/2}\right\}^2 \frac{1+\frac{S_{ij}}{T}}{1+\frac{S_i}{T}} \tag{8-2-9}$$

The constants required to calculate A_{ij}, such as viscosity, molecular weight and boiling temperature of each gas can be found in the NIST Chemistry WebBook [28]. The gas composition of foams analysed in this work was measured using gas chromatography [13,19]. It was found that the gas composition for all glass foams is a mixture of two volatile gases of different polarity, carbon monoxide, CO (polar) and carbon dioxide,

CO_2 (non-polar). Both gases are produced during the foaming of the sample in a low oxygen atmosphere, as a result of the redox reaction that takes place between the foaming agent, carbon black, and the oxidising agent, Mn_3O_4, that are added to the panel glass to promote the foaming [29]. Figure 8-2-4 (a) shows the contents of the gases for different foams. As it can be observed, there is a trend for the foams to have higher contents in CO_2 as their relative density gradually increases. The experimental values of gas content have been adjusted to a quadratic regression (Figure 8-2-4 (a)) that enables to estimate the gas composition for all the glass foams with other densities. Additionally, Figure 8-2-4 (b) represents the thermal conductivity of the mixture of CO_2/CO entrapped inside the closed cells of the materials. CO has a thermal conductivity of 25.43 mW $m^{-1}K^{-1}$ at 10 °C and a slope with temperature variation of 0.066 mW $m^{-1}K^{-1}$ per kelvin. Whereas, CO_2 thermal conductivity is 15.5 mW $m^{-1}K^{-1}$ at the same temperature but varies more rapidly with temperature, 0.083 mW $m^{-1}K^{-1}$ per kelvin [30–32]. At low densities, the thermal conductivity of the mixture is higher, due to the higher content of CO inside the cells, which has a higher thermal conductivity than CO_2. As the relative density increases, the cells are mainly filled with CO_2 gas of low thermal conductivity; thus, foams with high density have a gas inside the cells of lower thermal conductivity. The difference is significant, from 20 mW $m^{-1}K^{-1}$ for low-density foams to 16 mW $m^{-1}K^{-1}$ for high density foams.

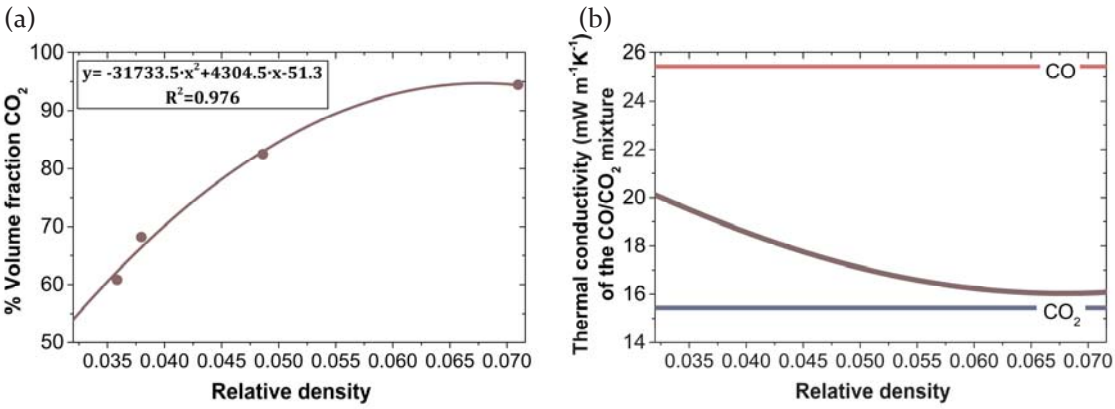

Figure 8-2-4: (a) Volume fraction of CO_2/(CO+ CO_2) against the relative density of the foam, as reported by J. König et al. [13]. (b) λ of the mixture of CO_2/CO at 10 °C. The straight lines represent the thermal conductivities of the two components alone.

However, it is to be noted that in the case of low-density foams, open porosity is not negligible (Table 8-2-2). Inside these cells, the gas composition will no longer be a mixture of the CO and CO_2. Since they are in contact with the exterior, they are filled with air, which has a thermal conductivity very similar to that of CO at 10 °C, 25.12 mW $m^{-1}K^{-1}$ and varies slightly faster with temperature, slope: 0.072 mW $m^{-1}K^{-2}$ [33]. Consequently, to correctly

predict the thermal conductivity due to the conductivity of the gas phase (air, CO and CO_2) inside the foams an additional term (eq. (8-2-10)) accounting for the open cells needs to be introduced in eq. (8-2-7):

$$\lambda_g = V_g \cdot \lambda_{air} \cdot OC + V_g \cdot \lambda_{gas}^{mix} \cdot (1 - OC) \quad (8\text{-}2\text{-}10)$$

In Figure 8-2-5 (a), the contribution of the open and closed cells to the gas conductivity can be seen. For low density foams where the open porosity is relatively high (around 0.23), the air that fills these cells contributes with about 8% to the gas conductivity. The impact of open porosity progressively decreases to almost zero for the high-density samples.

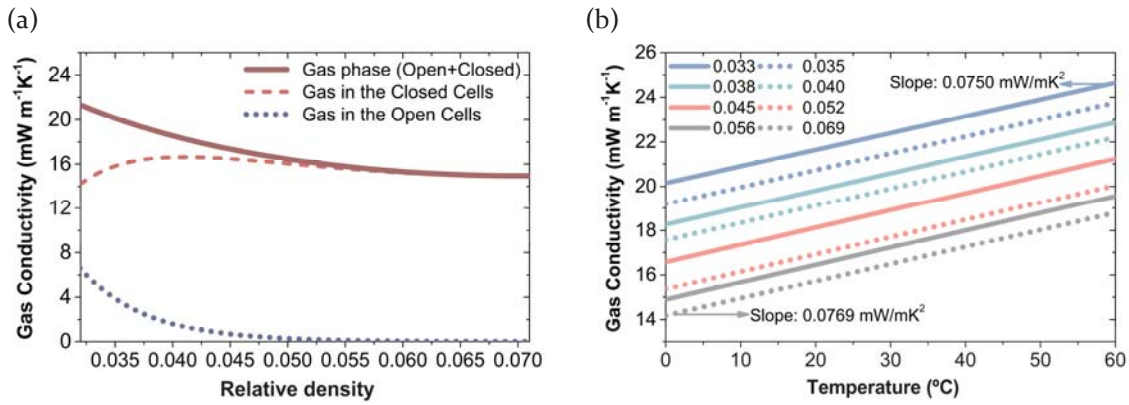

Figure 8-2-5: (a) Thermal conductivity of the gas phase at 10 °C. (b) Gas phase thermal conductivity of the foams in Table 8-2-2 as a function of temperature.

The thermal conductivity linked to gas conduction increases at low densities because of the three simultaneous mechanisms: firstly, higher content of CO in the closed cells, secondly, the higher degree of interconnectivity resulting in air filling the fraction of the open cells and thirdly, higher porosities which lead to larger amounts of gas inside the foams. Furthermore, it can be seen that the thermal conductivity increases linearly with temperature, with a slope that slightly rises as porosity decreases due to the larger heat transfer impinged by CO_2 molecules (Figure 8-2-5 (b)).

3.2.2. Solid phase conduction

In general, glass exhibits a low thermal conductivity among inorganic materials due to the lack of a long range order [34]. The thermal conductivity of CRT panel glass is around 0.93 W $m^{-1}K^{-1}$ [35,36]. Conventional foams in the market are usually based on polymeric materials whose matrix rarely has a thermal conductivity above 0.5 W $m^{-1}K^{-1}$ [37]. The majority of these foams have a low contribution of the solid conduction to the overall

material's thermal conductivity; below room temperature, it is seldom higher than 15% when considering the range of densities under subject in this study [16]. However, the higher thermal conductivity of glass leads to increased contribution of the solid matrix to the thermal conductivity of the foam.

In the literature, different equations have been proposed to analytically predict the thermal conductivity by conduction of the solid phase in a cellular material [38]. In this work, we have used an expression that has been proven to give good results in the case of polymeric foams [39]. It is known as Glicksman equation (eq. (8-2-11)) [17]. It breaks the conduction of the solid in two terms, one accounting for the conduction due to struts and the other one due to cell walls.

$$\lambda_s = \lambda_{struts} + \lambda_{walls} = \frac{\rho_r}{3} \cdot f_s \lambda_{glass} \sqrt{AR} + \frac{2}{3} \rho_r (1 - f_s) \lambda_{glass} AR^{1/4} \qquad (8\text{-}2\text{-}11)$$

All the parameters in eq. (8-2-11) except λ_{glass} are reported in Table 8-2-2. The conductivity of the CRT panel glass can be calculated using a theoretical approach. Based on the results of Primenko [40], the thermal conductivity of silicate glass at different temperatures, ranging from 0 to 600 °C can be calculated according to eq. (8-2-12) just by considering its composition. In eq. (8-2-12), λ_{glass}, stands for the thermal conductivity of the glass at a temperature T, $\%wt_i$ is the mass percentage of oxide i in the glass and P_i is the partial conductivity coefficient of each oxide (values for these coefficients and their variation with temperature can be found in the following references [40–42]).

$$\lambda_{glass} = \sum_i \%wt_i \cdot P_i \qquad (8\text{-}2\text{-}12)$$

After applying eq. (8-2-12) the thermal conductivity of CRT panel glass is found to increase linearly (slope: 1.5 mW $m^{-1}K^{-2}$) with temperature from 900 mW $m^{-1}K^{-1}$ at 10 °C up to 1100 when the temperature is increased to 150 °C. Despite the swifter increase of the panel glass thermal conductivity, Figure 8-2-6 (a) reveals that the solid conductivity increases more gradually with temperature than the gas one. However, as the proportion of solid inside the foam rises, the thermal conductivity due to the matrix rises more steeply with temperature (higher slope).

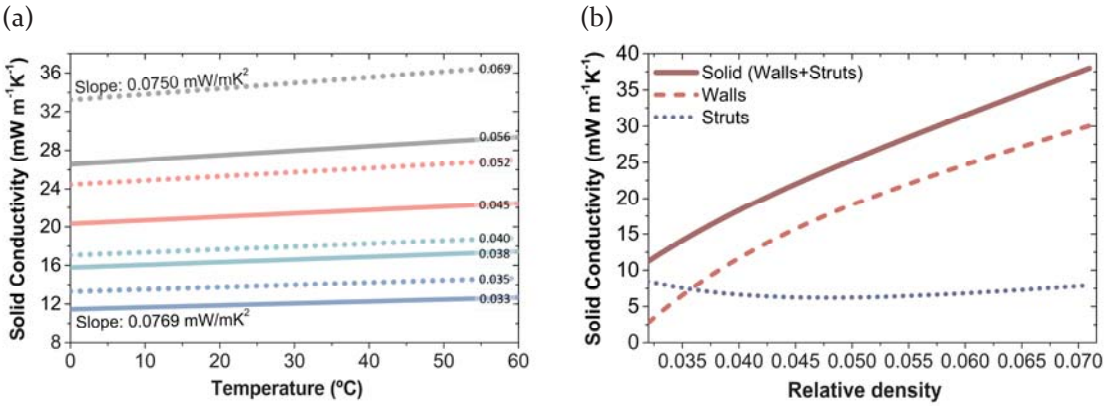

Figure 8-2-6. (a) Solid phase thermal conductivity of the foams in Table 8-2-2 as a function of temperature. (b) Thermal conductivity of the solid phase at 10 °C as a function of the relative density

Figure 8-2-6 (b) illustrates the importance of the mass fraction located in the cell walls on the conduction through the solid phase. As expected, an increase in the relative density promotes a rise in the solid conductivity. It can be seen how at medium to high densities, the walls account for the major part of conduction through the solid phase. At high densities, *i.e.* at low f_s, the majority of the mass is located in the walls which act as wires for the conduction of heat. In fact, the evolution of the solid phase conduction is mainly shaped by that of the cell walls. On the other hand, regardless of the foam density, the struts conductivity is always around 7 mW $m^{-1}K^{-1}$. Only at very low densities when the mass is predominantly in the struts, these elements have a considerable influence on the glass matrix conductivity. The intense porosity in the cell walls at low densities makes the conduction path through them more tortuous, reducing its impact on the overall conduction term. However, an increase in the relative density results in a decrease of the struts contribution to the solid conductivity, from 70% to less than 20%.

3.2.3. Radiation heat transfer

The third mechanism contributing to the thermal conductivity of foams is due to the electromagnetic radiation. Unlike convection and conduction, radiation does not need an intervening medium to be transported. All bodies at a temperature higher than absolute zero emit thermal radiation in the form of photons, which then can be absorbed, scattered, or transmitted to other bodies. Absorbed radiation has the capability of changing the material's internal energy and consequently, its temperature. The transmitted thermal radiation through a material, depends on its thickness and most importantly on its

Constr. Build. Mater. 274, 122000 (2021)

extinction coefficient, $K_{e,R}$, which accounts for all the absorption and scattering events that take place inside the material [17].

The extinction coefficient of foams can be modelled using an equation proposed by Glicksmann et al. [17]. The authors considered the foam as a combination of randomly oriented cell walls that absorb radiation and blackbody struts, which scatter all the radiation incident upon them. The struts have a contribution to the foam's extinction coefficient that depends on the cellular structure and density. Cell walls have an extinction coefficient, K_{ws}, that is a function of the amount of glass in the walls and the extinction coefficient of the material contained in the walls K_w (eq. (8-2-13)).

$$K_{e,R} = K_s + K_{ws} = 4.10\frac{\sqrt{f_s \cdot \rho_r}}{\Phi} + (1 - f_s)\rho_r K_w \tag{8-2-13}$$

Therefore, the foam's extinction coefficient is a combination of scattering by the struts and absorption of cell walls. In optically thick mediums, where –ln(T) ≥ 5 [43]; thermal radiation only travels a short distance before suffering from absorption or scattering. In such cases, the mean free path of photons inside the material is small in comparison to the dimensions of the insulator. Thus, it is possible to model radiative heat transport as a diffusion process inside the foam, result known as Rosseland diffusion equation (eq. (8-2-14)) [44]. This equation considers the foam's extinction coefficient, $K_{e,R}$, Stefan–Boltzmann constant, σ, and the sample's temperature, T.

$$\lambda_r = \frac{16\sigma T^3}{3K_{e,R}} \tag{8-2-14}$$

Spectral extinction coefficient

Table 8-2-2 collects all the cellular structure descriptors needed to obtain the foams extinction coefficient following Glicksmann equation. However, the optical properties of CRT panel glass, particularly its extinction coefficient K_w, is also required.

The standard experimental method to obtain the extinction coefficient of a material is based on the use of infrared spectroscopy in transmission mode for samples with varying thickness. The changes in transmitted infrared radiation are related to the material's extinction coefficient, K_λ, and the sample thickness, L, according to Beer-Lambert's law, $I_\lambda = I_{0,\lambda} \cdot e^{-L \cdot K_\lambda}$ [45]. We tested solids of the panel glass (composition shown in Table 8-2-1) with thicknesses from 100 μm up to 1000 μm. Due to the high absorption of SiO_2 stretching

band, the spectra were incomplete, and some peaks were saturated. For this reason, differences in transmittance could not be observed; ergo, it was not possible to apply Beer-Lambert's law to obtain an experimental value for the panel glass extinction coefficient. Hence, an alternative method to get a representative value of the glass extinction coefficient is proposed here. Considering that the composition of our panel glass and standard soda–lime glass is reasonably similar [46], it is possible to use the optical properties of soda–lime glass to exemplify the behaviour of the CRT panel glass inside the foams under study.

The reflectivity of soda–lime glass in the visible and infrared region was extensively studied by M. Rubin [47]. From his works, it is possible to obtain the transmissivity, τ_λ, of clear soda-lime glass sheets of thickness 0.01 to 100 mm. With this data and using a liner adjustment based on eq. (8-2-15), the spectral extinction coefficient was found for every wavelength, Figure 8-2-7 (a).

$$K_\lambda = \frac{-ln\,(T)}{L} \tag{8-2-15}$$

The material's mean extinction coefficient can be derived from the diffusion approximation to the radiative heat transfer, an expression known as Rosseland opacity. To compute the mean extinction coefficient of soda-lime glass, K_w, the spectral extinction coefficient is weighted by the temperature derivative of the monochromatic blackbody emissive power, $e_{b,\lambda}$ (eq. (8-2-16)).

$$K_w = \frac{\int_0^\infty \frac{1}{K_\lambda}\frac{\delta e_{b,\lambda}}{\delta T}\,d\lambda}{\int_0^\infty \frac{\delta e_{b,\lambda}}{\delta T}\,d\lambda} \tag{8-2-16}$$

From eq. (8-2-16) it is possible to obtain the glass extinction coefficient as long as the medium is optically thick. This condition is only satisfied in the near to far-infrared region, above 5 μm. For smaller wavelengths and in the visible range soda–lime glass is almost transparent to radiation. Nevertheless, bodies at standard conditions for temperature (20 °C) emit more than 99% of their thermal radiation at wavelengths longer than 2.5 μm (Figure 8-2-7 (a)). Only for wavelengths below 5 μm, soda-lime glass is optically thin, and Rosseland diffusion model does not apply. This range will not be taken into consideration to calculate K_w. The error associated with excluding those wavelengths is negligible since for the highest temperature considered 91.4% of the blackbody emission spectra is emitted for wavelengths higher than 5 μm.

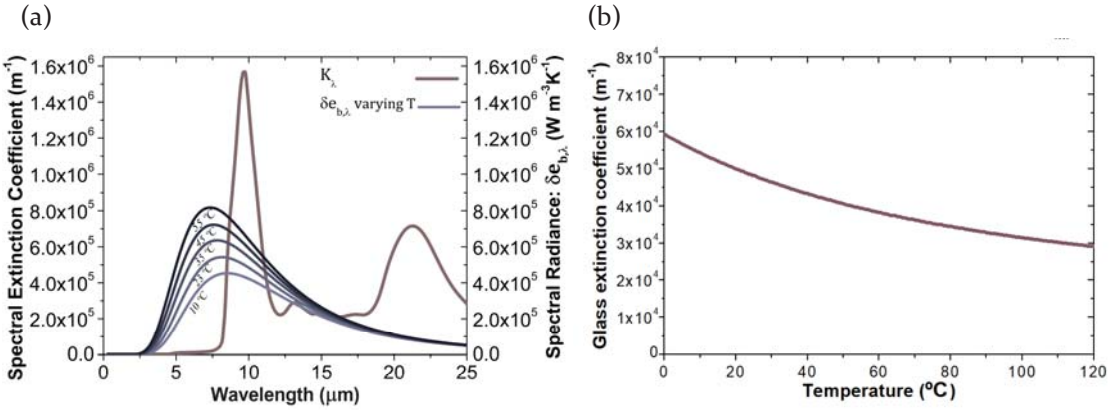

Figure 8-2-7: (a) Spectral extinction coefficient of soda–lime glass (left axis) and curves representing the spectral radiance temperature derivative at different temperatures, from bottom to top, 10, 23, 33, 43 and 55 °C (right axis), (b) soda–lime extinction coefficient as a function of temperature.

The change in glass extinction coefficient observed with increasing temperature (Figure 8-2-7 (b)) is a consequence of weighting the spectral extinction coefficient with the blackbody emission spectra. The spectral extinction coefficient through the foam remains constant with varying temperatures but as the material is heated the blackbody emission peak shifts to shorter wavelengths, where the material is more transparent to radiation. This fact translates to a reduction of K_w by a factor of two when the temperature rises from 0 to 120 °C.

Glass foams extinction coefficient

Once the optical properties of the glass matrix have been modelled, Glicksmann equation (eq. (8-2-13)) can be applied to study the foams extinction coefficient, Figure 8-2-8 (a). Thermal radiation in foams is the result of adding two independent extinction coefficients, one depicting the struts and another the walls. Logically, scattering due to the struts increases with the number of them in the foam. Additionally, the number of scattering events increases when cell size is reduced. The foams in this work present a highly heterogeneous as well as bimodal cellular structure. As described in section 3.1, the foams' porosity is due to the existence of large cells in the millimetric range and a high number of micrometric pores embedded in the solid phase. On average, it has been estimated that large cells account for more than 95% of the materials' porosity and the micrometric pores stand for less than 3% of the samples' porosity. Despite the apparent insignificance of the micrometric pores, they should not be ignored when it comes to analysing the scattering term of the extinction coefficient. In fact, it is to be expected that the existence of small

pores has a non-negligible impact on the absorption and scattering of radiation. On the one hand, as assessed in Section 3.1, internal porosity causes an unusual increase in the cell wall thickness at low densities which might in turn increase the absorption of radiation in the entirely solid regions of the skeleton. On the other hand, previous works have demonstrated that the scattering of thermal radiation is increased as cell size decreases – at least as long as cells are larger than the wavelength of the incident radiation [48]. Therefore, in order to estimate the impact of these pores we have modified Glicksmann equation (eq. (8-2-13)) by introducing the dependence of cell diameter as a combination of the millimetric and micrometric pore sizes weighted by their average porosity (eq. (8-2-17)).

$$K_{e,R} = K_s + K_{ws} = 4.10\sqrt{f_s \cdot \rho_r}\left(\frac{V_m}{\Phi_m} + \frac{V_\mu}{\Phi_\mu}\right) + (1 - f_s)\rho_r K_w \qquad (8\text{-}2\text{-}17)$$

In eq. (8-2-17) all terms have been described previously, with the exception of V_m which was calculated as the micrometric cells porosity, V_μ, subtracted from the foam's total porosity, V_g.

Despite the higher contribution of millimetric cells to the foams' porosity their considerable size (ϕ>900 μm) results in a relatively low scattering coefficient. Yet, micrometric pores produce strong scattering of infrared radiation traversing the cell walls. Thus, the solid phase micro pores are somewhat acting as radiation blockers, dispersing the radiation incident on them, and increasing the scattering inside the foam. Nonetheless, outside the low density region walls have a stronger role as radiation blockers than the struts, *i.e.* absorption in the cell walls is more critical than scattering by the cells. Only at very high porosities, when the density of struts and their mass fraction is high, their contribution will overpass that of the walls (Figure 8-2-8 (a)).

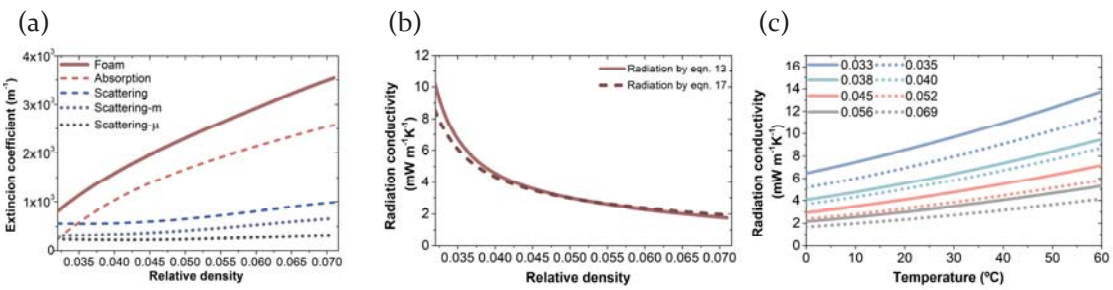

Figure 8-2-8: (a) Glicksmann extinction coefficient, $K_{e,R}$ and the corresponding absorption and scattering contributions (10 °C). (b) Radiation heat transfer calculated with eq. (8-2-13) and (8-2-17), as a function of relative density at 10 °C and (c) as a function of temperature for the foams in Table 8-2-2 (only for $K_{e,R}$).

Constr. Build. Mater. 274, 122000 (2021)

In general, radiation will have minor influence in foams where the solid fraction is high, due to the significant fraction of absorbing solid elements which will be efficiently absorbing radiation. However, when the porosity of the material is significantly raised, it becomes more transparent to radiation. Ultimately, all the data obtained of the foam's structure and the matrix's optical properties lead to a prediction of the density effect on the radiative heat transfer for glass foams, Figure 8-2-8 (b). It can be appreciated how indeed thermal conductivity due to radiation is constant and low for materials with high or medium relative density. Nonetheless, as the fraction of mass in the struts rises above 0.5, *i.e.*, at a density of 114 kg m^{-3}, the radiation term starts to increase considerably. In addition, it can be observed how the introduction of an additional scattering term (eq. (8-2-17)), accounting for the micro-porosity of the solid skeleton leads to a slowdown in the rate of thermal conductivity increase due to thermal radiation, Figure 8-2-8 (b). Moreover, the power of radiation is particularly noticeable for low density foams at high temperatures, Figure 8-2-8 (c). Not only does radiation increase with temperature following a cubic regression but also, the glass matrix extinction coefficient decreases quadratically with temperature. That is why the warmer the environment, the higher the radiation contribution is.

3.2.4. Glass foams thermal conductivity: Influence of temperature and density

Up until now, the influence of the density on each of the heat transfer mechanisms has been presented. As shown in eq. (8-2-6) the sum of all mechanisms results in the total thermal conductivity of the foam. From Figure 8-2-9 it is clear how the materials' thermal conductivity shows a nonlinear trend against density. For high density samples (above 110 kg m^{-3}) conduction through the glass phase is the main mechanism conditioning the thermal behaviour of the foams. This is due to the high amount of solid material inside the foams' skeleton. However, as the density decreases (below 100 kg m^{-3}), gas conduction has the largest impact on the foam's thermal conductivity, representing around 50% of the material's conductivity. Yet, radiation (calculated with the extinction coefficient that eq. (8-2-17) yields) has a considerable effect on the thermal conductivity of light foams accounting for almost 20%. Furthermore, the thermal conductivity plateau observed at around 100 kg m^{-3} points out to the growth of radiation heat transfer in these foams. The model predictions fit with previous observations made in thermoplastic foams, where for relative densities below a certain threshold, there is a shift in the course of thermal conductivity [16].

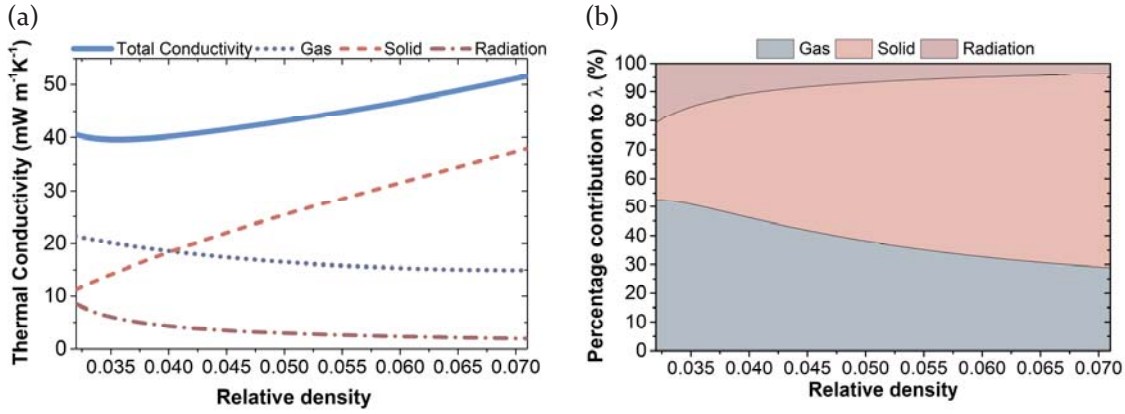

Figure8-2-9: (a) Model predicted values of λ and the impact of each heat transfer mechanism at 10 °C. (b) Relative contribution of each mechanism to the thermal conductivity at 10 °C.

As enlightening as the previous results might be, they only depict the impact of each term on the insulating capacity of the foams at a fixed temperature. However, in reality, glass foams can be employed in a variety of applications that require excellent performance regardless of the temperature conditions. As it has been mentioned previously, each heat transfer mechanism is affected differently by changes in temperature. The radiation contribution is the swiftest to grow, following a cubic increase. Conduction mechanisms grow almost linearly with temperature as it can be seen in Figure 8-2-10 (a). Yet, gas phase conductivity rises more swiftly with temperature than the solid phase conduction, since the fraction of gas inside the foam is always larger than the solid fraction. For this reason, regardless of the foam's density in conditions where the temperature is above ambient the relative contributions of gas conduction and radiation heat transfer grow, meanwhile the relative contribution of the solid matrix lessens. Therefore, in these applications minimising the effect of radiation heat transfer would be of vital importance. Figure 8-2-10 (b) also reveals how as the temperature rises the best insulation performance is achieved for higher densities foams. This result highlights that for applications in which glass foams work at elevated temperatures, it is not worth compromising other properties to reduce the relative density. Seeing that the lowest thermal conductivity plateau shifts to higher densities due to the impact of radiation.

Constr. Build. Mater. 274, 122000 (2021)

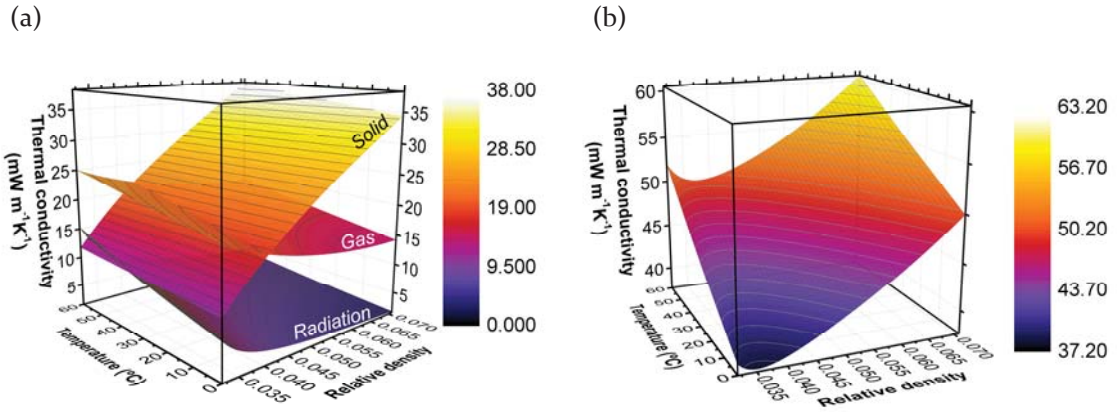

Figure 8-2-10: (a) Thermal conductivity due to every heat transfer mechanism and (b) total thermal conductivity as a function of temperature and density.

3.3. Experimental validation of the model

Figure 8-2-11 reveals that, in the range of assessed densities, the proposed model for glass foams conductivity concurs with the experimentally obtained values for the materials under study. In fact, the error is less than 2% for all temperatures and all densities. It is also remarkable how if radiation were to be ignored the model would fail to predict the experimental values (Figure 8-2-11, discontinuous lines). Moreover, in Figure 8-2-11 (dotted lines) it is possible to observe how neglecting the presence of micrometric pores in the solid matrix, when calculating the scattering extinction coefficient, results in a model that overestimates the weight of radiation heat transfer in these foams. Yet, in our model (continuous lines) there is still some deviation between the experimental and predicted values. This deviation is larger at elevated temperatures. This fact could be pointing out to a mismatch between the real extinction coefficient of CRT panel glass and the soda-lime glass that we have used to model the absorption infrared radiation. To obtain a better fitting, the predicted extinction coefficient of the panel glass should have been higher, as corresponding to a material with impurities due to its recycled nature, and its colour, dark [13] not transparent as standard window glass is. To evaluate this hypothesis some rough calculations have been performed in which the soda-lime glass extinction coefficient has been increased by around 20%, thus it has been possible to confirm that this slight increase is enough to reduce the error between experiment and model to just 0.5%.

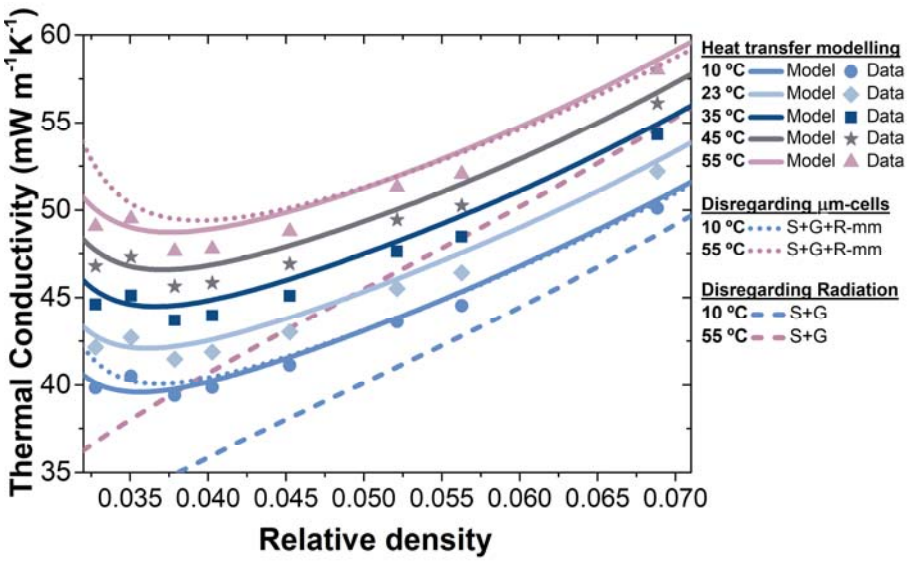

Figure 8-2-11: Experimental (scatter) and model predicted (continuous lines) values of λ at different temperatures of the foam. Model predictions without assessing the impact of micrometric cells on the extinction coefficient or without radiation heat transfer at all (discontinuous and dotted lines).

On the whole, the proposed method enables to predict the existence of a threshold density below which the thermal conductivity does not further decrease, a key point for further research in glass foams. This effect is well known in the field of low density polymeric foams but as far as the authors know this is the first time that it has been observed in glass foams. The experimental points also reveal how the thermal conductivity plateau moves to higher densities with rising temperatures due to the increasing weight of radiation as a route for thermal transport, as seen in Figure 8-2-10.

Nevertheless, there are still some open questions as to which are the main structural or compositional factors responsible for the plateau in the thermal conductivity, the model unquestionably proves that reducing the density is no longer a route to enhance insulation capacities. So, if further research is carried out, lower density foams of the same composition should be produced in order to assess whether thermal conductivity continues to grow or on the contrary it remains constant. The former would imply that the cell walls become more transparent to radiation, most likely due to the decrease in cell wall thickness around the micrometric pores, whereas the latter would indicate that scattering inside the foams is increased somehow.

Last but not least, the novelty of this model lies in the fact that previous works have only predicted linear dependences of thermal conductivity with density. Yet, this observation is only true for high density foams with porosities below 90% [35]. Therefore, models accounting merely for conduction mechanisms (Russel model, Landauer model and

Constr. Build. Mater. 274, 122000 (2021)

Schertz-Glicksmann model) would underestimate the thermal conductivity of the foams in this work as suggested by Figure 8-2-11. Moreover, here, the detailed characterisation of the gas phase and solid phase morphologies enables to obtain more accurate predictions of conduction heat transfer than those available in the current state of the art [35]. Provided that more samples were manufactured following the same production route as the one presented here the model should allow to estimate the sample's conductivity requiring virtually no change in the variables. Yet, if changes in the composition or production route were performed some information about the cellular structure descriptors would have to be provided to the model.

4. CONCLUSIONS

In this study, glass foams for insulation purposes were produced with different densities by changing the foaming temperature. The morphology and cellular structure of the foams have been analysed using SEM microscopy and X-ray tomography. All foams show irregularly shaped cells, cellular structures with bimodal distributions of cells ranging from some hundred microns to a few millimetres as well as porous glass matrix. Average cell size and content of open pores rise with increasing porosity, most probably as a consequence of cell degeneration mechanisms that cause coalescence of cells and ruptures in the cell walls. The fraction of mass in the struts increased with decreasing density, due to the thickening of struts as a result of drainage during the foaming process and the growth of the small pores embedded in the walls.

A detailed characterisation of both the solid and gas phase distribution has been essential to building a model able to predict the thermal conductivity of foams with very different densities. The gas composition was found to be a mixture of CO and CO_2 in the closed cells and, additionally, air in the open cells. The model introduces these variables and predicts lower gas phase conductivities in high-density materials due to the major content of CO_2. In contrast, gas phase conductivity is higher in low-density foams due to the higher content of CO and air.

The influence of temperature in the foams thermal conductivity was also modelled. As expected, the thermal conductivity increases with temperature. Still this increase is more substantial when the density of the material is low due to the presence of radiative heat transfer. Radiation is responsible for the lack of linearity in the measured values of thermal conductivity, where for very high porosities a plateau in the insulation capacities is reached.

Future research in these materials should explore new production routes to minimise degeneration mechanisms, increase the content of CO_2 inside the cells and reduce the radiative contribution by including IR blockers and reducing the cell size. These strategies would enable to reduce thermal conductivity due to radiation and gas conduction, which, additionally, would be extremely beneficial for applications which require good insulation at high temperatures.

5. ACKNOWLEDGEMENTS

This study has received funding from M.ERA.NET and was co-financed by ICE (Instituto para la competitividad empresarial; Castilla y León) (11/16/VA/0003), Slovenian Ministry of Higher Education, Science and Technology (C330-17-500103) and the Research and Innovation research program, Horizon 2020, (European Union). Financial support from Junta de Castilla y Leon predoctoral grant of P. Cimavilla-Román, co-financed by the European Social Fund is also acknowledged. Financial assistance from the Spanish Ministry of Science, Innovation and Universities (RTI2018-098749-B-I00) is gratefully acknowledged.

6. REFERENCES

[1] D. Eaves, Handbook of Polymer Foams, Rapra Technology Limited, Shrewsbury, 2004.

[2] L.J. Gibson, M.F. Ashby, Cellular solids: Structure and Properties, Cambridge: Cambridge Solid State Science Series, Cambridge, 1997.

[3] B. Wicklein, A. Kocjan, G. Salazar-Alvarez, F. Carosio, G. Camino, M. Antonietti, L. Bergström, Thermally insulating and fire-retardant lightweight anisotropic foams based on nanocellulose and graphene oxide, Nat. Nanotechnol. 10 (2015) 277–283.

[4] M. Santiago-Calvo, J. Tirado-Mediavilla, J.L. Ruiz-Herrero, F. Villafañe, M.Á. Rodríguez-Pérez, Long-term thermal conductivity of cyclopentane–water blown rigid polyurethane foams reinforced with different types of fillers, Polym. Int. 68 (2019) 1826–1835.

[5] C. Sainz Fernandez, L. Gutiérrez Villanueva, L.S. Quindós Poncela -, I. Fuente Merino -, RAD592-E2: Radon Diffusion coefficient in FOAMGLAS ® cellular glass thermal insulation, 2016.

[6] A.G. Ryan, S. Kolzenburg, A. Vona, M.J. Heap, J.K. Russell, S. Badger, A proxy for magmatic foams: FOAMGLAS®, a closed-cell glass insulation, J. Non-Crystalline Solids X. 1 (2019).

[7] T. Welter, R. Müller, J. Deubener, U. Marzok, S. Reinsch, Hydrogen Permeation Through Glass, Front. Mater. 6 (2020) 342. (accessed November 28, 2020).

[8] J. König, R.R. Petersen, Y. Yue, Influence of the glass – calcium carbonate mixture ' s characteristics on the foaming process and the properties of the foam glass, J. Eur. Ceram. Soc. 34 (2014) 1591–1598.

[9] Materials recovery from waste cathode ray tubes (CRTs) ICER (Industry Council for Electronic Equipment Recycling), 2004.

[10] J. König, R.R. Petersen, Y. Yue, Fabrication of highly insulating foam glass made from CRT panel glass, Ceram. Int. 41 (2015) 9793–9800.

[11] E. Bernardo, F. Albertini, Glass foams from dismantled cathode ray tubes, Ceram. Int. 32 (2006) 603–608.

[12] V. Göswein, C. Rodrigues, J.D. Silvestre, F. Freire, G. Habert, J. König, Using anticipatory life cycle assessment to enable future sustainable construction, J. Ind. Ecol. 24 (2020) 178–192.

[13] J. König, A. Lopez-Gil, P. Cimavilla-Roman, M.A. Rodriguez-Perez, R.R. Petersen, M.B. Østergaard, N. Iversen, Y. Yue, M. Spreitzer, Synthesis and properties of open- and closed-porous foamed glass with a low density, Constr. Build. Mater. 247 (2020) 118574.

[14] R.R. Petersen, J. König, Y. Yue, The mechanism of foaming and thermal conductivity of glasses foamed with MnO<inf>2</inf>, J. Non. Cryst. Solids. 425 (2015) 74–82.

[15] J. König, V. Nemanič, M. Žumer, R.R. Petersen, M.B. Østergaard, Y. Yue, D. Suvorov, Evaluation of the contributions to the effective thermal conductivity of an open-porous-type foamed glass, Constr. Build. Mater. 214 (2019) 337–343.

[16] E. Solórzano, M.A. Rodriguez-Perez, J. Lazaro, J.A. De Saja, Influence of solid phase conductivity and cellular structure on the heat transfer mechanisms of cellular materials: Diverse case studies, Adv. Eng. Mater. 11 (2009) 818–824.

[17] L.R. Glicksmann, Heat transfer in foams, in: N.C. Hilyard, A. Cunningham (Eds.), Low Density Cell. Plast., First Ed, 1994: pp. 104–152.

[18] FOAMGLAS® thermal insulation made of cellular glass, (n.d.). (accessed June 9, 2020).

[19] M.B. Østergaard, R.R. Petersen, J. König, M. Bockowski, Y. Yue, Impact of gas composition on thermal conductivity of glass foams prepared via high-pressure sintering, J. Non-Crystalline Solids X. 1 (2019).

[20] J. Pinto, E. Solorzano, M.A. Rodriguez-Perez, J.A. de Saja, Characterization of the cellular structure based on user-interactive image analysis procedures, J. Cell. Plast. 49 (2013) 555–575.

[21] S. Pérez-Tamarit, E. Solórzano, A. Hilger, I. Manke, M.A. Rodríguez-Pérez, Multi-scale tomographic analysis of polymeric foams: A detailed study of the cellular structure, Eur. Polym. J. 109 (2018) 169–178.

[22] M. V. Krishnaiah, G. Seenivasan, P. Srirama Murti, C.K. Mathews, Thermal conductivity of selected cermet materials, J. Alloys Compd. 353 (2003) 315–321.

[23] P.B. Kowalczuk, J. Drzymala, Physical meaning of the Sauter mean diameter of spherical particulate matter, Part. Sci. Technol. 34 (2016) 645–647.

[24] V. Bernardo, J. Martín-de León, E. Laguna-Gutiérrez, M.Á. Rodríguez-Pérez, PMMA-sepiolite nanocomposites as new promising materials for the production of nanocellular polymers, Eur. Polym. J. 96 (2017) 10–26.

[25] M.B. Østergaard, M. Zhang, X. Shen, R.R. Petersen, J. König, P.D. Lee, Y. Yue, B. Cai, High-speed synchrotron X-ray imaging of glass foaming and thermal conductivity simulation, Acta Mater. 189 (2020) 85–92.

[26] R. Hasanzadeh, M.M. Darvishi, T. Azdast, Synergetic effect of MWCNT/nanoclays on microcellular polystyrene hybrid nanocomposite foams, Carbon Lett. (2019).

[27] A.L. Lindsay, L.A. Bromley, Thermal Conductivity of Gas Mixtures, Ind. Eng. Chem. 42 (1950) 1508–1511.

[28] P.J. Linstrom, W.G. Mallard, eds., NIST Chemistry WebBook, NIST Standard Reference Database Number 69, n.d.

[29] J. König, R.R. Petersen, Y. Yue, D. Suvorov, Gas-releasing reactions in foam-glass formation using carbon and MnxOyas the

foaming agents, Ceram. Int. 43 (2017) 4638–4646.

[30] J. Millat, W.A. Wakeham, The Thermal Conductivity of Nitrogen and Carbon Monoxide in the Limit of Zero Density, J. Phys. Chem. Ref. Data. 18 (1989) 565–581.

[31] V. Vesovic, W.A. Wakeham, G.A. Olchowy, J. V. Sengers, J.T.R. Watson, J. Millat, The Transport Properties of Carbon Dioxide, J. Phys. Chem. Ref. Data. 19 (1990) 763–808.

[32] D. Thermodynamics Research Center, NIST Boulder Laboratories, Chris Muzny, Thermodynamics Source Database, in: NIST Chem. WebBook, NIST Stand. Ref. Database Number 69, Eds. P.J. Linstrom W.G. Mallard, Gaithersburg, MD, 20899, n.d.

[33] E.W. Lemmon, R.T. Jacobsen, Viscosity and Thermal Conductivity Equations for Nitrogen, Oxygen, Argon, and Air, 2004.

[34] C. Kittel, Interpretation of the thermal conductivity of glasses, Phys. Rev. 75 (1949) 972–974.

[35] R.R. Petersen, J. König, Y. Yue, The mechanism of foaming and thermal conductivity of glasses foamed with MnO2, J. Non. Cryst. Solids. 425 (2015) 74–82.

[36] M.B. Østergaard, R.R. Petersen, J. König, H. Johra, Y. Yue, Influence of foaming agents on solid thermal conductivity of foam glasses prepared from CRT panel glass, J. Non. Cryst. Solids. 465 (2017) 59–64.

[37] C. Huang, X. Qian, R. Yang, Thermal conductivity of polymers and polymer nanocomposites, Mater. Sci. Eng. R Reports. 132 (2018) 1–22.

[38] A.G. Leach, The thermal conductivity of foams. I: Models for heat conduction, J. Phys. D. Appl. Phys. 26 (1993) 733–739.

[39] S. Estravís, J. Tirado-Mediavilla, M. Santiago-Calvo, J.L. Ruiz-Herrero, F. Villafañe, M.A. Rodríguez-Pérez, Rigid polyurethane foams with infused nanoclays: Relationship between cellular structure and thermal conductivity, Eur. Polym. J. 80 (2016) 1–15.

[40] V.I. Primenko, Theoretical method of determining the temperature dependence of the thermal conductivity of glasses, Glas. Ceram. 37 (1980) 240–242.

[41] M.K. Choudhary, R.M. Potter, Heat Transfer in Glass-Forming Melts, in: Prop. Glas. Melts, CRC Press, Boca Raton, FL, 2005: pp. 249–293.

[42] L.D. Pye, A. Montenero, I. Joseph, Properties of Glass- Formaning Melts, First Edit, Taylor & Francis, Boca Raton, 2005.

[43] W.M. Rohsenow, J.P. Hartnett, Y.I. Cho, Handbook of Heat Transfer, 1198.

[44] J.R. Howell, Thermal Radiation Heat Transfer, 2010.

[45] R.A. Campo-Arnáiz, M.A. Rodríguez-Pérez, B. Calvo, J.A. De Saja, Extinction coefficient of polyolefin foams, J. Polym. Sci. Part B Polym. Phys. 43 (2005) 1608–1617.

[46] N. El Khiati, N. Dideron, D. Ricoult, P. LaBorde, Silica-soda-lime glass compositions and their applications, US6063718A, 1997.

[47] M. Rubin, Optical properties of soda lime silica glasses, Sol. Energy Mater. 12 (1985) 275–288.

[48] V. Bernardo, J. Martin-de Leon, J. Pinto, U. Schade, M.A. Rodriguez-Perez, On the interaction of infrared radiation and nanocellular polymers: First experimental determination of the extinction coefficient, Colloids Surfaces A Physicochem. Eng. Asp. 600 (2020).

C APT

Conclusions

CONCLUSIONS AND FUTURE WORK

9.1 CONCLUSIONS

The scientific papers presented in this thesis have allowed achieving several important conclusions relevant to the field of reactive foams and thermal insulation materials. The main conclusions of each topic are summarized in the following paragraphs:

9.1.1. Development and validation of experimental methods

About the newly developed method based on Dynamic Mechanical Analysis (DMA):

- Prior to this PhD thesis, DMA was mainly used to measure the mechanical properties of viscoelastic materials as a function of temperature or frequency as well as major polymer transitions [1]. Yet, in this thesis, we demonstrate that DMA can also be applied to measure the viscoelastic properties of curing and expanding thermosets. By employing a customised fixture, it is possible to keep a growing foam in contact with the measuring system while maintaining the foam's mass constant underneath it (Chapter 4, Section 4.2).
- DMA can also be used to determine the main stages of polymer morphology development during Polyurethane foaming (Chapter 2, Figure 2-5). The transformation of the reactive PU mixture from a liquid to a gel and from a gel into a glass material can be detected thanks to the gel and vitrification times, respectively. The gel and vitrification transformations are revealed in the DMA measurements as the crossover of the storage and loss modulus and as a shoulder in the loss modulus curve, respectively (Chapter 4, Section 4.2).
- The specificity of the DMA measuring methodology was proved using materials of different reactivity and expansion ratios. As a matter of fact, DMA could detect differences in the viscoelastic properties development of foams produced with formulations of only slightly different water and catalyst content (Chapter 4,

Section 4.2). In addition, the reproducibility of the method was studied by performing repeated experiments on the same formulations. This approach confirmed that the coefficient of variation was below 32% for the foams with low catalyst content and below 20% for the foams with a high catalyst dosage.

About the newly developed method based on Cryogenic X-ray tomography (Cryo-Tomo):

- The foaming process of RPU foams can be stopped at different reaction times by decreasing the sample temperature (Chapter 5). Sample freezing was achieved by plunging the samples into liquid nitrogen. The use of cryogenic temperatures permits freezing the internal cellular structure as well as solidifying the reacting matrix.
- A novel Cryogenic X-ray tomography set-up has been designed. The set-up comprises a pre-existing X-ray tomography system and a new cooling system. The latter permits keeping the samples at cryogenic temperatures for the duration of the X-ray tomography scan. The system cools the samples by making a flow of dry N_2 pass through liquid nitrogen and then directing this gas flow towards the sample. In addition, the dynamic generation of frost on the surface of the samples is avoided by keeping the sample inside an insulating container which is at the same time kept inside a chamber where N_2 gas at room temperature is constantly flowing.
- The analysis of the obtained Cryogenic X-ray tomographies permitted evaluating in 3D the main structural parameters of the foams: cell size, porosity or relative density, cell nucleation density and average matrix thickness.
- The specificity of the imaging approach was confirmed by studying formulations of different blowing agent (water) and catalyst concentrations.
- Cryogenic X-ray tomography experiments were performed on samples frozen at three different reactions times. The increase in the water concentration led to a 30% increase in the cell nucleation density with respect to the formulation with low water and catalyst (Reference). Being the higher concentration of CO_2 responsible for promoting the nucleation of more cells in the reactive mixture. In contrast increasing the catalyst concentration led to higher nucleation densities, from 8.7 10^5 to 1.3 10^6 cells cm^{-3}, practically 100% more than the

Reference formulation. The mechanism responsible for this increase was the faster viscosity build-up of the mixture at short reaction times.

Using the previous methods, it is possible to gain a deep understanding of reaction kinetics-rheological behaviour-structure generation relationship in standard RPU formulations prepared with different contents of water and catalyst:

- The use of complementary techniques such as DMA and FTIR Spectroscopy has permitted identifying the relationship between the modulus build-up kinetics and the speed of the chemical reactions. It was observed that a higher catalyst content implied a faster isocyanate consumption which translated into a faster modulus build-up. Moreover, faster isocyanate consumption also reduced the gelling and vitrification time of the matrix (Chapter 4).
- The cellular structure evolution was more significantly impacted by the initial viscosity of the reactive mixture and the modulus build-up speeds. X-ray radioscopy revealed that the structure of foams with low catalyst content (REF and BAF) suffered strong degeneration after the first 2-3 minutes of reaction and for nearly 14 minutes. In contrast, the cell nucleation density of foams with high catalyst content (GCF and GBF) had stabilised after 5-6 minutes of reaction. The different intensity of degeneration in the structure was motivated by the dissimilar modulus build-up profiles. The moduli of REF and BAF scarcely increase and remain below 500 Pa for the first 10 minutes of reaction. This effect together with the long gelling times (2.5 minutes) resulted in cell walls of low strength and stretching ability causing the structure to degenerate. The opposite effect was detected for foams GCF and GBF whose gelling time was below 1 minute, and the moduli rose sharply after less than 4 minutes of reaction. These mechanisms contributed to a fast crosslinking of the reactive mixture favouring the stabilisation of the cellular structure.
- The rheological behaviour and viscosity of the mixture was also responsible for the detected increase in cell nucleation density of foam GCF (high catalyst) detected with Cryogenic X-ray tomography. The early gelling and rise in viscosity (200 Pa s after 60 s of foaming, against the initial reactants viscosity, *ca.* 5 Pa s) facilitated the entrapment of air bubbles during mixing and the survival of the nucleated cells. Whereas, for foam BAF the viscosity of the mixture is low, *ca.* 20

Pa s, and the mechanism responsible for enhancing nucleation is the higher CO_2 gas released during the foam synthesis.

About the newly developed methods to characterise the solid matrix distribution in foams using low resolution X-ray tomography:

- The developed analysis methodologies permit estimating the fraction of mass in the struts of polymeric foams even when the pixel size of the imaging system is above the cell wall thickness (Chapter 6).
- The methods were found suitable for the analysis of the fraction of mass in the struts in materials of both thick and thin struts, such as RPU and XPS foams, respectively.
- The accuracy of each method and its specificity was proved by comparison with previous high resolution analysis of the fraction of mass in the struts for the same foams.

9.1.2. Applicability of the developed methodologies

The non-conventional methods to probe the synthesis and structure of RPU foams were also applied to understand the reaction kinetics-rheological behaviour-structure generation in RPU-Silica aerogel composite foams. In addition, the impact of the rheological behaviour of the initial reactants on the synthesis, final structure and properties was also evaluated.

About the rheological behaviour of the raw materials and reactive mixture during synthesis:

- The isocyanate/aerogel dispersions used to prepare the composite foams underwent a dramatic increase in their complex viscosity when moving from aerogel contents of 0 wt.% to 3 wt.%. Initially, the isocyanate was a Newtonian liquid of constant viscosity of 0.32 Pa s. Yet, the isocyanate/aerogel dispersions had a strong non-Newtonian behaviour with viscosities as high as 10^4 Pa s at low shearing frequencies and 3 wt.% aerogel content.
- The storage and loss modulus of the dispersions also point out to a transition from a liquid to gel behaviour at contents above 2.5 wt.%. This transition is the result of the generation of a percolated network of touching particles at high aerogel contents. Above this percolation threshold, the dispersion no longer exhibits liquid-like but gel-like response.

- The composite foams prepared with the isocyanate/aerogel dispersions show a modulus build-up profile which is significantly slower than that of the unfilled (Reference) foam. Foams with aerogel content below 1 wt.% see the initial increase in their complex moduli after approximately 5-10 minutes of reaction. In contrast, the moduli of foam 3% A remain practically unchanged, *ca.* 200 Pa, for the first 20 minutes of reaction.
- Vitrification times are delayed by approximately 4.5 min per 1 wt.% of aerogel added to the composite. Gelling times remain practically constant, with the exception of the foam 3% A. This material was produced with a percolated isocyanate/aerogel dispersion which was already in a gel state before polymerisation, hence no gelling of the reactive PU mixture was detected after stirring the components.

About the reaction kinetics during the synthesis of RPU-Aerogel composite foams:

- The introduction of particles modifies the normal chemical reaction balance of the RPU foam synthesis. The isocyanate consumption of the unfilled foam was increased by a 7% with the addition of 3 wt.% of aerogel particles. Conversely, the addition of a low content of aerogel particles (1 wt.%) decreased the isocyanate consumption in a 25% compared to the unfilled (Reference) foam.
- A possible rationale for this uneven change in the isocyanate consumption is the different conditioning mechanism of the reaction kinetics at different particle concentrations. At low concentration of particles, below the percolation threshold, the reaction kinetics are dominated by the increase in the viscosity of the isocyanate. In contrast, at high particle loadings when the particle interactions dominate over the polymer chains interactions the particles shape and type are the conditioning mechanism of the reaction. Hence, they act as catalyst of the reaction.
- Crosslinking density (related to the number of urethane groups) increased with the addition of 1 wt.% of aerogel particles. In contrast, the blowing reaction was enhanced for the material with a 3 wt.% of aerogel particles compared to the unfilled (Reference) foam.
- The modifications in the reaction kinetics led to changes in the foaming temperatures of the composites. It was observed that the maximum internal temperature of the composites was lower that the temperature of the unfilled

(Reference) foam. However, the faster isocyanate consumption of the foam with 3 wt.% of aerogels caused the composite to reach the maximum internal temperature faster than other foams. In addition, foam 3% A also presented higher heat dissipation speeds which are related with a higher cell opening in the structure.

About the changes in the foam formation dynamics with the addition of aerogel particles:

- The high viscosity of the isocyanate with particles causes the foam expansion to slow down particularly at low particle contents. For high particle contents, the initial foam expansion is the slowest, catching up at longer foaming times and finishing the process with a similar expansion ratio compared to the unfilled (Reference) foam. This change in foam expansion speed at high aerogel contents is motivated by a change in the reaction balance towards the blowing (urea) reaction.
- Degeneration of the cellular structure is present in all the composite foams. However, it is the most intense in foam 3% A. Of every 6 cells created only 1 survives at the end of the foaming process. From an initial cell nucleation density of 10^6 cells cm^{-3}, the final density was below 2 10^5 cells cm^{-3}
- Coalescence is the main mechanism responsible for the degeneration of the structure in these composite foams. The slow modulus build-up of foam 3% A together with the high particle content promotes cell wall ruptures while slowing the drainage of polymer mass from the walls to the struts.
- The final structure of the composite foams is the result of a combination of degeneration and enhanced nucleation. The materials with 1 wt.% of aerogel particles show a reduction in cell size from 412.5 to 290.7 μm meaning that nucleation was the predominant mechanisms. In contrast, for the foam 3% A the cell size has increased from 412.5 μm, for the unfilled foam, to 454.7 μm. In addition, the inclusion of 3 wt.% of aerogel caused cell wall ruptures which contribute to an increase in the open cell content.
- When producing large foams (mass of 387 g) their cellular structure showed symptoms of degeneration at aerogel contents lower than 3 wt.%. For a concentration of 0.5 wt.% of aerogel the average cell size had decreased in a 24% with respect to the unfilled (Reference) foam. However, at a concentration of 1

wt.% of aerogel particles the cell size had decreased only 16% with respect to the unfilled (Reference) foam. Moreover, the open cell content raised to nearly 40%.

- The structural changes in the large composite foams lead to a decrease in the thermal conductivity of 1.35 and 0.73 mW m^{-1} K^{-1} for foams 0.5% A and 1% A, respectively.
- Modelling of the heat transfer mechanisms revealed that the thermal insulation improvement for foam 0.5% A was owed to a decrease in radiative heat transfer mainly. In contrast, for foam 1% A the decrease of 0.73 mW m^{-1} K^{-1} was also due to a reduction in the polymer matrix conduction due to the presence of super insulating aerogel particles and a slight reduction in radiative heat transfer.

About the cellular structure and thermal insulation properties of recycled glass foams:

- Recycled glass foams present a characteristic structure with two distinct levels of porosity. On the one hand, the structure consists of cells in the millimetre range which represent more than 90% of the total porosity of the foam. On the other hand, the solid matrix, walls and struts, present micrometric cells of less than 50 μm in diameter.
- The average cell size of the foams increases in a liner fashion with decreasing cell size. In addition, the internal porosity of the solid matrix also rises with decreasing density, causing an increase in the fraction of material in the struts. Likewise, the content of open cells also rises with the density reduction probably due to degeneration of the structure as a consequence of the high expansion of the glass foams.
- After considering the peculiarities of the structure a model to predict the thermal conductivity was built. Such model predicts a decrease in the thermal conductivity from 50 mW m^{-1} K^{-1} to 40 mW m^{-1} K^{-1} with a reduction of 100 kg m^{-3} in density. Yet, at low densities a plateau in the thermal conductivity is reached at a value of 40 mW m^{-1} K^{-1}. Moreover, by studying the thermal conductivity at high temperatures (50 °C) an increase in the thermal conductivity with further density was detected, as well as a shift in the thermal conductivity plateau to higher densities.
- The thermal conductivity model for glass foams has been validated by comparing with experimental measurements of the thermal conductivity at different

temperatures. On average for all the samples the difference between predicted and experimental values of the thermal conductivity was below 2%.

- For the first time it has been proved that radiation heat transfer in glass foams is non-negligible. Moreover, radiation heat transfer can account for more than 20% of the thermal conductivity for foams of porosity above 96%.

9.2 FUTURE WORK

The present work is the continuation of a number of theses in CellMat devoted to investigating PU foams and developing methods to understand the foaming mechanisms. In addition, this is the first thesis to have considered the rheological behaviour as a key aspect in the synthesis of RPU foams. It is to be expected that from this work new studies can be conducted in the following topics:

Rheology of reacting PU foams:

- The rheological measurements were performed during the international research stay at KU Leuven. It would be interesting to implement the flooded parallel-plate measurement protocol at CellMat Laboratory. In such way it would be possible to investigate the impact of other formulation components and particles on the viscoelastic properties development of reactive foams.
- It is also worth trying to modify the current measuring method for performing shear rheology on reacting foams. In the current state of the art, the foam always grows over the plate and onto the shaft during the experiment [2]. This represents a setback as the modulus values obtained under this configuration are only apparent measurements. By designing a new measuring set-up, the foaming material could be evacuated to keep the material from flowing on top of the plate and affecting the measurement.
- The experimental results prove that there is a big impact of the rheology of the reactants and reactive mixture on the cellular structure development of PU foams. In this thesis, efforts have been put into simulating the cell growth in PU foams. Using other equations or models could permit to achieve a deeper understanding of the mechanisms of cell growth [3–5]. In addition, the models should be optimised to also consider degeneration mechanisms of the structure. It is also worth trying to simulate other magnitudes such as the cell wall and strut thickness.

- The shear rheology and DMA experiments have proved that it is possible to identify the main transformations during the cure of a thermoset, gelling and vitrification [6,7]. Other works have demonstrated that it is possible to measure the evolution of the glass transition temperature during cure using Differential Scanning Calorimetry (DSC) [8–10]. This approach could be followed to better understand the polymerisation of the matrix by performing experiments on non-foaming polyurethanes.

Cryogenic X-ray tomography:

- In this thesis only early reaction times have been studied using Cryogenic X-ray tomography. By investigating the foams at later reaction times, the evolution of drainage and degeneration with time could be better understood. To that end, the freezing method should be improved. The experimental research conducted during this thesis revealed that freezing was the most damaging to the internal structure of the foams when the porosity of the foams was high, and the matrix thickness was low. One possibility to improve the freezing method would be to apply a cooling ramp to the material so the freezing is not so aggressive on the material.
- In the PhD thesis of Saúl Pérez-Tamarit [11] real time synchrotron X-ray tomography was used to measure in-situ the evolution of the cellular with time for 90 s. It would be interesting to perform real time synchrotron X-ray tomography on the same materials that were studied by Cryogenic X-ray tomography in this thesis. In such way, a more precise validation of the Cryogenic X-ray tomography results could be achieved.
- The cooling system used for the Cryogenic X-ray tomography experiments could also be improved. Two important points to consider would be: improving the stability of the sample container and achieving computer control of the sample temperature [12]. On the one hand, the sample container could be a double walled cooper vessel like the one suggested by Jorgensen et al. [12,13]. In the previous set-up, cold nitrogen is conducted directly towards the vessel and the formation of frost is avoided by heating the exhaust N_2 gas. On the other hand, a Resistive Temperature Detector (RTD) within the chamber could be used to control the rate of inflow of the cold nitrogen gas and, in turn, the temperature in the sample [12].

Polyurethane-Silica aerogel composite foams:

- For the composite foams it has been detected that one of the reasons promoting degeneration of the structure were the large sized aerogel particles used to produce the foams. By employing a planetary ball mill and sieving the aerogel powder, the size of the particles could be reduced to near 1 μm or less. It is expected that this approach could minimise the degeneration effect induced by the particles and improve the thermal insulation performance of the RPU composite foams produced with the grinded aerogel powder.
- Another strategy to improve the properties of the RPU-Silica Aerogel composite foams would be modifying the current formulations to speed up the reaction kinetics and viscosity build-up to compensate the effect of high particle loadings. That is increasing the reactivity of the system 3% A to promote a quicker modulus build-up and more crosslinking of the polymer matrix which could potentially reduce the number of degeneration events.
- It is expected that a combination of the two previous points could lead to a decrease in the cell size of foams produced with a 3 wt.% of aerogel particles. This reduction of the cell size together with a high volume fraction of aerogel particles embedded in the matrix would lead to further decrease the thermal conductivity of the composite foams.

9.3 REFERENCES

[1] K.P. Menard, Dynamic Mechanical Analysis: A Practical Introduction, First Edit, CRC Press, Boca Raton, 2008.

[2] E. Mora, L.D. Artavia, C.W. Macosko, Modulus development during reactive urethane foaming, J. Rheol. 35 (1991) 921–940.

[3] P. Ferkl, I. Kršková, J. Kosek, Evolution of mass distribution in walls of rigid polyurethane foams, Chem. Eng. Sci. 176 (2018) 50–58.

[4] P. Ferkl, M. Karimi, D.L. Marchisio, J. Kosek, Multi-scale modelling of expanding polyurethane foams: Coupling macro- and bubble-scales, Chem. Eng. Sci. 148 (2016) 55–64.

[5] J. Kosek, P. Ferkl, I. Kršková, PU foams: Mathematical modelling of morphology development, in: Comput. Aided Chem. Eng., Elsevier, 2017: pp. 1009–1014.

[6] M.T. Aronhime, J.K. Gillham, Time-Temperature-Transformation (TTT) Cure Diagram of Thermosetting Polymeric Systems., Adv. Polym. Sci. 78 (1986) 83–113.

[7] P. Cimavilla-Román, M. Santiago-Calvo, M.Á. Rodríguez-Pérez, Dynamic Mechanical Analysis during polyurethane foaming: Relationship between modulus build-up and reaction kinetics, Polym. Test. 103 (2021) 107336.

[8] L.M. Chiacchiarelli, J.M. Kenny, L. Torre, Kinetic and chemorheological modeling of the vitrification effect of highly reactive

poly(urethane-isocyanurate) thermosets, Thermochim. Acta. 574 (2013) 88–97.

[9] N.C. Restrepo-Zapata, B. Eagleburger, T. Saari, T.A. Osswald, J.P. Hernández-Ortiz, Chemorheological time-temperature-transformation-viscosity diagram: Foamed EPDM rubber compound, J. Appl. Polym. Sci. 133 (2016) 43966.

[10] R.R. Rao, L.A. Mondy, K.N. Long, M.C. Celina, N. Wyatt, C.C. Roberts, M.M. Soehnel, V.E. Brunini, The kinetics of polyurethane structural foam formation: Foaming and polymerization, AIChE J. 63 (2017) 2945–2957.

[11] S. Pérez Tamarit, Structural characterization of solid cellular polymers by X-ray tomography and light scattering, University of Valladolid, 2019.

[12] S.M. Jorgensen, B. Blank, E.L. Ritman, Cryostatic micro-CT imaging of transient processes, Dev. X-Ray Tomogr. III. 4503 (2002) 140.

[13] B. Kantor, S.M. Jorgensen, P.E. Lund, M.S. Chmelik, D.A. Reyes, E.L. Ritman, Cryostatic micro-computed tomography imaging of arterial wall perfusion, Scanning. 24 (2002) 186–190.